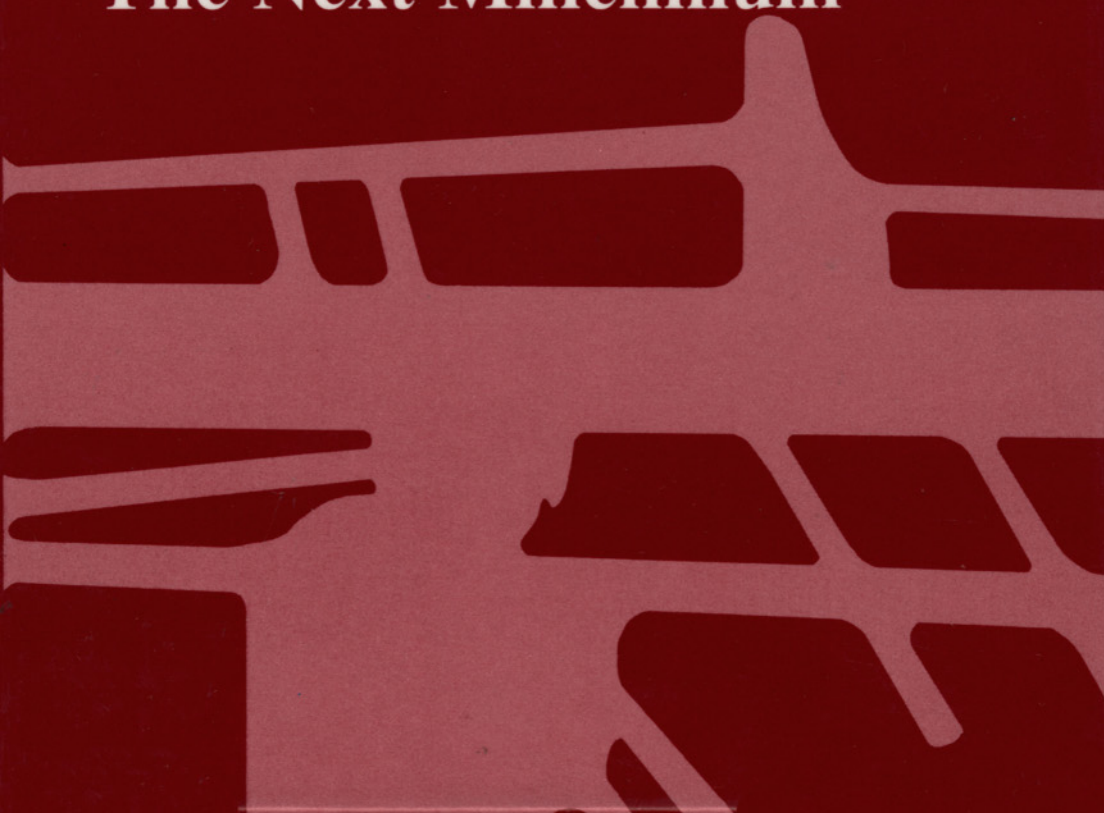


Biological Magnetic Resonance

14 Edited by
Lawrence J. Berliner

Spin Labeling The Next Millennium



Biological Magnetic Resonance
Volume 14

Spin Labeling
The Next Millennium

A Continuation Order Plan is available for this series. A continuation order will bring delivery of each new volume immediately upon publication. Volumes are billed only upon actual shipment. For further information please contact the publisher.

Biological Magnetic Resonance
Volume 14

Spin Labeling
The Next Millennium

Edited by

Lawrence J. Berliner

Ohio State University
Columbus, Ohio

KLUWER ACADEMIC PUBLISHERS
NEW YORK, BOSTON, DORDRECHT, LONDON, MOSCOW

eBook ISBN: 0-306-47072-1
Print ISBN: 0-306-45644-3

©2002 Kluwer Academic Publishers
New York, Boston, Dordrecht, London, Moscow

All rights reserved

No part of this eBook may be reproduced or transmitted in any form or by any means, electronic, mechanical, recording, or otherwise, without written consent from the Publisher

Created in the United States of America

Visit Kluwer Online at: <http://www.kluweronline.com>
and Kluwer's eBookstore at: <http://www.ebooks.kluweronline.com>

To Harden M. McConnell and Eduard G. Rozantsev

This page intentionally left blank

Contributors

R. L. Belford • Illinois EPR Research Center, Department of Chemistry, University of Illinois, Urbana, Illinois 61801

Albert M. Bobst • Department of Chemistry, University of Cincinnati, Ohio 45221-0172

R. B. Clarkson • Illinois EPR Research Center, College of Medicine and Veterinary Medicine, University of Illinois, Urbana, Illinois 61801

Jimmy B. Feix • National Biomedical ESR Center, Biophysics Research Institute, Medical College of Wisconsin, Milwaukee, Wisconsin 53226

Howard Halpern • Department of Radiation and Cellular Oncology, University of Chicago, Chicago, Illinois 60637

Marcus A. Hemminga • Department of Molecular Physics, Wageningen Agricultural University, 6703 HA Wageningen, The Netherlands

László I. Horváth • Biological Research Centre, H-6701 Szeged, Hungary

Seppo Kasa • Department of Biochemistry and Molecular Biology, University of Chicago, Chicago, Illinois 60637; *present address*: Department of Chemistry, University of Jyväskylä, SF-40500 Jyväskylä, Finland

Robert S. Keyes • Department of Chemistry, University of Cincinnati, Ohio 45221-0172

Valery V. Khrantsov • Institute of Chemical Kinetics and Combustion, Novosibirsk, Russia 630090

Candice S. Klug • National Biomedical ESR Center, Biophysics Research Institute, Medical College of Wisconsin, Milwaukee, Wisconsin 53226

Marvin W. Makinen Department of Biochemistry and Molecular Biology, University of Chicago, Chicago, Illinois 60637

Derek Marsh • Max-Planck-Institut für biophysikalische Chemie Abteilung Spektroskopie, D-37108 Göttingen Germany

Devkumar Mustafi • Department of Biochemistry and Molecular Biology, University of Chicago, Chicago, Illinois 60637

Tibor Páli • Biological Research Center, Institute of Biophysics, H-6701 Szeged, Hungary

M. B. Sankaram • DepoTech Corporation, San Diego, California 92121

Karl Shorn • Max-Planck-Institut für biophysikalische Chemie Abteilung Spektroskopie, D-37108 Göttingen, Germany

Alex I. Smirnov • Illinois EPR Research Center, College of Medicine, University of Illinois, Urbana, Illinois 61801

Harold M. Swartz • Department of Radiology, HB7785, Dartmouth Medical School, Hanover, New Hampshire 03755-3863

Ivon J. van den Dries • Department of Molecular Physics, Wageningen Agricultural University, 6703 HA Wageningen, The Netherlands

Leonid B. Volodarsky • Institute of Organic Chemistry, Novosibirsk, Russia 630090

Preface

We present here the second issue devoted entirely to the spin-labeling technique as part of *Biological Magnetic Resonance*. Volume 14 commemorates a modification in our editorial policy with the retirement of my esteemed coeditor, Jacques Reuben. From this juncture into the future, each issue will focus on some special topic in magnetic resonance. Each volume will be organized in most cases by guest editors, for example forthcoming issues will address the following topics:

^{13}C *in vivo* magnetic resonance (P. Robitaille and L. J. Berliner, eds.)

Modern techniques in proton NMR of proteins (R. Krishna and L. J. Berliner, eds.)

Instrumental techniques of EPR (C. Bender and L. J. Berliner, eds.)

The current volume, *Spin Labeling: The Next Millennium*, presents an excellent collection of techniques and applications that evolved during the past decade since the last volume, volume 8 (1989). Some obvious omissions, such as multi-quantum EPR and very high-frequency FT-ESR were unfortunately not possible for this volume. Perhaps they will appear in *Spin Labeling: 2001*.

Lastly it is a pleasure to honor two scientists whose contributions were both pioneering and pivotal to the spin label technique: Professor Eduard G. Rozantsev (Moscow), whose synthetic feats in nitroxyl chemistry set the broad stage for a versatile catalog of labels; and Professor Harden M. McConnell, last year's International ESR (EPR) Society Gold Medalist, who conceived and developed the spin label technique to address many biological problems (proteins, enzymes, membranes, cells, immune response, etc.).

Lawrence J. Berliner
Columbus, Ohio

This page intentionally left blank

Contents

Introduction: Reflections on the Beginning of the Spin Labeling Technique

Lawrence J. Berliner

Chapter 1

Analysis of Spin Label Line Shapes with Novel Inhomogeneous Broadening from Different Component Widths: Application to Spatially Disconnected Domains in Membranes

M. B. Sankaram and Derek Marsh

1.	Introduction	5
1.1.	Inhomogeneous Broadening Due to Unresolved Hyperfine Structure	6
1.2.	Inhomogeneous Broadening Due to Different Component Widths	8
2.	Theory	8
2.1.	Sum of Two Spectra with Different Widths	9
2.2.	Statistical Distribution of Spin Labels	11
2.3.	Methods to Determine the Existence of a Statistical Distribution of Spin Labels	13
2.4.	Experimental Considerations	16
3.	Applications	16
3.1.	Domain Structure in a Two-Component, Two-Phase Lipid Bilayer System	16
3.2.	Effect of a Peptide on Domain Structure	21
4.	Conclusions	21
	<i>References</i>	21

Chapter 2

Progressive Saturation and Saturation Transfer EPR for Measuring Exchange Processes and Proximity Relations in Membranes*Derek Marsh, Tibor Páli, and László I. Horváth*

1. Introduction	23
1.1. Continuous Wave Saturation	25
1.2. Effective Spin Lattice Relaxation Times	26
2. Contributions to Intrinsic Spin-Lattice Relaxation Rates	28
2.1. Electron Relaxation Mechanisms	28
2.2. Nuclear Relaxation Mechanisms	35
3. Paramagnetic Relaxation Enhancement	37
3.1. Paramagnetic Enhancement by Heisenberg Exchange	38
3.2. Paramagnetic Enhancement by Magnetic Dipole-Dipole Interactions	40
4. Spin Lattice Relaxation Enhancement by Exchange Processes	42
4.1. Two-Site Exchange	44
4.2. Heisenberg Spin Exchange	47
5. Continuous Wave Saturation Measurements	52
5.1. Progressive Saturation EPR	52
5.2. Saturation Transfer EPR	56
6. Applications	58
6.1. Two-Site Lipid Exchange and Lipid-Protein Interactions	59
6.2. Lipid and Protein Collision Frequencies: Translational Diffusion	63
6.3. Spin Label Location and Accessibility: Paramagnetic Relaxation	69
6.4. Distance Measurements: Dipolar Relaxation	72
6.5. Slow Rotational Diffusion and Saturation Studies	77
7. Conclusions	79
<i>References</i>	80

Chapter 3

Comparative Spin Label Spectra at X-Band and W-band*Alex I. Smirnov, R. L. Belford, and R. B. Clarkson*

1. Introduction	83
2. Comparative X- and W-Band EPR Spectra of Spin Labels in Isotropic Liquids	84
2.1. Solution of Perdeuterated Tempone in Toluene	85

2.2. Solution of 3-Doxyl-17 β -Hydroxy-5 α -Androstane in O-xylene	88
2.3. Resolution Enhancement in High Magnetic Fields: Mixtures of Phenyl- <i>tert</i> -butylnitron Spin Adducts	90
3. Sample Deoxygenation in CW HF EPR Experiments	93
4. Comparative X- and W-Band EPR Spectra of Spin-Labeled Phospholipids and Proteins	95
4.1. Small Spin Labels in Phospholipid Membranes	95
4.2. Doxyl Stearic Acid Labels in Phospholipid Membranes	97
4.3. Binding Spin-Labeled Fatty Acids to Bovine Serum Albumin	100
4.4. Spin-Labeled Proteins: Immobilized Labels	102
4.5. Spin-Labeled Proteins: Mobile Labels	104
<i>References</i>	106

Chapter 4

Use of Imidazoline Nitroxides in Studies of Chemical Reactions: ESR Measurements of the Concentration and Reactivity of Protons, Thiols, and Nitric Oxide

Valery V. Khramtsov and Leonid B. Volodarsky

1. Introduction	109
2. Stable Nitroxides in Proton Exchange Reactions	110
2.1. Theoretical Considerations	110
2.2. Effect of pH on ESR Spectra of Stable Nitroxides	112
2.3. pH-Sensitive Nitroxides in Studies of Proton Exchange Reactions	125
2.4. ESR Measurements of the Local Concentration of Protons	130
2.5. ESR Studies of Proton-Related Transport Processes	135
2.6. pH-Sensitive Spin Labels in Studies of Peptides, Proteins, and Biomembranes	140
3. Disulfide Biradicals in the Thiol-Disulfide Exchange	149
3.1. Physicochemical Backgrounds	149
3.2. Quantitatively Determining Thiol Groups in Biological Systems	155
3.3. ESR Studies of Thiol-Related Processes	157
3.4. Spin Labeling SH Groups in Proteins	159
4. Reactions of Nitronyl Nitroxides with Nitric Oxide	161
4.1. Trapping Nitric Oxide by Nitronyl Nitroxides: Physicochemical Studies	162

4.2. ESR Detection of Nitric Oxide in Chemical and Biological Systems	168
4.3. Antagonistic Action of NNR against Nitric Oxide	172
5. Conclusions	174
<i>References</i>	176

Chapter 5

ENDOR of Spin Labels for Structure Determination: From Small Molecules to Enzyme Reaction Intermediates

Marvin W. Makinen, Devkumar Mustafi, and Seppo Kasa

1. Introduction	181
2. EPR and ENDOR Spectroscopy of Nitroxyl Spin Labels	183
2.1. EPR of Nitroxyl Spin Labels	183
2.2. Basis of ENDOR	187
2.3. ENDOR of Nitroxyl Spin Labels	190
2.4. TRIPLE Spectroscopy of Nitroxyl Spin Labels	201
3. X-ray Structure and Conformation of Nitroxyl Spin Labels	203
3.1. Molecular Structure of Nitroxyl Spin Labels	203
3.2. Molecular Modeling of Nitroxyl Spin Labels	206
4. Structure and Conformation of Spin-Labeled Molecules by ENDOR	211
4.1. Spin-Labeled Amino Acids	211
4.2. Other Spin Label Derivatives	225
5. Intermediates of Enzyme-Catalyzed Reactions	229
5.1. Methods of Stabilizing Reaction Intermediates	229
5.2. Structural Characterization of True Intermediates of Enzyme-Catalyzed Reactions by ENDOR	231
6. Future Directions	240
6.1. Enhanced Resolution of ENDOR Spectra	240
6.2. Enzyme Reaction Intermediates	242
6.3. Spin-Labeled Proteins for ENDOR	244
<i>References</i>	245

Chapter 6

Site-Directed Spin Labeling of Membrane Proteins and Peptide-Membrane Interactions

Jimmy B. Feix and Candice S. Klug

1. Introduction	251
---------------------------	-----

2.	The SDSL Paradigm	252
2.1.	Spin Labeling Cysteine	253
2.2.	Spin Label Motion in SDSL	253
2.3.	CW Saturation in SDSL	255
3.	SDSL of Membrane Proteins	259
3.1.	Structure–Function Studies of α - Helical Membrane Proteins	259
3.2.	SDSL of the Ferric Enterobactin Receptor FepA	265
3.3.	Metal-Nitroxide Distance Measurements	271
4.	SDSL Studies of Peptide-Membrane Interactions	273
4.1.	Diphtheria Toxin	273
4.2.	Cecropins	274
4.3.	Alamethicin	276
4.4.	Influenza Virus Hemagglutinin	276
4.5.	Melittin	277
5.	Conclusion	278
	<i>References</i>	279

Chapter 7

Spin-Labeled Nucleic Acids

Robert S. Keyes and Albert M. Bobst

1.	Introduction	283
2.	Syntheses of Spin-Labeled Nucleic Acids	288
2.1.	Chemical Oligonucleotide Synthesis	288
2.2.	Enzymatic Incorporation of Spin-Labeled Substrates	292
2.3.	Spin Labeling Oligonucleotides by Spin Trapping	295
3.	Characterization of Spin-Labeled Nucleic Acids	297
3.1.	Free Spin Test	297
3.2.	EPR-Specific Activity of Spin-Labeled Nucleic Acids	298
3.3.	Influence of Spin Label on Native Nucleic Acid Duplex Conformation	301
3.4.	Evaluation of Spin-Label Rigid-Limit Tensors	302
4.	Motional Analysis of Spin-Labeled Nucleic Acids	304
4.1.	Theoretical Approaches to Modeling Nucleic Acid Dynamics	304
4.2.	Spin-Labeled Nucleic Acid Dynamics Detected by EPR	306
5.	Biological Applications of Spin-Labeled Nucleic Acids	319
5.1.	Spin-Labeled Nucleic Acids As Monitors in Biological Studies	319
5.2.	Spin-Labeled Hybridization Probes	320
5.3.	Detecting Local Z-DNA Conformations	323

5.4.	Detecting Local DNA Bending	325
5.5.	Relative Binding Affinities of Single-Strand Nucleic Acid Binding Proteins	327
5.6.	Monitoring the Dynamics of <i>EcoRI</i> Endonuclease and Homeodomain Protein Spin-Labeled Oligonucleotide Complexes	329
6.	Conclusions	334
	<i>References</i>	334

Chapter 8

Spin Label Applications to Food Science

Marcus A. Hemminga and Ivon J. van den Dries

1.	Introduction	339
2.	Spin Labels	340
3.	Analysis of ESR and ST-ESR Spectra	341
4.	Molecular Motion in Liquid Samples	344
4.1.	Glycerol Water Systems	345
4.2.	Sucrose Water Systems	347
5.	Molecular Mobility in Sugar Water Glasses	348
5.1.	Glassy State	349
5.2.	Sugar Water Systems	349
5.3.	Molecular Mobility in Maltooligosaccharide Water Glasses	351
5.4.	Glucose Water Systems	354
5.5.	Commercial Maltodextrin	355
5.6.	Activation Energy for Molecular Reorientation	356
6.	Gluten Systems	356
6.1.	ESR Spectra	357
6.2.	ST-ESR Spectra	358
7.	Conclusions	359
	Appendix: Calibration Procedure for ST-ESR Spectra	361
	Calibration of ST-ESR Spectra	361
	Notes	365
	<i>References</i>	365

Chapter 9

EPR Studies of Living Animals and Related Model Systems (*In Vivo* EPR)

Harold M. Swartz and Howard Halpern

1.	Introduction	367
----	------------------------	-----

2. Rationale for Developing and Using <i>in Vivo</i> EPR	368
3. Imaging and Spectroscopy	370
4. Potential Constraints on <i>in Vivo</i> EPR	371
4.1. Nonresonant Absorption of the Exciting Frequency (Usually Microwaves)	372
4.2. Concentration of Paramagnetic Species	372
4.3. Bioreduction	373
4.4. Excretion	374
4.5. Physiological Motions	374
4.6. Accurate Localization of Paramagnetic Materials	374
4.7. Penetration of Microwaves	374
5. Sensitivity Considerations for <i>in Vivo</i> EPR	375
5.1. Concentrations of Naturally Occurring Free Radicals and Other Paramagnetic Materials <i>in Vivo</i>	375
5.2. Sensitivity of <i>in Vivo</i> EPR Spectrometers	375
6. Results of <i>in Vivo</i> EPR Spectroscopy of Functional Biological Systems	376
6.1. Initial Studies	376
6.2. Types of Studies with <i>in Vivo</i> EPR Spectroscopy	377
6.3. Specific Results Obtained with <i>in Vivo</i> EPR Spectroscopy	378
7. Results of <i>in Vivo</i> EPR Imaging of Functional Biological Systems	390
7.1. Imaging Studies of Pharmacokinetics of Nitroxides	391
7.2. Imaging Studies of Tumors and Tumor Oxygenation	393
7.3. Imaging of Diffusion in Skin and Related Systems	393
7.4. Imaging Studies of the Concentration of Nitric Oxide	394
7.5. Imaging Studies at the Microscopic Level	394
7.6. Use of Gated and Pulsed Methods to Obtaining Images	394
7.7. Using of Pulsed Methods in <i>In Vivo</i> EPR	395
7.8. Review of Spectral Spatial-Imaging Studies	395
7.9. Issues in EPR Imaging	396
8. Summary and Conclusions	397
References	397

Appendix

Derek Marsh and Karl Schorn

References	409
----------------------	-----

Contents of Previous Volume in Series	411
--	------------

Index	415
------------------------	------------

This page intentionally left blank

Biological Magnetic Resonance

Volume 14

Spin Labeling

The Next Millennium

This page intentionally left blank

Introduction

Reflections on the Beginning of the Spin Labeling Technique

Lawrence J. Berliner

This volume is dedicated to the two pioneers who contributed seminally to the beginnings of the spin label technique, Eduard G. Rozantsev, who developed a broad range of nitroxyl compounds and reagents; and Harden M. McConnell, whose foresight into the areas of biological structure and function brought the world the broad leadership that guided this technique to where it is today.

As Harden McConnell's first graduate student assigned to spin labeling, I take great pride in reflecting on the early days and subsequent development of the technique from the early- to mid-60s when it first began. McConnell's lab was located in the Physical Chemistry Laboratories of the Department of Chemistry at Stanford University, where his research to that point had been heavily involved in areas of chemical physics, solid-state physics, and theoretical aspects of spin physics. Rozantsev's lab, then at the Institute of Chemical Physics, USSR Academy of Sciences, Moscow, was publishing extensively on the chemistry, synthesis and physical chemistry of several nitroxyl compounds (coined iminoxyl at the time); this research was published mainly in Russian academy journals. Since it was difficult to obtain samples from Moscow at that time, a major synthetic effort was launched in the McConnell lab to reproduce compounds synthesized in the Rozantsev

lab and to develop analogues of protein modification reagents. In fact early during this period, the first *in vivo* related experiment was done in the McConnell lab to assess toxicity of nitroxyl compounds to cells or living systems. Several grams of di-*t*-butyl nitroxide were dissolved in an aquarium where a goldfish swam. The goldfish survived the nitroxyl environment, but when someone allowed hot water to drip slowly into the aquarium, the animal died either from heat exposure or by falling out of the aquarium when the water level reached the top and overflowed into the sink! Another effort involved analyzing EPR lineshape and motional characteristics of the tumbling nitroxyl group. The first paper (Stone *et al.*, 1965) reflected the effort of three postdoctorates, two of whom were trained as organic chemists; the latter two authors (including McConnell) were experts in lineshape analysis. The major efforts in the McConnell laboratory from 1966–67 focused predominantly on protein and enzyme problems. There was another massive effort by a team of postdoctorates who attempted to apply, in a blanket fashion, a new maleimide spin label to a variety of enzymes and proteins (Griffith and McConnell, 1966).

The common attributes of McConnell and Rozantsev is that they were great scientists, interested purely in the joy of pursuing important fundamental problems (instead of what was currently politically in favor.) To the best of my knowledge, McConnell's conception of the spin-labeling technique was based heavily on the pioneering fluorescence work of Gregorio Weber (University of Illinois), who studied fluorescence depolarization, and other steady-state techniques with extrinsic fluorophores introduced into specific sites in proteins and enzymes. At the same time Stanford hired Lubert Stryer in the medical school (Department of Biochemistry), who was a consultant in protein structure/function. Nonetheless, it is fair to say that most of the driving force, motivation, and discovery came from within the McConnell group through the foresight and leadership of its mentor. This of course led to the applications of spin labeling in several other areas of biochemistry and medicine: lipids and membranes, cellular machinery (such as the complement system), studies of diffusion phenomena within lipid bilayers. Most recently there were impressive *in vivo* applications in animals, as outlined in the chapter by Swartz and Halpern. McConnell also applied nitroxyl groups as paramagnetic relaxation agents to probe protein structure by NMR. This was elegantly described in volume 8 of this series by Anglister (in Berliner and Reuben, 1989). McConnell was literally the father, grandfather, and great-grandfather of spin labeling. Rarely a publication on the subject does not cite at least one or two of his fundamental papers. It is certainly an honor and a tribute to recognize his contributions in this book.

Eduard Rozantsev was a prolific chemist who was also well-versed in physical chemistry and biochemistry as well. Under the tutelage of M. B. Neiman at the Institute of Chemical Physics, he grew to be an international giant in this field, collaborating frequently with other physical and biophysical chemists at the Institute on applications of nitroxyl compounds, some modeled after McConnell's early articles. Unfortunately during Soviet times the Institute of Chemical Physics was

not always headed by extremely benevolent directors. For reasons (all of which are not totally known to me) Rozantsev fell into disfavor with Director V. Buchachenko, who banished him from the Institute in the later 1970s. Rozantsev took a position in the Institute for Applied Biotechnology in Moscow, where he continued a research and teaching program, albeit much smaller than that at the Institute of Chemical Physics. During the time period of Buchachenko's reign, Rozantsev was frequently denied travel; for example he did not attend the First International Symposium on Nitroxyl Compounds in Pečs, Hungary nor the Second International Symposium in Novosibirsk in 1989. Nonetheless this editor had the pleasure and honor of meeting him twice in Moscow, once in 1981 on a National Academy of Sciences exchange visit to the Shemyakin Institute of Organic Chemistry, where we were allowed to have a private meeting. This was shortly after Rozantsev and Renat Zhdanov undertook the massive effort of translating the first volume of *Spin Labeling: Theory and Applications* (Berliner, 1976) into Russian (Rozantsev, 1979) for Mir Press. The second visit was in 1994 when I met him and one of his postdoctoral students (an excellent physical chemist who carried on the tradition of high-quality organic synthesis, characterization, and new insights into novel structures as a result of Rozantsev's excellent mentoring). Rozantsev was also a true giant in his field. His book, *Free Nitroxyl Radicals* (Rozantsev, 1970) still serves as a useful guide. In fact, it is noteworthy that we continue the tradition in every spin-labeling volume of including a complete chapter on new aspects of organic synthesis of nitroxyl compounds, each containing detailed methods and materials sections enabling a chemist to carry out synthesis without referring to the original publication.

The spin-labeling field blossoms even more as we head into the next millennium. As exemplified by the chapters here, it has been applied to systems in food chemistry, nucleic acid and nucleotide biochemistry, to cell applications, *in vivo* applications with small animals, and most recently as a tool for specifically incorporating spin labels at unique amino acid residue positions in mutated proteins. As described in other chapters, new instrumental advances combined with other techniques, such as NMR (ENDOR), allow us to probe detailed motional and structural characteristics, especially at very high frequencies (e.g., 95 GHz). No doubt there are many other techniques yet to come. In conclusion, speaking for the other authors as well, we hope that the subject matter in this volume and continuing contributions from the two honored scientists and their research groups inspire into even more applications and techniques in the millennium to come!

REFERENCES

- Berliner, L. J., 1976, *Spin Labeling: Theory and Applications* (Academic, New York).
Berliner, L. J., and Reuben, J., 1989, *Spin Labeling: Theory and Applications Biological Magnetic Resonance*, vol. 8 (Plenum, New York).
Griffith, O. H., and McConnell, H. M., 1966, *Proc. National Academy of Sciences, U.S.* **55**:8.

Rozantsev, E. G., 1970, *Free Nitroxyl Radicals* (Plenum, New York).

Rozantsev, E. G., 1979, trans., *Spin Labeling: Theory and Applications* (Mir, Moscow).

Stone T. J., Buckman, T., Nordio, P. L., and McConnell, H. M., 1965, *Proc. National Academy of Sciences*, U.S. **54**:1010.

Analysis of Spin Label Line Shapes with Novel Inhomogeneous Broadening from Different Component Widths Application to Spatially Disconnected Domains in Membranes

M. B. Sankaram and Derek Marsh

1. INTRODUCTION

Electron spin resonance (ESR) line shapes of nitroxide spin labels for axially symmetric or isotropic systems are usually Lorentzian or Voigt in nature (see, e.g., Bales, 1989). The Lorentzian line width of spin label ESR spectra is increased by such dynamic effects as molecular rotation, molecular diffusion, or spin exchange. For free radicals in solution, spin-spin relaxation determines the intrinsic line width of the Lorentzian line shape. When static dipolar interactions are averaged out, e.g., by lateral diffusion in the plane of a lipid bilayer membrane, line shapes are usually Lorentzian or Voigt. The pure Lorentzian shape arises at high concentration as a result of a homogeneous spin-spin exchange interaction, whereas the Voigt shape occurs at low spin concentrations, and it is due to inhomogeneous broadening from

M. B. Sankaram • DepoTech Corporation, San Diego, CA 92121 and **Derek Marsh** • Max-Planck-Institut für biophysikalische Chemie, Abteilung Spektroskopie, D-37108 Göttingen, Germany.

Biological Magnetic Resonance, Volume 14: Spin Labeling: The Next Millennium, edited by Berliner. Plenum Press, New York, 1998.

unresolved hyperfine structure. Another less common form of inhomogeneous broadening arises from unresolved lines of different widths. This gives rise to line shapes differing from those for conventional inhomogeneous broadening, and these are the subject of this chapter.

1.1. Inhomogeneous Broadening Due to Unresolved Hyperfine Structure

For nitroxide spin labels, the unresolved hyperfine structure arises from the interaction of the electron spin with neighboring nuclei. As a result of the interaction

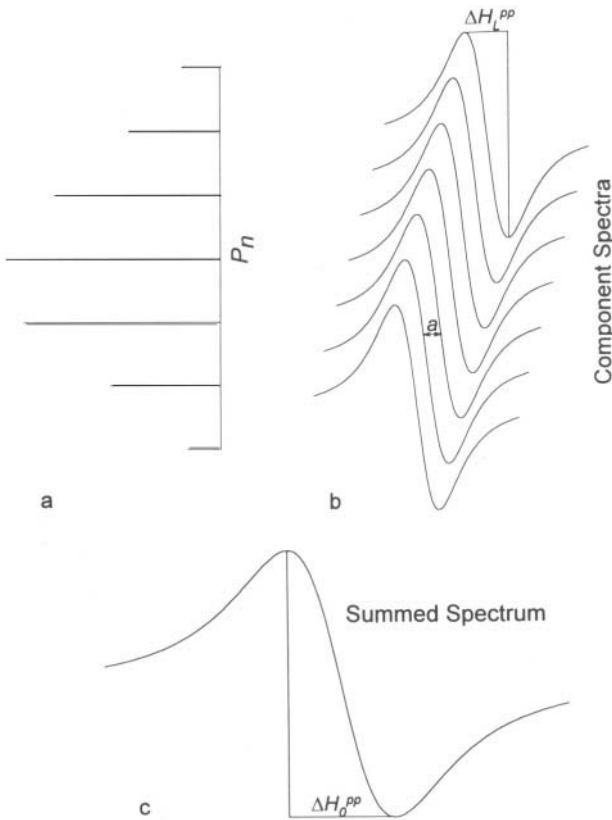


Figure 1. Illustration of inhomogeneous broadening of a Lorentzian line by proton hyperfine interaction. (a) The electron spin is coupled to six equivalent protons resulting in a hyperfine splitting into seven component lines whose intensities are determined by the binomial probability distribution function denoted by the stick plot. (b) The hyperfine coupling constant is given by a , the peak-to-peak line width of the original unsplit Lorentzian line from the electron spin is ΔH_L^{pp} ; and (c) the peak-to-peak line width of the unresolved composite envelope is ΔH_0^{pp} .

of the protons with the electron spin on the nitroxide, the otherwise single Lorentzian line is split into a number of Lorentzians. The hyperfine-split lines remain unresolved when the proton hyperfine coupling constant is small. Consequently the ESR spectrum of a nitroxide spin label is normally broadened by the proton hyperfine interaction. As shown in Fig. 1, the experimental spectrum may be understood as a superposition of spectra of the same line width but centered at different magnetic field strengths. For equivalent protons, the relative intensities of the hyperfine lines are distributed binomially. In practice the intensity distribution is usually well-represented by a Gaussian, and the resulting line shape is Voigt in nature (Bales, 1989).

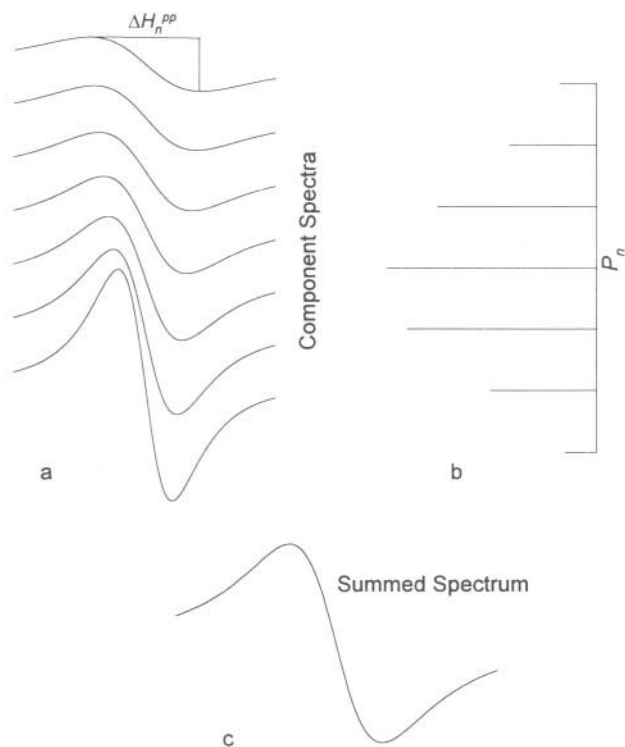


Figure 2. Illustration of inhomogeneous broadening of an ESR line arising from different component widths. (a) Individual ESR lines can be Lorentzian, Gaussian, or Voigt in shape. The component lines differ in peak-to-peak line width (ΔH_n^{pp}) depending on spin label concentration (n), and (b) relative intensities of the component lines are given by the Poisson probability distribution denoted by the stick plot. (c) The summed spectrum is an unresolved line, whose line shape can be distinguished from that of the component lines by the intensity ratio.

1.2. Inhomogeneous Broadening Due to Different Component Widths

Spectral broadening also arises when spectra centered at the same magnetic field strength but of different widths are superimposed (Fig. 2). This type of inhomogeneous broadening applies to systems in which nitroxide spin labels are spatially distributed. In general the resulting line shape is neither Gaussian, Lorentzian, nor Voigt in nature, and it can be distinguished from these. Domain structure in lipid monolayers formed at the air-water interface, and the reticulated domain structure of one- and two-component lipid bilayer systems are good examples of where this different type of inhomogeneous line shape is applicable.

If a nitroxide spin label is statistically distributed in a spatially disconnected system, the experimental ESR spectrum can be described as a superposition of spectra of the individual domains, weighted in the line width by the concentration of the label in the domain and in intensity by the probability that a domain contains that concentration of the label. In the following sections, this novel kind of inhomogeneity is developed theoretically, and examples from lipid binary mixtures and the effect of peptide incorporation on domain structure are discussed.

2. THEORY

Inhomogeneous broadening arising from a statistical distribution of labels among domains can be distinguished from other forms of spectral broadening (both homogeneous and inhomogeneous) by the diagnostic line shape intensity ratio R , which was introduced by Bales (1989) for analyzing conventional inhomogeneous broadening. The intensity ratio is defined as:

$$R = \frac{V'}{2V^{pp}} \quad (1)$$

where V^{pp} is the peak-to-peak amplitude of the first derivative ESR display; $V'/2$ is the height above the baseline at the diagnostic position in the spectral wings, which is defined to be $\pm 1.32\Delta H^{pp}$ distant from the central resonance position, where ΔH^{pp} is the peak-to-peak line width (see Fig. 3). This intensity ratio is a property only of the line shape, and it is independent of the magnitude of the spectral broadening. For a Lorentzian line, it has a value of $R^L = 0.2125$; for a Gaussian line, a value of $R^G = 0.067$. Voigt line shapes have intermediate values of R depending on the degree of Gaussian broadening arising from unresolved proton hyperfine structure. A method for determining the Gaussian broadening of a Voigt line from R is described by Bales (1982, 1989).

Intensity Ratio, $R = V/2V^{pp}$

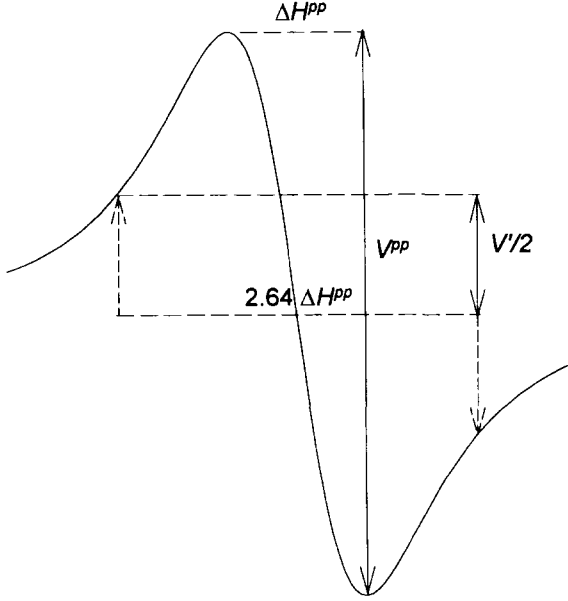


Figure 3. Definition of the internally normalized intensity ratio R .

2.1. Sum of Two Spectra with Different Widths

The simple case of adding two Lorentzians of different peak-to-peak line widths in different proportions illustrates that the intensity ratio is a valuable experimental measure for distinguishing homogeneous broadening and conventional inhomogeneous broadening due to hyperfine interaction from inhomogeneous broadening due to different widths. The amplitude of the summed spectrum is given by:

$$V = x \frac{8\sqrt{3}}{\pi(\Delta H_1^{pp})^2} \frac{\xi_1}{[3 + \xi_1^2]^2} + (1-x) \frac{8\sqrt{3}}{\pi(\Delta H_2^{pp})^2} \frac{\xi_2}{[3 + \xi_2^2]^2} \quad (2)$$

$$\xi_i = \frac{2(H - H_0)}{\Delta H_i^{pp}} \quad (3)$$

where x is the area fraction of the spectrum with peak-to-peak line width ΔH_1^{pp} , $(1-x)$ is the area fraction of the spectrum with peak-to-peak line width ΔH_2^{pp} , and both are centered at resonance position H_0 .

Figure 4 shows the effect on the intensity ratio of superpositioning two Lorentzians, as determined by computer simulations. When the fractional difference in line width between the two Lorentzians, i.e., $(\Delta H_2^{pp} - \Delta H_1^{pp})/\Delta H_1^{pp}$ is greater than 0.6, the summed spectrum remains two-component in nature. At lower values, summed spectra have an apparent single-component line shape for which R changes both with the fractional difference in line width and with the proportion of one spectrum to the other. The significant result is that the intensity ratio of the composite line shape is greater than the maximum that can be attained with conventional inhomogeneous broadening from unresolved hyperfine structure, which is given by $R^L=0.2125$. Intensity ratios greater than R^L are therefore diagnostic for inhomogeneous broadening arising from different component widths. When the fractional difference in line width is less than 0.1, R does not

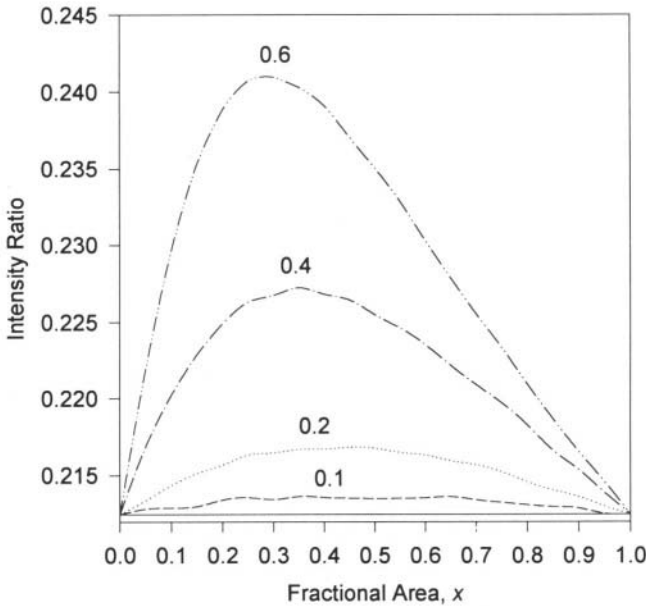


Figure 4. Dependence of the intensity ratio of the summed spectrum on the fractional area x when two Lorentzians of different peak-to-peak line width ΔH_1^{pp} and ΔH_2^{pp} are summed. The value of x is the fractional area of the spectrum with peak-to-peak line width ΔH_1^{pp} , and $(1-x)$ is the fractional area of the other spectrum. The fractional difference in peak-to-peak line width $(\Delta H_1^{pp} - \Delta H_2^{pp})/\Delta H_1^{pp}$ (from top to bottom) is 0.6, 0.4, 0.2, and 0.1. The horizontal solid line is the intensity ratio of the component Lorentzians, namely, $R^L = 0.2125$.

change significantly from its single-component value, which in this case is R^L . This is true irrespective of whether either or both two-component spectra are Lorentzian, Gaussian, or Voigt in shape.

2.2. Statistical Distribution of Spin Labels

In most practical applications, spin labels are not distributed just between two domains, but among several as previously described. In this case, a distinction is made between the number of host molecules that make up a domain l , the number of spin labels n in the domain of size l and the *average* number of host molecules *per* domain L , and the *average* number of spin labels *per* domain N .

When spin labels are statistically distributed among such domains, the experimental spectrum is calculated by simulating spectra from each domain and summing them by appropriate weighting. If the number of domains is N_{dom} and the total number of spin labels is $N_t (= N \cdot N_{dom})$, the probability P_n of finding n spin labels in a domain is given by a binomial distribution function:

$$P_n = \frac{N_t!}{n!(N_t - n)!} \left[\frac{1}{N_{dom}} \right]^n \left[1 - \frac{1}{N_{dom}} \right]^{N_t - n} \quad (4)$$

When the number of domains N_{dom} and the total number of spin labels N_t are large, the binomial probability P_n that a domain contains n spin labels can be approximated by the Poisson probability distribution function:

$$P_n = \frac{N^n}{n!} e^{-N} \quad (5)$$

where N is the average number of spin labels per domain. The condition that spin labels are distributed statistically among domains at all occupation numbers is that in general, the spin-labeled molecule must resemble as closely as possible the unlabeled parent molecule.

In the following, we ignore domain size heterogeneity. Thus the average number of host molecules per domain L is the same as the number of host molecules making up any given domain l . When the domain contains n spin labels, the peak-to-peak line width ΔH_n^{pp} is given by:

$$\Delta H_n^{pp} = \Delta H_0^{pp} + \frac{d\Delta H^{pp}}{dc} c_n \quad (6)$$

Here ΔH_0^{pp} is the limiting line width in the absence of spin-spin exchange and dipole-dipole interactions, c_n is the mole percent of spin label in a domain, and $d\Delta H^{pp}/dc$ is the gradient with concentration of the line width. The value of ΔH_0^{pp} is usually 1 G and $d\Delta H^{pp}/dc$ ranges from 0.1–0.8 G/mol% for a number of

different spin labels incorporated in fluid phase lipid bilayers (Sachse *et al.*, 1987). By taking representative experimental values for $d\Delta H^{pp}/dc$ from homogeneous systems, statistical factors corresponding to the dependence of Heisenberg spin exchange on the nuclear quantum numbers of the spin labels undergoing exchange are largely corrected for.

The mole percent of spin label in a domain c_n is given by:

$$c_n = \frac{100n}{L+n} \quad (7)$$

Similarly the average concentration of the spin label per domain C is given by:

$$C = \frac{100N}{L+N} \quad (8)$$

For a system consisting wholly of disconnected domains, this equals the net spin label concentration in the sample; otherwise changes in the two are proportional to one another. In the original formulation of Eq. 6 (Sankaram *et al.*, 1992), the approximation made was that the line width is directly proportional to n , i.e., $d\Delta H^{pp}/dn$ is constant. The present version, which involves linear proportionality with c_n , gives a more realistic representation of the fine structural details of concentration-dependent spin-spin broadening within domains. As we see later, this gives rise to a dependence of the diagnostic line height ratio plots on the domain size L .

When the Poisson probability distribution function is combined with the line shape function for a pure Lorentzian line, the amplitude of the summed spectrum is given by.

$$V = \sum_{n=1}^{\infty} n P_n \frac{8\sqrt{3}}{\pi(\Delta H_n^{pp})^2} \frac{(\xi_n)^2}{[3 + (\xi_n)^2]^2} \quad (9)$$

where

$$\xi_n = \frac{2(H - H_0)}{\Delta H_n^{pp}}$$

Similarly when the component spectra contain conventional inhomogeneous broadening, e.g., from an unresolved proton hyperfine structure, they can be represented by a Gaussian convolution of individual Lorentzian lines. The amplitude of the summed spectrum then consists of component spectra with Voigt line shapes, which is given by:

$$V = \sum_{n=1}^{\infty} n P_n S_n \quad (10)$$

where S_n is the Voigt line shape function (e.g., Bales, 1989).

While there are a number of algorithms available for a numerical simulation of S_n , a convenient method is given by Bales (Wertheim *et al.*, 1974; Bales, 1989). According to this method, S_n is given to a good approximation by a linear combination of Lorentzian and Gaussian line shapes.

$$S_n = \eta \frac{8\sqrt{3}}{\pi(\Delta H_n^{pp})^2} \frac{(\xi_n)^2}{[3 + (\xi_n)^2]^2} + (1 - \eta) \frac{4}{\sqrt{2\pi}(\Delta H_n^{pp})^2} \xi_n e^{-(\xi_n)^2/2} \quad (11)$$

where η is the fraction of the Lorentzian line shape in the Voigt function (Wertheim *et al.*, 1974; Bales, 1989).

2.3. Methods to Determine the Existence of a Statistical Distribution of Spin Labels

The intensity ratio of the summed spectrum for a statistical distribution of spin labels R can be calculated by numerical simulations. The value of R depends not only on the average number of spin labels per domain N (Fig. 5), and hence on the average mole percent of spin labels per domain C (Fig. 6), but also on the size of the domain L . The dependence on C offers a way of determining whether a spatially disconnected domain structure exists in a system. If the experimental intensity ratios attained are greater than R^L and a maximum is observed in the experimentally determined dependence of R on spin label concentration, we can conclude that the system possesses a spatially disconnected domain structure.

The shape of the predicted dependence of R on N (Fig. 5) changes systematically with L . A sharp maximum at a roughly fixed value of N is found for small values of the mean domain size. With increasing values of L , this peak becomes attenuated, and it is replaced by a broader maximum at higher values of N . When translated to a concentration axis (Fig. 6), the position of the sharp peak depends on the value of L that may in principle be used to determine the size of small domains. For larger domains, insufficient resolution is obtained in the broad maximum, so domain size must be determined from the absolute values of R ; differences between these values are rather small for large domains.

While Figs. 5 and 6 show the case of Lorentzian component line shapes, the characteristic maximum in R as a function of spin label concentration occurs for both Lorentzian and Voigt component line shapes. When the intensity ratio is measured at high enough concentrations of the spin label, so that exchange narrowing of the unresolved hyperfine structure (i.e., of the conventional Gaussian inhomogeneous broadening) is complete, the analysis can be simplified by assum-

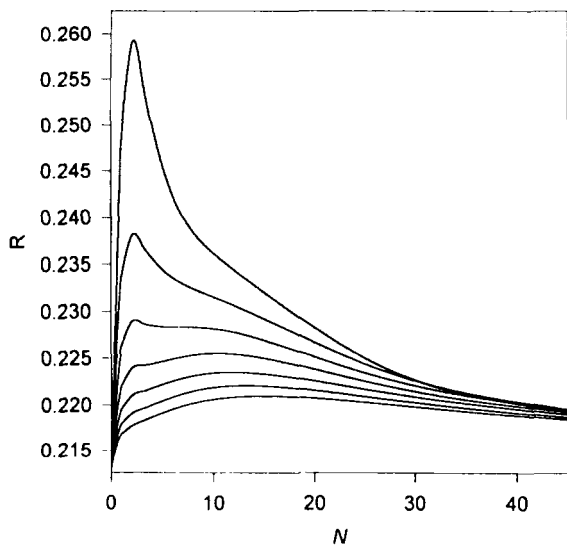


Figure 5. Dependence of the intensity ratio predicted from Eq. 9 on the average number of spin labels per domain N when a set of Lorentzians with a concentration-dependent peak-to-peak line width given by Eq. 6 and an intensity given by the Poisson probability distribution function (Eq. 5) are summed together, as illustrated in Fig. 2. The number of host molecules in the domain L is 200, 300, 400, 500, 600, 700, 800, 900, and 1000 (from top to bottom).

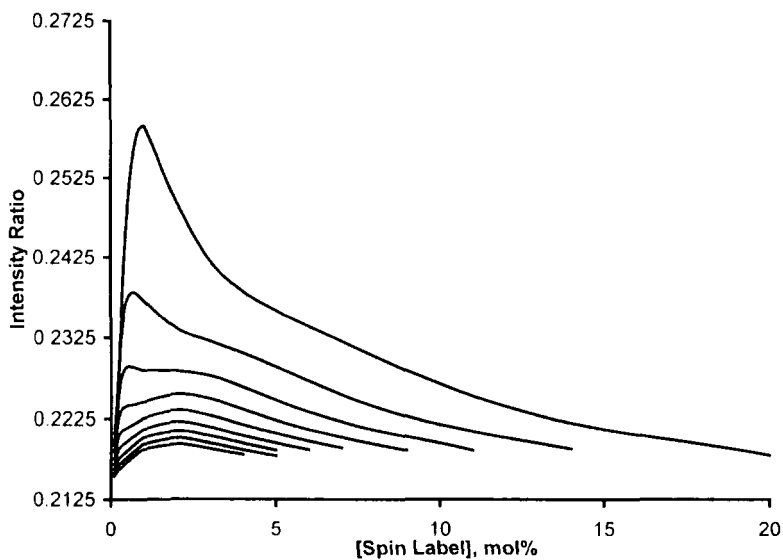


Figure 6. Dependence of the intensity ratio on the concentration of spin label, obtained by transforming data in Fig. 5 by using Eq. 8.

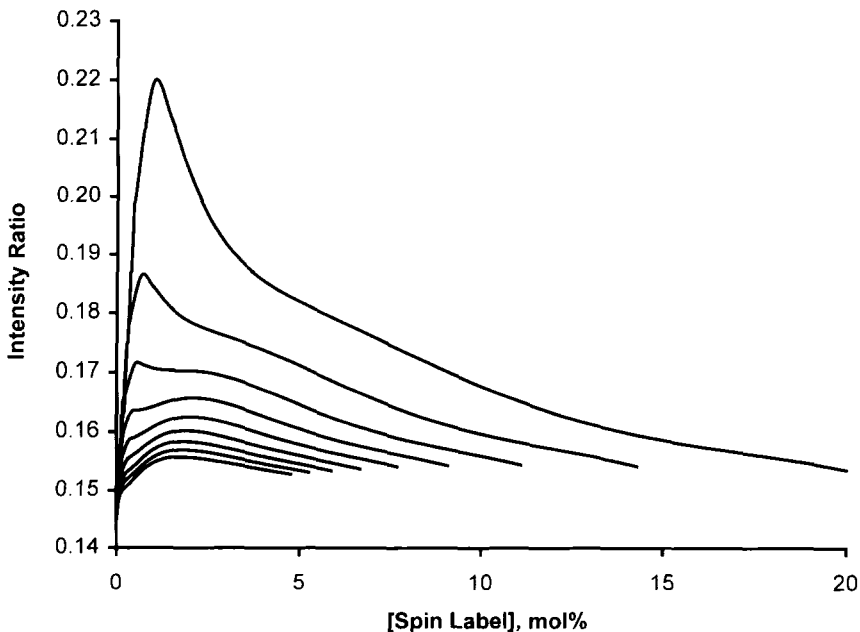


Figure 7. Dependence of the intensity ratio on the concentration of spin label, obtained when a set of Voigt lines with a concentration-dependent peak-to-peak line width given by Eq. 6, and an intensity given by the Poisson probability distribution function (Eq. 5) are summed together, as illustrated in Fig. 2. Voigt lines are simulated using Eq. 11 with a value for η of 0.2. The number of host molecules in the domain L is 200, 300, 400, 500, 600, 700, 800, 900, and 1000 (from top to bottom).

ing a Lorentzian line shape for the component spectra. The intensity ratio for a pure Lorentzian line shape R^L , is greater than that for Voigt lines regardless of line width. As a result, even when the component spectra are non-Lorentzian in shape, an experimentally determined value of R greater than R^L is a strong indication of the existence of a domain structure. Figure 7 shows representative results of the spin label concentration dependence of the diagnostic line height ratio parameter R for individual components that contain conventional (Gaussian) inhomogeneous broadening ΔH_G^{pp} . In comparison with Fig. 6, the dependence of the diagnostic ratio R on spin label concentration is very similar when the components have Gaussian inhomogeneous broadening to that for homogeneously broadened Lorentzian component line shapes. However depending on the degree of Gaussian inhomogeneous broadening and on domain size, the diagnostic line height ratios are not always greater than the value of R^L for a pure Lorentzian line. In the presence of strong conventional inhomogeneous broadening, this diagnostic feature of domain formation may therefore be lost. Information on the dependence of the

component line shapes on domain structure obtained by appropriate control experiments where possible can be used in the formalism developed in Section 2.2 to determine the exact dependence of R on C , N , and L .

The diagnostic line height ratio R has the advantage of being sensitive essentially only to line shape, with relatively little (or no) sensitivity to line widths (Bales, 1989). Other spectral parameters, such as peak heights and possibly line splittings, can be used, but these are sensitive to other variables. Line widths are of interest because their temperature dependence is used to detect the point of domain connectivity in disconnected systems (Sankaram *et al.*, 1992; 1994). The line widths also show dependence on connectivity and domain size, but with less sensitivity than the diagnostic ratio R . Part of the sensitivity of the line width to the point of connectivity may arise from this effect, possibly also with contributions from the underlying continuous phase.

2.4. Experimental Considerations

To determine the intensity ratio accurately, it is important that the field positions where the intensities are measured be determined precisely. The minimum spectral width required for measuring R is $2.64\Delta H^{pp}$; the maximum spectral width is usually $10\Delta H^{pp}$, so that the baseline can be well-defined. Therefore to locate the field position accurately to two significant digits relative to the line width, the spectrum of width $10\Delta H^{pp}$ must be stored as $1000\Delta H^{pp}$ points. For example, a peak-to-peak line width of 1.0 G requires a spectral width of 10 G digitized as 1000 points.

For a pure Lorentzian line $\partial R/\partial H \approx -0.167/\Delta H^{pp}$ and for lines consisting of a superposition of components with different widths, the dependence is even less steep. Therefore for a field resolution relative to ΔH^{pp} of two significant digits, the resolution in the intensity ratio should be close to three significant digits. This is sufficient for systems with small domains ($L < 600$), but it limits the accuracy with which the size of larger domains can be determined (cf. Fig. 6).

3. APPLICATIONS

3.1. Domain Structure in a Two-Component, Two-Phase Lipid Bilayer System

Lipid bilayers composed of two or more lipids have been shown to exhibit lateral phase separations into gel and fluid phases in a temperature range that depends on the composition. The two phases are laterally organized into domains with connectivity properties given by percolation theory. Thus in the gel-fluid coexistence region, a temperature exists above which the fluid phase is continuous, thereby disconnecting the gel phase into domains. Below this point, the gel phase

forms the continuous structure, and the fluid phase is disconnected. To illustrate this further, Fig. 8 shows the temperature-composition phase diagram for the binary system of 1,2-dimyristoyl-*sn*-glycero-3-phosphocholine (DMPC) and 1,2-distearoyl-*sn*-glycero-3-phosphocholine (DSPC).

The theoretical formalism just developed was applied to the DMPC-DSPC system, and average sizes of the gel and fluid domains were estimated (Sankaram *et al.*, 1992, 1994). The experimental strategy involves introducing either a spin-labeled DMPC, 1-myristoyl-2[13-(4,4-dimethyloxazolidine-N-oxyl)]-myristoyl-*sn*-glycero-3-phosphocholine (13-DMPCSL), or a spin-labeled DSPC, 1-stearoyl-2[16-(4,4-dimethyloxazolidine-N-oxyl)]-stearoyl-*sn*-glycero-3-phosphocholine (16-DSPCSL), then measuring the intensity ratio over a range of temperatures and composition. From the phase diagram in Fig. 8, the fraction F of the total lipid in the fluid phase at a mole fraction of the particular lipid X is given by the lever rule:

$$F = \frac{X_S - X}{X_S - X_F} \quad (12)$$

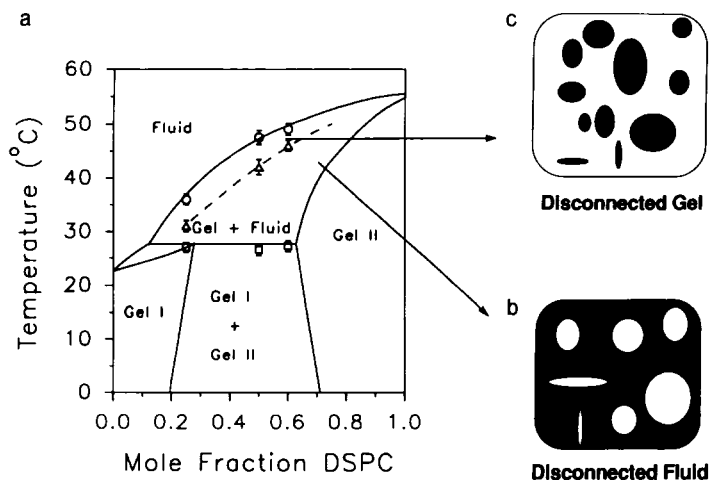


Figure 8. Temperature-composition phase diagram of the DMPC-DSPC system. (a) Solid lines represent phase boundaries. The dashed line in the gel-fluid coexistence region is the line where connectivity of the fluid phase and disconnection of the gel phase is achieved with increasing temperature. A schematic representation of the disconnected fluid/connected gel and the disconnected gel/connected fluid situations encountered (b) below and (c) above the point of connectivity, respectively, is included. The disconnected fluid and gel domains are shown to differ in both size and shape. (Data from Sankaram *et al.*, 1992)

where X_S and X_F are the mole fractions of the lipid at the solidus and fluidus boundaries of the tie line at the relevant temperature. The fraction of the particular lipid in the fluid phase is given by:

$$f = \frac{FX_F}{X} \quad (13)$$

It is assumed that the partitioning of the spin-labeled lipid is the same as that of the corresponding parent lipid. Thus the value for f is the same for DMPC and 13-DMPCSL, and for DSPC and 16-DSPCSL.

Figure 9 shows the temperature dependence of the experimental intensity ratio R_{obs} for the three ^{14}N -hyperfine ESR lines of the 13-DMPCSL spin label at a concentration of 3 mol% in a 50:50 (mol/mol) mixture of DMPC and DSPC. In the region of gel-fluid coexistence, R_{obs} is greater than that for a pure Lorentzian R^L .

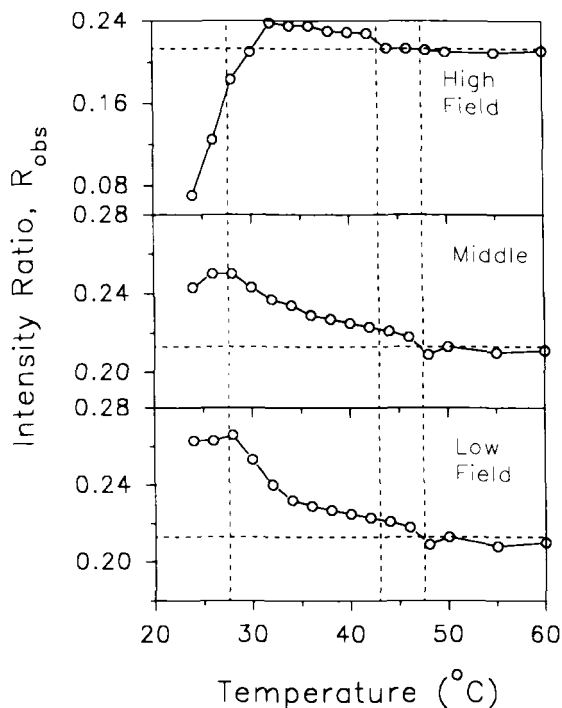


Figure 9. Temperature dependence of the experimental intensity ratio R_{obs} for the three ^{14}N -hyperfine ESR lines of the 13-DMPCSL spin label at a concentration of 3 mol% in a 50:50 (mol/mol) mixture of DMPC with DSPC. Vertical dashed lines from left to right represent the solidus, the line of connectivity, and the fluidus phase boundary, respectively (cf. Fig. 8). The horizontal dashed line is the value of the intensity ratio for a pure Lorentzian line R^L . (Data from Sankaram *et al.*, 1992)

indicating that disconnected domains are present in this region. Because the peak-to-peak line width does not decrease by more than 10% across the region of gel-fluid coexistence, the difference $R_{obs} - R^L$ cannot be entirely accounted for simply by the coexistence of gel and fluid domains per se. Simulations show that when the line width difference is less than 10%, the intensity ratio for the sum of two spectra in any proportion can be expressed as a weighted average of the individual intensity ratios of the two spectra (Sankaram *et al.*, 1992). This is because R does not vary much due to admixture under these conditions, as is shown in Fig. 4. The intensity ratio for the disconnected fluid phase R_f can thus be derived from the experimental intensity ratio R_{obs} , the fraction of the lipid in the fluid phase f ,

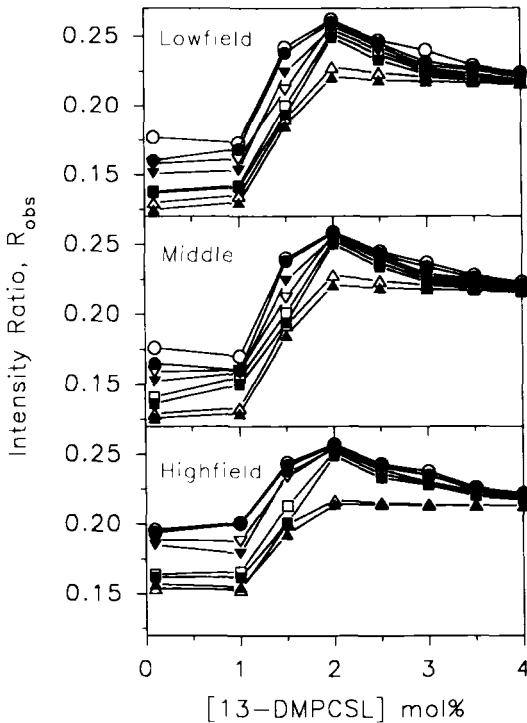


Figure 10. The value of R_{obs} as a function of concentration of the 13-DMPCSL spin label in equimolar mixtures of DMPC with DSPC. The temperatures at which spectra were recorded are (from upper to lower) 32, 34, 36, 38, 40, 42, 44, and 46 °C. At 44 and 46 °C, the gel phase is disconnected, and the fluid phase is connected; the fluid phase becomes disconnected and the gel phase is connected in the temperature range 32–42 °C. (Data from Sankaram *et al.*, 1992)

and the intensity ratio in the continuous gel phase R_g . The value for R_g can be measured from the spectrum at a temperature just below the solidus boundary:

$$R_{obs} = fR_f + (1-f)R_g \quad (14)$$

As the spin label concentration is increased, R_{obs} increases to reach a maximum followed by a decrease, as shown in Fig. 10. This behavior is characteristic of a disconnected domain structure, as discussed previously and shown in Fig. 6. Figure 10 also shows data at different temperatures for an equimolar mixture of DMPC and DSPC. At all temperatures, the maximum occurs in approximately the same region of spin label concentration. Most probably the domains are on the whole sufficiently large that the position of the maximum is not sensitively dependent on domain size. The size of the domains increases as the fraction of disconnected fluid phase or of disconnected gel phase is increased, as seen from changes in R_{obs} with temperature at fixed spin label concentration (of. Fig. 10).

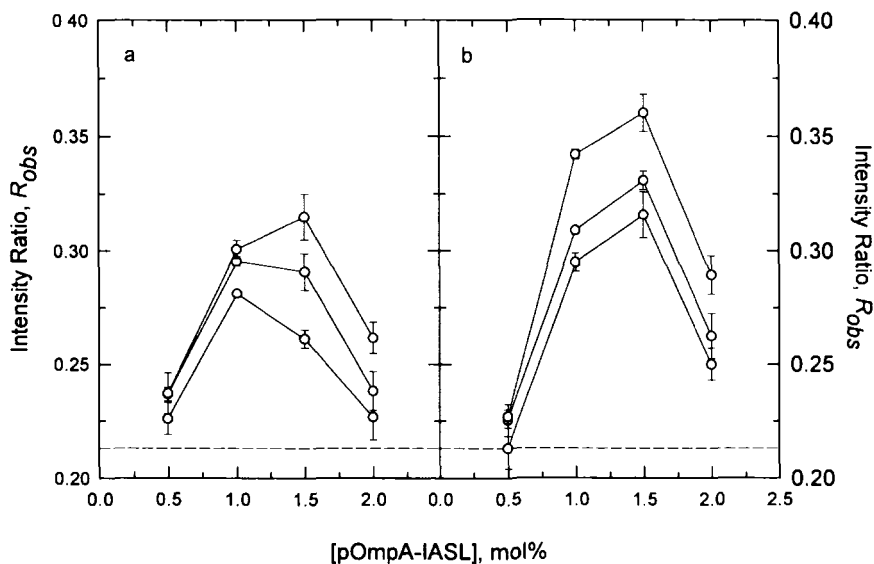


Figure 11. Dependence on the concentration of the spin-labeled peptide pOmpA-IASL of R_{obs} for the central hyperfine line in the ESR spectrum of pOmpA-IASL. Data obtained from (a) 50:50 (mol/mol) mixtures of DMPC/DSPC and (b) 40:60 (mol/mol) mixtures of DMPC/DSPC. In a, the temperatures at which the spectra were recorded are (from lower to upper) 32 °C, 34 °C, 38 °C, and in b, they are 34 °C, 38 °C, and 42 °C. The dashed line in both (a) and (b) is the maximum value for the intensity ratio $R^L = 0.2125$ for a Lorentzian line. (Data from Sankaram *et al.*, 1994)

3.2. Effect of a Peptide on Domain Structure

The intensity ratio method was also used to investigate the effect of incorporating *Escherichia coli* outer membrane protein A signal peptide, a transmembrane peptide, on the lipid domain structure in the same DMPC/DSPC system (Sankaram *et al.*, 1994). Figure 11 shows the dependence of the experimental intensity ratio R_{obs} on the concentration of the peptide labeled by the iodoacetamide spin label (pOmpA-IASL). Again, R_{obs} is much greater than R^L , suggesting the presence of a domain structure. The R_{obs} versus spin label concentration dependence also shows a maximum diagnostic of the presence of domain structure; however in this case, the position of the maximum in R_{obs} depends on the spin label concentration, at least for the equimolar DMPC/DSPC mixture. This suggests that the average domain size is smaller than in the lipid mixture without peptide and correspondingly phase conversion involves an increased number of domains in addition to an increase in domain size. Note: The temperature dependence in Fig. 11 is opposite from that in Fig. 10, indicating a pronounced change in lipid domain structure by the peptide.

4. CONCLUSIONS

Chapter 1 presents a theoretical formalism for the phenomenon of inhomogeneous broadening of spin label ESR spectra from different component widths. An internally normalized measure of the line shape, namely, the intensity ratio, is shown to be a diagnostic parameter for distinguishing between the conventional origins of line broadening, including unresolved hyperfine structure and spin label dynamics, and the novel mechanism of a statistical distribution of component lines differing in line width. The method is applied to characterize lipid domain connectivity in two-component, two-phase lipid binary mixtures and the effects of peptides on membrane in-plane domain structure. Experimental results show that intensity ratio measurements indicate the presence of disconnected domain structure in membranes, and such measurements are able to distinguish domain growth in size from growth in number.

REFERENCES

- Bales, B. L., 1982, *J. Mag. Res.* **48**:418.
Bales, B. L., 1989, Inhomogeneously broadened spin label spectra, in *Biological Magnetic Resonance*, vol. 8 (L. J. Berliner and J. Reuben, eds.) (Plenum., New York), pp. 77–130.
Sachse, J.-H., King, M. D., and Marsh, D., 1987, *J. Mag. Reson.* **71**:385.
Sankaram, M. B., Marsh, D., and Thompson, T. E., 1992, *Biophys. J.* **63**:340.
Sankaram, M. B., Marsh, D., Gierasch, L. M., and Thompson, T. E., 1994, *Biophys. J.* **66**:1959.
Wertheim, G. K., Butler, M. A., West, K. W., and Buchanan, D. N. E., 1974, *Rev. Sci. Instrum.* **45**:1369.

This page intentionally left blank

Progressive Saturation and Saturation Transfer EPR for Measuring Exchange Processes and Proximity Relations in Membranes

Derek Marsh, Tibor Páli, and László I. Horváth

1. INTRODUCTION

Conventional applications of spin label electron paramagnetic resonance (EPR) spectroscopy rely mostly on the sensitivity of line shapes and line widths of continuous wave (CW) spectra to rotational motions with correlation times ranging from 10^{-11} – 10^{-8} s, which are determined by the nitroxide spin-spin (i.e., T_2) relaxation processes (see, e.g., Marsh, 1989; Marsh and Horváth, 1989). Extension of the motional sensitivity of spin label methods to slower time scales is possible by using the microwave saturation properties of the EPR spectrum governed by the nitroxide spin lattice relaxation time T_1 , which for relevant cases lies in the microsecond time regime. A well-established application of this extended motional

Derek Marsh • Max-Planck-Institut für biophysikalische Chemie, Abteilung Spektroskopie, D-37108 Göttingen, Germany Tibor Páli and László I. Horváth • Biological Research Centre, H-6701 Szeged, Hungary.

Biological Magnetic Resonance, Volume 14: Spin Labeling: The Next Millennium, edited by Berliner. Plenum Press, New York, 1998.

sensitivity is determination of the slow rotational diffusion rates of membrane proteins and supramolecular aggregates by using saturation transfer (ST) EPR in which the nonlinear EPR signal in quadrature phase with respect to the field modulation is detected under conditions of partial microwave saturation (Thomas *et al.*, 1976; Marsh and Horváth, 1989; and Knowles and Marsh, 1991).

Recently, there has been an upsurge in the application of CW saturation EPR methods in spin labeling (Marsh, 1994). The reason for this lies in the unique sensitivity of enhancements in the nitroxide spin-lattice relaxation rate to a variety of slow exchange processes, including weak Heisenberg exchange, and to the distance-dependent dipolar interaction with paramagnetic ions and their complexes (Marsh, 1992a, 1993). Figure 1 shows different applications in membrane studies. Not only is progressive saturation of the CW spectrum with increasing microwave power used in these studies, but also a novel application of ST-EPR intensity measurements to determine spin-lattice relaxation rates. The latter has the advantage of increased sensitivity to T_1 -relaxation processes for spin labels undergoing slow rotational motion (Marsh and Horváth, 1992a). Although saturation recovery and electron-electron double resonance (ELDOR) methods have been used with great success in studying weak exchange phenomena (Yin *et al.*, 1987; Yin and Hyde, 1987; Hyde and Feix, 1989), part of the appeal of CW saturation methods just mentioned lies in the relative ease of application to complex biological systems;

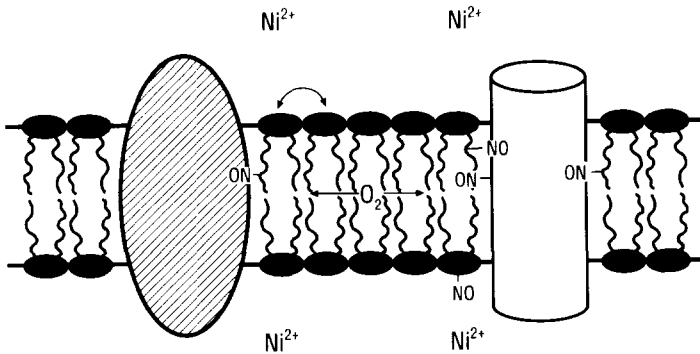


Figure 1. Spin label exchange processes, both molecular exchange and spin exchange, and interactions with aqueous paramagnetic ions that determine spin lattice relaxation enhancements in membranes. *Left-hand side:* Exchange of a spin-labeled (-NO) lipid between sites at the lipid-protein interface and in the lipid bilayer regions of the membrane. *Right-hand side:* Heisenberg spin exchange between spin-labeled lipids and a spin-labeled protein, depending on their mutual collisional accessibility. Heisenberg spin exchange also takes place with paramagnetic oxygen that is preferentially concentrated in the membrane, and with paramagnetic ions in the aqueous phase. In the absence of Heisenberg exchange with paramagnetic ions (i.e., direct accessibility), relaxation enhancement is determined by the separation-dependent magnetic dipole-dipole interactions.

they can also be performed straightforwardly on standard EPR spectrometers. A particularly fruitful application of CW saturation methods is in combination with site-directed spin labeling (Hubbell and Altenbach, 1994).

Chapter 2 deals in depth with the application of CW EPR methods, both progressive saturation and ST-EPR intensity measurements, to determine enhancements in spin-lattice relaxation rates of spin-labeled biological systems, particularly membranes. The different processes that can be studied by these techniques are the slow exchange of spin labels between different environments, Heisenberg exchange between different or the same spin-labeled species, Heisenberg exchange with paramagnetic relaxants, and dipolar-induced relaxation by paramagnetic ions. Regarding Heisenberg spin exchange and magnetic dipole interactions, the advantage of T_1 -based methods is that experiments may be restricted to low concentrations of both spin-labeled and paramagnetic species; in the case of dipolar interactions, the sensitivity may be extended to longer distances. Such studies provide important information not only on molecular dynamics of exchange processes, but also structural information from accessibilities to relaxants and other spin-labeled species and from distance measurements via the dipolar interactions (compare Fig. 1).

The initial sections of Chap. 2 deal individually with relaxation enhancements induced by different exchange processes and paramagnetic interactions and also with possible complications arising from competing relaxation and exchange processes. The next sections deal with extracting relaxation enhancements from CW saturation measurements. Particular attention is paid to using integrated intensities and the dependence of the latter on the T_1 -relaxation time for ST-EPR spectra. Finally different applications of various CW saturation studies are reviewed. These sections give a good indication of the power of the methods and the broad range of studies to which they are applicable.

1.1. Continuous Wave Saturation

Saturation of an EPR transition arises when the spin-lattice relaxation is no longer able to compete effectively with transitions induced by the microwave radiation field. Classically saturation of the intensity of the conventional EPR spectrum can be described in terms of the population differences n_i between the $M_{s_i} = \pm 1/2$ levels of the i th spin system, where $n_i = N_i^- - N_i^+$, with N_i^\pm the spin populations of the two levels (compare Fig. 2). The standard expression for the steady-state population difference under CW irradiation of the isolated k th two-level spin system is (Slichter, 1978):

$$n_k = n_k^0 / (1 + 2WT_{1,k}^{eff}) \quad (1)$$

where n_k^0 is the Boltzmann equilibrium population difference and W is the rate at which transitions are induced by the microwave H_1 field. As the transition rate W increases with increasing microwave power, the steady-state population difference n_k decreases, resulting in saturation of the EPR spectrum. The dependence of n_k on W given in Eq. (1) defines the effective spin lattice relaxation time $T_{1,k}^{eff}$ in a CW saturation EPR experiment. It is used here to derive the effective T_1 -relaxation times for more complex spin systems than a simple two-level scheme (compare Marsh, 1992b).

1.2. Effective Spin Lattice Relaxation Times

In a CW saturation EPR experiment, processes other than the intrinsic electron spin-lattice relaxation, which occurs at a rate given by $2W_e = 1/T_{1e}$, contribute to alleviating saturation. These additional processes contributing to the effective spin-lattice relaxation time T_1^{eff} include nuclear relaxation at a rate $2W_n$ and Heisenberg spin exchange at a rate ω_{HE} . It is this effective electron spin-lattice relaxation time that is measured in CW EPR saturation experiments.

For a nitroxide spin label system with ^{14}N nuclear spin $I = 1$, the possible transitions between the $S = 1/2$ electron spin states are indicated in Fig. 2. Cross relaxation from nonsecular terms of the electron-nuclear dipolar interaction is ignored in this scheme. We also assume that all three hyperfine levels have the same intrinsic spin-lattice relaxation rate (see later). Heisenberg spin exchange between radicals in different hyperfine states depends on the radical concentration; it is negligible at low concentrations. Steady-state rate equations for the spin population differences $n_{M_I} = N_{M_I}^- - N_{M_I}^+$ in the different hyperfine levels with nuclear magnetic quantum numbers $M_I = 0, \pm 1$, neglecting Heisenberg exchange, are given by (cf. Marsh, 1992b):

$$\frac{dn_0}{dt} = -2W_e(n_0 - n_0^0) + 2W_n(n_{+1} + n_{-1} - 2n_0) - 2Wn_0\delta_{0,m} = 0 \quad (2)$$

$$\frac{dn_{\pm 1}}{dt} = -2W_e(n_{\pm 1} - n_{\pm 1}^0) + 2W_n(n_0 - n_{\pm 1}) - 2Wn_{\pm 1}\delta_{\pm 1,m} = 0 \quad (3)$$

where $n_{M_I}^0$ is the spin population difference at Boltzmann equilibrium. Transitions are induced by the H_1 -field at a rate W , within the hyperfine manifold with $M_I = m$ (i.e., $\delta_{M_I,m} = 1$ for $M_I = m$ and 0 otherwise).

Solution of Eqs. (2) and (3) leads to a dependence on the microwave power (i.e., on W) that conforms to the standard expression for the saturation of a simple two-level ($S_I = 1/2$) system given by Eq. (1). *Effective* spin-lattice relaxation times governing the saturation behavior of the $M_I = 0, \pm 1$ manifolds are then, respectively (Marsh, 1992b):

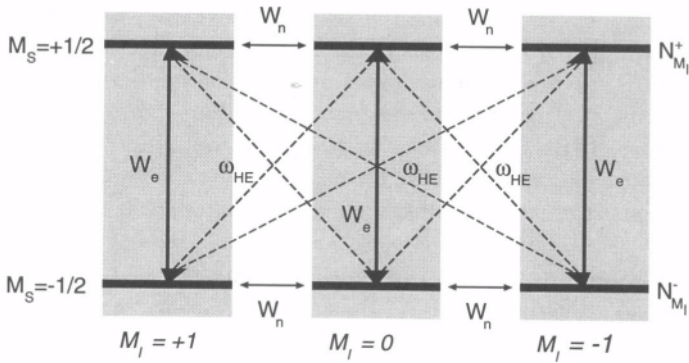


Figure 2. Energy level scheme for an $S=1/2$, $I=1$, ^{14}N -nitroxide spin label. Populations of the $M_S = \pm 1/2$ levels of the M_I -nuclear manifold are $N_{M_I}^{\pm}$; the corresponding spin population difference is $n_{M_I} = N_{M_I}^- - N_{M_I}^+$. The different relaxation pathways are indicated. Heisenberg exchange does not contribute at low concentration; it is indicated by dashed lines. The intrinsic electron spin-lattice relaxation rate is W_e ; the ^{14}N nuclear spin lattice relaxation rate is W_n ; and the Heisenberg electron spin exchange frequency is ω_{HE} .

$$T_1^{\text{eff}}(0) = \left(\frac{1+b}{1+3b} \right) \frac{1}{2W_e} \quad (4)$$

and

$$T_1^{\text{eff}}(\pm 1) = \frac{1+3b+b^2}{(1+b)(1+3b)} \cdot \frac{1}{2W_e} \quad (5)$$

where $b = W_n/W_e$ is the ratio of the nuclear to the electron relaxation rate. For $b \ll 1$, nuclear relaxation is unimportant, so each hyperfine state relaxes independently with its intrinsic rate $T_1^{-1}(0) = T_1^{-1}(\pm 1) = 2W_e$. For $b \gg 1$, the transitions are short-circuited by the nuclear relaxation, and all relax with a rate $T_1^{-1}(0) = T_1^{-1}(\pm 1) = 6W_e$. Otherwise the relaxation rate of the $M_I = 0$ transition is faster than that of the $M_I = \pm 1$ transitions; the maximum difference is 25%, obtained when $b = 1$.

The general case for Heisenberg spin exchange is considered in detail later. For the simple scheme shown in Fig. 2, the effective relaxation times including spin exchange between the different hyperfine manifolds are given by (compare Hyde, Chien, and Freed, 1968):

$$T_1^{\text{eff}}(0, b'') = \frac{1+b+b''}{1+3b+3b''} \cdot \frac{1}{2W_e} \quad (6)$$

and

$$T_1^{\text{eff}}(\pm 1, b'') = T_1^{\text{eff}}(0, b'') + \frac{b}{(1+b+3b'')(1+3b+3b'')} \cdot \frac{1}{2W_e} \quad (7)$$

where $b'' = \omega_{HE}/6W_e$ is the normalized Heisenberg exchange rate. Unlike those of nuclear relaxation, the effects of exchange are similar for all three hyperfine manifolds. For the $M_I = 0$ manifold, nuclear relaxation contributes to the effective relaxation time in a manner similar to exchange. For the $M_I = \pm 1$ manifolds, exchange is more effective than nuclear relaxation due to less restrictive selection rules for exchange relative to those for nuclear relaxation (compare Fig. 2). The question of determining Heisenberg exchange frequencies in the presence of nuclear relaxation is considered in more detail later.

Note: The intrinsic electron spin-lattice relaxation rate W_e corresponds exactly to the nonsecular contributions to T_{2e}^{-1} that arise solely from electron spin flips. This W_e -like term is therefore manifested in the line widths, and it can sometimes be resolved from other contributions to the line width by the characteristic dependence on the rotational correlation time (Goldman *et al.*, 1972). In principle this offers a means for determining the intrinsic spin-lattice relaxation rate rather than $(T_1^{eff})^{-1}$ by continuous wave EPR measurements (Hwang *et al.*, 1975).

2. CONTRIBUTIONS TO INTRINSIC SPIN-LATTICE RELAXATION RATES

Chapter 2 is concerned with enhancements in the spin-lattice relaxation rate of spin labels by paramagnetic species, and by Heisenberg spin exchange and other exchange processes. For such studies, the mechanism of intrinsic spin-lattice relaxation of the spin label is not of primary importance. However the intrinsic spin-lattice relaxation rate does affect the sensitivity of these methods; in particular it serves as the clock by which exchange rates are measured. Therefore it is helpful to know the intrinsic spin label relaxation rates and how these are affected by the rotational dynamics of the spin label and its environment. For these reasons, the present section is concerned with the mechanisms contributing to the intrinsic spin-lattice relaxation of nitroxide spin labels. Typical values of intrinsic spin-lattice relaxation times for different situations are also reviewed. Our discussion concentrates mainly on the commonly used ^{14}N -nitroxide spin labels, although currently more detailed information is available from ^{15}N -substituted spin labels whose relaxation pathways are somewhat simpler and quantitative results are likely to be different (Robinson *et al.*, 1994).

2.1. Electron Relaxation Mechanisms

Classically there are two principal liquid-state mechanisms of electron spin-lattice relaxation for nitroxide spin labels. The first is the modulation of the *hyperfine* and *g-value anisotropies*, which leads to a relaxation rate with a Debye-type spectral density that depends on the nuclear hyperfine manifold M_I . For

isotropic rotational diffusion, the contribution to the relaxation rate from this mechanism is given by (Wilson and Kivelson, 1966; Dalton *et al.*, 1976; Freed, 1979):

$$W_e^{anisot}(M_I) = \frac{1}{15} \left\{ \left(\frac{\beta_e H_o}{\hbar} \right)^2 [(\Delta g)^2 + 3(\delta g)^2] + 2 \left(\frac{\beta_e H_o}{\hbar} \right) (\Delta g \Delta A + 3\delta g \delta A) M_I + [(\Delta A)^2 + 3(\delta A)^2] M_I^2 \right\} \cdot \frac{\tau_R}{1 + \omega_e^2 \tau_R^2} \quad (8)$$

where $\tau_R (= 1/6D_R)$ is the rotational correlation time, H_o is the resonance magnetic field, and $\omega_e (= g_o \beta_e H_o / \hbar)$ is the electron Larmor frequency. Anisotropies of the principal g-tensor elements (g_{ii}) and of the ^{14}N hyperfine tensor elements (A_{ii}) are defined by:

$$\begin{aligned} \Delta g &= g_{zz} - \frac{1}{2}(g_{xx} + g_{yy}) \\ \delta g &= \frac{1}{2}(g_{xx} - g_{yy}) \\ \Delta A &= A_{zz} - \frac{1}{2}(A_{xx} + A_{yy}) \\ \delta A &= \frac{1}{2}(A_{xx} - A_{yy}) \end{aligned} \quad (9)$$

Hyperfine tensor elements are expressed in terms of *angular frequencies*: $H_{hf} = \hbar I \cdot A \cdot S$, i.e., $A_{ii}(\text{rad}\cdot\text{s}^{-1}) = (g_o \beta_e / \hbar) A_{ii}(\text{Gauss})$

For anisotropic rotational diffusion, the $(\Delta g)^2$, $\Delta g \Delta A$, and $(\Delta A)^2$ terms of Eq. (8) are characterized by a rotational correlation time $\tau_{2,0}^{-1} = 6D_{R//}$; and the $(\delta g)^2$, $\delta g \delta A$, and $(\delta A)^2$ terms by a correlation time $\tau_{2,\pm 2}^{-1} = 2D_{R\perp} + 4D_{R//}$ where $D_{R//}$, $D_{R\perp}$ are the rotational diffusion tensor components referred to the nitroxide z-axis and x,y-axis, respectively (Dalton *et al.*, 1976; Goldmann *et al.*, 1972). For anisotropic motion with limited excursions of the z-axis specified by an order parameter S , the $(\Delta g)^2$, $\Delta g \Delta A$, and $(\Delta A)^2$ terms are multiplied by a factor $(1 - S^2)$ (Shlenkin *et al.*, 1993). Note: The electron spin-lattice relaxation rate arising from modulation of the hyperfine and g-tensor anisotropies is maximum for rotational diffusion at the Larmor frequency ω_e . Because this corresponds to rather rapid motions ($\tau_R = 1/\omega_e \sim 2 \cdot 10^{-11}\text{s}$), it is likely that fast internal motions contribute appreciably to relaxation by this mechanism.

The second liquid-state mechanism is the *spin-rotation interaction*, which gives rise to a relaxation rate that is essentially orientation-independent and also

does not depend on the nuclear spin quantum number. For isotropic rotational diffusion, the contribution to the spin-lattice relaxation rate from this mechanism is (Atkins and Kivelson, 1966):

$$W_e^{SR} = \sum_i \frac{(g_{ii} - g_e)^2}{18\tau_R} \quad (10)$$

where g_e ($= 2.0023$) is the free electron g -value. Here the reasonable assumption is made that the correlation time τ_J for the molecular angular momentum is short for all cases of interest; i.e., it is always in the motional-narrowing regime. Further, the correlation time τ_J is related (inversely) here to that for molecular reorientation τ_R by the Stokes–Einstein relation.

A third liquid state mechanism for the spin-lattice relaxation of nitroxide spin labels was recently suggested (Robinson *et al.*, 1994). This is *spin diffusion* that arises from coupling of the electron spin to the nuclear spins of solvent protons. Such a mechanism gives rise to non-Debye spectral densities characterized by the solvent-spin label translational diffusion time, which is proportional to the rotational correlation time of the spin label. Making the approximation that the diffusion time equals the rotational correlation time, the contribution from spin diffusion to the electron relaxation rate is given by (Robinson *et al.*, 1994):

$$W_e^{sd} = R_{e,o}^{sd} \left[\frac{\tau_R}{1 + (\omega_e \tau_R)^{3/2}} \right]^{1/4} \quad (11)$$

where $R_{e,o}^{sd}$ is a parameter determined by the strength of the proton-electron spin interactions and by the efficiency of spin diffusion. For a spin-labeled system of considerably greater size than the solvent molecules, this equality with the spin label correlation time does not hold; the diffusion time is then better determined from the rotational correlation time of the solvent molecules. This mechanism appears to be particularly significant at longer correlation times because of the much weaker dependence of the spectral density on τ_R . At long correlation times ($\omega_e \tau_R \gg 1$), the spin diffusion mechanism [Eq. (11)] predicts that the spin-lattice relaxation rate varies as $\tau_R^{-1/8}$. This mechanism makes its maximum contribution [$W_e^{sd} \approx R_{e,o}^{sd} / (2\omega_e)^{1/4}$] to the overall rate in the shorter correlation time regime for $\tau_R = 2^{2/3} / \omega_e$ ($\approx 3 \times 10^{-11}$ s), although in this region the classic liquid state mechanisms are likely to dominate. Note: because this spin diffusion mechanism is described in terms of intermolecular interactions, it may make a considerably smaller contribution to the relaxation of spin labels in complex biological systems where solvent accessibility may be limited.

Saturation recovery EPR measurements with spin labels indicate no strong dependence of the electron spin-lattice relaxation rate on the nuclear manifold, unlike that predicted by Eq. (8) for the contribution from modulation of the

hyperfine and g -tensor anisotropies (Percival and Hyde, 1976). Figure 3 shows data obtained for ^{14}N -hydroxy-TEMPO in *sec*-butyl benzene. Also the dependence on rotational correlation time, as shown in Fig. 3 ($T_{1e}^{-1} \propto \tau_R^{-1/2}$), is weaker than that predicted for either of the classic liquid-state mechanisms given by Eqs. (8) and (10). At short correlation times (high temperatures), spin rotation can account numerically for an appreciable part of the relaxation, but at longer correlation times (lower temperatures), neither mechanism is adequate. This suggests that an additional mechanism, presumably spin diffusion, proposed by Robinson *et al.* (1994), contributes to the electron relaxation. In a detailed study with ^{15}N hydroxy-TEMPO in glycerol-water solutions over an extremely wide range of rotational correlation times, it was found that both electron and nuclear spin-lattice relaxation rates could be fit consistently with the combined contributions from electron-nuclear dipolar interactions, spin rotation, and spin diffusion without recourse to nonliquid-state relaxation mechanisms (Robinson *et al.*, 1994). This indicates that with a single

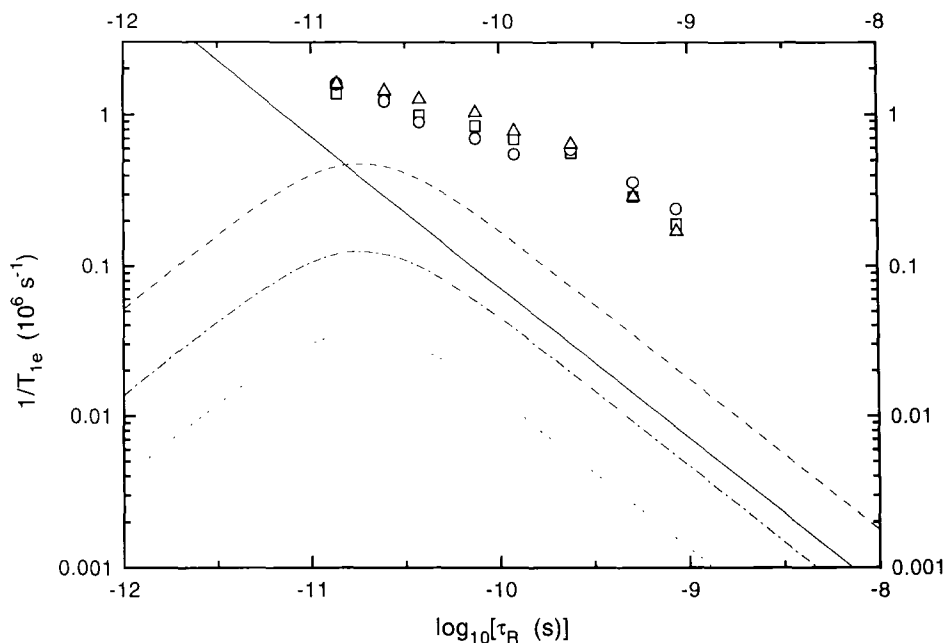


Figure 3. Dependence of the electron spin-lattice relaxation rate T_{1e}^{-1} of 4-hydroxy-2,2,6,6-tetramethylpiperidine-1-oxyl (hydroxy-TEMPO) on rotational correlation time τ_R , in *sec*-butyl-benzene. Calculated contributions from modulation of the hyperfine and g -tensor anisotropies according to Eq. (8) and from the spin-rotation mechanism according to Eq. (10) (solid line) are also given. (Data from Percival and Hyde, 1976)

adjustable parameter ($R_{e,o}^{sd}$), the spin diffusion mechanism is capable of describing the otherwise anomalous dependence of the electron T_1 on rotational correlation time.

Previously values of the electron spin-lattice relaxation rate $W_e(0)$, obtained from the M_J -independent contribution to the line widths, were found to depend on rotational correlation time, which suggested that the nonsecular spectral densities may differ from the simple Debye form. This was attributed to the contribution from fluctuating torques (Hwang *et al.*, 1975). At very high viscosities, little dependence of the electron spin-lattice relaxation rate of hydroxy-TEMPO in supercooled *sec*-butyl-benzene was found on the rotational correlation time in an early study. The value of T_{1e} remained approximately constant at 15 μ s for $\tau_R = 2 \times 10^{-7} - 2 \times 10^{-4}$ s (Hyde, 1979).

For spin-labeled hemoglobin in aqueous glycerol solutions, no dependence of the electron spin-lattice relaxation rate was found on either the nuclear manifold or the spectral anisotropy (Fajer *et al.*, 1986). The dependence of the relaxation rate on rotational correlation time was found to be very weak ($T_{1e}^{-1} \propto \tau_R^{-0.12}$) in this case over the range $\tau_R = 2.10^{-8} - 2.10^{-3}$ s. This dependence is that predicted for the spin diffusion mechanism at long correlation times and also that found experimentally for ^{15}N -hydroxy-TEMPO in glycerol-water mixtures at correlation times greater than a microsecond (Robinson *et al.*, 1994; Haas *et al.*, 1993a). The absolute values of the spin-lattice relaxation rate of spin-labeled hemoglobin were no more than a factor of ten smaller than those for small nitroxides in the much faster correlation time regime (see Table 1). At these long correlation times, the two classical liquid-state relaxation mechanisms considered above contribute negligibly to the overall relaxation rate measured (compare Fig. 3).

Earlier, it had been pointed out that the temperature dependence of the electron spin-lattice relaxation rate of hydroxy-TEMPO and TEMPONE in *sec*-butyl-benzene, was consistent with the excess relaxation rate, over that estimated for the two classic liquid-state mechanisms, being contributed by solid-state relaxation (local mode and two-phonon Raman) mechanisms for rotational correlation times longer than 10^{-10} s (Hyde and Dalton, 1979). The temperature dependence of the experimental relaxation rate was found to be characterized by the following expression (compare Thomas *et al.*, 1976):

$$T_{1e}^{-1} = 2W_e^{SR} + 2W_e^{aniso} + A \exp(-B/T) + CT^2 \quad (12)$$

where the first two terms are contributions from the classic liquid-state mechanisms [Eqs. (8) and (10)] and the temperature-dependent terms, with A , B , and C as constants, represent the excess relaxation rate. The extensive saturation recovery and pulse ELDOR studies of Robinson *et al.* (1994) on ^{15}N -hydroxy-TEMPO in aqueous glycerol solutions indicate however that such solid-state mechanisms are

Table 1
Representative Values of Electron Spin-Lattice Relaxation Times T_{1e} and ^{14}N
Nuclear Spin-Lattice Relaxation Times T_{1n} Obtained from Saturation Recovery
and Pulsed ELDOR Measurements for Nitroxide Spin Labels

Nitroxide ^a	Environment	Temperature (°C)	τ_R^b (ns)	T_{1e} (μs)	T_{1n} (μs)	b	Ref. ^c
Small nitroxides							
TANOL	SBB	-73	0.52	2.37			1
		31	0.014	0.38			1
TEMPONE	SBB	-60	0.21	2.25	0.6	3.5	1,2
		22	0.012	0.47			1
	Paraffin oil	20		0.61			3
	DMSO	20		0.77			3
	Water	20		0.64			3
DTBN	Paraffin oil	20		0.24			3
	DMSO	20		0.41			3
TEMPO	Paraffin oil	20		0.51			3
CTPO	Mineral oil	-5	43	1.7	0.7	2.4	4
		52	0.05	0.55	1.20	0.46	4
Lipid nitroxides							
16-SASL	DMPC	4		6			9
		27	0.9	2.25	0.16	13.8	5
		54		1.7	0.8	2.1	6
		57	0.2	1.2	1.0	1.2	5
		DOPC	54		1.6	0.7	2.2
CSL	DMPC	20		3.1			3
		27		4.2	0.37	11.3	8
	37		3.3	0.86	3.8	8	
	Paraffin oil	20		4.9			3
ASL	Paraffin oil	20		3.8			3
9-SASL	Paraffin oil	20		4.8			3
5-SASL	DMPC	4		8			9
		37		5			9
		45		3			10
TEMPO-PC	DMPC	4		5			10
		45		2.5			10

(continued)

Table 1
Continued

Nitroxide ^a	Environment	Temperature (°C)	τ_R^b (ns)	T_{1e} (μ s)	T_{1n} (μ s)	b	Ref. ^c
4-PCSL	DPPC	1		9			11
6-PCSL	DPPC	1		8.5			11
8-PCSL	DPPC	1		8			11
10-PCSL	DPPC	1		6			11
14-PCSL	DPPC	1		5			11
16-PCSL	DPPC	1		13			11
Protein nitroxides							
MSL-Hb	Water	20	20	4.1 ± 0.1			12
	Water	-20	∞	7			12
	88% Glycerol	21	2.10 ³	8.2 ± 0.1			12
	88% Glycerol	-4	2.10 ⁴	13.5 ± 0.5			12
	88% Glycerol	-37	2.10 ⁶	16.1 ± 0.2			12
	Precipitated	24	∞	7			12
¹⁵ N-MSL-Hb	Aqueous glycerol		1.1 × 10 ³	10.7	0.50	21.1	13
	Aqueous glycerol		1.5 × 10 ³	15.3	0.36	42.5	13

^aAbbreviations: TANOL, 4-hydroxy-2,2,6,6-tetramethylpiperidine-1-oxyl; TEMPONE, 2,2,6,6-tetramethylpiperidone-1-oxyl; DTBN, di-*tert*-butyl-nitroxide; TEMPO, 2,2,6,6-tetramethylpiperidine-1-oxyl; CTPO, 3-carbamoyl-2,2,5,5-tetramethyl-3-pyrroline-1-oxyl; n-SASL, n-(4,4-dimethyl-oxazolidine-*N*-oxyl)stearic acid; CSL, 4',4'-dimethylspiro[5 α -cholestane-3,2'-oxazolidin]-3'-yloxy; ASL, 17- β -hydroxy-4',4'-dimethylspiro[5 α -androstane-3,2'-oxazolidin]-3'-yloxy; TEMPO-PC, *N,N*-dimethyl-*N*-(2,2,6,6-tetramethyl-4-piperidinyl-1-oxyl)-phosphatidylethanolamine, n-PCSL, 1-acyl-2-[n-(4,4-dimethyl-oxazolidine-*N*-oxyl)]stearoyl-*sn*-glycero-3-phosphocholine; MSL, *N*-(1-oxyl-2,2,6,6-tetramethyl-4-piperidinyl)-maleimide, SBB, *sec*-butyl-benzene; DMSO, dimethylsulphoxide; DMPC, 1,2-dimyristoyl-*sn*-glycero-3-phosphocholine; DOPC, 1,2-dioleoyl-*sn*-glycero-3-phosphocholine; DPPC, 1,2-dipalmitoyl-*sn*-glycero-3-phosphocholine; Hb, hemoglobin.

Unless otherwise noted, data are for ¹⁴N-nitroxides.

^bWhere available the rotational correlation time τ_R is also given.

not required for nitroxides with rotational correlation times less than 10⁻⁴ s; presumably these mechanisms must become operative at yet lower temperatures.

Table 1 gives representative values of electron spin-lattice relaxation times for ¹⁴N-nitroxide spin labels. For small nitroxides in low-viscosity media, T_{1e} is about 0.4–0.7 μ s; for nitroxide-labeled lipids in fluid lipid bilayers, T_{1e} is about 1–5 μ s,

depending to some extent on the position of chain labeling. For nitroxide-labeled lipids in gel-phase bilayers, T_{1e} lies in the approximate range of 5–10 μs . For spin-labeled hemoglobin, T_{1e} increases from 4 μs to 16 μs over a range of rotational correlation times spanning five orders of magnitude, starting from the submicrosecond region. The value of 7 μs obtained for a frozen solution and for precipitated hemoglobin is however substantially less than that obtained for the longest rotational correlation time.

2.2. Nuclear Relaxation Mechanisms

The principal mechanism for spin label nuclear relaxation is modulation of the electron-nuclear dipolar (END) interaction. The ^{14}N relaxation rate for an END mechanism and isotropic rotational diffusion is given by (Dalton *et al.*, 1976; Freed, 1979):

$$W_n = \frac{1}{60} [(\Delta A)^2 + 3(\delta A)^2] \frac{\tau_R}{1 + \omega_a^2 \tau_R^2} \quad (13)$$

where ω_a ($\approx \frac{1}{2}a_N$) is the ^{14}N nuclear Larmor frequency, and the A-tensor (and the isotropic hyperfine constant a_N) are again specified as an angular frequency. Note: The coefficient in this equation is just one-fourth times that of the M_I^2 (i.e., END) term for the electron relaxation rate in Eq. (8).

A spin diffusion mechanism involving solvent nuclear spins can contribute to the nuclear relaxation of the spin label in much the same way as it does to the electron relaxation (Robinson *et al.*, 1994). The relaxation rate is given by an expression analogous to Eq. (11), with the electron Larmor frequency ω_e replaced by the ^{14}N nuclear resonance frequency ω_n ($\approx 6.3 \times 10^6 \text{ s}^{-1}$). The maximum contribution from this process occurs for a rotational correlation time (equal to the translational diffusion time) of $\tau_R = 2^{2/3}/\omega_n \approx 2.5 \times 10^{-7} \text{ s}$. Experiments on ^{15}N -hydroxy-TEMPO in aqueous glycerol show that this mechanism makes a significant contribution compared to END only for correlation times longer than approximately 1 μs (Robinson *et al.*, 1994).

Figure 4 shows the dependence on rotational correlation time of the nuclear relaxation rate of a small spin label CTPO in heavy mineral oil, derived from pulse ELDOR combined with saturation recovery measurements (Hyde *et al.*, 1984). The magnitude of the relaxation rates agrees roughly with that calculated for an END mechanism, but the dependence on rotational correlation time is much weaker than that predicted. Electron spin-lattice relaxation rates obtained in these experiments were comparable to those found for hydroxy-TEMPO in *sec*-butyl benzene (compare Fig. 3), again with a weak dependence on rotational correlation time ($T_{1e}^{-1} \propto \tau_R^{-0.3}$).

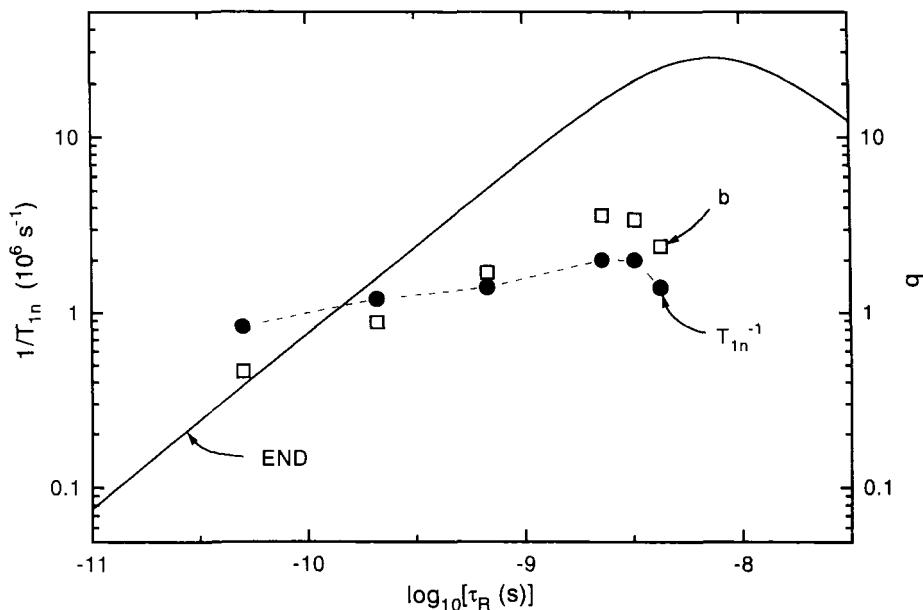


Figure 4. Dependence of the ^{14}N nuclear spin-lattice relaxation rate T_{1n}^{-1} of 3-carbamoyl-2,2,5,5-tetramethyl-3-pyrroline-1-oxyl (CTPO) on rotational correlation time τ_R in heavy mineral oil. The normalized nuclear relaxation rate $b = W_n/W_e$ is also shown. The solid line represents the calculated relaxation rate for an END mechanism according to Eq. (13). (Data from Hyde *et al.*, 1984)

Nuclear relaxation rates, normalized to the electron spin relaxation rates, were found to be in the range of $b \sim 0.5\text{--}5$ (Hyde *et al.*, 1984). Considerably larger values were reported for lipid spin labels in bilayer membranes: $b \sim 5\text{--}50$ (Popp and Hyde, 1982; Yin *et al.*, 1990). It appears that in many cases, nuclear relaxation is rapid relative to electron relaxation. For an END mechanism, the maximum ^{14}N nuclear relaxation rate $W_n^{END}(\text{max.}) \sim 2.8 \cdot 10^7 \text{ s}^{-1}$ is predicted to occur for a rotational correlation time of $\tau_R = 1/\omega_a \sim 7.4 \cdot 10^{-9} \text{ s}$.

For ^{15}N -hydroxy-TEMPO in aqueous glycerol, the ^{15}N nuclear relaxation was found to be dominated by an END mechanism for rotational correlation times shorter than $1 \mu\text{s}$; in this range it can be described essentially quantitatively by this mechanism (Robinson *et al.*, 1994). Over the entire correlation time range from 100 ps – $100 \mu\text{s}$, the nuclear relaxation can be accounted for by END and spin diffusion mechanisms. In all cases nuclear relaxation was faster than electron relaxation; values of b ranged from 4–600, with $b \approx 24$ for $\tau_R = 1 \mu\text{s}$.

Some representative values of the ^{14}N nuclear spin-lattice relaxation times for spin labels in different environments are collected in Table 1.

3. PARAMAGNETIC RELAXATION ENHANCEMENT

Coupling a nitroxide spin system with a fast-relaxing paramagnetic species (e.g., molecular oxygen or a paramagnetic ion) by either Heisenberg spin exchange or a magnetic dipole-dipole interaction increases the true spin-lattice relaxation rate rather than simply effecting a cross relaxation. The measurement of paramagnetic effects on the saturation behavior of the spin label is important in determining location/proximity relationships of the spin label in the case of Heisenberg spin exchange, or intermolecular separations in the case of the dipole-dipole interaction.

Because paramagnetic species produce a true spin-lattice relaxation sink, the steady-state rate equations for population differences between the energy levels of the spin label (compare Fig. 5) are given by Eqs. (2) and (3) with W_e replaced ($W_e + \omega_x$), where ω_x is the rate of the additional (paramagnetic) spin-lattice relaxation process (Marsh, 1995a). Effective spin lattice relaxation times, as determined by CW saturation methods for the $M_I = 0$ and $M_I = \pm 1$ hyperfine manifolds are, respectively (compare Subczynski and Hyde, 1981; Marsh, 1995a):

$$T_{1e}^{eff}(0, b''') = \frac{1 + b + b'''}{1 + 3b + b'''} \cdot \frac{1}{2W_e(1 + b''')} \tag{14}$$

and

$$T_{1e}^{eff}(\pm 1, b''') = \frac{(1 + b''')^2 + 3b(1 + b''') + b^2}{(1 + b + b''')(1 + 3b + b''')} \cdot \frac{1}{2W_e(1 + b''')} \tag{15}$$

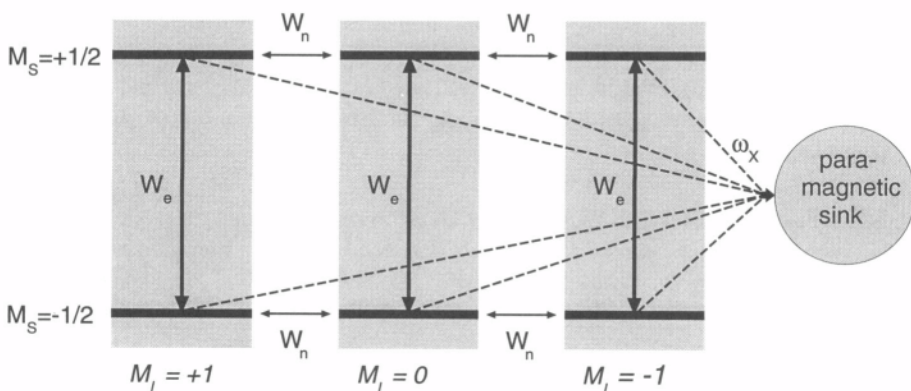


Figure 5. Energy level scheme for an $S = 1/2, I = 1, {}^{14}\text{N}$ -nitroxide spin label in the presence of a paramagnetic relaxation sink. The intrinsic electron spin-lattice relaxation rate W_e and the ${}^{14}\text{N}$ nuclear spin-lattice relaxation rate W_n are the same as in Fig. 2. Additional relaxation pathways with rates ω_x that arise from interaction with the fast relaxing paramagnetic species are indicated by dashed lines.

where as before the normalized nuclear relaxation rate is $b = W_n/W_e$, and $b''' = \omega_x/W_e$ is the normalized paramagnetic relaxation enhancement rate. Thus although the paramagnetic relaxation is a true T_1 -process, complications may arise in extracting the corresponding relaxation rate b''' if nuclear relaxation cannot be ignored. If paramagnetic relaxation is fast compared to the nuclear relaxation rate ($b''' > b$) and/or the nuclear relaxation rate is very slow compared to the electron relaxation rate ($b \ll 1$), then a simple spin-lattice relaxation enhancement is obtained: $T_1^{eff}(0, b''')^{-1} = T_1^{eff}(\pm 1, b''')^{-1} = 2W_e(1 + b''')$. Correspondingly if the nuclear relaxation rate is very fast ($b \gg b''', 1$), then: $T_1^{eff}(0, b''')^{-1} = T_1^{eff}(\pm 1, b''')^{-1} = 6W_e(1 + b''')$. The paramagnetic relaxation enhancement rate b''' can then be obtained in a straightforward manner.

In general the enhancement in relaxation rate of the spin label relative to the absence of the paramagnetic sink is given by:

$$\frac{T_1^{eff}(0)}{T_1^{eff}(0, b''')} = \frac{1 + b'''/(1 + 3b)}{1 + b'''/(1 + b)} \cdot (1 + b''') \quad (16)$$

and

$$\frac{T_1^{eff}(\pm 1)}{T_1^{eff}(\pm 1, b''')} = \frac{[1 + b'''/(1 + b)][1 + b'''/(1 + 3b)]}{1 + b'''(2 + 3b + b''')/(1 + 3b + b^2)} \cdot (1 + b''') \quad (17)$$

Thus for intermediate values of nuclear or paramagnetic relaxation rates, a knowledge of b from other experiments, such as ELDOR, may be required to determine an exact value for the paramagnetic relaxation enhancement from CW saturation experiments, if measurements are made at only one concentration of the relaxant. The correction factor, given by the first term on the right in Eqs. (16) and (17), in principle ranges from 1–0.333, but for useful values of the paramagnetic relaxation enhancement, it is restricted to values closer to 1 (see Fig. 6).

3.1. Paramagnetic Enhancement by Heisenberg Exchange

The enhancement in the spin-lattice relaxation rate of the spin label due to Heisenberg spin exchange interaction is linearly proportional to the concentration c_R of the relaxant; it is given by:

$$\omega_x = k_{RL} \cdot c_R \quad (18)$$

where k_{RL} is a rate constant dependent on the collisional kinetics and steric and electrostatic factors affecting the mutual accessibility of spin label and relaxant. In

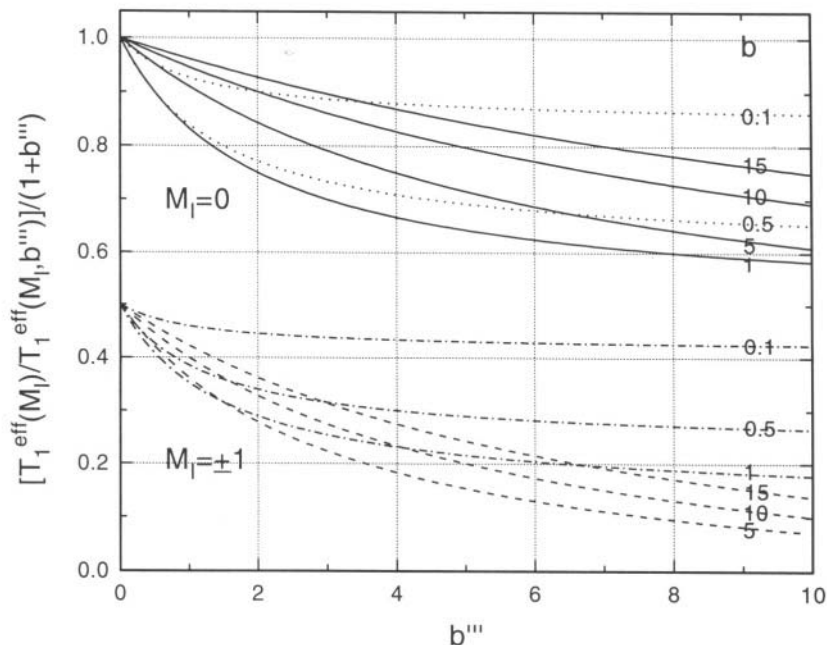


Figure 6. Dependence of the effective electron spin lattice relaxation rate $1/T_1^{\text{eff}}(M_I, b''')$ for a ^{14}N nitroxide spin label on the normalized paramagnetic relaxation enhancement $b''' = \omega_x/W_e$, calculated according to Eqs. (16) and (17) for the $M_I = 0$ and ± 1 nuclear manifolds, respectively. The relaxation rate is normalized to that in the absence of paramagnetic relaxation enhancement $1/T_1^{\text{eff}}(M_I)$ and to the value $1 + b'''$ expected for this normalized relaxation rate in the absence of nuclear relaxation. Upper curves are for the $M_I = 0$ nuclear manifold and various values of the normalized nuclear relaxation rate $b = W_n/W_e$; lower curves are correspondingly for the $M_I = \pm 1$ nuclear manifolds, and these were shifted downward by 0.5 for clarity. For $b = 0$, the ordinate has a constant value of 1. (Data from Marsh, 1995a)

general for fast exchange, this collision rate constant is given by the Smoluchowski solution of the diffusion equation:

$$k_{RL} = 4\pi\sigma_{RL}r_{RL}D_R \cdot \exp(-z_R e\psi_L/kT) \quad (19)$$

where D_R is the translational diffusion coefficient of the relaxant (that of the spin-labeled system is assumed to be negligible by comparison), r_{RL} is the interaction distance between relaxant and spin label, σ_{RL} is a steric factor, $z_R e$ is the electrical charge on the relaxant, and ψ_L is the electrostatic surface potential of the spin-labeled system.

For molecular oxygen as the paramagnetic relaxant, $r_{RL} \approx 4.5 \text{ \AA}$ (Windrem and Plachy, 1980), and the diffusion coefficient in water at 37°C , obtained with $\sigma_{RL} = 1$, is $D_{o_2} = 2.8 \cdot 10^{-5} \text{ cm}^2 \cdot \text{s}^{-1}$ (Hyde and Subczynski, 1984). In fluid lipid bilayers, the diffusion coefficient is not much smaller: $D_{o_2} = 1 - 1.8 \cdot 10^{-5} \text{ cm}^2 \cdot \text{s}^{-1}$ in dimyristoyl phosphatidylcholine at 40°C (Subczynski and Hyde, 1981). Thus for oxygen where exchange is diffusion-controlled, the bimolecular rate constant is in the region of $10^{10} \text{ M}^{-1} \cdot \text{s}^{-1}$ (Subczynski and Hyde, 1984). For a detailed discussion of the application of such methods in spin label oximetry, see Hyde and Subczynski (1989); this includes consideration of the factor p , which represents the probability that a productive exchange event occurs on collision, and is expected to be close to unity for strong exchange (Molin *et al.*, 1980).

For paramagnetic ions, electrostatic effects may play an important role in controlling collisional kinetics. Second-order exchange rate constants for small uncharged spin labels and paramagnetic ions (or small paramagnetic complexes) lie in the range of $1 - 3 \cdot 10^9 \text{ M}^{-1} \cdot \text{s}^{-1}$ (Molin *et al.*, 1980); examples of data for electrostatic effects are found in the same reference. Shin and Hubbell (1992) apply the method to measuring electrostatic surface potentials by using spin label EL-DOR.

3.2. Paramagnetic Enhancement by Magnetic Dipole-Dipole Interactions

Fast relaxing paramagnetic ions can contribute to the T_1 relaxation of spin labels not only by the contact exchange interaction, but also through the distance-dependent magnetic dipole-dipole interaction. For molecular oxygen, the contribution of dipole-dipole interactions to the relaxation enhancement is thought to be negligible (Subczynski and Hyde, 1981), but this is not the case for paramagnetic ions—especially if these do not contact the spin label directly. For the static limit, the paramagnetic dipolar contribution to the spin label relaxation is given by (Bloembergen, 1949; Solomon, 1955):

$$2\omega_x = g_{pm}^2 \beta^2 S(S+1) \gamma_e^2 \times \sum_k \frac{|F_0(\theta_k)|^2 J(\omega_M - \omega_e) + |F_1(\theta_k)|^2 J(\omega_e) + |F_2(\theta_k)|^2 J(\omega_M + \omega_e)}{r_k^6} \quad (20)$$

where r_k is the distance of the k th paramagnetic ion from the spin label center; ω_e and ω_M are the electron Larmor frequencies of the spin label and paramagnetic ion, respectively; g_{pm} and S are the g -value and spin of the paramagnetic ion, respectively; and γ_e is the electron gyromagnetic ratio of the spin label. Terms depending on the angle θ_k between the interdipole vector and the static magnetic field direction

are related to the absolute values of the corresponding spherical harmonics; spectral densities are defined by: $J(\omega) = T_{1pm}/(1 + \omega^2 T_{1pm}^2)$ where T_{1pm} is the spin-lattice relaxation time of the paramagnetic ion. See Bertini and Luchinat (1986) for typical values for the latter. The static dipolar limit holds except when the spin label and relaxant are diffusing very rapidly relative to one another (Pfeifer, 1961, 1963). Methods for discriminating between static and diffusional dipolar mechanisms are considered in Páli *et al.* (1992).

If the angular dependence in Eq. (20) is neglected relative to the steep distance dependence of the dipolar interaction (of. Hyde *et al.*, 1979), integration over the paramagnetic ion distribution yields a linear dependence of the relaxation enhancement on the paramagnetic ion concentration, i.e., a form similar to that given in Eq. (18). The strength of the concentration dependence of the paramagnetic relaxation enhancement is then given in terms of Eq. (18) by (Páli *et al.*, 1992):

$$2k_{RL} = f^o \int \frac{d^3r}{|r|^6} = \frac{f_m}{R^m} \quad (21)$$

where R is the distance of closest approach of the paramagnetic ions to the spin label, and f^o and f_m are constants that contain all other parameters in Eq. (20). The exponent m depends on the dimensionality of the paramagnetic ion distribution: $m = 3$ for a three-dimensional distribution, and $m = 4$ for an adsorbed surface layer. Figure 7 shows these two cases for spin labels situated within the lipid chain region of a biological membrane with paramagnetic ions in the aqueous environment. For spherically symmetric systems, values of $f_3/f^o = 4\pi/3$ and $f_4/f^o = 4\pi K$ are obtained, where K is effectively a binding constant of the paramagnetic ions to the surface in the latter case. If the angular dependences are neglected, then for a planar surface defining the distance of closest approach, values of $f_3/f^o = \pi/6$ and $f_4/f^o = K\pi/2$ are obtained. In the case of spherically symmetrical systems, the angular integrals can be readily obtained to yield the coefficients appearing in the Solomon-Bloembergen equation (Bertini and Luchinat, 1986). If we assume that the paramagnetic ion relaxation is very fast, the spectral densities can be approximated by $J(\omega) \approx T_{1pm}$. The Solomon-Bloembergen equation then yields the following approximation for f^o in spherically symmetrical systems:

$$f^o \approx \left(\frac{4}{3}\right) g_{pm}^2 \beta^2 S(S+1) \gamma_e^2 T_{1pm} N_A \cdot 10^{-3} \quad (22)$$

where β is the Bohr magneton, N_A is Avogadro's number, and the paramagnetic ion concentration is expressed in molar units.

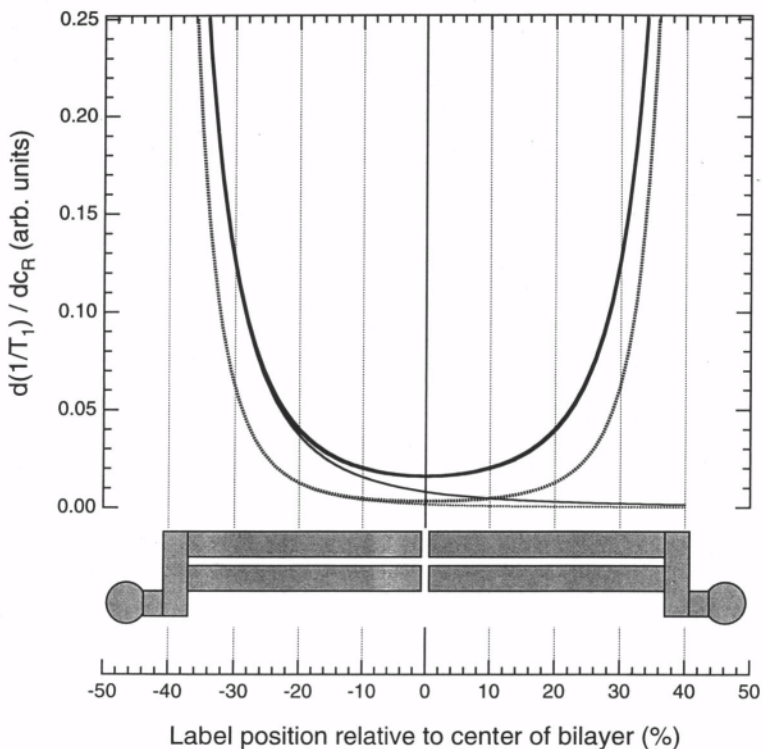


Figure 7. Illustration of the positional dependence of the dipolar spin-lattice relaxation enhancement $d(1/T_1)/dc_R$ of spin labels located in the interior of a bilayer membrane by external paramagnetic relaxants. *Solid lines*: Three-dimensional distribution of external relaxants ($m=3$). *Dotted lines*: Surface distribution of relaxants ($m=4$). The relaxation enhancement of the spin label by magnetic dipole-dipole interaction with the fast relaxing paramagnetic species is calculated from Eq. (21). *Bold lines*: Symmetric distribution of relaxants. *Light lines*: Relaxants restricted to the left-hand side.

4. SPIN-LATTICE RELAXATION ENHANCEMENT BY EXCHANGE PROCESSES

Exchange processes can alleviate saturation in spin label EPR spectra. This occurs either by transferring spin polarization in the case of physical or chemical exchange, or by mutual antiparallel spin flips (cross relaxation) in the case of Heisenberg exchange (see Fig. 8). Two different situations can be distinguished: Exchange between spin labels at two distinct sites and concentration-dependent Heisenberg exchange between spin labels of the same type. Measurements of spin label saturation behavior can therefore be used to determine rates of

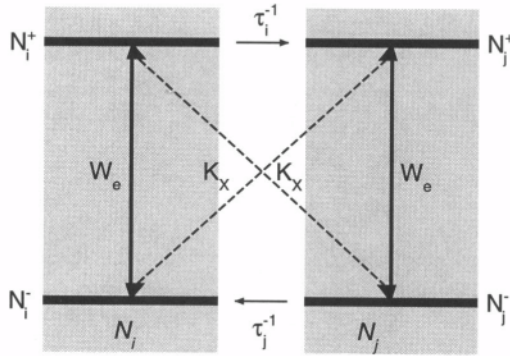
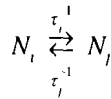


Figure 8. Energy levels, spin populations (N_i^\pm), and transitions for two spin environments i and j in an EPR line shape. Hyperfine structure is not included; i.e., nuclear relaxation is neglected. The spin population difference is given by $n_i = N_i^- - N_i^+$. The transition rate for spin-lattice relaxation is $2W_e = 1/T_1^0$. The rate of Heisenberg spin exchange between spins i and j is $2K_x N_i^\pm N_j^\mp$; that for chemical (or physical) exchange is $N_i \tau_i^{-1} = N_j \tau_j^{-1}$.

physical exchange; frequencies of collision, and hence translational diffusion rates; and in the case of different spin-labeled species, mutual accessibilities and locations.

Formally physical exchange between inequivalent sites and the Heisenberg spin exchange between spin labels in inequivalent states are indistinguishable (Eastman *et al.*, 1969; Marsh, 1992b). Physical exchange between two general sites i and j is considered first:



where τ_i^{-1} is the rate of transfer per unit time from site i and τ_j^{-1} that from site j (compare Fig. 8). If N_i is the total spin population at site i and N_j that at site j , then the rate constants are related by detailed balance:

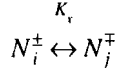
$$N_i \tau_i^{-1} = N_j \tau_j^{-1} = N_i N_j K_E \tag{23}$$

where K_E is a constant. Because physical exchange occurs with conservation of spin orientation, the rate equation for the population difference at site i is given by:

$$\frac{dn_i}{dt} = -(n_i \tau_i^{-1} - n_j \tau_j^{-1}) \tag{24}$$

and similarly for the population difference at site j .

The situation for Heisenberg spin exchange is somewhat more complicated. Heisenberg exchange between spin labels at the two sites takes place between spins of opposite orientations (i.e., cross relaxation):



where K_x is the bimolecular rate constant for spin exchange (compare Fig. 8). The net rate equation for the population difference at site i is therefore:

$$\frac{dn_i}{dt} = -2K_x(N_i^-N_j^+ - N_i^+N_j^-) \quad (25)$$

where N_i^{\pm} are the spin populations of the $M_{S_i} = \pm 1/2$ energy levels and similarly for N_j^{\pm} . This equation can be rewritten in terms of population sums and differences as (Marsh, 1992b):

$$\frac{dn_i}{dt} = -K_x(N_i n_i - N_j n_j) \quad (26)$$

where $N_i = N_i^+ + N_i^-$, and similarly for N_j ; a similar rate equation can be derived for the population difference at site j . The exchange frequency is defined in the usual bimolecular formalism by $\tau_{ex}^{-1} = K_x(N_i + N_j)$. We then see that Eqs. (24) and (26) are formally equivalent, with identities $\tau_i^{-1} = f_j \tau_{ex}^{-1}$ and $\tau_j^{-1} = f_i \tau_{ex}^{-1}$ [where the fractional population is $f_i = N_i/(N_i + N_j)$ and similarly for f_j], which are fully consistent with Eq. (23). Alternatively Eq. (24) can be expressed in the same form as Eq. (26) by replacing K_x with K_E . Thus only one of the two cases must be considered to cover both. For convenience the physical exchange formalism is adopted in treating two-site exchange, and the Heisenberg exchange formalism is adopted for spin exchange between a single species.

4.1. Two-Site Exchange

To differentiate from the general case, the two sites undergoing exchange are designated b and f . If spin transitions at site b are induced by the H_1 microwave field, the net steady-state condition for the spin population difference at this site is

$$\frac{dn_b}{dt} = -2Wn_b + \frac{(n_b^0 - n_b)}{T_{1,b}^0} - n_b \tau_b^{-1} + n_f \tau_f^{-1} = 0 \quad (27)$$

where the first term on the right represents transitions induced by the microwave field, the second is the spin-lattice relaxation, and the final terms represent the exchange between sites (compare Fig. 8). The corresponding steady-state condition for spins at site f which is not irradiated by the microwave field is

$$\frac{dn_f}{dt} = \frac{(n_f^0 - n_f)}{T_{1,f}^0} - n_f \tau_f^{-1} + n_b \tau_b^{-1} = 0 \quad (28)$$

Solving Eqs. (27) and (28), together with Eq. (23), which also holds for population differences, yields the standard expression for saturation of the spin system at site b ; i.e., Eq. (1), where the effective spin-lattice relaxation time $T_{1,b}^{eff}$ at site b is given by (compare Marsh, 1993; Horváth *et al.*, 1993a):

$$\frac{T_{1,b}^0}{T_{1,b}^{eff}} = 1 + \frac{T_{1,b}^0 \tau_b^{-1}}{1 + T_{1,f}^0 \tau_f^{-1}} \quad (29)$$

This equation can be expressed in terms of a single exchange rate by means of the following relation for detailed balance derived from Eq. (23): $f_b \tau_b^{-1} = f_f \tau_f^{-1}$, where f_b and f_f are the fractional spin populations at sites b and f , respectively ($f_b + f_f = 1$), for two-site exchange. The corresponding result for two-site Heisenberg spin exchange is (Snel and Marsh, 1994):

$$\frac{T_{1,b}^0}{T_{1,b}^{eff}} = 1 + \frac{f_f T_{1,b}^0 \tau_{ex}^{-1}}{1 + f_b T_{1,f}^0 \tau_{ex}^{-1}} \quad (30)$$

which is obtained from the identities between the exchange rates in the two cases. Equivalent expressions can be derived for site f by permutating the indices in Eqs. (29) and (30).

Contributions that nuclear relaxation may make to effective spin-lattice relaxation times of spin labels undergoing two-site exchange (compare Sec. 1.2) were considered by Marsh (1995b). Effective spin-lattice relaxation times for the $M_I = 0$ and $M_I = \pm 1$ hyperfine manifolds of the spin label at site b are found to be given by, respectively:

$$T_{1,b}^{eff}(0) = \frac{1 + (T_{1,b}^{(2,si)}/T_{1,b}^0)b}{1 + 3(T_{1,b}^{(2,si)}/T_{1,b}^0)b} \cdot T_{1,b}^{(2,si)} \quad (31)$$

$$T_{1,b}^{eff}(\pm 1) = \left[1 + \left(\frac{b}{1+b} \right) \frac{1}{1 + (T_{1,b}^{(2,si)}/T_{1,b}^0)b} \right] T_{1,b}^{eff}(0) \quad (32)$$

where $T_{1,b}^{(2,si)}$ is the effective spin-lattice relaxation time for two-site exchange ignoring nuclear relaxation that is given by Eq. (29), and $b = W_{n,b}/W_{e,b}$ is the ratio of the nuclear to the electron spin-lattice relaxation rate for the spin label at site b . Figure 9 shows the relaxation enhancement by two-site exchange in the presence of nuclear relaxation $T_{1,b}^{(n)}(M_I)/T_{1,b}^{eff}(M_I)$, where $T_{1,b}^{(n)}(M_I)$ is the effective spin-lattice relaxation time in the presence of nuclear relaxation but in the absence of two-site

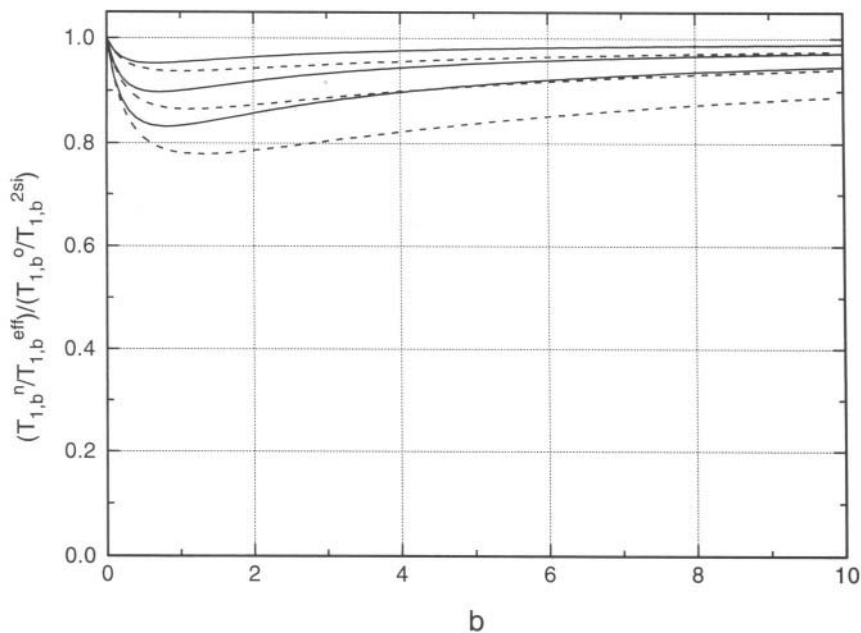


Figure 9. Dependence of the effective electron spin lattice relaxation rate $1/T_{1,b}^{eff}$ for two-site exchange in the presence of nuclear relaxation relative to that for a simple two-site exchange model $1/T_{1,b}^{(2si)}$ on the normalized nuclear relaxation rate b for a ^{14}N nitroxide spin label ($I = 1$). Effective relaxation rates $1/T_{1,b}^{eff}$ are obtained from Eqs. (31) or (32). Values for $1/T_{1,b}^{(n)}$ and $T_{1,b}^{(2si)}$ are normalized to the corresponding values [$1/T_{1,b}^{(n)}$ and $1/T_{1,b}^o$, respectively] in the absence of two-site exchange. Solid lines denote $M_1 = 0$ and dashed lines for $M_1 = \pm 1$. From upper to lower, each set of curves corresponds to $T_{1,b}^o/T_{1,b}^{(2si)} = 1.2, 1.5$ and 2.0 . (Data from Marsh, 1995b)

exchange [Eqs. (4) and (5)]. The rate enhancement is normalized relative to that for two-site exchange in the absence of nuclear relaxation $T_{1,b}^o/T_{1,b}^{(2si)}$ given by Eq. (29). It appears that over most of the likely range of nuclear relaxation rates (compare Sec. 2.2), the simple model neglecting nuclear relaxation [Eq. (29)] provides a reasonable approximation. Effects of internal exchange processes at a single site (and equivalently of rotational diffusion) on the effective spin-lattice relaxation times of spin labels undergoing two-site exchange are considered in a later section dealing with Heisenberg spin exchange in the general (i.e., multisite) case.

Equations (29) and (30) are exactly of the form required for analyzing progressive saturation or saturation transfer measurements. If the ratio $T_{1,j}^0/T_{1,b}^0$ is known, e.g., from the ratio of the saturation transfer EPR intensities in the absence of exchange, the effective T_1 can be expressed solely in terms of a single dimensionless exchange rate, e.g., $T_{1,b}^0\tau_b^{-1}$. Depending on conditions, useful sensitivity can be obtained for exchange rates up to five times the intrinsic spin-lattice relaxation rate.

The greatest sensitivity is found at low exchange rates less than the intrinsic spin-lattice relaxation rate (Marsh, 1993).

4.2. Heisenberg Spin Exchange

We now consider the effects of Heisenberg spin exchange between spin labels of a single species on their EPR saturation properties. In contrast to the two-site case, many different distinct transitions are coupled by exchange. These may correspond to different hyperfine states or to different orientations of the spin labels relative to the external magnetic field direction in a powder sample (see Fig. 10). Equation (26) must then be summed over all states j with which the state i is exchanging. The general steady-state rate equation for the population difference of the i th transition is then (Marsh, 1992b):

$$\frac{dn_i}{dt} = -2Wn_k\delta_{i,k} + \frac{(n_i^0 - n_i)}{T_1^0} - K_x(Nn_i - N_in) \quad (33)$$

where $N = \sum_j N_j$ and $n = \sum_j n_j$. In Eq. (33) transitions are assumed to be induced by the microwave field in the k th spin system; i.e., $\delta_{i,k} = 1$ for $i = k$ and is zero otherwise. Summing Eq. (33) over all i gives the following relation:

$$-2Wn_k + \frac{(\sum n_i^0 - n)}{T_1^0} = 0 \quad (34)$$

Solving Eqs. (33) and (34) for $i = k$ yields the standard expression for saturation of the k th spin system, i.e., Eq. (1), with the effective spin-lattice relaxation time given by (Marsh, 1992b):

$$T_{1,k}^{eff} = \frac{T_1^0(1 + Z_k T_1^0 \tau_{ex}^{-1})}{(1 + T_1^0 \tau_{ex}^{-1})} \quad (35)$$

where the exchange frequency is $\tau_{ex}^{-1} = K_x N$, and $Z_k = N_k/N$ is the fractional population (or degeneracy) of the transition being saturated. This equation was also derived quantum mechanically for exchange between hyperfine manifolds under the condition that nuclear relaxation can be neglected (Eastman *et al.*, 1969). For powder saturation transfer EPR spectra from unoriented systems (e.g., membranes), this relaxation enhancement reduces the intensity of the spectrum without appreciable changes in line shape (see Fig. 10 and Marsh and Horváth, 1992a).

Figure 11 shows the dependence of the reduction in effective spin-lattice relaxation time predicted from Eq. (35) on the Heisenberg spin exchange frequency. When the exchange frequency is low ($T_1^0 \tau_{ex}^{-1} \ll 1$), a linear relation is obtained.

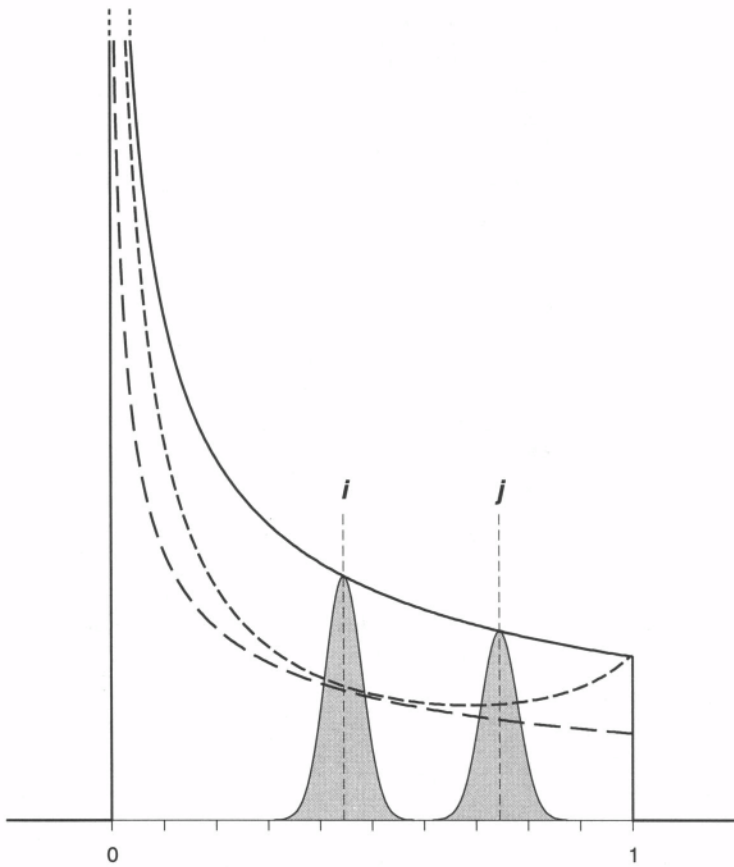


Figure 10. Exchange between spin packets i and j in a powder spectral line shape from randomly oriented spin labels. A given spin packet i undergoes Heisenberg spin exchange with all other spin packets j . This results in a powder line shape given by the long-dashed line (see Marsh and Horváth, 1992a). For rotational diffusion, a spin packet at position i undergoes an angular displacement to position j , where the size of the displacement depends on the diffusion mechanism. For Brownian diffusion, this produces a powder line shape given by the short-dashed line (see Marsh and Horváth, 1992a).

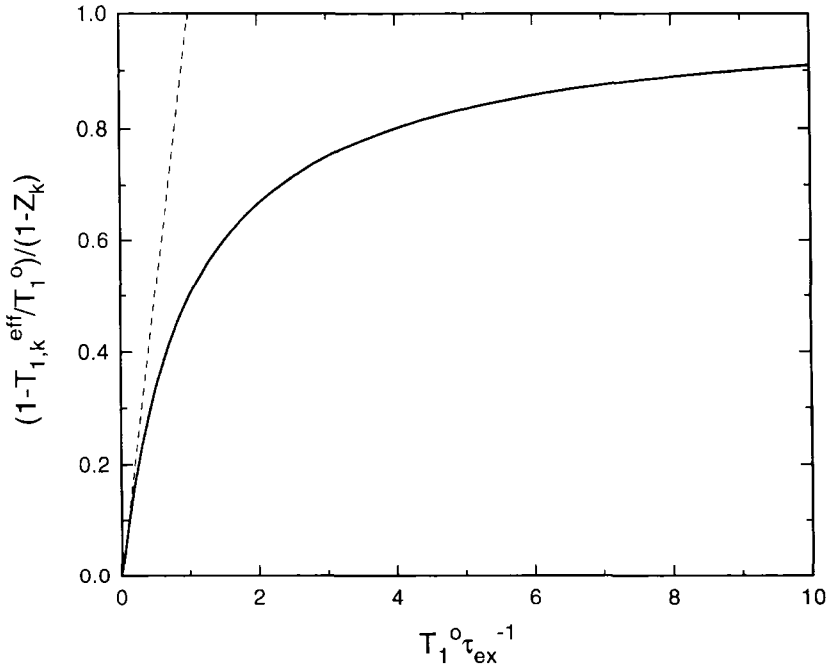


Figure 11. Dependence of the normalized reduction in effective spin-lattice relaxation time $(1 - T_{1,k}^{eff}/T_1^0)$ on the scaled Heisenberg spin exchange frequency $T_1^0 \tau_{ex}^{-1}$ obtained from Eq. (35). The ordinate is expressed in terms of the redistribution factor $(1 - Z_k)$. At high exchange rates, the normalized reduction in effective T_1 reaches a limiting value of 1. The dashed line indicates the initial linear dependence on exchange frequency. (Data from Marsh and Horváth, 1992a)

When the degree of degeneracy is also high (i.e., $Z_k \approx 0$), Heisenberg exchange has the effect expected for a true relaxation enhancement rather than a cross relaxation, because the redistribution of saturation between the different exchange-coupled states does not limit the effective relaxation. In this limiting case, the effective relaxation rate is given by the following expression:

$$\frac{1}{T_1^{eff}} = \frac{1}{T_1^0} + \tau_{ex}^{-1} \quad (36)$$

This is found to be applicable in many cases of interest when the exchange frequency is low. At high exchange frequencies, on the other hand, $T_{1,k}^{eff}$ tends to a limiting value of $Z_k T_1^0$ that represents the maximum redistribution of saturation throughout the various distinct spin label states. Beyond this limit, the spin-spin relaxation time T_2 becomes sensitive to the spin exchange process, so the exchange

frequency can be determined conventionally from line widths and line shapes of the in-phase EPR spectra (Marsh, 1989).

Possible contributions from nuclear relaxation to the effective spin-lattice relaxation time of spin labels undergoing Heisenberg exchange are considered by Marsh (1992b). Effective spin-lattice relaxation times for the $M_I = 0$ and $M_I = \pm 1$ hyperfine manifolds are found to be, respectively:

$$T_{1,k}^{eff}(0) = T_1^0 \frac{[1 + Z_k T_1^0 \tau_{ex}^{-1} + b(1 + 3Z_k T_1^0 \tau_{ex}^{-1}) / (1 + T_1^0 \tau_{ex}^{-1})]}{1 + T_1^0 \tau_{ex}^{-1} + 3b} \quad (37)$$

$$T_{1,k}^{eff}(\pm 1) = T_{1,k}^{eff}(0) + \frac{bT_1^0}{(1 + T_1^0 \tau_{ex}^{-1} + 3b)(1 + T_1^0 \tau_{ex}^{-1} + b)} \quad (38)$$

In general for equivalent intrinsic rates, nuclear relaxation is far less effective in alleviating saturation than is Heisenberg exchange. This is because the $\Delta M_I = \pm 1$ END selection rule is far more restrictive than that for Heisenberg exchange, for which there is no restriction. Nuclear relaxation exerts its maximum effect for the $M_I = 0$ manifold in an isotropic spectrum. Then it is equivalent to Heisenberg exchange, and Eq. (35) applies with T_1^0 replaced by $T_{1,n}^{0,n}$ [given by Eq. (4)]; the exchange rate is scaled by the factor $1/(1 + b)$ and the degeneracy factor $Z_k = 1/3$ by the factor $(1 + 3b)/(l + b)$. For further discussion, see Marsh (1992b).

The situation of internal (Heisenberg) exchange at a single site for spin labels undergoing two-site exchange has also been analyzed (Marsh, 1995b). For the case when two-site exchange takes place only between equivalent spins at the two sites (e.g., preserving angular orientation), the effective spin-lattice relaxation time is given by Eq. (35), where $T_{1,b}^0$ is replaced by $T_{1,b}^{(2si)}$ from Eq. (29) for two-site exchange in the absence of internal exchange. The effective relaxation time in the presence of Heisenberg exchange and two-site exchange is therefore:

$$T_{1,b,k}^{eff} = \frac{1 + Z_{b,k} T_{1,b}^{(2si)} \tau_{ex,b}^{-1}}{1 + T_{1,b}^{(2si)} \tau_{ex,b}^{-1}} \cdot T_{1,b}^{(2si)} \quad (39)$$

Internal (Heisenberg) exchange rates can then be extracted in the normal way, yielding values $T_{1,b}^{(2si)} \tau_{ex,b}^{-1}$, which are normalized by the effective spin-lattice relaxation time for two-site exchange in the absence of Heisenberg exchange. Viewed from the standpoint of the two-site exchange process, the relaxation rate enhancement $T_{1,b}^{(x)} / T_{1,b}^{eff}$, where $T_{1,b}^{(x)}$ is the effective spin-lattice relaxation time in the presence of internal (Heisenberg) exchange [Eq. (35)] but in the absence of two-site exchange is given in Fig. 12. The rate enhancement is normalized relative to that for two-site exchange in the absence of internal exchange $T_{1,b}^0 / T_{1,b}^{(2si)}$, which is given by Eq. (29). If the restriction that exchange takes place only between

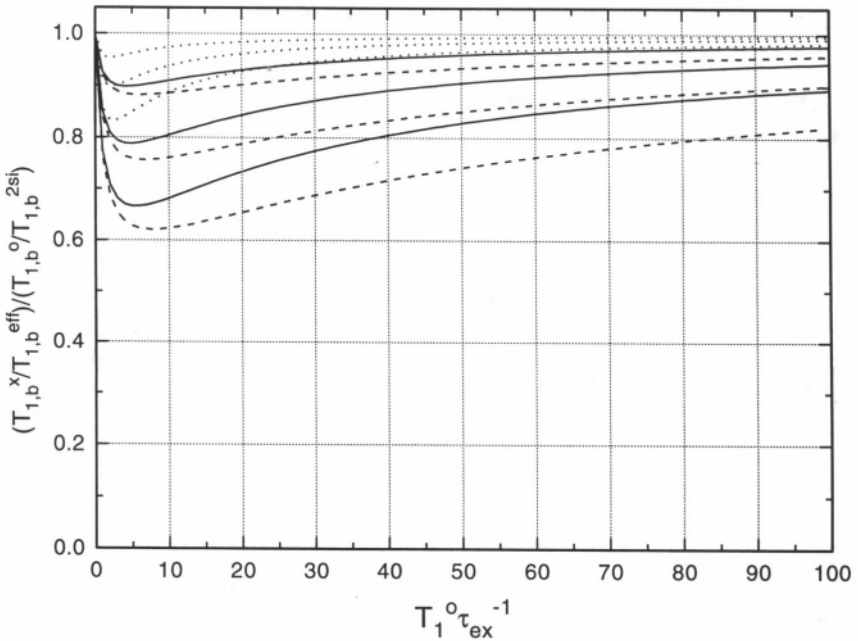


Figure 12. Dependence of the effective electron spin-lattice relaxation rate $1/T_{1,b}^{eff}$ for two-site exchange in the presence of internal exchange, relative to that for a simple two-site exchange model $1/T_{1,b}^{(2si)}$, on the normalized internal exchange frequency $T_{1,b}^0 \tau_{ex}^{-1}$. Effective relaxation rates $1/T_{1,b}^{eff}$ are obtained from Eq. (39). Values for $1/T_{1,b}^{eff}$ and $1/T_{1,b}^{(2si)}$ are normalized to the corresponding values ($1/T_{1,b}^{(x)}$ and $1/T_{1,b}^0$, respectively) in the absence of two-site exchange. (----) for $Z_{b,k} = 1/30$, (—) for $Z_{b,k} = 1/15$, and (····) for $Z_{b,k} = 1/3$. From upper to lower, each set of curves corresponds to $T_{1,b}^0/T_{1,b}^{(2si)} = 1.2, 1.5$ and 2.0 . (Data from Marsh, 1995b)

equivalent spins at the two sites is lifted, then the effective spin-lattice relaxation time is given by a similar expression except that the Heisenberg spin exchange frequency is augmented by a term that depends on the two-site exchange, being replaced by:

$$\tau_{ex,b}^{*-1} = \tau_{ex,b}^{-1} + \frac{T_{1,f}^0 \tau_f^{-1}}{1 + T_{1,f}^0 \tau_f^{-1}} \cdot \tau_b^{-1} \tag{40}$$

This expression is substituted for $\tau_{ex,b}^{-1}$ in Eq. (39). These considerations are important for extracting Heisenberg exchange frequencies in systems undergoing two-site exchange and for determining rates of two-site exchange in the presence of internal exchange processes (or rotational diffusion). For further discussion, see Marsh (1995b).

5. CONTINUOUS WAVE SATURATION MEASUREMENTS

There are two main methods for determining effective spin-lattice relaxation times from continuous wave EPR spectroscopy. The first and standard method uses progressive saturation of the conventional EPR spectrum with increasing microwave power. The second and more novel method uses intensities of the nonlinear EPR spectra that are detected in phase quadrature with respect to the field modulation.

5.1. Progressive Saturation EPR

The rate W of spin transitions induced by the microwave field is given from standard radiation theory by (Portis, 1953):

$$W = \left(\frac{\pi}{2} \right) \gamma_e^2 H_1^2 g(\omega - \omega_k) \quad (41)$$

where γ_e is the electron gyromagnetic ratio, ω is the angular microwave frequency, and $g(\omega - \omega_k)$ is the line shape function for the spin packet centered at ω_k . This is the quantity required to express the microwave power dependence of the EPR saturation under CW-irradiation given in Eq. (1).

Because the EPR absorption is proportional to both W and the spin population difference n_k (i.e., to the microwave susceptibility) given by Eq. (1), the line height of the absorption spectrum is given by (compare Portis, 1953):

$$a(\omega - \omega_k) = a_0 g(\omega - \omega_k) / [1 + \pi \gamma_e^2 H_1^2 g(\omega - \omega_k) T_{1,k}^{eff}] \quad (42)$$

where the absorption line height in the absence of saturation is obtained by setting $T_{1,k}^{eff} = 0$. For Lorentzian spin packets, as is the usual case, the normalized line shape is given by:

$$g(\omega - \omega_k) = \frac{(T_{2,k}/\pi)}{[1 + (\omega - \omega_k)^2 T_{2,k}^2]} \quad (43)$$

where $T_{2,k}$ is the transverse (spin-spin) relaxation time. From Eqs. (42) and (43), saturation of the absorption line shape for a homogeneously broadened Lorentzian resonance is given by:

$$a(\omega - \omega_k) = \frac{a_0}{\sqrt{1 + \sigma_k^{eff}}} \cdot \frac{(T_{2,k}/\sqrt{1 + \sigma_k^{eff}})/\pi}{[1 + (\omega - \omega_k)^2 (T_{2,k}/\sqrt{1 + \sigma_k^{eff}})^2]} \quad (44)$$

where $\sigma_k^{eff} = \gamma_e^2 H_1^2 T_{1,k}^{eff} T_{2,k}$ is the effective saturation parameter. Therefore for a homogeneously broadened resonance, the line shape remains Lorentzian during saturation. The integrated intensity of the resonance is reduced by a factor of

$1/(1 + \sigma_k^{eff})^{1/2}$ and line width is increased by a factor of $(1 + \sigma_k^{eff})^{1/2}$ with progressively increasing microwave power. The saturation behavior of the maximum amplitude of the n th derivative spectrum for a homogeneously broadened line is given from Eq. (44) by:

$$S_k^{(n)} = \frac{S_{0,k}^{(n)}}{(1 + \sigma_k^{eff})^{n/2+1}} \tag{45}$$

where $S_{0,k}^{(n)}$ is the value that the maximum amplitude has if there were no saturation. For the absorption maximum, $n = 0$, and Eq. (45) also holds for saturation of the integrated intensity of the absorption with $n = -1$.

Figure 13 shows dependences of the degree of saturation of the integrated intensity, absorption maximum, and peak line height of the first-derivative for a homogeneously broadened line. The different extents of saturation of the line height displays relative to integrated intensity arise from the progressively increasing

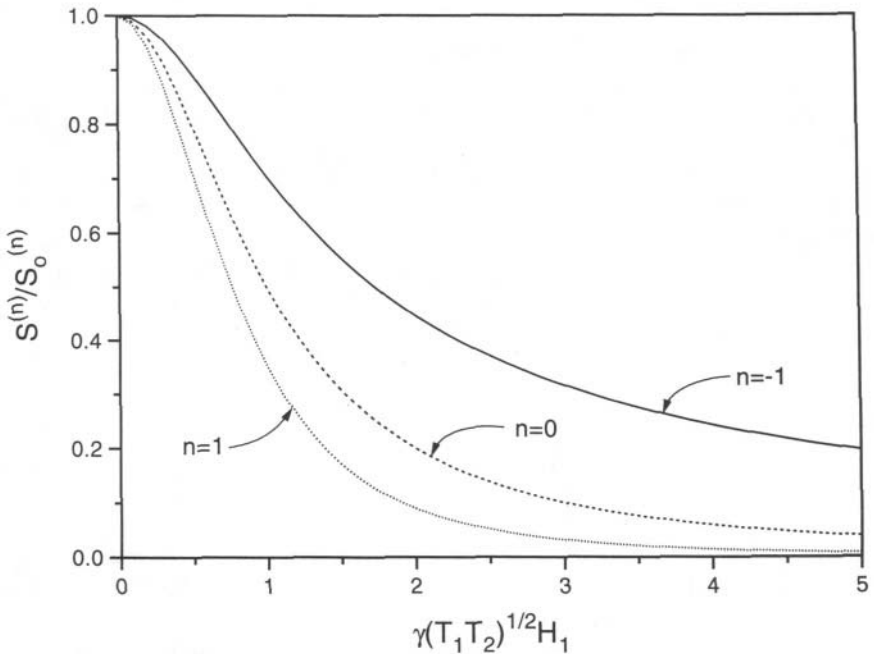


Figure 13. Dependence of the degree of saturation $S^{(n)}/S_0^{(n)}$ from Eq. (45) on the scaled microwave H_1 -field for the saturation of the integrated absorption (solid line, $n = -1$), absorption line height (dashed line, $n = 0$), and first derivative of the absorption (dotted line, $n = 1$) for a homogeneously broadened line. For the integrated absorption, the saturation behavior remains the same in the presence of inhomogeneous broadening but not for the two line height displays.

Lorentzian broadening induced by saturation. For inhomogeneously broadened lines in which inhomogeneous broadening completely outweighs saturation broadening, all line height displays saturate simply as does the integrated intensity [i.e., with $n = -1$ in Eq. (45)]. Frequently with spin labels in randomly oriented systems, we are dealing with an isotropic powder line shapes whose outer wings of the first derivative spectra are those of the absorption line shape; these also saturate as does the absorption (i.e., with $n = 0$ for homogeneous broadening) rather than exhibiting normal first-derivative behavior (Fajer *et al.*, 1992).

Because individual spin packets saturate independently and contribute additively to the total intensity, the integrated intensity saturates as $1/(1 + \sigma_k^{eff})^{1/2}$ irrespective of the degree of inhomogeneous broadening. This also holds for anisotropic powder patterns if anisotropy in T_1 and T_2 may be neglected (Páli *et al.*, 1993a). For inhomogeneously broadened lines, the spin packets k are distributed according to a normalized envelope function $h(\omega_k - \omega_o)$ centered about ω_o . The absorption EPR line shape for a randomly oriented sample with axial anisotropy is then given by (compare Fajer *et al.*, 1992):

$$A_{inh}(\omega, H_1) = \int_{\omega_{\perp}}^{\omega_{\parallel}} \int_{-\infty}^{\infty} I(\omega_o) \cdot h(\omega_k - \omega_o) \cdot a(\omega - \omega_k, H_1) \cdot d\omega_k \cdot d\omega_o \quad (46)$$

where $I(\omega_o)$ is the distribution of inhomogeneously broadened lines corresponding to the different orientations with respect to the static magnetic field direction. This distribution ranges from $\omega_o = \omega_{\perp}$ to $\omega_o = \omega_{\parallel}$, which are the resonance positions corresponding to the static magnetic field oriented perpendicular and parallel, respectively, to the principal magnetic axis of the spin system. The total integrated intensity of the absorption (or equivalently the double integral of the first-derivative EPR display) $S = \int A_{inh}(\omega, H_1) \cdot d\omega$ is therefore given by:

$$S(H_1) = \int_{\omega_{\perp}}^{\omega_{\parallel}} I(\omega_o) \int_{-\infty}^{\infty} h(\omega_k - \omega_o) \int_{-\infty}^{\infty} a(\omega - \omega_k, H_1) \cdot d\omega \cdot d\omega_k \cdot d\omega_o \quad (47)$$

A simple change of variables in Eq. (47) shows that the three integrals are separable. The integral over the line shape of the envelope function is then given by the normalization condition $\int h(\omega_k - \omega_o) \cdot d\omega_k = 1$. Therefore the integral over the entire line shape $S(H_1)$ saturates as does the integrated intensity of the individual spin packets $a(\omega - \omega_k, H_1)$. It is clear that this result must hold quite generally, i.e., independent of the degree of inhomogeneous broadening provided $h(\omega_k - \omega_o)$ varies slowly over the width of a spin packet $a(\omega - \omega_k)$, which is the case when inhomogeneous broadening exerts an appreciable effect. For individual spin packets with a Lorentzian line shape [i.e., Eq. (43)], the integral over $a(\omega - \omega_k, H_1)$ with

respect to ω is given by $a_o/(1 + \sigma^{eff})^{1/2}$. The saturation of the overall integrated line shape then has the form:

$$S(H_1) = \frac{A_o(H_1)}{(1 + \sigma^{eff})^{1/2}} \quad (48)$$

where A_o contains the integral over the powder line shape function $\int I(\omega_o) \cdot d\omega_o$, and $\sigma^{eff} = \gamma_e^2 H_1^2 T_1^{eff} T_2^{eff}$ is the effective saturation parameter averaged over the powder line shape.

This simple result [i.e., Eq. (48)] obtained for the integrated intensity is not true however for saturation curves normally deduced from the absorption line heights, because these depend strongly on the degree of inhomogeneous broadening relative to that of saturation broadening (Castner, 1959). Thus in complex spin systems, CW saturation is best analyzed in terms of the second integral of the conventional first-derivative absorption spectrum. In treating multicomponent systems, the integrated intensity of the absorption spectrum has the further advantage of being directly additive; saturation of the total integral in such multicomponent systems is described by:

$$S_{tot} = S_{0,tot} \sum_i \frac{f_i}{(1 + \sigma_i^{eff})^{1/2}} \quad (49)$$

where f_i and $S_{0,tot}$ are the fractional intensity of component i and the total integrated absorption intensity, respectively, in the absence of saturation. An alternative expression in terms of relaxation enhancements, which are of principal interest, is:

$$S_{tot} = S_{0,tot} \sum_i \frac{f_i}{[1 + \sigma_i^0 (T_{1,i}^{eff}/T_{1,i}^0)]^{1/2}} \quad (50)$$

where σ_i^0 and $T_{1,i}^0$ are the effective saturation parameter and value of T_1 , respectively, in the absence of additional relaxation enhancement. In this case appropriate to the situations to be considered, we assume that T_2 is unchanged because it is much shorter than T_1 and therefore far less sensitive to the additional relaxation processes than is T_1 .

The effects of rotational motion on saturation of conventional EPR line heights were analyzed by spectral simulation for the homogeneous case (Haas *et al.*, 1993b). It is found that the saturation curves can be described empirically by a microwave power dependence similar to that in Eq. (45) but with the exponent in the denominator treated as a fit parameter. For the first-derivative spectrum, the exponent is then not always close to the value of three-halves expected for a single homogeneous line. The apparent saturation parameter determined in this way is directly proportional to the spin-lattice relaxation time.

Spectral simulations were also performed to investigate the effects of rotational motion and Zeeman modulation frequency on the saturation of the integrated spectral intensity by using the uncorrelated jump model (Livshits *et al.*, 1998). The saturation curves are still independent of the degree of inhomogeneous broadening and can be described by Eq. (48) with the fixed exponent of one-half in the denominator. The saturation parameters extracted from the saturation curves are directly related to T_1 . For slow rotational frequencies, the saturation parameters approximate reasonably well to those expected in the absence of rotational motion. For intermediate rotational frequencies comparable to the anisotropy in spectral splittings, the apparent saturation parameter is independent of T_2 because of extreme motional broadening. In this case T_1 itself rather than the $T_1 T_2$ product, can be determined directly from the saturation curves.

5.2. Saturation Transfer EPR

The experimental normalized intensity of the phase quadrature, second-harmonic, absorption (V'_2) saturation transfer EPR spectrum is defined by (Horváth and Marsh, 1983):

$$I_{ST} = \frac{\int V'_2(H).dH}{\iint V_1(H).d^2H} \quad (51)$$

where V_1 represents the conventional in-phase, first-harmonic, absorption EPR signal. Early theoretical simulations of the V'_2 saturation transfer spectra showed that their intensity depends directly on the effective spin-lattice relaxation time T_1^{eff} (Thomas *et al.*, 1976). Experimental support for direct proportionality between the ST-EPR intensity and T_1^{eff} comes from the linear dependence of $1/I_{ST}$ for the spin label on paramagnetic ion concentration, confirming that $1/I_{ST}$ is directly determined by the spin-lattice relaxation rate of the spin label that is enhanced by paramagnetic relaxation (Páli *et al.*, 1992). The dependence of the saturation transfer integral on the effective spin label T_1 is expressed in this linear approximation as:

$$I_{ST,k} = \left(\frac{I_{ST,k}^0}{T_{1,k}^0} \right) T_{1,k}^{eff} \quad (52)$$

where $I_{ST,k}^0$ and $T_{1,k}^0$ are the intrinsic saturation transfer integral and spin label T_1 , respectively, in the absence of additional relaxation enhancement.

Comparing Eqs. (48) and (52) therefore suggests that the integrated intensity of the V'_2 saturation transfer spectrum is more sensitive to changes in T_1 than is the saturation of the conventional V_1 EPR spectrum; this is confirmed experimentally for the integrated intensities. Using integrated ST-EPR intensities also allows

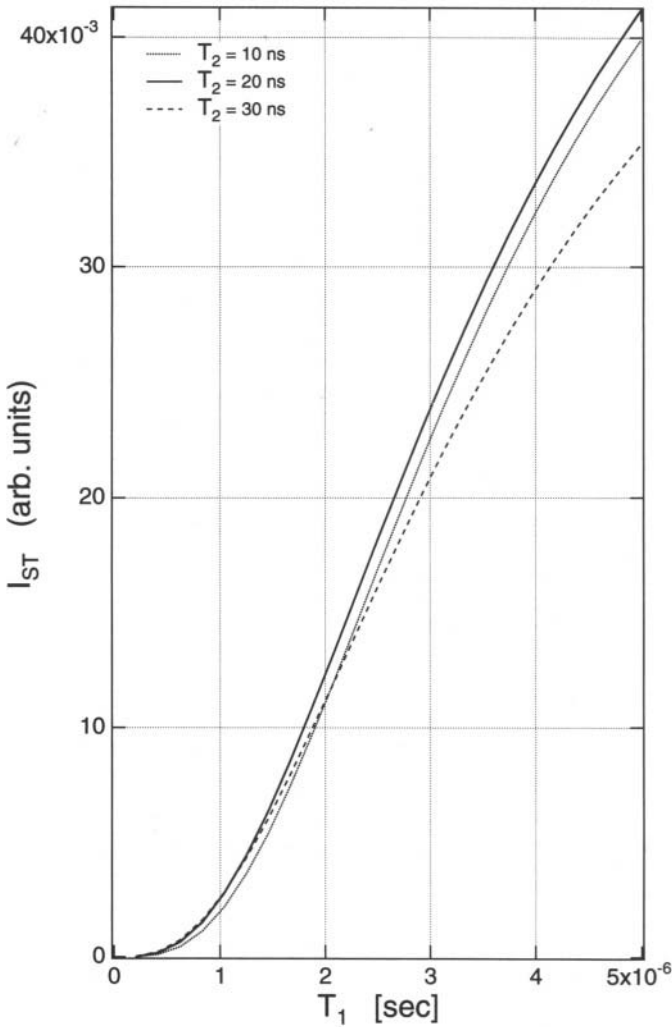


Figure 14. Theoretical dependence of the integrated intensity of 90° out-of-phase, second-harmonic, absorption ST-EPR spectra on the spin-lattice relaxation time T_1 . The first integral of the ST-EPR spectrum I_{ST} is normalized to the second integral of the conventional EPR spectrum. Calculated dependences are given for three values of the spin-spin relaxation time ($T_2 = 10, 20,$ and 30 ns) and for $H_1 = 0.25$ G and a Zeeman modulation frequency of 50 kHz. Calculations were performed with the Bloch equations using an expansion to lowest order in the Zeeman modulation amplitude [cf. Páli *et al.* (1996); Halbach (1954)].

simplifications in the analysis of more complex systems, because of the direct additivity of the component intensities. In the linear approximation given by Eq. (52), the total integrated ST-EPR spectral intensity for a multicomponent system is given by:

$$I_{ST,tot} = I_{ST,tot}^0 \sum_i f_i (T_{1,i}^{eff}/T_{1,i}^0) \quad (53)$$

where f_i and $I_{ST,tot}^0$ are the fractional intensity in the conventional V_1 spectrum of component i and the total saturation transfer integral, respectively, in the absence of additional relaxation processes. The usefulness of this method is demonstrated experimentally for both two-component lipid membranes and reconstituted lipid-protein membranes (Horváth and Marsh, 1983; Horváth *et al.*, 1993a,b).

A more detailed analysis of the dependence of the ST-EPR intensity on T_1 can be obtained theoretically by the Fourier expansion method of Halbach (1954). The second harmonic EPR signal is to lowest order directly proportional to the square of the Zeeman modulation amplitude; the corresponding Fourier component of the magnetization is given by (compare Páli *et al.*, 1996):

$$V'_2(0) \approx \omega_m T_2 \cdot \frac{\gamma_e H_1 T_2}{1 + \gamma_e^2 H_1^2 T_1 T_2} \cdot \left(3 - \frac{2\gamma_e^2 H_1^2 T_1^2}{1 + 2\gamma_e^2 H_1^2 T_1 T_2 + 4\omega_m^2 T_1^2} \right) \quad (54)$$

for the 90° out-of-phase signal, where ω_m is the Zeeman modulation frequency. For simplicity this expression refers to the amplitude at the center of the spectrum. The second factor on the right of Eq. (54) represents saturation of the normal, zeroth-harmonic EPR absorption. The third factor represents additional sensitivity of the second-harmonic, out-of-phase EPR spectrum to spin-lattice relaxation.

Figure 14 shows numerical calculations for the dependence of the normalized integrated ST-EPR intensity (I_{ST}) on spin-lattice relaxation time. These results are obtained from spectral simulations by using the above theoretical methods and are given for different values of the spin-spin relaxation time T_2 . It is seen that, within limited ranges of values of practical interest, the integrated ST-EPR intensity, I_{ST} , is reasonably linearly dependent on T_1 . Typically, enhancements in relaxation rate might be expected to reduce T_1 from the intrinsic value T_1^0 over a region in which the dependence of I_{ST} on T_1 remains approximately linear. This is found to be the case experimentally for spin label relaxation enhancement by Heisenberg exchange and by paramagnetic ions (Páli *et al.*, 1996).

6. APPLICATIONS

The following sections are devoted to experimental results obtained by using the CW saturation properties of the spin label EPR spectrum. Both progressive saturation of the conventional EPR spectrum and nonlinear displays of the EPR

signal in phase quadrature with the Zeeman modulation field at saturating microwave field intensities (i.e., ST-EPR) are used. Analysis is restricted to integrated spectral intensities because this eliminates effects of inhomogeneous broadening and additionally because spectral intensities are linearly additive in multicomponent systems. Illustrations are given of how parameters directly related to spin-lattice relaxation rates are obtained from experimental measurements. A broad range of different types of experiment based on different physical processes by which saturation can be alleviated in the spin label EPR spectra are included to demonstrate the versatility of application of the methods. These mechanisms include two-site lipid exchange, lipid and protein collisions, and relaxation enhancement by both Heisenberg spin exchange and magnetic dipole-dipole interactions. Rotational diffusion is also included briefly to illustrate parallels between standard ST-EPR experiments and some of the newer methods. Biophysical data related to both the dynamics and the structure of spin-labeled systems are obtained in this way.

6.1. Two-Site Lipid Exchange and Lipid-Protein Interactions

Continuous wave saturation of the integrated EPR intensity proved to be sensitive to the physical exchange of spin-labeled lipids at the hydrophobic interface with integral proteins in membranes (Horváth *et al.*, 1993a)—compare Fig. 1. This is illustrated by saturation curves for spin-labeled lipids in myelin proteolipid protein/dimyristoyl phosphatidylcholine membrane recombinants in Fig. 15. In the gel-phase membranes at 4 °C, where lipid chain mobility is extremely low, the intensity of the conventional EPR spectrum from the lipid-protein membrane recombinant saturates as predicted for a linear combination of the two environments in which the lipid spin label is situated [compare Eq. (49)]. In fluid lipid membranes at 30 °C, the intensity of the conventional EPR spectrum from the recombinant saturates less readily than predicted from the saturation behavior in the fluid bilayer and protein-associated environments in isolation. The alleviation of saturation arises from exchange of the spin-labeled lipid between these two environments, indicating that in fluid membranes, lipid exchange must take place on the time scale of the spin-lattice relaxation. [The two-component spectral line shapes obtained from recombinant membranes indicate that exchange is slow on the conventional EPR time scale (Horváth *et al.*, 1988)].

Quantitative conclusions regarding lipid exchange rates were reached from measuring intensities of the saturation transfer EPR spectra. Figure 16 gives data on the ST-EPR intensity I_{ST} for spin-labeled phosphatidylcholine in lipid bilayer membranes, associated with the protein alone, and in protein-lipid membrane recombinants. Data are also included for other spin-labeled lipids in membrane recombinants of the same lipid/protein ratio. Because these other lipids display a preferential interaction with the protein (compare Brophy *et al.*, 1984), the frac-

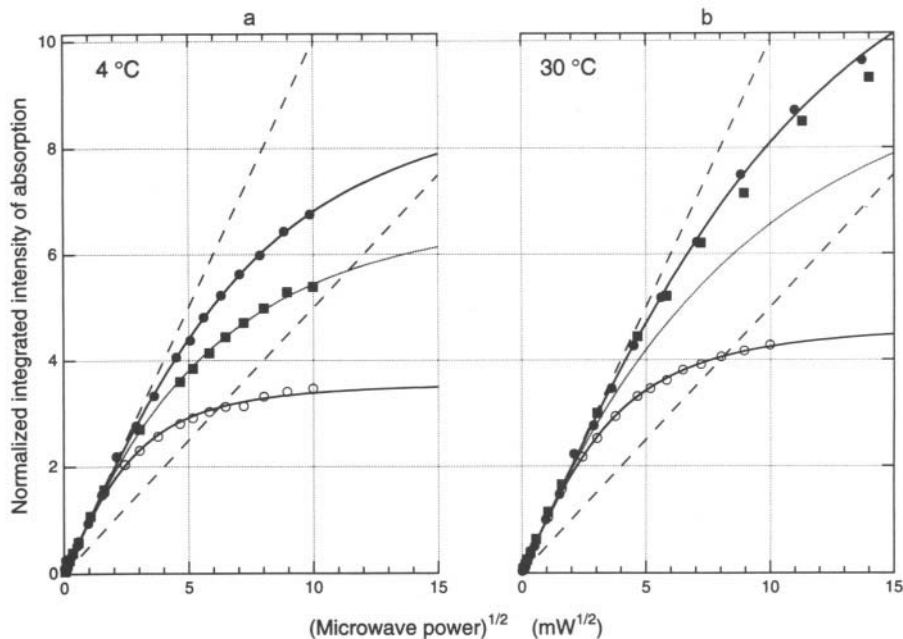


Figure 15. Continuous wave saturation curves for the integrated intensity of the conventional EPR spectra from spin-labeled phosphatidylcholine (14-PCSL) in dimyristoyl phosphatidylcholine bilayer membranes alone (\bullet), associated with the delipidated myelin proteolipid protein (\circ), and in myelin proteolipid protein/dimyristoyl phosphatidylcholine membranes of lipid/protein ratio 24:1 mol/mol (\blacksquare). (a) Microwave power dependence of the double-integrated spectral intensity is recorded at 4 °C in the lipid gel phase and (b) at 30 °C in the lipid fluid phase. Solid lines represent fits to the saturation of single components according to Eq. (48); dotted lines represent the predicted saturation behavior of the lipid/protein membranes, assuming no exchange between the two components and a fraction $f_b = 0.4$ of the protein-associated component. The dashed straight lines correspond to predicted dependences for no saturation and half-saturation (upper and lower, respectively). (Data from Horváth *et al.*, 1993a)

tional population of spin-labeled lipid associated with the protein f_b differs among the different spin-labeled lipid species for membranes of fixed lipid/protein ratio. In gel-phase membranes, the ST-EPR intensity increases linearly with the fraction of spin-labeled lipid associated with the protein. The linear additivity of the spectral intensity, as also that for the conventional EPR spectra under saturation, is consistent with lipid exchange in gel-phase membranes being considerably slower than spin-lattice relaxation of the nitroxide spin label.

In fluid-phase membranes however, I_{ST} is reduced very considerably below the values predicted by linear additivity. The reduction in intensity represents alleviation of saturation by lipid exchange at the intramembranous surface of the protein (compare Fig. 1). The dependence of I_{ST} on f_b in the fluid membranes can be fit by

assuming a constant (i.e., diffusion-controlled) on-rate τ_f^{-1} and an off-rate τ_b^{-1} determined by the selectivity of the different lipid species for the protein (see Sec. 4.1 and caption to Fig. 16). The measured on-rate is $T_{1,b}^0 \tau_f^{-1} = 2.9$ for membranes of lipid/protein ratio 37:1 mol/mol. This translates into intrinsic off-rates of $\tau_b^{-1} = 0.7, 0.9, 2.5,$ and $4.9 \times 10^6 \text{ s}^{-1}$ for spin-labeled stearic acid, phosphatidic acid, phosphatidylserine, and phosphatidylcholine, respectively, derived from detailed balance and assuming that $T_{1,b}^0 \approx 1 \mu\text{s}$ (Horváth *et al.*, 1993a).

Results in Figs. 15 and 16 indicate that the saturation properties of spin-labeled lipids associated with integral membrane proteins differ considerably from those in lipid bilayers because of differences in lipid mobility in the two environments. In principle this can be used to determine the rotational mobility of the protein-associated lipids (compare Sec. 6.5). This has been done for spin-labeled lipids associated with the Ca-ATPase in sarcoplasmic reticulum membranes (Squier and

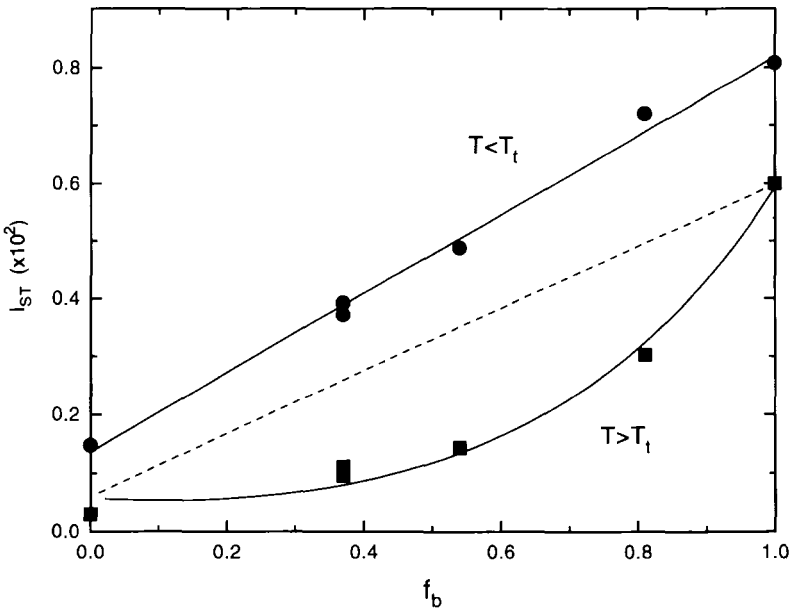


Figure 16. Dependence of the normalized integrated intensity I_{ST} of the saturation transfer EPR spectra from different spin-labeled lipids on the fraction f_b of each lipid species associated with the myelin proteolipid protein in dimyristoyl phosphatidylcholine membranes of fixed protein/lipid ratio (1:37 mol/mol). Data correspond to spin labels with different selectivities for the protein; they were recorded in the gel phase at 4 °C (●) and in the fluid phase at 30 °C (■). Solid lines are fits to Eqs. (29) and (53), obtained by a linear regression appropriate to negligible exchange for data at 4 °C, and a nonlinear least-squares fit for data at 30 °C, yielding a normalized lipid exchange rate of $T_{1,b}^0 \tau_f^{-1} = 2.9$. The dashed line is the dependence expected in the absence of exchange at 30 °C. (Data from Horváth *et al.*, 1993a)

Thomas, 1989), although effects of lipid exchange were neglected. The latter is probably a good approximation at low temperature, but not at higher temperatures (compare East *et al.*, 1985).

Although lipid exchange rates in gel-phase membranes are slower than the spin-lattice relaxation, the difference in saturation properties in the two environments can still be used to study static properties of the lipid-protein interactions (Horváth *et al.*, 1993b). This is particularly useful because standard methods of two-component line shape analysis are not applicable in gel-phase membranes due to a lack of resolution of the spectra from the two environments (compare Marsh, 1989). In these cases, the two spectral components can be distinguished only by their saturation properties.

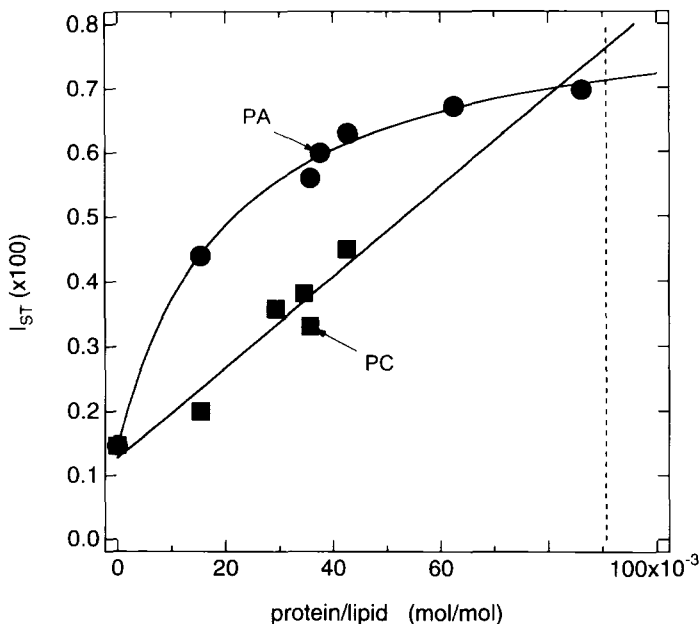


Figure 17. Dependence on the protein/lipid ratio of the normalized integrated intensity I_{ST} of the saturation transfer EPR spectra from the 14-PCSL phosphatidylcholine spin label (■) and 14-PASL phosphatidic acid spin label (●) in membrane recombinants of the myelin proteolipid protein with dimyristoyl phosphatidylcholine in the gel phase at 0 °C. The solid straight line represents a linear regression to data for 14-PCSL, assuming no exchange and no selectivity for interaction with the protein of spin-labeled phosphatidylcholine relative to unlabeled phosphatidylcholine (i.e., $K_r^{PC} = 1$). The curved line is a nonlinear least-squares fit to data for 14-PASL with Eq. (53) and (55), yielding $K_r^{PA} = 5.2$ and $N_b = 11.4$. The vertical dashed line corresponds to a lipid/protein stoichiometry of $N_b = 11$. (Data from Horváth *et al.*, 1993b)

Figure 17 shows the dependence of the ST-EPR intensities of spin-labeled phosphatidylcholine and spin-labeled phosphatidic acid on the protein/lipid ratio in membrane recombinants of the myelin proteolipid protein with dimyristoyl phosphatidylcholine in the gel phase. For the phosphatidylcholine spin label, the ST-EPR intensity increases linearly with the protein/lipid ratio, demonstrating little selectivity between spin-labeled and unlabeled phosphatidylcholine for interaction with the protein. Spin-labeled phosphatidic acid exhibits a selectivity relative to phosphatidylcholine for interaction with the protein in gel-phase membranes. This results in a higher integrated ST-EPR spectral intensity than for spin-labeled phosphatidylcholine and a highly nonlinear dependence on protein/lipid ratio (see Fig. 17).

The fraction of protein-associated lipid spin label L with relative association constant K_r^L is given by (Marsh, 1989):

$$f_b = \frac{K_r^L}{(n_t/N_b + K_r^L - 1)} \quad (55)$$

where n_t is the total lipid/protein ratio of the membrane and N_b is the number of lipid association sites on the protein. Using Eq. (55) for the equilibrium lipid-protein association to express the total ST-EPR intensity, as given by Eq. (53), allows us to determine the stoichiometry (N_b) and specificity (K_r^L) of lipid-protein interaction in gel-phase membranes. Values determined for phosphatidic acid ($N_b = 11.4$, $K_r^{PA} = 5.2$) are close to those found also in fluid-phase membranes (compare Brophy *et al.*, 1984). Data for phosphatidylcholine are also consistent with a lipid/protein stoichiometry of $N_b \approx 11$ in gel-phase membranes (Horváth *et al.*, 1993b).

6.2. Lipid and Protein Collision Frequencies: Translational Diffusion

A principal application of CW saturation methods is in determining weak Heisenberg exchange interactions. These can be related directly to collision frequencies between the spin-labeled partners. Heisenberg exchange frequencies are low whenever collision rates are intrinsically slow or the concentration of spin-labeled species is low. In these cases, the exchange interaction is too weak to affect T_2 ; hence it is not amenable to conventional line shape analysis, such as that used to determine translational diffusion rates of spin-labeled lipids in fluid membranes (compare Marsh, 1989).

Figure 18 illustrates the determination of the biomolecular rate constants for Heisenberg exchange between spin-labeled lipids in gel-phase membranes, for which the collision rates are low. The ST-EPR intensity decreases progressively with an increasing concentration of spin-labeled lipid, as described by Eq. (35), for gel-phase membranes of both dimyristoyl and dipalmitoyl phosphatidylcholine.

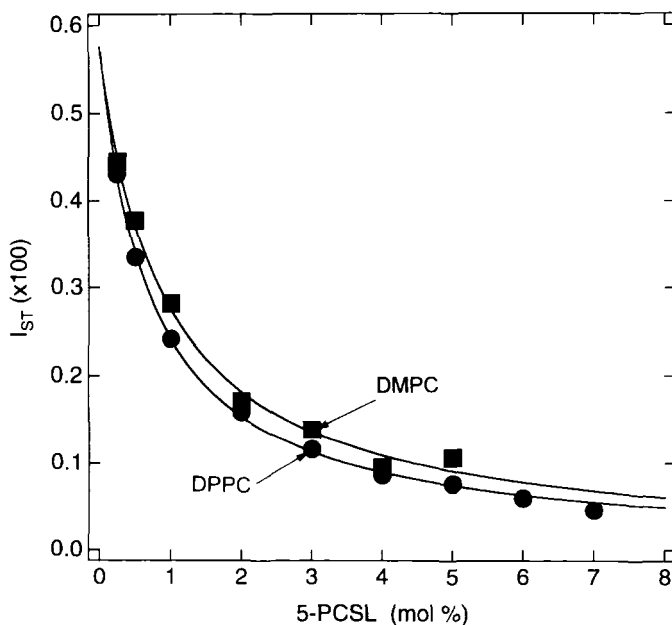


Figure 18. Normalized integrated intensity I_{ST} of the saturation transfer EPR spectra of the 5-PCSL phosphatidylcholine spin label in gel-phase bilayer membranes of dipalmitoyl phosphatidylcholine (DPPC) at 20 °C (●) and of dimyristoyl phosphatidylcholine (DMPC) at 3 °C (■) as a function of the spin label concentration. Solid lines are nonlinear least-squares fits to Eqs. (35) and (52), which yield a normalized rate constant for the spin exchange of $T_1^0 k_{ex} = 1.1$ and 1.4/mol% in DMPC and DPPC, respectively. (Data from Marsh and Horváth, 1992a)

The decrease in ST-EPR intensity can be distinguished from that arising from slow rotational diffusion because it takes place with relatively little change in ST-EPR line shape, and it is more sensitive to exchange than is saturation of the conventional EPR intensity (Marsh and Horváth, 1992a). The magnitude of the exchange rate constants obtained suggests that translational diffusion is taking place along defect regions rather than in the bulk lipid gel phase.

A converse application of this method is used with suitable calibrations to determine local concentrations of spin-labeled probe molecules in heterogeneous systems. This approach has been applied successfully to study nucleation and the growth of lipid domains in a model membrane system (Páli *et al.*, 1993b).

Of most interest is the application to the translational diffusion of proteins, where diffusion rates are slower than for small molecules and high concentrations of the spin-labeled species often cannot be realized. Methods for studying local translational diffusion of proteins in membranes are largely lacking; those based on spin label saturation are therefore of special relevance. Viability of an approach

based on ST-EPR intensities was demonstrated with spin-labeled human serum albumin in homogeneous aqueous solution (Khrantsov and Marsh, 1991). Translational diffusion coefficients were obtained that agreed with those determined by other methods; these depended on temperature and viscosity as predicted by hydrodynamic theory.

Figure 19 shows a strategy for measuring translational diffusion rates with spin-labeled integral membrane proteins. Detergent-solubilized, spin-labeled protein is combined with unlabeled protein at different relative proportions, then membranes are reconstituted at the same total protein/lipid ratio to ensure a constant effective intramembrane viscosity. By this method of varying spin concentration rather than simply varying the spin-labeling level, intramolecular spin-spin interactions that can also affect the EPR saturation properties are maintained constant (compare Horváth *et al.*, 1990). For spin-labeled Na,K-ATPase ion pump reconstituted at a lipid/protein ratio corresponding to that of the native membranes, the dependence of the ST-EPR intensity on relative spin concentration was found to conform to that predicted by Eqs. (36) and (52) up to 100% spin-labeled protein (Esmann and Marsh, 1992). Local translational diffusion coefficients deduced from the resulting bimolecular collision rate constants ($T_1^0 k_{ex} \sim 0.2-0.4$) are in the expected range ($\approx 2-6 \times 10^{-8} \text{ cm}^2 \text{ s}^{-1}$, depending on temperature); these are

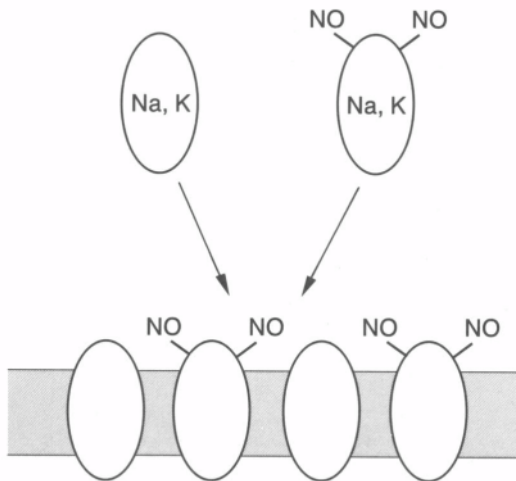


Figure 19. Scheme for measuring the translational diffusion rate of the Na,K-ATPase in reconstituted membranes of identical protein/lipid ratios but different fractions of spin-labeled protein. Solubilized, spin-labeled (-NO) protein is mixed with solubilized, unlabeled protein at different proportions; membranes are then reconstituted by precipitation from the detergent solution. The Heisenberg exchange frequency is determined by the relative concentration of spin-labeled protein and by the collision rate between proteins in the membrane.

significantly slower than those for spin-labeled lipids in fluid membranes ($\approx 1-2 \times 10^{-7} \text{ cm}^2\text{s}^{-1}$; compare Marsh, 1989). They are however much larger than corresponding values found for long-range protein diffusion coefficients in whole-cell systems by photobleaching techniques. This comparison indicates considerable barriers to long-range diffusion in cells that presumably are associated with the cytoskeleton.

Mutual collisions between different spin-labeled species can be studied by determining Heisenberg exchange frequencies in double-labeling experiments (Snel and Marsh, 1994). Here exchange frequencies are likely to be relatively low because concentrations must be limited to minimize Heisenberg exchange within the single-labeled species. Using CW saturation methods based on integrated intensities obviates the necessity for spectral resolution of the two spin-labeled species provided their individual saturation properties differ sufficiently. Figure 20 shows the principles for determining the location of spin-labeled segments of proteins in their surface-bound or membrane-penetrant forms by using spin-labeled lipids. Apocytochrome *c* is the haem-free precursor of the holoprotein cytochrome *c*, which is a peripheral membrane constituent of the mitochondrial electron transport chain. The apoprotein binds strongly to negatively charged lipid membranes, and this is thought to constitute an essential part of the mechanism by which newly synthesized protein enters the mitochondrion. The degree of penetration of the precursor protein into the membrane therefore is likely to be a determining

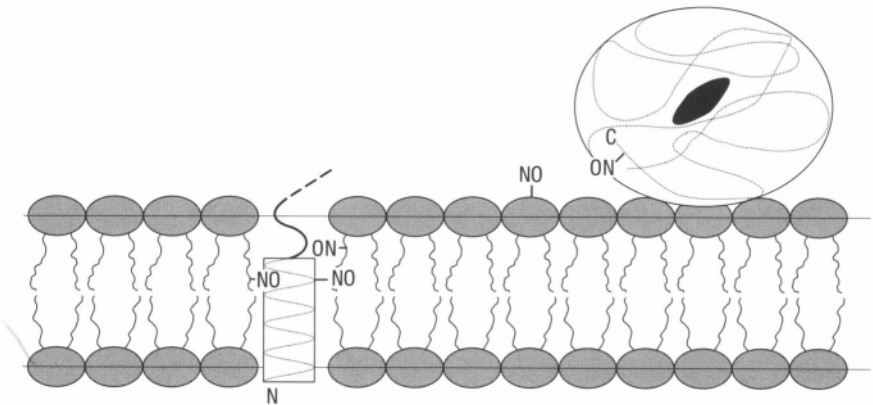


Figure 20. Illustration of relative locations of spin-labeled (-NO) lipids and proteins that give rise to mutual Heisenberg spin exchange between the two spin-labeled species. *Left side:* Membrane insertion of the spin-labeled N-terminal segment of apocytochrome *c*. *Right side:* Membrane surface location of holocytochrome *c* spin-labeled at the C-terminal. The highest collisional, spin exchange frequency is expected for the spin label on the lipid positioned at the same depth in the membrane as that on the protein.

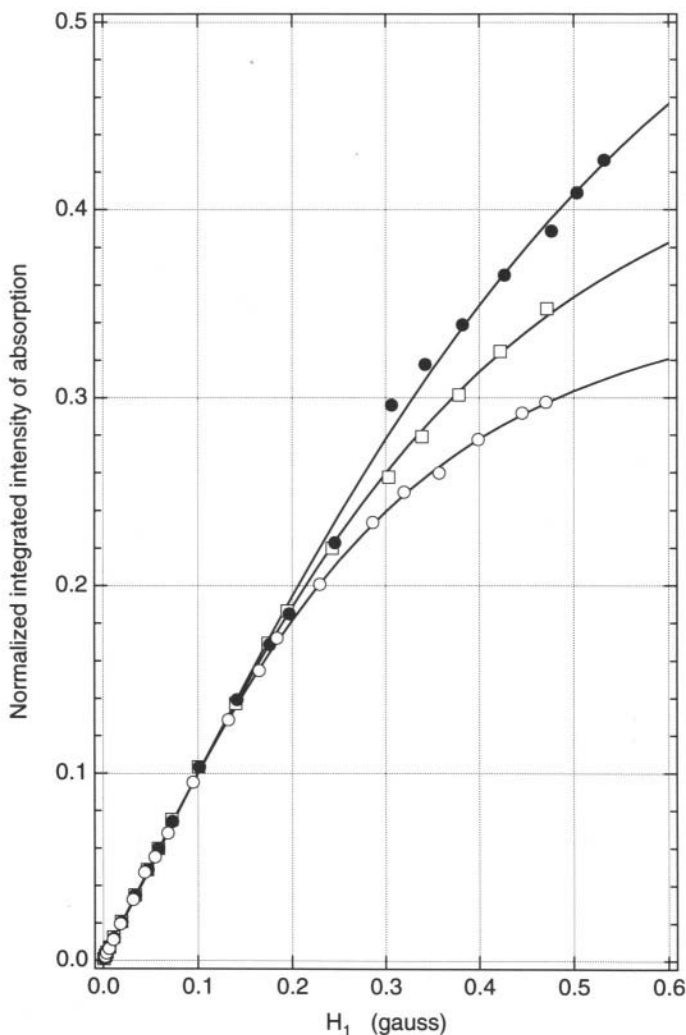


Figure 21. Saturation curves for the double-integrated intensity of conventional EPR spectra from singly and doubly spin-labeled complexes of apocytochrome *c* with dimyristoyl phosphatidylglycerol (DMPG) membranes. Dependence on the microwave magnetic field (H_1) is given for spin-labeled apocytochrome *c* bound to DMPG membranes (\circ), unlabeled apocytochrome *c* bound to DMPG membranes containing 1 mol % 14-PGSL phosphatidylglycerol spin label (\square), and spin-labeled apocytochrome *c* bound to DMPG membranes containing 1 mol % 14-PGSL (\bullet). Solid lines give fits of saturation curves to Eq. (48), yielding $(T_1 T_2^{eff})_p = 2.5 \times 10^{-14} \text{ s}^2$ for spin-labeled apocytochrome *c* bound to DMPG, $(T_1 T_2^{eff})_L = 1.4 \times 10^{-14} \text{ s}^2$ for 14-PGSL in DMPG with unlabeled apocytochrome *c* bound, and $(T_1 T_2^{eff})_{PL} = 6.9 \times 10^{-15} \text{ s}^2$ for the doubly labeled complex of apocytochrome *c* and DMPG containing 14-PGSL. (Data from Snel and Marsh, 1994)

parameter in the translocation of the precursor protein across the outer mitochondrial membrane.

Figure 21 shows progressive saturation curves for apocytochrome *c* spin-labeled on cys-14 or cys-17 in the N-terminal region and bound to negatively charged lipid membranes. When bound to membranes containing a phospholipid spin-labeled at a chain position close to the center of the membrane (i.e., 14-PGSL), the doubly labeled system saturates less readily than either of the corresponding singly labeled systems. This is a direct effect of Heisenberg exchange by collision between the spin-labeled segment of the apoprotein and the spin label on the 14-C atom of the lipid chains; it is a clear demonstration that the N-terminal of the apoprotein penetrates deeply into the lipid membrane. Table 2 lists reciprocal effective T_1T_2 products deduced from progressive saturation for spin-labeled apocytochrome *c* bound to membranes containing lipids spin-labeled at various positions. Also given are values predicted for the absence of mutual Heisenberg spin exchange from progressive saturation measurements on the singly spin-labeled systems. For spin label positions on the lipid that are in the head group region or close to the polar end of the chains, the saturation properties are similar to those of the isolated systems. There are strong mutual collisions as reflected in the exchange

Table 2
Experimental Relaxation Rates $(1/T_1T_2)_{PL}$ for Spin-Labeled Lipid and Spin-Labeled Protein in Complexes of Apocytochrome *c* (apo *c*) and Holocytochrome *c* (cyt *c*) with Negatively Charged Lipid Membranes (DMPG or DOPG) together with values $(1/T_1T_2)_{PL}^0$ Predicted from Eq. (49), Assuming no Heisenberg Exchange between Spin Labels, and Estimates of the Normalized Spin Exchange Frequency $T_{1,P}^0\tau_{ex}^{-1}$, from Eqs. (30) and (50). $T = 30^\circ\text{C}$

Lipid Spin Label ^a	$(1/T_1T_2)_{PL} (10^{13}\cdot\text{s}^{-2})$	$(1/T_1T_2)_{PL}^0 (10^{13}\cdot\text{s}^{-2})$	$T_{1,P}^0\tau_{ex}^{-1}$
apo <i>c</i> /DMPG			
14-PGSL	14.5	6.0	≥ 5
5-PGSL	5.6	5.3	0.2
T-PASL	6.3	6.8	0
cyt <i>c</i> /DOPG			
14-PGSL	5.7	6.4	0
5-PGSL	7.3	7.1	0.1
T-PASL	8.0	6.4	0.8

Source: Data from Snel and Marsh, 1994

^an-PGSL, phosphatidylglycerol spin-labeled on the n-C atom of the *sn*-2 chain; T-PASL, phosphatic acid spin-labeled on the phosphate polar headgroup; DMPG, dimyristoyl phosphatidylglycerol; DOPG, dioleoyl phosphatidylglycerol.

frequencies deduced from the T_1T_2 products only for spin labels close to the terminal methyl of the chains. This provides clear evidence of penetration of the N-terminal segment of apocytochrome *c* deep into the hydrophobic region of the lipid membrane. For a spin label on cys-102 close to the C-terminal of yeast holocytochrome *c*, the largest exchange frequency is obtained with the lipid spin-labeled in the polar head group region, as expected for a native peripheral membrane protein bound at the membrane surface.

6.3. Spin Label Location and Accessibility: Paramagnetic Relaxation

Another way of determining the location of spin-labeled segments in proteins uses paramagnetic relaxation agents with preferential solubilities in polar or apolar environments. This method's most powerful application is in connection with site-directed spin labeling (Hubbell and Altenbach, 1994). Figure 22 illustrates the

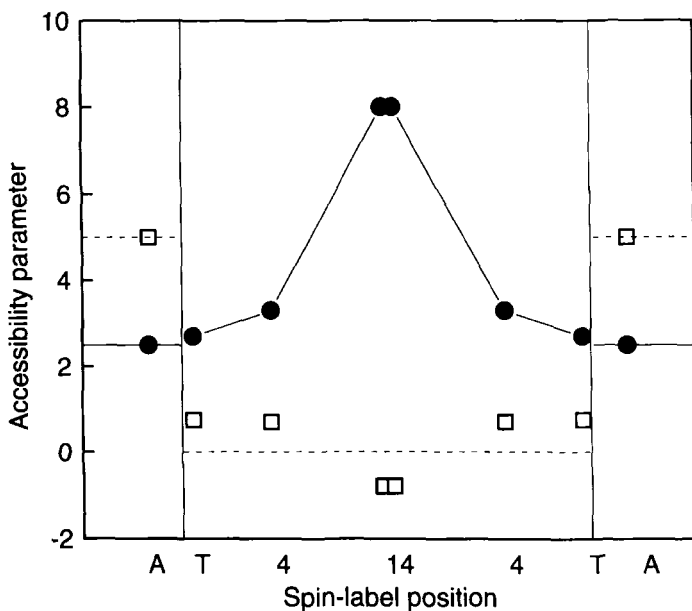


Figure 22. Dependence on the location of the spin label group in dimyristoyl phosphatidylcholine bilayer membranes of the accessibility to oxygen (●, solid line) and to chromium oxalate (□, dashed line). The accessibility parameter is the enhancement in relaxation rate $1/T_1T_2$ corrected by the central line width (in units of $10^{13} \text{ s}^{-2} \text{ G}^{-1}$). The Tempostearamide (T) is a spin label in the lipid headgroup region; 4 and 14 are spin labels on the 4 and 14 C-atoms, respectively, of the *m*-2 chain of phosphatidylcholine; and A (spin-labeled apocytochrome *c*) is a spin label in the aqueous phase. Vertical lines indicate the surface of the membrane; these have a separation of $\sim 4 \text{ nm}$. $T = 30^\circ \text{C}$. (Data from Snel and Marsh, 1993)

principles for lipid spin labels in bilayer membranes in the presence of paramagnetic molecular oxygen or a negatively charged paramagnetic ion complex. Both are efficient relaxants; oxygen is preferentially concentrated in the hydrophobic region of the membrane with a well-defined intramembranous concentration profile, and chromium oxalate is restricted to the aqueous phase. The efficiency of relaxation enhancement is defined in terms of the accessibility parameter, which is the increase in the effective $1/T_1T_2$ relaxation rate by the relaxant normalized with respect to line width (Snel and Marsh, 1993).

This method was applied to determine the membrane location of spin-labeled apocytochrome *c* and cytochrome *c* (Snel *et al.*, 1994). Figure 23 shows accessibility parameters for molecular oxygen obtained from progressive saturation meas-

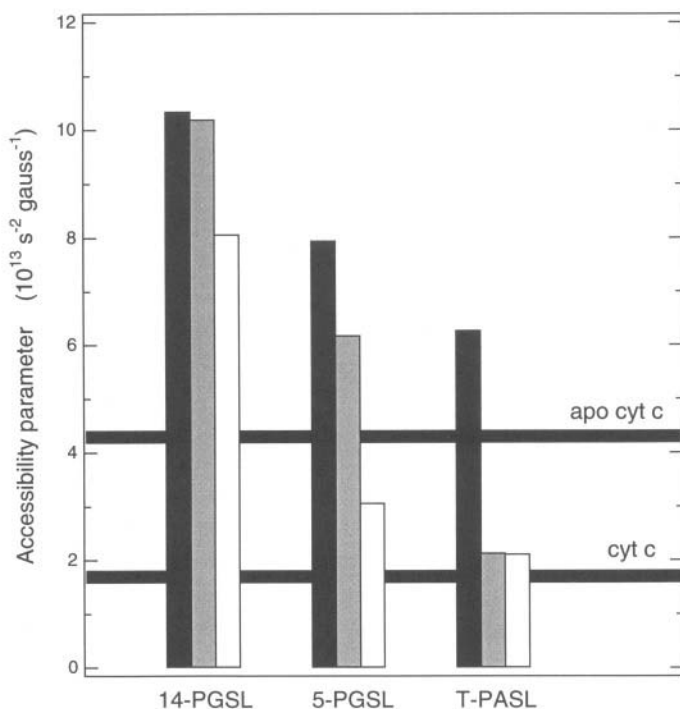


Figure 23. Accessibility parameters for negatively charged phospholipids spin-labeled in the head group (T-PASL), or at the 5- or 14-position in the *sn*-2 chain (5-PGSL and 14-PGSL, respectively), to oxygen are given for bilayer membranes of dioleoyl phosphatidylglycerol (DOPG) alone (solid bars); for DOPG membranes with unlabeled cytochrome *c* bound at a lipid/protein ratio of 13 mol/mol (gray bars); and for DOPG membranes with unlabeled apocytochrome *c* bound at a lipid/protein ratio of 11 mol/mol (white bars). Accessibility parameters to oxygen for spin-labeled cytochrome *c* and apocytochrome *c* bound to unlabeled DOPG membranes at a lipid/protein ratio of 13 and 14 mol/mol, respectively, are shown as horizontal lines. (Data from Snel *et al.*, 1994)

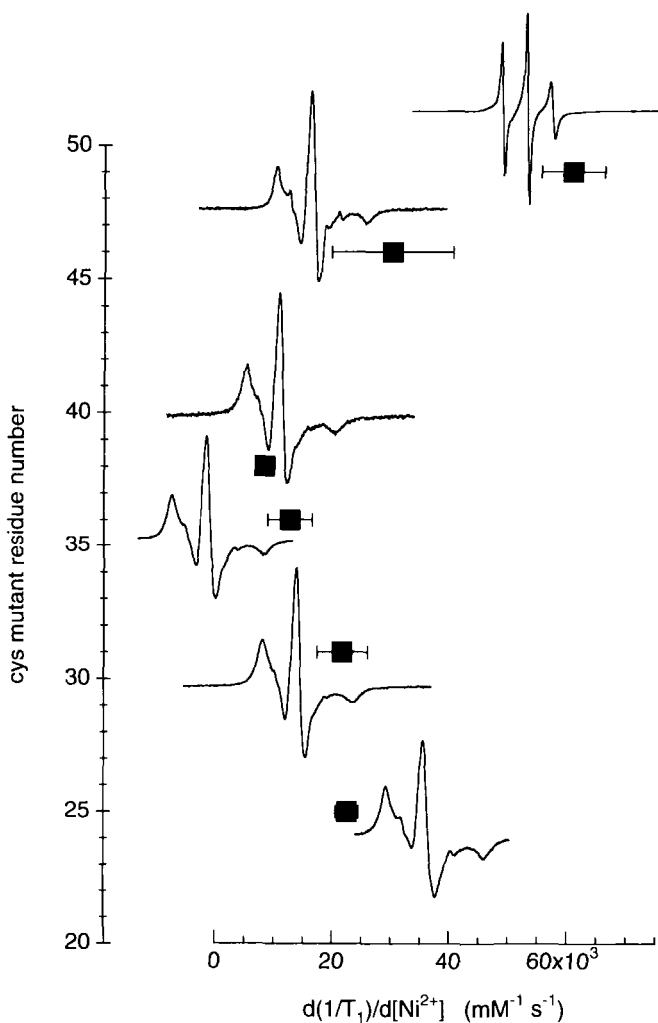


Figure 24. Extent of paramagnetic relaxation enhancement by aqueous Ni^{2+} ions $d(1/T_1)/d[Ni^{2+}]$ for spin-labeled cysteine mutants of the M13 bacteriophage coat protein reconstituted into dioleoyl phosphatidylglycerol bilayer membranes, as a function of the position of the cysteine substitution. Effective values for T_1 were obtained from progressive saturation curves and line width measurements. Spectra indicate conventional EPR line shapes in the absence of Ni^{2+} recorded at 20 °C and a subsaturating microwave power with a scan width of 100 or 160 G. (Data from Stopar *et al.*, 1997)

urements. Results for spin-labeled lipids serve as calibrations. Protein binding was found to have a considerable effect on local concentrations of oxygen within the lipid bilayer membranes. Accessibilities of spin-labeled proteins relative to those obtained for phospholipids labeled at various positions identify the location of the spin-labeled cysteine residues in the phospholipid bilayer membrane. The spin label on apocytochrome *c* bound to phosphatidylglycerol membranes lies between the 5- and 14-C positions of the lipid acyl chain. The spin label on the holoprotein cytochrome *c* is located at the membrane surface. These different extents of membrane penetration also correlate with the reduction in local oxygen concentration experienced by spin-labeled phospholipids on binding of apo- and holocytochrome *c* (compare Fig. 23). This approach was also used to determine the membrane location of a spin label on the single cysteine residue in the presequence of yeast cytochrome oxidase subunit IV when bound to bilayer membranes of phosphatidylglycerol, cardiolipin, or their (1:4) mixtures with phosphatidylcholine by using molecular oxygen and chromium oxalate as relaxants (Snel *et al.*, 1995). Another application involves cysteine mutants in the precursor and native parts of the *E. coli* PhoE outer membrane protein (Keller *et al.*, 1996).

Figure 24 shows the paramagnetic relaxation induced by aqueous Ni^{2+} ions for a series of spin-labeled cysteine mutants of the M13 bacteriophage coat protein in its transmembrane form. Effective values for the spin-lattice relaxation time were deduced from progressive saturation experiments combined with line width measurements (Stopar *et al.*, 1997). Close to the C-terminal (cys-49), the spin label is relaxed efficiently by collisional Heisenberg exchange with the aqueous Ni^{2+} ions. On proceeding closer to the membrane surface, the efficiency of collision-induced relaxation decreases. On entering the membrane from cys-38 onward, the spin label is shielded from direct contact with the paramagnetic ions, and the residual relaxation enhancement is induced by magnetic dipole-dipole interactions. The profile of paramagnetic relaxation enhancement is mirrored by the rotational mobility of the spin label, as reflected in the conventional spectral line shapes. At the C-terminal, the spin label is very mobile, and spectral anisotropy increases as the labeling position approaches the membrane surface. For spin labels positioned within the membrane, rotational mobility is reduced considerably, and line shapes (e.g., for cys-25) approach the rigid limit of sensitivity of conventional EPR spectroscopy.

6.4. Distance Measurements: Dipolar Relaxation

When paramagnetic ions are unable to come in direct contact with the spin label, Heisenberg spin exchange is absent. The paramagnetic relaxation enhancement of the spin label then occurs solely by through-space magnetic dipole-dipole interactions. Because of the explicit dependence of the dipole-dipole interaction on the separation r of the spin dipoles ($\sim 1/r^6$ for individual dipole pairs), relaxation

enhancements can be used for distance measurements on the molecular scale. In general the relaxation enhancement depends directly on the concentration of the paramagnetic ion. Using saturation measurements allows measurement of longer distances and/or lower concentrations of paramagnetic species than is possible with measurements of paramagnetic line broadening.

Figure 25 shows the method using integrated intensities of the ST-EPR spectra for a spin-labeled phospholipid (5-PCSL) in gel-phase lipid bilayer membranes dispersed in aqueous solutions with increasing concentrations of paramagnetic Ni^{2+} ions. The ST-EPR spectral line shapes do not change much with increasing Ni^{2+} ion concentration, indicating little change in the rotational motion of the lipid spin label. The ST-EPR spectral intensities however decrease pronouncedly with increasing Ni^{2+} concentration, as seen most clearly from the first integrals of the ST-EPR spectra. The normalized reciprocal integrated ST-EPR intensities $1/I_{ST}$ increase linearly with Ni^{2+} ion concentration (Páli *et al.*, 1992), corresponding to a paramagnetic enhancement in the spin-lattice relaxation rate of the spin label according to Eqs. (18) and (52). Because the spin label is situated in the hydrocarbon chain region of the lipid bilayer, and therefore not directly accessible to the aqueous Ni^{2+} ions, this relaxation enhancement must occur through the magnetic dipole-dipole interaction.

The upper part of Figure 26 shows the dependence of the relaxation enhancement induced by the Ni^{2+} ions on the position of the spin label group in the *sn*-2 chain of phosphatidylcholine in normal, gel-phase bilayer membranes of dipalmitoyl phosphatidylcholine. The increase in reciprocal ST-EPR integral intensity induced by aqueous Ni^{2+} decreases progressively with increasing distance of the spin label position from the polar-apolar interface toward the membrane interior. The positional dependence can be described by the following expression derived from Eqs. (18) and (21) (Páli *et al.*, 1992):

$$\frac{1}{I_{ST}(c_{Ni})} = \frac{1}{I_{ST}(0)} + k_m [R^{-m} + (d_l - R)^{-m}] c_{Ni} \quad (56)$$

where R is the distance of the spin label from the membrane surface, d_l is the membrane thickness, c_{Ni} is the Ni^{2+} ion concentration, and k_m is a constant directly related to f_m in Eq. (21) that also contains the proportionality between ST-EPR intensity and T_1 [cf. Eq. (52)]. The second term in the square brackets in Eq. (56) represents the contribution to the paramagnetic relaxation from Ni^{2+} ions on the opposite face of the membrane from that in which the spin-labeled lipid is located. Distances R and d_l in Eq. (56) can be related to the spin label position in the chains because lipid chains are in the all-*trans* configuration and tilted at a known angle in gel-phase bilayer membranes. It is therefore possible to determine both bilayer thickness d_l and the distance of the origin of the chain numbering from the membrane surface (i.e., the thickness of the polar region d_p) from the positional

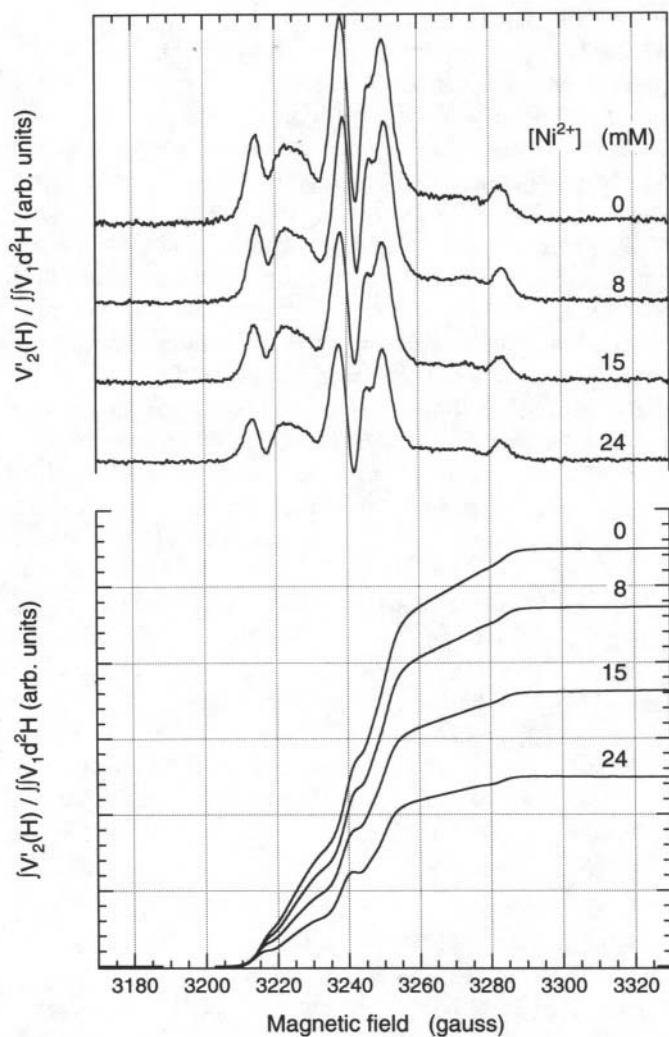


Figure 25. *Upper panel:* Second harmonic, out-of-phase ST-EPR spectra (V'_2 -display) of the 5-PCSL phosphatidylcholine spin label (0.5 mol%) in dispersions of gel-phase dipalmitoyl phosphatidylcholine bilayer membranes containing increasing concentrations of Ni^{2+} ions. Spectra are scaled to reflect their relative intensities by normalizing with respect to the second integral of the corresponding conventional EPR spectra. *Lower panel:* Normalized first integrals of ST-EPR spectra shown in the upper panel. Total scan width = 160 G. $T = 0^\circ\text{C}$. (Data from Páli *et al.*, 1992)

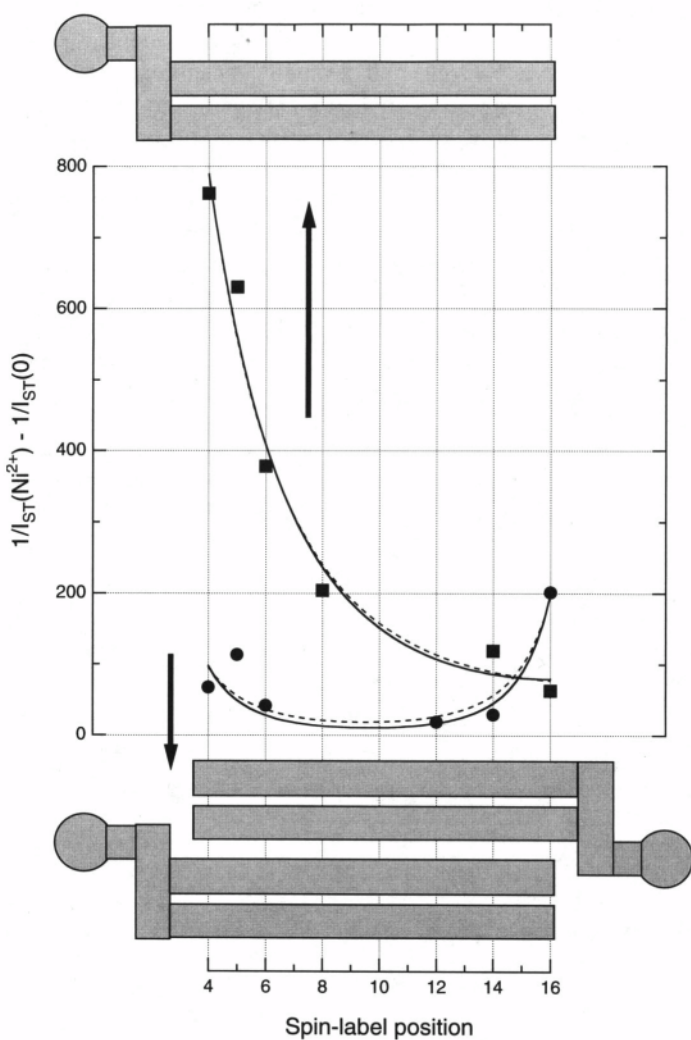


Figure 26. Dependence of the difference in the reciprocal saturation transfer EPR integral in the presence and the absence of 30-mM Ni^{2+} , $1/I_{ST}(Ni^{2+}) - 1/I_{ST}(0)$, on the nitroxide position in the *sn*-2 chain of phosphatidylcholine spin labels in gel-phase dipalmitoyl phosphatidylcholine membranes dispersed in water (■) or glycerol (●) at 0 °C. Lines are nonlinear least-squares fits to Eq. (56) with $m = 3$ (dashed lines) and $m = 4$ (solid lines). Schematic indications of the positions of the lipid molecules in a normal gel-phase bilayer membrane (*top*) and an interdigitated gel-phase membrane (*bottom*) are given. (Data from Páli *et al.*, 1992)

dependence of the relaxation enhancement given in Fig. 26. Values deduced in this way are in good agreement with those obtained from independent studies with x-ray diffraction (see Páli *et al.*, 1992).

Comparable data on Ni^{2+} -induced relaxation enhancements obtained from gel-phase dipalmitoyl phosphatidylcholine membranes dispersed in glycerol are given in the lower part of Fig. 26. Under these conditions, gel-phase membranes are not of the normal lipid bilayer type but correspond to a structure in which lipid chains from opposing bilayer faces are fully interdigitated throughout the entire hydrophobic membrane thickness. The membrane profile of the relaxation enhancement is changed drastically, and it becomes symmetric for membranes in glycerol rather than monotonic, which is the case for membranes in water. While the spin label at C-atom position 16 in the normal bilayer has the smallest relaxation enhancement, in the interdigitated bilayer its relaxation enhancement is the largest, indicating that it comes in closest proximity to Ni^{2+} ions. Fitting the relaxation

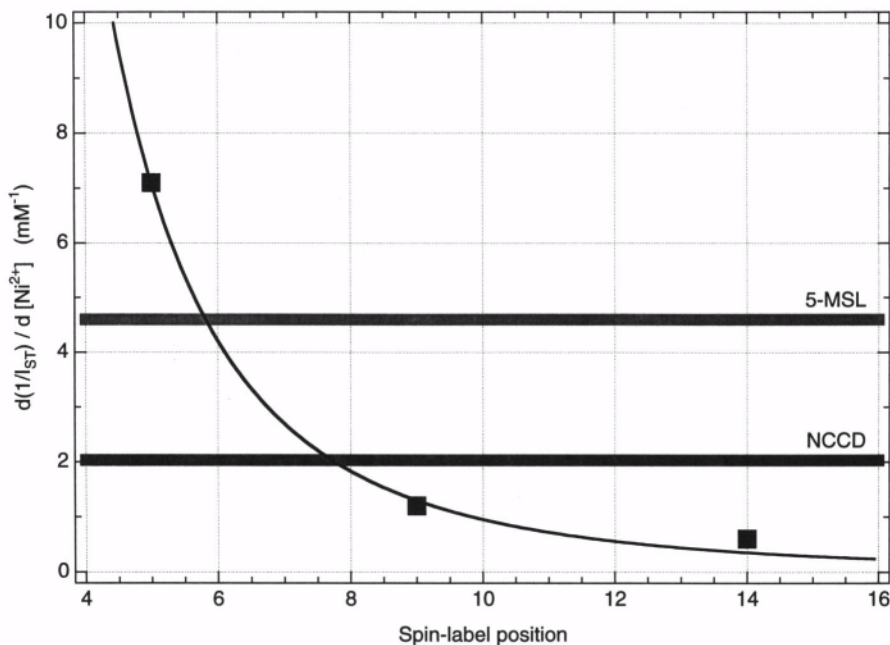


Figure 27. Dependence of the slopes of the reciprocal saturation transfer EPR integral with respect to Ni^{2+} ion concentration $d(1/I_{ST})/d[\text{Ni}^{2+}]$ on the nitroxide position in the chain of spin-labeled stearic acid in 16-kDa channel polypeptide-containing membranes from *Nephrops norvegicus* (■). The solid line represents a fit to Eqs. (18) and (21), with $m = 3$. Horizontal bars indicate corresponding values for the protein spin-labeled at cys-54 (5-MSL) and glu-140 (NCCD), respectively. (Data from Páli *et al.*, 1998)

profile indicates that overall membrane thickness is reduced by 40% for the interdigitated bilayer relative to the normal bilayer and the C-atom 16 is located in the region of the C-3 position of the chains of the oppositely oriented phospholipid molecules (Páli *et al.*, 1992). The latter represents the sort of fine-structural detail that cannot easily be obtained from diffraction methods.

The same method was applied to membranes containing the 16-kDa channel polypeptide from *Nephrops norvegicus* that has sequence homology with the proteolipid subunit of the vacuolar ATPases (Páli *et al.*, 1998). On the basis of its sequence, molecular modeling, and other studies (compare Holzenburg *et al.*, 1993; Páli *et al.*, 1995), this rather hydrophobic protein is thought to possess four transmembrane segments that most probably are in an α -helical conformation. Figure 27 shows paramagnetic relaxation enhancements by aqueous Ni^{2+} ions $d(1/I_{ST})/d[\text{Ni}^{2+}]$ for both stearic acid spin-labeled at different positions in the lipid chain and for spin labels attached at two different residues in the protein. Measurements in the presence of Ni^{2+} ions indicate that both protein labeling sites are located within the hydrophobic region of the membrane. Using calibrations established by the dipolar relaxation enhancement of spin-labeled lipids locates the maleimide spin label (5-MSL) on the single cysteine residue, cys-54 in putative transmembrane segment 2, as positioned in the region of the C-6 atom of the lipid chain. Correspondingly the carbodiimide spin label (NCCD) on glu-140 in putative transmembrane segment 4 is located somewhat deeper in the membrane, in the region of the C-8 atom of the lipid chain. Complementary studies with double labeling (compare Sec. 6.2) indicate that these residues are also exposed to the lipid chains.

6.5. Slow Rotational Diffusion and Saturation Studies

This section draws parallels between the exchange processes already considered and the standard application of ST-EPR in studying slow rotational diffusion [compare Thomas *et al.* (1976); Marsh and Horváth (1989)]. We do this primarily because it leads to a particularly simple formulation of the dependence of diagnostic ST-EPR line shape parameters on rotational correlation time (Marsh and Horváth, 1992b). Section 4 shows that two-site physical exchange and Heisenberg spin exchange are kinetically equivalent. Rotational diffusion of a spin-labeled molecule can be approximated as physical exchange in small steps. This results in a spectral diffusion of saturation analogous to that of the Heisenberg spin exchange between distinct transitions in an anisotropic powder spectrum of a single spin-labeled species (compare Fig. 10).

The spectral diffusion rate arising from spin label rotation is determined by parameters governing the angular dependence of the resonance positions and the width of a spin packet; it is inversely proportional to the rotational correlation time τ_R , defined by $\tau_R = 1/(6D_R)$, where D_R is the rotational diffusion coefficient (Fajer *et al.*, 1986). This spectral diffusion rate ($\propto \tau_R^{-1}$) is equivalent to the exchange

Table 3
Parameters for Fitting Experimental ST-EPR Rotational Correlation Time Calibrations
(Horváth and Marsh, 1983) from Spin-Labeled Hemoglobin to Eq. (58) for the Diagnostic
Spectral Line Height Ratios (L''/L , H''/H , C'/C) and Normalized Integrals (I_{ST}).
Fits to the Calibration Curves Are Given in Marsh and Horváth (1992b).

R	Range Fitted	R_0	k (μs)	b (μs)
L''/L^a	0.2, 2.0	1.825	105.6	63.8
H''/H	0.2, 2.0	2.17	407	210
C'/C	0.2, 1.0	1.01	21.3	21.1
	-0.4, 1.0	0.976	11.9	7.82
I_{ST} (total)	0.15, 1.0	1.07×10^{-2}	0.400	43.6
$I_{ST}(m_I = -1)^b$	0.06, 0.6	6.97×10^{-4}	2.85×10^{-2}	45.0

^aValues of L'' correspond to the maximum in the low-field diagnostic region. For values corresponding to the position one-third of the way in from the low-field turning point (L), as given originally in Horváth and Marsh (1983), see Marsh (1992a).

^bIntegrated intensity for the high-field manifold alone (used to detect anisotropic rotational diffusion; see Horváth and Marsh (1983)).

frequency $\tau_{e\alpha}^{-1}$, introduced in Sec. 4.2. In this case however, because the spectral diffusion rate depends on the angular dependence of the resonance positions, the resulting reduction in intensity varies throughout the spectrum, producing a large change in the saturation transfer EPR line shape [see Fig. 10 and Marsh and Horváth (1992a,b)]. Assuming line heights and intensities of the saturation transfer EPR spectra are directly proportional to the effective T_1 [compare Eq. (52)], the spectral line height ratios and integrated intensities R normally used to establish rotational correlation time calibrations (compare Horváth and Marsh, 1983), may be expressed in analogy with Eq. (35) by the following general form:

$$R = R_0 \frac{(1 + a/\tau_R)}{(1 + b/\tau_R)} \quad (57)$$

where R_0 is the value of the measured parameter R in the absence of rotational diffusion, a and b are constants to be fitted that depend only on intrinsic spectral parameters, and the ratio a/b is equal to the orientational degeneracy parameter ($\approx \sin^2\theta$). Equation (57) describes rather well the dependence on rotational correlation time of diagnostic line height ratios and intensities of the saturation transfer EPR spectra from spin-labeled hemoglobin in glycerol-water mixtures (Marsh and Horváth, 1992b). It can therefore be used to give the following simple expression for correlation time calibrations of the experimental ST-EPR spectra:

$$\tau_R = \frac{k}{(R_0 - R)} - b \quad (58)$$

where values of the experimental calibration constants k , R_0 , and b for different diagnostic spectral parameters are given in Table 3. This is a much more readily accessible form for calibrations of rotational correlation time than hitherto presented and has the additional advantage of reflecting directly the underlying spectral diffusion process.

In principle slow rotational diffusion can also be studied from the power saturation of the conventional EPR spectra. Squier and Thomas (1986) do this in terms of saturation factors determined from the ratio of integrated intensities of conventional first-derivative EPR spectra recorded at low (subsaturating) and high (partially saturating) microwave powers [compare Eq. (48)]. For calibrations for this method equivalent to those given for ST-EPR by Eq. (58), see Marsh (1995c).

7. CONCLUSIONS

Exploitation of the characteristic T_1 time scale for nitroxide spin labels allows us to extend the spin-label EPR method to determine slower rate processes and weaker magnetic interactions than is possible with conventional spectral line shape analysis. In addition to the standard application of saturation transfer EPR to measuring slow rotational diffusion rates in the submillisecond time regime, a broad range of different new applications are possible. These include the study of two-site physical (or chemical) exchange, determining weak Heisenberg exchange interactions and slow collision and translational diffusion rates, detecting mutual accessibilities of different paramagnetic species from their (weak) spin-spin interactions, and measuring relatively large intermolecular separations by using magnetic dipole-dipole interactions. The great advantage of methods based on spin-lattice relaxation is not only that sensitivity to intrinsically slow processes is increased, but also lower concentrations of paramagnetic species can be used to obtain detectable relaxation enhancements or for instance larger intermolecular distances can be measured. Such methods can be used to investigate many different dynamic processes and structural properties of biological systems, as illustrated in Sec. 6.

All of this class of measurements can be performed by CW EPR methods: Either progressive saturation EPR or nonlinear EPR, of which saturation transfer EPR is a particular example. The general use of integrated spectral intensities for such measurements circumvents problems associated with inhomogeneous broadening; it is especially useful in analyzing multicomponent systems, including those involving double labeling. The wide availability of CW instrumentation will contribute greatly to future applications of these novel spin label methods, most

notably in rather complex areas, such as structural biology and membrane dynamics.

REFERENCES

- Atkins, P. W., and Kivelson, D., 1966, *J. Chem. Phys.* **44**:169.
- Bertini, I., and Luchinat, C., 1986, *NMR of Paramagnetic Molecules in Biological Systems* (Benjamin/Cummins, Menlo Park, CA).
- Bloembergen, N., 1949, *Physica* **15**:386.
- Brophy, P. J., Horváth, L. I., and Marsh, D., 1984, *Biochemistry* **23**:860.
- Castner, T. G., Jr., 1959, *Phys. Rev.* **115**:1506.
- Dalton, L. R., Robinson, B. H., Dalton, L. A., and Coffey P., 1976, *Adv. Magn. Reson.* **8**:149.
- East, J. M., Melville, D., and Lee, A. G., 1985, *Biochemistry* **24**:2615.
- Eastman, M. P., Kooser, R. G., Das, M. R., and Freed, J. H., 1969, *J. Chem. Phys.* **51**:2690.
- Esmann, M., and Marsh, D., 1992, *Proc. Natl. Acad. Sci. USA* **89**:7606.
- Fajer, P., Thomas, D. D., Feix, J. B., and Hyde, J. S., 1986, *Biophys. J.* **50**:1195.
- Fajer, P., Watts, A., and Marsh, D., 1992, *Biophys. J.* **61**:879.
- Freed, J. H., 1979, Theory of multiple resonance and EPR saturation in liquids and related media, in *Multiple Electron Resonance Spectroscopy* (M. M. Dorio and J. H. Freed, eds.) Plenum, New York and London), pp. 73–142.
- Goldman, S. A., Bruno, G. V., Polnaszek, C. R., and Freed, J. H., 1972, *J. Chem. Phys.* **56**:716.
- Halbach, K., 1954, *Helv. Phys. Acta* **27**:259.
- Haas, D. A., Sugano, T., Mailer, C. and Robinson, B. H., 1993a, *J. Phys. Chem.* **97**:2914.
- Haas, D. A., Mailer, C., and Robinson, B. H., 1993b, *Biophys. J.* **64**:594.
- Holzenburg, A., Jones, P. C., Franklin, T., Páli, T., Heimberg, T., Marsh, D., Findlay, J. B. C., and Finbow, M. E., 1993, *Eur. J. Biochem.* **213**:21.
- Horváth, L. I., and Marsh, D., 1983, *J. Magn. Reson.* **54**:363.
- Horváth, L. I., Brophy, P. J., and Marsh, D., 1988, *Biochemistry* **27**:46.
- Horváth, L. I., Dux, L., Hankovszky, H. O., Hideg, K., and Marsh, D., 1990, *Biophys. J.* **58**:231.
- Horváth, L. I., Brophy, P. J., and Marsh, D., 1993a, *Biophys. J.* **64**:622.
- Horváth, L. I., Brophy, P. J., and Marsh, D., 1993b, *Biochim. Biophys. Acta* **1147**:277.
- Hubbell, W. L., and Altenbach, C., 1994, Site-directed spin labeling of membrane proteins, in *Membrane Protein Structure. Experimental Approaches* (S. H. White, ed.) (Oxford University Press, New York), pp. 224–248.
- Hwang, J. S., Mason, R. P., Hwang, L.-P., and Freed, J. H., 1975, *J. Phys. Chem.* **79**:489.
- Hyde, J. S., 1979, Saturation recovery methodology, in *Time Domain Electron Spin Resonance* (L. Kevan and R. N. Schwartz, eds.) (Wiley, New York), pp. 1–30.
- Hyde, J. S., and Dalton, L. R., 1979, Saturation transfer spectroscopy, in *Spin Labelling II. Theory and Applications* (L. J. Berliner, ed.) (Academic, New York), pp. 1–70.
- Hyde, J. S., and Feix, J. B., 1989, Electron-electron double resonance, in *Biological Magnetic Resonance. Spin Labeling Theory and Applications*, vol. 8 (L. J. Berliner and J. Reuben, eds.) (Plenum, New York), pp. 305–37.
- Hyde, J. S., and Subczynski, W. K., 1984, *J. Magn. Reson.* **56**:125.
- Hyde, J. S., and Subczynski, W. K., 1989, Spin-label oximetry, in *Biological Magnetic Resonance. Spin Labeling Theory and Applications*, vol. 8 (L. J. Berliner and J. Reuben, eds.) (Plenum, New York), pp. 399–425.
- Hyde, J. S., Chien, J. C. W., and Freed, J. H., 1968, *J. Chem. Phys.* **48**:4211.

- Hyde, J. S., Swartz, H. M., and Antholine, W. E., 1979, The spin-probe, spin-label method, in *Spin Labelling II. Theory and Applications* (L. J. Berliner, ed.) (Academic, New York), pp. 71–113.
- Hyde, J. S., Froncisz, W., and Mottley, C., 1984, *Chem. Phys. Lett.* **110**:621.
- Keller, R. C. A., ten Berge, D., Nouwen, N., Snel, M. M. E., Tommassen, J., Marsh, D., and de Kruijff, B., 1996, *Biochemistry* **35**:3063.
- Khrantsov, V. V., and Marsh, D., 1991, *Biochim. Biophys. Acta* **1068**:257.
- Knowles, P. F., and Marsh, D., 1991, *Biochem. J.* **274**:625.
- Kusumi, A., Subczynski, W. K., and Hyde, J. S., 1982, *Proc. Natl. Acad. Sci. USA* **79**:1854.
- Livshits, V. A., Páli, T., and Marsh, D., 1998, *J. Magn. Reson.*, in press.
- Marsh, D., 1989, Experimental methods in spin-label spectral analysis, in *Biological Magnetic Resonance. Spin Labeling Theory and Applications*, vol. 8 (L. J. Berliner and J. Reuben, eds.) (Plenum, New York), pp. 255–303.
- Marsh, D., 1992a, *Appl. Magn. Reson.* **3**:53.
- Marsh, D., 1992b, *J. Magn. Reson.* **99**:332.
- Marsh, D., 1993, *Chem. Soc. Rev.* **22**:329.
- Marsh, D., 1994, Spin-Labeling in Biological Systems, in *Electron Spin Resonance*, vol. 14 (N. M. Atherton, M. J. Davies, and B. C. Gilbert, eds.) (Royal Society of Chemistry, Cambridge, UK), pp. 166–202.
- Marsh, D., 1995a, *Spectrochim. Acta A* **51**:L1 and **A 51**:1453 (correction).
- Marsh, D., 1995b, *J. Magn. Reson. A* **114**:248.
- Marsh, D., 1995c, *Spectrochim. Acta* **51A**: 111.
- Marsh, D., and Horváth, L. I., 1989, Spin-Label Studies of the Structure and Dynamics of Lipids and Proteins in Membranes, in *Advanced EPR. Applications in Biology and Biochemistry* (A. J. Hoff, ed.) (Elsevier, Amsterdam), pp. 707–52.
- Marsh, D., and Horváth, L. I., 1992a, *J. Magn. Reson.* **97**:13.
- Marsh, D., and Horváth, L. I., 1992b, *J. Magn. Reson.* **99**:323.
- Molin, Yu. N., Salikov, K. M., and Zamarev, K. I., 1980, *Spin Exchange. Principles and Applications in Chemistry and Biology* (Springer-Verlag, Berlin).
- Páli, T., Bartucci, R., Horváth, L. I., and Marsh, D., 1992, *Biophys. J.* **61**:1595.
- Páli, T., Horváth, L. I., and Marsh, D., 1993a, *Magn. Reson.* **A101**:215.
- Páli, T., Bartucci, R., Horváth, L. I., and Marsh, D., 1993b, *Biophys. J.* **64**:1781.
- Páli, T., Finbow, M. E., Holzenburg, A., Findlay, J. B. C., and Marsh, D., 1995, *Biochemistry* **34**:9211.
- Páli, T., Livshits, V. A., and Marsh, D., 1996, *J. Magn. Reson.* **B113**:151.
- Páli, T., Finbow, M. E., and Marsh, D., 1998, to be published.
- Percival, P. W., and Hyde, J. S., 1976, *J. Magn. Reson.* **23**:249.
- Pfeifer, H., 1961, *Ann. Physik* **8**:1.
- Pfeifer, H., 1963, *Biochim. Biophys. Acta* **66**:434.
- Popp, C. A., and Hyde, J. S., 1982, *Proc. Natl. Acad. Sci. USA* **79**:2559.
- Portis, A. M., 1953, *Phys. Rev.* **91**:1071.
- Robinson, B. H., Haas, D. A., and Mailer, C., 1994, *Science* **263**:490.
- Shin, Y.-K., and Hubbell, W. L., 1992, *Biophys. J.* **61**:1443.
- Shlenkin, V. I., Fushman, D. A., Vylegzhanina, N. N., Jagodina, L. O., and Fedotov, V. D., 1993, *Appl. Magn. Reson.* **5**:285.
- Slichter, C. P., 1978, *Principles of Magnetic Resonance*, 2d ed. (Springer-Verlag, Berlin/Heidelberg/New York).
- Snel, M. M. E., and Marsh, D., 1993, *Biochim. Biophys. Acta* **1150**:155.
- Snel, M. M. E., and Marsh, D., 1994, *Biophys. J.* **67**:737.
- Snel, M. M. E., de Kruijff, B., and Marsh, D., 1994, *Biochemistry* **33**:11150.
- Snel, M. M. E., de Kroon, A. I. P. M., and Marsh, D., 1995, *Biochemistry* **34**:3605.
- Solomon, I., 1955, *Phys. Rev.* **99**:559.

- Squier, T. C., and Thomas, D. D., 1986, *Biophys. J.* **49**:921.
- Squier, T. C., and Thomas, D. D., 1989, *Biophys. J.* **56**:735.
- Stopar, D., Jansen, K., Pali, T., Marsh, D., and Hemminga, M A., 1997, *Biochemistry* **36**:8261.
- Subczynski, W. K., and Hyde, J. S., 1981, *Biochim. Biophys. Acta* **643**:283.
- Subczynski, W. K., and Hyde, J. S., 1984, *Biophys. J.* **45**:743.
- Subczynski, W. K., Hyde, J. S., and Kusumi, A., 1989, *Proc. Natl. Acad. Sci. USA* **86**:4474.
- Thomas, D. D., Dalton, L. R., and Hyde, J. S., 1976, *J. Chem. Phys.* **65**:3006.
- Wilson, R., and Kivelson, D., 1966, *J. Chem. Phys.* **44**:154.
- Windrem, D. A., and Plachy, W. Z., 1980, *Biochim. Biophys. Ada* **600**:655.
- Yin, J.-J., and Hyde, J. S., 1987, *Z. Phys. Chem. NF* **153**:57.
- Yin, J.-J., Pasenkiewicz-Gierula, M., and Hyde, J. S., 1987, *Proc. Natl. Acad. Sci. USA* **84**:964.
- Yin, J.-J., Feix, J. B., and Hyde, J. S., 1988, *Biophys. J.* **53**:525.
- Yin, J.-J., Feix, J. B., and Hyde, J. S., 1990, *Biophys. J.* **58**:713.

Comparative Spin Label Spectra at X-Band and W-band

Alex I. Smirnov, R. L. Belford, and R. B. Clarkson

1. INTRODUCTION

Most electron paramagnetic resonance (EPR) experiments on spin-labeled systems are carried out at X-band (8.8–9.5 GHz), although a few are done at Q-band (35 GHz) and higher frequencies. At X-band the main source of spin rotational relaxation for nitroxide spin labels is modulation of the nitrogen hyperfine A tensor. For nitroxides this tensor is very close to axial, which limits the amount of information on the anisotropy of rotational motion that can be obtained from X-band spin label EPR spectra (e.g., Budil *et al.*, 1993). At Q-band (35 GHz), contributions to spectral densities determined by rotational modulation of the electronic Zeeman term become comparable to those from the hyperfine tensor, making this frequency an important tool for elucidating different models of motion (e.g., Hwang *et al.*, 1975; Griffith and Jost, 1976), for assigning components for spin label spectra of lipid-protein complexes (e.g., Marsh, 1989; Horvath *et al.*,

Alex I. Smirnov • Illinois EPR Research Center, College of Medicine, University of Illinois, Urbana, IL 61801 R. L. Belford • Illinois EPR Research Center, Department of Chemistry, University of Illinois, Urbana, IL 61801 and R. B. Clarkson • Illinois EPR Research Center, College of Medicine and Veterinary Medicine, University of Illinois, Urbana, IL 61801.

Biological Magnetic Resonance, Volume 14: Spin Labeling: The Next Millennium, edited by Berliner. Plenum Press, New York, 1998.

1994), and for measuring g -matrices of the spin labels more accurately (e.g., Goldman *et al.*, 1972; Gaffney and McConnell, 1974).

At EPR fields corresponding to frequencies of 90 GHz and higher, the Zeeman term in the spin Hamiltonian of a typical nitroxide radical dominates hyperfine interactions. Electronic spin relaxation then becomes even more sensitive to the rotational modulation of the g -matrix, which for most nitroxides has a rhombic structure. Thus EPR at such high magnetic fields (HF) provides different information on the anisotropy of rotational motion than conventional X-band EPR. For example it was recently shown that by combining 9.5 and 250 GHz EPR data, one can determine the full rotational diffusion tensor (Budil *et al.*, 1993). Other features include enhanced sensitivity to both fast and slow motion, angle selectivity, and sensitivity of spectral simulations to models of rotational motion and solvent interactions.

Although the advantages of HF EPR in spin-labeling experiments were already demonstrated, these experiments were carried out by only a few research groups, primarily because HF EPR instrumentation was not available commercially. Recent announcements of commercial HF EPR spectrometers, 95 GHz in particular, are likely to stimulate more groups to undertake applications of the spin-labeling method at these frequencies. Chapter 3 compares continuous-wave spectra from several selected spin-labeled systems at W-band (94 GHz) with those at the conventional 9.5-GHz (X-band) EPR frequency to illustrate the kind of behavior we can expect. We provide here only a general discussion of observed spectra and leave a detailed analysis to the original literature and other chapters of this book. We also include some essential experimental details on sample handling and deoxygenation in HF EPR experiments.

2. COMPARATIVE X- AND W-BAND EPR SPECTRA OF SPIN LABELS IN ISOTROPIC LIQUIDS

One of the features of HF EPR of spin labels is enhanced sensitivity to both fast and slow motional regimes. In the fast motional regime, the line width of each of the nitrogen hyperfine transitions can be expressed in terms of spectral parameters A , B , and C :

$$T_2^{-1}(m_I) = (A + A') + Bm_I + Cm_I^2 \quad (1)$$

where m_I is the nitrogen nuclear quantum number and all frequency-independent contributions to line width are included in the A' term.

Secular spectral densities contributing to these line width parameters have very different frequency dependencies. For example the secular spectral density arising solely from rotational modulation of the electronic g -matrix depends quadratically on the resonance frequency ν , resulting in a large (by a factor of a hundred)

enhancement of parameter A at 95 GHz over 9.5 GHz. Rotational modulation of both \mathbf{g} - and hyperfine \mathbf{A} tensors contributes to parameter B in a correlated way, resulting in an approximate proportionality of this parameter to ν (if pseudosecular and nonsecular spectral densities are neglected). Parameter C remains approximately unchanged because the contributing secular spectral density arises from rotational modulation of the nitrogen hyperfine tensor, and it is frequency-independent. This characteristic frequency dependence of line width parameters is illustrated here in examples of two different nitroxides. A more detailed analysis of the frequency dependence of spectral densities for a general case of fully anisotropic rotational diffusion is given by Budil *et al.* (1993).

2.1. Solution of Perdeuterated Tempone in Toluene

Rotational dynamics of a small molecule, perdeuterated 2,2',6,6'-tetramethyl-4-piperidone-1-nitroxide (perdeuterated Tempone, or PDT), in toluene was addressed in X- and Q-band studies (e.g., Hwang *et al.*, 1975; Zager and Freed, 1982), 150 GHz (Grinberg *et al.*, 1980), and recently reexamined at 250 GHz (Budil *et al.*, 1993). The PDT represents a six-membered ring nitroxide without resolved superhyperfine structure. Figure 1 shows experimental 9.0- and 95-GHz EPR spectra from a 0.05-mM PDT solution in toluene- d_8 recorded at different temperatures. Both samples were prepared in quartz tubes, carefully deoxygenated by a freeze-pump-thaw technique, then sealed with a torch.

It is apparent that at room temperature, the X-band EPR spectrum of PDT falls into the extreme narrowing regime, resulting in almost equal amplitudes of the nitrogen hyperfine lines (Fig. 1, 291 K). The width of those lines (ca., 0.2 G peak-to-peak) is determined primarily by inhomogeneous broadening (ca., 0.1 G peak-to-peak) caused by unresolved hyperfine interactions with deuterons and by homogeneous contributions from mainly the Heisenberg nitroxide-nitroxide spin exchange and spin rotation coupling. Homogeneous line width arising from rotational modulation of \mathbf{g} - and \mathbf{A} -tensors is small and difficult to measure under these conditions. For example line width parameter B (Eq. 1) is only 9 ± 1 mG.

Although the 94-GHz spectrum at the same temperature (Fig. 1, 291 K) also falls in the line width narrowing regime, the enhanced sensitivity of EPR spectra at this frequency to the rotational motion manifests itself in unequal peak-to-peak amplitudes of the nitrogen hyperfine components. Figure 2 summarizes line width parameters ($A + A'$), B , and C measured for 0.05-mM PDT toluene- d_8 solutions at 9.0 and 94 GHz as a function of $\log(\eta/T)$. It is apparent that at 94 GHz, parameters ($A + A'$) and B are substantially enhanced compared to 9.0 GHz, while parameter C remains approximately the same. Figure 2 also illustrates that at $\eta/T < 10^{-2}$ cPK $^{-2}$, the sum ($A + A'$) measured from 94 GHz is dominated by parameter A , which is determined primarily by rotational modulation of the \mathbf{g} -tensor; thus it is useful for analyzing rotational dynamics (see also Budil *et al.*, 1993). At 9.0 GHz this sum is

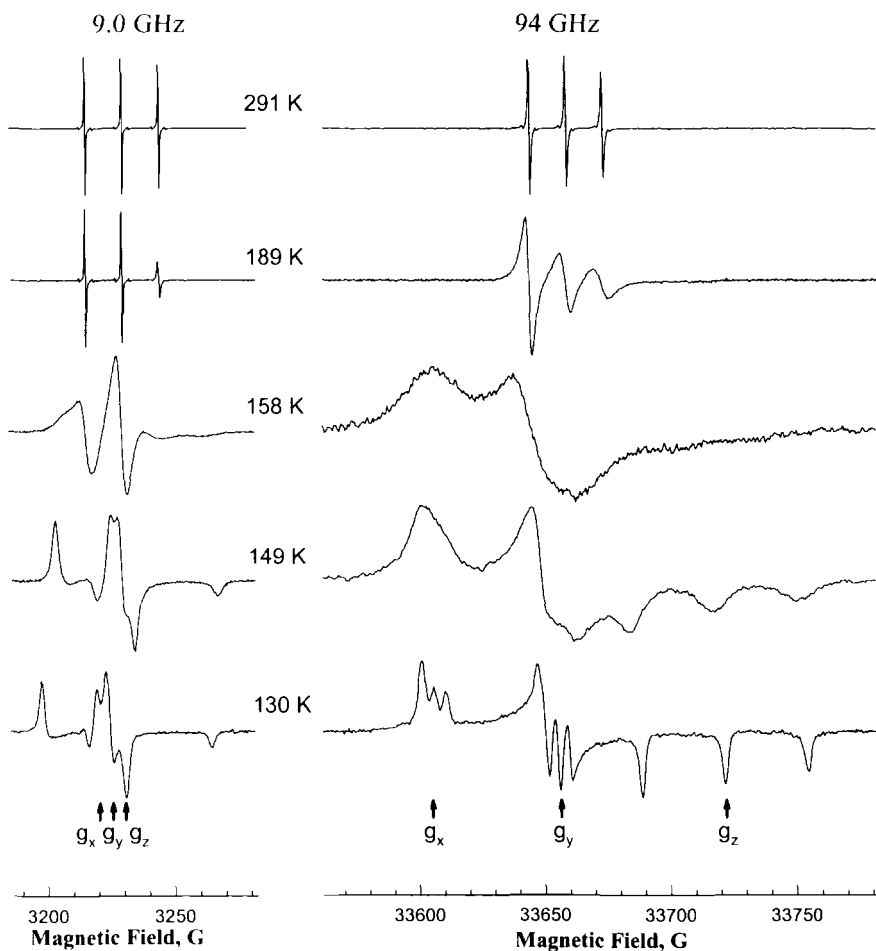


Figure 1. Experimental 9.0- and 95-GHz EPR spectra from 0.05-mM solution of perdeuterated 2,2',6,6'-tetramethyl-4-piperidone-1-nitroxide (Tempone or PDT) in toluene- d_8 recorded at several temperatures. Samples for measurements at both EPR frequencies were carefully deoxygenated. Approximate positions of the g -matrix principal axis' orientations are indicated by arrows in the 130-K spectra, which approach the rigid limit.

dominated by A' . This part of the relaxation includes field-independent Heisenberg spin-spin exchange, and spin-orbital coupling which causes a noticeable increase in $(A + A')$ with the decrease of η/T ; this complicates data analysis. Overall Fig. 2 demonstrates the enhanced sensitivity of HF EPR to fast molecular motion.

Comparing 9.0- and 94-GHz EPR spectra at different temperatures (Fig. 1) also illustrates that at W-band, the onset of slow motional effects for the same nitroxide

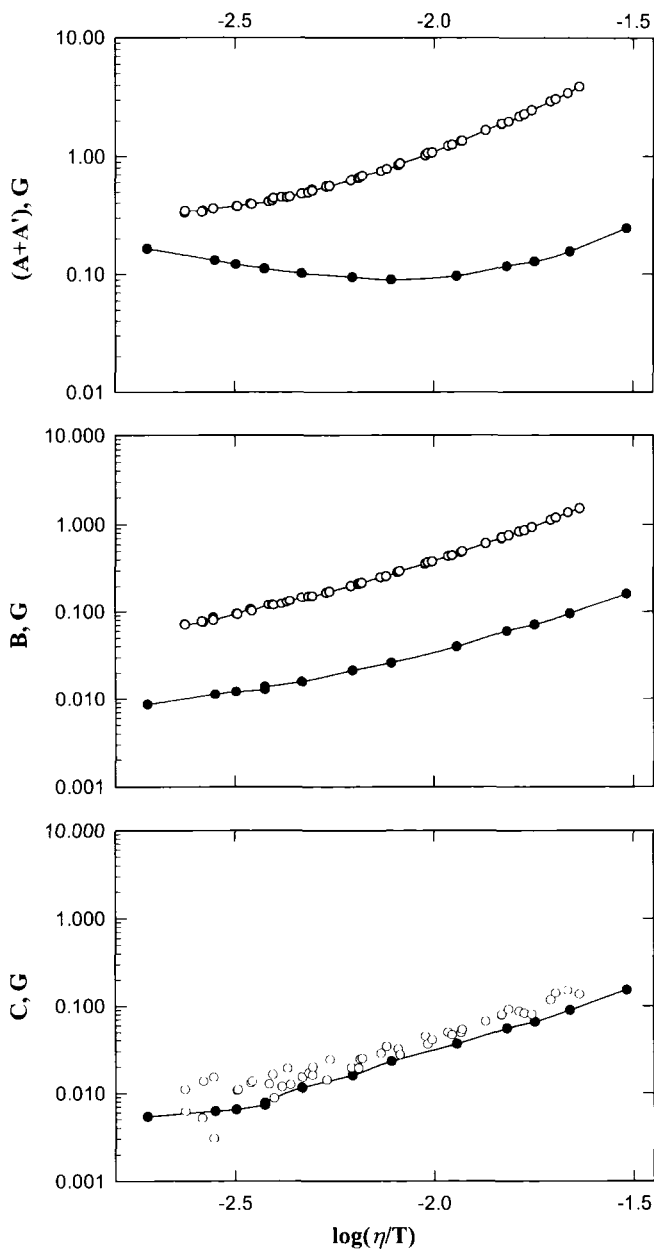


Figure 2. Line width parameters $(A + A')$, B , and C (Eq. 1) measured at 9.0 GHz (solid circles, ●) and 94 GHz (open circles, ○) for 0.05-mM solution of perdeuterated 2,2',6,6'-tetramethyl-4-piperidone-1-nitroxide (PDT) in toluene- d_8 . At 94 GHz parameters $(A + A')$ and B are substantially enhanced compared to 9.0 GHz, while parameter C remains approximately the same.

solvent system occurs at a higher temperature than it does at X-band. This effect is also described by Budil *et al.* (1993) for 250 GHz. Another feature of HP EPR spin label spectra in a slow motional regime is enhanced sensitivity to rotational dynamics. Comparing X- and W-band spectra of PDT in toluene (Fig. 1) shows that the EPR spectra at 130 and 149 K demonstrate more pronounced changes in line width and field position of the characteristic features at 95 than at 9.5 GHz.

Rotational dynamics of spin labels can be analyzed if their magnetic parameters are known to a high accuracy, having been obtained for example from the rigid-limit (or “powder pattern”) spectrum. As previously shown (e.g., Ondar *et al.*, 1985), these measurements are more accurate at high magnetic fields (EPR frequencies > 90 GHz). At these frequencies, turning points of spin label spectra corresponding to principal axis orientations of the **g**-matrix are separated from those of the **A**-matrix. For some nitroxides, nitrogen hyperfine components are resolved at 95 GHz, as illustrated in Fig. 1 (130 K) for PDT in toluene. Then both **g**- and **A**-matrices can be accurately determined accurately by computer simulations. If resolution of the nitrogen hyperfine structure is lost in the HF EPR spectrum, then least-squares analysis of the rigid-limit spectra at two frequencies (9.0 and 95 GHz) can be used to measure magnetic parameters accurately (e.g., Smirnov *et al.*, 1995). Magnetic parameters for many nitroxides in different solvents from measurements at 150 GHz were published by Lebedev and coworkers (e.g., Lebedev *et al.*, 1992; Lebedev, 1994; and papers cited therein). Some of these values were further refined by experiments at 249 GHz and computer simulations (e.g., Budil *et al.*, 1993; Earle *et al.*, 1993, 1994). Most differences among values of magnetic parameters reported by different laboratories for the same nitroxide/solvent are probably attributable to errors in magnetic field calibration (e.g., see also Budil *et al.*, 1993).

2.2. Solution of 3-Doxyl-17 β -Hydroxy-5 α -Androstane in *O*-xylene

The 3-Doxyl-17 β -hydroxy-5 α -androstane (or ASL) represents a 5-membered ring nitroxide whose solution X-band EPR spectrum displays a well-resolved complex superhyperfine structure when the sample is deoxygenated (Fig. 3). This spin label has a cigarlike shape, therefore anisotropy parameters for this molecule in an effectively isotropic solvent, such as *o*-xylene ($\rho_x = 1.6 \pm 0.5$, $\rho_y = 5.8 \pm 1.0$; Smirnova *et al.*, 1995), are larger than those for PDT in toluene ($\rho_x = 1.8 \pm 0.2$, $\rho_y = 1.5 \pm 0.3$; Budil *et al.*, 1993).

Figure 3 shows comparative EPR spectra from a 0.5-mM ASL solution in *o*-xylene at different temperatures. At temperatures ≥ 10 °C, ASL spectra at 9.0 GHz fall into the extreme motional narrowing regime, where a complex superhyperfine structure makes the measurement of rotational dynamics inaccurate (Smirnova *et al.*, 1995). This is typical for room temperature X-band spectra of many other solutions of nondeuterated spin labels in organic solvents. In contrast the 94-GHz spectrum at 293 K for the same system shows visible differences in peak-to-peak

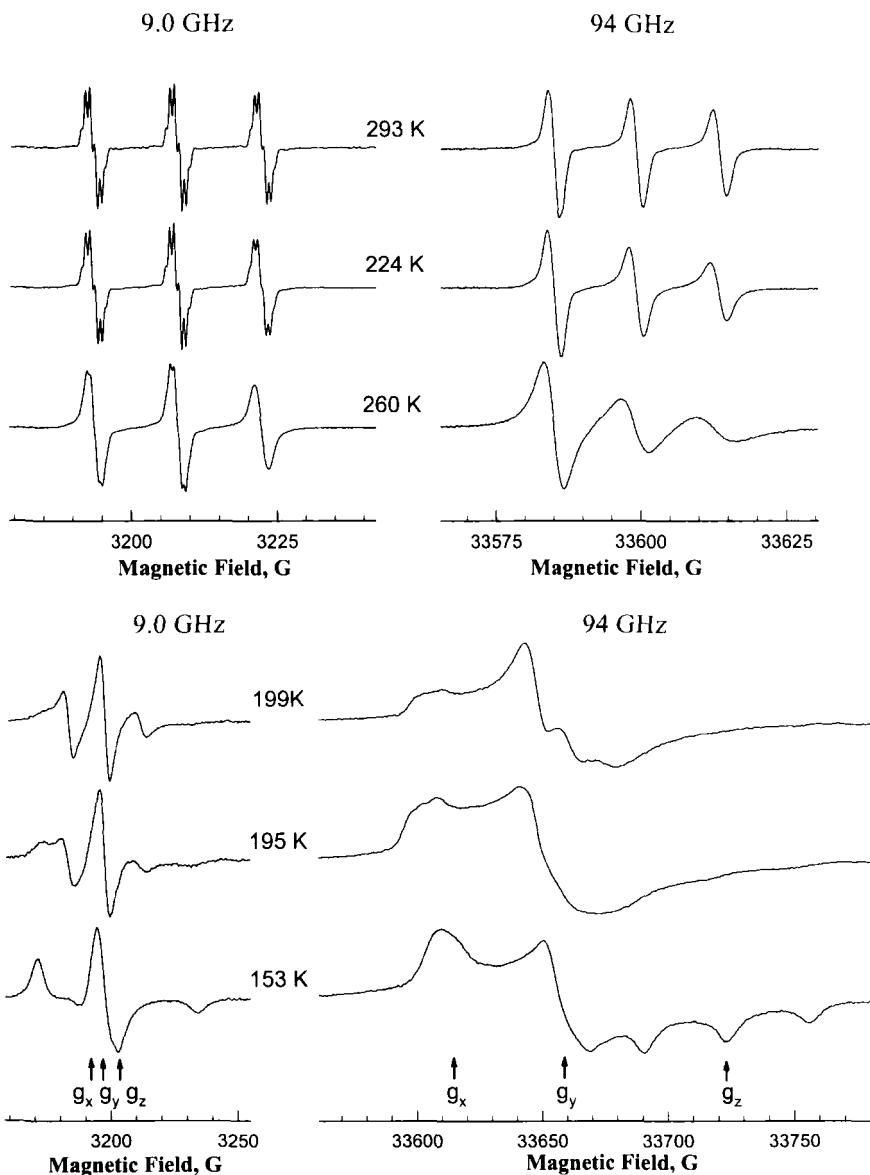


Figure 3. Comparative experimental 9.0- and 94-GHz EPR spectra from a 0.5-mM solution of 3-doxyl-17 β -hydroxy-5 α -androstane (ASL) in *o*-xylene for several temperatures. Spectra at $T = 293$, 224, and 260 K fall into the fast motional regime at both frequencies. At temperatures ≥ 10 °C, ASL spectrum at 9.0 GHz exhibits extreme motional narrowing for which the presence of a complex superhyperfine structure makes measurements of rotational dynamics inaccurate (Smirnova *et al.*, 1995). The approximate positions of the g -matrix principal axis' orientation are indicated by arrows in the 153-K spectra, which approach the rigid limit.

amplitudes of the three nitrogen hyperfine components (Fig. 3, 94 GHz, $T = 293$ K). These unequal amplitudes are attributed to different homogeneous component line widths, and they arise from enhanced contribution to the relaxation from rotational modulation of the g -matrix. Because of the increased homogeneous line width, the proton superhyperfine structure becomes unresolved even at room temperature and for a carefully deoxygenated sample.

Fast motional EPR spectra in Fig. 3 are clearly asymmetric. This asymmetry is caused by an admixture of dispersion into the absorption spectrum; it is usually present in CW EPR spectra obtained with single-channel detection. A more expensive quadrature detection scheme can eliminate this problem. Another approach accounts for the phase shift in data post processing either by calculating a quadrature signal (generated from the Hilbert transform of the measured signal), then adding this calculated spectrum to the experimental one until the integrated combined spectrum displays a flat baseline (Earle *et al.*, 1993); or simulating the experimental spectrum with an arbitrary phase, then adjusting this phase during the fitting procedure (e.g., Smirnov and Belford, 1995; Smirnova *et al.*, 1995).

Slow motional effects for ASL in *o*-xylene become more apparent at higher temperatures at 94 GHz than at 9.0 GHz in a manner similar to that seen for PDT. Other features in this system are the sensitivity of slow motional HF EPR spectra to diffusional anisotropy and the sensitivity of simulations to the rotational diffusion model employed. For example Earle and coworkers (1993) found significant differences in rotational anisotropy for an approximately spherical PDT molecule and a cigar-shaped 3-doxylcholestane (CSL) probe. The best fit of 250-GHz EPR spectra for CSL in a slow motional limit suggested even greater anisotropy than in the fast motional limit. Since ASL has a shape similar to CSL, its rotational dynamics at low temperatures should differ from PDT. Indeed W-band slow motional spectra for ASL at 199 K (Fig. 3) and PDT at 158 K (Fig. 1) are quite different, while X-band spectra at the same temperatures are more nearly similar.

In the rigid limit (Fig. 3, 153 K), the X-band ASL spectra contain little information on the g -matrix because of a large inhomogeneous line width, primarily caused by proton hyperfine interactions. In a contrast 95-GHz spectra at the same temperature demonstrate well-resolved features corresponding to the principal axis' orientations of the g -matrix. Components of the A -matrix are not resolved, with the exception of A_z .

2.3. Resolution Enhancement in High Magnetic Fields: Mixtures of Phenyl-*tert*-butylnitron Spin Adducts

A major established advantage of high-field EPR spectroscopy is enhanced g -factor resolution (e.g., Ondar *et al.*, 1985). The ability to resolve two spectra from a mixture of different species is defined by the difference in the field position of the spectra ΔH and the line width $\Delta H_{p-p}(\nu)$ at a given resonance frequency ν :

$$\Delta H \approx \frac{h\nu}{g_{el}^2 \beta} \Delta g \quad (2)$$

Most spin labels have close g -factors ($\Delta g < 1 \times 10^{-3}$), which results in strongly overlapping X-band EPR spectra from mixtures of different nitroxides (e.g., Wang *et al.*, 1994) or a spin probe partitioned between the membrane aqueous and lipid phases (e.g., Smirnov *et al.*, 1995). The same spectral overlapping occurs for the spin adducts formed by the same spin trap and different radical precursors.

In Fig. 4 curve *A* shows an X-band (9.5-GHz) spectrum from a mixture of adducts formed by spin trap phenyl-*tert*-butylnitron (PBN) and phenyl- and trichloromethyl- radicals. Only the high-field line ($m_1 = -1$ nitrogen hyperfine component) has some small extra broadening on the line shoulder (shown by an arrow) that may suggest two species. This strong overlap of the X-band spectra makes accurately determining the number of species as well as nitrogen and β -hydrogen hyperfine coupling parameters a difficult task. In Fig. 4 curve *B* shows the 94.5-GHz EPR spectrum from the same mixture of spin adducts at the same temperature.

Because spectral separation ΔH is proportional to the resonance frequency ν at the same Δg , the presence of two radical adducts becomes clear at W-band. An increase in microwave frequency also results in broader lines at 95 GHz; however as can be seen from curve *B* in Fig. 4, line broadening at 95 GHz is much too small to defeat the gain in resolution due to Δg . The latter is explained by considering the frequency dependence of spectral densities contributing to line width. As discussed in references to PDT, the line width parameter *A* is enhanced the most at high fields because it contains the secular spectral density J^{GG} , arising solely from the rotational modulation of the electronic g -matrix, which increases as ν^2 . Although this spectral density at W-band is larger by a factor of 100 than at X-band, the peak-to-peak width of the $m_1 = 0$ nitrogen transition, as seen in Fig. 4, increases only moderately. One reason is that at X-band, the homogeneous width of the $m_1 = 0$ line is dominated by rotational modulation of the hyperfine tensor, and it also contains frequency-independent contributions (denoted as A') in equation 1, such as spin rotation coupling and Heisenberg spin exchange. The relative contribution from the electronic g -matrix spectral density J^{GG} is rather small. For example according to data by Smirnova *et al.* (1997) for methyl-PBN in toluene at 260 °K, the contribution from rotational modulation of the nitrogen hyperfine matrix is $A = 20.4$ mG, while the contribution from the electronic g -matrix spectral density is almost negligible ($J^{GG} = 1.0$ mG). At 94.5 GHz (W-band), the line width parameter *A* is 121 mG, and it is dominated by J^{GG} ($= 107$ mG). Therefore although J^{GG} is increased more than 100-fold, overall broadening of the $m_N = 0$ line for this viscosity/temperature arising solely from the rotational modulation of g -matrix is only about 100 mG.

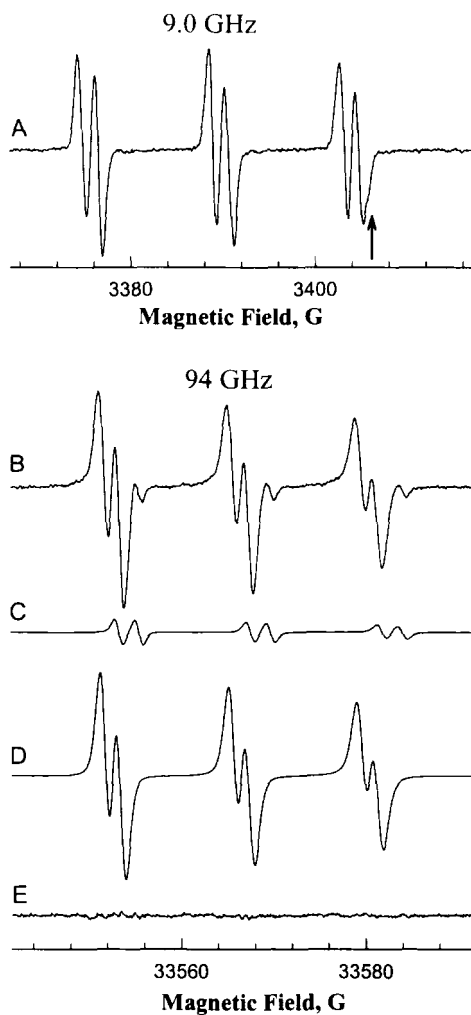


Figure 4. A: X-band (9.5-GHz) EPR spectrum from a mixture of phenyl-PBN and trichloromethyl-PBN adducts in benzene at 24 °C. Arrow points to some extra broadening on the line shoulder, which is caused by the presence of two species.

B, C, and D: Experimental W-band (95-GHz) spectrum of the mixture and the corresponding least-squares-simulated spectra of phenyl-PBN and trichloromethyl-PBN adducts, respectively. Reprinted with permission from Smirnova *et al.*, 1997 © 1997 American Chemical Society.

The second reason for only very moderate line broadening for this spin adduct at the W-band is a large inhomogeneous line width (≈ 1 G), which is typical of many nondeuterated nitroxide spin labels and spin adducts. Inhomogeneous line width caused by unresolved and partially resolved hydrogen hyperfine interactions is typically about 0.6–1.0 G. Thus for solutions of methyl-PBN adduct in non-viscous solvents, inhomogeneous broadening dominates the line width at both X- and W-bands. Therefore relative broadening of the $m_N = 0$ transition for these and many other nondeuterated spin adducts at W-band EPR frequency is expected to be quite moderate ($\leq 20\%$; about 10% for methyl-PBN), while the difference in the field position ΔH among species with different g-factors proportionally increases with the EPR frequency ν [see Eq. (2)].

Secular spectral densities increase proportionally with rotation correlation time τ_R , and the relative line width broadening at W-band also increase as the viscosity-to-temperature ratio increases. Estimates show that the gain in spectral resolution at W-band disappears only when the HF EPR spectrum falls into an intermediate motional regime.

3. SAMPLE DEOXYGENATION IN CW HF EPR EXPERIMENTS

For many spin-labeled systems, line width at W-band increases primarily because of rotational averaging of the g-factor, which decreases the relative weight of other contributions to the line width, such as for example Heisenberg spin exchange with dissolved molecular oxygen. For aqueous solutions of a typical nitroxide spin label equilibrated with air at room temperature, oxygen broadening is only ≈ 0.13 G (X-band data, Smirnova *et al.*, 1995b). However, this effect accounts for most homogeneous line width in the nitroxides at X-band; especially for deuterated nitroxides, it represents a substantial portion of the overall peak-to-peak line width (≈ 0.30 G for PDT). At 94 GHz, the peak-to-peak line width of the $m_I = 0$ nitrogen hyperfine component for PDT increases to ≈ 0.68 mG; the relative magnitude of the oxygen effect is somewhat smaller. However for many other solvents (and particularly organic solvents), the product of oxygen solubility and the diffusion coefficients significantly exceeds that for water, so careful sample deoxygenation may be necessary.

Sample sizes for HF EPR experiments are determined by the resonator and spectrometer configuration. For example for the Cornell 250-GHz EPR spectrometer equipped with a Fabry-Perot resonator, Budil and coworkers (1993) prepared a PDT toluene solution in a quartz tube [4–5 mm outer diameter (o.d.), ≈ 1 mm wall thickness], which they then deoxygenated by a freeze-pump-thaw method and sealed with a torch about 20 mm from the end. Cylindrical resonators developed for W-band EPR spectroscopy easily can accommodate longer sample tubes but of smaller diameter (e.g., tube length ≈ 26 mm, o.d. ≈ 1 mm, (Wang *et al.*, 1994). For

example in a split-coil superconductive magnet, the cavity axis is typically directed along the bore of the magnet, so the length of the sample tube is not limited to the size of the cavity. Nonlossy spin-labeled samples can be placed in a quartz capillary 5-10 cm long, deoxygenated with the freeze-pump-thaw technique, then easily flame-sealed when the sample is kept under liquid nitrogen. For solenoid-type magnets, sample length is usually limited by the diameter of the room temperature bore or cryostat, it is typically $\leq 3-5$ cm. For such a configuration, the quartz capillaries can be custom bent to form an L-shape and sealed at the short ends, as described by Smirnova *et al.* (1995a). Under vacuum, spin label solutions can be drawn into such capillaries (primarily into the short ends), deoxygenated by the freeze-pump-thaw method, then sealed with a torch while the solution is kept under liquid nitrogen away from the heat.

Unfortunately aqueous solutions of biological interest (spin-labeled proteins and membranes) cannot be handled in 95-GHz EPR experiments the same way for two reasons: (1) Freezing can often destroy the integrity of the sample, and (2) the optimal diameter of the capillary for an aqueous sample at this frequency is only 0.1-0.2 mm, which makes freeze-pump-thawing a viscous solution quite difficult due to excessive bubbling. At the Illinois EPR Research Center, we adapted a degassing method based on gas-permeable plastic capillaries from a procedure previously described for X-band (e.g., Windrem and Plachy, 1980; Hyde and Subczynski, 1989). In brief an aqueous sample is drawn into a microbore Teflon (poly(tetrafluoroethylene), or TFE) tubing [inner diameter (i.d.) = 0.152 ± 0.025 mm, wall thickness 0.127 ± 0.025 , Cole-Parmer Instrument Co., Vernon Hills, IL], and the capillary ends are sealed with Critoseal tube sealant (Sherwood Medical, purchased from Fisher Scientific, Pittsburgh, PA). The capillary is positioned through the center of a cylindrical W-band TE_{012} resonator so that the ends remain outside the cavity. A gas flow with the desired oxygen content is directed to the cryostat enclosing the cavity and through the waveguide directly to the sample. At room temperature, reequilibration of an aqueous PDT solution drawn inside such a capillary occurred with a time constant of $t_{1/2} \approx 4$ min; this is acceptable in many experiments. At elevated temperatures, the oxygen permeability coefficient for TFE increases, decreasing the time necessary for sample reequilibration (e.g., see Smirnov *et al.*, 1994).

Figure 5 shows the effect of deoxygenation on 9.0- and 94-GHz EPR spectra taken at 41 °C in a multibilayer aqueous dispersion of 1,2-dimyristoyl-*sn*-glycero-3-phosphocholine (DMPC, 20% v/v, 1.1-M borate buffer at pH 9.5) labeled with 16-doxyyl stearic acid (16-DS, label-to-lipid ratio 1:100). Under these conditions, EPR spectra of the 16-DS label at the X-band fall into the motional narrowing regime. The nitroxide moiety of 16-DS is located within the center of the bilayer, where oxygen permeability is maximal (e.g., see Kusumi *et al.*, 1982; Smirnov *et al.*, 1996); thus the oxygen effect on the shape of X-band EPR spectra that are normalized by the double integral value is seen primarily as changes in peak-to-

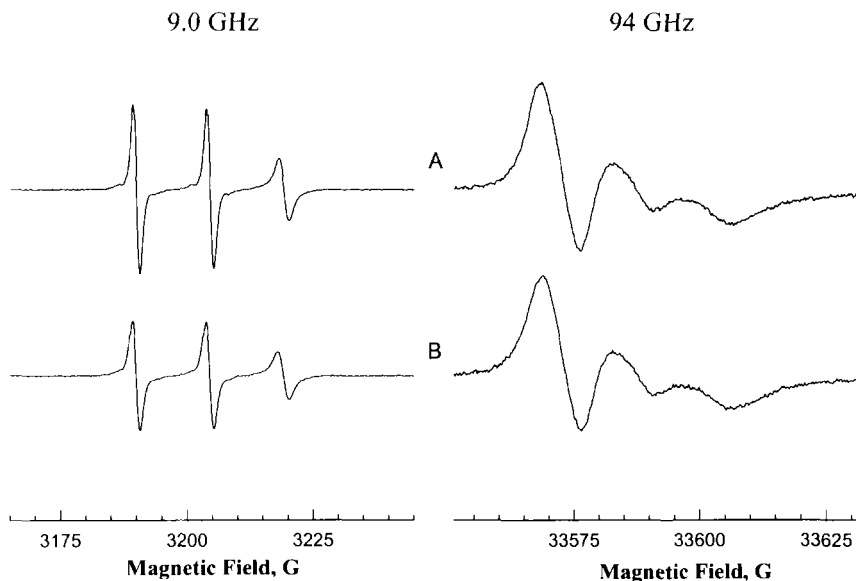


Figure 5. Comparative experimental 9.0- and 94-GHz EPR spectra from multibilayer aqueous dispersion of 1,2-dimyristoyl-*sn*-glycero-3-phosphocholine (DMPC, 20% v/v, 1.1-M borate buffer at pH 9.5) labeled with 16-doxyl stearic acid (DS) (16-DS; label-to-lipid ratio 1:100). Sample was drawn into a microbore Teflon tubing (i.d. = 0.152 ± 0.025 mm, wall thickness = 0.127 ± 0.025) and equilibrated at 41 °C with nitrogen (A) and air (B).

peak amplitude (Fig. 5, 9.0 GHz). Oxygen-induced broadening for this sample, as measured by a convolution-based algorithm (Smirnov *et al.*, 1996), was 0.267 ± 0.005 G; the peak-to-peak line width of the middle-nitrogen hyperfine component was ≈ 1.36 G. A W-band spectrum from the same carefully deoxygenated sample has much broader lines (ca. 10 G); therefore the oxygen effect on the overall shape of the spectrum is much smaller than at X-band (Fig. 5).

4. COMPARATIVE X- AND W-BAND EPR SPECTRA OF SPIN-LABELED PHOSPHOLIPIDS AND PROTEINS

4.1. Small Spin Labels in Phospholipid Membranes

Small nitroxide probes, such as 2,2,6,6-tetramethylpiperidine-1-oxyl (Tempo) and di-*tert*-butyl nitroxide (DTBN) are useful in determining the fluid/lipid fraction in bilayers and in monitoring phase properties of membranes (e.g., Griffith and Jost, 1976; McConnell, 1976). Partitioning these small probes between different phases

(e.g., aqueous and lipid phases of the membrane) results in some splitting of the HF component of the X-band EPR spectra. The relative magnitude of this splitting is used to characterize phase properties of the membrane system.

Figure 6 shows comparative experimental 9.0- and 94-GHz spectra from multilamellar vesicles made from 1,2-dipalmitoyl-*sn*-glycero-3-phosphatidylcholine (DPPC) and labeled with the small nitroxide Tempo. Liposomes were

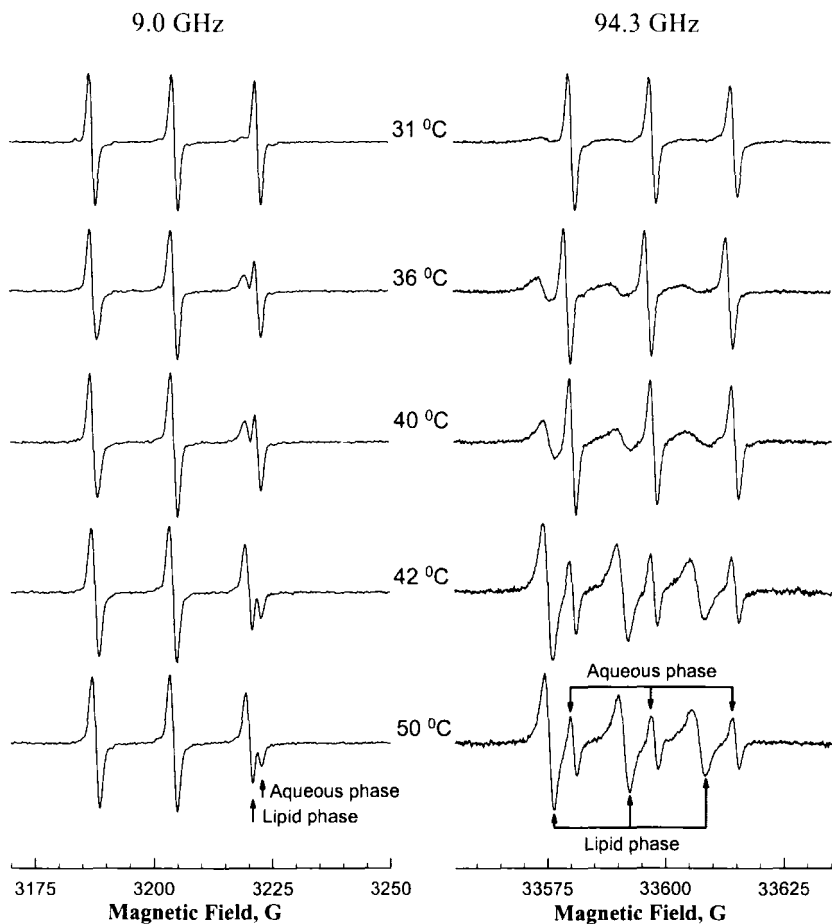


Figure 6. Experimental 9.0- and 94-GHz EPR spectra at various temperatures of multilayer vesicles made from 1,2-dipalmitoyl-*sn*-glycero-3-phosphatidylcholine (DPPC) and labeled with a small nitroxide, Tempo (2,2,6,6,-tetramethylpiperidine-1-oxyl). Liposomes prepared in a phosphate-buffered saline (0.15-M NaCl, 5-mM phosphate buffer, pH 7.0) with a final concentration of DPPC in an aqueous media of 200 mg/ml; concentration of Tempo was 620 μ M. The effect of partitioning Tempo between aqueous and lipid phases of the membrane indicated is by arrows in the spectra taken at 50 °C and discussed in the text.

prepared in a phosphate-buffered saline (0.15-M NaCl, 5-mM phosphatebuffer, pH 7.0) with a final concentration of DPPC in aqueous media of 200 mg/ml; the concentration of Tempo was 620 μM . Figure 6 shows that at $T > 31^\circ\text{C}$, EPR spectra at both frequencies reveal partitioning of the Tempo between lipid and aqueous phases of the membrane, but spectral resolution is very different. At 94 GHz Tempo signals arising from aqueous and hydrocarbon membrane phases are clearly resolved. Spectra corresponding to the lipid phase are shifted down-field because g_{iso} for Tempo is greater in the lipid phase than in the aqueous phase. In contrast X-band spectra from the same system show only partial resolution of the high-field component.

According to calorimetric and EPR data (e.g., Chen and Sturtevant, 1981; Shimshick and McConnell, 1973), phase transitions in a DPPC membrane occur at $\approx 34\text{--}35^\circ\text{C}$ (gel phase - ripple phase) and 40.5°C (ripple phase - fluid bilayer phase). The W-band EPR spectra clearly mark these transitions as abrupt changes in partitioning and rotational dynamics of Tempo molecules in the lipid phase of the membrane (Smirnov *et al.*, 1995). The same research also shows that the high spectral resolution achieved at 94 GHz is necessary to ensure uniqueness of least-squares simulations; 9.0 GHz data may lead to multiple solutions with essentially the same goodness of fit.

Figure 6 also demonstrates that the effect of the label microenvironment polarity is easier to measure from HF EPR spectra than from conventional X-band spectra. Some significant variations in g_x and A_z with the solvent polarity were found in several HF EPR studies (e.g., Ondar *et al.*, 1985; Krinichnyi *et al.*, 1985; Lebedev *et al.*, 1992; Earle *et al.*, 1994). Changes in g_x usually correlate with A_z (see also Kawamura *et al.*, 1967). For many spin-labeled systems, polarity effects on the probe EPR spectrum can be measured more accurately from HF EPR g -factor data than from changes in A . For example for the Tempo/DPPC system, the field shift of lipid versus aqueous signal exceeds changes in isotropic hyperfine coupling by a factor of three if expressed in the magnetic field scale; thus it can be measured more accurately. For rigid- and close-to-the-rigid-limit spectra another important factor is the gain of spectral resolution at 95 GHz, which in many cases separates g - and A -features of the spectrum.

4.2. Doxyl Stearic Acid Labels in Phospholipid Membranes

Spin-labeled fatty acids with a nitroxide moiety attached at different positions along the hydrocarbon chain are informative EPR probes for studying phospholipid bilayers and lipid-protein systems (e.g., Griffith and Jost, 1976; Hyde *et al.*, 1979; Marsh, 1989). Figures 7–9 show representative spectra from multibilayer aqueous dispersions of 1,2-dimyristoyl-*sn*-glycero-3-phosphocholine [(DMPC, 20% v/v) labeled with 5-, 12-, and 16-doxyl-stearic acids (5-, 12-, and 16-DS, label-to-lipid ratio 1:100)]. Sample preparation procedures are found elsewhere (e.g., Smirnov

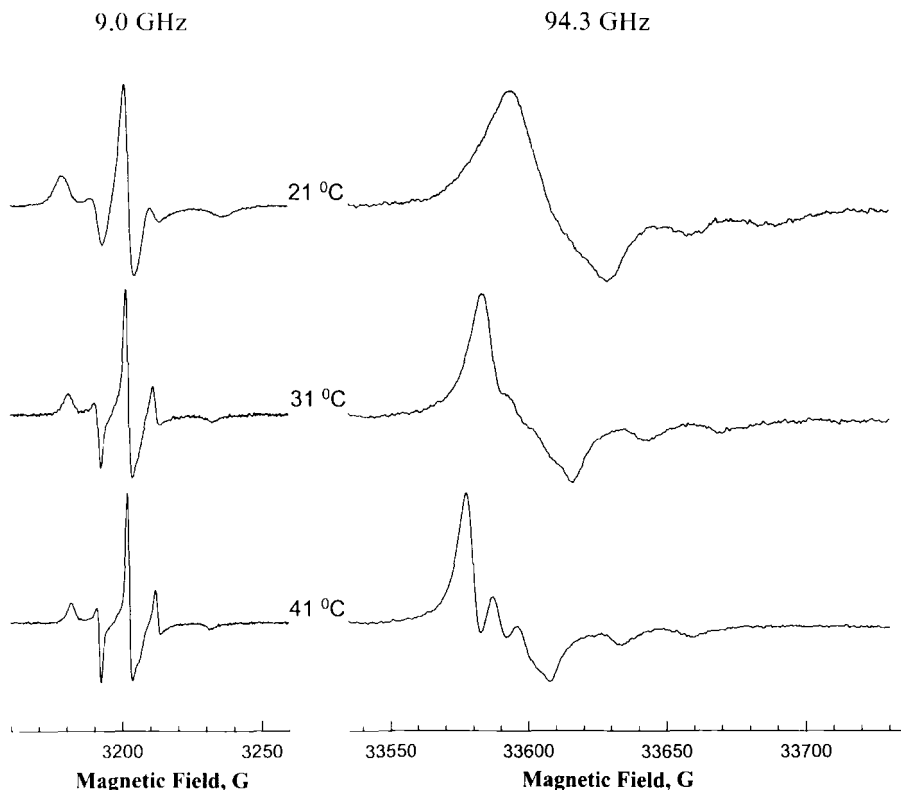


Figure 7. Representative 9.0- and 94-GHz EPR spectra of multibilayer aqueous dispersions of 1,2-dimyristoyl-*sn*-glycero-3-phosphocholine (DMPC; 20% v/v) labeled with 5-doxy-stearic acid (5-DS, label-to-lipid ratio 1:100, pH 9.5). The main phase transition of DMPC occurs at about 23 °C.

et al., 1996). A rather high pH, 9.5, was chosen to ensure that all carboxyl groups of the doxyl probes are ionized in the DMPC membrane (1.1-M borate buffer at pH = 9.5; see Subczynski *et al.*, 1989; Träube and Eibl, 1974).

The EPR spectra from the spin-labeled DMPC membrane demonstrate how local chain motion of the lipids depends on position in the membrane. When the nitroxide doxyl group is translated from C-5 (5-DS) into C-12 (12-DS) and C-16 (16-DS), outside peaks positions on 9.0-GHz spectra move closer, then disappear, and line width becomes narrower (see also Griffith and Jost, 1976). This is a result of an increase in motional freedom of the phospholipid chains from the polar lipid head region to the center of the bilayer. Increased motional freedom is also observed for each doxyl label with an increase in temperature; this is particularly noticeable in spectra recorded at 21 and 31 °C, because the main phase transition for DMPC occurs at about 23 °C and the membrane is more fluid above this temperature.

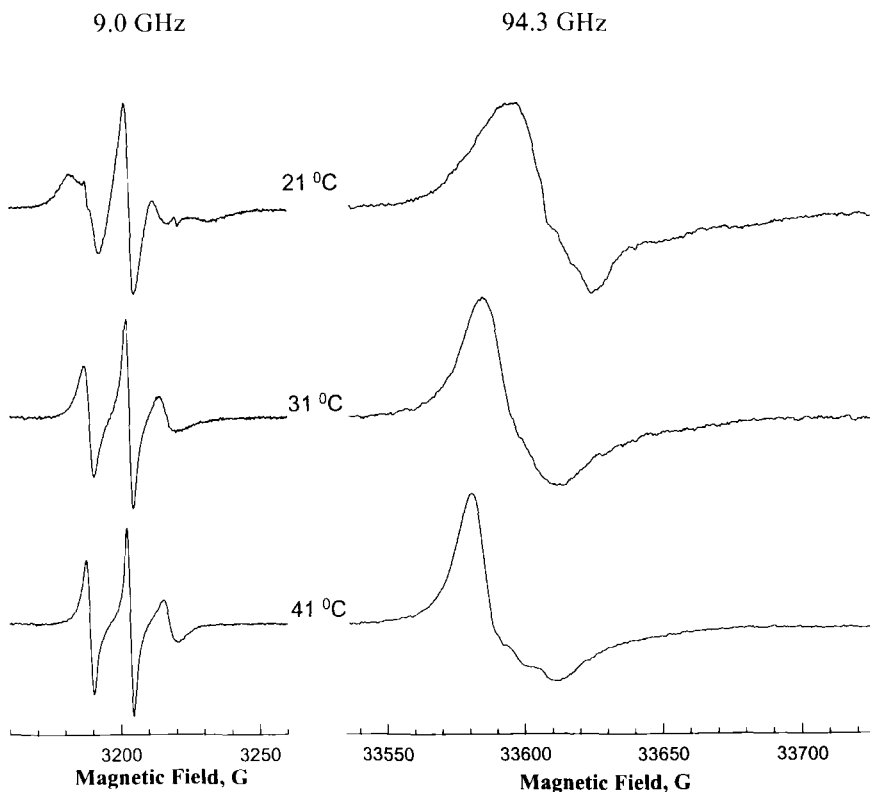


Figure 8. Representative 9.0- and 94-GHz EPR spectra of multibilayer aqueous dispersions of 1,2-dimyristoyl-*sn*-glycero-3-phosphocholine (DMPC, 20% v/v) labeled with 12-doxyl-stearic acid (12-DS, label-to-lipid ratio 1:100, pH 9.5).

Microscopic ordering of spin-labeled fatty acids is relatively high for 5-DS over the entire temperature range shown; this ordering is substantially decreased for 12-DS, and it is almost absent for 16-DS at temperatures above the main phase transition. The X-band EPR spectra by characterization the order parameter and some characteristic spectra of spin-labeled fatty acids are found elsewhere (e.g., Gaffney, 1976). The W-band spectra of these systems show trends similar to those observed at X-band: The overall spread of the W-band spectra decreases from 5- to 12-DS and then a little further to 16-DS because of a decrease in molecular ordering (Figs. 7–9). However this spectral feature spread is primarily determined by contributions from anisotropic averaging of the *g*-matrix at 94 GHz rather than from the *A*-matrix, as at 9.0 GHz. This last observation explains why the spectrum from 5-DS is substantially broader at W-band than X-band (Fig. 7).

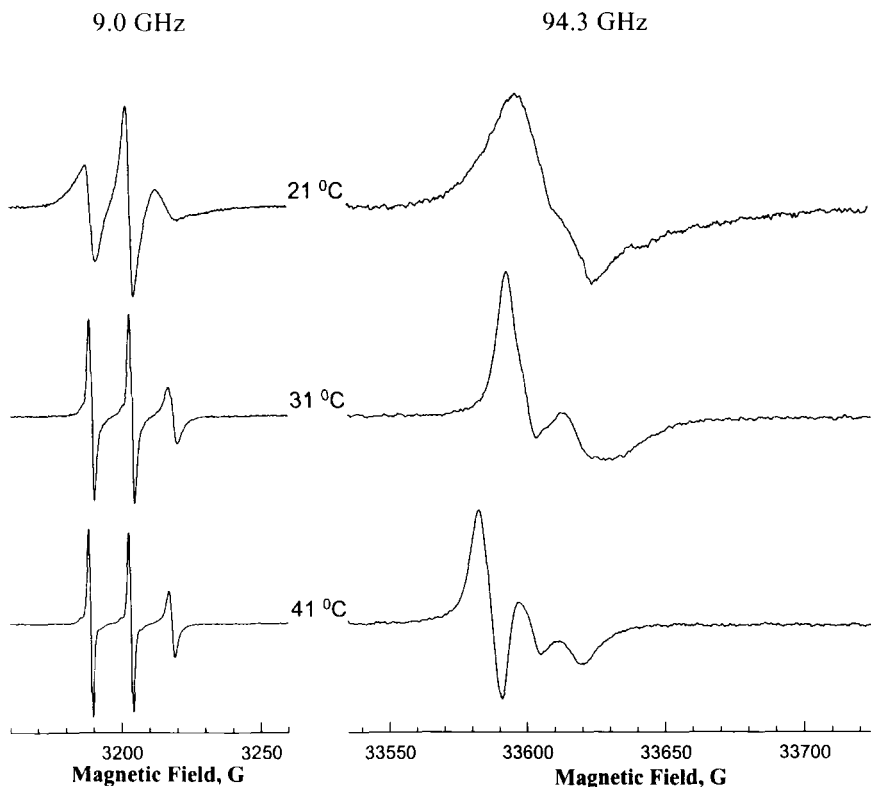


Figure 9. Representative 9.0- and 94-GHz EPR spectra of multibilayer aqueous dispersions of 1,2-dimyristoyl-*sn*-glycero-3-phosphocholine (DMPC, 20% v/v) labeled with 16-doxyl-stearic acid (16-DS, label-to-lipid ratio 1:100, pH 9.5).

At temperatures below the main phase transition of DMPC (e.g., at 21 °C), W-band EPR spectra from spin-labeled fatty acids fall close to the intermediate motional regime, and these are not very characteristic (Figs. 7–9). At $T = 31$ °C (above the main phase transition) the line width for all the probes is decreased; some new spectral features appear with a further increase in temperature ($T = 41$ °C). Note: Changes in the corresponding X-band spectra from 31–41 °C are relatively small. Thus HF EPR spectra from spin-labeled membranes appear to be quite sensitive to the phase state of the membrane and the local dynamics of phospholipids.

4.3. Binding Spin-Labeled Fatty Acids to Bovine Serum Albumin

Ability of the blood pool protein serum albumin to bind and transport fatty acids was studied extensively by various experimental techniques (e.g., Peters and

Sjöholm, 1978). As shown in several studies, applying the EPR spin-labeling method to this problem can reveal details of the molecular motion of fatty acids bound to albumin, and provide information on the structure of the binding site (e.g., see Perkins *et al.*, 1982; Ge *et al.*, 1990, and papers cited therein).

Figure 10 shows 9.5- and 94-GHz EPR spectra taken from spin-labeled fatty acids (5-, 12-, and 16-DS) added to an aqueous solution of bovine serum albumin (BSA) at pH 7.0 and $T = 20^\circ\text{C}$ (concentration of BSA was 1.0 mM, ratio of fatty acids to BSA was 1 to 1). The X-band EPR spectra correspond to a slow motional regime, and these demonstrate that fatty acids are bound to BSA, so there is no

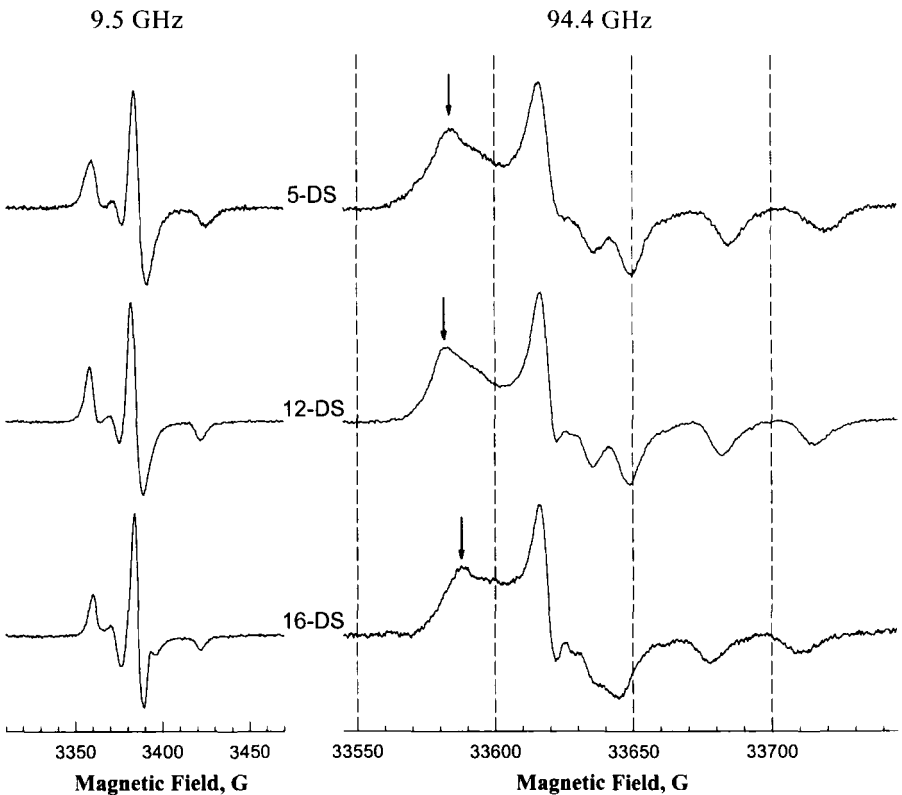


Figure 10. Experimental 9.5- and 94-GHz EPR spectra of spin-labeled fatty acids (5-, 12-, and 16-doxyl stearic acids) added to an aqueous solution of bovine serum albumin (BSA) at pH 7.0 and $T = 20^\circ\text{C}$ (concentration of BSA was 1.0 mM, ratio of fatty acids to BSA was 1 to 1). Approximate position of motionally averaged g_x components is indicated by arrows. Sample volume for W-band measurements was 70 nl; data acquisition time 8 min.

detectable fraction of unbound fatty acids in solution. These spectra are in agreement with those in the literature (Perkins *et al.*, 1982; Ge *et al.*, 1990).

The W-band spectra of the bound doxyl stearic acids all fall into the slow motional regime. Although W-band experimental spectra were taken at slightly different frequencies (because of different resonator tuning), field positions of the spectra shown in Fig. 9 we readjusted to exactly 94.4-GHz resonance frequency. Spectral features corresponding to motionally-averaged x-, y-, and z-components of the g-matrix and z-components of the A-matrix all are resolved in experimental HF EPR spectra. There are also no traces of unbound fatty acids in the 94-GHz spectra.

Previous studies by Ge and coworkers (1990) show that rotational diffusion coefficients R_{\parallel} and R_{\perp} for 5- and 12-DS are about the same, while R_{\parallel} for 16 DS increases by more than one order of magnitude. Indeed comparing of 94-GHz data (Fig. 10) shows that the overall width of the 16-DS spectrum is the narrowest in the series, thus it corresponds to the fastest rate of rotational diffusion.

Figure 10 also demonstrates that the feature corresponding to the motional averaging of the g_x component for 12-DS is higher than g_x for 5-DS (shown by the arrows). If rotational correlation time for both spin labels is about the same (e.g., Ge *et al.*, 1990), then 94-GHz data indicate that g_x for 12 DS is higher than for 5 DS. Previously by analyzing X-band spectra, Ge and coresearchers found that a_{180} and A_z for 12 DS bound to BSA are lower than values observed for 5 DS. Because of the correlation between g_x and A_z established earlier for many nitroxide labels (e.g., Ondar *et al.*, 1985; Krinichnyi *et al.*, 1985; Lebedev *et al.*, 1992; Earle *et al.*, 1994), smaller nitrogen hyperfine couplings correspond to a higher g_x factor. Thus the 94-GHz data in Fig. 10 are indeed in agreement with the X-band data (Ge *et al.*, 1990). It is anticipated that a global multifrequency simulation analysis of these data will reveal new information on the binding potentials of BSA. Recently 250-GHz EPR experiments on several model spin-labeled systems demonstrated that HF EPR is particularly sensitive to molecular interaction details when systems are in the slow motional regime (Polimonto and Freed, 1995).

4.4. Spin-Labeled Proteins: Immobilized Labels

The maleimide spin label [(MSL, N-(1-oxyl-2,2,6,6-tetramethyl-4-piperidinyl) maleimide)] is one of the nitroxides that can be attached rigidly to a protein by entering a hydrophobic protein pocket and covalently binding to a sulfur of the sulfhydryl (SH) group (e.g., see Ohnishi *et al.*, 1966; Thomas *et al.*, 1976; Beth *et al.*, 1980; Singh *et al.*, 1995). The BSA has a single sulfhydryl group, which can be labeled with MSL (e.g., Beth *et al.*, 1980). We chose this spin-labeled protein system as a model of a strongly immobilized label to compare X- and W-band spectra.

The BSA was labeled with MSL following the procedure given by Beth *et al.* (1980) except that excess from the unbound label was removed by dialysis over 12 hr. Curve *A* in Fig. 11 compares of 9.5- and 94-GHz spectra from a lyophilized, spin-labeled BSA sample. Principal axis components of the *g*-matrix are clearly resolved in the W-band spectrum, while a considerable overlap is seen in X-band results. Previously only a partial resolution of *g*-components was observed for a BSA sample labeled with deuterated MSL (Beth *et al.*, 1980). In Fig. 11 curve *B* compares 9.5- and 94-GHz EPR spectra from a 0.5-mM solution of spin-labeled BSA (phosphate buffer at pH 8.0, $T = 20^\circ\text{C}$). Both spectra show the presence of a small fraction of a mobile component overlapping with a broad spectrum corresponding to the immobilized label. The W-band spectra demonstrate that the overall width of solution spectrum decreases compared to the lyophilized sample, primarily because of some motional averaging. This demonstrates the sensitivity of HF EPR in the slow motional regime. We anticipate that least-squares simulations of W-band data will provide more accurate rotational diffusion coefficients for the protein as a whole and also trace solvent (polarity) effects at the spin-labeled site under physiologically relevant conditions. Previously some solvent effects on magnetic parameters of spin-labeled human serum albumin (HSA) were described from a 150-GHz EPR study of rigid-limit spectra at 140 K (Krinichnyi *et al.*, 1985).

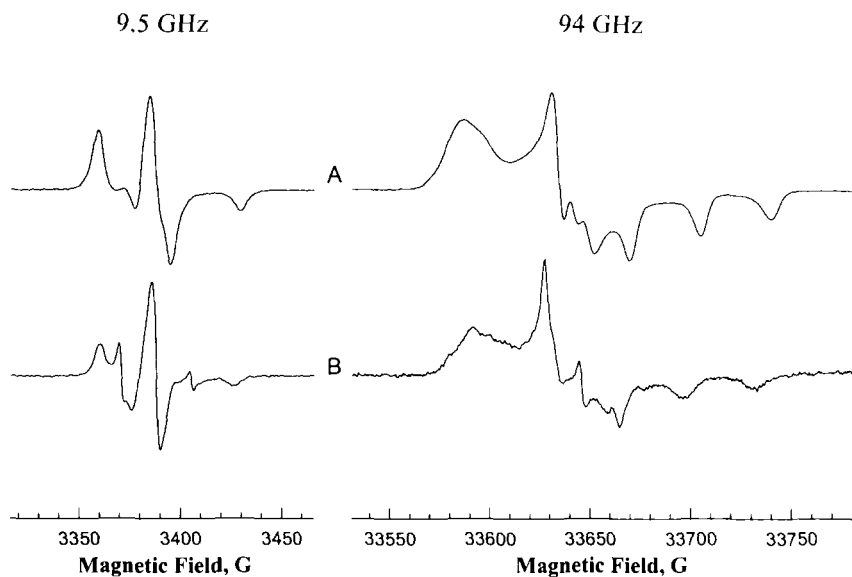


Figure 11. Curve *A* compares 9.5- and 94-GHz EPR spectra of lyophilized bovine serum albumin (BSA) labeled with maleimide spin label (MSL). Curve *B* compares 9.5- and 94-GHz EPR spectra of a 0.5-mM solution of spin-labeled BSA (phosphate buffer at pH 8.0, $T = 20^\circ\text{C}$).

Another instructive EPR study of immobilized nitroxide spin labels at X-, Q-, and W-bands is presented by Hustedt and coauthors (1997). By analyzing multifrequency EPR data from N° -spin-labeled coenzyme NAD⁺ bound to spin-labeled microcrystalline, tetrameric glyceraldehyde-3-phosphate dehydrogenase (GAPDH), molecular distances and angles defining the relative orientation of dipole-coupled nitroxide labels are determined. Analyzing simulations at W-band frequency demonstrates an exquisite sensitivity along all three principal axes of the nitroxides' CW EPR spectra to the magnitude of dipolar coupling and a remarkable line shape sensitivity to angles determining the mutual orientation of the probes (Hustedt *et al.*, 1997).

Note: Studies of spin-labeled biological samples at W-band require only a very small sample volume because of an increased absolute point sensitivity of HF EPR (e.g., see Lebedev, 1990). For example for a 95-GHz EPR spectrometer constructed at the Illinois EPR Research Center, the optimal size of an aqueous sample within the sensitive region of the cylindrical TE_{012} cavity is only ≈ 70 nl. This can be advantageous when only very small sample amounts are available (e.g., spin-labeled protein or DNA). This sensitivity advantage can also be useful for samples with lower dielectric losses.

4.5. Spin-Labeled Proteins: Mobile Labels

Nitroxide spin labels attached to proteins may exhibit substantial motional mobility on the scale of conventional EPR (9.5 GHz) (e.g., see spectra presented by Shin *et al.*, 1993, and Singh *et al.*, 1995). The X-band EPR spectra of such labels usually reveal only a relatively small degree of the anisotropy, and these are difficult to analyze unambiguously. Quite often the nitroxide moiety of such labels is exposed to the aqueous phase, so that EPR spectra from those labels may severely overlap with spectra from unbound labels in solution.

Figure 12 shows one example of such a label—succinimidyl 2,2,5,5-tetramethyl-3-pyrroline-1-oxyl-3-carboxylate (SSL)—attached to free amino groups of lysine residues of recombinant human growth hormone (rhGH, m.w. = 22,500). Spin labeling this protein was carried out by Dr. B. Variano (Emisphere Technologies, Hawthorne, NY) by placing a mixture of 5 mg of rhGH, 0.8 mL of 10-mM sodium phosphate buffer (pH 6.8), 10 mM of SSL, and 0.2 mL of acetonitrile in a 37 °C water bath for 2.5 hr with a consequent 48-hr, dialysis of spin-labeled rhGH against PBS at 4 °C. In some cases, e.g., after storing the protein sample, some free labels can be present with those bound to the protein. Whether this is the case is rather difficult to determine by comparing X-band spectra from the free label (Fig. 12, curve *A*) and the spin-labeled protein sample (Fig. 12, curve *B*). The HF EPR spectra (Fig. 12, 94 GHz) partially resolve three narrower peaks overlapping with much broader lines from the bound label. (Approximate positions of the lines from unbound label are shown with dashed lines.) It is

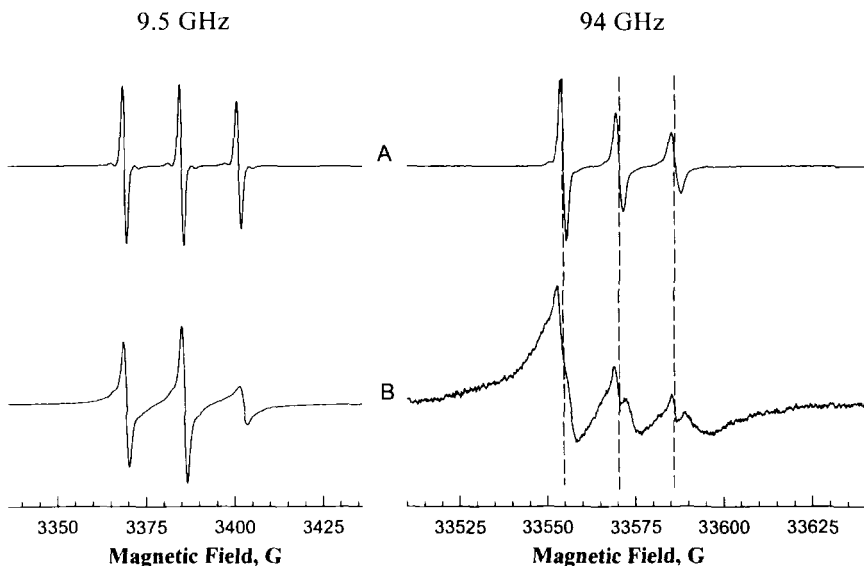


Figure 12. Comparison of 9.5- and 94-GHz EPR spectra of curve *A*: 1-mM solution of succinimidyl 2,2,5,5-tetramethyl-3-pyrroline-1-oxyl-3-carboxylate (SSL); measurements were carried out in an aqueous flat cell; curve *B*: SSL attached to free amino groups of lysine residues of the recombinant human growth hormone (rhGH); sample was placed in 0.15-mm i.d. quartz capillary; data acquisition time 8 min. All spectra were taken at 21 °C, both solutions were prepared in a sodium phosphate pH 6.8 buffer, at a protein concentration of 88 μ M. Approximately four spin labels were attached to each protein molecule, as determined by double integration of 9.5-GHz EPR spectra.

also clear that the fraction of unbound label is small and its W-band spectrum is shifted down-field compared to the bound one; thus it corresponds to a more polar environment. The onset of such slow motional effects as asymmetry and extensive line broadening are noticeable in 94-GHz spectra, while 9.5-GHz spectra are almost isotropic.

ACKNOWLEDGMENTS. The authors wish to thank Dr. T. Smirnova (University of Illinois) for providing some experimental data and preparing many spin-labeled samples. We are also thankful to Drs. E. G. Janzen and Y. Kotake (Oklahoma Medical Research Foundation) for providing PBN spin adducts. Many useful discussions with Dr. P. D. Morse II (Illinois State University) are greatly acknowledged. Resources for this work were provided by the Illinois EPR Research Center, an NIH biotechnology research resource (RR01811).

REFERENCES

- Beth, A. H., Perkins, R. C., Jr., Venkataramu, S. D., Pearson, D. E., Park, C. R., and Park, J. H., 1980, *Chem. Phys. Lett.* **69**:24.
- Budil, D. E., Earle, K. A., and Freed, J. H., 1993, *J. Phys. Chem.* **97**:1294.
- Chen, S. C., and Sturtevant, J. M., 1981, *Biochem.* **20**:713.
- Earle, K. A., Moscicki, J. K., Ge, M., Budil, D. E., and Freed, J. H., 1994, *Biophys. J.* **66**:1213.
- Earle, K. A., Budil, D. E., and Freed, J. H., 1993, *J. Phys. Chem.* **97**:13289.
- Gaffney, B. J., 1976, Practical Considerations for the Calculation of Order Parameters for Fatty Acids or Phospholipid Spin Labels in Membranes, in *Spin Labeling, Theory and Applications* (L. J. Berliner, ed.) (Academic, New York), pp. 567–71.
- Gaffney, B. J., and McConnell, H. M., 1974, *J. Magn. Reson.* **16**:1.
- Ge, M., Rananavare, S. B., and Freed J. H., 1990, *Biochim. Biophys. Acta* **1036**:228.
- Goldman, S. A., Bruno, G. V., Polnaszek, C. F., and Freed J. H., 1972, *J. Chem. Phys.* **56**:716.
- Grinberg, O. Ya., Dadali, A. A., Dubinskii, A. A., Vasserman, A. M., Buchachenko, A. L., and Lebedev, Ya. S., 1980, *Theor. Exp. Chem.* (Eng. Translation) **15**:457.
- Griffith, O. H., and Jost, P. C., 1976, Lipid Spin Labels in Biological Membranes, in *Spin Labeling, Theory and Applications* (L. J. Berliner, ed.) (Academic, New York), pp. 454–524.
- Horvath, L. I., Brophy, P. J., and Marsh, D., 1994, *J. Magn. Reson. B.* **105**:120.
- Hustedt, E. J., Smirnov, A. I., Laub, C. F., Cobb, C. E., and Beth, A. H., 1997, *Biophys. J.* **74**:1861.
- Hwang, J. S., Mason, R. P., Hwang, L.-P., and Freed, J. H., 1975, *J. Phys. Chem.* **79**:489.
- Hyde, J. S., Swartz, H. M., Antholine, W. E., 1979, Spin-Probe-Spin-Label Method, in *Spin Labeling II, Theory and Applications* (L. J. Berliner, ed.) (Academic, New York), pp. 71–114.
- Hyde, J. S., and Subczynski, W. K., 1989, Spin-Label Oximetry, in *Biological Magnetic Resonance*, vol. 8 (L. J. Berliner and J. Reuben, eds.) (Plenum., New York), pp. 399–425.
- Kawamura, T., Matsunami, S., and Yonezawa, T., 1967, *Bull. Chem. Soc. Jpn.* **40**:1111.
- Krinichnyi, V. I., Grinberg, O. Ya., Bogatyrenko, V. R., Likhtenshtein, G. I., and Lebedev, Ya. S., 1985, *Biophysics* **30**:233.
- Lebedev, Ya. S., 1994, High-Field ESR, in *Electron Spin Resonance*, vol. 14 (N. M. Atherton, M. J. Davies, and B. C. Gilbert, senior reporters) (Royal Society of Chemistry, Cambridge, UK) pp. 63–87.
- Lebedev, Ya. S., Grinberg, O. Ya., Dubinskii, A. A., and Poluektov, O. G., 1992, Investigation of Spin Labels and Probes by Millimeter Band EPR, in *Bioreactive Spin Labels* (R. Zhdanov, ed.) (Springer., Berlin), pp. 228–78.
- Lebedev, Ya. S., 1990, High-Frequency Continuous-Wave Electron Spin Resonance, in *Modern Pulsed and Continuous-Wave Electron Spin Resonance* (L. Kevan and M. K. Bowman, eds.) (Wiley., New York), pp. 365–403.
- Marsh, D., 1989, Experimental Methods in Spin-Label Spectral Analysis, in *Biological Magnetic Resonance*, vol. 8 (L. J. Berliner and J. Reuben, eds.) (Plenum., New York), pp. 255–304.
- McConnell, H. M., 1976, Molecular Motion in Biological Membranes, in *Spin Labeling, Theory and Applications* (L. J. Berliner, ed.) (Academic, New York), pp. 525–61.
- Ondar, M. A., Grinberg, O. Ya., Dubinskii, A. A., and Lebedev, Ya. S., 1985, *Sov. Chem. Phys.* **3**:781.
- Ohnishi, S., Boeyens, J. C. A., and McConnell, H. M., 1966, *Proc. Natl. Acad. Sci. USA.* **56**:809.
- Perkins, R. C., Jr., Abumrad, N., Balasubramanian, K., Dalton, L. R., Beth, A. H., Park, J. H., and Park, C. R., 1982, *Biochem.* **21**:4059.
- Peters, T., and Sjöholm, I., eds., 1978, Albumin: Structure, Biosynthesis, Function, *Proceedings of the 11th FEBS Meeting*, vol. 50 (Pergamon., Oxford, UK), p. 79.
- Polimento, A., and Freed, J. H., 1995, *J. Phys. Chem.* **99**:10995.
- Shin, Y-K, Levinthal, C., Livinthal, F., and Hubbell, W. L., 1993, *Science* **259**:960.
- Shimshick, E. J., and McConnell, H. M., 1973, *Biochem.* **12**:2351.

- Singh, R. J., Feix, J. B., Mchaourab, H. S., Hogg, N., and Kalyanaraman, B., 1995, *Arch. Biochem. Biophys.* **320**:155.
- Smirnov, A. I., and Belford, R. L., 1995, *J. Magn. Reson. A* **98**:65.
- Smirnov, A. I., Clarkson, R. B., and Belford R. L., 1996, *J. Magn. Reson. B* **III**: 149.
- Smirnov, A. I., Smirnova, T. I., and Morse II, P. D., 1995, *Biophys. J.* **68**:2350.
- Smirnov, A. I., Norby, S.-W., Weyhenmeyer, J. A., and Clarkson, R. B., 1994, *Biochim. Biophys. Acta* **1200**:205.
- Smirnova, T. I., Smirnov, A. I., Clarkson, R. B., Belford, R. L., Kotake, Y., and Janzen, E. G., 1997, *J. Phys. Chem. B* **101**:3877. *Natl.*
- Smirnova, T. I., Smirnov, A. I., Clarkson, R. B., and Belford, R. L., 1995a, *J. Phys. Chem.* **99**:9008.
- Smirnova, T. I., Smirnov, A. I., Clarkson, R. B., and Belford, R. L., 1995b, *Magn. Reson. Med.* **33**:801.
- Subczynski, W. K., Hyde, J. S., and Kusumi, A., 1989, *Proc. Natl. Acad. Sci. USA.* **86**:4474.
- Thomas, D. D., Dalton, L. R., and Hyde, J. S., 1976, *J. Chem. Phys.* **65**:3006.
- Träube, H., and Eibl, H., 1974, *Proc. Natl. Acad. Sci. USA.* **71**:214.
- Wang, W., Belford, R. L., Clarkson, R. B., Davis, P. H., Forrer, J., Nilges, M. J., Timken, M. D., Walczak, T., Thurnauer, M. C., Norris, J. R., Morris, A. L., and Zwang, Y., 1994, *Appl. Magn. Reson.* **6**:195.
- Windrem, D. A., and Plachy, W. Z., 1980, *Biochim. Biophys. Acta* **600**:655.
- Zager, S. A., and Freed, J. H., 1982, *J. Chem. Phys.* **77**:3360.

This page intentionally left blank

Use of Imidazoline Nitroxides in Studies of Chemical Reactions

ESR Measurements of the Concentration and Reactivity of Protons, Thiols, and Nitric Oxide

Valery V. Khrantsov and Leonid B. Volodarsky

1. INTRODUCTION

Nitroxides have been widely used as paramagnetic molecular probes in chemistry and biochemistry for about 30 years. The grounds of these applications are extremely stable nitroxyl fragment and sensitivity of their Electron Spin Resonance (ESR) spectra to parameters of the probe's local environment. Chemical reactions of nitroxides are mostly considered a factor limiting the stability of the paramagnetic fragment and an instrument for synthesizing of new spin labels and spin-labeled macromolecules. Of special interest are reactions of functional groups of nitroxides resulting in changes in spin density delocalization without loss of paramagnetic properties. The difference in magnetic resonance parameters of radical reagent, R1 and radical product R2 of the reactions of nitroxides, $R1 + A1 \leftrightarrow R2 + A2$,

Valery V. Khrantsov • Institute of Chemical Kinetics and Combustion, Novosibirsk, Russia 630090
and **Leonid B. Volodarsky** • Institute of Organic Chemistry, Novosibirsk, Russia 630090.

Biological Magnetic Resonance, Volume 14: Spin Labeling: The Next Millennium, edited by Berliner. Plenum Press, New York, 1998.

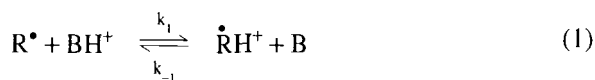
provides the possibility of measuring reactivity and concentration of corresponding substances A1 and A2. We review studies of three different types of chemical reactions of imidazoline nitroxides, namely, reactions with protons, thiols, and nitric oxide. The ESR spectroscopy allows us to follow these reactions and measure local concentration and reactivity of proton-, thiol- or NO-donating compounds, which are of principal importance for many biological functions. Our two groups at the Scientific Center in Novosibirsk are largely responsible for development and applications of imidazoline nitroxides for measuring local concentration and reactivity of protons and thiols (Volodarsky, 1988a, 1988b; Khramtsov *et al.*, 1982, 1985a, 1989b, 1991a, 1992, 1997). Recent data demonstrate the efficiency of imidazoline nitroxides applications as paramagnetic traps for nitric oxide (Akaike *et al.*, 1993; Joseph *et al.*, 1993; Woldman *et al.*, 1994).

2. STABLE NITROXIDES IN PROTON EXCHANGE REACTIONS

All cases of reversible pH effect on ESR spectra of radicals known at present are associated with proton exchange reactions in these radicals. First ESR studies of proton exchange in solution were done for short-lived radicals (Carrington and Smith, 1964; Fisher, 1965; Zeldes and Livingston, 1966); these were previously overviewed by Khramtsov and Weiner (1988a, 1988b). These studies demonstrate that the presence of ionizable groups in the radical structure close to the radical center leads to the difference in ESR spectra of protonated RH^+ and nonprotonated R forms of the radical. The ability of ESR spectroscopy to obtain information about equilibrium constants of the reactions and to measure bimolecular protonation constants was concluded. Applications of these radicals as pH probes create problems due to their instability. It is difficult for organic chemistry to obtain in one molecular structure the ionizable functional group and stable paramagnetic fragment in a distance of a few bonds. Imidazoline radicals were the most promising structures applied as spin pH-probes (Keana *et al.*, 1982; Khramtsov *et al.*, 1982) due to the presence of protonatable nitrogen atom N-3 in the radical heterocycle.

2.1. Theoretical Considerations

The reaction of a proton exchange between conjugated bases, radical R, and an acid, BH^+ , is described by:



The necessary condition for the reaction to be observed in the ESR spectra is the difference in magnetic resonance parameters of the radical in protonated and

unprotonated forms. In this case, chemical proton exchange results in a frequency exchange between respective components of the ESR spectra of R and RH^+ forms. The corresponding line shape of the ESR signal is described by (Emsley *et al.*, 1965; Khramtsov and Weiner, 1987, 1988a):

$$G(H_0 - H_R) = J m \left\{ i \cdot G_0 \cdot \frac{\tau_{\text{RH}^+} + \tau_R + \tau_{\text{RH}^+} \cdot \tau_R \cdot (p_{\text{RH}^+} \cdot \alpha_R + p_R \cdot \alpha_{\text{RH}^+})}{(1 + \alpha_R \cdot \tau_R) (1 + \alpha_{\text{RH}^+} \cdot \tau_{\text{RH}^+}) - 1} \right\} \quad (2)$$

where τ_R and τ_{RH^+} are lifetimes of the radical in the forms R and RH^+ ; H_0 and H_R are the constant magnetic field and the field corresponding to the center of the ESR signal for form R, respectively; G_0 is the numerical coefficient; $p_R = \tau_R / (\tau_R + \tau_{\text{RH}^+})$, $p_{\text{RH}^+} = \tau_{\text{RH}^+} / (\tau_R + \tau_{\text{RH}^+})$, $\alpha_R = (1/T_2)_R - i \cdot \gamma \cdot (H_0 - H_R + \Delta\omega/\gamma)$, and $\alpha_{\text{RH}^+} = (1/T_2)_{\text{RH}^+} - i \cdot \gamma \cdot (H_0 - H_R)$, where $\Delta\omega$ is the difference in frequencies of corresponding lines in the ESR spectrum of the radical in the R and RH^+ forms; $(T_2)_R$ and $(T_2)_{\text{RH}^+}$ are transverse relaxation times of the forms R and RH^+ , respectively; γ is the electron gyromagnetic ratio.

Analyzing the line shape in the case of intermediate frequency exchange ($1/\tau_R$, $1/\tau_{\text{RH}^+} \approx \Delta\omega$) allows us to determine lifetimes of the radical in each form (Khramtsov and Weiner, 1987, 1988a) and to calculate the corresponding rate constants of reaction (1):

$$k_1 = [\text{BH}^+]/\tau_R \quad k_{-1} = [\text{B}]/\tau_{\text{RH}^+} \quad (3)$$

In the case of fast ($1/\tau_R$, $1/\tau_{\text{RH}^+} \gg \Delta\omega$) or slow ($1/\tau_R$, $1/\tau_{\text{RH}^+} \ll \Delta\omega$) frequency exchange in terms of the ESR time scale, only the ratio $\tau_R/\tau_{\text{RH}^+}$ can be determined from the ESR spectrum using Eq. (2). It allows us to calculate the equilibrium constant K:

$$K = k_{-1}/k_1 = \frac{[\text{BH}^+] \cdot [\text{R}]}{[\text{B}] \cdot [\text{RH}^+]} = \frac{\tau_R}{\tau_{\text{RH}^+}} \cdot \frac{[\text{BH}^+]}{[\text{B}]} \quad (4)$$

When the reaction (1) describes exchange with a solvated proton ($\text{BH}^+ \equiv \text{H}^+$), Eq. (4) allows us to measure proton concentration $[\text{H}^+]$:

$$[\text{H}^+] = K \cdot \frac{\tau_{\text{RH}^+}}{\tau_R} \quad (5)$$

which leads to the possibility in principle of using radicals as pH probes. Note: The important consequence of Eqs. (2) and (5) for the case of fast frequency exchange between radicals R and RH^+ with different values of hyperfine interaction (hfi) constants $a(\text{R})$ and $a(\text{RH}^+)$. We can show that only the averaged hfi constant a is present in the ESR spectrum; its dependence on pH (H^+) is determined by the conventional titration curve (Khramtsov and Weiner, 1988a):

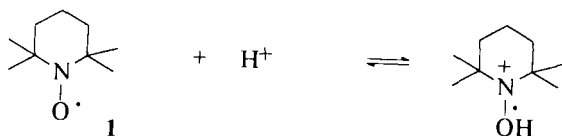
$$a(\text{H}^+) = a(\text{R}) \cdot \frac{\tau_{\text{R}}}{\tau_{\text{R}} + \tau_{\text{RH}^+}} + a(\text{RH}^+) \cdot \frac{\tau_{\text{RH}^+}}{\tau_{\text{R}} + \tau_{\text{RH}^+}} = \frac{a(\text{R}) + a(\text{RH}^+) \cdot [\text{H}^+]/K}{1 + [\text{H}^+]/K} \quad (6)$$

2.2. Effect of pH on ESR Spectra of Stable Nitroxides

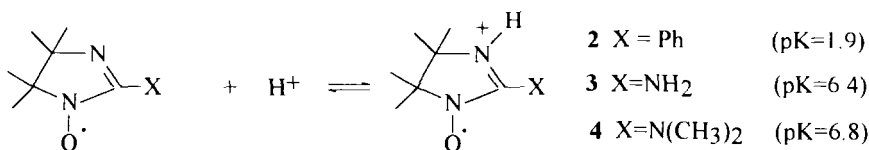
2.2.1. Protonation of the Radical Center of Nitroxides

Protonation of the N-O• fragment of di-tert-alkylnitroxides is realized in very acid media (Hogeveen *et al.*, 1967; Hoffman and Eames, 1969; Malatesta and Ingold, 1973). The protonation of widely used spin probe TEMPO in 80% aqueous solution of sulfuric acid is described (Malatesta and Ingold, 1973) by Scheme 1. This results in an increase in the hyperfine interaction constant hfi ($\Delta a_{\text{N}} = 5.7 \text{ G}$), a decrease in the g-factor ($\Delta g = 0.0013$), and the appearance of doublet splitting due to hyperfine interaction with a joined proton ($a_{\text{H}} = 3.12 \text{ G}$). Osiecki and Ullman (1968) observed the protonation of an N-O fragment of nitronyl nitroxides in benzene resulting in a decrease in hfi constants with both nitrogen atoms of the radical heterocycle ($\Delta a_{\text{N}_1} \approx 1.8 \text{ G}$, $\Delta a_{\text{N}_3} \approx 2.8 \text{ G}$) and the appearance of doublet splitting with a joined proton ($a_{\text{H}} \approx 4.7 \text{ G}$). Note: For most nitroxides, protonation of nitroxyl fragment in aqueous solution cannot be observed due to their disproportionation in the acid medium (Golubev *et al.*, 1965; Osiecki and Ullman, 1968).

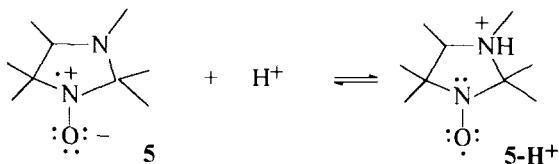
Strong pH effect on ESR spectra of iminonitroxides ($\Delta a_{\text{N}_1} \approx 3.5 \text{ G}$, $\Delta a_{\text{N}_3} \approx 0.5 \text{ G}$) were observed under the protonation of the nitrogen atom of an imino group with a radical center (Ullman and Osiecki, 1970; Helbert *et al.*, 1975) according to Scheme 2. Radicals **3** and **4** could be used as pH probes in a pH range of practical value. However interpreting ESR spectra of these radicals at $\text{pH} \approx \text{pK}$ is rather



Scheme 1.



Scheme 2.



Scheme 3.

complicated due to spectra superposition of R and RH^+ forms, each of which exhibits hfi constants with three nonequivalent nitrogen atoms and protons of the substituent at C-2. Another limitation to their possible application as pH probes is the recently obtained extremely high reduction rates of this type of nitroxides in biological systems; in the case of thioglycerol-induced reduction, this exceeds corresponding rates for di-tert-alkylnitroxides by about 10^4 times (Woldman *et al.*, 1994).

2.2.2. Protonation of the N-3 Atom of Imidazoline Radicals

Among stable nitroxides, only the imidazoline and imidazolidine radicals have a protonatable group, atom N-3, directly in the radical heterocycle in the vicinity of two σ -bonds to a radical center. The pH effect on the ESR spectra of nitroxides of imidazoline and imidazolidine series was first described by Keana *et al.* (1982) and Khramtsov *et al.* (1982). Figure 1 shows the reversible influence of pH on the ESR spectra of the imidazolidine radical 5. In the pH range from 5-7, the high-field component of the ESR spectrum in the X band (Fig. 1a) is split into two resolved components whose relative intensities vary reversibly with pH. This type of the spectrum is shown to be due to the superposition of two triplet ESR spectra with different hfi constants $a_N(\text{R})$ and $a_N(\text{RH}^+)$ and g-factors ($\Delta a_N = 1.25 \text{ G}$ and $\Delta g = 0.0002$) for R and RH^+ forms (Khramtsov *et al.*, 1982, 1985) participating in proton exchange according to Scheme 3.

In terms of resonance theory, the increase of unpaired electron density at the nitrogen atom N-1 depends on the relative contribution of the ionic resonance structure of nitroxide moiety (indicated as the preferable structure for the unprotonated form), which is destabilized by the positive charged at N-3 in the RH^+ form. Quantum chemical calculations of a_N and g-factor in R and RH^+ forms support the conclusion that observed changes in these parameters are induced by the direct influence of the positive charge field of the joined proton on the radical electronic structure and spin density redistribution (Khramtsov *et al.*, 1985a). The difference in the line positions caused by Δg depends on microwave frequency. Therefore different spectral patterns were obtained when ESR spectra of radical 5 were registered at microwave frequencies 1.1 GHz, 9.9 GHz (X band), 35.5 GHz (Q band) and 140 GHz (2-mm band) (Fig. 1). The most distinguished signals of R and

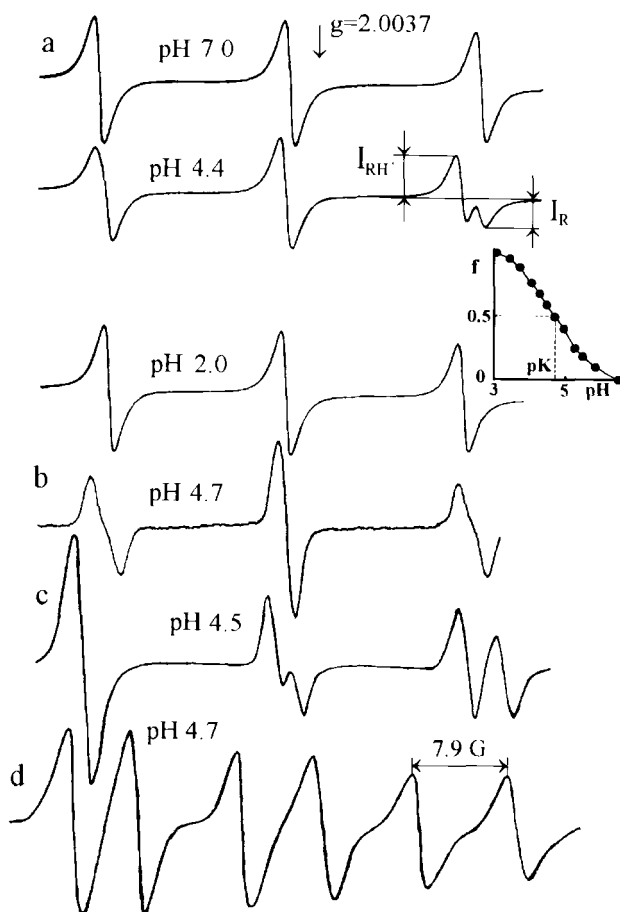


Figure 1. The ESR spectra of an aqueous solution of imidazolidine nitroxide **5** at different pHs and microwave frequencies: (a) 9.9 GHz, (b) 1.1 GHz, (c) 35.5 GHz, (d) 140 GHz. (From Khramtsov and Weiner, 1988, with permission; data at 1.1 GHz taken from Mäder *et al.*, 1996, with permission.) *Inset:* The pH dependence of function $f = I_{RH^+} / (I_R + I_{RH^+})$ on pH for the radical **5**; pK measured by the ESR method is 4.7 ± 0.1 .

RH^+ forms observed at 140 GHz clearly demonstrate the superposition of two triplet ESR spectra (Fig. 1d), while only a slight disturbance of low-field and high-field components of the triplet were obtained at 1.1 GHz (Fig. 1b). In contrast to changes in g-factors, the difference in the hfi constants of R and RH^+ forms does not depend on microwave frequency.

Figure 2 shows the pH dependencies of hyperfine splitting for the pH-sensitive radicals **5-11** (Table 1) and **40** (Table 2). Fitting the intrinsic pK of the radical to a

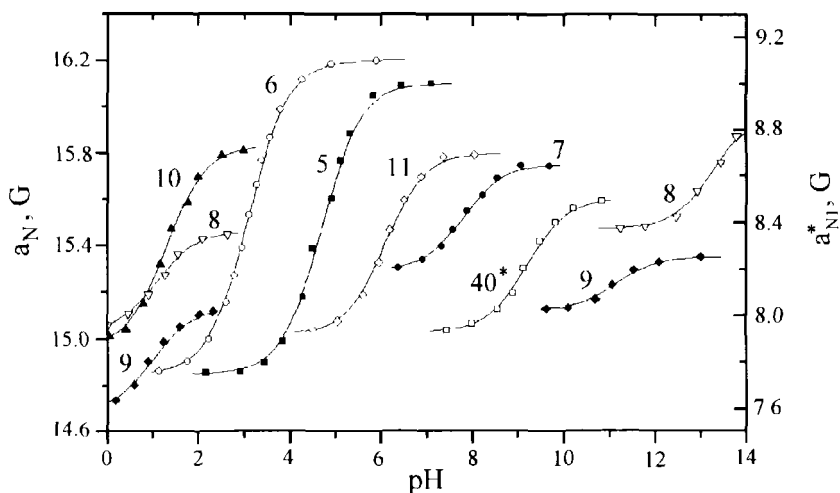
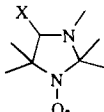
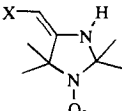
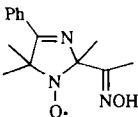


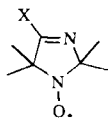
Figure 2. The pH-induced changes of hfi splittings for aqueous solution of nitroxides 5–11 (Table 1) and 40 (Table 2). Hyperfine interaction constant a_N was measured as the distance between the baseline crossing point of the low-field and central lines of ESR triplet spectra for radicals 5–11. The two pK values for radicals 8 and 9 are explained by the presence of two ionizable groups in their structures (Khramtsov *et al.*, 1985). Low values for the hfi constant a_N^* for radical 40 is due to the delocalization of spin density between two nitrogen atoms of the nitronylnitroxyl fragment with $a_{N1} = a_{N2} \approx 8$ G resulting in quintet ESR spectrum. (The a_N^* is the average value of a_{N1} of R and RH^+ forms taken with their fractions, which were obtained by computer simulation of experimental spectra.) Solid curves were calculated using Eq. (6) with parameters $a_N(R)$, $a_N(RH^+)$, and pK_a for radicals 5–11 in Table 1 and $a_N(R) = 8.5$ G, $a_N(RH^+) = 7.93$ G, and $pK = 9.2$ for 40 (Khramtsov *et al.*, 1986).


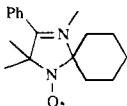
conventional titration curve (6) yields a good agreement between experimental and calculated data (Fig. 2) and provides the value of pK. Note: Equation (6) was obtained (Sec. 2.1) for the case of fast frequency exchange on an ESR time scale, which is valid only for the radicals 8 ($pK^1 = 1.1$, $pK^2 = 13.3$), 9 ($pK = 1.0$), and 10 ($pK = 1.3$). Variations of pH for these radicals remain in the triplet form of the spectrum, but these lead to a reversible change in a_N constants and g-factor values. However applying Eq. (6) to the case of slow frequency exchange between unresolved ESR lines can be considered a satisfactory approximation of experimental data (Fig. 2). Moreover pK radical values can be determined from the pH value corresponding to the hfi constant $a_N(pK) = (a_N(RH^+) + a_N(R))/2$ as well as from the function $f = I_{RH^+}/(I_R + I_{RH^+})$ (I_R and I_{RH^+} are the peak intensities of ESR lines of R and RH^+ forms, respectively; see Fig. 1a, inset). Both pH dependencies of a_N and function f can be used as calibration curves for pH measurement by spin pH probes. The pH values accessible for ESR measurement using one of the imidazoline radicals range from $pK - 1.5$ to $pK + 1.5$; the accuracy of pH measurements is about

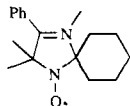
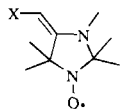
Table 1
Structures of Radicals 5–33 of the Imidazoline and Imidazolidine Types, ESR-Determined pK Values, g-Factors and a_N of R and RH^+ Forms, and the Character of the Frequency $R \Leftrightarrow RH^+$ Exchange

Structure	Nu	X	pK	a_N (± 0.02 G)		g (± 0.0001)		Ex ^a
				RH^+	RH	RH^+	R	
	5	CH ₃	4.7	14.85	16.12	2.0057	2.0054	s
	6	Ph	3	14.85	16.20	2.0057	2.0054	s
	7	NO ₂	7.8	15.29	15.75	2.0056	2.0055	s
	8	COCH ₃	1.1	15.03	15.46	2.0057	2.0056	f
			13.25	15.47	15.98	2.0056	2.0055	f
	9		1.0	14.69	15.13	2.0058	2.0057	f
			11.15	15.12	15.35	2.0057	2.0056	-

10	CH ₃	1.3	14.95	15.85	2.0057	2.0055	f
11	NH ₂	6.1	15.02	15.81	2.0057	2.0055	s
12	CH=NNHC(S)NH ₂	0.2	14.80	15.66	2.0057	2.0055	f
13	CH=NOH	0.1	14.85	15.64	2.0057	2.0055	f
14	COCH ₃	-0.2	14.93	15.81	2.0057	2.0055	f
15	CH(CH ₃) ₂	0.8	15.00	15.85	2.0057	2.0054	f
16	C ₆ H ₄ OCH ₃ -p	1.2	15.00	15.86	2.0057	2.0054	f
17	C(CH ₃)=NNH ₂	2.5	15.03	15.77	2.0057	2.0055	m
18	CH=NNHCH ₃	3.3	15.02	15.81	2.0057	2.0055	m
19	NH-C ₆ H ₄ Cl-p	5.1	14.96	15.83	2.0057	2.0055	s
20	NH-Ph	4.95	14.95	15.84	2.0057	2.0055	s
21	NH- α C ₁₀ H ₇	5.0	14.98	15.85	2.0057	2.0055	s
22	NH(CH ₂) ₂ Cl	5.6	14.94	15.83	2.0057	2.0055	s
23	NH-cC ₆ H ₁₁	6.45	14.98	15.86	2.0057	2.0055	s
24	NHC ₂ H ₅	6.4	15.01	15.85	2.0057	2.0055	s
25	NH-Bu	6.6	15.00	15.84	2.0057	2.0055	s

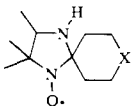
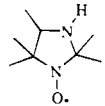
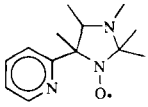
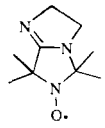


26	COCH ₂ N 	-0.7	14.20	15.41	2.0058	2.0055	s
27	COCH ₂ I	0.2	14.40	15.57	2.0058	2.0055	s
28		0.6	14.95	15.65	2.0057	2.0055	f



(continued)

Table 1
Continued

Structure	Nu	X	pK	a_N (± 0.02 G)		a_H (± 0.0001)		Ex ^a
				RH ⁺	RH	RH ⁺	R	
	29^b	CH ₂	2.0	14.36	15.64	–	–	f
	30^b	NH	4.5	14.98	16.22	–	–	f
	31		4.35	15.02	16.18	2.0057	2.0055	s
	32		4.5	14.72	15.89	2.0057	2.0055	s
	33		7.2	15.25	15.70	2.0056	2.0055	s

^aCharacter of exchange on ESR time scale: f, fast; m, moderate; s, slow.

^bData obtained by Keana *et al.* (1982).

Table 2
Structures of Radicals 34–59, ESR-Determined pK Values, Changes in a_N Constants on the Protonation of Functional Groups, and Character of the Frequency $R \leftrightarrow RH^+$ Exchange on ESR Time Scale

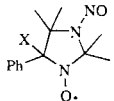
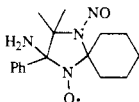
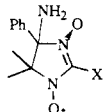
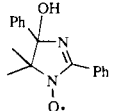
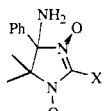
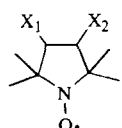
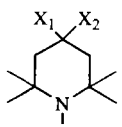
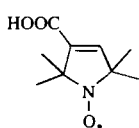
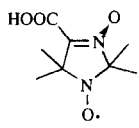
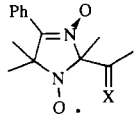
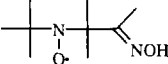
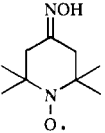
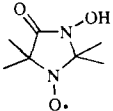
Structure	Nu	X	pK	Δa_N	Exchange
	34	NH ₂	2	1.9, 1.93 ^g	Fast
	35	NHCH ₃	2	1.36, 2.26 ^g	Fast
	36		2	1.8, 2.2 ^g	Fast
	37	Ph	1.75	0.45, 1.0 ^g	Fast
	38	(CH ₂) ₄ CONH ₂	1.75	0.45, 1.0 ^g	Fast
	39		4.5	0.89, 1.1 ^g , 0.37 ^h	Slow
	40 ^a	Ph	9.2	0.57, 0.07 ^h	Slow
	41 ^a	CH ₃	9.2	0.67, 0.28 ^h	Slow
	42 ^a	(CH ₂) ₄ CHO	9.2	0.73, 0.22 ^h	Slow

Table 2
Continued

Structure	Nu	X ₁	X ₂	pK	Δa _N	Exchange
	43 ^b	CO ₂ H	H	3.6	0.25	—
	44 ^c	NH ₂	H	—	0.5	—
	45 ^d	NH ₂	CO ₂ H	—	0.52	—
	46 ^d	CO ₂ H	CO ₂ H	—	0.5	—
	47 ^d	CONH ₂	CONH ₂	—	0.45	—
	48 ^d	CN	CN	—	0.3	—
	49 ^e	NH ₂	H	9.5	0.13	—
	50 ^f	NH ₂	CO ₂ H	8.0	0.3	Slow
	51 ^f	NH ₂	CONHCH ₂ CO ₂ H	5.8	0.18	Slow
	52 ^f	NHCOCH ₃	CO ₂ H	3.7	0.3	Slow
Structure	Nu	X		pK	Δa _N	Exchange
	53			3.5	0.31	—
	54			1.9	0.15	—

	55	NNHCH ₃	1.6	0.47	Fast
	56	NOH	10.7	0.22	—
	57		11.55	0.34	—
	58		11.35	0.16	—
	59		7.0	0.24	Slow

^aCompounds were obtained in aqueous solutions where they are stable for month (Khramitsov *et. al.*, 1986).

^bData from Mäder *et al.* (1996).

^cFrom Smith *et al.* (1972).

^dFrom Mathew and Dodd (1985).

^eFrom Hsia and Boggs (1972) and Quintanilha and Melhorn (1978).

^fFrom Nakaie *et al.* (1981, 1983).

^gChanges in the hf_i constant with a nitrogen nucleus of amino group.

^hChanges in a_N with a nitrogen nucleus N-3 of the radical heterocycle.

0.05 pH units. Up to the present, the pH effect on the ESR spectra of a large number of imidazoline and imidazolidine radicals was described. Table 1 lists structures of radicals **5-33**, their pK values, a_N constants, and g-factors for R and RH^+ forms; and the character of the R-RH^+ exchange in an ESR time scale. According to Table 1 and Fig. 2, radicals with different functional groups, lipophilicity, and charge cover total pH range from 0–14, providing the basis for spin pH probes applications (see also Sec. 2.6.1. for pH-sensitive spin-labeling reagents).

2.2.3. Protonation of Functional Groups of Stable Nitroxides

This section summarizes observed data of the effects of pH titration on ESR spectra of stable nitroxides derived from the protonation of functional groups distanced from the radical center and different from atom N-3 of the imidazoline and imidazolidine nitroxides. Table 2 lists the structures of radicals **34-59**, their pK values, changes in hfi constants on protonation/deprotonation and the character of the R-RH^+ exchange in the ESR time scale. The largest pH effects were found for radicals **34-42**, with the ionizable groups located at a distance of two σ -bonds from the radical center (Table 2). Figure 3 shows the influence of pH on the ESR spectra of radicals **34** and **37** with an amino group within two bonds to nitroxyl and a nitronyl nitroxyl fragment, respectively. Decreasing the pH from 5 to 0.5 results in a strong decrease in a_{N1} and an increase in $a_{\text{N}}(\text{NH}_2)$ for these radicals with $\text{pK} \approx 2$ (Table 2). Aqueous solutions of nitronyl nitroxides **40-42** with the OH-group at C-4 of the radical heterocycle show the dependencies of their hfi constant a_{N1} (see

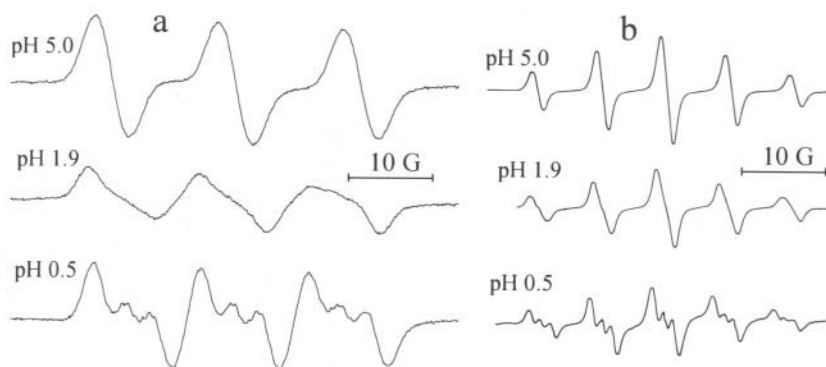
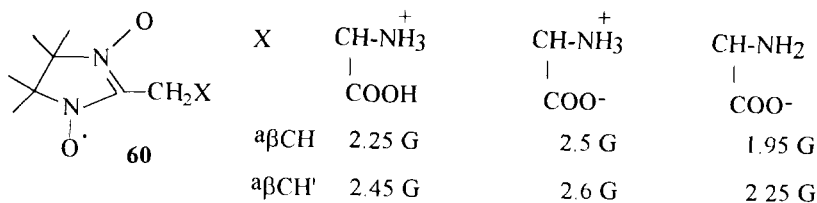


Figure 3. The ESR spectra of a 100- μM aqueous solution of (a) radicals **34** and (b) **37** at various pHs. Decreasing intensity of the signal at pH 0.5 for radical **37** is due to the disproportionation of nitronyl nitroxides in acid media. Additional triplet splitting of ESR spectra at acidic pHs is due to a strong increase in the hfi constant with a nitrogen nucleus of the amino group in the α -position to the radical center and a fast frequency exchange between R and RH^+ forms of the radicals. (Data for radical **37** are taken from Khramtsov *et al.*, 1986, with permission.)



Scheme 4.

Fig. 2 for radical **40**) and splitting the high-field component of the ESR spectrum of **40** in the pH range from 7.5–10.5 similar to that for imidazoline radical **5** (Fig. 1).

The increasing distance between the ionizable group and the radical center results in a strong decrease in the pH sensitivity of their ESR spectra. The pH effect of the hfi constant Δa_{N1} decreases from 1.9 G for the radical **34** (Fig. 3) to 0.5 G for radical **44** (Smith, 1972) and **45** (Mathew and Dodd, 1985), and to 0.13–0.3 G for **49** (Hsia and Boggs, 1972) and **50**, **51** (Nakaie *et al.*, 1981, 1983) for the amino group located in α -, β -, and γ -positions to nitroxide moiety, respectively.

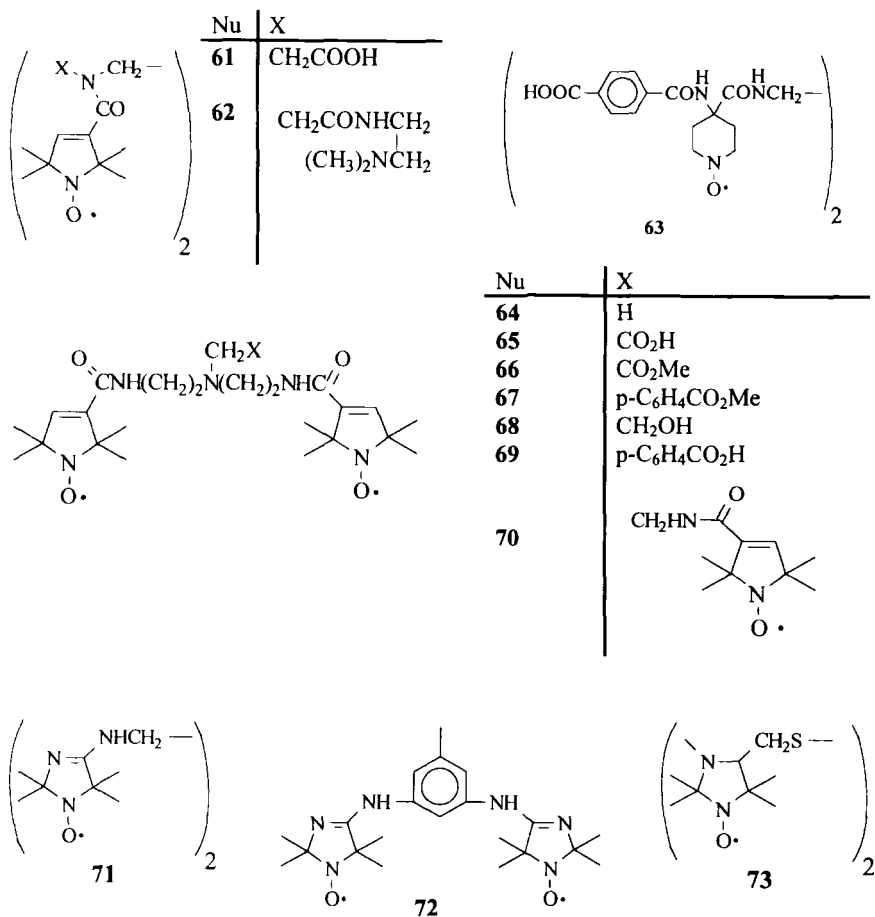
Regardless of protonatable (deprotonatable) group and nitroxide type, the increase in positive molecule charge results in a decrease in a_N and an increase in g-factor (when detected), which can be qualitatively explained in terms of resonance theory (see Sec. 2.2.2, diagram). Intramolecular and intermolecular interactions are other factors that can influence the pH sensitivity of ESR spectra of nitroxides. Weinkman and Jorgensen (1971a) show that protonation of the carboxy group in the radical analogue of histidine **60** disturbs the ion dipole interaction between the electron-deficient nitronylnitroxyl ring and the carboxylate anion, which alter hfi constants with the nonequivalent β -protons of methylene group (see Scheme 4). The influence of protonation of functional groups of nitroxides on their intermolecular interaction with the model and biological membranes and its manifestation in the ESR spectra is well-known (Barrat and Laggner, 1974; Cafiso and Hubbel, 1981; Sankaram *et al.*, 1990; Bonnet *et al.*, 1990; Khramtsov *et al.*, 1992).

2.2.4. Di- and Triradical pH-Sensitive Spin Labels

Biradical ESR spectra are markedly influenced by pairwise spin exchange between free radical subunits. When approximating single, effective conformation of the radical in liquids of low viscosity, they can be accounted for by the isotropic spin Hamiltonian (Luckhurst, 1976):

$$H_S = g\beta H_0(S_1 + S_2) + a_N(S_1 I_1 + S_2 I_2) + J S_1 S_2 \quad (7)$$

where β is the electron Bohr magneton, S_1, S_2 , and I_1, I_2 are electron and nuclear spin operators, respectively, and J is an exchange integral characterized by the overlap of orbitals of unpaired electrons of the two radical fragments. This results in additional biradical components with intensities and positions determined by the J value in the spectrum. However analysis of most experimental situations requires more complicated consideration of several effective conformations with nonequivalent J as well as an intramolecular exchange between conformations. In this case electrostatic interaction arising from the ionization of the monoradical fragment should affect the statistical weight of conformations resulting in changes in the ESR spectrum.



Scheme 5.

Ferruti *et al.* (1969, 1970) show for biradicals **61–63** (Scheme 5) that protonating or neutralizing functional groups of biradicals modifies electrostatic repulsion between radical subunits, resulting in changes in intensities of biradical components of the ESR spectrum. Recently Martin and Keana (1995) reported the synthesis of pH-sensitive nitroxide bi- and triradical spin labels **64–70** (Scheme 5). The authors observed an increase in the effective exchange integral J on protonation of the central nitrogen atom, apparently due to an decrease in angles between substituents. That results in favoring conformations with closer nitroxide centers.

We observed the pH effect on ESR spectra of the imidazoline and imidazolidine biradicals **71–73** (Fig. 4). Intensities of biradical spectral components were found to be temperature- and viscosity-dependent, indicating the presence of several effective conformations. It was observed in the disappearance of biradical components in the ESR spectrum of **72** and their strong decrease in the spectrum of biradical **73** at low pH (Figs. 4 and 5). This can be explained by the electrostatic repulsion of charged monoradical fragments of fully protonated forms, which result in favoring the effective conformation with a greater distance between fragments with $J \approx 0$.

In addition characteristic changes in the hf_i constant a_N and g -factor described in Sec. 2.2.2 for protonation of the N-3 atom of imidazoline monoradicals were also observed (Fig. 5). For some applications, this bifunctional behavior of imidazoline biradicals may be of special advantage—for example to distinguish contributions from different environmental parameters (pH, temperature, or viscosity). For instance Fig. 4 shows that viscosity changes induced by a small addition of glycerol can easily be detected from a decrease in the intensity of biradical spectral components; the hf_i constant measured as the distance between monoradical components can be used for pH measurement. Note: The pH dependence of a_N for radical **72** (Fig. 5) clearly demonstrates the presence of two nonequivalent pK of monoradical fragments due to the influence of the charge of the first protonated group on the equilibrium of the protonation of the second group. In agreement with this conclusion, the decrease in amplitudes of biradical components was observed only on the protonation of the second monoradical fragment when electrostatic repulsion is switched on (see Fig. 5). For radicals **71** (pK = 5.0) and **73** (pK = 2.8) with N-3 atoms of monoradical fragments separated by a longer chain, the single pK was observed (compare pH dependence of a_N for **72** and **73** in Fig. 5).

2.3. pH-Sensitive Nitroxides in Studies of Proton Exchange Reactions

Proton exchange is one of the most common reactions in organic chemistry and plays an important role in acid and alkaline catalysis and in technological and biological processes. High rates of proton exchange reactions in solution give rise to methodological complexities in their kinetics studies. The ESR method, which is highly sensitive and makes it possible to follow the paramagnetic reactant and obtain quantitative information about the kinetics of proton exchange, is promising

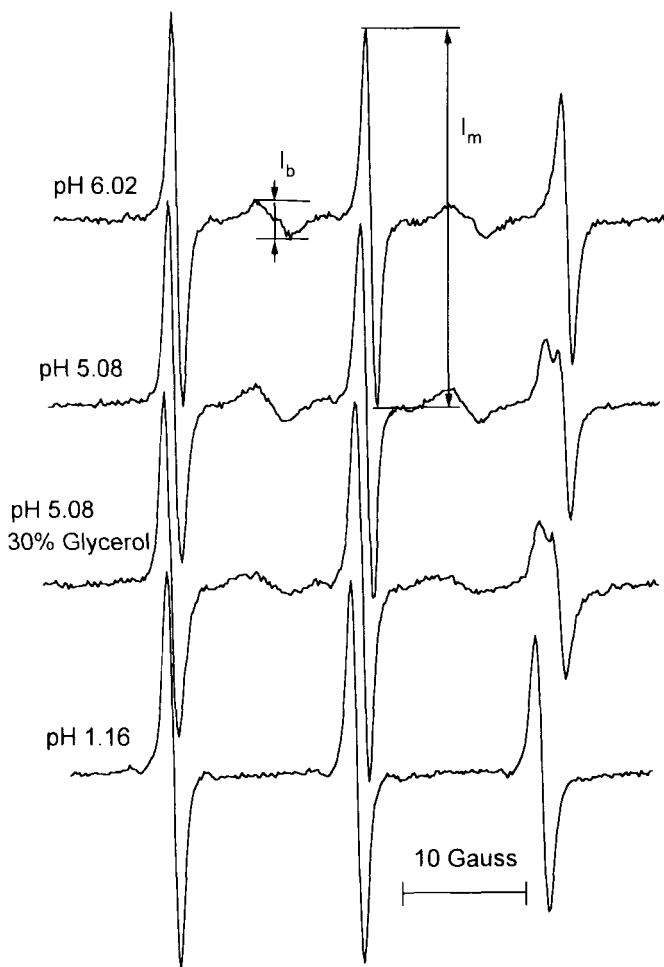


Figure 4. The ESR spectra of 0.1-mM imidazoline biradical **72** at 23 °C at different pH values. The ESR spectra at pH 5.08 in water and in 30% aqueous glycerol have the same values of the $h\nu$ constant (15.56 G) and function f ($f = 0.38$, as obtained from amplitudes of partially resolved high-field components of ESR signals of R and RH^+ forms; see Sec. 2.2.2). The relative decrease in the amplitude of the biradical component induced by glycerol addition is equal to 1.55 ± 0.05 .

(Khramtsov and Weiner, 1987). The application of ESR to the study of proton exchange reactions in stable radicals may allow reaction data to be used as models for obtaining quantitative information on the influence of the steric factor, the solvent, and electron-donating and accepting substituents on kinetics and equilibrium parameters of the proton exchange. (For an earlier review, see Khramtsov and Weiner, 1988a).

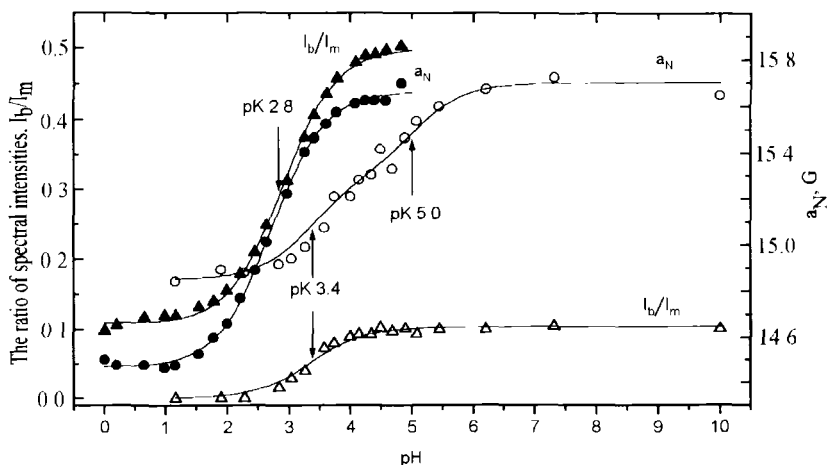
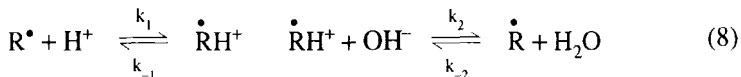


Figure 5. The pH dependence of the hfi constant a_N and peak intensity ratio I_b/I_m (see Fig. 4) of biradical and monoradical components of ESR spectra of radicals **72** and **73**. Solid curves for a_N dependence were calculated using Eq. (6) with parameters $a_N(R) = 15.66$ G, $a_N(RH^{++}) = 14.47$ G, and $pK = 2.8$ for radical **73**; Eq. $a_N(H^+) = \{a_N(R) + a_N(RH^+) \cdot [H^+]/K_1 + a_N(RH_2^{++}) \cdot ([H^+]/K_1) \cdot ([H^+]/K_2)\} / (1 + [H^+]/K_1 + ([H^+]/K_1) \cdot ([H^+]/K_2))$ with parameters $a_N(R) = 15.70$ G, $a_N(RH^+) = 15.28$ G, $a_N(RH_2^{++}) = 14.85$ G, and $pK_1 = -\lg K_1 = 5.0$, $pK_2 = -\lg K_2 = 3.4$ for radical **72**. Solid curves for I_b/I_m dependence were calculated using the conventional titration equation, $I_b/I_m(pH) = \{I_b/I_m(R) + I_b/I_m(RH_2^{++}) \cdot [H^+]/K\} / (1 + [H^+]/K)$ with $I_b/I_m(R) = 0.5$, $I_b/I_m(RH_2^{++}) = 0.108$, $pK = 2.8$ for **73** and $I_b/I_m(R) = 0.103$, $I_b/I_m(RH_2^{++}) = 0$, $pK = 3.4$ for **72**. The hyperfine interaction constant a_N was measured as the distance between the baseline crossing point of the low-field and central monoradical components of ESR spectra.

2.3.1. Equilibrium Constants of Proton Exchange

The equilibrium constant of proton exchange reaction in aqueous solution or pK of pH-sensitive radical can be determined as shown in Figs. 1 and 2; Tables 1 and 2 give the results. Values of pK for imidazoline and imidazolidine radicals (Table 1) strongly depend on substituents at the C-4 of radical heterocycle. For imidazoline radicals, pK values increase from -0.2 to 6.6 according to electron-donating ability of the substituent. The radical center itself is affected on the pK of the nitroxides' functional groups. The radical center decreases pK values of the ionizable groups compared with that of the diamagnetic analogs in agreement with its electron-accepting properties. The reduction of radical **10** (pK 1.3) to a corresponding diamagnetic hydroxylamine increases the pK value to 3.85 (Khramtsov *et al.*, 1985a). Values of $pK \approx 2$ for the NH_2 group in radicals **34–38** and of $pK \approx 9.2$ for the OH group in **40–42** are lower by about seven units compared with those of corresponding aliphatic amines and alcohols.

Of special interest is the relation between the character of the frequency $R \leftrightarrow RH^+$ exchange in the ESR spectra and the pK value. As we see from Tables 1 and 2, slow frequency exchange is observed for radicals whose pK lies in the range from 3–9, while fast frequency exchange is found for radicals with a very low (pK < 3) or high (pK \approx 13) pK. This correlation is explained (Khramtsov *et al.*, 1985a) by two mechanisms of proton exchange favoring an acid or alkaline medium, respectively:



Taking Eqs. (4) and (5), which relate the rate constants with lifetimes of the radical in R and RH^+ forms, the following slow exchange requirement ($1/\tau_R, 1/\tau_{RH^+} \ll \Delta\omega$) is easily obtained (Khramtsov *et al.*, 1985a):

$$\lg(k_1/\Delta\omega) < pK < 14 - \lg(k_2/\Delta\omega) \quad (9)$$

For imidazoline radicals ($\Delta\omega \approx 3 \times 10^7 \text{ s}^{-1}$) in the case of diffusion-controlled reactions ($k_1 \approx k_2 \approx 10^{10} \text{ M}^{-1} \text{ s}^{-1}$), this results in the numerical condition of slow frequency exchange:

$$3 < pK < 11 \quad (10)$$

which describes most experimental data. Rare contradictory data should be considered in terms of Eq. (9); the lower value of k_1 indicates a specific mechanism of the protonation. Contradictory data for enaminketones **26** and **27** (slow exchange for pK \leq 0) are explained by low values for the bimolecular rate constant k_1 derived from protonation of the oxygen atom in the enaminketone group of the radical followed by intramolecular charge redistribution for nitrogen atom N-3 (Khramtsov *et al.*, 1985b).

2.3.2. Kinetic Parameters of Proton Exchange

From the analysis of Eq. (2) for the ESR signal shape, the kinetic parameters (k_1 and k_{-1}) for the proton exchange reaction (1) can be obtained only for the intermediate frequency $R \leftrightarrow RH^+$ exchange. For the proton exchange with solvated proton ($BH^+ \equiv H_3O^+$), intermediate frequency exchange is observed for radicals **6**, **17**, **18** (see Fig. 6a), with pK \sim 3 in agreement with Eq. (10). For the proton exchange reaction (1) with buffer molecule ($BH^+ = H_2PO_4^-, CH_3COOH$), frequency exchange can be accelerated without shifting the equilibrium $R \leftrightarrow RH^+$ by increasing the buffer concentration, with the pK close to radical pK (Fig. 6b). This agrees with Eq. (3) (Khramtsov and Weiner, 1987). This approach allows us to measure rate constants of proton exchange reactions between buffer molecules and radicals,

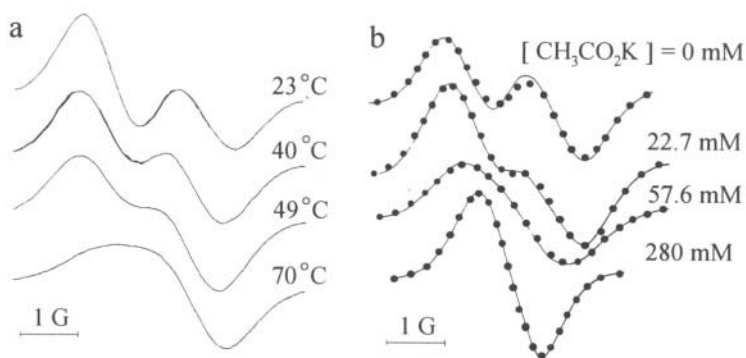


Figure 6. (a) Temperature dependence of the ESR spectrum (high-field component) of 0.1-mM radical **6** (pH = 2.85 at 23 °C); (b) high-field component of the ESR spectrum of 0.05-mM radical **31** in K-Ac buffer, pH 4.35 at different buffer concentrations. In the simulated spectra indicated by points, the unresolved hyperfine structure was taken into account using a convolution of the function calculated by Eq. (2) and the Gaussian distribution function, with the following parameters: $\Delta\omega/\gamma = 1.54$ G, $\gamma\chi(1/T_2)_R = 0.18$ G, $\gamma\chi(1/T_2)_{RH^+} = 0.21$ G, width of Gaussian distribution 0.65 G. The obtained rates constants are given in Table 3.

which show a slow frequency exchange in the absence of the buffer; this approach can be applied to all radicals with $3 < \text{pK} < 11$ (Table 1, except for **30**).

Computer simulation of the high-field component of the ESR spectrum allows us to determine lifetimes of the radical in the R and RH^+ forms and the respective rate constants of the proton exchange k_1 and k_{-1} (Fig. 6). Table 3 lists rate constants for a series of proton exchange reactions between radicals and the partner BH^+ . Note: There is a correlation between bimolecular protonation constants and the steric accessibility of atom N-3. The rate constant k_1 for the exchange with solvated proton is more than one order of magnitude higher for radical **17** compared with that for radical **6**, which has the bulky CH_3 group at the N-3 atom. Replacement of

Table 3
Rate Constants of the Proton Exchange Reaction of Nitroxides with Different Partners as Solvated Proton, Deuteron, and Compounds BH^+ at 21 °C Measured by ESR Method

Radical	Partner	$k_1 \times 10^{-8}, \text{M}^{-1} \text{s}^{-1}$	$k_{-1} \times 10^{-8}, \text{M}^{-1} \text{s}^{-1}$
17	H_3O^+	85 ± 9	$0.27 \pm 0.03 \text{ s}^{-1}$
17	D_3O^+	31 ± 2	$0.039 \pm 0.004 \text{ s}^{-1}$
6	H_3O^+	≈ 5	$\approx 0.005 \text{ s}^{-1}$
11	H_2PO_4^-	2 ± 0.2	20 ± 2
5	CH_3COOH	0.93 ± 0.06	0.93 ± 0.06
31	CH_3COOH	2 ± 0.15	5.3 ± 0.3

the hydrogen atom at N-3 in radical **31** by the CH_3 group (radical **5**) also results in a significant decrease in the bimolecular protonation constant of the proton exchange reaction with an acetic acid molecule. Values of the kinetic isotopic effect observed for radical **17** by comparing ESR spectra in H_2O and D_2O (2.7 ± 0.2 for k_1 and 6.9 ± 0.4 for k_{-1} at 294 K) are usual for reactions of this type, and these do not require references to the tunneling effect.

2.4. ESR Measurements of the Local Concentration of Protons

Measurement of pH is one of the most important problems of chemistry and biology, since many catalytic reactions, processes of vital cell activities and cellular organelles depend on the pH value. Application of stable pH-sensitive nitroxides to study the acidity of the medium in the local environment of the probe seems promising due to the high sensitivity of the ESR method and well-developed organic chemistry of nitroxides (Volodarsky *et al.*, 1994), and the possibility of working in nontransparent, heterogeneous, and nonconducting systems. Recent data demonstrating these advantages of spin pH-probes are reviewed in this section.

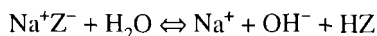
2.4.1. pH Measurements in Micropores of Cross-Linked Polyelectrolytes

Circumstantial evidence suggests that the state of water in ionite micropores and the acidity of the medium significantly differ from the ones in solution contacting the sorbent (Zundel, 1969). Therefore these parameters in the interior of ionite grains, which determine complexing and catalytic processes, may not be approximated by measurements in solution. Recently Molochnikov *et al.* (1996) applied pH-sensitive nitroxides **5**, **6**, and **11** (covering the pH range from 2–7) to measure local pH in the micropores of carboxylic cationites. The method provides direct pK determination of carboxylic acid groups, which were found to be substantially lower compared to that determined according to potentiometric titration. Authors conclude that using pH-sensitive radicals opens up new possibilities for studying acid base properties of cross-linked polyelectrolytes and polycomplexonates on their base and for critically evaluating concepts previously formed in this field.

2.4.2. pH Measurements in Mesopores of Zeolites and Kaolin

Mineral theories of the origin of life (Ferris and Ertem, 1992) assume that adsorption and catalysis on mineral surfaces considerably facilitate the polymerization of aminoacids and nucleotides. Among other minerals with catalytic properties, zeolites and certain kinds of layer silicates present unique catalytic, adsorption, and ion exchange properties. Zamaraev *et al.* (1995, 1997) consider the possible catalytic role of these minerals in prebiotic oligopeptide synthesis. The formation of linear dipeptide was found to be a rate-determined stage in the

oligomerization of glycine, which is dramatically accelerated by the alkaline medium or the presence of zeolites and kaolin. Actually in aqueous suspensions of silicate cation exchangers (zeolites and clays), the equilibrium of the water dissociation shifts toward higher OH^- concentration according to:



where Z is an anionic aluminosilicate framework in a zeolite or the layer in the layer silicate. The pH-sensitive nitroxides **7**, **9**, **25**, and **40** (covering the pH range from 5.5–12.5) have been applied to measure pH in mesopores of molecular size of zeolites and kaolin. The ESR spectra were observed to represent narrowing lines corresponding to fast rotation of the probe with a pH sensitivity of a_N and a g-factor described in Sec. 2.2. The pH values measured by ESR were found to be higher than those determined using a pH meter in suspension (to 1.8 pH units for most alkaline systems). This supports the conclusion about markedly higher OH^- concentration in mesopores of zeolites and kaolin compared to a bulk solution.

2.4.3. Determining pH in Nontransparent W/O Systems

Monitoring the pH in various drug delivery systems, such as liposomes or water-in-oil ointments (w/o systems) is of principal importance in the field of pharmacy. Important applications include adjusting the pH value in the various drug delivery systems and monitoring drug degradation. Such commonly used methods of pH measurement as glass electrodes or pH-sensitive fluorescent probes are not applicable for nonconducting or nontransparent systems, since these do not allow

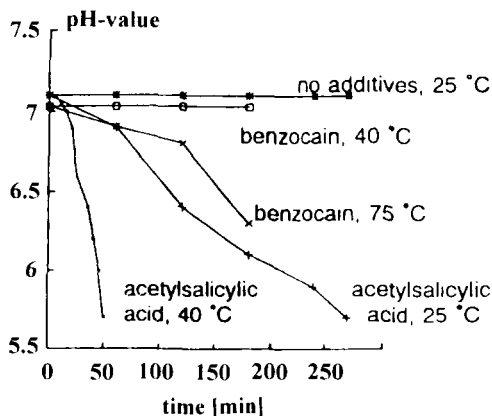
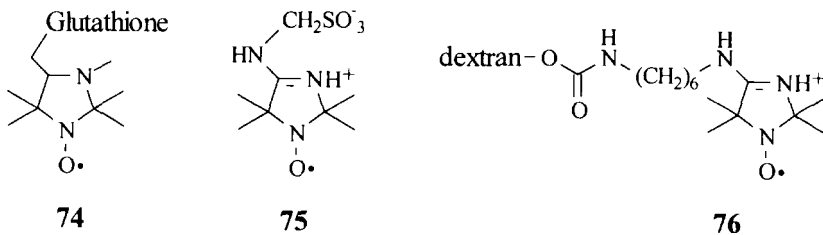


Figure 7. Change in the pH value of the water phase in the w/o Eucerinum^R ointment (Beiersdorf AG, Germany). Data were monitored continuously by ESR using the pH dependence of the hf1 constant a_N of radical **11** (from Kroll *et al.*, 1995, with permission).

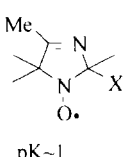
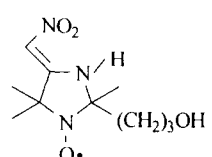
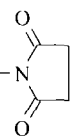
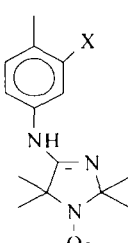
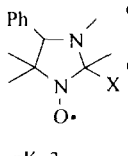
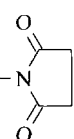
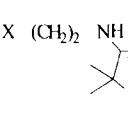
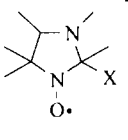
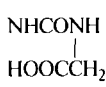
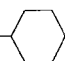
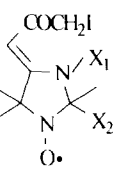
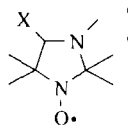
direct, real-time pH monitoring of w/o systems. The application of pH-sensitive nitroxides is the method of choice for overcoming these problems. The hydrophilic imidazoline radical **11** was recently used for pH monitoring in the aqueous phase of a w/o system during decomposition of hydrolyzable drugs (Kroll *et al.*, 1995). While hydrolysis of acetylsalicylic acid caused a rapid decrease in the pH value during 5 h at room temperature within the emulsion, benzocain exhibited a relatively higher stability (Fig. 7). Results proved the possibility of pH determination in nontransparent w/o systems using spin pH probes without expensive and disturbing sample preparation. The high sensitivity of ESR spectroscopy allows us to use samples with a volume of a few microliters.

2.4.4. Determining pH in the Inner Volume of Phospholipid Vesicles

Determining intraliposomal pH is of basic interest due to the wide spectrum of liposome applications (Gregoriadis, 1993), including drug delivery and studies of biomembrane transport processes. Molecular pH probes are usually used to measure intraliposomal pH by fluorescence (Eidelman and Cabantchik, 1989; Norris and Powell, 1990), Nuclear Magnetic Resonance (NMR) (Taylor and Deutsch, 1988), and ESR (Bragadin and Viola, 1983; Perkins and Cafiso, 1986, 1987) spectroscopies. However the application of fluorescent pH probes is restricted by the optical transparency requirement of samples. The NMR is limited owing to low sensitivity. Spin-labeled amphiphiles (Perkins and Cafiso, 1986, 1987) are restricted to systems where calibration of the distribution sensitivity of spin probes between water and lipid phases to the transmembrane pH gradient can be performed. The application of pH-sensitive nitroxides for these purposes seems to be promising, since it allows direct, real-time monitoring of intraliposomal pH. The limitation of the approach is the requirement that the hydrophilic structure of the radical not be penetrated across the membrane barrier for its localization in the inner volume of liposomes. Spin-labeled glutathione **74** (Khramtsov *et al.*, 1989a), sulfonic acid **75**, and dextran **76** (Balakirev and Khramtsov, 1993) covering the pH range from 1.7–7.2 were synthesized for these purposes (Scheme 6). Incorporo-



Scheme 6.

	Nu	X		Nu	X		
 <p>pK~1</p>	77	(CH ₂) ₂ COOH	 <p>92</p> <p>pK~7.8</p>	78	C ₆ H ₄ -NCS-p		
	79			93	CH ₂ CHO		
					94	(CH ₂) ₂ OH	
 <p>pK~4.8-5.0</p>	80	COCH ₂ I	 <p>pK~3</p>	81	NCS	95	(CH ₂) ₂ COOH
	82	N ₃		96	(CH ₂) ₃ OH		
	83	NHCONHCH ₂ CO ₂ H		97			
	84	NH ₂		98	CH ₂ NCS		
				99	CH ₂ Br		
 <p>pK~5-6</p>	85	COOH	 <p>pK~4.7</p>	86	CH ₂ OH	100	CH ₂ N ₃
	87	CH ₂ NH ₂		101	CH ₂ COOH		
	88			102	CH ₂ OH		
				103 ^a	CH ₂ -NCN- 		
 <p>pK~0-1</p>	89	Me	Me	 <p>pK~3-5</p>	90	Me	(CH ₂) ₂ COOH
	91	H	Me		103 ^a		

Scheme 7. Structures of pH-sensitive imidazoline and imidazolidine labels 103 (103^a from Schanding et al., 1996).

ration of these spin pH probes in the inner water volume of the liposomes were performed by repetitive procedures (3-4 times) of sedimentation while changing the supernatant. These probes do not penetrate across the membrane of phosphatidylcholine liposomes for 5-10 h, which allows us to follow intraliposomal pH variations induced by changing external parameters or degradation processes (see Sec. 2.5.2).

2.4.5. *In Vivo* ESR Measurement of pH in Biodegradable Polymers

Progress in the development of low-frequency spectrometers during recent years permits noninvasive *in vivo* measurements (Swartz and Halpern, 1998). Recently Mäder *et al.* (1995) applied pH-sensitive nitroxides **5**, **6**, **11**, **33** (Table 1), **43** (Table 2), and **77** (see Scheme 7) covering a pH range from 0-9 for *in vivo* pH measurements in biodegradable implants using a 1.1-GHz ESR spectrometer (for a 1.1-GHz ESR spectrum of **5** at $\text{pH} \approx \text{pK}$, see Fig. 1b). The authors focused their study on poly(D,L-lactide-co-glycolide) 50:50 (PLGA), which is of therapeutic importance (Schmitt *et al.*, 1993). Tablets from a nitroxide-loaded polymer were made by means of a hydraulic press and implanted in the backs of anaesthetized mice. Nitroxides were observed in the mobile environment after about 1 week except for lipophilic radical **6**. The decrease in pH from 4 to 2 was observed during the second and third weeks, as shown in Fig. 8. After about three weeks, a rapid

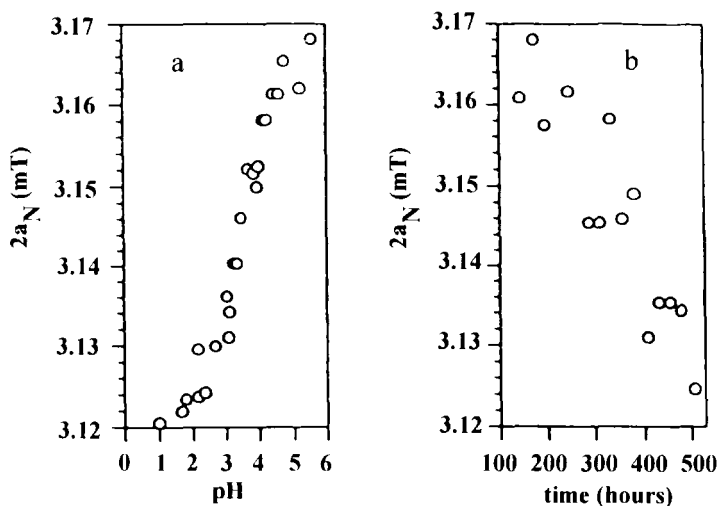


Figure 8. (a) Calibration curve and (b) *in vivo* time dependency of $2a_N$ values of a nitroxide **43**-containing PLGA implant. The $2a_N$ values were determined as the difference between maxima of the first and third peaks of the integrated ESR spectra (data taken from Mäder *et al.*, 1996, with permission).

decay of the ESR signal was observed. The authors conclude that the formation of acidic compartments (pH 4 to pH 2) with low viscosity in the delivery system catalyze the degradation of the polymer. These results may have significant effects on drug stability and solubility, bioavailability, pharmacokinetics, and therefore on therapeutic efficiency. These first data on pH-sensitive nitroxides applications *in vivo* offer new perspectives on *in vivo* ESR spectroscopy. Recently *in vivo* applications of pH-sensitive nitroxides for noninvasive ESR measurement of the pH inside the gut of mice have been demonstrated (Gallez *et al.*, 1996).

2.5. ESR Studies of Proton-Related Transport Processes

2.5.1. Diffusion of Proton in Aqueous Glycerol

Studies of diffusion processes in glassy and supercooled liquids in a wide temperature range are of principal interest for understanding their dynamic properties. Stable nitroxides were previously applied in studies of slow diffusion in glassy and supercooled liquids (Dzuba *et al.*, 1987; Popov *et al.*, 1988; Mogutnov *et al.*, 1994). The approach is based on the concentration dependence of ESR spectra of stable nitroxides caused by spin exchange and dipolar interactions. It results in time dependence of the sample's ESR spectrum, with an initial gradient of nitroxide concentration creating the possibility of following spin probe diffusion. The limitation of the approach is the requirement of high probe concentration (to 0.8 M) and the possibility of the probe disturbing the local environment. Recently we used spin pH probes to study proton diffusion in similar systems (Paschenko *et al.*, 1998). Advantages of applying pH-sensitive nitroxides include the possibility of directly measuring the diffusion of a solvated proton in proton-containing solvents and the avoidance of high probe concentration.

Figure 9 shows the ESR spectra of imidazolidine radical **6** in 85% aqueous glycerol at 220 K and different proton concentrations. Spectra corresponds to the slow rotation region of a strongly immobilized spin probe. The difference in $2A_{zz}$ between R and RH^+ equals 5.1 G (Fig. 9); and it seems to be mostly responsible for changes in isotropic hfi constant $\Delta a_N \sim 1G$ of imidazoline nitroxides observed in aqueous solutions at room temperature (Table 1). The pH dependence of the ESR signal intensity at fixed value of a constant magnetic field I_H (see inset, Fig. 9) shows a conventional titration curve. It can be used as calibration when measuring proton concentration at this temperature. To prepare samples for proton diffusion studies, a thin layer of aqueous glycerol containing radical **6** was created at the outer surface of glass capillary, cooled by the liquid nitrogen, then placed in the larger capillary containing the water-glycerol solution with a lower pH, and immediately frozen at 77 K. The prepared sample was transferred to the cavity of an ESR spectrometer, where proton diffusion was initiated by rapidly heating this sample to the required temperature. Figure 10 shows time evolution of the ESR spectra induced by proton

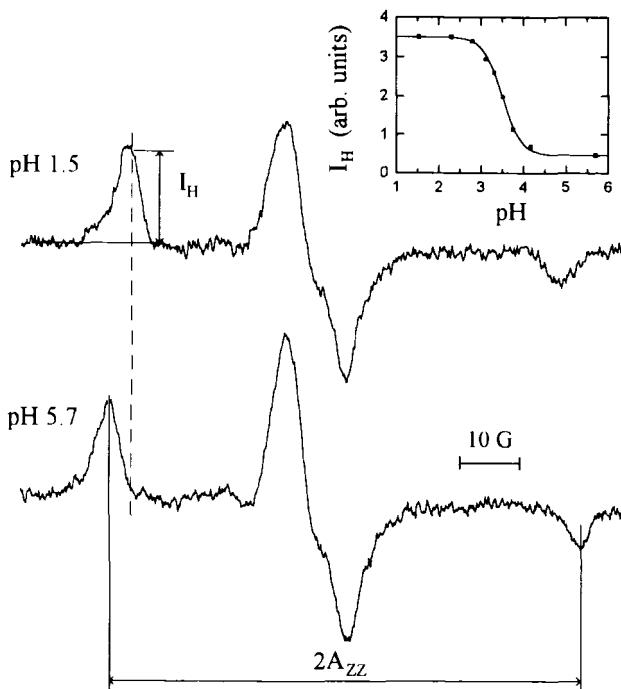


Figure 9. The ESR spectra of radical **6** in 85% aqueous glycerol at 220 K corresponding to fully protonated (pH 1.5) and fully unprotonated (pH 5.7) forms of the radical ($\text{pH} = -\lg[\text{H}^+]$) was calculated according to calibration of the pH meter in an aqueous glycerol with HCl, namely, $\text{pH} = \text{pH}_{\text{obs}} + 0.8$, where pH_{obs} is the value measured by the pH meter at 23 °C). *Inset:* The pH dependence of ESR spectral intensity I_{H} measured at a fixed position of constant magnetic field refer to the line position of Mn^{2+} in CaO used as a standard.

diffusion at 220 K. The linear time dependence of intensity squared $[I_{\text{H}}(t) - I_{\text{H}}(0)]^2$ at the beginning of diffusion is predicted by detailed analysis by Dzuba *et al.* (1987) and Popov *et al.* (1988). The slope of this dependence allows the quantitative determination of the diffusion coefficient. Values of the proton diffusion coefficient measured using spin probe **6** for 85% aqueous glycerol at different temperatures were found to range from 10^{-7} – 3×10^{-9} cm²/s for viscosity varying from 10^2 – 10^5 P.

In contrast to the Stokes–Einstein equation, there was an empirical relation between diffusion coefficient D and viscosity η , namely, $D \sim \eta^{-1/2}$. Similar deviation in the dependence of the diffusion coefficient on viscosity from that predicted by the Stokes–Einstein equation ($D \sim \eta^{-1}$) was previously reported by Popov *et al.* (1988) and Mogutnov *et al.* (1994) for the diffusion of stable nitroxide in supercooled liquids. Analogous anomalous with viscosity dependence were

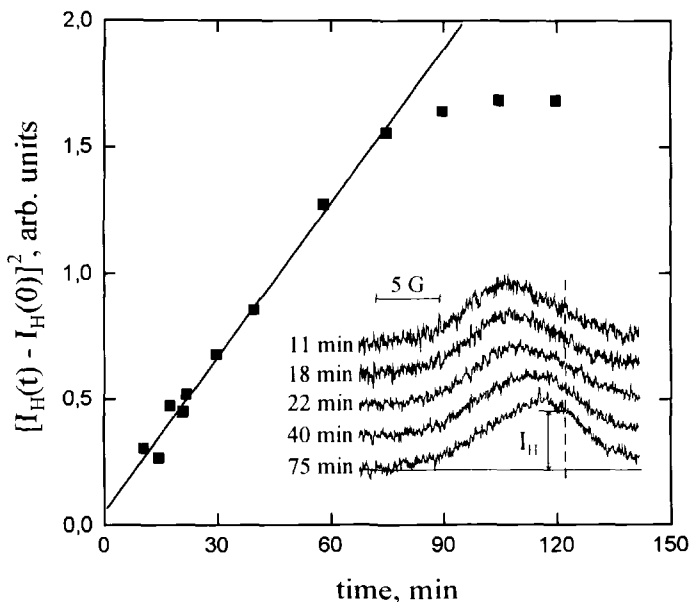


Figure 10. Time evolution of the low-field component of the ESR spectrum of the radical **6** (*inset*) and dependence of the square of ESR signal intensity changes in 85% aqueous glycerol after a fast temperature increase from 77 K to 220 K in the sample containing two layers with pH 4.17 (inner thin layer is about $10\ \mu\text{m}$ wide with 0.1-mM of radical **6**) and pH 0.95. (The $\text{pH} = -\lg[\text{H}^+]$ was calculated according to calibration of the pH meter in the aqueous glycerol with HCl, namely, $\text{pH} = \text{pH}_{\text{obs}} + 0.8$, where pH_{obs} is the value measured by the pH meter at $23\ ^\circ\text{C}$). The diffusion coefficient calculated from the slope of the linear dependence according to the equation obtained by Dzuba *et al.* (1987) equals $(9 \pm 5) \times 10^{-9}\ \text{cm}^2/\text{s}$.

observed for some diffusion-controlled reactions (Leone and Hamill, 1968; Mayer *et al.*, 1988) as well as for biochemical processes (Schlitter, 1988). These are explained by possible microheterogeneity of glassy and supercooled liquids in higher viscosity ranges (Mogutnov *et al.*, 1994). The applications of spin pH probes in proton diffusion studies in these systems seems to be promising especially when we take into account the wide spectrum of available nitroxides with sensitivity to different proton concentration in the range of 14 orders of value (Tables 1 and 2), which allows us to vary characteristic kinetic time by changing the initial proton gradient and, respectively, increasing the range of diffusion coefficients available for measuring.

2.5.2. Proton Transport Across Phospholipid Vesicles

Proton transfer across biological membranes is of great importance in bioenergetics and in the functional regulation of cell processes. Many significant results in the study of transmembrane proton transport are obtained by measuring the

relaxation of the pH gradient across cellular and model membranes using molecular pH probes (Eidelman and Cabantchik, 1989; Norris and Powell, 1990; Perkins and Cafiso, 1986, 1987). Recently pH-sensitive nitroxides were specially designed for pH measurement in the inner volume of phospholipid vesicles (see Sec. 2.4.4). Spin-labeled glutathione **74**, sulfonic acid **75**, and dextrane **76** covering a pH range from 1.7–7.2 (Scheme 6) were used with ESR to follow the kinetics of pH variations inside large unilamellar liposomes after creating a transmembrane proton gradient. Figure 11 shows the kinetics of intraliposomal pH changes calculated from corresponding time dependencies of the hfi constant a_N . The plateau in the kinetics demonstrates the establishment of the transmembrane proton gradient, whose value depends on the initial ΔpH and remains for some hours.

These results are explained (Balakirev and Khramtsov, 1993) by a transmembrane electric potential that causes the transmembrane proton gradient to equilibrate (see Fig. 11 captions). In agreement with this conclusion, the addition of counterion for the protons or proton carriers (Cl^- , K^+ and K-valinomycin, Tl^+) results in further proton influx into the liposome due to a proton counterion exchange (Fig. 12). The

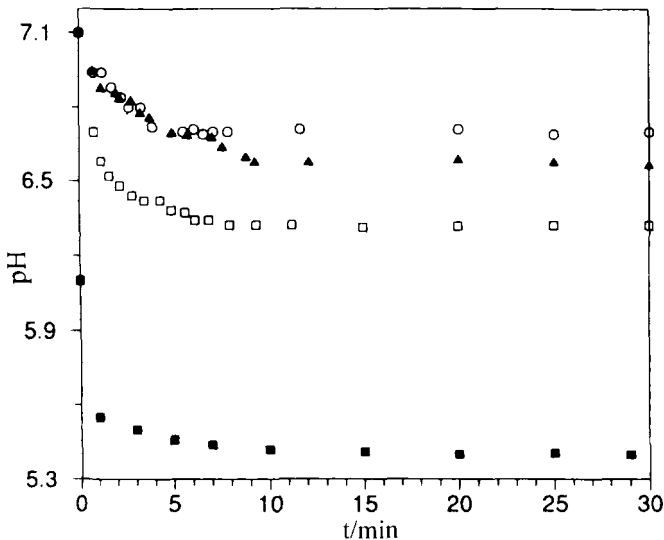


Figure 11. Kinetics of the decrease in intraliposomal pH after applying different proton gradients across phospholipid vesicle membranes measured by means of spin probe **75** (■), $\Delta\text{pH} = 1.1$, or **76** (○), $\Delta\text{pH} = 0.76$; (▲) $\Delta\text{pH} = 1.13$; (□) $\Delta\text{pH} = 1.89$. The final pH gradients are equilibrated by establishing a transmembrane electric potential according to the Nernst equation (Clement and Gould, 1981) $\Delta\phi \approx 60 \log[\text{H}^+]_{\text{out}}/[\text{H}^+]_{\text{in}}$; thus $\Delta\phi$ equals 21 mV (○), 36 mV (▲), 66 mV (□), and 24 mV (■). Note: Values of $\Delta\phi$ display a reasonably linear dependence on changes in the internal H^+ concentration (from Balakirev and Khramtsov, 1993, with permission).

biphasic kinetics of intraliposomal pH changes in the presence of 0.1-M KCl was explained by relaxation of transmembrane electric potential due to Cl^- transport with a permeability coefficient of 10^{-10} cm/s, in reasonable agreement with the literature data (Deamer, 1987). The addition of K-valinomycin accelerates this slow phase of the kinetics (Fig. 12) due to a transfer of K^+ by valinomycin. The proton permeability coefficient obtained from the kinetics (see Fig. 12 captions) is about 5×10^{-4} cm/s, which also agrees with literature data (Deamer, 1987). Studies of proton transport in acidic pH range ($\text{pH} \sim 3$, $\Delta\text{pH} \sim 1$) were performed using spin-labeled glutathione 74.

In contrast to data observed at neutral pH, relaxation of ΔpH in acidic medium does not result in the establishment of transmembrane electric potential, but it proceeds within a few minutes with complete equilibration of the inner and outer pH (Khramtsov *et al.*, 1989a). Characteristic times for the kinetics were found to depend strongly on the type of acid used to create the proton gradient; in the case of H_2SO_4 , liposomes kept ΔpH for an hour. It was concluded that in an acidic region,

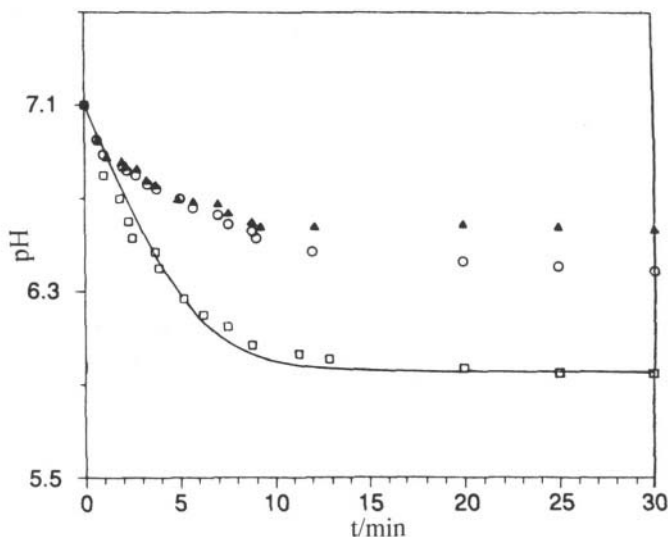


Figure 12. Kinetics of the decrease in the intraliposomal pH after applying a proton gradient across phospholipid vesicle membranes measured by spin probe 76: $\Delta\text{pH} = 1.13$ (▲); $\Delta\text{pH} = 1.13$, 0.1-M KCl added (○); $\Delta\text{pH} = 1.13$, 0.1-M KCl, 30- μM K-valinomycin (□). Estimation of the permeability coefficient of Cl^- from the slope of the slow phase of the kinetics (○) gives a value of $(1 \pm 0.3) \times 10^{-10}$ cm/s. The solid curve is a nonlinear least-squares fit of data to the Nernst-Planck equation (Clement and Gould, 1981) $\text{dpH}_{\text{in}}(t)/\text{dt} = 3\text{pH}_+ \cdot ([\text{H}^+]_{\text{out}} - [\text{H}^+]_{\text{in}})/\text{B} \cdot r$, where buffer capacity B and outer proton concentration $[\text{H}^+]_{\text{out}}$ are assumed to be constant during the kinetics; $\text{B} = 25$ mM and $[\text{H}^+]_{\text{out}} = 10^{-5.97}$; liposome radius $r \approx 200$ nm, giving proton permeability coefficient $\text{pH}_+ = (5 \pm 1.5) \times 10^{-4}$ cm/s (from Balakirev and Khramtsov, 1993, with permission).

the main transmembrane proton transfer mechanism is transport of a proton in the form of undissociated acid. Membrane permeability coefficients were determined for a series of acids: (2 ± 1) cm/s for HCl, (2.2 ± 1) cm/s for HClO₄, $(1.4 \pm 0.7) \times 10^{-4}$ cm/s for HNO₃, and less than 10^{-7} cm/s for H₂SO₄. These values agree with those measured for HCl, HNO₃, and H₂SO₄ for planar lipid bilayers (Gutknecht and Walter, 1981). Data demonstrate the efficiency of the application of spin pH probes in studying biomembrane transport processes.

2.6. pH-Sensitive Spin Labels in Studies of Peptides, Proteins, and Biomembranes

2.6.1. pH-Sensitive Spin-Labeling Reagents

The most important targets of spin labeling are probably proteins and biomembranes. For pertinent reviews see Wenzel *et al.* (1983) and Hideg and Hankovszky (1989). To develop really promising methods of labeling proteins and biomembranes with pH-sensitive nitroxides, we must design labeling reagents capable of reacting with different functional groups. Table 2 (43–54) lists some pH-sensitive radicals of piperidine, pyrroline, and pyrrolidine types containing labeling amino or carboxyl group. The application of pH-sensitive imidazoline and imidazolidine labels seems to be of particular interest due to the higher pH effect on their ESR spectra (Table 1) and the well-developed organic chemistry of radicals of these types (Volodarsky, 1988a, 1988b). Scheme 7 shows structures of synthesized imidazoline and imidazolidine spin labels.

Among these the radicals containing CH₂Br (99), iodoacetamido (80, 89–91), isothiocyanate (78, 81, 98), succinimido (79, 97), azide (82, 100), carbodiimide (103), amino (84, 87), COOH (77, 83, 85, 88, 90, 95, 101), OH (86, 92, 94, 96), and keto (93) groups are available. For most of these labels, the pK value should not change markedly after the labeling procedure, values are indicated near the structures (see Table 1). For biological studies, labels with pH sensitivity in physiological pH range are of particular interest. In this respect amidine derivatives of imidazoline 80–88 (pK ≈ 4.5–6.6) and imidazolidine 92 (pK = 7.8) can be useful. Recently we described (Balakirev *et al.*, 1992) modifying different chemical functions by the compound 105 with a free isocyanate group followed by alkaline hydrolysis of the perhydrooxadiazole cycle of modified products 106 and 107 (see Scheme 8). The resulting imidazoline nitroxides contain the pH-sensitive amidine group with pK in the range from 4.8–6.4; these can be used in biochemical applications.

Spin-labeled dextran 76 was applied in studies of transmembrane transport (Balakirev and Khramtsov, 1993); label 88 was used for modification of human serum albumin (Khramtsov *et al.*, 1990, 1992). Compounds 109–111 with a long methylene chain or cholesteryl substitutor can be incorporated into the phospholipid

membranes similar to **118** ($n = 16$) and **119** ($n = 16$) (Scheme 9) (Khramtsov *et al.*, 1992). Structures of other pH-sensitive lipophylic derivatives of imidazoline and imidazolidine radicals designed for biomembrane studies are shown in Scheme 9.

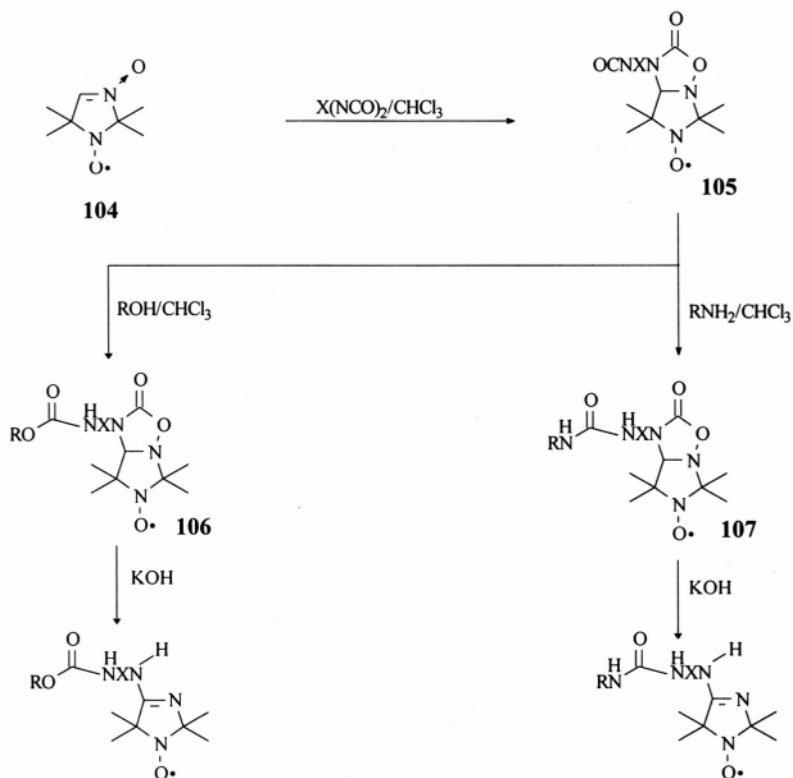
2.6.2. Spin-Labeled pH-Sensitive Peptides

Spin-labeled pH-sensitive derivatives of the peptide hormone angiotensin are used to study pH-induced conformational transitions and intramolecular interactions in this octapeptide (Weinkam and Jorgensen, 1971b; Nakaie *et al.*, 1983). The pH dependence of ESR spectra of radical analogues of angiotensin II containing nitronyl nitroxide instead of imidazole ring of histidine was shown to be (Weinkam and Jorgensen, 1971b) similar to that for the radical analogue of histidine **60** (Weinkam and Jorgensen, 1971a). An intramolecular ion dipole bond was postulated as an important feature in the conformational stability of certain nitronyl nitroxide peptides. These results were used to describe a conformation of angiotensin II that involves an intramolecular ion dipole bond between the phenylalanine carboxylate anion and the imidazole ring. The pH-induced conformational change of angiotensin was also studied by Nakaie *et al.* (1983) using angiotensin derivatives, containing as their N-terminal residue spin-labeled amino acid **50** (Table 2). It was concluded that ESR spectra of the three spin-labeled angiotensins are remarkably sensitive to the conformational change that occurs on deprotonation of the N-terminal amino group.

The pH-sensitive analogue of tripeptide glutathione **74** was synthesized by modifying the SH group of glutathion by alkylating imidazolidine radical **99**. Parameters of the ESR spectrum of spin-labeled glutathione are effected by pH to a much higher extent ($\Delta a_N = 1.17$ G; $\Delta g \approx 0.0002$) compared to that for radical analogues of angiotensin ($\Delta a_N \leq 0.3$ G; $\Delta g \leq 0.0001$). This made it possible to use spin-labeled glutathione in studying proton transport through model biomembranes (Khramtsov *et al.*, 1989a; Sec. 2.5.2).

2.6.3. Studies of Surface Potential and Polarity of Phospholipid Membranes and Proteins

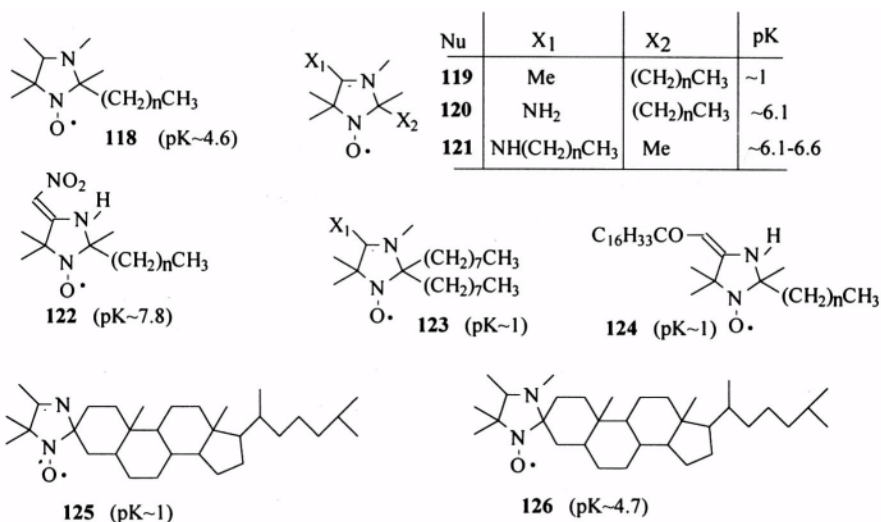
The electrostatic surface potential plays a significant role in many biological functions, such as transmembrane transport, membrane-protein interactions, enzyme catalysis, etc. Methods used to measure surface electric potential can be either indirect, as when estimating the ζ -potential through electrophoretic mobility or conductance measurements (Cafiso *et al.*, 1989; Rottenberg, 1989) or direct approaches using NMR methods (Cafiso *et al.*, 1989), fluorescence spectroscopy (Fromherz, 1989), or spin probes (Cafiso and Hubbel, 1981; Sankaram *et al.*, 1990; Bonnet *et al.*, 1990). Advantages of spin probes lie mainly in the possibility of direct spectral readout related to probe location and the ability to handle opaque or highly scattering samples as well as higher sensitivity relative to NMR. The ESR spectra



Nu	X	R
108		Et
109		n-C ₁₀ H ₂₁
110		n-C ₁₈ H ₃₇
111		cholesteryl
112	(CH ₂) ₂	Et
113	(CH ₂) ₂	Bu
114	(CH ₂) ₄	Bu
76	(CH ₂) ₆	dextran

Nu	X	R
88	(CH ₂) ₂	CH ₂ CO ₂ H
115		
116		
117	(CH ₂) ₂	polylysine

Scheme 8.



Scheme 9.

of radicals previously used (Cafiso and Hubbel, 1981; Sankaram *et al.*, 1990; Bonnet *et al.*, 1990) are not intrinsically sensitive to pH (nor electrostatic potential) in homogeneous solutions. Their use for surface potential, or for surface polarity, depends on changes in interactions between the radical and membrane phases, either directly with surface potential or indirectly with pH. Such methods so far have not proved amenable to measuring electrostatic potentials at the surface of proteins. Therefore the application of spin labels with intrinsic spectral sensitivity to pH seems promising for studying the electrostatic surface potential of membranes and particular proteins.

2.6.3.1. Measuring the Surface Potential and Polarity of DMPC/DMPG Bilayers. The imidazolidine radical **118** ($n = 16$) (Scheme 9) was used in surface potential and polarity studies of mixed bilayers composed of dimyristoylphosphatidylglycerol (DMPG) and dimyristoylphosphatidylcholine (DMPC) (Khrantsov *et al.*, 1992). The intrinsic pK of nitrogen atom N-3 of the radical **118** ($n = 16$) with very low solubility in water is expected to have a value of 4.6 close to that measured for water soluble radicals **118** with shorter methylene chains ($n = 0$, pK = 4.7; $n = 6$, pK = 4.6). Figure 13 shows the effect of pH on ESR spectra of radical **118** ($n = 16$) incorporated in DMPC bilayers derived from the protonation of N-3 atom. For radical **119** ($n = 16$) incorporated in DMPC bilayers on the other hand, no spectral changes were observed over the same pH range; this agrees with the very acidic pK (about 1) of this particular radical. Note: The main reason for the pH sensitivity of the ESR spectrum of radical **118** ($n = 16$) in liposomes is not changes in Δa_N and

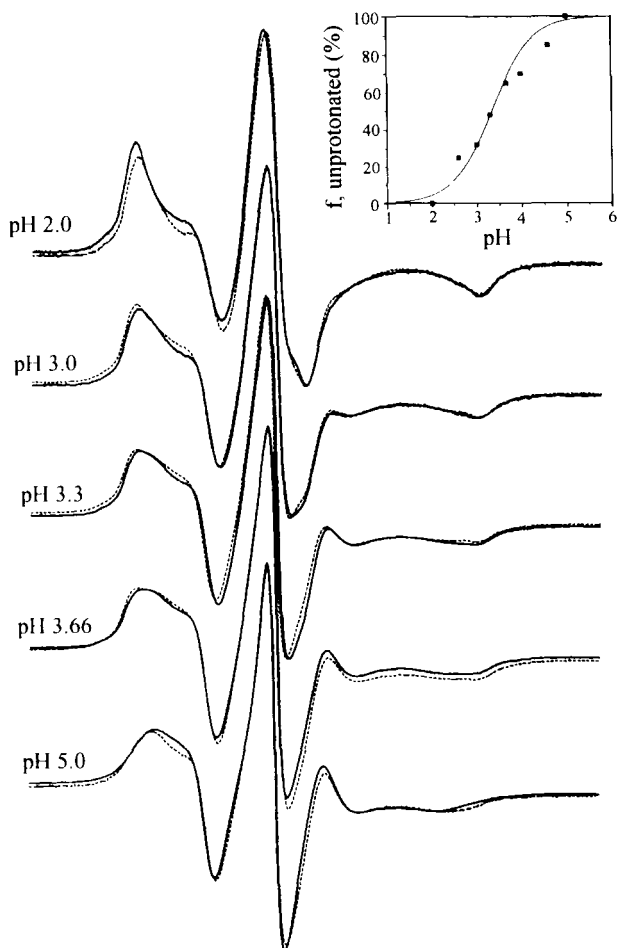


Figure 13. The ESR spectra of radical **118** ($n = 16$) as a function of pH in DMPC bilayer dispersions in a 10-mM NaOAc buffer at 17 °C. Solid lines: Original experimental spectra; dashed lines: Results of spectral subtraction and addition. Spectra were normalized to the same double-integrated intensity for spectral subtractions and additions, but these are scaled to the same maximum line heights in the plots. Total scan width = 100 G. *Inset:* The pH dependence of the fraction f of the unprotonated form of radical **118** ($n = 16$) in DMPC bilayer dispersions determined from ESR spectra using the procedure of spectral subtractions and additions. The solid line is a nonlinear least-squares fit of data to a conventional titration curve $f = 1/(1+[H^+]/K_i)$, yielding a value of $pK_i = 3.3$ (from Khramtsov *et al.*, 1992, with permission).

Δg between R and RH^+ forms, as in the case of a homogeneous solution (see Fig. 9 for imidazoline radical **6** in aqueous glycerol), but the change in interaction between the radical and membrane on protonation of the imidazolidine moiety. The observed greater restriction of rotational mobility of the protonated radical may result from a change in the vertical localization of the probe, as in spin-labeled fatty acids (Sanson *et al.*, 1976) or from direct interaction of the charged moiety with the phospholipid head groups.

An interfacial pK_i of the **118** ($n = 16$) in DMPC as well as DMPC/DMPG mixtures can be calculated by fitting pH dependencies of the fraction of RH^+ form (Fig. 13, *inset*) or spectral peak intensities ratio of the central and low-field components (Fig. 14) as conventional titration curves. Both approaches give the value $\text{pK}_i = 3.3 \pm 0.1$ in uncharged DMPC bilayers at 17 °C. The polarity-induced shift $\Delta\text{pK}_{\text{pol}} = -1.3$ from the value of pK in water allows us to estimate the effective dielectric constant at the membrane surface ϵ_i in the region of the radical heterocycle using calibration of $\Delta\text{pK}_{\text{pol}}$ of the radical in water-ethanol solutions; $\Delta\text{pK}_{\text{pol}} = 0.032 \times (\epsilon - 78)$, where the dielectric constant of the solution ϵ ranges from 30–78. This gives $\epsilon_i = 37$, corresponding to lower polarity at the membrane surface than in a bulk solution, which agrees with literature data (Fromherz, 1989). The polarity-

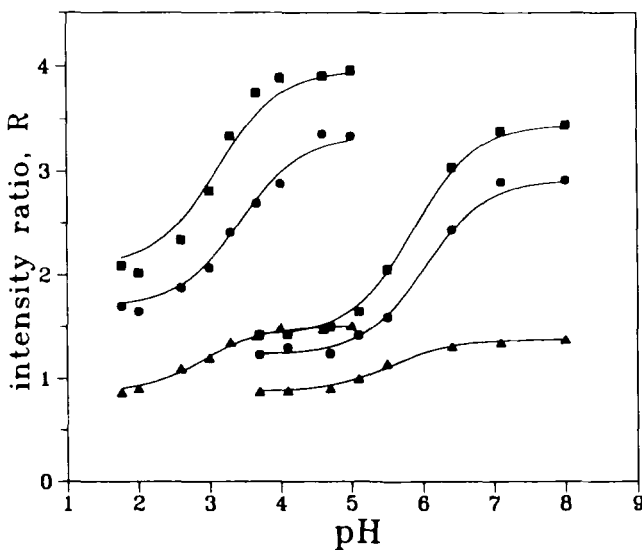


Figure 14. The pH dependence of the ratio of ESR spectral peak height intensities of the central ($m_l = 0$) and low-field ($m_l = +1$) components for radical **118** ($n = 16$) in DMPC (three left-hand curves) and in DMPG (three right-hand curves) bilayer dispersions in a 10-mM NaOAc buffer; ●, data at 9 °C; ■, at 17 °C; ▲, at 50 °C. Solid lines represent nonlinear least-squares fits of data to the standard titration equation (from Khramtsov *et al.*, 1992, with permission).

induced shift of pK_i is temperature-dependent, as seen in Fig. 14; it corresponds to a temperature coefficient of $\Delta pK_{\text{pol}}/dT \approx -0.01$ per degree. For a carboxylic acid spin probe in DMPC bilayers, a similar temperature-induced shift in pK_i was found (Bonnet *et al.*, 1990) but of the opposite sign to that found here, as expected for the dissociation of a molecular acid as opposed to a cationic acid.

When radical **118** ($n = 16$) is incorporated into negatively charged DMPG bilayers, a positive shift is observed in the pK_i of the radical (Fig. 14). This is due to both the polarity-induced shift and the electrostatic shift ΔpK_{el} (Fromherz, 1989; Cevc and Marsh, 1987):

$$pK_i = pK + \Delta pK_{\text{pol}} + \Delta pK_{\text{el}} \quad (11)$$

The electrostatic shift is related to the surface potential ϕ by the following equation (Cevc and Marsh, 1987):

$$\Delta pK_{\text{el}} = -\frac{e\phi}{\ln(10)kT} \quad (12)$$

where T is the absolute temperature, e is the elementary charge, and k is Boltzmann's constant. Using $pK = 4.6$ in water, $pK_i = 5.9$ in DMPG (Fig. 14), $\Delta pK_{\text{pol}} = -1.3$ in DMPC yields electrostatic surface potential $\phi = -150$ mV at the interface of DMPG bilayers in a 10-mM NaOAc at 17 °C. The ionic strength dependence of the surface potential of DMPG bilayers measured in the preceding manner is given in Fig. 15a. The value of $\phi = -95$ mV at 0.1 M KCl agrees with other data (Cevc *et al.*, 1980). Dependencies of the electrostatic surface potential on ionic strength (Fig. 15a) and charge density in bilayers composed of mixtures of the negatively charged lipid DMPG with the zwitterionic lipid DMPC are in reasonable agreement with those predicted by the Gouy–Chapman equation from the electrostatic double-layer theory (Khramtsov *et al.*, 1992).

Thus radical **118** ($n = 16$) extends the class of spin labels with ionizable head groups that are useful for surface electrostatic measurements by ESR (Sankaram *et al.*, 1990; Bonnet *et al.*, 1990; Horvath *et al.*, 1988), and it also extends the pH range of their applicability. Note: Other pH-sensitive analogues are available with a higher value of intrinsic pK as well as different lengths of alkyl chain (Scheme 9).

2.6.3.2. Measuring Surface Potential of the Protein HSA. The electrostatic potential at the surface of a protein can be measured using pH-sensitive radicals by comparing the pK of the radical in bulk solution with that at the surface of the protein. The choice of the length of the linkage between the protonatable group and the point of covalent attachment, and of the intrinsic pK of the radical, is important for such determinations. For instance when the imidazoline spin label **88** was covalently bound to human serum albumin (HSA) (Khramtsov *et al.*, 1990, 1992), a highly mobile ESR spectrum of the radical was observed (Fig. 16a). In addition the pK of the bound radical was found to equal that of radical **88** in bulk solution

(Fig. 16b). The motional freedom of the bound label suggests that the protonatable atom N-3 of the radical heterocycle is located at a remote position from the protein surface. Therefore the label pK is insensitive to the protein's surface electrostatics and remains unshifted from the intrinsic value ($pK = 4.75$, Fig. 16b), which is close to the isoelectric point of the protein $pI = 4.9$.

Modification of the -SH group of HSA by spin label **99** with a short distance between protonatable nitrogen N-3 and alkylating $-CH_2Br$ group (Khramtsov *et al.*, 1985a, 1992) results in a moderately immobilized ESR spectrum of the radical (Fig. 16a). A clear shift of pK of the label bound to the -SH group located at the surface of HSA was found relative to that for label **99** bound to the -SH group of the low

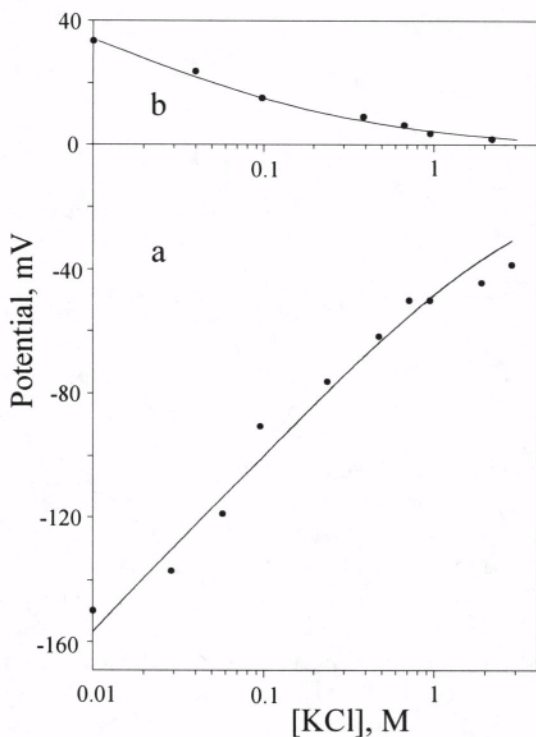


Figure 15. (a) Dependencies of the electrostatic surface potential ϕ of DMPG bilayer dispersions in a 10-mM NaOAc buffer at 17 °C on KCl concentration. The solid curve is a nonlinear least-square fit to the standard Gouy–Chapman equation from electrostatic double-layer theory (Cevc and Marsh, 1987). (b) Dependencies of the electrostatic surface potential at the location of the N-3 atom of spin label **99** covalently bound to HSA on a KCl concentration. Experimental points were determined from the pK shift in the radical, as illustrated in Fig. 16b; the solid curve is a nonlinear least-squares fit to Eq. (13), with $r_p = 2.8$ nm, yielding $\Delta r = 0.2$ nm and $\phi_0 = +65$ mV (data from Khramtsov *et al.*, 1992, with permission).

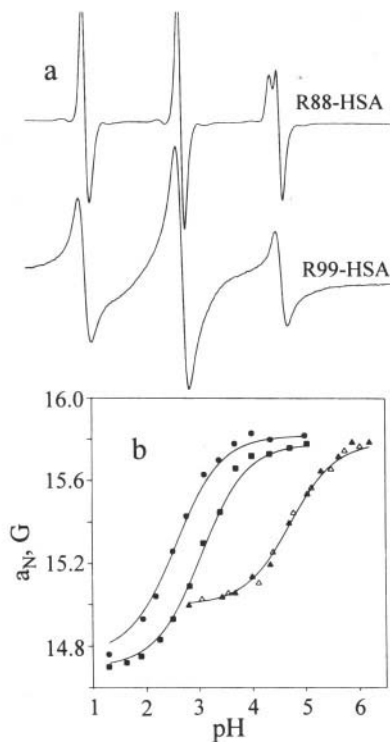


Figure 16. (a) The ESR spectra recorded at 23 °C of radicals **88** and **99** covalently bound to HSA in 10-mM KCl at pH 4.9 and pH 5.0, respectively. The hfi constant a_N is measured as the distance between baseline crossing points of low-field ($m_l = +1$) and central ($m_l = 0$) lines. Total scan widths = 60 G. (b) The pH dependence of a_N for the radicals **88** (▲) and **99** (●) covalently bound to HSA, radical **99** bound to GSH (■), and radical **88** alone (Δ) in 10-mM KCl at 23 °C.

molecular weight compound glutathione (Fig. 16b). The similar values of a_N for radical **99** bound to GSH and to HSA, in both protonated and unprotonated forms of the radical (Fig. 16b), indicates that polarity at the location of the label bound to HSA is similar to that in bulk solution. (For the dependence of a_N on polarity, see Griffith *et al.*, 1974). Therefore the main reason for the shift in the radical pK at its binding site on HSA is the nonzero electrostatic potential at the surface of the protein. Using Eq. (12) with ΔpK_{el} given by the difference between the pK for radical **99** bound to GSH and HSA yields a value for the protein surface potential of +33 mV at pH 2.5–3 in 10-mM KCl; the sign is consistent with the isoelectric point of the protein (pI = 4.9).

Figure 15b shows screening the surface potential with increasing ionic strength I . Data fit well with the linearized Poisson–Boltzmann equation for an isolated spherical surface of radius r_p (Cevc and Marsh, 1987):

$$\phi = \phi_0 \left[\frac{\lambda}{(\lambda + r_p)} \right] \exp(-\Delta r / \lambda) \quad (13)$$

where $\Delta r = r - r_p$ is the distance of the N-3 atom from the protein surface, ϕ_0 is the surface potential at zero ionic strength ($I = 0, \Delta r = 0$), and λ is the Debye screening length ($\lambda = 0.304/I^{1/2}$ nm at 294 K for monovalent salt). Agreement of the ionic strength dependence with the Debye-Hückel theory and the nearly complete screening at a KCl concentration of approximately 2 M further confirm that shifts in pK for radical **99** bound to HSA are dominated by electrostatic effect; hence these give a reliable method for estimating surface potential.

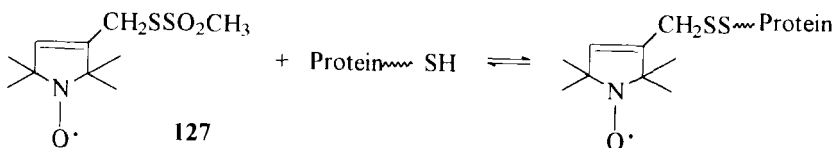
3. DISULFIDE BIRADICALS IN THE THIOL-DISULFIDE EXCHANGE

The key role of thiols and the thiol-disulfide status of the cell in a wide array of biochemical and biological responses is documented (Packer, 1995). Disulfide bond formation is used biologically in such diverse processes as enzyme catalysis, protecting against oxidative damage, stabilizing extracellular proteins, and regulating biological activity. Determining sulfhydryl groups in proteins and low molecular weight compounds is one of the most important procedures in analytical biochemistry. Optical and chromatographic methods are used to determine quantitatively sulfhydryl groups (Boyne and Ellman, 1972; Kosower and Kosower, 1995; Newton and Fahey, 1995). Their limitations are the requirement of the optical transparency of samples on the one hand, and labor-consuming procedures in case of chromatographic methods, in particular HPLC, on the other hand. We propose an ESR method of quantitatively determining sulfhydryl groups (Khramtsov *et al.*, 1989b) which allows us to overcome some of these limitations. The method is based on applying a disulfide biradical that participates in reactions of thiol-disulfide exchange with thiols, resulting in dramatic changes in the ESR spectrum. We and others demonstrated the usefulness of this ESR approach in many chemical and biological systems (Khramtsov *et al.*, 1989, 1991a, 1991b, 1997; Weiner *et al.*, 1991; Yelinova *et al.*, 1993, 1995, 1996; Dolginova *et al.*, 1992; Busse *et al.*, 1992a, 1992b, 1993; Dikalov *et al.*, 1996a). For recent pertinent reviews, see Weiner *et al.* (1995) and Nohl *et al.* (1995).

3.1. Physicochemical Backgrounds

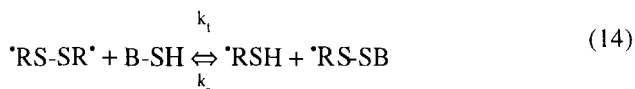
3.1.1. Basis of the ESR Applications of Paramagnetic Disulfides

Berliner *et al.* (1982) shows the usefulness of paramagnetic disulfide **127** in assaying reactive thiol groups in protein through their modification by a thiol-disulfide exchange reaction according to Scheme 10. The label is a highly reactive thiol-specific reagent, which is easily reversible in the presence of an excess of dithiothreitol. One of the disadvantages of the approach is the requirement of the



Scheme 10.

procedure to release the unreacted radical from the protein by gel filtration, dialysis, or precipitation before ESR measurement. The other is insensitivity of ESR spectra of **127** to the reaction with low molecular weight thiols. To overcome these limitations, disulfide biradicals $\cdot\text{RS-SR}\cdot$ can be used (Khrantsov *et al.*, 1989b). The necessary requirement for this approach is a spin-spin interaction of two paramagnetic fragments $\cdot\text{R}$, resulting in the appearance of the biradical ESR spectral components in addition to sharp three-line ESR spectrum of nitroxide monoradicals (see Sec. 2.2.4). The thiol-disulfide exchange reaction of $\cdot\text{RS-SR}\cdot$ with thiols (B-SH):



results in splitting the disulfide bond of the biradical and formation of two monoradicals, $\cdot\text{RSH}$ and $\cdot\text{RS-SB}$, which show conventional triplet ESR spectra. This approach keeps all advantages of disulfide monoradical **127**, allowing protein reversible modification. In addition the application of disulfide biradicals makes it possible to use ESR spectroscopy to follow the kinetics of the reaction (14) as well as to determine quantitatively low molecular weight thiols.

3.1.2. Spectral Parameters of Disulfide Biradicals of Imidazoline and Imidazolidine Types

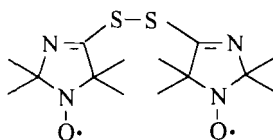
The presence of a disulfide bond in the structure of imidazolidine biradical **73** and imidazoline biradical **128** (Scheme 11) as well as the high intensity of biradical components in their ESR spectra (Fig. 17) opens the possibility of applying them in ESR studies of their reaction with thiols. The ESR spectrum of imidazoline disulfide biradical **128** is shown in Fig. 17. The ESR spectrum was found not to vary with temperature in the range from 10–80 °C, which was interpreted in the terms of a single effective conformation of the biradical with $J = 3.5 a_N$ (Khrantsov *et al.*, 1989b). The stability of the disulfide bond of biradical **128** was found to decrease strongly with pH. In an alkaline medium (pH > 11), biradical **128** decomposes spontaneously in a few seconds, forming two monoradicals, in an acidic medium (pH < 6), it is stable for days. The complete splitting of the disulfide

bond of biradical **128** results in the disappearance of biradical spectral components and an increase in the peak intensity of monoradical ones to 18.2 times followed by the decrease of their line width from 1.35 G to 0.95 G, while the double integral of the spectrum does not change. This means that the initial integral intensity of monoradical components is about 0.11 of total ESR signal intensity, which is in very good agreement with the theoretical prediction of $1/(2I + 1)^2 = 1/9$ (Parmon *et al.*, 1980) for the single effective conformation of symmetric nitroxyl biradicals. Nitrogen nuclear spin is $I = 1$. The rate of spontaneous disulfide bond splitting at physiological pH is low ($\tau_{1/2} \approx 18$ h in 10-mM sodium phosphate, pH 7.5, 23 °C); it is not critical for most of biological applications.

Figure 17 shows the ESR spectrum of the imidazolidine disulfide biradical **73**. The intensity of biradical components I_b was found to depend on temperature and pH (at pH < 4, see Sec. 2.2.4), which indicates the contribution of several effective conformations with an averaged exchange integral $J \approx a_N$ in ESR spectra of this biradical. Protonation of monoradical fragments at pH < 3 results in a decrease of both the hfi constant a_N and peak intensity of biradical components I_b (Fig. 5). It opens the additional possibility of applying this disulfide label as a pH-sensitive one (see Sec. 3.4.1). The disulfide bond of biradical **73** is extremely stable in an aqueous solution in a wide pH range from 1–12 for days or weeks.

3.1.3. Titration of ESR Spectra of Disulfide Biradicals with Low Molecular Weight Thiols

Figure 17 shows typical changes in ESR spectra of biradicals **73** and **128** induced by the addition of thiols. Regardless of the thiol structure, ESR spectra changes were similar for both radicals, and these include a decrease in biradical spectral components while monoradical ones were increasing. Rates of the observed spectral transformation strongly depend on pH (see Sec. 3.1.4); it takes a few seconds (for radical **128**) or minutes (for **73**) for conditions shown in the figure captions. Double integration of ESR spectra of biradicals obtained at different concentrations of thiols indicates preservation of the integral intensity of the ESR signal. Thus reduction of the nitroxide moiety by SH groups of the thiols has not occurred appreciably at these conditions.



128

Scheme 11.

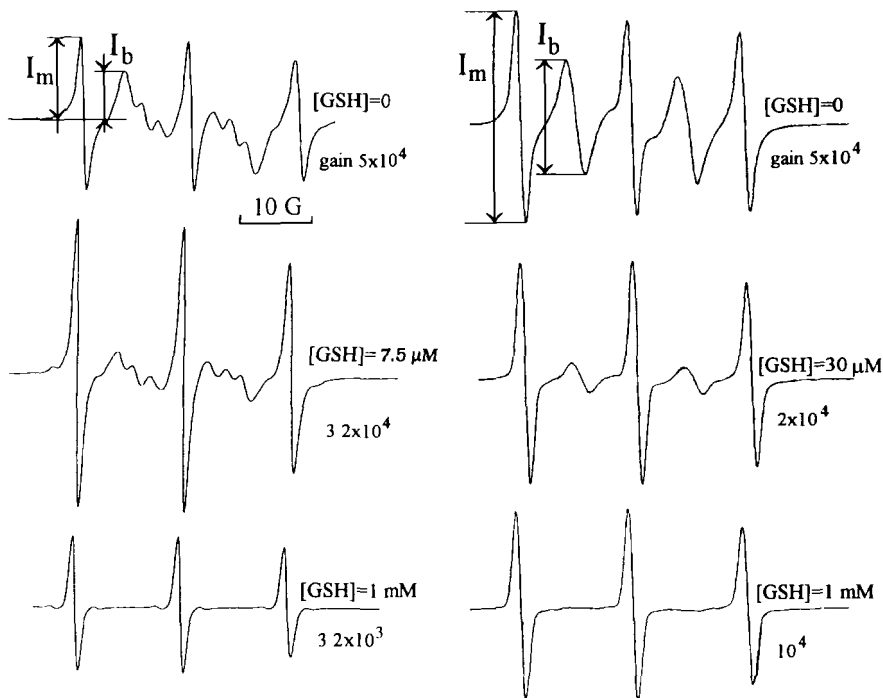


Figure 17. The ESR spectra of disulfide biradicals **128** (0.1 mM) in a 10-mM Na-phosphate buffer, pH 7.5 (*left-hand spectra*) and **73** (0.1 mM) in a 10-mM $\text{Na}_2\text{B}_4\text{O}_7$ buffer, pH 11.3 (*right-hand spectra*) at different concentrations of GSH. Spectrometer settings were the same except for the gain indicated near the spectra: Microwave power 20 mW, modulation amplitude 0.8 G. Note: Splitting the S-S bond of biradical **128** results in a decrease in the line widths of its monoradical component from $\Delta H_{pp}^1 = 1.35$ G to $\Delta H_{pp}^1 = 1.05$ G; for radical **73**, these changes were less than 2% (from 1.46 G to 1.44 G).

Observed ESR spectra changes agree with splitting the disulfide bond of the biradical and the formation of two monoradicals with conventional triplet ESR spectra according to Eq. (14). The maximal increase in the integral intensity of the monoradical components in excess of GSH or Cys (Fig. 17) is about 9.1 times for radical **128**, which is close to the theoretical prediction for biradicals with a single effective conformation (see Sec. 3.1.2). For radical **73**, this value is lower and equals 4.6, which is consistent with the contribution of several effective conformations in the ESR spectrum of **73**. Figure 18 shows dependencies of relative changes in intensities of monoradical ($\Delta I_m/I_m^0$) and biradical ($\Delta I_b/I_b^0$) components of ESR spectra of disulfide probes **73** and **128** on the ratio of the concentration of thiols and biradicals. Deviation from linear dependence is due to an increasing contribution from the reverse reaction (14) at high thiol concentrations (Khramtsov *et al.*, 1991a). The linear part of the dependencies is described by:

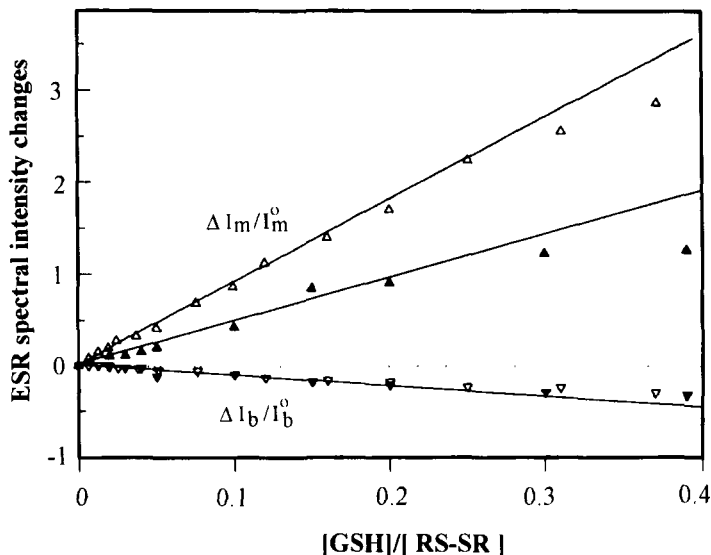


Figure 18. Dependencies of relative changes in peak intensities of monoradical ($\Delta I_m/I_m$) and biradical ($\Delta I_b/I_b^0$) components of ESR spectra of disulfide labels **73** (\blacktriangledown and \blacktriangle) and **128** (\triangle and ∇) (data obtained as shown in Fig. 17). To reflect changes in the integral intensity of the monoradical component for radical **128**, values of $\Delta I_m/I_m$ were normalized on the ratio of their squared line widths, $(\Delta H_{pp}^i/\Delta H_{pp}^t)^2 = 1.65$ (see Fig. 17 captions).

$$\Delta I_b/I_b^0 = -[BSH]/[*RS-SR^*] \quad \Delta I_m/I_m^0 = \alpha[BSH]/[*RS-SR^*] \quad (15)$$

The tangent of the angle of the slope of dependencies $\Delta I_b/I_b^0$ on $[BSH]/[*RS-SR^*]$ equals 1, in agreement with the stoichiometry of reaction (14), it does not depend on the nature of thiol B-SH or the biradical $*RS-SR^*$. The slope α of dependencies ($\Delta I_m/I_m^0$) depends on the integral intensity of the biradical ESR signal compared to that of monoradicals and as a consequence, on the nature of both the thiol and biradical (see Fig. 18). In the case of GSH and cystein, similar thiol-induced ESR changes were observed, supporting the weak influence of the nature of low molecular weight thiol on magnetic resonance parameters of the resulting monoradical $*RS-SB$. However the structure of B-SH must be considered when SH groups of larger molecules or the total content of different thiols are determined. Thus the obtained dependencies (Fig. 18) can be used as calibrations for the ESR static method of measuring SH-groups. Applications of the ratio $\Delta I_m/I_m^0$ is more favorable due to higher sensitivity, while the advantage of the ratio $\Delta I_b/I_b^0$ is its independence on the thiol structure.

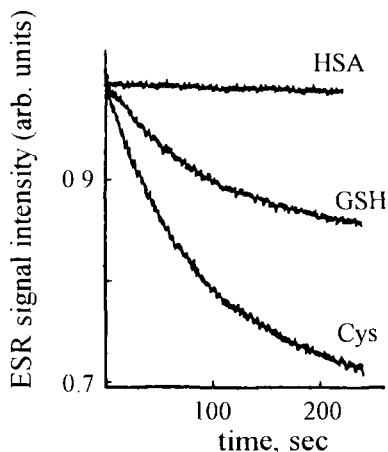


Figure 19. Kinetics of the change in peak intensity of the biradical component of the ESR spectrum of biradical **128** (0.1 mM in a 0.2-mM NaOAc buffer, pH 4.0, temperature 23 °C) after adding 40 μ M of cysteine, glutathione, and human serum albumin.

3.1.4. ESR Studies of the Kinetics of the Thiol-Disulfide Exchange

Kinetics of the thiol-disulfide exchange (14) strongly decrease with a pH decrease, and these can be easily registered at $\text{pH} \leq 10$ for radical **73** and at $\text{pH} \leq 5$ for **128** (see Fig. 19). The rate constant of the forward reaction (14) is determined from the initial part of the kinetics of the decrease of biradical component I_b and the increase of the monoradical component I_m by the following equation obtained from Eqs. (14) and (15):

$$k_f = -(1/I_b^0[\text{BSH}]_0) (dI_b/dt) \quad k_f = (1/\alpha I_m^0[\text{BSH}]_0) (dI_m/dt) \quad (16)$$

where $[\text{BSH}]_0$ is the initial concentration of sulfhydryl groups. The rate constants k_f of reaction (14) of biradicals **73** and **128** with series of thiols are listed in Table 4. The strong dependence of k_f on the pH value confirms the conclusion that the main mechanism of reaction (14) is the reaction with mercaptide ion BS^- (Torchin-skii, 1974). Equation (16) is the basis for the kinetic approach in assessing concentrations of SH compounds when the rate constant k_f is measured in advanced. Of particular interest is the enormous difference in the reactivity of the disulfide bond of radicals **73** and **128** compared to the same concentration of mercaptide ion or pH value. This allows us to use **73** and **128** as complementary labels for different tasks. For example, they can be used to study reaction (14) as well as to measure thiols concentrations by the kinetic approach in different pH ranges ($\text{pH} \geq 7$ for radical **73** and $\text{pH} < 6$ for radical **128**). Another important application involves measuring absolute concentrations of thiols particular to biological systems at $\text{pH} \approx 7$. For example radical **128** was successfully used (Khramtsov *et al.*, 1991a, 1991b; Weiner *et al.*, 1991) in the static approach described in Sec. 3.1.3. The

Table 4
Rate Constants, k_f , for the Reaction (14) of Thiol-Disulfide Exchange of the Disulfide Biradicals **128 (pH < 6) and **73** (pH \geq 7) with Series of Thiols at 21 °C**

Thiol	Rate Constant k_f ($M^{-1} s^{-1}$)						
	pH 4.0	pH 4.67	pH 5.34	pH 7.0	pH 7.4	pH 8.0	pH 8.5
Cysteamine	61 \pm 6	74 \pm 8	290 \pm 30	—	—	—	—
Cysteine	41 \pm 5	92 \pm 10	240 \pm 30	0.37 \pm 0.04	0.97 \pm 0.1	2.3 \pm 0.3	4.2 \pm 0.5
Glutathione	14 \pm 2	32 \pm 4	150 \pm 20	0.26 \pm 0.03	0.76 \pm 0.1	2.6 \pm 0.3	4.6 \pm 0.5
HSA	—	0.2 \pm 0.04	0.7 \pm 0.1	—	—	—	\approx 0.01

disadvantage of the static approach is the required excess of the biradical compared to thiols content, which does not allow its application to SH-groups measurement *in vivo*.

The application of biradical **73** in thiols measurements at physiological pH by the static method is limited by the slow kinetics of reaction (14). Biradical **73** can be used for SH-group measurement by the kinetic approach at pH \approx 7 when using biradical **128** creates problems due to very fast S-S bond splitting in the reaction with thiols ($\tau \approx 1/k_f[\text{BSH}] \leq 0.1$ s at $[\text{GSH}] \approx 1$ mM). For instance the rate constant k_f for the reaction of **73** with GSH at pH = 7.4 equals 0.76 $M^{-1} s^{-1}$ (Table 4), and, the characteristic time of S-S bond splitting of the biradical τ is about 1 hour for millimolar concentrations of GSH, which is reasonable for *in vivo* applications.

Note: The comparatively low values of k_f for the reaction of biradicals with protein human serum albumin, which is of methodological importance, since it allows us to ignore the protein background when the content of low molecular weight thiols in the presence of the protein is measured.

3.2. Quantitatively Determining Thiol Groups in Biological Systems

3.2.1. Intracellular Glutathione Measurement

Among low molecular weight compounds GSH is particularly important because it is present in all animal cells and blood in concentrations to a few millimolars, and it is responsible for the redox state of organisms (Meister and Anderson, 1983). Biradical **128** was used to measure GSH content in erythrocytes (Khrantsov *et al.*, 1989b), Chinese hamster ovary cells (Weiner *et al.*, 1991), murine neuroblastoma and malignant melanoma cells (Busse *et al.*, 1992a, 1992b), and tumor HeLa cells (Busse *et al.*, 1993), including those during treatment by anticancer antibiotics. Noninvasive measurement of intracellular GSH by the static ESR approach is based on the dominant contribution of GSH in the reaction with

biradical, fast diffusion of the biradical across the cellular membrane, and comparatively low reduction of its paramagnetic fragment. The sensitivity of the method is sufficiently high to perform the measurements in a few (~ 100) cells (Weiner *et al.*, 1991).

3.2.2. Thiols Determination in the Blood

The concentration of thiols in the blood is an important biochemical parameter particular for GSH. Both kinetic (Khramtsov *et al.*, 1989b, 1997) and static (Yelinova *et al.*, 1995, 1996) approaches for measuring of GSH in erythrocytes, cystein in blood plasma, as well as total thiols content in the blood were applied using biradical **128** and **73**. Recent ESR studies of thiols in human and rat blood show an increased level of oxidized GSH in blood plasma under oxidative stress conditions, including such human pathologies as kyphoscoliosis (Yelinova *et al.*, 1996). The ESR assay for thiols measurement in blood meets the requirements of a sensitive and convenient method for express analysis that does not need complicated procedures for sample preparation.

3.2.3. Noninvasive Measurement of Thiols in Isolated Organs

Nohl *et al.* (1995) described the application of biradical **128** to determining thiol levels in isolated perfused hearts. Measurements were performed at a constant rate of biradical infusion, Fig. 20, and shows results of a typical experiment. Monoradicals released into the perfusate were considered to represent tissue GSH levels. Maximal thiol levels of the particular organ available for thiol-disulfide

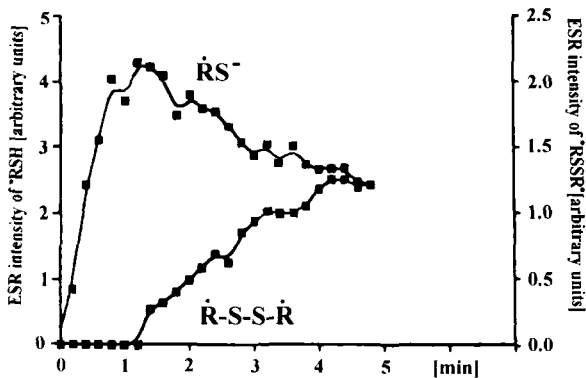


Figure 20. Time profiles of ESR peak intensities of mono- ($\dot{R}S\cdot$) and biradicals ($\dot{R}-S-S-\dot{R}$) collected from the effluent perfusate of a Langendorff heart. The isolated rat heart was perfused for 20 minutes with a Krebs–Henseleit buffer (95% O_2 , 5% CO_2) followed by a 5-minute perfusion period in which 0.5-mM $\dot{R}-S-S-\dot{R}$ was added to the perfusate. Perfusion flow was kept constant at 6 ml/min (from Nohl *et al.*, 1995, with permission).

exchange reactions are indicated by maxima of monoradical release kinetics (Fig. 20). Reappearance of the biradical in the effluent perfusion medium indicates exhaustion of tissue GSH, since the excess of the biradical was used (0.5 mM). To estimate the protein-bound thiols, authors proposed measuring ESR spectra of the homogenate obtained from the organ after washing from all radicals. The $K_3Fe(CN)_6$ was added to retransform the diamagnetic species formed due to reduction of radicals by incidental biochemical reactions to an ESR-sensitive paramagnetic compound. Application of the preceding approach to a rat heart studies under oxidative stress induced by ischemia/reperfusion shows a clear difference in thiol levels compared to those in the control study (Nohl *et al.*, 1995). One of the disadvantages of this approach is the consumption of the thiols to be detected, which irreversibly damages the system under study.

3.3. ESR Studies of Thiol-Related Processes

3.3.1. Monitoring Enzymatic Activity *in Situ* by ESR

Disulfide biradicals can be used to determine the activity of enzymes, including glutathione-dependent ones, whose substrates or products are low molecular weight thiols (Khramtsov *et al.*, 1991a). We applied this approach to measure the activity of acetylcholinesterase (AChE). The AChE is one of the most important enzyme

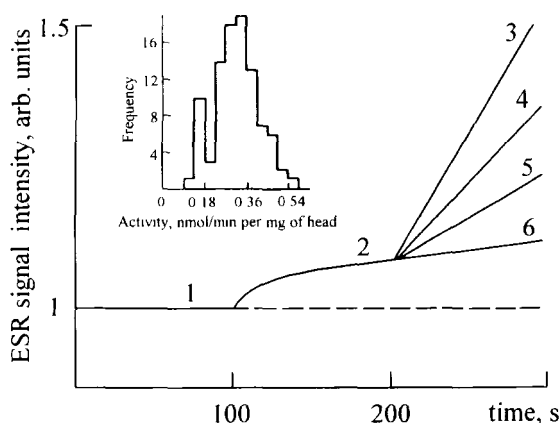


Figure 21. Time course of the peak intensity of the monoradical component I_m of the ESR spectrum of biradical **128**: The initial solution of a 0.1-mM 'RS-SR' in a 10-mM Na-phosphate buffer, pH 7.5 (1); after adding homogenate from the head of larvae, protein concentration 0.15 mg/ml (2); after adding 0.4-mM ATCh (3); before adding ATCh, the inhibitor, phenylmethylsulfonyl fluoride, was added in concentrations of 0.34 mM (4), 0.66 mM (5), and 2 mM (6). Slow kinetics (2) can be explained by the reaction of the biradical with protein SH-groups. *Inset*: The frequency distribution of individual AChE activity in the laboratory population of a fifth-instar bollworm *Heliothis armidera* Hbn measured by ESR for 69 individual insects.

responsible for terminating neuronal transmission at cholinergic synapses by rapid hydrolysis of the neurotransmitter acetylcholine (Quinn, 1987). The widely used method of determining AChE activity is based on the spectrophotometric measurement of the content of thiocholine (TCh) accumulated during the course of enzymatic hydrolysis of acetylthiocholine (ATCh). To follow enzymatic reaction by measuring TCh accumulation, we used biradical disulfide **128** (Khramtsov *et al.*, 1991). This ESR approach is similar to the spectrophotometric one applying a disulfide reagent proposed by Ellman *et al.* (1961). Figure 21 shows the typical kinetics of TCh accumulation after adding the substrate ATCh to the homogenate from the heads of individual bollworm larvae.

The kinetic process is linear in the presence of the ATCh, and AChE activity is easily determined. The kinetic characteristic of the enzymatic reaction was found to be $K_m = (30 \pm 5) \mu\text{M}$, $V_{\max} = (12.3 \pm 2) \text{ nmol/min per mg of protein}$, which is in good agreement with data obtained by Ellman's reagent. The high sensitivity of the approach allows express analysis (a few minutes, as in Fig. 21) of AChE activity in homogenates with a protein concentration of a few $\mu\text{g/ml}$ (to be compared with $\sim 1 \text{ mg/ml}$ in the case of Ellman's reagent). This makes it possible to use the ESR approach to measure AChE activity in individual insects and to carry out populational analysis (see Fig. 21, *inset*).

3.3.2. Determining the Rate Constants of Thiols Reaction with a Superoxide Radical

Superoxide radical generation occurs in all aerobic organisms and leads to superoxide-mediated cell damage. Thiols are well-known antioxidants, and their scavenging properties are of particular interest (Winterbourn and Metodieva, 1995). Two commonly used spectrophotometric approaches for measuring the rate constant of thiols with superoxide radical are based on competition between thiols and cytochrome c (Fridovich, 1986) or epinephrine (Suzuki *et al.*, 1991) for the superoxide radical. However authors applying both approaches must take into account reactions of thiols with cytochrome c and adrenochrome (the product of the reaction of epinephrine with superoxide radical) as possible sources of errors. To overcome these drawbacks, a new ESR approach based on competition between thiols and spin trap 5,5-dimethyl-1-pyrroline-N-oxide (DMPO) for superoxide radical was developed (Dikalov *et al.*, 1996, 1997). The ESR spectroscopy was used to determine both the spin adduct DMPO-OOH formation and the thiol concentration using disulfide biradical **128**. Rates of thiol oxidation by superoxide radical were obtained from the decrease in the amount of SH groups measured by disulfide biradical. Rate constants of the reaction of superoxide radicals with GSH ($1.8 \times 10^5 \text{ M}^{-1} \text{ s}^{-1}$) as well as with a widely used therapeutic agent, α -lipoic acid ($4.8 \times 10^5 \text{ M}^{-1} \text{ s}^{-1}$), were found to be close to the value of $2 \times 10^5 \text{ M}^{-1} \text{ s}^{-1}$ obtained for lipid-soluble antioxidant α -tocopherol (Bielski *et al.*, 1985). Taking into account

that the amount of thiols in membrane compartments is at least 10 times higher than that for tocopherol, we can deduce the important role of thiols in radical trapping and thereby in inhibiting oxidative damage.

3.4. Spin Labeling SH Groups in Proteins

3.4.1. Reversible Modification of Proteins by Biradical Disulfides

Reversibility of the reaction of thiol-disulfide exchange (14) gives the basis for reversibly modifying proteins illustrated by Eqs. (17) and (18):



where BSH is low molecular weight thiols, such as GSH, dithiotreitol, etc. Berliner *et al.* (1982) used paramagnetic disulfide **127** for the reversible modification of Cys-25 in papain. The disulfide biradical **128** was used for the reversible modification of human serum albumin (HSA) and human hemoglobin (Khramtsov *et al.*, 1989b), NADPH-cytochrome P-450 reductase (Yelinova *et al.*, 1989, 1993; Khramtsov *et al.*, 1991), acetylcholinesterase from *Torpedo californica* (Dolginova *et al.*, 1992), and alcohol dehydrogenase from *Thermoanaerobium brockii* (Wciner, 1995). Figure 22 shows the ESR spectrum of HSA modified by disulfide biradical **73**. The spectrum is typical for a moderately immobilized radical; the modification degree of HSA equals 0.95 ± 0.1 , which agrees with one available SH-group in this protein (Markus and Karush, 1957). Labeling is easily reversible according to Eq. (18). Indeed the addition of excess GSH results in the complete disappearance of the immobilized spectrum, while the mobile triplet spectrum of the unbound radical with the same integral signal intensity appears. In addition we observe reversible changes in the ESR spectrum of HSA labeled with biradical **73** in an acidic medium at $\text{pH} < 3.5$. This fact is explained by the protonation of the N-3 atom of the radical fragment of **73** in acidic region ($\text{pK} \approx 3$; see Sec. 2.2.4, Fig. 5). As for radical **128**, both free and bound to HSA, its pK is too low to be detected at $\text{pH} > 1$. (See Table 1 for imidazoline radicals of similar structure.)

The observed decrease in the $h\nu$ constant for **73** bound to HSA at a low pH, $\Delta a_N = 1.2 \text{ G}$, is a characteristic feature of the process of N-3 protonation of imidazoline and imidazolidine radicals (Sec. 2.2.2). The higher mobility of the protonated label bound to HSA indicates its weaker association with the protein surface, which is naturally enough due to electrostatic repulsion of positively charged radical fragments from the surface of a positive electric potential ($\phi \approx +30 \text{ mV}$ for HSA at a pH from 2.5–3; see Sec. 2.6.3.2).

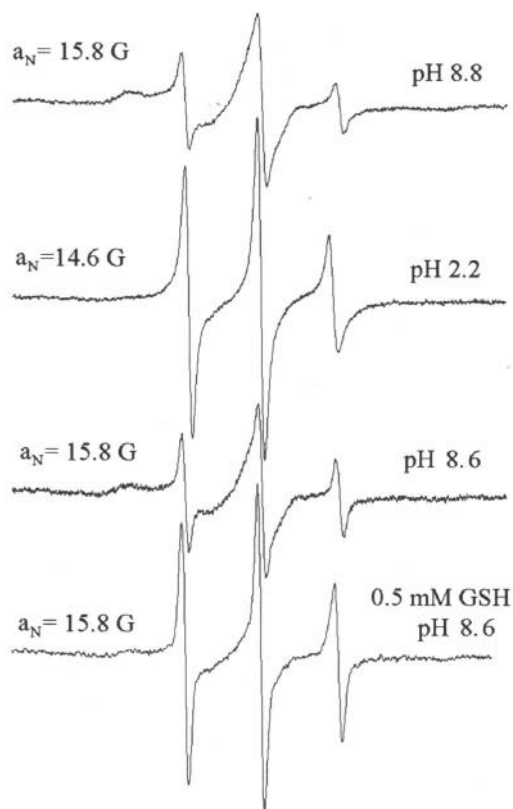


Figure 22. The ESR spectra of HSA labeled by biradical **73**, modification degree $n = 0.98$, protein concentration $50 \mu\text{M}$. Reversible spectral changes in an acidic medium (pH 8.8 \rightarrow pH 2.2 \rightarrow 8.6) demonstrate reversible protonation of the radical. The ESR spectrum at pH 8.6 recorded after adding 1-mM GSH indicates removal of the spin label from the HSA due to the reaction of the thiol-disulfide exchange (18). Spectrometer settings were: microwave power 20 mW, modulation amplitude 0.8 G, receiver gain 1.25×10^5 for immobilized spectra (pH 8.8 and pH 8.6), and 5×10^4 for mobile spectra (pH 2.2 and pH 8.6 after adding GSH).

The reversible modification of SH groups of enzymes by disulfide biradicals allows us to study the influence of structural changes in protein on their enzymatic activity. Chemical modification of NADPH-cytochrome P-450 reductase (Yelinova *et al.*, 1989, 1993) and alcohol dehydrogenase (Weiner, 1995) by the biradical **128** were found to result in the complete inactivation of enzymes. An immediate reactivation of enzymes to 95% was observed after removing the radical from these enzymes by an excess of GSH or dithiothreitol. Recently we used a similar approach to regulate the activity of NADPH-cytochrome P-450 reductase with a natural disulfide compound, α -lipoic acid, widely used as a therapeutic agent (Slepneva *et al.*, 1995). In contrast to these examples, Dolginova *et al.* (1992) observed that removing biradical label **128** from modified AChE does not result in the reversibility of its enzymatic activity. It was proved by different physicochemical methods that both modified and demodified enzymes are in a partially unfolded molten globule state.

3.4.2. Determining the Availability and Molecular Surrounding of SH Groups in Proteins

As shown in the previous section, covalent binding of spin labels to protein is usually followed by the appearance of the immobilized ESR spectrum of the label (Fig. 22), which can be obtained only after release of the unreacted radical from the reaction mixture. Direct registration of the spectrum of the bound radical during modification is impossible due to the weak peak intensity of its ESR signal compared to that for the unbound radical. Taking advantage of biradicals, we can follow the kinetics of protein modification (17) directly by measuring the kinetics of the decrease of the biradical component I_b and/or the increase of the monoradical component I_m (Fig. 17). Using $I_m(t)$ has the advantage of higher sensitivity, while $I_b(t)$ does not need a calibration procedure (see Sec. 3.1.3). The kinetics of demodifying the protein (18) can be registered by detecting the reappearance of monoradical ESR spectrum in the bulk solution after adding low molecular weight thiol. Such studies give important information about the availability of SH groups in the protein. In principle the treatment of surrounding protein SH groups as well as using $^*RS-SR^*$ and B-SH compounds with different structural properties, such as charge, size, and polarity, provide an additional instrument for studying SH groups and their local environment. For example the treatment of alcohol dehydrogenase with *o*-phenantroline to remove a Zn^{2+} atom from its active site results in an increase in the modification rate of the protein by biradical **128** (Weiner *et al.*, 1995). The authors interpreted these data as indicating the appearance of an additional SH group accessible for interaction with the biradical, which is a probable ligand of Zn^{2+} .

4. REACTIONS OF NITRONYL NITROXIDES WITH NITRIC OXIDE

Nitric oxide (NO) was shown to be permanently synthesized in living organisms and involved in many physiological processes, including vasodilatation, neurotransmission, and cellular toxicity (Moncada and Higgs, 1993; Bredt and Snyder, 1994; Schmidt and Walter, 1994). The methods of NO detection in biological systems are limited because of its short half-life *in vivo* from less than 1 to several seconds. These methods are mostly indirect, such as those measuring stable metabolites (nitrite, nitrate, L-citrulline); chemical reaction products, such as methemoglobin; or biological activity (cyclic GMP, smooth muscle relaxation, inhibition of platelet aggregation). Despite the fact that NO is a paramagnetic molecule, it cannot be detected by ESR under normal circumstances, though solid-state spectra were reported at 77 K (Bloom *et al.*, 1972). Therefore methods of NO detection in solution by ESR are based on trapping nitric oxide with a formation of a comparatively stable paramagnetic species using (1) oxyhemoglo-

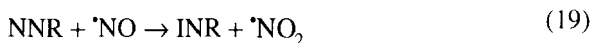
bin, HbFe^{II} , with a formation of the nitrosyl derivative $\text{HbFe}^{\text{II}}\text{-NO}$ (Naschimento *et al.*, 1991); (2) metal-chelator complexes of reduced iron (Fe^{2+}) with dithiocarbamate derivatives (Mordvintcev *et al.*, 1991); (3) cheletropic spin traps (Korth *et al.*, 1994); and (4) nitronyl nitroxyl radicals, NNR, which react with NO forming stable iminonitroxides (Akaike *et al.*, 1993; Joseph *et al.*, 1993; Woldman *et al.*, 1994). Scavenging NO by NNR in chemical and biological systems was used for NO detection by means of ESR spectroscopy as well as to antagonize biological action of both exogenous and endogenous nitric oxide (Yoshida *et al.*, 1993, 1994; Az-ma *et al.*, 1994; Maeda *et al.*, 1994a, 1994b; Singh *et al.*, 1995; Khramtsov *et al.*, 1995; Hogg *et al.*, 1995, 1996; Fukuyama *et al.*, 1995; Konorev *et al.*, 1995; Rand and Li, 1995; Pietraforte *et al.*, 1995; Zamora *et al.*, 1995; Utepbergenov *et al.*, 1995; Balakirev and Khramtsov, 1996).

4.1. Trapping Nitric Oxide by Nitronyl Nitroxides: Physicochemical Studies

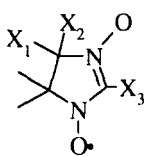
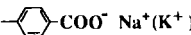
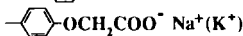
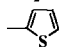
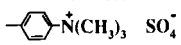
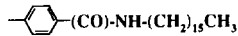
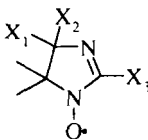
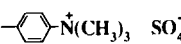
4.1.1. Titration of ESR Spectra of NNR with Nitric Oxide

Nitronyl nitroxides (see Scheme 12) as a new class of stable nitroxides were obtained by Ullman *et al.* (1970). Later we proposed (Grigor'ev *et al.*, 1985; Khramtsov *et al.*, 1986) synthesizing NNR, which allows us to obtain NNR with various substituents in positions 4 and 5 of the radical heterocycle (see structures **135–137**, **140–142** in Scheme 12).

For the first time, NNR was applied to measure an NO concentration in the gas phase by Nadeau and Boocock (1977). The reaction of NNR with nitric oxide in an aqueous solution is described by Akaike *et al.* (1993) for radicals **129–131**, by Joseph *et al.* (1993) for radicals **132** and **133**, and by Woldman *et al.* (1994) for radicals **134–137**. Figure 23 shows typical changes in the ESR spectrum of **134** NNR, induced by adding an NO-saturated buffer solution. The ESR spectra of NNR consist of a characteristic quintet of lines with the intensity ratio 1:2:3:2:1 due to similar hyperfine interaction constants with nuclear spins of atoms N1 and N3 ($a_{\text{N1}} = a_{\text{N3}} = 8.1 \text{ G}$) (Fig. 23a). Treating NNR **134** with nitric oxide leads to the formation of a distinctly different ESR spectrum (Fig. 23c) of seven lines ($a_{\text{N1}} = 9.8 \text{ G}$, $a_{\text{N3}} = 4.6 \text{ G}$), which coincides with that for the corresponding INR, **144** (Fig. 23c, *dotted line*). This transformation proceeds while preserving the integral intensity of the ESR spectrum, which supports stoichiometric conversion of NNR into the corresponding INR by the reaction:



Titration of the ESR spectrum of NNR with nitric oxide is best performed by monitoring low-field components of the ESR spectra of NNR and INR that show negligible overlap (see Figs. 23b and 24a). Titration results show linear depend-

	Nu	X ₁	X ₂	X ₃
	129	Me	Me	Ph
	130	Me	Me	 COO ⁻ Na ⁺ (K ⁺)
	131	Me	Me	 OCH ₂ COO ⁻ Na ⁺ (K ⁺)
	132	Me	Me	
	133	Me	Me	C(CH ₃) ₃
	134	Me	Me	 N ⁺ (CH ₃) ₃ SO ₄ ⁻
	135	Ph	OCH ₃	m-Py
	136	Ph	NH ₂	m-Py
	137	2-Furyl	NH ₂	m-Py
	138	Me	Me	 (CO)-NH-(CH ₂) ₁₅ CH ₃
	139	Me	Me	C ₆ H ₄ -OCH ₃ -p
	140	Ph	OCH ₃	3-Pyridyl
	141	Ph	Ph	Ph
	142	Ph	OCH ₃	Ph
143	Me	Me	C(CH ₃) ₂ -CH ₂ OH	
	144	Me	Me	 N ⁺ (CH ₃) ₃ SO ₄ ⁻

Scheme 12. The structures of nitronitroxides **129–143** and iminonitroxide **144**.

encies of a decrease in ESR amplitude for low-field components of NNR and an increase in ESR amplitude for the low-field components of INR (Fig. 23, *inset*, for **134**; Fig. 24b for **130**); these results can be used as calibration for NO determination using these NNR. Note: The transformation of NNR into INR is a specific reaction of NNR with nitric oxide, and it was not observed in the presence of ¹⁵NO₂, O₂⁻ or ¹OH (Akaike *et al.*, 1993; Joseph *et al.*, 1993).

4.1.2. Stoichiometry of the Reaction between NO and NNR

Figures 23 (*inset*) and 24b clearly demonstrate that the Stoichiometry of the reaction between NNR and NO is approximately 1:2.0 and 1:1.6 for radicals **134** and **130**, respectively. The distinction of this value from 1:1 was carefully discussed by Hogg *et al.*, (1995). Reaction (19) in solution is followed by reactions (20) and (21), which affect both Stoichiometry and the kinetics (see Sec. 4.1.3) of the reaction of NNR with NO:

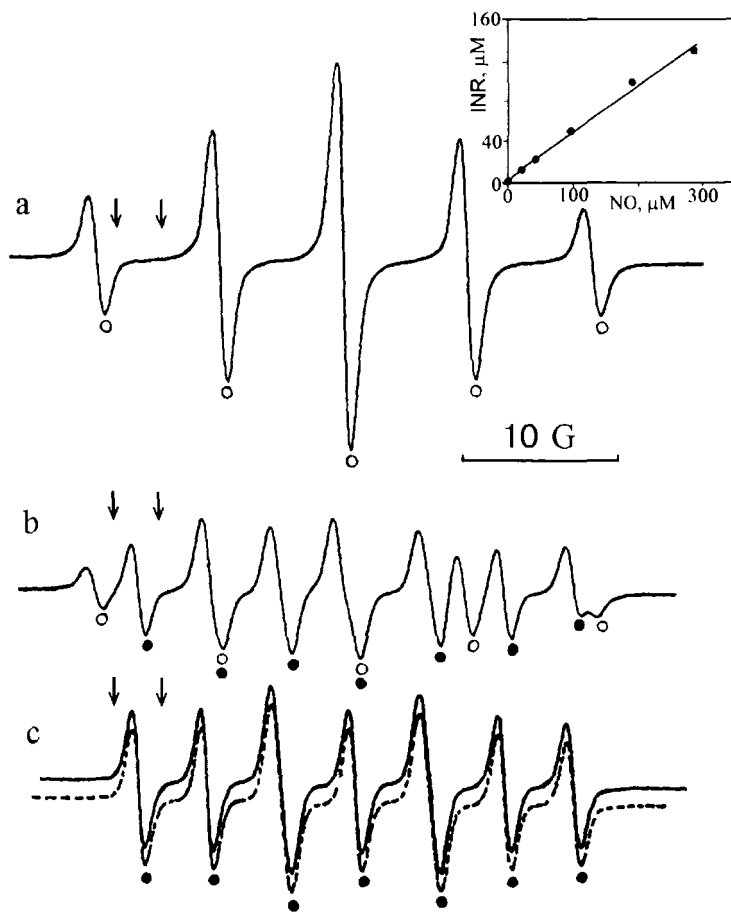


Figure 23. The ESR spectrum of 0.15-mM NNR **134** in a 50-mM K-phosphate buffer, pH 7.4, (a) before and (b) after adding NO-saturated solutions in a final NO concentration 0.2 mM and (c) 0.35 mM. Dotted line: The ESR spectrum of 0.15-mM INR **144**. Hyperfine interaction constants determined by comparing experimental and simulated spectra are (a) $a_{N1} = a_{N3} = 8.1$ G for **134** and (c) $a_{N1} = 9.8$ G, $a_{N3} = 4.6$ G for **144**. Symbols (O) and (●) denote line positions of radicals **134** and **144**, respectively. Arrows denote the field range used to detect the appearance of the radical **144** during NO production by NO synthase (see Fig. 28). Spectrometer settings were: microwave power, 10 mW; modulation amplitude, 0.8 G; receiver gain, 10^4 . *Inset*: Dependence of the concentration of INR **144** formed due to the reaction of NNR **134** with nitric oxide on NO concentration.

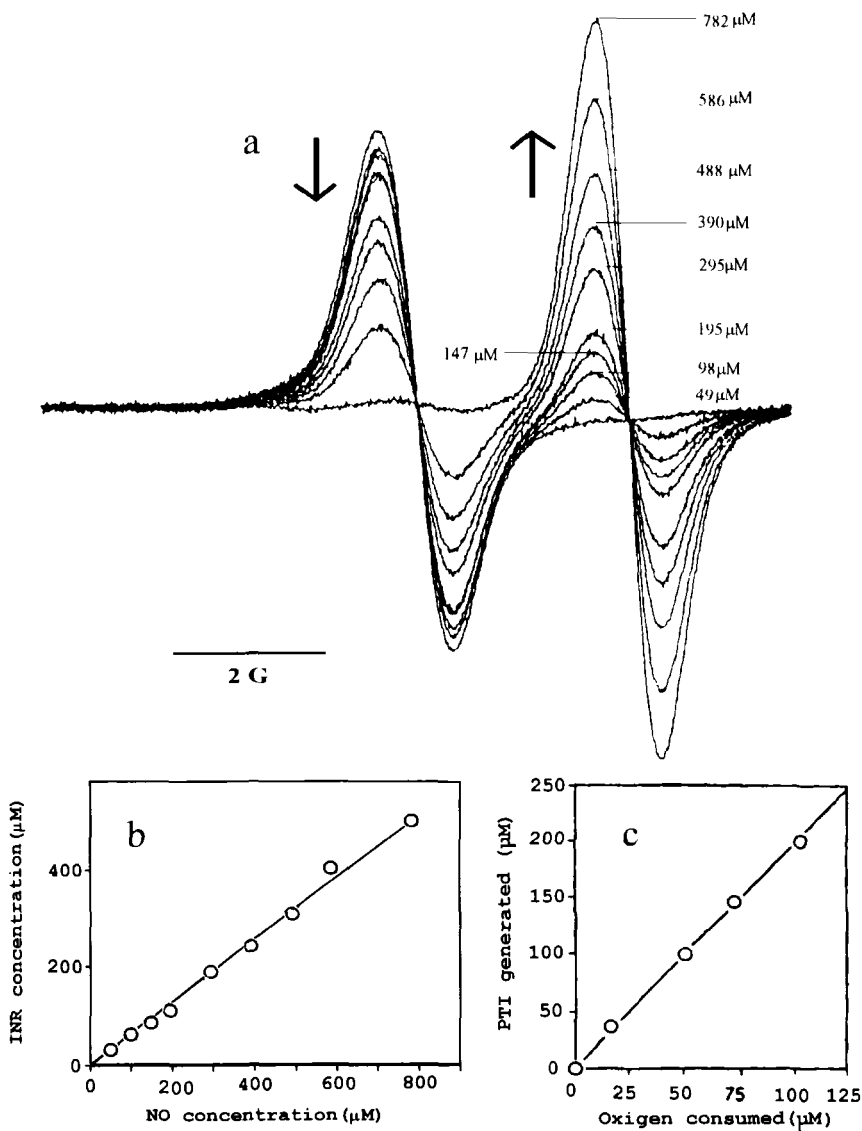
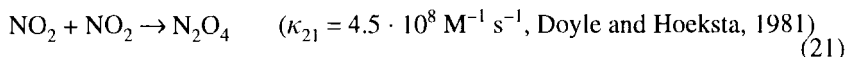
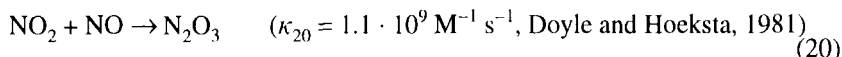
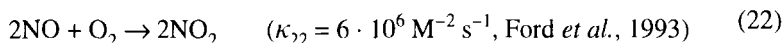


Figure 24. (a) Titration of NNR **130** with NO. Nitric oxide (0–782 μM) was added to NNR **130** (530 μM) in Dulbecco's phosphate-buffered saline, and ESR spectra of low-field lines of NNR and INR were monitored. Arrows \uparrow and \downarrow denote the increase and decrease in the spectral intensity of NNR and INR, respectively. Note: Due to the decrease in INR line widths compared to those for NNR, spectral intensity of INR is greater than that of NNR at the same concentration (reprinted from Hogg *et al.*, 1995, with permission). (b) Dependence of the INR concentration formed due to the reaction of NNR **130** with nitric oxide on NO concentration (calculated from the data in Fig. 24a). (c) Correlation between oxygen consumption and INR (PTI) generation in the reaction of NNR **129** with NO. After adding various amounts of NO to a 0.25-M sodium phosphate buffer (pH 7.4) with or without NNR **129**, oxygen consumption was measured with a Clark-type oxygen electrode. The amount of INR formed was quantified by ESR (reprinted from Akaike *et al.*, 1993, with permission).



In aqueous solution N_2O_3 and N_2O_4 formed hydrolyze to give nitrite and nitrate. Computer analysis of reactions (19)–(21) results in the stoichiometry $[\text{NNR}]/[\text{NO}] = 1:2$ at the high rates of NO generation or at the bolus addition of NO due to the negligible contribution of reaction (21) in NO_2 decay. However the stoichiometry $[\text{NNR}]/[\text{NO}]$ increases to 1:1 at the rate of NO generation less than 1 nM/s at an NNR concentration about 1 mM (Hogg *et al.*, 1995) when reaction (21) becomes essential. Note: Rates of NO generation in biological systems depend on cell types containing variable amounts of isoforms of NO synthase with different mechanisms for regulating enzyme activity; they are usually in the range of 1-10 nM/s (Kelm and Schrader, 1988; Beckman and Crow, 1993). The reaction of NO with oxygen:



does not effectively compete with the reaction between NO and NNR. Experimental data of Akaike *et al.* (1993) on oxygen consumption induced by the bolus addition of NO in the presence and absence of NNR **129** are in agreement with stoichiometry 1:2 between NNR and NO (Fig. 24c). Indeed in the absence of NNR, reactions (20) and (22) give the stoichiometry between O_2 and NO in an aqueous phase as 1:4, as shown by Wink *et al.* (1993). The amount of oxygen consumed was exactly 50% of the INR generated from NNR in the reaction with NO (Fig. 24c). This means that stoichiometry between NNR and NO is 1:2.

4.1.3. The Studies of the Kinetics of NNR with Nitric Oxide

Kinetics of the reaction of NNR with NO was studied by the stopped flow method using ESR (Akaike *et al.*, 1993) and the spectrophotometric method (Woldman *et al.*, 1994). Figure 25 shows the kinetics of the decrease of the concentration of radical **134** in reaction with NO added to a buffer solution. To obtain satisfactory agreement between experimental and calculated kinetics curves, reactions (19) and (20) were taken into account as supporting the stoichiometry between NNR and NO 1:2 (Fig. 25).

Rate constants for the reaction of a series of NNR with nitric oxide are listed in Table 5. Present data demonstrate the possibility of applying NNR as an effective scavenger of nitric oxide. The characteristic time of NO trapping by NNR ($\tau \approx 1/k_1[\text{NNR}] \leq 1 \text{ s}$ at $[\text{NNR}] \geq 0.1 \mu\text{M}$) is close to or less than the lifetime of NO *in vivo* (Ignarro, 1990; Kelm and Schrader, 1990). The ability of NNR and INR to follow ESR spectra allows us to carry out quantitative measurements of a concentration of trapped nitric oxide; the sensitivity of the approach is $1 \mu\text{M}$ for detecting

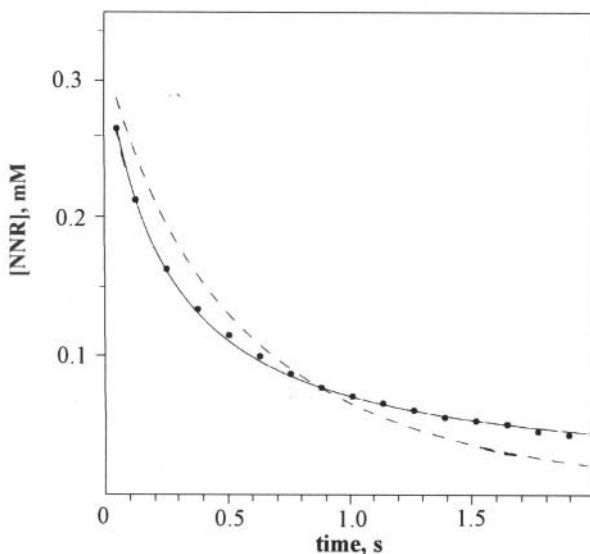


Figure 25. Kinetics of the radical concentration decrease in the reaction of NNR 134, 0.32 mM with NO, 0.6 mM, in a 0.1-M K-phosphate buffer at 22 °C. Solid and dotted curves are nonlinear least-squares fits of data to numerical solutions. Computer calculations taking into account only reaction (19) (*dotted line*, $k_{19} = 0.34 \times 10^4 \text{ M}^{-1} \text{ s}^{-1}$) do not allow us to explain experimental dependence. Considering reactions (19) and (20) gives good agreement between experiment and calculation (*solid line*, $k_{19} = 0.6 \times 10^4 \text{ M}^{-1} \text{ s}^{-1}$). (reprinted from Woldman *et al.*, 1994, with permission).

NO concentration and 0.3 nM/s for measuring rates of NO generation for 1 hour in a sample of 0.2 ml. The method can be applied in optically nontransparent samples. It has one order higher of sensitivity compared with that for widely used spin trappings of NO by dithiocarbamate complexes of iron (Mordvintcev *et al.*, 1991; Komarov *et al.*, 1993) due to comparatively narrow lines of NNR and INR ESR

Table 5
Rate Constants k_{19} of Reaction (19) of NNR 129–131, 134–137 with Nitric Oxide

NNR	129	130	131	134	135	136	137
$k_{19} \times 10^{-3}, \text{ M}^{-1} \text{ s}^{-1}$	5.15 ^a , 5.9 ± 0.4 ^b	10.1 ^a	5.27 ^a	6.0 ± 0.4 ^b	6.4 ± 0.4 ^b	8.2 ± 0.5 ^b	11 ± 0.5 ^b

^aData obtained in a 0.25-M sodium phosphate buffer, pH 7.4, by the stopped flow ESR approach by Akaike *et al.* (1993).

^bData obtained in a 0.1-M K-phosphate buffer, pH 7.5, at 22 °C by the stopped flow spectrophotometric method by Woldman *et al.* (1994).

spectra. The serious limitation of the method is the reduction of nitroxyl radicals into diamagnetic products in biological samples.

4.2. ESR Detection of Nitric Oxide in Chemical and Biological Systems

4.2.1. ESR Studies of NO Release from NO Donors

Recently NNR was used as traps of nitric oxide to study NO donors in both chemical and biological systems. Joseph *et al.* (1993) and Singh *et al.* (1995) applied NNR **130**, **132**, **133**, and **138** to study NO release during photolytic decomposition of sodium nitroprusside. The application of hydrophylic NNR **130** with carboxy group and hydrophobic NNR **138** with a long methylene chain may be used to assay NO production by NO donors in both aqueous and lipid environments (Singh *et al.*, 1995). The NNR **130** was successfully used to study NO release from S-nitroso adducts of glutathione and bovine serum albumin (Pietraforte *et al.*, 1995), as well as from spontaneous NO releaser FK409, (\pm)-(E)-4-ethyl-2-[(E)-hydroxyimino]-5-nitro-3-hexenamamide (Fukuyama *et al.*, 1995). Zamora *et al.* (1995) used NNR **139** to detect NO formation under an oxidative breakdown of Piloxy's acid. We used ESR spectroscopy to study NO liberation by 3,4-dihydro-1,2-diazete 1,2-dioxides, DDD, using NNR traps **134** and **140** (Utepbergenov *et al.*, 1995), by NN-bis(arylsulfonyl)hydroxylamines using NNR **141** (Balakirev and Khramtsov, 1996), and by the derivatives of *N*-methoxy-*N*-nitrosoamines using NNR **142** (Khlestkin *et al.*, 1996). Figure 26 shows a typical transformation of the low-field component of the ESR spectrum of NNR **134** during incubation with a DDD derivative; this corresponds to the initial linear part of the kinetics of spontaneous decomposition of DDD, and it allows us to calculate the rate constant of the process.

4.2.2. Quantitative Measurement of NO Released from Cultured Endothelial Cells

The endothelium-derived relaxing factor EDRF, which is responsible for relaxation of vascular smooth muscle cells, was proposed to be nitric oxide itself (Palmer *et al.*, 1987) or an NO-containing molecule from which NO is subsequently released to target cells (Myers *et al.*, 1990). The NO released from endothelial cells was measured by means of chemiluminescence (Palmer *et al.*, 1987), but because the subject for this method is nitrite, measured data are affected in the presence of nitrite. Az-ma *et al.* (1994) proposed using NNR **130** to measure NO release from endothelial cells by ESR spectroscopy. Endothelial cells cultured on microcarriers were packed in a column, perfused with Krebs solution, then the effluent was mixed with the NNR. The mixture was collected in tubes with a fraction collector, and an ESR signal amplitude of INR formed from NNR **130** due to the reaction with NO was measured (Fig. 27). The signal amplitude was increased by adding endothelium-dependent vasodilator bradykinin in a concentration-de-

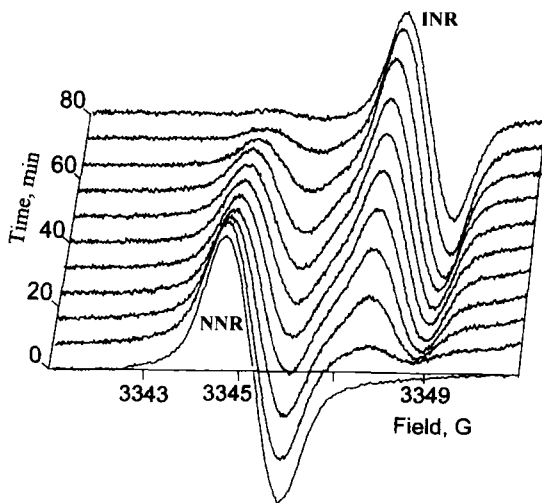


Figure 26. Time profile of the low-field component of the ESR spectrum of 25- μM NNR **134** in the presence of 10 mM of an NO donor, 3-methyl-3,4-tetramethylene-3,4-dihydro-1,2-diazete 1,2 dioxide, DD, in deoxygenated a 50-mM Tris-HCl buffer at 37 °C. Rates of decrease of the NNR component as well as increase of the INR component allow us to measure the rate constant of spontaneous NO liberation by the DD compound. It was found to equal $(6.5 \pm 0.7) \times 10^{-7} \text{ s}^{-1}$ (Utepbergenov *et al.*, 1995). Spectrometer settings were: microwave power, 10 mW; modulation amplitude, 0.8 G; receiver gain, 3.2×10^5 .

pendent manner; reduced by preincubation with an NO synthase inhibitor, N^G-monomethyl- L-arginine; and reversed by following incubation with the substrate of an NO synthase, L-arginine. These data support the usefulness of applying NNR to measure the amount of endothelium-derived NO.

4.2.3. Measuring the Activity of NO Synthase from Rat Cerebellum

The applications of NNR to detect NO by ESR in biological systems is limited due to the fast reduction of NNR into a diamagnetic product in biological samples. We compared reduction rates of different types of nitroxides in the model system with thioglycerol as a reductant (Woldman *et al.*, 1994). Reduction rates were found of NNR and INR by thioglycerol to be much higher compared with those for nitroxide with an isolated N-O[•] fragment, hydroxy-TEMPO (Table 6). This limitation requires an additional defense of NNR against reduction for effective application in biological systems. For that purpose we propose using charged NNR **134** incorporated into the inner volume of a large unilamellar phosphatidylcholine liposomes (Woldman *et al.*, 1994, Khramtsov *et al.*, 1995). The presence of a charge

Table 6
Initial Reduction Rates (V) of 50 μ M of the Radicals of Different Types in a 0.1-M
K-Phosphate Buffer pH 7.5 at 22 °C

Radical	Reducing Agent	V, nM/s
Hydroxy-TEMPO ^a	Thyoglycerol, 2.5 mM	2.4 \pm 0.3
NNR 134	Thyoglycerol, 2.5 mM	175 \pm 20
INR 144	Thyoglycerol, 0.23 mM	5700 \pm 600
NNR 134	Rat cerebellum cytosol, 2 mg of protein per 1 ml, 100- μ M NADPH	1200 \pm 600
NNR 134 in liposomes	Rat cerebellum cytosol, 2 mg of protein per 1 ml, 100- μ M NADPH	3.3 \pm 2.5

^a4-Hydroxy-2,2,6,6-tetramethyl-piperidine-1-oxyl.

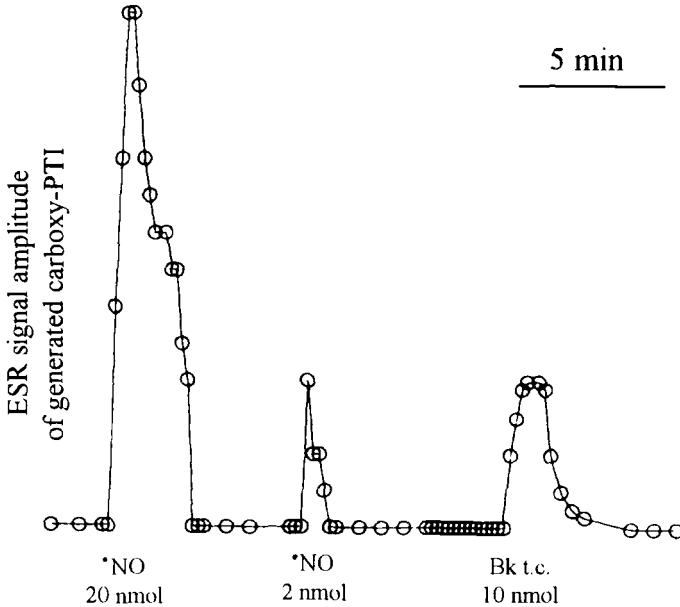


Figure 27. The course of the appearance of generated INR (carboxy-PTI) observed by the assay system. The 2, 20 nmol ^{*}NO injected into a Krebs solution (1 ml min⁻¹), or an effluent from an endothelial cell column stimulated by 10 nmol of bradykinin through the column (Bk t.c.) increased the signal (reprinted from Az-ma *et al.*, 1994, with permission).

in the structures of NNR **134** and corresponding INR **144**, allows us to locate definitely these radicals in the inner volume of liposomes with the characteristic time of their efflux through the membrane $\tau_{1/2} \approx 10$ h. Meanwhile the low molecular weight hydrophobic molecule NO freely diffuses across lipid bilayer. The membrane barrier was found to decrease the availability of radicals **134** and **144** for biological reductants, resulting in a strong decrease in radical reduction rates. In the case of rat cerebella cytosol, the reduction rate of NNR **134** decreases from 10% per second to 0.01% per second due to its location in liposomes (see Table 6). This allows us to follow arginine-dependent NO production by ESR spectroscopy (Fig. 28). Rates of NO trapping by NNR **134** in rat cerebella cytosol were found to be in the range (0.01–0.03) $\mu\text{M}/\text{min}$ per mg of protein, which is about 10% of NO synthase activity measured spectrophotometrically using the oxyhemoglobin method (Doyle and Hoeksta, 1981). Applications of NNR incorporated into

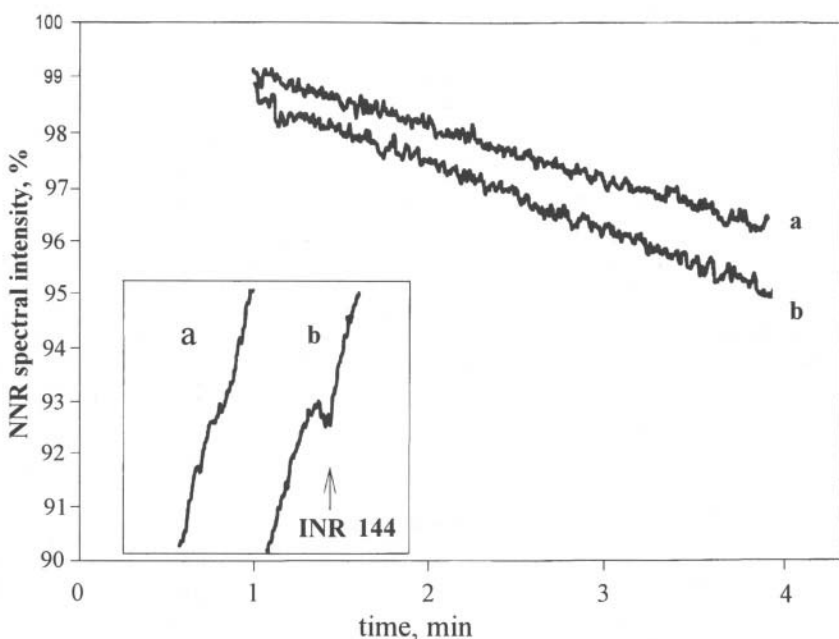


Figure 28. Kinetics of the decrease in low-field peak intensity of NNR **134** ($60 \mu\text{M}$) incorporated into the inner volume of liposomes in the presence of rat cerebella cytosol (6 mg/ml of protein and 0.5-mM NADPH). Kinetics were registered after adding (a) NO synthase inhibitor, L-N^G-nitroarginine or (b) substrate of NO synthase, L-arginine. *Inset:* The EPR spectra of NNR **134** 10 minutes after initiating the kinetics. The field range is shown in Fig. 23 by arrows; it corresponds to the low-field component of the EPR spectrum of INR **144**. Spectrometer settings were as indicated in the caption for Fig. 23 except that gain was 5×10^5 .

liposomes seems to be useful for increasing their efficiency and prolongating their action as antagonists against nitric oxide both *in vitro* and *in vivo* (see Sec. 4.3).

4.3. Antagonistic Action of NNR against Nitric Oxide

Biological functions of NO are so profound, diverse, and crucial in various biological systems that the importance of using NO scavengers or inhibitors of NO synthase (NOS) is increasing. The advantage of NNR scavengers over widely used NOS inhibitors is that NNR directly removes NO from the system and hence abolishes its biological activity without inhibiting NOS. On the contrary, applying NOS inhibitors *in vivo* may cause undesirable long-term inhibition of NOS and as a consequence, of vascular, hepatocytic, or neuronal functions. Therefore the study of this antagonistic action of NNR appears to be helpful not only in understanding the pathophysiological role of NO but also in treating various diseases caused by an overproduction of NO.

4.3.1. Inhibition of Endothelium-Dependent Vasorelaxation

A potent antagonistic action of NNR **129–131** against EDRF-dependent muscle relaxation was demonstrated by Akaike *et al.* (1993) in experiments with acetylcholine-induced vasorelaxation of rabbit aorta. The authors determined that the inhibitory potency of these three NNR was similar to, or greater than, that of NOS inhibitors, N^ω-nitro-L-arginine and N^ω-monomethyl-L-arginine. These NOS inhibitors prevented both consumption of NNR and formation of INR in the vascular system, indicating a direct reaction of NNR with NO.

Recently Rand and Li (1995) observed that NNR **130** produced concentration-dependent reductions of relaxations elicited by exogenous NO and relaxation mediated by acetylcholine and ATP in rings of rat aorta. The authors support the conclusion that EDRF is free radical NO.

4.3.2. NNR As Probes for Studying the Mechanism of Action of Exogenous Vasodilators

Despite widespread clinical use of nitrovasodilators for over a century, their mechanisms of action are not well understood. Konorev *et al.* (1995) proposed NNR as probes for studying the possible role of NO in the vasodilatory action of nitrovasodilators, nitrone spin traps, and nitroxides. The authors demonstrate that NNR **130** and **143** antagonize vasodilatory effects of sodium nitroprusside, SNP, and S-nitroso-N-acetylpenicillamine, SNAP, in isolated rat hearts but did not counteract the vasodilatory action of α -(4-pyridyl-1-oxide)-N-tert-butyl nitrone, POBN, and 4-hydroxy-2,2,6,6-tetramethylpiperidinyloxy free radical, TEMPOL. The authors concluded that coronary vascular relaxation induced by SNP and SNAP

is mediated by NO and the mechanism of the vasodilatory effect of POBN and TEMPOL does not involve NO release.

4.3.3. Therapeutic Effect of NNR 130 against Endotoxin Shock

Endotoxin (septic) shock is mediated through excessive production of NO; it is characterized by a gradual fall in blood pressure, a high cardiac output, an impairment in tissue perfusion, and a lack of response to vasoconstrictors. Yoshida *et al.* (1994) clearly demonstrate pronounced therapeutic effects of NNR 130 on lipopolysaccharide(LPS)-induced endotoxin shock in Wistar rats. The time profile of LPS-induced hypotension and the restoration of blood pressure by NNR 130 are shown in Fig. 29. Administering 130 at 0.17 or 1.7 mg/kg/min completely reversed the effects of LPS on mean arterial blood pressure, heart rate, and lethality. About 82% of the NNR 130 injected was recovered in the urine in the forms of NNR 130 and corresponding INR by treatment with 1-mM potassium ferricyanide. The

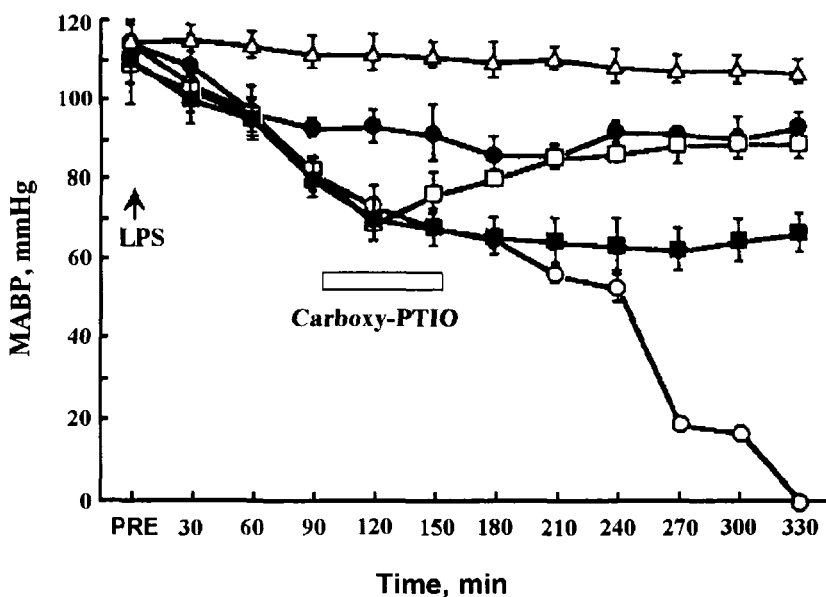


Figure 29. Effects of NNR 130 (carboxy-PTIO) on mean arterial blood pressure (MABP) of rats with endotoxin shock. Various concentration of NNR 130 were administered by continuous intravenous (i.v.) infusion for 1 hour at the rate of 6 ml/h, 90 minutes after i.v. injection of lipopolysaccharide (LPS) (*E. coli*, 10 mg/kg). The MABP was measured continuously through the catheter connected to a pressure transducer. (Δ), control rats (vehicle treated, $n = 5$); (○), rats with LPS-induced endotoxin shock ($n = 5$); (●), LPS + NNR 130 (1.7 mg/kg/min, $n = 5$); (◻), LPS + NNR 130 (0.17 mg/kg/min, $n = 5$); (■), LPS + NNR 130 (0.056 mg/kg/min, $n = 5$). Data are means \pm SEM (from Yoshida *et al.*, 1994, with permission).

formation of the INR in LPS-treated rats was markedly inhibited by administering an NOS inhibitor, N^{ω} -monomethyl-L-arginine, which indicates the action of NNR through its direct reaction with NO.

4.3.4. Modulation of the Pathogenic Function of Nitric Oxide by NNR

The pathological role of nitric oxide, oxygen radicals, and peroxynitrite formed in the reaction of NO with superoxide is widely discussed (Beckman and Crow, 1993). Maeda *et al.* (1994a) observed that treating mice infected with the influenza virus pneumonitis with NNR **130** resulted in a significant improvement in their survival rate, which supports the role of NO in the development of this disease. Enhanced vascular permeability in solid tumors was found to be mediated by NO and inhibited by NOS inhibitors and NNR **130** (Maeda *et al.*, 1994b). Yoshida *et al.* (1993) reported a pronounced enhancement of NO-dependent antimicrobial action with treatment by NNR **130**. Therefore it seems that NNR is a useful instrument in studying the pathophysiological functions of NO as well as in treating various diseases caused by an overproduction of NO.

5. CONCLUSIONS

Stable nitroxides with ESR spectra sensitivity to local chemical environment open new field of applications to spin labeling. In this respect imidazoline and imidazolidine nitroxides were found to be the most promising by offering the possibility of following their reactions with protons, thiols, and nitric oxide by ESR.

Due to the ability of the protonation of the nitrogen atom N3 in radical heterocycle, imidazoline and imidazolidine radicals are the most effective spin pH probes and labels (Khramtsov *et al.*, 1982, 1985a). These spin pH probes are useful in measuring local pH values within the pH range from 0–14; the accuracy of determination is 0.05 pH units. The application of these radicals provides quantitative information about thermodynamic and kinetic characteristics of proton exchange reactions, including isotopic effects. The use of spin pH probes in biological systems seems extremely promising. Measuring local pH in nontransparent water-in-oil ointments and the inner volume of phospholipid vesicles provides new ESR approaches for pH monitoring in these drug delivery systems, including studies of drugs degradation (Kroll *et al.*, 1995) and the kinetics of transmembrane transport processes (Khramtsov *et al.*, 1989; Balakirev and Khramtsov, 1993). The pH titration of radicals located at the surface allows us to estimate surface polarity and the electrostatic surface potential of biological membranes and proteins (Khramtsov *et al.*, 1992). We hope that recent applications of pH sensitive labels for measurement of pH inside the gut of mice (Gallez *et al.*, 1996) and in

biodegradable polymers *in vivo* (Mäder *et al.*, 1996) will stimulate further development of *in vivo* pH studies by ESR.

Disulfide biradicals with imidazoline and imidazolidine radical fragments are convenient labels for SH group titration in both high and low molecular weight compounds, as well as for reversible modification of proteins. These labels are shown to participate in thiol-disulfide exchange reactions, with dramatic changes in ESR spectra. This creates the possibility of measuring the local concentration (to 0.1 μM) and the reactivity of SH groups even in colored and highly absorbing samples. The method proved highly sensitive and reproducible for intracellular GSH measurement (Khramtsov *et al.*, 1989b, 1991b; Weiner *et al.*, 1991; Busse *et al.*, 1992a, 1992b, 1993) and thiol determination in the blood (Khramtsov *et al.*, 1989; Yelinova *et al.*, 1995, 1996). The method is useful for measuring rates of enzymatic reactions, whose products or substrates are thiols (Khramtsov *et al.*, 1991a), and reaction rates of thiols with a superoxide radical (Dikalov *et al.*, 1996). Nohl *et al.* (1995) demonstrated the applicability of the imidazoline disulfide biradical for determination thiol in isolated organs. However the authors indicate a limitation of the approach due to the ultimate consumption of thiols and irreversible damage to the system. In this chapter we show that thiol determination by a new imidazolidine disulfide biradical allows the application of a much lower concentration of the label without essentially consuming thiols. We hope that this new disulfide label opens the possibility of *in vivo* ESR measurements of thiols.

Recently the 2-imidazoline-3-oxides (nitronyl nitroxides) were shown to be effective scavengers of nitric oxide in aqueous solutions under physiological conditions (Akaike *et al.*, 1993; Joseph *et al.*, 1993; Woldman *et al.*, 1994). Their applications include both ESR quantification of NO in chemical and biological systems and neutralization of biological functions of NO. An extremely fast reduction of nitronyl nitroxides by biological reductants compared to that for di-tert-alkylnitroxides limits their applications in biological systems and requires special defense against the reduction, for instance, by using nitronyl nitroxides incorporated in liposomes (Woldman *et al.*, 1994).

We hope that future developments in the application of stable nitroxides in chemical reactions will extend both the field of ESR applications described here as well as a number of the chemical functions available for evaluation by ESR spectroscopy.

ACKNOWLEDGMENTS. We would like to acknowledge the contributions of our coworkers whose names appear in referenced papers. We thank Prof. I. A. Grigor'ev, Prof. V. A. Reznikov, and Dr. T. A. Berezina for helpful discussions and their synthesis of some of the radicals; Dr. V. I. Yelinova, D. I. Utepbergenov, Yu. I. Glazachev, and S. I. Paschenko for their assistance in some experiments and illustrations. This work was partly supported by grant No. 95-04-12506 from the

Russian Foundation of Basic Research and grant No. TW05234 from the Fogarty International Center, National Institutes of Health.

REFERENCES

- Akaike, T, Yoshida, M., Miyamoto, Y., Sato, K., Kohno, M., Sasamoto, K., Miyazaki, K., Ueda, S., and Maeda, H., 1993, *Biochemistry* **32**:827.
- Az-ma, T., Fujii, K., and Yuge, O., 1994, *Life Sciences* **54**:PL185.
- Balakirev, M. Yu., and Khramtsov, V. V., 1993, *J. Chem. Soc. Perkin Trans. 2* **11**:2157.
- Balakirev, M. Yu., and Khramtsov, V. V., 1996, *J. Org. Chem.* **61**:7263.
- Balakirev, M. Yu., Khramtsov, V. V., Berezina, T. A., Martin, V. V., and Volodarsky, L. B., 1992, *Synthesis* **12**:1223.
- Barrat, M. D., and Laggner, P., 1974, *Biochim. Biophys. Acta* **363**:127.
- Beckman, J. S., and Crow, J. P., 1993, *Biochemical Society Transactions* **21**:330.
- Berezina, T. A., Martin, V. V., Volodarsky, L. B., Khramtsov, V. V., and Weiner, L. M., 1990, *Bioorganicheskaja Khimija (Russian)* **16**:262.
- Berliner, L. J., Grünwald, J., Hankovszky, H. O., and Hideg, K., 1982, *Anal. Biochem.* **119**:450.
- Bielski, B. H. J., Cabelli, D. E., Arudi, R. L., and Ross, A. B., 1985, *J. Phys. Chem. Ref. Data* **4**:1041.
- Bloom, N. B. D., Raynor, J. B., and Symons, M. C. R., 1971, *J. Chem. Soc. A* **23**:3843.
- Bonnet, P.-A., Roman, V., Fatome, M., and Berleur, F., 1990, *Chem. Phys. Lipids* **55**:133.
- Boyne, A. F., and Ellman, G., 1972, *Anal. Biochem.* **46**:639.
- Bragadin, M., and Viola, E. R., 1983, *Inorganica Chimica Acta* **80**:L1-L2.
- Bredt, D. S., and Snyder, S. H., 1994, *Annu. Rev. Biochem.* **63**:175.
- Busse, E., Zimmer, G., and Kornhuber, B., 1992a, *Strahlentherapie und Onkologie* **168**:419.
- Busse, E., Zimmer, G., and Kornhuber, B., 1993, *Anneim.-Forsch./Drug Res.* **43**:378.
- Busse, E., Zimmer, G., Schopohl, B., and Kornhuber, B., 1992b, *Arzneim.-Forsch./Drux Res.* **42**:829.
- Cafiso, D., and Hubbel, W. L., 1981, *Annu. Rev. Biophys. Bioeng.* **10**:217.
- Cafiso, D., McLaughlin, A., McLaughlin, S., and Winiski, A., 1989, *Methods Enzymol.* **171**:342.
- Carrington, A., and Smith, I. C. P., 1964, *Mol. Phys.* **8**:101.
- Cevc, G., and Marsh, D., 1987, *Phospholipid Bilayers, Physical Principles, and Models* (Wiley, New York).
- Cevc, G., Watts, A., and Marsh, D., 1980, *FEBS Lett.* **120**:267.
- Clement, N. R., and Gould, J. M., 1981, *Biochemistry* **20**:1534.
- Deamer, D. W., 1987, *J. Bioenerg. Biomembr.* **19**:457.
- Dikalov, S., Khramtsov, V., and Zimmer, G., 1996, *Arch. Biochem. Biophys.* **326**:207.
- Dikalov, S., Khramtsov, V., and Zimmer, G., 1997, Reaction of lipoate and its derivatives with reactive oxygen species, in *Lipoic Acid in Health and Disease* (J. Fuchs, L. Packer, and G. Zimmer, eds.) (Marcel Dekker, New York), pp. 47-66.
- Dolginova, E. A., Roth, E., Silman, I., and Weiner, L. M., 1992, *Biochemistry* **31**:12248.
- Doyle, M. P., and Hoeksta, J. W., 1981, *J. Inorg. Biochemistry* **14**:351.
- Uzuba, S. A., Popov, V. I., and Moralev, V. M., 1987, *Zh. Fiz. Khim.* (Russian) **61**:2188.
- Eidelman, O., and Cabantchik, Z. I., 1989, *Methods Enzymol.* **172**:122.
- Ellman, G. L., Courtney, K. D., Anders, V. ,Jr., and Featherstone, R. M., 1961, *Biochem. Pharmacol.* **7**:88.
- Emsley, J. W., Feeney, J., and Sutcliffe, L. H., 1965, *High-Resolution Nuclear Magnetic Resonance Spectroscopy*, vol. 1 (Pergamon, Oxford, UK).
- Ferris, J. P., and Ertem, G., 1992, *Science* **257**:1387.
- Ferruti, P., Gill, D., Klein, M. P., and Calvin, M., 1969, *J. Am. Chem. Soc.* **91**:7765.

- Ferruti, P., Gill, D., Klein, M. P., Wang, H. H., Entine, G., and Calvin, M., 1970, *J. Am. Chem. Soc.* **92**:3704.
- Fisher, H., 1965, *Mol. Phys.* **9**:149.
- Ford, P. C., Wink, D. A., and Stanbury, D. M., 1993, *FEBS Letters* **326**:1.
- Fridovich, I., 1986, Cytochrome c, in *CRC Handbook of Methods for Oxygen Radical Research* (R. A. Greenwald, ed.) (CRC, New York), pp. 121–122.
- Fromherz, P., 1989, *Methods Enzymol.* **171**:376.
- Fukuyama, S., Kita, Y., Hirasawa, Y., Azuma, T., Sato, A., Morokoshi, N., Koda, S., Yasuda, T., Sakurai, S., and Sakurai, H., 1995, *Free Rad. Res.* **23**:443.
- Gallez, B., Mäder, K., and Swartz, H. M., 1996, *Magn. Reson. Med.* **36**:694.
- Golubev, V. A., Rozantcev, E. C., and Neiman, M. B., 1965, *Izv. Akad. Nauk S.S.S.R., Ser. Khim.* **1965**:1927.
- Gregoriadis, G., ed., 1993, *Liposome Technology*, vols. 1–3 (CRC, Boca Raton, FLA).
- Griffith, O. H., Dehlinger, P. J., and Van, S. P., 1974, *J. Membr. Biol.* **15**:159.
- Grigor'ev, I. A., Schukin, G. I., Khramtsov, V. V., Weiner, L. M., Starichenko, V. F., and Volodarsky, L. B., 1985, *Izv. AN SSSR, Ser. Khim.* (Russian) **10**:2342.
- Gutknecht, J., and Walter, A., 1981, *Biochim. Biophys. Acta*, **641**:183.
- Helbert, J. N., Kopf, P. W., Poindexter, E. M., and Wagner, B. E., 1975, *J. Chem. Soc. Dalton Trans.* **94**:998.
- Hideg, K., and Hankovszky, O. H., 1989, Chemistry of spin-labeled amino acids and peptides. Some new mono- and bifunctionalized nitroxide free radicals, in *Biological Magnetic Resonance*, vol. 8, *Spin Labelling. Theory and Applications* (L. J. Berliner, ed.) (Plenum, New York and London), pp. 427–88.
- Hoffman, B. M., and Eames, T. B., 1969, *J. Am. Chem. Soc.* **91**:2169.
- Hogeveen, H., Germann, H. R., and Proat, A. P., 1967, *Rec. Trav. Chim.* **86**:1063.
- Hogg, N., Singh, R. J., and Kalyanaraman, B., 1996, *FEBS Letters* **382**:223.
- Hogg, N., Singh, R. J., Joseph, J., Neese, F., and Kalyanaraman, B., 1995, *Free Rad. Res.* **22**:47.
- Horvath, L. I., Brophy, P. J., and Marsh, D., 1988, *Biochemistry* **27**:5296.
- Hsia, J. C., and Boggs, J. M., 1972, *Bioch. Bioph. Acta* **266**:18.
- Ignarro, L. J., 1990, *Annu. Rev. Pharmacol. Toxicol.* **30**:535.
- Joseph, J., Kalyanaraman, B., and Hyde, J. S., 1993, *Biochem. Biophys. Res. Commun.* **192**:926.
- Keana, J. F. W., Acarregui, M. J., and Boyle, S. L. M., 1982, *J. Am. Chem. Soc.* **104**:827.
- Kelm, M., and Schrader, J., 1988, *European J. Pharmacology* **155**:317.
- Kelm, M., and Schrader, J., 1990, *Circ. Res.* **66**:1561.
- Khlestkin, V. K., Mazhukin, D. G., Tikhonov, A. Ya., Bagryanskaya, I. Yu., Gatilov Yu. V., Utepbergenov, D. I., Khramtsov, V. V., and Volodarsky, L. B., 1996, *Tetrahedron Lett.* **37**(33):5997.
- Khramtsov, V. V., and Weiner, L. M., 1987, *Khim. Fizika* (Russian) **6**(4):499.
- Khramtsov, V. V. and Weiner, L. M., 1988a, Proton exchange in stable nitroxyl radicals: pH-sensitive spin probes, in *Imidazoline Nitroxides*, vol. 2 (L. B. Volodarsky, ed.) (CRC, Boca Raton) pp. 37–80.
- Khramtsov, V. V., and Weiner, L. M., 1988b, *Russian Chemical Reviews* **57**(9):824.
- Khramtsov, V. V., Goryunova, T. E., and Weiner, L. M., 1991a, *Bioch. Bioph. Res. Comm.* **179**:520.
- Khramtsov, V. V., Yelinova, V. I., Goryunova, T. E., and Weiner, L. M., 1991b, *Biokhimiya* (Russian) **56**:1567.
- Khramtsov, V. V., Marsh, D., Weiner, L. M., and Reznikov, V. A., 1992, *Bioch. Bioph. Acta* **1104**:317.
- Khramtsov, V. V., Panteleev, M. V., and Weiner, L. M., 1989a, *J. Bioch. Biophys. Methods*, **18**:237.
- Khramtsov, V. V., Yelinova, V. I., Weiner, L. M., Berezina, T. A., Martin, V. V., and Volodarsky, L. B., 1989b, *Analytical Biochemistry* **182**:58.
- Khramtsov, V. V., Weiner, L. M., Eremenko, S. I., Belchenko, O. I., Schastnev, P. V., Grigor'ev, I. A., Reznikov, V. A., 1985a, *J Magn. Res.* **61**:397.

- Khrantsov, V. V., Weiner, L. M., Grigor'ev, I. A., Reznikov, V. A., Schukin, G. I., and Volodarsky, L. B., 1985b, *Khim. Fizika* (Russian) **4**:637.
- Khrantsov, V. V., Weiner, L. M., Gogolev, A. Z., Grigor'ev, I. A., Starichenko, V. F., and Volodarsky, L. B., 1986, *Magn. Res. Chem.* **24**:199.
- Khrantsov, V. V., Weiner, L. M., Grigor'ev, I. A., and Volodarsky, L. B., 1982, *Chem. Phys. Lett.* **91**:69.
- Khrantsov, V. V., Weiner, L. M., Rar, V. A., Berezina, T. A., Martin, V. V., and Volodarsky, L. B., 1990, *Biokhimija* (Russian) **55**:1014.
- Khrantsov, V. V., Woldman, Ya. Yu., Grigor'ev, I. A., Kiriljuk, I. A., and Utepbergenov, D. I., 1995, *Magnetic Resonance in Medicine* **6**:282.
- Khrantsov, V. V., Yelinova, V. I., Glazachev, Yu. I., Reznikov, V. A., and Zimmer, G., 1997, *Biochem. Biophys. Methods* **35**:115.
- Komarov, A., Mattson, D., Jones, M. M., Singh, P. K., and Lai, C. S., 1993, *Biochem. Biophys. Res. Commun.* **195**:1191.
- Konorev, E., Margaret, M. T., Joseph, J., Baker, J. E., and Kalyanaraman, B., 1995, *Free Radic. Biol. Med.* **18**:169.
- Korth, H.-G., Sustmann, R., Lommes, P., Paul, T., Ernst, A., de Groot, H., Hughs, L., and Ingold, K. U., 1994, *J. Am. Chem. Society* **116**:2767.
- Kosower, E. M., and Kosower, N. S., 1995, *Methods Enzymol.* **251**:133.
- Kroll, C., Milder, K., Stöffer, R., and Borchert, H. H., 1995, *European J. Pharmaceutical Sciences* **3**:21.
- Leone, J. A., and Hamill, W. H., 1968, *J. Chem. Phys.* **49**:5294.
- Luckhurst, G. R., 1976, Biradicals as spin probes, in *Spin Labeling. Theory and Application* (L. J. Berliner, ed.) (Academic, New York), pp. 133–81.
- Mäder, K., Gallez, B., and Swartz, H. M., 1996, *Biomaterials* **17**:457.
- Maeda, H., Akaike, T., Yoshida, M., and Suga, M., 1994a, *J. Leukocyte Biology* **56**:588.
- Maeda, H., Noguchi, Y., Sato, K., Akaike, T., 1994b, *Jpn. J. Cancer Res.* **85**:331.
- Malatesta, V., and Ingold, K., 1973, *J. Am. Chem. Soc.* **95**:6404.
- Markus, G., and Karush, F., 1957, *J. Am. Chem. Soc.* **79**:134.
- Martin, V. V., and Keana, J. F. W., *J. Chem. Soc., Chem. Commun.* **7**:723.
- Mathew, A. E., and Dodd, J. R., 1985, *J. Heterocyclic Chem.* **22**:225.
- Mayer, J., Szadkowska-Nicze, M., and Kroh, J., 1988, *Radiat. Phys. Chem.* **32**:519.
- Meister, A., and Anderson, M. E., 1983, *Annu. Rev. Biochem.* **52**:711.
- Mogutnov, O. S., Dz.uba, S. A., and Tscvetkov, D. I., 1994, *Zh. Fiz. Khim.* (Russian) **68**:1235.
- Molochnikov, L. S., Kovalyova, E. G., Grigor'ev, I. A., and Reznikov, V. A., 1996, Determination of acidity in the interior of the cross-linked polyelectrolyte grain by the use of pH-sensitive probes, in *Metal-Containing Polymeric Materials* (C. U. Pittman, C. E. Carraher, M. Zeldin, J. E. Sheats, and B. M. Culbertson, eds.) (Plenum, New York and London), pp. 395–401.
- Moncada, S., and Higgs, A., 1993, *Engl. J. Med.* **329**:2002.
- Mordvintsev, P., Mulsh, A., Busse, R., and Vanin, A., 1991, *Anal. Biochem.* **199**:142.
- Myers, P. R., Minor, R. L., Guerra, R., Bates, J. N., and Harrison, D. G., 1990, *Nature* **345**:161.
- Nadeau, J. S., and Boocock, D. G. B., 1971, *Anal. Chem.* **49**:1672.
- Nakaie, C. R., Goissis, G., Schreier, S., and Paiva, A. C. M., 1981, *Brazilian J. Med. Biol. Res.* **14**:173.
- Nakaie, C. R., Schreier, S., and Paiva, A. C. M., 1983, *Biochim. Biophys. Acta* **742**:63.
- Naschimento, L. M., Neto, L. M., and Wajnberg, J., 1991, *J. Chem. Phys.* **95**:2265.
- Nohl, H., Stolze, K., and Weiner, L. M., 1995, *Methods Enzymol.* **251**:191.
- Norris, F. N., and Powell, G. L., 1990, *Biochem. Biophys. Acta* **1030**:165.
- Newton, G. L., and Fahey, R. C., 1995, *Methods Enzymol.* **251**:148.
- Osiecki, J. H., and Ullman, E. E., 1968, *J. Am. Chem. Soc.* **90**:1078.
- Packer, L. (ed.), 1995, Biothiols, *Methods Enzymol.* **251**:3.
- Palmer, R. M. J., Ferrige, A. G., and Moncada, S., 1987, *Nature* **327**:524.

- Parmon, V. N., Kokorin, A. I., and Zhidomirov, G. M., 1980, *Stable Biradicals* (Russian) (Nauka, Moscow).
- Paschenko, S.V., Dzuba, S.A., Khramtsov, V.V., and Tsvetkov, Yu.D., 1998, *Ber. Bunsenges. Phys. Chem.* **102**:224.
- Perkins, W. R., and Cafiso, D. S., 1986, *Biochemistry* **25**:2270.
- Perkins, W. R., and Cafiso, D. S., 1987, *J. Bioenerg. Biomembr.* **19**:443.
- Pietraforte, D., Mallozzi, C., Scorza, G., and Minetti, M., 1995, *Biochemistry* **34**:7177.
- Popov, V. I., Dzuba, S. A., and Moralev, V. M., 1988, *Zh. Fiz. Khim.* (Russian) **62**:472.
- Quintanilha, A. T., and Melhorn, R. J., 1978, *FEBS Lett.* **91**:104.
- Rand, M. J., and Li, C. G., 1995, *Brit. J. Pharmacol.* **116**:1906.
- Quinn, D. M., 1987, *Chem. Rev.* **87**:955.
- Rottenberg, H., 1989, *Methods Enzymol.* **171**:364.
- Sankaram, M. B., Brophy, P. J., Jordi, W., and Marsh, D., 1990, *Binchim. Biophys. Acta* **1021**:63.
- Sanson, A., Ptac, M., Rigaud, J. L., and Gary-Boobo, C. M., 1976, *Chem. Phys. Lipids* **17**:435.
- Schanding, T., Vogel, P. D., Trommer, W. E., and Wise, J. G., 1996, *Tetrahedron* **52**(16):5783.
- Schlitter, J., 1988, *Chem. Phys.* **120**:187.
- Schmitt, E. A., Flanagan, D. R., and Linhardt, R. J., 1993, *J. Pharm. Sci.* **82**:326.
- Schmidt, H., and Walter, U., 1994, *Cell* **78**:919.
- Singh, R. J., Hogg, N., Neese, F., Joseph, J., and Kalyanaraman, B., 1995, *Photochemistry and Photobiology* **61**:325.
- Slepneva, I. A., Sergeeva, S. V., and Khramtsov, V. V., 1995, *Bioch. Biophys. Res. Comm.* **214**:1246.
- Smith, I. C. P., 1972, Spin label method, in *Biological Applications of Electron Spin Resonance* (H. M. Swartz, J. R. Bolton, and D. C. Borg, eds.) (Wiley, New York), pp. 483–539.
- Stöber, R., Mäder, K., Borchert, H.-H., Hermann, W., Schneider, G., and Liero, A., 1995, Pharmaceutical aspects of ESR investigations on drug delivery systems, tissues, and living systems, in *Bioradicals Detected by ESR Spectroscopy* (H. Ohya-Nishiguchi and L. Packer, eds.), (Birkhäuser Verlag, Basel), pp. 301–20.
- Suzuki, Y. J., Tsuchiya, M., and Packer, L., 1993, *Free Radical Res. Commun.* **15**:255.
- Swartz, H. M., and Halpern, H., 1998, chapter in this book.
- Taylor, J., and Deutsch, C., 1988, *Biophys. J.* **53**:227.
- Torchinskii, Yu. M., 1974, *Sulphydryl and Disulfide Groups of Proteins* (Consultants Bureau, New York).
- Ullman, E. F., Call, L., and Osiecki, J. H., 1970, *J. Org. Chem.* **35**:3623.
- Utepergenov, D. I., Fink, B., Skatchkov, M. P., Khramtsov, V. V., and Bassenge, E., 1996, *FASEB J.* **10**:A569.
- Utepergenov, D. I., Khramtsov, V. V., Vlassenko, L. P., Markel, A. L., Mazhukin, D. G., Tikhonov, A. Ya., and Volodarsky, L. B., 1995, *Bioch. Biophys. Res. Comm.* **214**:1023.
- Volodarsky, L. B., ed., 1988a, *Imidazoline Nitroxides*, vol. 1, *Synthesis and Properties* (CRC, Boca Raton).
- Volodarsky, L. B., ed., 1988b, *Imidazoline Nitroxides*, vol. 2, *Applications* (CRC, Boca Raton).
- Volodarsky, L. B., Reznikov, V. A., and Ovcharenko, V. I., 1994, *Synthetic Chemistry of Stable Nitroxides* (CRC, Boca Raton).
- Weiner, L. M., 1995, *Methods Enzymol.* **251**:87.
- Weiner, L. M., Hu, H., and Swartz, H. M., 1991, *FEBS Lett.* **290**:243.
- Weinkam, R. J., and Jorgensen, E. C., 1971a, *J. Am. Chem. Soc.* **93**:7028.
- Weinkam, R. J., and Jorgensen, E. C., 1971b, *J. Am. Chem. Soc.* **93**:7033.
- Wenzel, H. R., Tschesche, H., and Goldammer, E., 1983, Spin-labeled amino acids, peptides, and proteins—Synthesis and applications, in *Modern Methods in Protein Chemistry* (H. Tschesche, ed.) (de Gruyler, Berlin), pp. 385–408.
- Wink, D. A., Derbyshire, R. W., Nims, R. W., Saavedra, J. E., and Ford, P. C., 1993, *Chemical Research in Toxicology* **6**:23.

- Winterbourn, C. C., and Metodieva, D., 1995, *Methods Enzymol.* **251**:86.
- Woldman, Ya. Yu., Khramtsov, V. V., Grigor'ev, I. A., Kiriljuk, I. A., and Utepergenov, D. I., 1994, *Biochem. Biophys. Res. Commun.* **202**:195.
- Yelinova, V., Glazachev, Yu., Khramtsov, V., Kudryashova, L., Rykova, V., and Salganik, R., 1996, *Biochem. Biophys. Res. Commun.* **221**:300.
- Yelinova, V. I., Khramtsov, V. V., Salganik, R. I., Solovjova, N. A., and Kudryashova, L. N., 1995, *Magnetic Resonance in Medicine* **6**:285.
- Yelinova, V. I., Slepneva, I. A., and Weiner, L. M., 1989, Affinity modification of NADPH-cytochrome P-450 reductase by reversible inhibitors, in *Cytochrome P-450: Biochemistry and Biophysics* (I. Schuster, ed.) (Taylor & Francis, London), pp. 411–14.
- Yelinova, V. I., Weiner, L. M., Slepneva, I. A., and Levina, A. S., 1993, *Biochem. Biophys. Res. Commun.* **193**:1044.
- Yoshida, M., Akaike, T., Doi, T., Sato, K., Ijiri, S., Suga, M., Ando, M., and Maeda, H., 1993, *Infect. Immun.* **61**:3552.
- Yoshida, M., Akaike, T., Wada, Y., Sato, K., Ikeda, K., Ueda, S., and Maeda, H., 1994, *Biochem. Biophys. Res. Commun.* **202**:923.
- Zamaraev, K. I., Salganik, R. I., Romannikov, V. N., Wlassoff, W. A., and Khramtsov, V. V., 1995, *Dokladi Akademii Nauk* (Russian) **340**:779.
- Zamaraev, K. I., Salganik, R. I., Romannikov, V. N., Wlassoff, W. A., and Khramtsov, V. V., 1997, *Origins of Life and Evolution of the Biosphere* **27**:325.
- Zamora, R., Grzesiok, A., Weber, H., and Feelisch, M., 1995, *Biochem. J.* **312**:333.
- Zeldes, H., and Livingston, R., 1966, *J. Chem. Phys.* **45**:1946.
- Zundel, G., 1969, *Hydration and Intermolecular Interaction* (Academic, New York).

ENDOR of Spin Labels for Structure Determination: From Small Molecules to Enzyme Reaction Intermediates

**Marvin W. Mäkinen, Devkumar Mustafi, and
Seppo Kasa**

1. INTRODUCTION

Electron paramagnetic resonance (EPR) is a sensitive method for probing the electronic and molecular structure of paramagnetic sites because the energies of microwave-induced transitions of unpaired electrons are modulated by interactions with nearby magnetic nuclei. This phenomenon is known as hyperfine (hf) interaction; measuring the strength of this interaction yields precise information about the electronic structure of the paramagnetic site and the geometric arrangement of magnetic nuclei in its immediate environment. While the most detailed information

Marvin W. Mäkinen and Devkumar Mustafi • Department of Biochemistry and Molecular Biology, University of Chicago, Chicago, Illinois 60637 **Seppo Kasa** • Department of Biochemistry and Molecular Biology, University of Chicago, Chicago, Illinois 60637; *present address*: Department of Chemistry, University of Jyväskylä, SF-40500 Jyväskylä, Finland

Biological Magnetic Resonance, Volume 14: Spin Labeling: The Next Millennium, edited by Berliner. Plenum Press, New York, 1998.

is obtained from measurements in single crystals, such studies may be time consuming when compared to the ease of experimental accessibility possible with polycrystalline materials or frozen solutions and glasses. However, in disordered, solid systems, spectra are a superposition of multiple orientations of the paramagnetic sites with random variations in their immediate environments. Therefore, resonance features are broadened, and the relationships between magnetic resonance parameters and structural or physical properties may be difficult to extract. Furthermore, hf interactions generally cannot be resolved in EPR spectra of polycrystalline and frozen solution samples. These difficulties may be overcome by applying electron nuclear double resonance (ENDOR), developed first by Feher (1956, 1959).

In the ENDOR method, the spin system is irradiated by a microwave field to saturate partially the EPR transition while simultaneously sweeping the sample with radiofrequency radiation through nuclear resonance transitions. Not only does ENDOR provide a means of measuring the hf and nuclear Zeeman interactions directly, but it also yields these measurements with high precision. Since EPR spectra of polycrystalline and amorphous systems are an average over all molecular orientations with respect to the magnetic field, the critical objective is to determine the angular dependence of the hf energies of ligand nuclei on the settings of the static laboratory magnetic field. Only on this basis can the geometric location of nearby magnetic nuclei and the spatial distribution of unpaired spin be determined. Chapter 5 discusses spectroscopic principles through which molecular geometry can be assigned by applying ENDOR of nitroxyl spin labels as the paramagnetic probe in polycrystalline, amorphous glassy, and frozen solution systems. We discuss theoretical relationships underlying the interpretation of ENDOR spectra of nitroxyl free radicals, and we outline guiding principles for assigning molecular structure and conformation through application of ENDOR-determined electron nucleus dipolar distances as constraints. Illustrations are provided ranging from small molecule spin label systems to true intermediates of enzyme-catalyzed reactions. We also point out future directions in which this methodology may be applied.

The general chemical bonding structure of nitroxyl spin labels is illustrated in Fig. 1. Because nitroxyl free radicals exhibit chemical inertness that is uncharacteristic of other organic free radicals, they continue to be the subject of extensive investigations, particularly in the study of biological macromolecules. After the first synthesis of stable nitroxyl free radicals by Rozantsev and coworkers (Neiman *et al.*, 1962; Rozantsev *et al.*, 1963; Rozantsev, 1970), labeling biological macromolecules with nitroxyl free radicals as spectroscopic probes was first introduced by McConnell and coworkers (Stone *et al.*, 1965; Ohnishi and McConnell, 1965; Hamilton and McConnell, 1968). Since that time the use of these free radical probes was largely directed toward evaluating equilibrium effects and only qualitatively assessing changes in the conformational flexibility of macromolecules. Direct

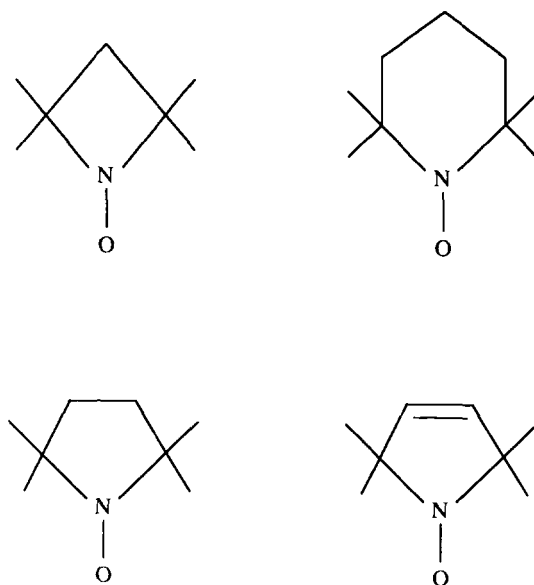


Figure 1. Schematic drawing of general chemical bonding structures of four-, five-, and six-membered nitroxyl spin labels.

structural information in terms of stereochemical and steric interactions has generally not been achieved except in a relatively small number of single-crystal EPR studies to determine spin label orientation and conformation (Chien and Dickinson, 1981; Makinen and Kuo, 1983) or in studies to determine the radial separation between the nitroxyl group and a paramagnetic cation immobilized in freely tumbling macromolecules in a fluid solution (Leigh, 1970; Morrisett, 1976; Berliner, 1978). On the other hand, the emphasis of this chapter is to demonstrate that application of the ENDOR method with spin label probes results in analysis of the structure and conformation of molecules in frozen solutions at a level of accuracy exceeded only by that of single crystal x-ray diffraction.

2. EPR AND ENDOR SPECTROSCOPY OF NITROXYL SPIN LABELS

2.1. EPR of Nitroxyl Spin Labels

2.1.1. EPR Properties of Spin Labels

Nitroxyl spin labels are widely employed in chemical, biochemical, and biophysical studies because of their paramagnetism due to the unpaired electron in

the nitroxyl group and their chemical stability provided by the four methyl groups attached to the carbon atoms adjacent to the NO group (Hamilton and McConnell, 1968; McConnell and McFarland, 1970; Rozantsev, 1970). The EPR spectroscopy of spin labels is thoroughly reviewed elsewhere (Berliner, 1976, 1978) as well as in this volume. These studies are primarily directed to the EPR of spin labels in single crystals, polycrystalline systems, and fluid and frozen solutions and glasses. In contrast, our discussion of the EPR spectroscopy of nitroxyl spin labels concentrates only on those aspects germane to understanding the application of ENDOR for molecular structure determination. We initially present a series of EPR and ENDOR spectra of specifically deuteriated analogs of spin-labeled compounds to identify the underlying spectroscopic principles for structure analysis. To this end Fig. 2 shows the structural formulae of a series of site specifically deuteriated analogs of spin-labeled methyl L-alanate. These derivatives were synthesized to facilitate spectroscopic analysis of EPR and ENDOR spectra of spin labels for structure determination (Mustafi *et al.*, 1990b).

The first-derivative EPR absorption spectrum of nitroxyl spin labels in fluid solutions of low viscosity consists of three sharp lines resulting from the hf interaction of the nitroxyl ^{14}N with the unpaired electron. In solution, rapid tumbling averages out anisotropic hyperfine contributions, and in degassed solutions, well-resolved superhyperfine structure can be observed in the spectrum due to the Fermi contact interactions of the unpaired electron with protons in the spin label. As paramagnetic dioxygen is introduced into the sample, the resolution of the superhyperfine structure deteriorates because of Heisenberg exchange, and the resonance features are broader than in degassed samples. In contrast EPR spectra of spin labels in frozen solutions or polycrystalline samples exhibit a spreading of the absorption envelope because of g and A anisotropy (Hwang *et al.*, 1975; Lee *et al.*, 1984), as seen in Fig. 3.

The EPR and ENDOR spectra of spin labels can be described by the spin Hamiltonian in Eq. (1), which includes the electronic Zeeman interaction (H_1) and the nuclear Zeeman interaction (H_2); hf interactions of the unpaired electron with different classes of nuclei are contained within H_3 :

$$\begin{aligned}
 H_S &= |\beta_e| \mathbf{H}_0 \cdot \mathbf{g}_e \cdot \mathbf{S} - g_n |\beta_n| \mathbf{H}_0 \cdot \mathbf{I} + \mathbf{S} \cdot \mathbf{A} \cdot \mathbf{I} \\
 &= H_1 + H_2 + H_3
 \end{aligned}
 \tag{1}$$

In Eq. (1), β_e and β_n represent the Bohr electron and nuclear magneton, \mathbf{g}_e the electronic Zeeman interaction matrix, g_n the nuclear g -factor, \mathbf{H}_0 the external (laboratory) magnetic field, \mathbf{S} and \mathbf{I} the electron and nuclear spin operators, respectively, and \mathbf{A} the electron nucleus hf matrix. The principal axes of the \mathbf{g}_e matrix defining field orientation are designated, as shown in Diagram 1, with the

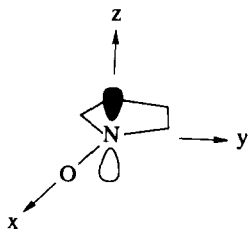


Diagram 1.

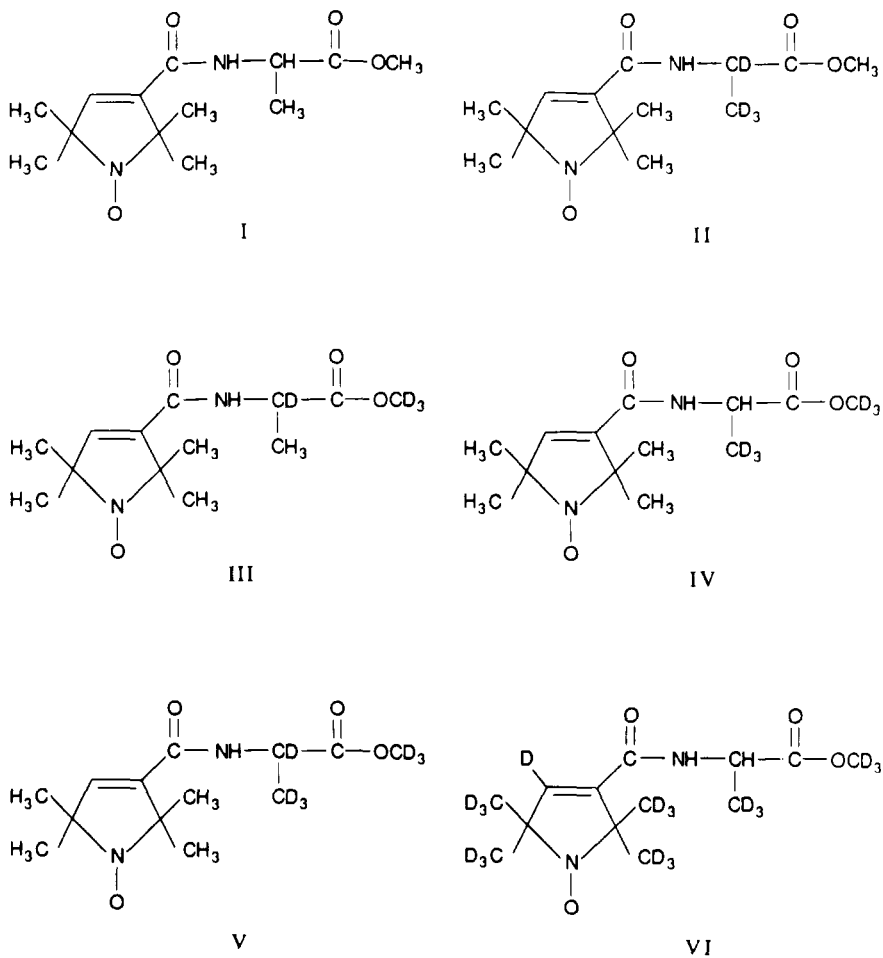


Figure 2. Illustration of the structural formulae of methyl *N*-(2,2,5,5-tetramethyl-1-oxypyrrolinyl-3-carbonyl)-*L*-alanate (I) and of specifically deuterated analogs (II-VI) synthesized for analysis of ENDOR spectra. Reprinted with permission from Mustafī *et al.* (1990b), American Chemical Society.

x -axis lying along the N–O bond, z parallel to the nitrogen $2p_z$ orbital, and y perpendicular to the x,z -plane (Griffith *et al.*, 1965; Capiomont *et al.*, 1974).

In Fig. 3, the EPR spectrum of spin-labeled methyl L-alanate with a perdeuterated spin label is well-resolved because the dipolar broadening of nearby deuterons is weaker than that of hydrogens. The values of A_z and g_z can be obtained directly from the spectrum, while estimates of the other principal values of \mathbf{g}_e and \mathbf{A} require either a single-crystal study or accurate computer simulation of EPR spectra. Following the analysis of Hwang *et al.* (1975) and Lee *et al.* (1984), we estimated from EPR studies the values of the principal components of the \mathbf{g}_e and \mathbf{A} matrices for methyl *N*-(2,2,5,5-tetramethyl-1-oxypyrrolinyl-3-carbonyl)-L-alanate in solutions at room temperature and 40 K. Results are given in the legend to Fig. 3. The isotropic ^{14}N hf coupling of this five-membered nitroxyl spin label attached to the amino group of methyl L-alanate in methanol at room temperature was 14.96

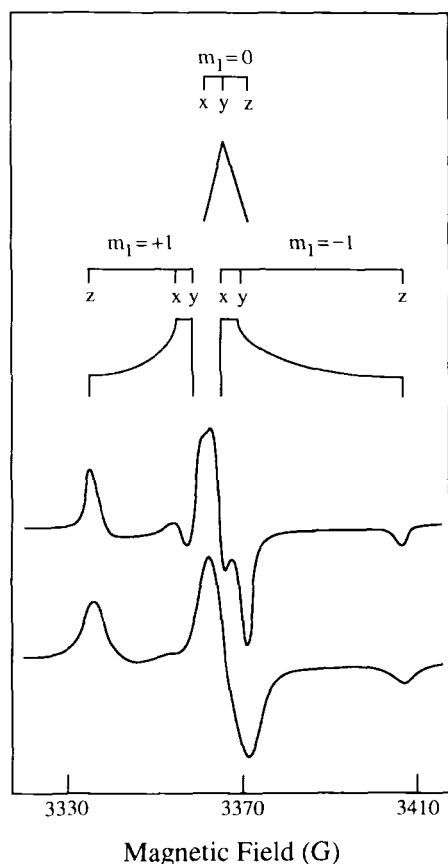


Figure 3. Schematic diagram of the rigid-limit EPR powder pattern of methyl *N*-(2,2,5,5-tetramethyl-1-oxypyrrolinyl-3-carbonyl)-L-alanate in frozen solutions of d_4 -methanol. In the upper half of the figure, stick diagrams identify different components of the electronic spin transition according to g_x , g_y , and g_z and values of m_l . With reference to Fig. 2, the upper spectrum is of compound VI, where the spin label moiety is perdeuterated, and the lower spectrum is of compound I. Parameters used to calculate the stick diagrams are $g_x = 2.0089$, $g_y = 2.0064$, $g_z = 2.0027$; and $A_x = A_y = 4.9$ G, $A_z = 35.1$ G at a microwave frequency of 9.45 GHz, temperature, 40 K.

G at 9.46 GHz. These results are in excellent agreement with the single-crystal EPR study of 2,2,5,5-tetramethyl-1-oxypyrroline-3-carboxaniide (Griffith *et al.*, 1965; Capiomont *et al.*, 1974).

2.1.2. Orientation Selection on the Basis of the EPR Spectrum

The EPR absorption spectra of spin labels in Fig. 3 are equivalent to a powder pattern in the rigid limit of a polycrystalline sample. Under these conditions, the spectrum is a composite of spectra from three sets of molecules differing by their projection of the ^{14}N nuclear moment onto the laboratory magnetic field \mathbf{H}_0 designated by the values of $m_1 = +1, 0$, and -1 . As Fig. 3 shows, ^{14}N hf contributions to the spectrum produce three step shoulders at magnetic fields $H_z = (h\nu - m_1 A_z)/g_z \beta_e$ and six divergences at $H_{x,y} = (h\nu - m_1 A_{x,y})/g_{x,y} \beta_e$, where h is Planck's constant (Lee *et al.*, 1984). Since the ^{14}N hf interaction is associated with large anisotropy, the two step shoulders corresponding to $m_1 = +1$ and -1 are well-separated at X-band frequency from the dominant central feature of the spectrum. Therefore, if the magnetic field is set to the high-field or low-field turning point of the EPR absorption spectrum, the absorption feature arises from those molecules immobilized in the frozen or polycrystalline sample for which the laboratory magnetic field is oriented perpendicularly to the plane of the spin label. On the other hand, the dominant central region corresponding primarily to $m_1 = 0$ arises from a collection of randomly oriented molecules.

Values of \mathbf{H}_0 corresponding to alignment of $m_1 = +1$ along g_x and of $m_1 = 0$ along g_z , the two extreme features in the central region of the EPR spectrum in Fig. 3, differ by only about 15 G at a microwave frequency of 9.45 GHz. Consequently, microwave power saturation of the central region of the EPR spectrum for ENDOR results essentially in selection of all molecular orientations, leading to a condition that we previously termed the *isotropic approximation* (Wells and Makinen, 1988). On the other hand, saturating the low-field or the high-field region of the EPR spectrum, where \mathbf{H}_0 is oriented perpendicularly to the molecular plane, selects a single orientation. Orientation selection on the basis of \mathbf{H}_0 thus allows discrimination of ENDOR absorption features due to parallel and perpendicular hf interactions.

2.2. Basis of ENDOR

The physical basis of ENDOR is diagrammatically illustrated in Fig. 4. ENDOR spectroscopy is performed by saturating the electronic transitions of the paramagnetic system under high microwave power and sweeping the system simultaneously with a strong radiofrequency (rf) field through nuclear resonance transitions. When the frequency of the rf field is scanned and resonance of a nucleus interacting with the unpaired electron is reached, a forbidden transition involving

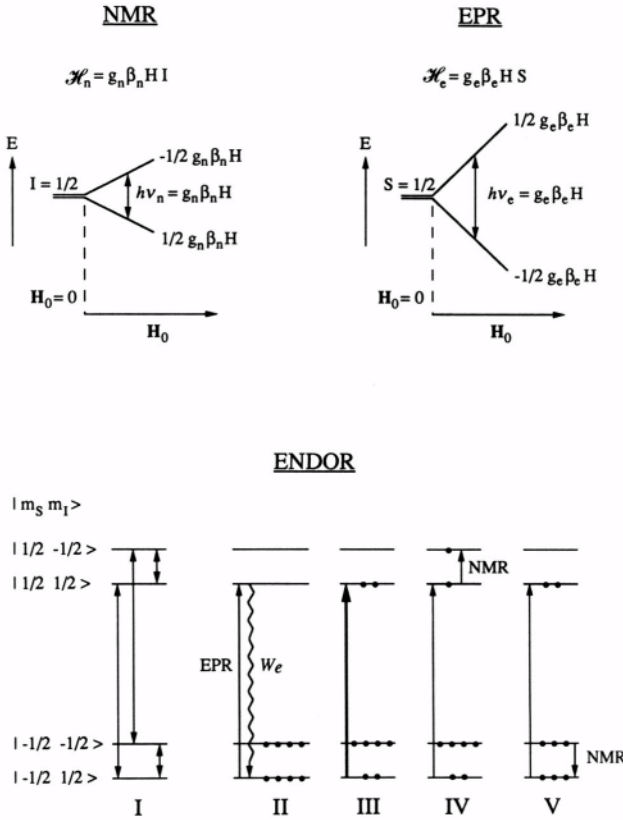


Figure 4. Schematic illustration of the physical basis of ENDOR. The upper part of the figure illustrates energy level diagrams for a magnetic nucleus with $I = 1/2$ and an unpaired electron with $S = 1/2$ placed in a magnetic field. Nuclear and electronic transitions between lower and upper levels are detected correspondingly by nuclear magnetic resonance (NMR) and EPR. Combining the two energy level schemes to correspond to a molecule with an unpaired electron interacting with a nearby magnetic nucleus results in the four-level scheme illustrated in I, where levels are denoted by magnetic spin quantum numbers $|m_s m_I\rangle$. In I allowed transitions are indicated that are detected by EPR according to selection rules $\Delta m_s = \pm 1, \Delta m_I = 0$ and by NMR for selection rules $\Delta m_s = 0, \Delta m_I = \pm 1$. In II four particles in each of the two lower levels are shown to illustrate that the Boltzmann population of spins in the lower manifold is greater than that in the upper manifold. An electronic transition induced under low microwave power from a lower level to an upper level does not disturb the Boltzmann equilibrium significantly because of the decay of electron spins from the excited state to the ground state, indicated by W_e . This situation corresponds to detecting EPR absorption under nonsaturating conditions. In III the thick arrow represents EPR transitions induced under high microwave power, a condition corresponding to saturation, which now perturbs lower and upper levels away from their Boltzmann defined populations. If a strong saturating rf field is now applied, upper or lower level populations are altered through rf induced nuclear transitions, as illustrated in IV and V. This condition “desaturates” the system and restores levels to their Boltzmann defined equilibrium. The intensity of the EPR transition is correspondingly increased. This situation corresponding to detection of EPR absorption by inducing an NMR transition, thus, depicts physical processes that underlie ENDOR. Reprinted from Makinen and Mustafi (1995) by courtesy of Marcel Dekker, Inc.

simultaneous electron and nuclear “spin flips” is stimulated, as illustrated in Fig. 4 by diagrams IV and V. The populations of the upper and lower levels are then “desaturated,” giving rise to increased EPR signal amplitude. Thus, the ENDOR method is equivalent to detection of nuclear resonance absorption by observing changes in the absorption intensity of an EPR line.

ENDOR spectroscopy is optimally carried out with paramagnetic probes that are characterized by relatively long electronic spin-lattice relaxation times (T_{1e}), allowing microwave power saturation of the paramagnetic center to be easily achieved. Since EPR absorption of spin labels can be detected at room temperature, subsequent lowering of the temperature results in achieving an electronic spin-lattice relaxation time favorable for ENDOR spectroscopy. ENDOR spectroscopy provides the most precise method for measuring the strength of electron-nucleus hf interactions; its application results in very high resolving power for assigning molecular structure. The high resolution of ENDOR spectroscopy is based on three factors:

- the density of nuclear spectral lines for a multinuclear system is much smaller for ENDOR than for EPR.
- the resonance absorption lines are much narrower for ENDOR than for EPR.
- the direct interaction of the nucleus with the static magnetic field and the electron-nucleus hf interaction can be measured separately by ENDOR, but not by EPR.

Since an ENDOR spectrum is a nuclear resonance spectrum, we must determine the total field at the nucleus to calculate the transition frequency. If we begin with the spin Hamiltonian in Eq. (1), it can be shown that the first-order transition frequencies ν_{\pm} for a nucleus are given by Eq. (2) where the l_i are the direction cosines of \mathbf{H}_0 in the molecular axis system, A_{ji} is the orientation

$$\nu_{\pm} = \left[\sum_{i=1}^3 \left[m_s / g_e \left(\sum_{j=1}^3 g_j l_j A_{ji} \right) - l_i \nu_n \right]^2 \right]^{1/2} \quad (2)$$

dependent value of the hf coupling (hfc), ν_n is the nuclear Larmor frequency, m_s is the electron spin quantum number, and g_e represents the effective g -value defined by the relation:

$$g_e = [l_1^2 g_{xx}^2 + l_2^2 g_{yy}^2 + l_3^2 g_{zz}^2]^{1/2}$$

In systems of low g anisotropy, we assume the axis of quantization of the unpaired electron spin to be the direction of the applied field \mathbf{H}_0 . If the applied field is oriented

parallel to the principal axis j of the hf tensor A , Eq. (2) is then simplified to that of Eq. (3) where the

$$\nu_{\pm} = \nu_n \pm \frac{|A_{jj}|}{2} \quad (3)$$

separation of ν_{\pm} about ν_n is called the ENDOR shift. For symmetric separations, the hfc is thus twice the value of this frequency spacing. Eq. (3) applies to the condition $\nu_n > |A|/2$. For some nuclei, the condition $\nu_n < |A|/2$ may apply; in this case Eq. (3) becomes $\nu_{\pm} = |A|/2 \pm \nu_n$. In this chapter, we are concerned only with ENDOR of ^1H and ^{19}F for which Eq. (3) applies directly.

Within the strong-field approximation, the observed hfc component A is given by Eq. (4) as a function of r and α :

$$A = \frac{g_e |\beta_c| g_n |\beta_n|}{hr^3} \cdot (3\cos^2\alpha - 1) + A_{\text{iso}} \quad (4)$$

where r is the modulus of the electron-nucleus position vector \mathbf{r} and α is the angle between \mathbf{H}_0 and \mathbf{r} . For spin labels the axially symmetric, principal hfc components A_{\parallel} and A_{\perp} correspond, respectively, to the maximum and minimum ENDOR shifts that are observed. The principal hfc components due to the dipole-dipole interaction A_{\parallel}^D and A_{\perp}^D correspond to the first term of Eq. (4) for values of $\alpha = 0^\circ$ and 90° , respectively. Under conditions:

$$|A_{\text{iso}}| \ll |A_{\parallel}| \text{ and } |A_{\perp}|, \text{ and } A_{\parallel}^D > 0 > A_{\perp}^D$$

the traceless dipolar hfc components A_{\parallel}^D and A_{\perp}^D can be calculated under the constraint $(A_{\parallel} + 2A_{\perp}) = 3A_{\text{iso}}$.

2.3. ENDOR of Nitroxyl Spin Labels

2.3.1. Angle-Selected ENDOR of Nitroxyl Spin Labels

2.3.1.1. Theoretical Basis. The concept of “angle-selected” ENDOR by microwave saturation of the turning points in the EPR spectrum yielding single-crystal-like spectra of molecules in polycrystalline matrices or frozen glassy solutions was first noted by Rist and Hyde (1970). Following this seminal observation, Hoffman *et al.* (1984, 1985, 1989) and Kreilick and coworkers (Hurst *et al.*, 1985; Henderson *et al.*, 1985; Kim *et al.*, 1995) provided insightful theoretical analysis of ENDOR spectra of polycrystalline or frozen glassy systems including arbitrary field settings.

The EPR spectrum of a polycrystalline sample is a superposition of resonances from randomly oriented molecules; the applied magnetic field \mathbf{H}_0 takes all possible orientations with respect to the molecular frame. ENDOR is performed at fixed

magnetic field strength H_0 . Therefore the ENDOR response from a polycrystalline sample arises only from the subset of molecules having orientations such that they contribute to the EPR intensity at H_0 . However, analysis of ENDOR spectra from polycrystalline samples requires knowledge of all polar angles (θ, ϕ) that contribute to fixed resonance fields in the EPR spectrum. The contribution of g and A anisotropy to the EPR spectrum is well-described by the following equations:

$$H_0 = \left[\frac{h\nu - m_1 A(\theta, \phi)}{\beta_e g(\theta, \phi)} \right] \quad (5)$$

$$g(\theta, \phi) = \left[\sum_{i=1}^3 (g_i h_i)^2 \right]^{1/2} \quad (6)$$

$$A(\theta, \phi) = \left[\sum_{i=1}^3 \left(\sum_{j=1}^3 A_{ij} g_j h_j \right)^2 \right]^{1/2} / g(\theta, \phi) \quad (7)$$

$$H = [h_1, h_2, h_3] H_0 \quad (8)$$

where H_0 is the resonant field, $h_1 = \cos\phi\sin\theta$, $h_2 = \sin\phi\sin\theta$, and $h_3 = \cos\theta$. Angles θ and ϕ are field orientation parameters in the g -axis system, where θ represents the angle between the g_z axis and \mathbf{H}_0 . The solution of Eq. (5) gives the θ and ϕ values that contribute to the resonance at any field value. When g and A anisotropy are axial with coincident axes, as occurs to a good, first-order approximation in spin labels, the ϕ dependence in Eqs. 5-8 vanishes and resonant field values depend only on the angle θ .

To determine structural information by ENDOR, we must (1) identify the surrounding nuclei contributing to hf interactions and (2) determine the dependence of ENDOR spectra on external magnetic field settings with respect to magnetic axes in the molecule. For nitroxyl spin labels, the g_z component of the \mathbf{g}_e matrix is coincident with the molecular z -axis and perpendicular to the molecular x, y -plane. Also in spin labels, g anisotropy is very small, A anisotropy is axially symmetric, and the \mathbf{g}_e and \mathbf{A} axes are coincident. Therefore applying \mathbf{H}_0 separately at different EPR absorption features, namely, along the molecular z -axis and along the x, y -plane, should provide a means for selecting different molecular orientations for ENDOR with correspondingly distinguishable hfc components that depend only on the dipolar angle between the applied magnetic field and the electron nucleus dipolar vector. Such examples are given in the following section.

2.3.1.2. *Characteristics of ENDOR Spectra of Nitroxyl Spin Labels at Selected Molecular Orientations.* In a system of low g anisotropy, as for nitroxyl spin labels (Griffith *et al.*, 1965; Capiomont *et al.*, 1974), the observed hf couplings A are functions of the electron-nucleus separations r and the dipolar angle α , as given by Eq. (4). Since g_e remains essentially constant over the range of \mathbf{H}_0 for a spectral scan of a nitroxyl spin label, Eq. (4) implies dependence of the value of A on the angle α . These relationships are illustrated in Fig. 5 by the series of ENDOR spectra of compound VI from Fig. 2, a specifically deuteriated form of methyl *N*-(2,2,5,5-tetramethyl-1-oxypyrrolinyl-3-carbonyl)-L-alanate synthesized to contain only one hydrogen as the sole source of proton resonance absorption. This is \mathbf{H}^α covalently bonded to \mathbf{C}^α in the amino acid (Mustafi *et al.*, 1990b).

When the magnetic field is set to either the low-field or high-field turning point in the EPR spectrum, a single molecular orientation is selected, such that \mathbf{H}_0 is aligned perpendicularly to the oxypyrrolinyl ring. The corresponding observed hfc is illustrated in the topmost ENDOR spectrum. The subsequent ENDOR spectra illustrated in descending order correspond to \mathbf{H}_0 settings, approaching and finally coinciding with the center of the prominent, central EPR feature. The splitting of the innermost pair of ENDOR features does not change perceptibly with change in \mathbf{H}_0 , while the splitting of the outermost pair of features gradually increases and reaches a maximum value.

The ENDOR splittings in Fig. 5 are readily explained with the aid of Fig. 6. This latter diagram illustrates schematically the expected pattern of observed ENDOR splittings as a function of the position of the proton and the orientation of \mathbf{H}_0 with respect to the molecular plane. When \mathbf{H}_0 is aligned parallel to g_z and therefore, perpendicular to the molecular plane, the A_{\parallel} hfc component of a proton located along the symmetry axis or the A_{\perp} hfc component of a proton located near or in the molecular plane are observed. As \mathbf{H}_0 is set to correspond closer and closer to an orientation in and finally parallel to the molecular plane, ENDOR absorption due to the A_{\perp} hfc component of a proton in the molecular plane is detected together with the absorption due to its A_{\parallel} hfc component. On this basis, if the topmost ENDOR spectrum in Fig. 5 belongs to an axially located proton, the parallel hfc component decreases monotonically with respect to both line splitting and intensity, while the perpendicular hfc component appears and gradually increases in intensity as \mathbf{H}_0 is moved toward the central region of the EPR spectrum. However, the innermost pair of features in Fig. 5 is observed with \mathbf{H}_0 perpendicular to the molecular plane; the value of this splitting is independent of the \mathbf{H}_0 setting. The observation that the value of this splitting is less than the largest splitting observed with \mathbf{H}_0 in the molecular plane, thus, identifies \mathbf{H}^α in spin-labeled methyl L-alanate as lying in or nearly coincident with the plane of the oxypyrrolinyl ring.

The assignment of the principal hfc components of \mathbf{H}^α according to Figs. 5 and 6 is confirmed by calculating the field dependence of hf interactions, as illustrated in Fig. 7. This diagram compares the \mathbf{H}_0 dependence of the ENDOR shift of \mathbf{H}^α

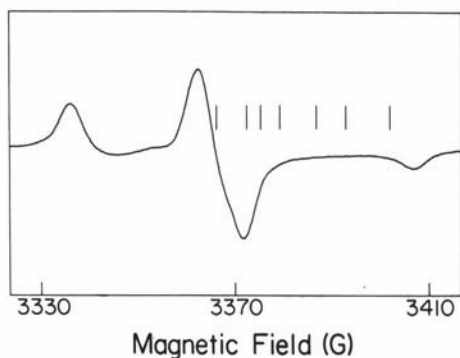


Figure 5. Proton ENDOR spectra of (d_3)-methyl N -(d_{13} -2,2,5,5-tetramethyl-1-oxypyrrrolinyl-3-carbonyl)-(d_3 - β 1, β 2, β 3)-L-alanate in d_4 -methanol as a function of magnetic field settings in the EPR spectrum. The descending order of the ENDOR spectra in the lower panel corresponds to \mathbf{H}_0 settings indicated by the right-to-left series of vertical lines in the top panel containing the EPR spectrum. The ENDOR absorption features in each spectrum are equally spaced about the free proton Larmor frequency. Minimum and maximum ENDOR splittings corresponding to principal hfc components $A_{||}$ and A_{\perp} are identified in the stick diagram. Resonance features belong exclusively to H^{α} because the pseudo-peptide H^{N} was exchanged with solvent deuterons; temperature, 20K. Reprinted with permission from Mustafı *et al.* (1990b), American Chemical Society.

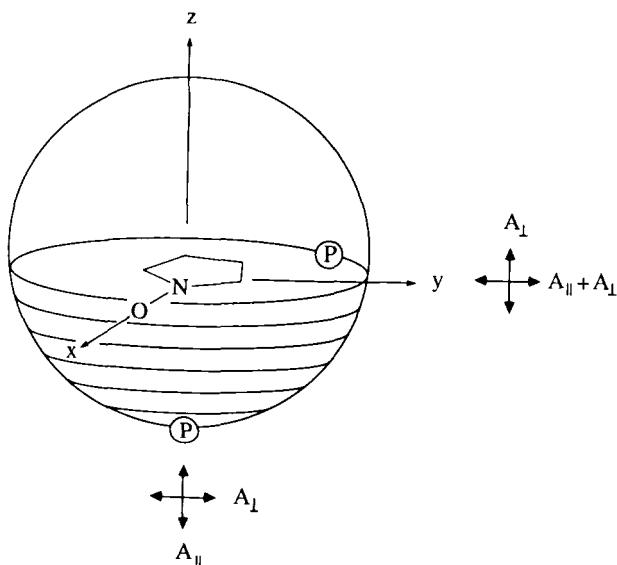


Figure 6. Schematic illustration of relationships of symmetry axes of the nitroxyl spin label to principal axes of the g_e matrix and the A tensor of nearby protons. Each circle represents the field orientation within the g axis system that is selected for saturation in the ENDOR experiment. Relative positions of protons in the molecular x,y plane or on the z axis are also indicated. The diagram also illustrates the principal hfc components detected for protons according to whether \mathbf{H}_0 is aligned parallel or perpendicular to the z -axis. Reprinted with permission from Mustafi *et al.* (1990b), American Chemical Society.

measured experimentally and calculated according to Eq. (2). When \mathbf{H}_0 is applied to g_z at the high-field or low-field edge of the EPR spectrum, the intensity feature is single-crystal like with ENDOR transitions at $\nu_{\pm} = \nu_n \pm |A_{\perp}|/2$. As \mathbf{H}_0 is gradually shifted from the high-field or low-field edge toward the central region of the EPR spectrum, a second pair of absorption features is observed for which the ENDOR shift increases smoothly until a maximum value is reached; the other two features remain fixed at their originally observed transition frequencies. The maximum ENDOR shift of the outer pair of resonance features occurs when \mathbf{H}_0 is applied within the central feature of the EPR spectrum and is coincident with g_x and g_y .

Thus, when the central feature of the EPR spectrum of a nitroxyl spin label is saturated for ENDOR, both the parallel and perpendicular hfc components of a proton in the molecular plane are observed while only the perpendicular hfc component is observed when the low-field or high-field EPR feature is saturated. This is explained with the aid of Fig. 8, which shows an EPR-selected orientation superposed on the hf coordinate system of a proton located in the molecular x,y -plane of a free radical with low g anisotropy. The surface of the sphere represents

the isotropic distribution of molecular orientations present in a randomly oriented sample. When g anisotropy is small compared to the average g value, the maximum hf interaction energy occurs for a field oriented along the electron-nucleus vector (A_z axis); the minimum occurs when the field is in the A_x, A_y plane. For a proton in the x, y -plane, well-resolved features corresponding to A_{\perp} are observed that persist with an essentially constant ENDOR shift at all H_0 values, because on selecting any value of θ , an orientation set intersects the A_x, A_y plane. This relationship is seen in Figs. 5–7, and it provides the basis for analyzing hf interactions in terms of nuclear coordinates with respect to the molecular axes of nitroxyl spin labels. In this manner, as presented in Figs. 5–8, selection of molecular orientation can be achieved with identification of both principal hfc components.

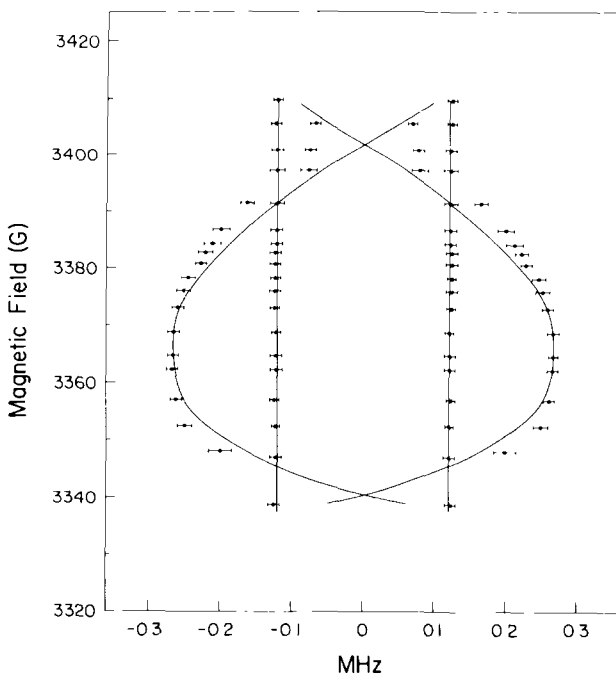


Figure 7. Magnetic field dependence of the ENDOR shift of H^{α} of spin-labeled methyl L-alanate. Experimentally observed ENDOR absorption features with H_0 , as illustrated in Fig. 5, are indicated by small solid circles with error bars drawn as uncertainties on the basis of ENDOR linewidths. Solid lines are calculated according to Eq. (2) under the condition $A_{\parallel} \perp g_{\parallel}$. Parallel ENDOR features exhibit larger deviations from calculated values at the high-field and low-field regions of the plot than in the central region. These larger deviations are ascribable to a greater uncertainty in assigning the position of parallel resonance absorptions with closely overlapping perpendicular features, as seen in Fig. 5. Reprinted with permission from Mustafi *et al.* (1990b), American Chemical Society.

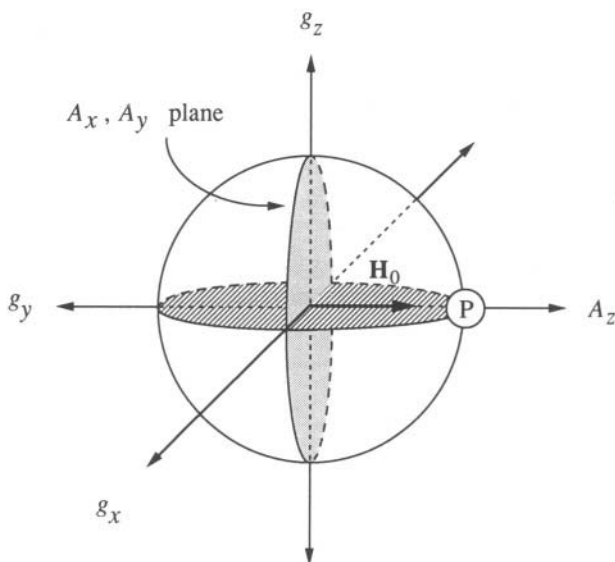


Figure 8. Superposition of principal axes of the g_e matrix and the A tensor. The proton is located in the molecular x,y plane. The electron-proton vector defines the principal hf axes: A_z axis along the vector; and the A_x, A_y plane is perpendicular to the vector (indicated by dots). The circle represented by the hatched area indicates the orientation of the applied magnetic field H_0 coincident with the molecular x,y plane. Reprinted from Makinen and Mustafi (1995) by courtesy of Marcel Dekker, Inc.

2.3.2. Point-Dipole Approximation in Nitroxyl Spin Labels

2.3.2.1. Evaluating Quantitative Limits of Structure Determination by ENDOR.

Structures of molecules determined through ENDOR studies depend on estimates of electron-nucleus dipolar separations, which are ordinarily calculated on the basis of Eq. (4). Therefore it is essential to develop an accurate working model of the spatial distribution of spin angular momentum. Although the spatial part of the wave function of the unpaired electron spin describes the region of space to which unpaired spin is localized, calculations to include the integrated wave function are generally not carried out, and the unpaired electron in the paramagnetic center is often considered as a point-dipole for purposes of simplification. To justify this simplification, two important questions must be addressed: How localized in space is the unpaired electron? and What fraction of the unpaired spin density has been transferred to nearby atoms through chemical bonds? These questions cannot be answered uniquely through theoretical calculations; therefore an experimental approach must be developed to assign the effective position of the unpaired spin. For certain types of paramagnetic systems, it has been established that the spin

density of the unpaired electron behaves very closely to that of a point-dipole. Hutchison and coworkers have shown in ENDOR studies that *f*-electrons of the lanthanide ions Nd^{3+} and Gd^{3+} exhibit behavior very close to that of a point magnetic dipole (Hutchison and McKay, 1977; Fields and Hutchison, 1985). Atherton and Shackleton (1980, 1984) demonstrated through single-crystal ENDOR studies that the hf interactions of VO^{2+} doped into crystals of $\text{Mg}(\text{NH}_4)_2(\text{SO}_4)_2 \cdot 6\text{H}_2\text{O}$ adhere closely to the point-dipole model. For these metal ions, the traceless dipolar hfc components were shown to exhibit axial symmetry, as expected for point-dipole interactions.

For purposes of structural analysis, we assess here the quantitative limits of application of Eq. (4) to nitroxyl spin labels, following the earlier discussion of Wells and Makinen (1988). Firstly, the accuracy of the strong-field approximation improves as the *g* factor anisotropy decreases. Following Hutchison and McKay (1977), we evaluate the expectation value of the electronic magnetic moment $\langle \mu_e \rangle_{\pm}$ associated with the unpaired electron of the nitroxyl group by Eq. (9):

$$\langle \mu_e \rangle_{\pm} = -|\beta_e| \mathbf{g}_e \cdot \langle \mathbf{S} \rangle_{\pm} = -\frac{|\beta_e|}{2g_e} \begin{bmatrix} g_{xx}^2 I_1 \\ g_{yy}^2 I_2 \\ g_{zz}^2 I_3 \end{bmatrix} \quad (9)$$

where \mathbf{g}_e is considered a diagonalized matrix, the quantity $\langle \mathbf{S} \rangle_{\pm}$ is the expectation value of \mathbf{S} , and g_e is the effective value of \mathbf{g}_e . The two extreme principal values g_x and g_z of model spin label systems differ by only 0.31%. On this basis, if we apply *g* as the average value of g_x , g_y , and g_z , then Eq. (9) reduces to $\langle \mu_e \rangle_{\pm} \approx -|\beta_e|g/2$.

Secondly, the accuracy of the strong-field approximation increases with increasing *r*. For a spin system with $g_e = 2.0060$ at 3500 G, the maximum magnetic field \mathbf{h}_e generated by an unpaired electron at an electron-nucleus separation of 5 Å is ~ 150 G. This value is small compared to that of the applied laboratory field \mathbf{H}_0 , and it is less for larger values of *r*. Correspondingly, the maximum angle between \mathbf{H}_0 and the effective field $(\mathbf{H}_0 \pm \mathbf{h}_e)$ at a nucleus 5 Å from the nitroxyl group is $\sim 2^\circ$ for $\alpha = 45^\circ$. This angle is 0° for $\alpha = 0^\circ$ or 90° , the orientations that give rise to ENDOR features corresponding to A_{\parallel} and A_{\perp} . The ratio of \mathbf{h}_e to \mathbf{H}_0 is even smaller for larger values of *r*.

Thirdly, the accuracy of the point-dipole approximation improves with increasing *r*. For a nucleus at $r = 5$ Å, the error in applying the point-dipole approximation for a nitroxyl group can be evaluated according to McConnell and Strathdee (1959). For an effective nuclear charge *Z* ranging from 3.5 to 4.5 and with all of the spin density localized in a *pπ*-type orbital of the nitrogen, deviation of the hfc components from values obtained under the point-dipole approximation ranges from 4.9 to 3.0%. The deviation decreases as *r* increases. Thus, the point-dipole and strong-field approximations together contribute less than 5% error to estimates of the principal dipolar hfc components. In view of the $1/r^3$ dependence of the electron-

nucleus separation on the hfc component, the effect is to contribute less than 3% error to estimates of $r \geq 5 \text{ \AA}$.

2.3.2.2. *Effective Electronic Dipole Position in the N-O Group.* It has been shown that the unpaired electron of spin labels is almost entirely localized to the nitroxyl group (Hayat and Silver, 1973; Davis *et al.*, 1975). Since spin density is distributed over both atoms of the nitroxyl group, the measured dipolar hf interaction of a nearby magnetic nucleus must be viewed as a composite interaction of the unpaired spin confined individually to the oxygen and the nitrogen atoms. On this basis, the separate dipolar interactions depend on the interaction of the total spin density associated with the nitrogen atom and the oxygen atom of the nitroxyl group. The *effective* position \mathbf{r}_e of the unpaired spin acting as a point dipole through composite contributions from both the nitrogen and oxygen atoms of the nitroxyl group can then be represented by the relationship $\mathbf{r}_e = \rho_N \mathbf{r}_N + \rho_O \mathbf{r}_O$, where \mathbf{r}_N is the position vector of the nitrogen atom, \mathbf{r}_O is the position vector of the oxygen atom, and the ρ s represent the corresponding fraction of spin density. The distribution of spin density can be estimated directly from the EPR measured isotropic nitrogen hf constant of the nitroxyl group according to the relationship $A_{\text{iso}} = \rho_N Q_N + \rho_O Q_O$, originally derived by Karplus and Fraenkel (1961). Constants Q_N and Q_O have values of 24.2 and 3.6 G, respectively (Cohen and Hoffman, 1973). Based on the value of $14.96 \pm 0.05 \text{ G}$ estimated from the isotropic ^{14}N hfc of spin-labeled methyl L-alanate in methanol, values of 0.552 and 0.448 for ρ_N and ρ_O , respectively, are calculated.

Since the unpaired electron is distributed over the nitroxyl group, we expect that the hfc component of the dipole-dipole interaction of a given proton is weighted according to the spin density distribution associated with the nitrogen and oxygen atoms of the nitroxyl group. On this basis we can calculate the dipolar coupling components of the *i*th class of protons according to Eq. (10):

$$A_i^D = g_e |\beta_e| g_n |\beta_n| \sum_{j=1}^2 \rho_j \frac{(3\cos^2\alpha_{ij} - 1)}{r_{ij}^3} \quad (10)$$

where ρ_j is the EPR-determined spin density of the unpaired electron at the *j*th nitroxyl atom, α_{ij} is the angle between the laboratory magnetic field \mathbf{H}_0 and the *i-j* internuclear vector, r_{ij} is the corresponding *i-j* internuclear distance; the remaining symbols have their classical definitions.

To establish the effective point-dipole behavior of the nitroxyl group of spin labels, we chose a simple spin label molecule, namely 2,2,5,5-tetramethyl-1-oxyproline-3-carboxamide, whose atomic structure is well-defined by x-ray crystallography (Turley and Boer, 1972). By ENDOR we determined both parallel and perpendicular hfc components of the vinylic proton and of each of the two carboxamide protons (Mustafi *et al.*, 1991). In Table 1 we compare values of A_{\perp}^D

Table 1
Comparison of Calculated and ENDOR-Determined Proton Dipolar hfc Components (in MHz) in 2,2,5,5-tetramethyl-1-oxypyrraline-3-carboxamide

Proton	A_{\perp}^D (Calculated)		A_{\perp}^D (ENDOR) ^c
	I ^a	II ^b	
H1	-0.572	-0.544	-0.570 (± 0.010)
H2	-0.351	-0.338	-0.344 (± 0.008)
H ^v	-1.540	-1.494	-1.480 (± 0.012)

^aUsing Eq. (10) dipolar hfc components were calculated as the sum of two separate interactions for each of the three protons with the EPR-determined spin density assigned to the nucleus of the nitrogen and to the nucleus of the oxygen atom of the nitroxyl group.

^b A_{\perp}^D were calculated as the sum of two separate interactions for each proton, with spin density on both nitroxyl atoms. In this case two point spins were positioned at 0.66 Å above and below the nitroxyl N and O atoms.

^cENDOR-determined values of A_{\perp}^D are from Mustafi *et al.* (1991).

for the three protons calculated according to two methods. For Method I, the dipolar hfc components were calculated as the sum of two separate interactions for each proton with the spin density assigned to the nucleus of each of the two nitroxyl atoms. For Method II, the dipolar hfc components were calculated by replacing the $2p_z$ orbital of each nitroxyl atom by a point spin in each lobe. By this method, point spins are positioned at a separation of 0.66 Å in each lobe of the $2p_z$ orbitals of the nitroxyl atoms, yielding a value of 3.5 for the effective nuclear charge Z for each nitroxyl atom. Comparing calculated dipolar hfc components with ENDOR-determined values shows a maximum discrepancy of only 4%, consistent with our discussion in Sec. 2.3.2.1. While this comparison shows expected agreement between calculated values and experimental results, this approach requires full knowledge of the molecular geometry; therefore it cannot be applied *ab initio* to determine structure and conformation.

We, therefore, established a geometrical solution for the effective position of the electronic point-dipole of the nitroxyl group. The effective position of the electronic point-dipole of the nitroxyl group \mathbf{r}_e can be defined as the common intersection point of spheres of radii r_1 , r_2 , and r^V centered, respectively, on the two carboxamide protons H1 and H2 and the vinylic proton H^V in the oxypyrrrolinyl moiety. For $\rho_j = 1$ and r_{ij} determined by ENDOR, this common intersection point should then simultaneously satisfy Eq. (10) for each nucleus relating the value of its observed hfc component to the electron-nucleus separation. Two intersection points of the three spheres were identified, as illustrated in Fig. 9. One lies almost exactly at the midpoint of the N-O bond and deviates less than 0.04 Å from \mathbf{r}_e defined by EPR; this is within experimental uncertainty. The other mathematical

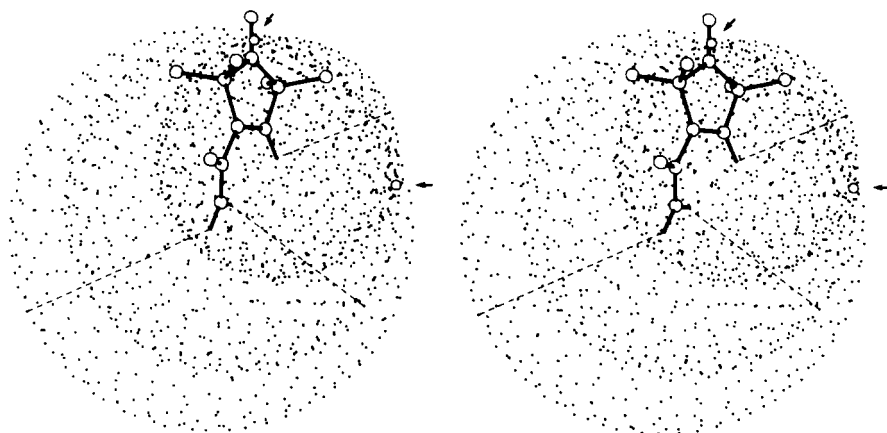


Figure 9. Stereodiagram of the skeletal structure of 2,2,5,5-tetramethyl-1-oxypyrroline-3-carboxamide contained within the three spheres of radius r^v , r_1 , and r_2 for the vinylic proton (H^v) and two carboxamide protons (H_1 and H_2), respectively. The calculated positions of the vinylic and two carboxamide hydrogens are shown in the diagram in addition to nonhydrogen atoms. Three spheres shown as dotted surfaces are drawn for ENDOR-determined radii of 3.78, 5.18, 6.13 Å centered on the calculated positions for H^v , H_1 , and H_2 , respectively. A radius in a general position is illustrated for each hydrogen with its corresponding sphere by a dashed line. The two common intersection points of the three spheres are also illustrated by small open circles indicated by arrows. One of these points lies nearly exactly at the midpoint of the N-O bond (see text). The other is distant from the nitroxyl group and is not contained within the van der Waals volume of spin label atoms. Intersection points of the three spheres were found by applying the Newton-Raphson method (Press *et al.*, 1986) within tolerance limits of ± 0.03 Å, consistent with experimental uncertainty. Identical solutions were also obtained with smaller tolerance limits. Reprinted with permission from Mustafi *et al.* (1991).

solution defines a point in space that is not contained within the van der Waals volume of the spin label and, therefore, does not represent a physically meaningful result. Since the unpaired electron is localized almost entirely on the nitroxyl group, the intersection point of the three spheres along the N-O bond represents a physically meaningful solution for \mathbf{r}_e , and it defines the effective position of the electronic point-dipole. This position is precisely 0.569 Å along the N-O bond from the nitrogen atom for the oxypyrroline spin label in a high-dielectric solvent, such as methanol. This distance corresponds to a value for ρ_N of 0.552, precisely identical to that obtained by estimating the ^{14}N isotropic hfc on the basis of the EPR spectrum of the molecule in fluid methanol. Since the ^{14}N isotropic hfc of the nitroxyl group is known to vary according to the polarity of the solvent (Jost and Griffith, 1978), we estimated the maximum shift of \mathbf{r}_e that may occur along the N-O bond in spin labels of the oxypyrroline type. In toluene, as a representative apolar solvent, the value of the ^{14}N isotropic hfc is 14.30 G (Mustafi and Joela, 1995). This yields an effective position at 0.610 Å along the N-O bond from the nitrogen atom, corre-

sponding to a shift of the point-dipole $\leq 0.041 \text{ \AA}$ from its position in a solvent of high-dielectric constant. Assigning the position of the effective dipole of the unpaired electron spin along the N-O bond in the oxypyrrolinyl spin label, thus, provides a reference point defined with high precision from which all ENDOR-determined electron-nucleus distances can be measured and correspondingly modeled by molecular graphics methods.

2.4. TRIPLE Spectroscopy of Nitroxyl Spin Labels

For purposes of reviewing studies of nitroxyl spin labels based on electron magnetic resonance methods that are important for structure assignment, we include here a brief summary of the application of electron-nuclear-nuclear triple resonance (TRIPLE) spectroscopy. Several monographs and review articles describe well the theory, instrumentation, and applications of TRIPLE spectroscopy (Möbius and Biehl, 1979; Möbius and Lubitz, 1987; Kurreck *et al.*, 1988). Consequently they are not discussed here.

The application of TRIPLE spectroscopy to nitroxyl spin labels is limited because it depends entirely on the presence of a sizable isotropic hfc associated with the nucleus under study. Isotropic hfc in nitroxyl spin labels are observed only for nuclei associated with the molecular ring of the spin label, since isotropic couplings of distant nuclei in attached groups are essentially negligible, as discussed in the previous section on ENDOR of spin labels. We, therefore, review only those TRIPLE studies where determining signs of hfc constants confirms evaluation of ENDOR absorptions of nitroxyl spin labels and where assignment of molecular structure or rotamer conformation was achieved.

TRIPLE is an extension of the ENDOR method in which two NMR frequencies are used instead of one. There are two kinds of TRIPLE techniques, known as special and general TRIPLE. In special TRIPLE, two nuclear transitions belonging to a set of equivalent nuclei are irradiated in addition to saturating the electron spin transition with microwave power. Since there are no applications of special TRIPLE to nitroxyl spin labels, this spectroscopic technique is not discussed here. The general TRIPLE technique was first introduced by Biehl *et al.* (1975) for radicals in solution. The analogous procedure for solid-state samples, called double ENDOR, was first performed by Cook and Whiffen (1964). In the general TRIPLE experiment, transitions of different nuclei are driven simultaneously. One ENDOR transition is irradiated with saturating rf power at constant frequency. The entire ENDOR frequency range is then swept to obtain the TRIPLE spectrum. If other protons or nuclei belong to the same paramagnetic molecule, the TRIPLE spectrum exhibits redistribution of intensities relative to the ENDOR spectrum.

In the specific example of the nitroxyl spin-label 2,2,5,5-tetramethyl-1-oxypyrroline-3-carboxylic acid in Fig. 10, methyl and vinylic protons associated with the oxypyrroline ring give rise to transitions. When the high-frequency ENDOR

transition of the vinylic proton is irradiated, the intensity of the corresponding low-frequency transition increases. A similar pattern is observed for the methyl protons. These observations demonstrate that the sign of the isotropic hfc of the methyl protons and the vinylic proton is the same (Mustafi and Joela, 1995). For the methyl protons, this was demonstrated to be negative (Kreilick, 1967). This observation, establishing the sign of the isotropic hfc of the vinylic proton, confirms the assessment of the sign of A_{iso} of the vinylic proton made earlier in ENDOR

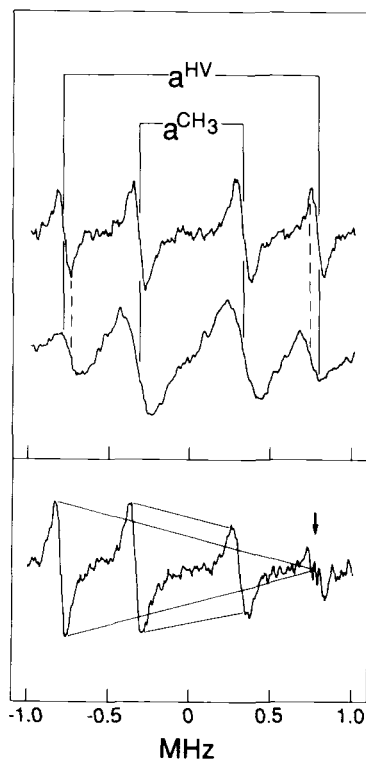


Figure 10. ENDOR and TRIPLE resonance spectra of spin label 2,2,5,5-tetramethyl-1-oxyproline-3-carboxylic acid in a fluid solution of d_4 -methanol. In the top panel, upper and lower ENDOR spectra were recorded at sample temperatures of 183 and 226 K, respectively. The ENDOR splittings for the vinylic and methyl protons of the spin label are indicated in a stick diagram by a^{HV} and a^{CH_3} , respectively. The decreased line splitting for the vinylic proton at higher temperatures is indicated by dashed vertical lines associated with the lower ENDOR spectrum. In the bottom panel, the general TRIPLE spectrum was recorded at 183 K and the high-frequency transition of the vinylic proton indicated by the arrow was pumped. Solid lines connecting high-frequency peaks to low-frequency peaks of the vinylic and methyl protons and sloping in the same direction are drawn to indicate that the sign of the isotropic hfc components of the vinylic and methyl protons is the same. Reprinted with permission from Mustafi and Joela (1995), American Chemical Society.

studies to define the effective dipole position of the unpaired electron of the nitroxyl group (Mustafi *et al.*, 1991). It is of interest to note that the value of A_{iso} of the vinylic proton is temperature-dependent while A_{iso} of the methyl protons is not (Hyde and Subczynski, 1984). The temperature dependence is due to an out-of-plane displacement of the vinylic proton (Mustafi and Joela, 1995).

General TRIPLE was also applied to determine signs of hfc constants in diphenylnitroxide and in a mixed biradical nitroxyl derivative of galvinoxyl (Kirste *et al.*, 1982). In a study by Jenzen *et al.* (1986) to determine the signs of the hfc of spin-trap adducts of α -phenyl-*N*-*t*-butylnitron using TRIPLE, changes in the magnitude of the measured hfc constants as a function of group substitution and temperature provided a means of assigning preferred rotamer conformations of these aminoxyl free radical species.

3. X-RAY STRUCTURE AND CONFORMATION OF NITROXYL SPIN LABELS

3.1. Molecular Structure of Nitroxyl Spin Labels

For purposes of discussion of ENDOR results, we briefly review the salient properties of nitroxyl spin labels that are important for spectroscopic and structural analysis by application of EPR and ENDOR. Although a large variety of nitroxyl spin labels have been synthesized and employed in biophysical and biochemical investigations, there are structurally three basic types, dependent on the number of atoms forming the closed ring into which the nitrogen atom of the nitroxyl group is incorporated (McConnell and McFarland, 1970; Berliner, 1976; Keana, 1978). These three categories are compared in Fig. 1. We comment here on the tendency of each type to exhibit multiple conformations in order to identify species unlikely to be gainfully employed as spectroscopic probes of molecular structure and function.

While it is probable that the spin label comprised of a four-membered ring in Fig. 1 is conformationally rigid, only its synthesis was reported (Espie and Rassat, 1971), and there are no studies in which it was employed as a spectroscopic probe. Oxypiperidinyl spin labels with a six-membered ring are probably the most frequently employed in biophysical studies. However, crystallographic analyses demonstrate that they undergo chair-chair inversion motions (Capiomont, 1972; Capiomont *et al.*, 1972), which must also occur for the spin label attached to macromolecules in solution. As we point out later, nitroxyl spin labels exhibiting multiple conformations in solution are associated with broadening and reduced amplitudes of ENDOR absorption features. These characteristics, thus, render six-membered spin labels of limited usefulness for ENDOR-based structural analysis.

In contrast to oxypiperidinyl spin labels, where the C(NO)C grouping of atoms assumes a pyramidal shape and the N-O bond makes an angle of a 17° with the

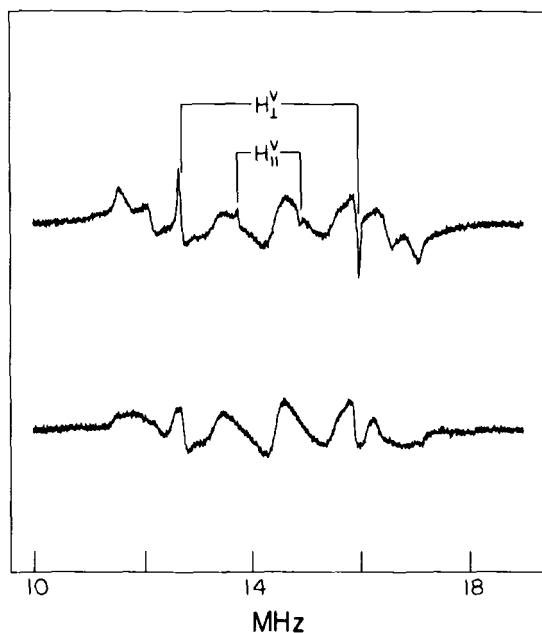


Figure 11. Proton ENDOR spectra of 2,2,5,5-tetramethyl-1-oxypyrroline-3-carboxylic acid (*upper*) and of 2,2,5,5-tetramethyl-1-oxypyrrolidine-3-carboxylic acid (*lower*) in d_4 -methanol with H_0 at setting B of the EPR spectrum. Both of the principal hfc components of the vinylic proton, assigned on the basis of specific deuteration, are labeled in the upper spectrum. Reprinted with permission from Mustafi *et al.* (1990c).

C-N-C plane (Berliner, 1970), the C(NO)C moiety is planar in the saturated (Ament *et al.*, 1973; Lajzerowicz-Bonneteau, 1976) and unsaturated (Boeyens and Kruger, 1970; Turley and Boer, 1972) five-membered spin labels. In the oxypyrrolidine spin label with a saturated ring, the C(3) atom of the ring is out of the molecular plane, in contrast to the completely planar structure of the unsaturated, five-membered oxypyrroline ring. For the saturated spin label, it is probable that multiple conformations are associated with the ring, so that alternatively the C(3) or the C(4) atom is out of the plane and both deviate from the mean plane to a variable extent. Furthermore the saturated chemical bonding structure of five-membered oxypyrrolidine spin labels, constrained by the planarity of the C(NO)C group, gives rise to enantiomers with a chiral center at C(3). Although oxypyrrolidine derivatives are generally synthesized as racemic mixtures, it was demonstrated that *R*(+) and *S*(-) isomers give rise to differential reactivity with macromolecules (Bauer and Berliner, 1979).

Comparing the ENDOR spectra of the 3-carboxylic acid derivatives of oxypyrroline and oxypyrrolidine spin labels in Fig. 11 shows that resonance absorptions

of protons in the saturated spin label are broader and of diminished amplitude, characteristic of the presence of multiple conformers (Mustafi *et al.*, 1990c). On the other hand, resonance features of the oxypyrrolinyl spin label are narrower and more indicative of a conformationally inflexible molecule. This circumstance is readily confirmed through our observations that ENDOR splittings of the methyl and vinylic protons in the oxypyrrolone derivative remain invariant when dissolved in a wide variety of solvents, indicating no or undetectable changes in molecular structure within the resolution of the resonance absorptions (Mustafi *et al.*, 1991). Also, as discussed in Sec. 2.3.2.2, r_e defining the effective position of the electronic point dipole is essentially invariant with solvent polarity, indicating again no change in molecular structure or conformation of the five-membered ring.

As pointed out earlier by Makinen and Kuo (1983), the five-membered oxypyrrolone spin label exhibits no chiral centers and retains a completely planar structure. The invariance of the molecular structure of the five-membered oxypyrrolinyl spin label was recently demonstrated in an interesting manner through x-ray crystallographic studies (Kasa *et al.*, 1996). In Table 2 bond lengths and bond angles are compared for five-membered oxypyrrolinyl ring systems with a carboxamide and a propenamide side chain; the atomic numbering scheme for the ring is shown in Diagram 2.

Parameters in Table 2 show that the two structures are identical within the standard deviations of x-ray results. Furthermore, determination of the molecular structure of 3-(2,2,5,5-tetramethyl-1-oxypyrrolinyl)-2-propenamide in crystals grown from solutions of ethyl acetate shows that there are three molecules in the asymmetric unit of the crystal of space group $C2/c$ that exhibit identical structural parameters within the standard deviations of the x-ray data. Figure 12 gives a stereo view of one of the molecules in the asymmetric unit. Not only is the N-O group coincident with the plane of the molecular ring, but the side chain also exhibits near coplanarity with the oxypyrrolinyl ring. The coplanar structure of the side chain is in complete agreement with the assessment of ENDOR absorptions of olefinic and carboxamide hydrogens (Kasa and Makinen, 1996, unpublished observations).

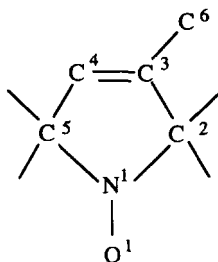


Diagram 2.

Table 2
Comparison of Bond Angles (in Degrees) and Bond Lengths (in Ångstroms) of the
Oxypyrrolinyl Ring in 2,2,5,5-Tetramethyl-1-oxypyrrolinyl-3-carboxamide and
3-(2,2,5,5-tetramethyl-1-oxypyrrolinyl)-2-propenamide

Bond lengths	SL-carboxamide ^{a,b}	SL-propenamide ^{b,c}
N(1)–O(1)	1.267(5)	1.277(7)
N(1)–C(2)	1.486(6)	1.470(9)
C(2)–C(3)	1.511(7)	1.470(10)
C(3)–C(4)	1.319(7)	1.318(9)
C(4)–C(5)	1.487(7)	1.506(9)
C(5)–N(1)	1.477(7)	1.469(9)
<i>Bond angles</i>		
N(1)–C(2)–C(3)	99.2	97.9(6)
C(2)–C(3)–C(4)	112.5	110.3(7)
C(3)–C(4)–C(5)	113.8	116.2(7)
N(1)–C(5)–C(4)	99.7	99.6(5)
C(2)–N(1)–O(1)	122.2	121.7(9)
C(5)–N(1)–O(1)	123.0	122.4(6)
C(2)–N(1)–C(5)	114.8	116.0(6)
C(2)–C(3)–C(6)	122.4	125.8(7)
C(4)–C(3)–C(6)	125.1	123.9(7)

^aTurley and Boer (1972); the uncertainty associated with bond angles is stated as approximately 0.5°.

^bSL represents the five-membered oxypyrrolinyl ring with the side chain attached at the C(3) position. See atomic numbering scheme in the text.

^cKasa *et al.* (1996).

3.2. Molecular Modeling of Nitroxyl Spin Labels

Since x-ray defined coordinates are not available for spin-labeled systems subjected to ENDOR structural analysis, it is necessary to generate their atomic coordinates through computer-based methods for assigning structure and conformation on the basis of ENDOR distance constraints. In these studies we applied general principles of structural chemistry to generate suitable molecular models for ENDOR data analysis, and through this experience we developed useful guidelines for applying this approach to a wide range of molecules. All of these studies employed the five-membered oxypyrrolinyl nucleus as the structural probe; models were constructed on the basis of x-ray defined molecular fragments.

Since a number of our ENDOR studies are based on using derivatives of *N*-acylated amino acids, we employed the acyl moiety of the x-ray defined structure of 2,2,5,5-tetramethyl-1-oxypyrroline-3-carboxamide (Turley and Boer, 1972) as

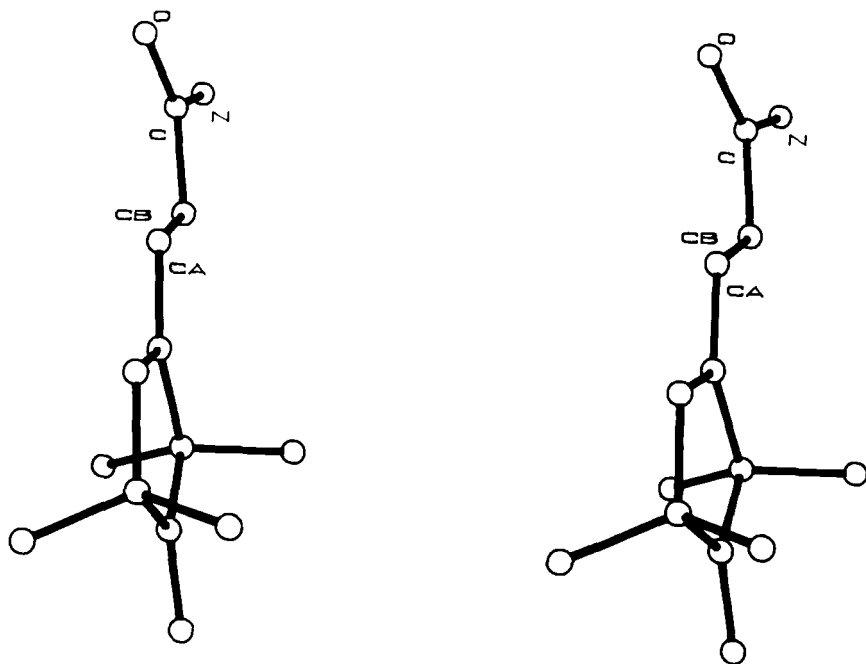


Figure 12. Stereodiagram of the x-ray determined structure of 3-(2,2,5,5-tetramethyl-1-oxypyrrolinyl)-2-propenamamide. Nonhydrogen atoms of the side chain attached to the 3-position of the oxypyrrolinyl ring are labeled. From Kasa *et al.* (1996).

a molecular fragment for modeling (Mustafi *et al.*, 1990b,c; Wells *et al.*, 1990; Joela *et al.*, 1991). With respect to the atomic numbering scheme of the oxypyrroline ring shown previously, molecular models of *N*-acylated amino acids were constructed initially by least-squares superpositioning the C(3), C(6), O(2), and N(2) atoms of the carboxamide side chain of the spin label onto the C $^{\alpha}$, C, O, and peptide N of a dipeptide containing the desired amino acid as the C-terminal portion. For these four spin label atoms, this approach resulted in root-mean-square deviations of 0.032 and 0.012 Å from the corresponding atoms of L-alanyl-*O*-*N*-dimethyl-L-tyrosinyl-L-alanate (Bates *et al.*, 1979) and methyl *N*-acetyl-L-tryptophanate (Cotrait and Barrans, 1974), respectively. While the superpositioning is adequately close and yields sterically acceptable assignments of conformation, this method led to difficulties for spin-labeled L-phenylalanine derivatives because the C $^{\alpha}$ -C bond length in the peptide was not equivalent to the C(3)-C(6) bond length in the spin-labeled carboxamide (Joela *et al.*, 1991). Since this approach overlooks the subtle differences in chemical-bonding structure between a carboxamide group and a peptide bond, in that study we developed the method illustrated in Fig. 13. We,

therefore, describe the general principles in Fig. 13 that should be applied in constructing the model with use of molecular graphics methods. Figure 13 specifically illustrates generating atomic coordinates of spin-labeled penicillin for which ENDOR results are described later.

In Fig. 13 bond lengths and valence angles of individual fragments are preserved, so the resulting model resembles more closely that expected according to its chemical bonding structure. For instance, as illustrated in Fig. 13, the C(3)-C(6) bond length and the valence angles around C(3) are preserved, as are the C(6)-O(2) bond length and the valence angles around C(6) in the spin-labeled compound. The C(6) and O(2) atoms of the spin-labeled carboxamide are first superpositioned onto the C(15) and O(16) atoms of the pseudo-peptide linkage of amoxicillin (Boles *et al.*, 1978). Then the C(6)-C(3) and C(6)-N(2) bond vectors

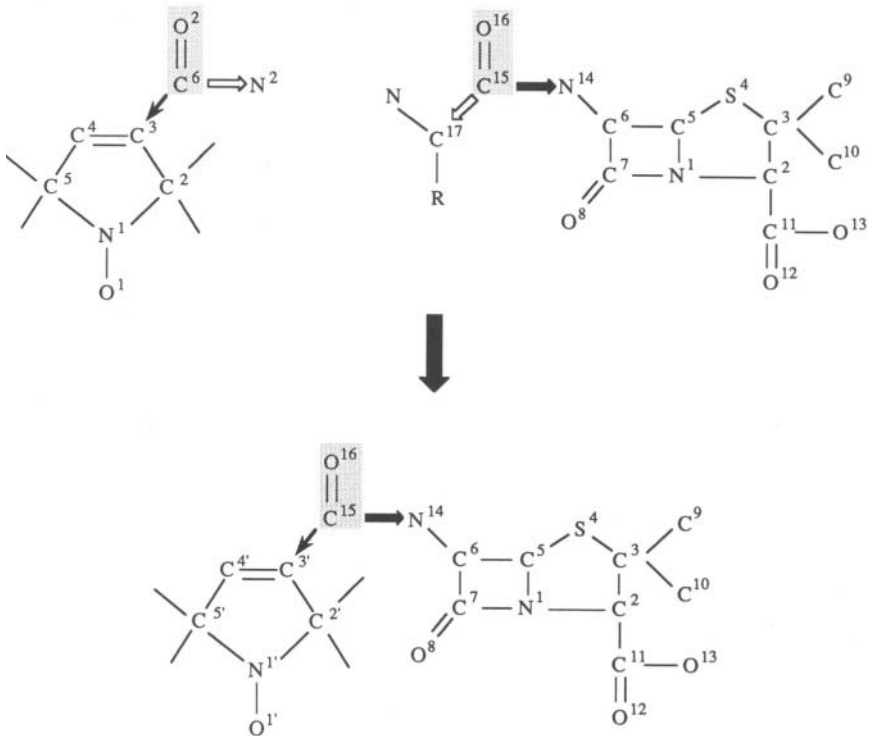


Figure 13. Illustration of the method of generating atomic coordinates for the molecular model of 6-*N*-(2,2,5,5-tetramethyl-1-oxypyrraline-3-carbonyl)-penicillanic acid by joining molecular fragments of x-ray defined molecules, in this case, 2,2,5,5-tetramethyl-1-oxypyrraline-3-carboxamide (Turley and Boer, 1972) and amoxicillin (Boles *et al.*, 1978).

of the spin label fragment are brought into coincidence with the C(15)-C(17) and C(15)-N(14) bond vectors of the penicillin molecule, respectively, thereby joining the two fragments with stereochemical parameters that closely reflect the chemical-bonding structure of the spin-labeled penicillin molecule. We calculate positions of hydrogen atoms according to idealized bond length and geometry (Coppens, 1967), but we prefer to employ atomic coordinates of x-ray defined molecules for nonhydrogen atoms rather than derive them on the basis of idealized bond lengths and bond angles. Through use of highly refined, atomic coordinates of x-ray defined molecules, we conclude that the least amount of bias is subsequently associated with assignment of resultant conformations derived through torsion angle calculations constrained by the ENDOR determined electron-nucleus dipolar distances.

Beginning with the atomic coordinates of the molecular model obtained, as previously described by joining molecular fragments, the conformation of the molecule is then assigned on the basis of torsion angle search calculations constrained by ENDOR-determined electron-nucleus distances. In our laboratory we found that the SEARCH option contained within the program package SYBYL* is ideal for analysis of molecular structure and conformation. The calculation involves a systematic conformational analysis by checking first for van der Waals contacts around all rotatable bonds. Within the sterically accessible conformational space, torsional angle search calculations are then carried out to identify which conformers accommodate the specified ENDOR distance constraints and their respective linewidth-determined uncertainties. A check is then made to ensure that the conformer geometrically satisfying the distance constraints is compatible spectroscopically with the observed pattern of ENDOR shifts and their dependence on H_0 .

As may be expected, the choice of parameters for defining van der Waals contact radii is important, and we have tested two different models to examine which best reproduce x-ray results. For this study we compared van der Waals radii described by Iijima *et al.* (1987) for amino acids and peptides, in which, covalent hydrogens are explicit, to van der Waals radii of Bondi (1964), in which heavy atom radii are spherically expanded to account for covalent hydrogens (Joela *et al.*, 1991). With respect to the x-ray structure of 2,2,5,5-tetramethyl-1-oxypyrroline-3-carboxamide (Turley and Boer, 1972), use of the van der Waals radii of Bondi (1964) resulted in a two-fold degeneracy of the conformation of the molecule so that the tilt of the plane of the carboxamide group with respect to the plane of the oxypyrrolinyl ring, as defined by the [C(4)=C(3)-C(6)-N(2)] torsion angle, was -45° or $+20^\circ$. Applying the parameters of Iijima *et al.* (1987) yielded only one

*Further details about this program package can be obtained from Tripos Associates, Inc., 1600 S. Hanley Road, St. Louis, Missouri 63144.

conformation with a value of -39° for the torsion angle. The value of the torsion angle calculated on the basis of the atomic coordinates is -31° . On this basis we preferred to apply the parameters of Iijima *et al.* (1987) to assign molecular conformation on the basis of ENDOR-determined electron-nucleus distance constraints. In the case of bonds within the molecule that are not rotated during the calculation and have no direct influence in determining conformation, such as the C-C bonds of the four methyl groups to the C(2) and C(5) atoms of the oxypyrrolinyl ring, hydrogens are assigned to idealized staggered conformations with respect to their [H-C-C(2)-C(3)] or [H-C-C(5)-C(4)] torsional angles.

It should be noted that the assignment of molecular conformation, as defined on the basis of ENDOR-constrained torsional angle search calculations, yields calculated conformers that accommodate electron-to-nucleus distances for hard-sphere interactions only and are not based on minimization of the potential energy. Although we have not been necessitated to apply potential energy minimization methods in our studies thus far, such computational methods may be useful for further refinement if multiple conformers satisfy ENDOR distance constraints. For spin-labeled methyl L-tryptophanate (Wells *et al.*, 1990), direct inspection of relevant dihedral angle relationships ruled out as unlikely one of the conformers of the side chain satisfying distance constraints because the resultant χ_2 torsion angle yielded an orientation of the side chain in an eclipsed conformation. This inspection in principle constituted the equivalent of a potential energy calculation, albeit carried out on the basis of visual inspection of the molecule by molecular graphics display. These results are further described in Sec. 4.1.2.

In our studies of methyl esters of spin-labeled amino acids, we noted that the average electron-to-(ester methyl) proton distance constraint is not a sensitive index of conformation of the $-\text{COOCH}_3$ group (Mustafi *et al.*, 1990a; Wells *et al.*, 1990; Joela *et al.*, 1991) due to both the experimental uncertainty associated with the corresponding distance and the circumstance that rotation around the carboxylate C-O bond results in the electron-to-nucleus probe vector describing a cone with a small apical angle. In this terminal region of the molecule, there are no steric constraints to rotation around the ester C-O bond. This situation may also be one where potential energy minimization more adequately assigns the lowest energy conformation of the $-\text{COOCH}_3$ group that satisfies the electron-to-(methyl) proton distance constraint.

As further studies are carried out to analyze molecular structure and conformation on the basis of ENDOR distance constraints, it is likely that potential energy minimization methods will be useful for further refinement of the approach. However, since no published force field parameters for the spin-label moiety exist for such calculations, it will be necessary to develop and refine them first against structural and spectroscopic data.

4. STRUCTURE AND CONFORMATION OF SPIN-LABELED MOLECULES BY ENDOR

4.1. Spin-Labeled Amino Acids

From ENDOR studies of molecules in frozen solutions, the molecular structures and conformations of several spin-labeled amino acid derivatives have been reported from this laboratory, including L-alanine (Mustafi *et al.*, 1990b), L-tryptophan (Wells *et al.*, 1990), and L-phenylalanine (Joela *et al.*, 1991) acylated at the amino nitrogen position with the nitroxyl spin label 2,2,5,5-tetramethyl-1-oxyproline-3-carboxylic acid. In these studies resonance assignments were made on the basis of site-specific deuteration or by use of fluorine substituted analogs. To demonstrate the precision of determining molecular structure and conformation of molecules in frozen solutions by ENDOR, we discuss particular aspects of each spin-labeled amino acid to illustrate the unique structural information that can be obtained.

4.1.1. Planarity of the Peptide Bond

In Fig. 2 we compared the series of specifically deuteriated analogs of spin-labeled methyl L-alanate synthesized to assign resonance features (Mustafi *et al.*, 1990b). Figure 14 illustrates spectra showing that resonance features of H^N in the pseudo-peptide bond are readily identified through exchange with solvent deuterons, in this instance, from d_4 -methanol. As discussed with respect to Figs. 5-7, the resonance features of H^α correspond to principal hfc components. Similarly the features for H^N were also shown to correspond to principal hfc components. While the assignment of resonance features belonging to an exchangeable proton is readily accomplished, comparing spectra in Fig. 15 illustrates the need to identify specific resonance features of each class of protons by using site-specifically deuteriated analogs. In this comparison with H_0 set to the central feature of the EPR spectrum, both the perpendicular hfc component and the parallel hfc component of each class of protons are identified, as discussed in Sec. 2.3. Spectra in Fig. 15 exhibit two sets of resonance features that are resolved for the β -methyl protons. One set was assigned to a single proton, the other set to the geometric mean of the other two β -methyl protons. Also, for the ester methyl protons, only one set of resonance features was observed; therefore, it was assigned to the geometrically averaged position of the three methyl protons of the ester group. In Table 3 the observed principal hfc components of each class of protons of spin-labeled methyl L-alanate are listed with estimates of A_{iso} values and corresponding values of r calculated on the basis of the dipolar equation. The results show that the isotropic hfc component is essentially negligible, as expected for protons at a distance greater than 5 Å from the nitroxyl group. The results also show that very small uncertainties

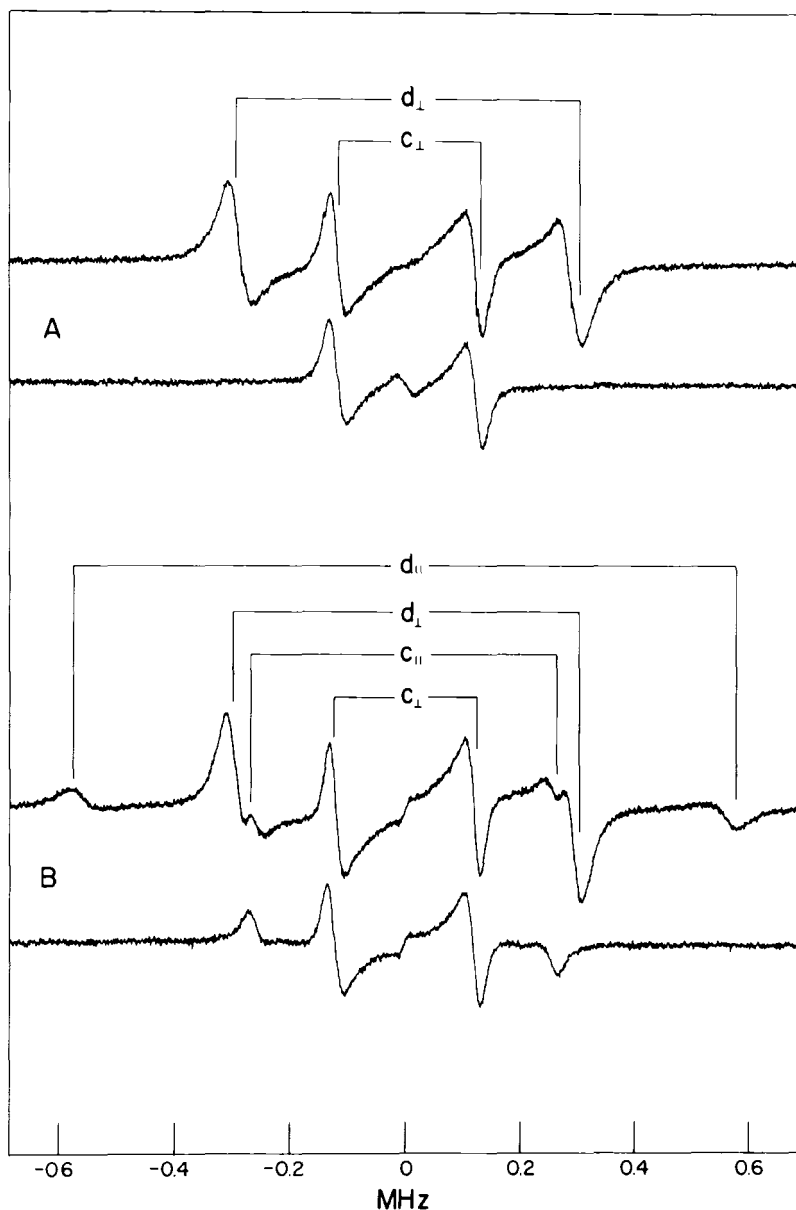


Figure 14. Proton ENDOR spectra of (d_{13})spin-labeled (d_3)methyl (d_3 - $\beta 1, \beta 2, \beta 3$)-L-alanate in d_4 -methanol. Letters A and B correspond to H_0 settings at the low-field edge and the central region of the EPR spectrum, respectively, that were saturated for ENDOR. For each field setting, the bottom spectrum was taken after exchanging H^N with solvent deuterons. The ENDOR splittings of H^α and H^N are identified in the stick diagram by c_{\parallel} , c_{\perp} and d_{\parallel} , d_{\perp} , respectively, for the principal components of each nucleus. Reprinted with permission from Mustafi *et al.* (1990b), American Chemical Society.

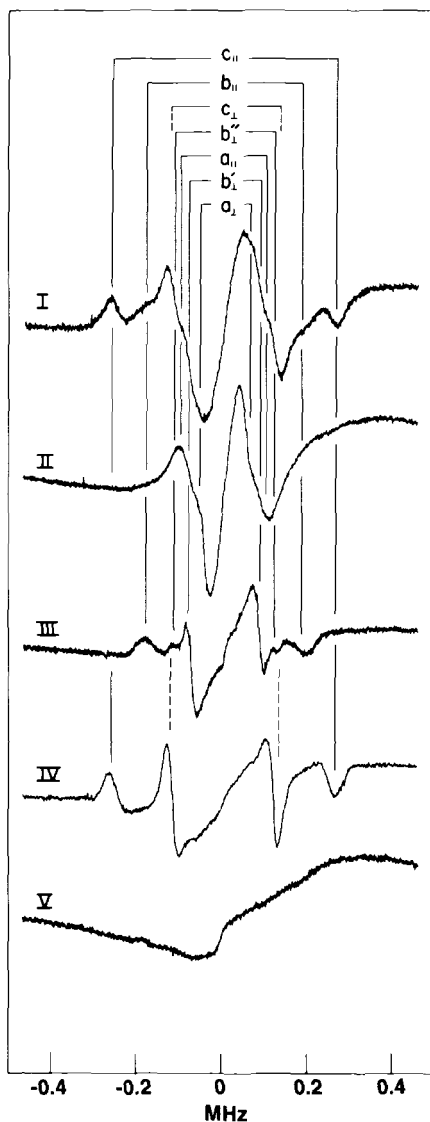


Figure 15. Proton ENDOR spectra of a series of site-specifically deuterated analogs of spin-labeled L-alanate in d_4 -methanol. Roman numerals refer to derivatives in Fig. 2: **I**, methyl alanate; **II**, methyl(d_4 - α , β 1, β 2, β 3)-alanate; **III**, (d_3)methyl (d - α)-alanate; **IV**, (d_3)methyl (d_3 - β 1, β 2, β 3)-alanate; and **V**, (d_3)methyl (d_4 - α , β 1, β 2, β 3)-alanate. Spectra were collected with H_0 at setting B of the EPR spectrum. Therefore for each class of protons, two line pairs are seen equally spaced about the free proton Larmor frequency; these are assigned to parallel and perpendicular hfc components. Assigning parallel and perpendicular hfc components is based on analysis of spectra at both field settings A and B. For H^β protons, two perpendicular hfc components are observed, but their corresponding parallel components are closely overlapping and labeled as $b_{||}$. Reprinted with permission from Mustafi *et al.* (1990b), American Chemical Society.

in r arise because of the high resolution of ENDOR spectra and relatively narrow linewidths of resonance features.

To assign the conformation of a molecule, a torsional angle search calculation is carried out, as described above (*cf.*, Sec. 3.2.), to identify conformational space within nonbonded, hard-sphere limits (Iijima *et al.*, 1987; Naruto *et al.*, 1985)

Table 3
Summary of hfc Components (A , MHz) and Estimated Electron-Proton Distances (r , Ångstrom) in Methyl *N*-(2,2,5,5-tetramethyl-1-oxypyrrolinyl-3-carbonyl)-L-alanate

Proton	Line Pairs ^a	A_{\parallel}	A_{\perp}	A_{iso}	A_{\parallel}^{D}	A_{\perp}^{D}	r^b
H ^E	a_{\parallel}, a_{\perp}	0.204	0.103	0.000	0.204	-0.103	9.19 ± 0.22
H ^{β1}	b_{\parallel}, b_{\perp}	0.384	0.237	-0.030	0.414	-0.207	7.30 ± 0.04^c
H ^{β2}	$b'_{\parallel}, b'_{\perp}$	0.346	0.173	0.000	0.346	-0.173	7.71 ± 0.06^d
H ^{α}	c_{\parallel}, c_{\perp}	0.525	0.244	0.013	0.513	-0.256	6.76 ± 0.04
H ^N	d_{\parallel}, d_{\perp}	1.152	0.605	-0.019	1.172	-0.586	5.13 ± 0.02

^aLine pairs are assigned in Figs 14 and 15.

^bUncertainty in frequency of 0.015–0.020 MHz due to the line width of each ENDOR absorption is included in the calculation of electron-proton distances.

^cH ^{β 1} is assigned to a single methyl proton

^dH ^{β 2} is assigned to the geometric mean of two methyl protons (H ^{β 2} and H ^{β 3}).

compatible with ENDOR-determined electron-nucleus dipolar distances and their respective uncertainties. The results of such a calculation for spin-labeled methyl L-alanate to define the planarity of the pseudo-peptide bond are represented by the angle map in Fig. 16. We discuss these results as a function of the number of ENDOR-determined distance constraints applied. The low-density dots represent conformational space allowed only by nonbonded van der Waals interactions. The small region of high-density dots represents the conformational space compatible with nonbonded van der Waals limits and distance constraints only to H^N and H ^{α} .

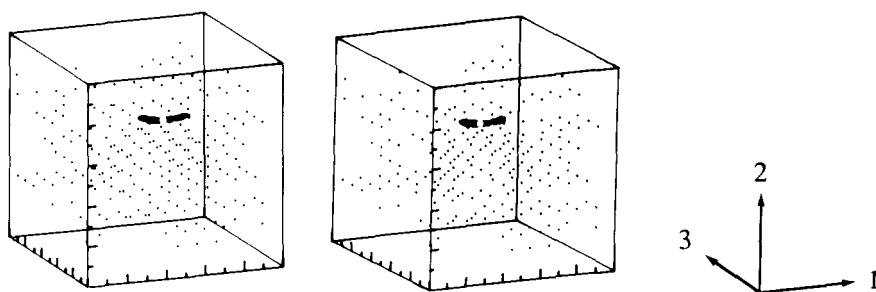


Figure 16. Stereodiagram of the angle map of spin-labeled methyl L-alanate defining the conformation of the molecule from the nitroxyl group to the C ^{α} and C ^{β} atoms of the alanine moiety. Axes 1–3 represent 0–360° rotation around the N–C ^{α} , C(6)–N, and C(3)–C(6) bonds, respectively. Each dot in the cube represents a set of three calculated torsion angles. Reprinted with permission from Mustafi *et al.* (1990b), American Chemical Society.

Applying the distance constraint to $H^{\beta 1}$ does not significantly change the volume of conformational space calculated for H^N and H^α constraints alone. On the other hand, adding the fourth distance constraint of $7.71 \pm 0.06 \text{ \AA}$ to the geometrically averaged position of the other two β -methyl protons listed in Table 3 sharply reduced the allowed conformational space to almost a single point represented by the white dot within the volume of high-density dots.

Simultaneous application of distance constraints to H^N and H^α limited the [C(3)-C(6)-N-C $^\alpha$] dihedral angle to values between 171° and 201° , as seen in Fig. 16. This dihedral angle in spin-labeled methyl L-alanate is analogous to the dihedral angle ω , which defines the planarity of the peptide bond in protein structure analysis (*cf.*, Schulz and Schirmer, 1979). Further application of distance constraints to the β -methyl protons of the alanine side chain restricts the value of this dihedral angle to $-170^\circ \pm 4^\circ$, in good agreement with that of a *trans* peptide bond expected through x-ray studies of a variety of simple peptides. (A *cis* conformation of the peptide bond joining the spin-label moiety to alanine is incompatible with the ENDOR-determined distance constraint of $5.13 \pm 0.02 \text{ \AA}$ to H^N alone.) Similar ENDOR studies of spin-labeled derivatives of L-tryptophan and L-phenylalanine demonstrated that the pseudo-peptide bond in these compounds also retains a planar *trans* structure. Furthermore, the dihedral angle [C(4)=C(3)-C(6)-N] retains a value of $\sim -35^\circ$ in each of these spin-labeled amino acids, essentially identical to that (-31°) of 2,2,5,5-tetramethyl-1-oxypyrroline-3-carboxamide in crystals (Turley and Boer, 1972). This particular structural detail is probably due to the tendency of π -conjugation between the carbonyl group in the peptide bond with the olefinic bond in the oxypyrrolinyl ring.

4.1.2. Conformation of Aromatic Side Chains

The conformational properties of aromatic side chains in amino acids and peptides are not well-defined by NMR for oligopeptides in solution. While the value of the χ_1 dihedral angle of the side chain measuring rotation around the C $^\alpha$ -C $^\beta$ bond can generally be estimated on the basis of NMR data, it is often not feasible to assign the value of the χ_2 dihedral angle for rotation around the C $^\beta$ -C $^\gamma$ bond, because it is difficult to assign the individual proton resonances of the -C $^\beta$ H $_2$ - group of the side chain.

While ENDOR spectra of spin-labeled methyl L-tryptophanate and of the corresponding $\zeta 3$ -fluoro- and $\eta 2$ -fluoro-tryptophanate analogs exhibit well-resolved resonance features readily assigned to H^N , H^α , $H^{\beta 1,2}$, and ester methyl protons, the resonance features of protons in the aromatic ring are broad and overlapping (Wells *et al.*, 1990). However, the conformation of the side chain can be readily determined on the basis of the hf interaction of the nitroxyl group with fluorine substituents in the indole ring. Figure 17 illustrates proton and fluorine ENDOR spectra of spin-labeled methyl $\zeta 3$ -fluoro-tryptophanate in two different

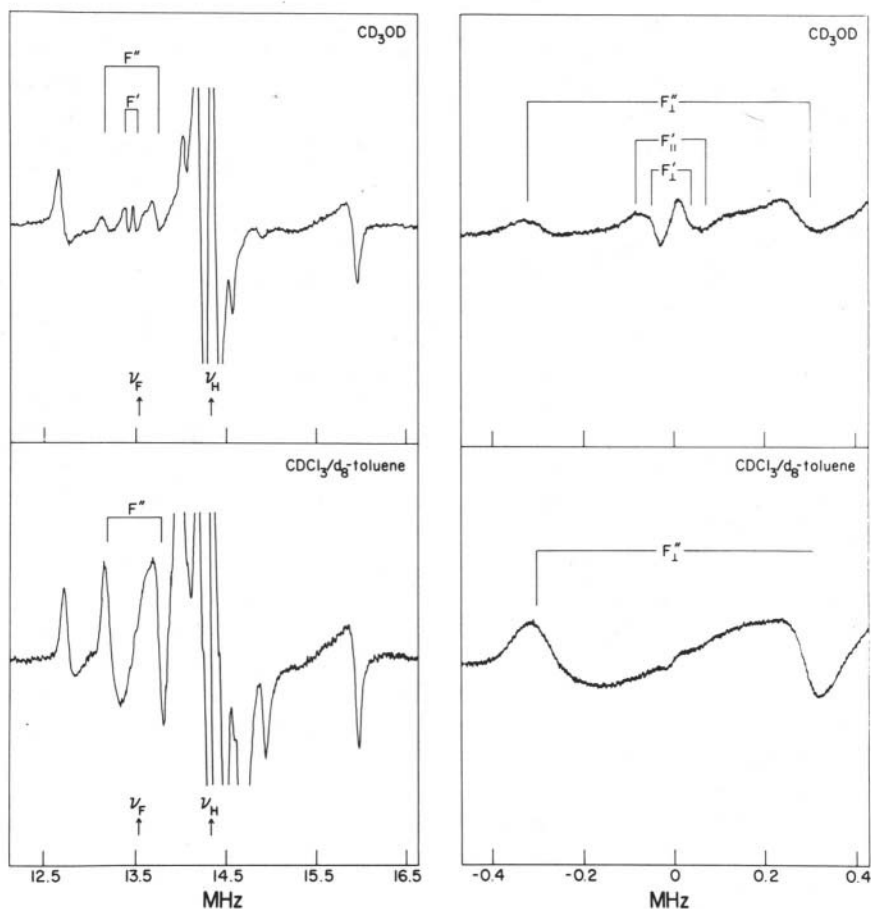


Figure 17. Proton and fluorine ENDOR spectra of (d_3)methyl *N*-(2,2,5,5-tetramethyl-1-oxypyrrolinyl-3-carbonyl)-D,L-(ζ - 3 -F)-tryptophanate in d_4 -methanol or perdeuterated 50:50 chloroform/toluene with \mathbf{H}_0 at setting *B* of the EPR spectrum. The right-hand panel shows only fluorine ENDOR features that are symmetric around the free fluorine Larmor frequency at 13.5 MHz. Two sets of fluorine resonances (F' , F'') are identified in methanol in the upper panel while in the lower panel for the nonpolar solvent, only one set is observed, identified as F_I'' .

solvent systems. On the right-hand side, only the ^{19}F ENDOR spectra are compared for the molecule in methanol as a polar solvent and in chloroform/toluene as an aprotic, nonpolar solvent. In the upper panel, the broad ^{19}F ENDOR features, labeled F_I'' for the molecule in methanol, exhibit splittings identical with those in chloroform/toluene but of diminished peak-to-peak amplitude. However, a second set of resonance features, labeled F_{II}'' and F_I' , acquire greater amplitude in methanol

and are essentially absent for the spin-labeled molecule in chloroform/toluene. These results indicate the presence of an equilibrium between two conformers differing in their electron-fluorine separations that is influenced by the dielectric constant of the solvent. In Table 4, the values of electron-nuclear distances for these two conformers are compared. In the solvent of low dielectric constant, only the conformer with the shorter electron-fluorine distance is detectable. In methanol both conformers exist in equilibrium.

The atomic numbering scheme of spin-labeled methyl tryptophanate is shown in Diagram 3 for purposes of discussion. Results of the conformational analysis based on ENDOR-determined values of r in Table 4 are illustrated in Fig. 18. As seen in Figure 18, the distance constraints for the molecule in chloroform/toluene limit the number of ENDOR compatible conformations to a very small range, resulting in a nearly unique conformation of the amino acid side chain with respect to the nitroxyl group of the spin label. This corresponds to the top-most conformer in Fig. 18, and the distance constraints defining this structure are labeled *closed* in Table 4. This conformer is also detected in methanol as evidenced by the spectra in Fig. 17. The set of distance constraints labeled *extended* in Table 4 corresponds to the second set of resonances for the molecule in methanol. Two families of conformers are illustrated by the central and bottom-most structures in Fig. 18 that satisfy the *extended* distance constraints in Table 4. This set of values for r is observed for the spin-labeled amino acid only in a solvent of high dielectric constant.

The conformation of the side chain of tryptophan is defined on the basis of two dihedral angles χ_1 [$N-C^\alpha-C^\beta-C^\gamma$] and χ_2 [$C^\alpha-C^\beta-C^\gamma-C^{\delta 1}$]. Torsion angle search calculations show that conformers for each of the three families in Fig. 18 are clustered around the value of $\chi_1 \approx -60^\circ$, corresponding to a g^- (*gauche*⁻) rotamer; g^+ (*gauche*⁺, $\chi_1 \approx +60^\circ$) and t (*trans*, $\chi_1 \approx 180^\circ$) rotamers are incompatible with ENDOR data. In Fig. 18 Newman projections correspond to χ_2 . The top and bottom

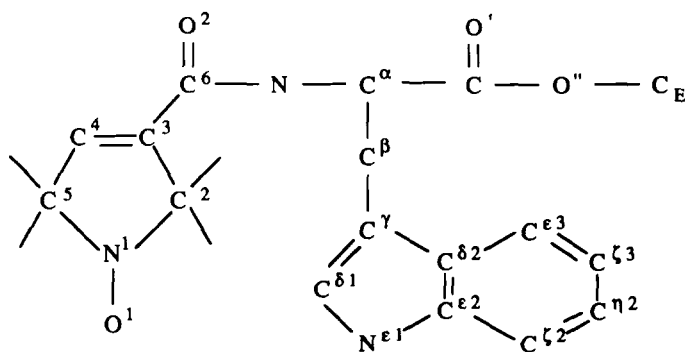


Diagram 3.

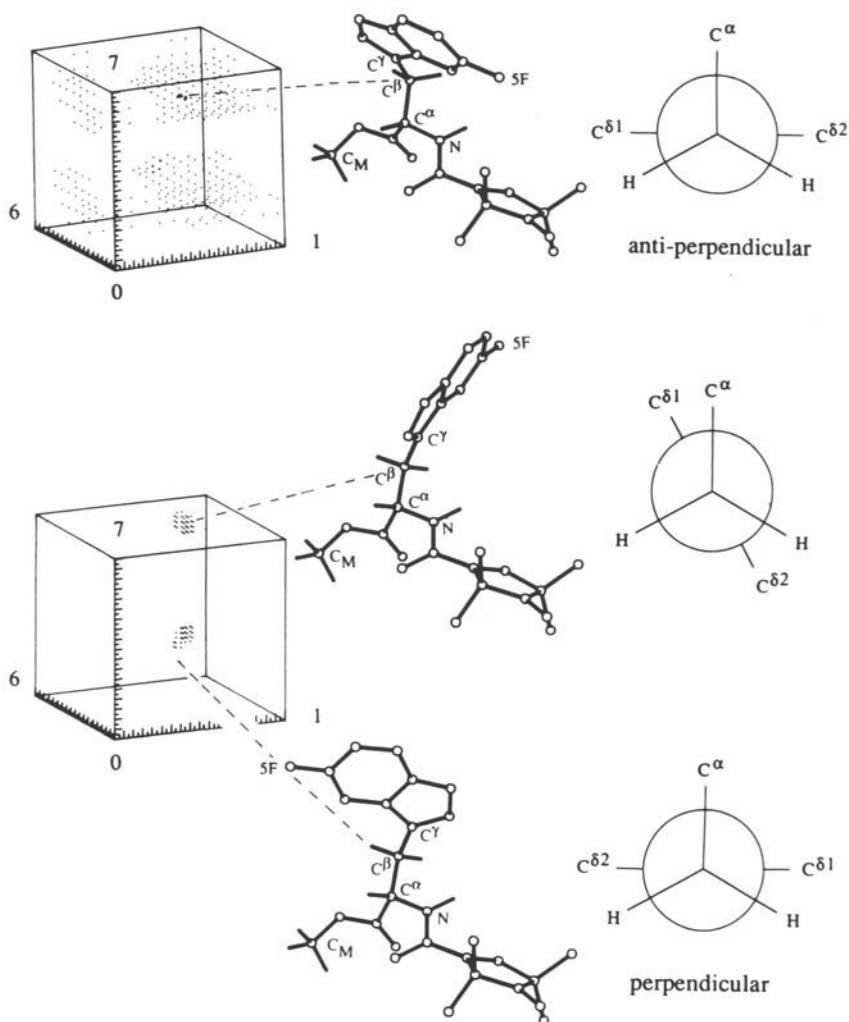


Figure 18. Conformations of spin-labeled methyl L-tryptophan determined on the basis of ENDOR-defined electron-nucleus dipolar distances. The left-hand side shows angle maps. Axes 1, 6, and 7 represent 0–360° rotation around the N–C^α, C^α–C^β, and C^β–C^γ bonds, respectively, which correspond to ϕ , χ_1 , and χ_2 dihedral angles in proteins (*cf.*, Schultz and Schirmer, 1979). In the upper angle map, low-density dots represent conformational space compatible with nonbonded van der Waals constraints. Also in the upper angle map, the small circumscribed set of high-density dots refers to the *closed* structure, and it identifies an essentially unique conformation of the molecule. This conformation is defined by *closed* distance constraints in Table 4. In the lower angle map, high-density dots identify two families of rotamers that satisfy the set of *extended* distance constraints in Table 4 for the molecule in the polar solvent methanol. The central part of the diagram shows structures of spin-labeled methyl (F³)-tryptophan drawn according to mean values of dihedral angles in the angle maps. The ENDOR-defined hydrogens and the F³ substituent in the indole ring, labeled as 5F, are shown in addition to nonhydrogen atoms. On the right-hand side, Newman diagrams are drawn projected along the C^β–C^γ bond (χ_2 dihedral angle) for each of the three conformations according to the respective ENDOR distance constraints.

Table 4
Estimated Electron-Proton Distances (r , Ångstrom) in Methyl
***N*-(2,2,5,5-tetramethyl-1-oxypyrrolinyl-3-carbonyl)-l-tryptophanate in Solutions of Frozen**
***d*₄-Methanol and Perdeuterated Chloroform/Toluene**

Nucleus	r (closed) ^{a,b}	r (extended) ^{a,b}
H ^N	5.08 ± 0.06	5.11 ± 0.06
H ^α	6.68 ± 0.08	6.70 ± 0.07
H ^{β1}	7.02 ± 0.10	7.54 ± 0.08
H ^{β2}	8.20 ± 0.18	8.29 ± 0.30
H ^E	9.67 ± 0.35	9.05 ± 0.22
F ^{γ,3}	5.01 ± 0.14	10.10 ± 1.02
F ^{η,2}	7.58 ± 0.12	10.22 ± 1.02

^aUncertainty in frequency of 0.015–0.020 MHz due to the linewidth of each ENDOR absorption is included in the calculation of electron-proton distances.

^bThe conformation of spin-labeled tryptophanate with shorter electron-fluorine distances, obtained from ENDOR results for molecules in chloroform/toluene is designated *closed*. For molecules in the polar solvent methanol, two sets of electron-fluorine distances are obtained from ENDOR. One is identical to the *closed* conformation, while the second conformation designated *extended* exhibits larger electron-to-nucleus distances for the fluorine substituents in the indole ring.

conformers belong to the classical antiperpendicular ($-\perp$) and perpendicular ($+\perp$) rotamers, respectively. The structure in the middle of Fig. 18 corresponds to a nearly eclipsed conformation with $\chi_2 \approx -30^\circ$; therefore it is expected to be associated with higher potential energy. Its relative population estimated on the basis of electrostatic dipole-dipole interactions is less than 2% under the solvent and temperature conditions used to prepare spin-labeled tryptophan for spectroscopy (Wells *et al.*, 1990). We consequently conclude that this nearly eclipsed conformer satisfies geometric distance constraints by calculation, but it does not represent a molecular species that accounts for the observed ENDOR absorption features in Fig. 17. Furthermore, we point out that the g^- , $+\perp$ conformer corresponding to the structure at the bottom of Fig. 18, defined by ENDOR distance constraints for the *extended* conformer of spin-labeled methyl L-tryptophanate in a polar solvent, is virtually identical to the x-ray defined structure of methyl *N*-acetyl L-tryptophanate crystallized from methanol (Cotrait and Barrans, 1974).

For spin-labeled L-phenylalanine and methyl L-phenylalanate, the conformation of the side chain was similarly assigned by using fluorine-substituted analogs (Joela *et al.*, 1991). Results of conformational search calculations are compared in Fig. 19 for this amino acid. While regions corresponding to g^+ , t , and g^- conformers are sterically allowed for both perpendicular and antiperpendicular conformations of an *ortho*-fluoro-phenyl side chain, electron-proton distance constraints restrict accessible conformational space to only the g^- manifold. Adding the electron-to-F^ε

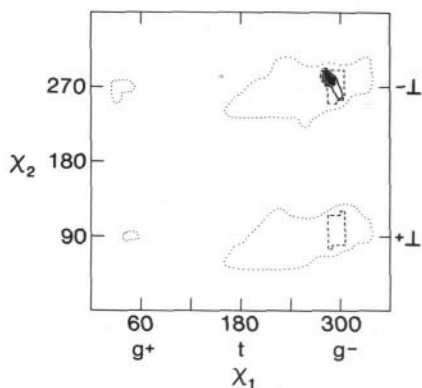


Figure 19. Angle maps of χ_1 and χ_2 for spin-labeled L-phenylalanine as a function of ENDOR-defined distance constraints. Axes representing values of χ_1 and χ_2 are indicated in degrees, and values are labeled on the axes for the classical conformers. Conformational space is indicated according to the following distance constraints: Only van der Waals constraints (---); $H^N, H^\alpha, H^{\beta 1,2}$ (---); $H^N, H^\alpha, H^{\beta 1,2}, F^{\delta 1}$ (—); $H^N, H^\alpha, H^{\beta 1,2}, F^{\delta 1}, F^{\zeta}$ (solid area). Reprinted with permission from Joela *et al.* (1991), American Chemical Society.

distance constraint did not alter results, whereas the distance constraint to $F^{\delta 1}$ limits the accessible space to the classical g^- rotamer with an antiperpendicular orientation of the *ortho*-fluoro-phenyl ring in both polar and apolar solvents. The structural similarity of spin-labeled methyl L-phenylalanate to that of methyl L-tryptophanate

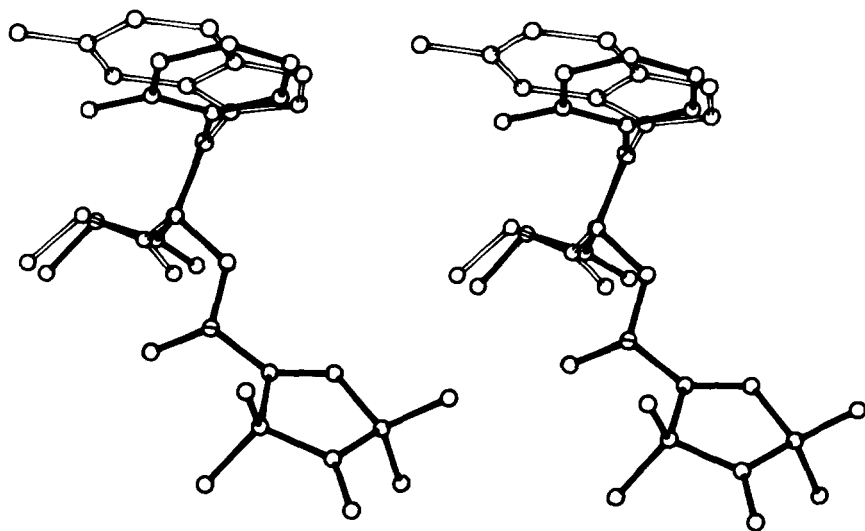


Figure 20. Stereodiagram comparing the structure of the $g^-, -\perp$ conformer of spin-labeled methyl (δ -F)-phenylalanate to the *extended* conformation of spin-labeled methyl (ζ 3-F)-tryptophanate. With respect to the dihedral angle χ_2 , the *ortho*-fluoro substituent of phenylalanine is in an $-\perp$ orientation, and the *extended* conformer of the tryptophan side chain is in a $+\perp$ orientation. The two ENDOR-determined structures are superposed only according to the six atoms of the oxyprolinyl ring. Reprinted with permission from Joela *et al.* (1991), American Chemical Society.

is illustrated in Fig. 20. Results of electrostatic dipole-dipole calculations show that the g^- , $-\perp$ orientation of the $\delta 1$ -fluoro-phenyl side chain is energetically favored over the g^- , $+\perp$ orientation and that 90% of the molecules exhibit this conformation (Joela *et al.*, 1991).

4.1.3. Spin-Labeled Penicillin—an Amino Acid Like System

While spin-labeled esters of L-tryptophan and L-phenylalanine proved to be kinetically specific substrate probes of α -chymotrypsin, as discussed below in Sec. 5, we found that a similarly spin-labeled derivative of 6-aminopenicillin is as kinetically specific and catalytically reactive towards the enzyme β -lactamase as is the classical substrate benzylpenicillin (Mustafi and Makinen, 1995). This spin-labeled derivative provided a sensitive structural probe not only of the enzyme-catalyzed reaction but also of the solvolytic reaction that the free β -lactam group undergoes in solution.

The atomic numbering scheme for spin-labeled penicillin given in Fig. 13 preserves the classical atomic numbering scheme of the fused thiazolidine ring system of penicillins. While assigning resonance features for H(14) and H(6) was critical for applying distance constraints to determine conformation, this aspect is essentially identical to that for H^N and H^α of spin-labeled α -amino acids. Consequently we summarize only the spectroscopic results in Table 5, and we emphasize

Table 5
Summary of hfc Components (A , MHz) and Estimated Electron-Proton Distances (r , Ångstrom) in 6-*N*-(2,2,5,5-tetramethyl-1-oxypyrrolinyl-3-carbonyl)-Penicillanic Acid

Proton	A_{\parallel}	A_{\perp}	A_{iso}	A_{\parallel}^D	A_{\perp}^D	r^a
<i>Penicillin</i> ^b						
H(14)	1.173	0.580	0.004	1.169	-0.584	5.13 ± 0.03
H(6)	0.535	0.265	0.002	0.533	-0.267	6.67 ± 0.04
H(5) ^c	—	0.153	—	—	-0.153	8.01 ± 0.16
H(2) ^c	—	0.121	—	—	-0.121	8.68 ± 0.30
H(CH ₃) ^c	—	0.085	—	—	-0.085	9.77 ± 0.45
<i>Solvent</i>						
H ^{OH}	0.874	0.436	0.001	0.873	-0.437	5.67 ± 0.04

^aUncertainty in frequency of 0.010–0.015 MHz due to the linewidth of each ENDOR absorption is included in the calculation of electron-proton distances.

^bSee Fig. 13 for the atomic numbering scheme of spin-labeled penicillin.

^cFor these three classes of protons, electron-proton distances are calculated from the perpendicular hfc components alone. Assignments of these dipolar distances to specific protons are based on molecular modeling studies (Mustafi and Makinen, 1995).

in our discussion that ENDOR investigations have revealed the probable mechanism of hydrolysis of the β -lactam group in solution.

Important ENDOR absorptions are identified in Fig. 21, where spectra of spin-labeled penicillin in neat methanol are compared to that of the molecule in an aprotic ternary solvent system to which methanol was added in 1:1 stoichiometry. Both principal hfc components for H(14) and H(6), labeled a_{\parallel} , a_{\perp} and b_{\parallel} , b_{\perp} , respectively, were assigned directly from the spectra. Two line pairs are present in the middle spectrum that are not seen in the top spectrum, and these are assigned to the parallel and perpendicular hfc components of the hydroxyl proton of the methanol molecule on the basis of the dependence of spectra on H_0 setting and solvent isotope composition. Despite line broadening with loss of resolution in spectrum C due to the presence of methanol as bulk solvent, it is clear that all ENDOR features observed in spectrum B are also evident in spectrum C. The sharp

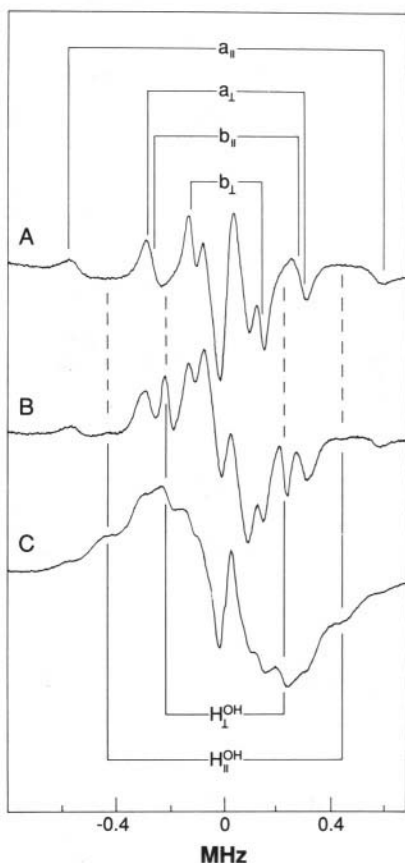


Figure 21. Proton ENDOR spectra of 6-*N*-(2,2,5,5-tetramethyl-1-oxypyrrrolinyl-3-carbonyl)-penicillanic acid in deuterated solvents illustrate a tightly bound methanol molecule. **A:** 50:25:25 (v/v) perdeuterated DMSO: toluene: chloroform to which d_4 -methanol was added in 1:1 stoichiometry with the spin-labeled penicillin. **B:** The same ternary solvent system to which a 1:1 molar equivalent of d_3 -methanol was added. **C:** Pure d_3 -methanol. These spectra were taken with H_0 at setting *B* of the EPR spectrum. Both parallel and perpendicular hfc components of the methanol hydroxyl proton are identified in spectra **B** and **C**. Other line pairs are assigned to H(14) and H(6), as listed in Table 5. Reprinted from Mustafi and Makinen (1995), by courtesy of Marcel Dekker, Inc.

resonance features in spectrum B, thus, indicate the presence of a methanol OH group tightly bound to the spin-labeled penicillin. In Table 5, the principal hfc components of the hydroxyl proton of the bound methanol molecule and its respective dipolar distance are also summarized.

The conformer of the spin-labeled penicillin molecule assigned on the basis of ENDOR-determined values of r in Table 5 and on the basis of molecular modeling (Mustafi and Makinen, 1995) proved to be essentially identical to the x-ray defined structure of amoxicillin trihydrate (Boles *et al.*, 1978). Since hydrogen bonding is the most likely basis for tight binding of the methanol molecule, the only group of hydrogen bonding potential satisfying these structural constraints is the -NH- of the pseudo-peptide bond. The location of the hydrogen-bonded methanol identified in spectrum B of Fig. 21 is illustrated in Fig. 22. The main spectroscopic criteria

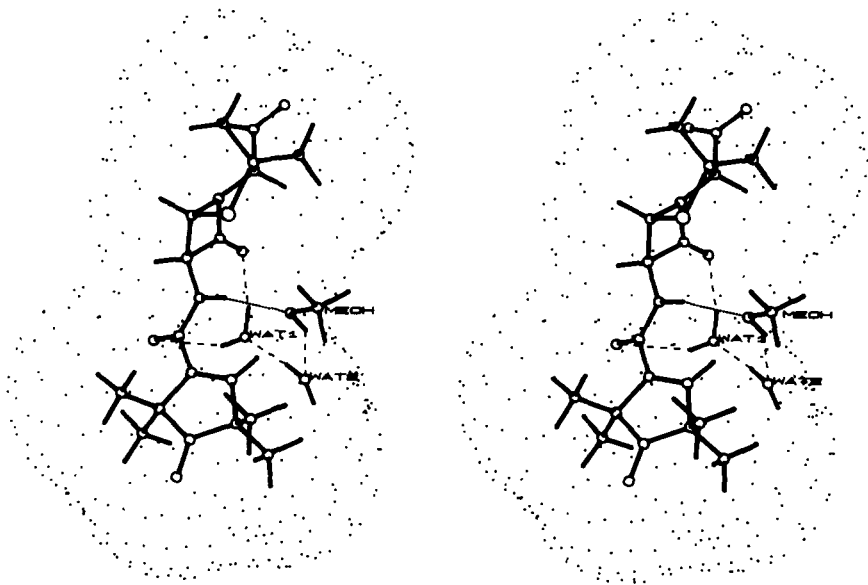


Figure 22. Stereodiagram of the ENDOR-determined conformation of spin-labeled penicillin and the hydrogen-bonded methanol molecule. The dotted surface shows the solvent-accessible surface of the spin-labeled penicillin calculated according to the algorithm of Lee and Richards (1971). Two water molecules are also illustrated in this diagram with open bond structures labeled WAT1 and WAT2. Their positions are defined by x-ray crystallographic studies of amoxicillin trihydrate (Boles *et al.*, 1978). The third water molecule is not included here for purposes of clarity because its oxygen atom is almost exactly superposed onto the hydroxyl oxygen of the hydrogen-bonded methanol molecule identified by ENDOR. Dashed lines indicate possible hydrogen bonds between these two water molecules and other hydrogen-bonding donors and acceptors in this complex; the dotted line indicates the hydrogen bond between the pseudo-peptide -NH- and O_{MeOH} . Reprinted with permission from Mustafi and Makinen (1995), American Chemical Society.

and the pattern of resonance features indicating that the OH group is essentially in or very close to the plane of the oxypyrrolinyl ring. As Fig. 22 shows, the hydroxyl group of the methanol molecule hydrogen bonded to the amide group of the spin-labeled penicillin molecule satisfies these requirements, and it is accommodated sterically by the solvent accessible surface. The ENDOR data are not compatible with hydrogen bonding of the methanol molecule to the β -lactam O(8) alone, to the β -lactam carbonyl O and the amide -NH- group simultaneously, or to the carbonyl O(16) atom alone (*cf.*, Fig. 13). This position of the methanol OH group overlaps with a similarly hydrogen-bonded water molecule in the crystal structure of amoxicillin trihydrate (Boles *et al.*, 1978). The other two water molecules from that structure shown in Fig. 22 illustrate that they can form a hydrogen-bonded network that can catalyze polarization of the solvent OH bond in solvolysis of the β -lactam group by a general base-catalyzed mechanism.

An interesting contradiction concerning the reactivity of the β -lactam group, originally pointed out by R. B. Woodward, is that "exo" attack, while sterically preferred, is not stereoelectronically allowed while "endo" attack, as the stereoelectronically favored approach, is sterically hindered (Benner, 1988). As Fig. 22 shows, the hydroxyl group of the methanol molecule is located on the *endo*, or concave side of the fused β -lactam ring. Nucleophilic attack on the β -lactam C=O group from the *endo* side is viewed as sterically incompatible for the reaction to proceed (Page, 1987; Sinnott, 1988). However, nucleophilic attack from the *endo* side is favored on the basis of stereoelectronic grounds; i.e., the incoming nucleophile is antiperiplanar to the lone pair orbital of the β -lactam N atom (Kirby, 1983; Deslongchamps, 1983), as Diagram 4 illustrates.

On the basis of molecular modeling studies, the ENDOR-defined methanol molecule can become a nucleophile from its hydrogen-bonded position on the *endo* surface of the penicillin moiety to form the tetrahedral adduct (Mustafi and Makinen, 1995). Detecting a hydrogen-bonded methanol molecule (see Fig. 21) coupled with structural data defining the path of approach of nucleophilic O \cdots C=O interactions (Bürgi *et al.*, 1974a,b), thus, provides strong arguments against the assumption that the *endo* side of the fused β -lactam ring is too sterically crowded for chemistry.

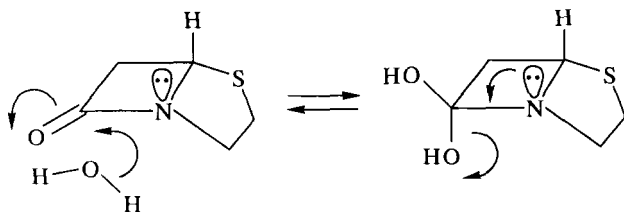


Diagram 4.

4.2. Other Spin Label Derivatives

4.2.1. Parent Spin Labels

Although ENDOR spectroscopy was applied to nitroxyl spin labels in solution by Leniart *et al.* (1970) over 25 years ago, until recently ENDOR studies of nitroxyl spin labels were limited mainly to characterizing electronic and structural properties of five- or six-membered spin labels only. A single-crystal ENDOR study of a saturated, six-membered spin label was reported by Ohzeki *et al.* (1982). Values of the principal hfc components and direction cosines of protons in the spin label moiety and of the nitroxyl nitrogen atom were assigned from this study. Brustolon *et al.* (1985) and Kotake *et al.* (1985) reported ENDOR studies of nitroxyl spin labels, including both the five-membered and six-membered ring in polycrystalline materials or disordered matrices. From these studies, they reported hfc components of ring protons in spin labels. However, these studies were not carried out with site-specific deuteration to assign the chemical origins of observed resonance features.

From this laboratory ENDOR studies of parent nitroxyl spin labels including 3-carboxamide, 3-carboxylic acid, and 3-formaldehyde derivatives of 2,2,5,5-tetramethyl-1-oxypyrrolidine were reported. Unambiguous assignments of principal hfc components for the vinylic proton and the methyl protons in the oxypyrrolidine ring were made on the basis of selectively deuterated spin label analogs (Mustafi *et al.*, 1990c; Mustafi and Makinen, 1992). ENDOR features of the formaldehyde proton and the exchangeable carboxylic acid proton and carboxamide protons were assigned, and their electron-proton dipolar distances were determined. For the 3-formaldehyde and 3-carboxylic acid derivatives, ENDOR results indicate that the [C(4) = C(3)-C(6)-O(2)] torsion angle defining side chain conformation was $180^\circ \pm 20^\circ$, which is in agreement with the x-ray defined structure of the 3-carboxylic acid derivative (Boeyens and Kruger, 1970). As noted earlier (Sec. 3.2), the ENDOR-defined conformation of the 3-carboxamide side chain is also in good agreement with x-ray results.

4.2.2. Oxypyrrolidine Spin Labels with Extended Side Chains

Molecular structures and conformations of oxypyrrolidine derivatives with conjugated polyene side chains having acid, ester, alcohol, and aldehyde functionalities were determined by ENDOR spectroscopy and molecular modeling (Mustafi *et al.*, 1993a,b). We review here special aspects of these studies to illustrate the intricate structural detail that can be achieved through ENDOR spectroscopy.

Figure 23 compares the proton ENDOR spectra of 5-(2,2,5,5-tetramethyl-1-oxypyrrolidine)-2,4-pentadienoic acid and the corresponding spin-labeled pentadienal. Table 6 lists values of principal hfc components and electron proton separations for each type of proton in these two compounds. While resonance

features corresponding to A_{\parallel} and A_{\perp} components for H^{α} , H^{β} , H^{γ} , and H^{δ} for the acid and the aldehyde derivatives as well as the aldehydic proton H^{al} of pentadienal were assigned from spectra like those in Fig. 23 on the basis of site-specific deuteration, resonance features for H^{COOH} are assigned on the basis of spectra of the pentadienoic acid derivative in an aprotic solvent system. Because of the spectral resolution achieved with use of selectively deuterated analogs, uncertainties associated with values of r were less than 2% for electron-proton distances over a 4.9–10.3 Å range. It was shown that only a completely planar *trans* structure of the side chain is fully compatible with all of the ENDOR-determined distances (Mustafi *et al.*, 1993a). Furthermore, ENDOR-determined values of r to H^{al} and H^{COOH} protons are compatible only with an *s-trans* conformation for the terminal C=O group of pentadienal and with an *s-cis* conformation for the C=O group of the pentadienoic acid. Figure 24 compares the ENDOR-constrained conformation of spin-labeled pentadienal to an ideal fully planar, all *trans*, *s-trans* structure. In the ENDOR-constrained structure of the pentadienal in Fig. 24, the side chain deviates $< 15^{\circ}$ from the plane of the oxypyrrolyl ring, the deviation beginning at the C^{β} atom.

For spin-labeled derivatives containing π -conjugated aldehyde, acid, and ester groups, the single preferred conformation of the side chain is explained in terms of its extended π -resonance structure. The ENDOR spectra of 3-(2,2,5,5-tetramethyl-1-oxypyrrolyl)-2-propen-1-ol, on the other hand, show multiple conformers of the terminal $-CH_2OH$ group (Mustafi *et al.*, 1993b). Since the terminal carbon atom is not sp^2 -hybridized and rotation around the terminal C^{β} - C^{γ} bond is not restricted as in conjugated systems, multiple conformers are not unexpected. This is directly

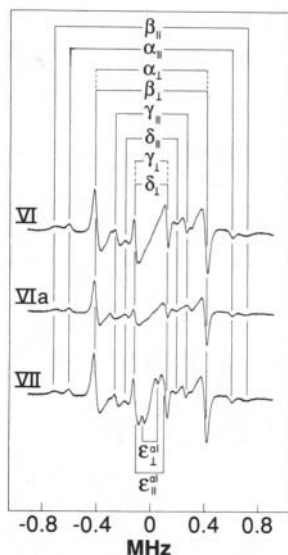


Figure 23. Proton ENDOR spectra of 5-(2,2,5,5-tetramethyl-1-oxypyrrolyl)-2,4-pentadienoic acid (top and middle spectra) and the corresponding spin-labeled pentadienal (bottom spectrum) in d_4 -methanol with H_0 at setting B. For the middle spectrum, a γ -deutero analog of the spin-labeled pentadienoic acid (SL - $C^{\alpha}H = C^{\beta}H - C^{\gamma}D = C^{\delta}H - C^{\epsilon}OOH$) was used. The ENDOR splittings that correspond to principal hfc components for each type of proton are identified by stick diagrams. Reprinted with permission from Mustafi *et al.* (1993a). ©1993 American Chemical Society.

Table 6
Summary of hfc Components (A, MHz) and Estimated Electron-Proton Distances (r , Ångstrom) in 5-(2,2,5,5-Tetramethyl-1-oxypyrrolinyl)-2,4-Pentadienoic Acid and 5-(2,2,5,5-Tetramethyl-1-oxypyrrolinyl)-2,4-Pentadienal

Proton	A_{\parallel}	A_{\perp}	A_{iso}	A_{\parallel}^{D}	A_{\perp}^{D}	r^a
H $^{\alpha}$	1.208	0.811	-0.138	1.346	-0.673	4.91 \pm 0.02
H $^{\beta}$	1.410	0.821	-0.077	1.487	-0.744	4.73 \pm 0.02
H $^{\gamma}$	0.519	0.230	0.020	0.499	-0.250	6.83 \pm 0.05
H $^{\delta}$	0.395	0.238	-0.027	0.422	-0.211	7.20 \pm 0.06
H $^{\text{COOH}}$	0.142	0.076	-0.003	0.145	-0.073	10.30 \pm 0.16
H $^{\text{al}}$	0.215	0.112	-0.003	0.218	-0.109	8.99 \pm 0.08

^aUncertainty in frequency of 0.010–0.015 MHz due to the linewidth of each absorption is included in the calculation of electron-proton distances.

confirmed by analyzing ENDOR spectra. The ENDOR spectra of spin-labeled propenol in Fig. 25 show at least two sets of hfc components for the hydroxyl protons labeled H $^{\text{OH}'}$ and H $^{\text{OH}''}$.

By using a specifically γ -deuteriated, enantiomorphically pure analog synthesized enzymatically as R-CHDOH (Mustafi *et al.*, 1993b), two sets of principal hfc components for H $^{\gamma}$ can be identified. On the other hand, in the bottom spectrum of Fig. 25, two well-resolved, sharper features are evident that belong to the principal hfc components of the carboxylic acid proton of the spin-labeled propenoic acid.

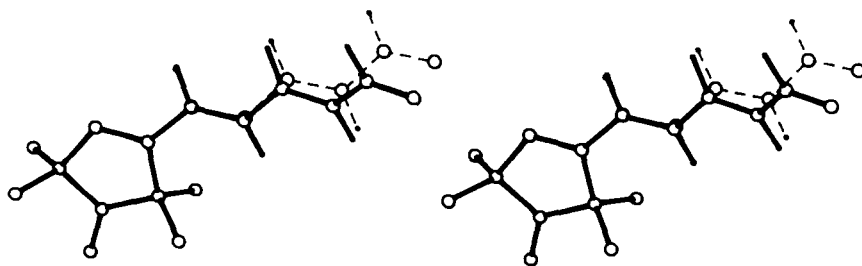


Figure 24. Stereodiagram comparing the ENDOR-constrained conformation (*solid bonds*) to the fully planar *trans, s-trans* conformation (*broken bonds*) of spin-labeled pentadienal. The ENDOR-determined structure is drawn according to the mean values of dihedral angles obtained from torsion angle search calculations constrained by ENDOR-determined electron-proton distances given in Table 6. For these calculations, 360° of rotation was permitted around each bond of the side chain, although the chemical bonding structure was known by synthesis to be that of a conjugated polyene. The ENDOR-active hydrogens H $^{\alpha}$, H $^{\beta}$, H $^{\gamma}$, H $^{\delta}$, and H $^{\text{al}}$ are shown in addition to nonhydrogen atoms. Reprinted with permission from Mustafi *et al.* (1993a), American Chemical Society.

These sharp resonance absorptions indicate a single conformation of the spin-labeled propenoic acid molecule.

The conformers identified for the terminal $-\text{CH}_2\text{OH}$ group are illustrated in the form of Newman diagrams in Figure 26. The ENDOR data yield two rotamers around the $\text{C}^\beta\text{-C}^\gamma$ bond in the upper diagram of Fig. 26. The predominant conformer is staggered with a value of -115° for the dihedral angle $[\text{C}^\alpha\text{=C}^\beta\text{-C}^\gamma\text{-O}]$. The second conformer is almost totally eclipsed; it is therefore, expected to be of low population. Rotamers defined by ENDOR with respect to the $\text{C}^\gamma\text{-O}$ bond are illustrated in the lower diagram of Fig. 26. In this figure the conformation of the hydroxyl group is either *gauche* or *trans* with respect to the C^β atom.

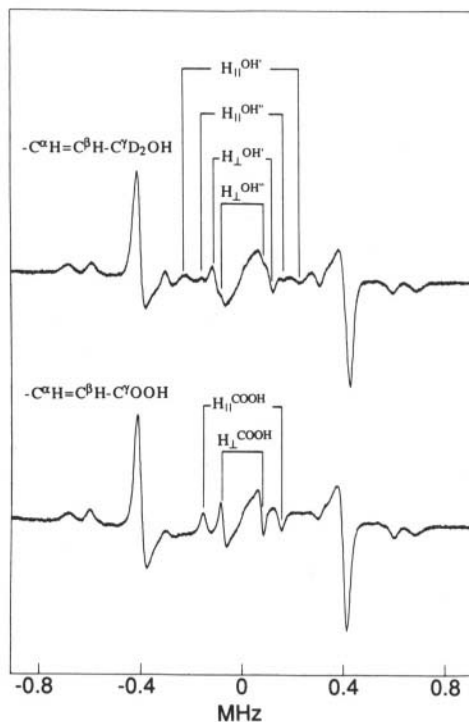
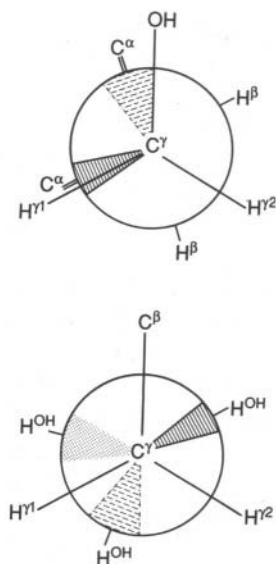


Figure 25. Proton ENDOR spectra of 3-(2,2,5,5-tetramethyl-1-oxypyrrolinyl)-2-propen-1-ol and the corresponding spin-labeled propenoic acid in perdeuterated DMSO:chloroform:toluene::50:25:25 (v/v) with H_0 at setting B of the EPR spectrum. Two sets of hfc components are identified for H^{OH} of the propenol; one set of hfc components are observed for H^{COOH} of the propenoic acid. The ENDOR features for H^α and H^β are not labeled. These spectra were collected in conjunction with studies reported by Mustafi *et al.* (1993b).

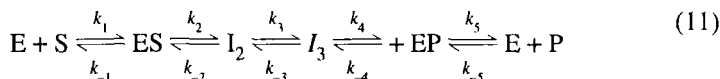
Figure 26. Newman diagrams illustrating the range of ENDOR-constrained dihedral angles [$C^\alpha = C^\beta - C^\gamma - O$] and [$C^\beta - C^\gamma - O - H$] in 3-(2,2,5,5-tetramethyl-1-oxypyrrolinyl)-2-propen-1-ol. The top diagram corresponds to a projection down the $C^\gamma - C^\beta$ bond and the lower diagram illustrates the projection down the $C^\gamma - O$ bond. In the top diagram the area indicated by solid lines corresponds to the range of the dihedral angle [$C^\alpha = C^\beta - C^\gamma - O$] compatible with the ENDOR-determined distance constraint $r^{\gamma 1}$ and the area indicated by dashed lines is obtained by applying the $r^{\gamma 1}$ distance constraint. The average positions of C^α and H^β for these two conformers are also indicated in the diagram. Three regions of conformational space are illustrated. The area with the solid line hatch marks is obtained using $r^{\gamma 1}$ and $r^{OH'}$ as distance constraints, while the area with the dashed lines is obtained using $r^{\gamma 1}$ and $r^{OH''}$; the area indicated by dots is obtained by applying distance constraints $r^{\gamma 1'}$ and $r^{OH'}$. Reprinted with permission from Mustafi *et al.* (1993b), American Chemical Society.



5. INTERMEDIATES OF ENZYME-CATALYZED REACTIONS

5.1. Methods of Stabilizing Reaction Intermediates

Enzyme-catalyzed reactions occur via the sequential formation of a series of intermediates illustrated by Eq. (11) for a one-substrate reaction.



In this scheme ES represents the initial collision (Michaelis) complex; EP, the enzyme-product complex, and I_2 and I_3 are intermediates of the reaction. To understand the molecular basis of enzyme function, we must determine (1) kinetic and thermodynamic parameters governing each step; (2) structures of reaction intermediates, the free enzyme, and the free substrate and products; and (3) the time-dependent atomic rearrangements involving the enzyme and substrate. While a variety of pre-steady-state and steady-state methods can be applied to estimate kinetic rate constants and equilibrium binding constants, the main obstacle to achieving goals (2) and (3) stems from the rapidity of enzyme catalytic action itself, for ordinarily intermediates of enzyme catalyzed reactions are short-lived and inaccessible to three-dimensional structure analysis. Consequently enzyme mechanisms are generally inferred on the basis of x-ray determined structures of enzyme-inhibitor complexes or on the basis of x-ray structures of enzyme-substrate

complexes formed under such conditions as low pH, in which the enzyme is inactive. Since *non-productive* structural relationships between the enzyme and inhibitor or the enzyme and a sluggish substrate are responsible for the long-term stability of such complexes, the observed relationships revealed by such x-ray crystallographic studies cannot correspond entirely to those required for the catalytic conversion of substrate to product. For these reasons, we must find methods for determining structures of true catalytically competent intermediates of enzyme-catalyzed reactions.

It has been appreciated for some time that methods of three-dimensional structure analysis coupled with cryoenzymology can provide a means of determining molecular structures of true intermediates of enzyme-catalyzed reactions (Makinen and Fink, 1977; Douzou, 1977; Cartwright and Fink, 1981). Cryoenzymology is a methodology for kinetically isolating an enzyme reaction intermediate by using fluid cryosolvents and subzero temperatures; it is based on the fact that different steps in the overall reaction, such as that depicted in Eq. (11), usually have kinetically distinguishable rate constants and activation barriers. In general, at suitably low temperatures in fluid, organic-aqueous cosolvent mixtures, an intermediate can be accumulated for which $k_i \gg (k_{-i} + k_{i+1})$. In favorable cases concentrations of such isolated intermediates may be stoichiometric with added enzyme, much greater than attainable, for instance, by rapid-mixing methods followed by freeze-quenching. Also, depending on the enthalpy of activation, the half-life of such intermediates can be increased from milliseconds at ambient, room temperature to hours in the -40° to -80° C range.

The choice of methodology for structural analysis of reaction intermediates is not straightforward however. Under subzero temperature conditions, cryosolvent mixtures acquire high viscosities, which limit their usefulness. The diffusion of substrates through solvent channels of protein crystals, already the rate-limiting process for crystals of the dimensions required for x-ray analysis (Makinen and Fink, 1977), becomes even slower. To circumvent the problem of viscosity and the rate-limiting diffusion of ligands, time-resolved crystallography has been applied to enzymes with catalytically inert, photocleavable ligands bound in the active site which are converted to catalytically reactive species upon photoactivation (Hajdu *et al.*, 1988; Moffat, 1989; Duke *et al.*, 1994). While this method still holds considerable promise for the future, studies carried out thus far, namely, formation of heptulose 2-phosphate by phosphorylase *b* (Hajdu *et al.*, 1988; Duke *et al.*, 1992), hydrolysis of GTP by *ras* p21 (Schlichting *et al.*, 1990; Scheidig *et al.*, 1992), and photochemical deacylation of a cinnamyl derivative of α -chymotrypsin (Stoddard *et al.*, 1991), yield data at relatively low resolution that lack the precision of structural detail to define catalytic events.

The high viscosity of cryosolvents at low temperatures also limits application of NMR methods to characterize enzyme reaction intermediates in solution, since the linewidth of resonances is determined by the correlation time of the macromole-

cule. A means of circumventing the problem of short lifetimes of reaction intermediates is to freeze-quench the reaction mixture in aerosolized droplets for structural characterization by solid-state NMR. While hitherto only preliminary studies have been published demonstrating the feasibility of the method (Evans *et al.*, 1993), this approach holds promise since there is no upper limit on the molecular weight of the enzyme as there is for NMR of macromolecules in fluid solutions. Another method based on nuclear magnetic resonance involves rotational-echo double resonance spectroscopy (Gullion and Schaefer, 1989; Jarvie *et al.*, 1996), which is similarly applied to solid-state samples and could be used to characterize enzyme reaction intermediates in frozen droplets.

5.2. Structural Characterization of True Intermediates of Enzyme-Catalyzed Reactions by ENDOR

5.2.1. α -Chymotrypsin

Since hydrolysis of ester and peptide substrates by α -chymotrypsin involves formation of an acylenzyme, it is expected that a tetrahedral adduct with the side chain of Ser-195 and the substrate is formed along the reaction pathway. Consequently, aldehydes form tightly bound complexes with serine proteases and are considered transition-state inhibitor analogs according to reaction Diagram 5 (Wolfenden, 1976). Jiang *et al.* (1998) synthesized the spin-labeled transition-state inhibitor analog *N*-(2,2,5,5-tetramethyl-1-oxypyrrolinyl-3-carbonyl)-L-phenylalaninal. The spin-labeled aldehyde displayed pure competitive inhibition with a K_1 of 0.18×10^{-3} M at pH 7; thus it is a tighter binding inhibitor analog than the *N*-benzoyl ($K_1 \sim 1.1 \times 10^{-3}$ M) and *N*-acetyl-L-phenylalaninal ($K_1 \sim 0.7 \times 10^{-3}$ M) inhibitors employed in NMR studies by others (Chen *et al.*, 1979).

Table 7 summarizes ENDOR-determined hfc components and estimates of electron-nucleus dipolar distances for a tetrahedral methanol adduct of the transition-state inhibitor analog in solution and for the inhibitor bound in the active site of α -chymotrypsin. Figure 27 provides a stereoview of the inhibitor modeled into the active site of α -chymotrypsin according to ENDOR distance constraints; this is similar to our study of the acylenzyme reaction intermediate formed with spin-labeled methyl L-tryptophanate, whose description follows (Wells *et al.*, 1994). Conformation of the enzyme-bound inhibitor was assigned on the basis of

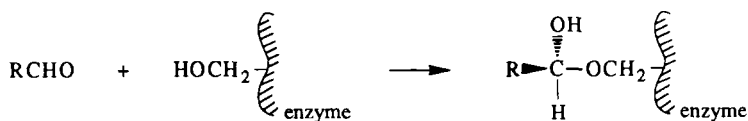


Diagram 5.

Table 7
Summary of hfc Components (A , MHz) and Estimated Electron-Nucleus Distances (r , Ångstrom) for the Tetrahedral Adduct of N -(2,2,5,5-tetramethyl-1-oxypyrrolinyl-3-carbonyl)- L -Phenylalaninal in Solution and with Ser-195 in the Active Site of α -Chymotrypsin

Nucleus	A_{\parallel}	A_{\perp}	A_{iso}	r^a
<i>Methanol Adduct</i>				
H^{N}	1.193	0.577	0.013	5.12 ± 0.04
H^{α}	0.542	0.262	0.018	6.64 ± 0.10
H^{al}	0.402	0.227	-0.017	7.24 ± 0.10
F^{x}	0.245	0.135	-0.008	8.56 ± 0.33
<i>Enzyme Adduct</i>				
H^{α}	—	0.259	—	6.73 ± 0.2^b
H^{al}	—	0.223	—	7.10 ± 0.2^b
F^{x}	0.229	0.110	0.003	8.70 ± 0.4

^aUncertainty in frequency due to the linewidth of each ENDOR absorption is included in the calculation of electron-nucleus distances.

^bBecause of the overlapping background resonance absorption of the enzyme, ENDOR features belonging to A_{\parallel} could not be identified. Resonances corresponding to A_{\perp} are identified on the basis of specific deuteration, and r is directly calculated from the value of A_{\perp} .

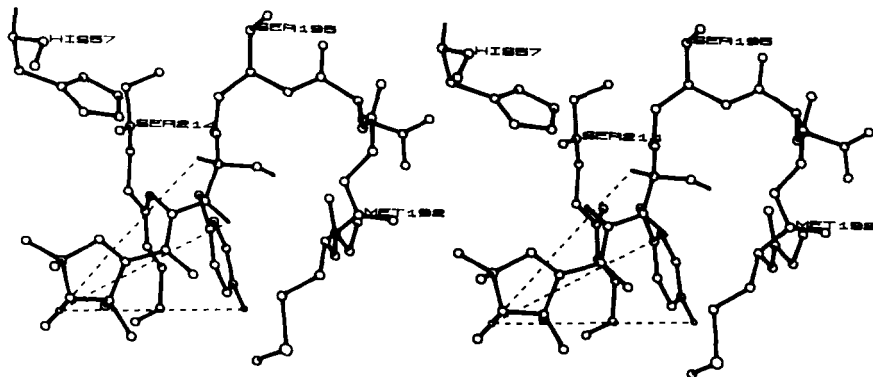
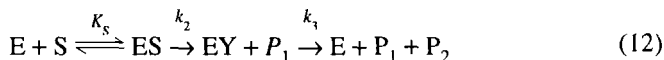


Figure 27. Stereoview of the transition-state inhibitor analog N -(2,2,5,5-tetramethyl-1-oxypyrrolinyl-3-carbonyl)- L -phenylalaninal modeled into the active site of α -chymotrypsin constrained by ENDOR-determined values of r in Table 7. The three electron-nucleus distances to H^{α} , H^{al} , and F^{x} are indicated by broken lines. Enzyme active site residues close to the inhibitor are also shown. On the basis of the inhibitor binding constant, it was possible to ensure for ENDOR samples that more than 91% of the spin-labeled L -phenylalaninal was bound to the enzyme at a concentration of 1.5×10^{-3} M in the EPR tube. From Jiang *et al.* (1998).

the three electron-to-nucleus distances in Table 7 and the requirement, according to the observed ^{19}F hf coupling of the $\zeta\text{F-phenylalaninal}$ analog, that the ^{19}F nucleus lie in, or be positioned very close to, the plane of the oxypyrrolinyl ring. According to these constraints, only an *S* configuration of the hemiacetal adduct of the aldehyde group with the nucleophilic O^γ of Ser-195 can be accommodated by ENDOR data (Jiang *et al.*, 1998). That the torsional angle relationships for χ_2 in the enzyme bound spin-labeled L-phenylalaninal were comparable to those illustrated by the middle Newman diagram in Fig. 18 and are similar to those found for the spin-labeled tryptophanyl acylenzyme reaction intermediate.

It was also demonstrated that when free in solution, the transition-state analog formed a hemiacetal adduct with solvent water; in neat methanol, it formed an adduct chemically analogous to that with the side chain of Ser-195 (Jiang *et al.*, 1998). The ENDOR electron-nucleus dipolar distances (*cf.*, Table 7) for the methanol adduct were compatible with both *R* and *S* configurations of the aldehyde carbonyl carbon; for the enzyme inhibitor adduct, only an *S* configuration was accommodated by the ENDOR data. Comparing the hemiacetal formed in neat methanol with the adduct formed in the active site of $\alpha\text{-chymotrypsin}$ illustrates how exacting ENDOR spectroscopic constraints can be in assigning molecular conformation and structure. In this respect, the requirement that the ^{19}F nucleus lie in the plane of the oxypyrrolinyl ring, as required by the \mathbf{H}_0 dependence of the hfc components (Jiang *et al.*, 1998), becomes particularly important, since the electron-nucleus distances for the free and enzyme-bound inhibitor in Table 7 are not distinguishably different. This situation illustrates the importance of applying not only distance constraints when assigning structure and conformation but also the requirement that the conformer is compatible with the pattern of the hfc components observed spectroscopically.

Methodology for employing a paramagnetic spin-labeled substrate to analyze the structure of an enzyme reaction intermediate is perhaps best illustrated by our studies using methyl *N*-(2,2,5,5-tetramethyl-1-oxypyrrolinyl-3-carbonyl)-L-tryptophanate as a substrate of $\alpha\text{-chymotrypsin}$. Conformational properties of the free spin-labeled molecule in solution are described in Sec. 4.1.2. The mechanism of $\alpha\text{-chymotrypsin}$ catalyzed hydrolysis of peptides and esters has been established to proceed according to the reaction Scheme in Eq. (12):



where ES is the Michaelis complex, EY is an acylenzyme intermediate formed through nucleophilic attack of the $-\text{CH}_2\text{OH}$ side chain of Ser-195 on the substrate, P_1 is the first product (in this case methanol) released from the active site on formation of the acylenzyme, and P_2 is the second product (in this case spin-labeled L-tryptophan) formed by breakdown of the acylenzyme intermediate, K_s is the

equilibrium constant for formation of the Michaelis complex, and rate constants k_2 and k_3 govern the reaction in the forward direction. (Backward reactions are omitted for ease of discussion, since formation of the reaction intermediate is considered here only under initial velocity conditions.) In general, it has been shown for a variety of substrates that k_2 is rate-determining in the hydrolysis of peptides, while k_3 is rate-limiting in the hydrolysis of esters (Hess, 1971). Since in Eq. (12) S, ES, EY, and P_2 contain the paramagnetic spin label, reaction conditions for the enzyme in solution must be found where only the acylenzyme species EY overwhelmingly predominates to facilitate straightforward spectroscopic and structural analysis.

Reaction conditions favoring formation of EY as the predominant species were determined by investigating the pH and temperature dependence of kinetic rate constants governing the reaction (Wells, 1987; Wells *et al.*, 1994). Since formation of the Michaelis complex ES occurs under diffusion controlled conditions, we need concern ourselves in Eq. 12 only with steps governed by the rate constants k_2 and k_3 under initial velocity conditions corresponding to two consecutive unimolecular reactions. For two consecutive unimolecular steps, differential equations describing the time-dependent formation and disappearance of each chemical species can be solved exactly, as illustrated in Fig. 28. In this figure the acylenzyme species EY has a maximum concentration approximately 2 minutes after initiating the reaction at 0° C and pD 4.7. Since other paramagnetic species are at low concentrations at this time, kinetic relationships favor a brief "window" approximately 2 minutes after mixing for maximum buildup of the paramagnetic spin-labeled acylenzyme reaction intermediate. The reaction is then quenched by rapid freezing to ensure

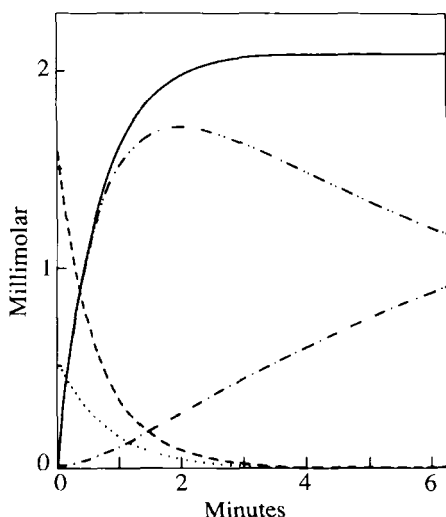


Figure 28. Simulation of the time course of hydrolysis of spin-labeled methyl L-tryptophan catalyzed by α -chymotrypsin. Enzyme and substrate concentrations were 2.7×10^{-3} and 2.1×10^{-3} M, respectively, as employed for ENDOR experiments. Simulation of the time course is based on estimates of K_s , k_2 , and k_3 from separate experiments (Wells, 1987; Wells *et al.*, 1994). Concentrations varying with time according to the reaction diagram in Eq. (12) are S (\cdots), ES ($--$), EY ($-\cdots-$), P_1 ($---$), P_2 ($-\cdot-\cdot-$). From Wells *et al.* (1994).

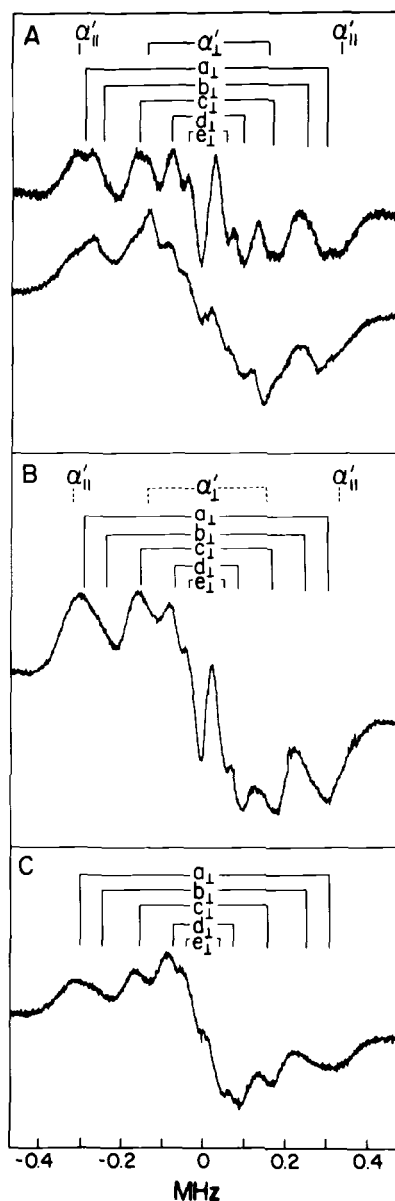


Figure 29. Proton ENDOR spectra of reaction mixtures of spin-labeled methyl *L*-tryptophanate with α -chymotrypsin with H_0 at setting *B*. Panel A: Top and bottom spectra of fully protonated substrate incubated with α -chymotrypsin for 3.5 min and for 5 h, respectively, at 0°C and pD 4.7. Incubation periods greater than ~ 1.5 min and up to 3.5 min produced essentially a constant spectrum, identical to that shown in the panel. A spectrum taken after 20 min of incubation was identical to the bottom spectrum in Panel A obtained after 5 h of incubation. This observation confirms the spectral properties of products in the reaction mixture upon hydrolysis of the substrate by α -chymotrypsin. Panel B: The ENDOR spectrum for the α -deuterio analog of the substrate incubated with α -chymotrypsin for 3.5 min. The hfc components for H^α are indicated by dashed line, as observed in Panel A. Panel C: the ENDOR spectrum for the reaction intermediate formed with a fully deuterated substrate analog. Line pairs labeled a–e are from active site residues in the enzyme. The cryosolvent mixture was d_6 -DMSO: D_2O (8:82 v/v) buffered to pD 4.7 with 0.05 M sodium cacodylate 0.1 M NaCl. Reprinted with permission from Wells *et al.* (1994).

preservation of the acylenzyme as the predominant species in the frozen solution. Such facile formation and breakdown of a reaction intermediate with a specific substrate having a short lifetime stands in marked contrast to the situation with nonspecific substrates e.g., *p*-nitrophenyl 2-(5-*n*-propyl)-furoate, for which the corresponding acylenzyme species has a half-life of approximately 15 minutes at 22° C (Wang *et al.*, 1981). For the latter substrate, *nonproductive* relationships between substrate and enzyme are responsible for its long-term stability while catalytically productive relationships account for the lability of reaction intermediates formed with highly specific substrates. Clearly the objective of structurally characterizing intermediates of enzyme catalyzed reactions should be carried out using only kinetically specific substrates.

Figure 29 shows proton ENDOR spectra of the acylenzyme reaction intermediate, spin-labeled L-tryptophanyl- α -chymotrypsin. The spectra indicate that resonances for H $^{\alpha}$ of the amino acid substrate can be identified through their absence upon specific deuterium substitution. Similarly using a fluorine-substituted tryptophan leads to identifying ^{19}F resonance features that specify side chain orientation (Wells *et al.*, 1994). The conformation of the acyl portion of the substrate was then modeled according to the electron-nucleus distances estimated on the basis of the ENDOR splittings. Figure 30 shows the acyl portion of the substrate and its relationship to critical active site residues constructed on the basis of such ENDOR experiments. The indole side chain was positioned in the hydrophobic pocket of

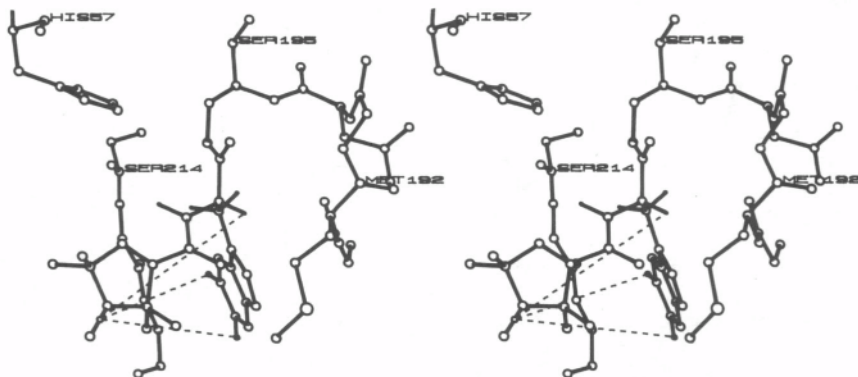


Figure 30. Stereo diagram of the acyl moiety of the spin-labeled tryptophanyl-acylenzyme reaction intermediate of α -chymotrypsin. Active site residues close to the acyl moiety are labeled. The conformation is constrained within van der Waals hard-sphere limits of active site residues by ENDOR determined electron-nucleus distances for H $^{\alpha}$ (6.5 ± 0.2 Å) and the F C3 - and F M2 -substituents of the indole ring (10.3 Å each) (indicated by broken lines). Although no difluoro-substituted substrate was used in these studies, ENDOR-determined r values for F C3 and F M2 substituents were determined in separate experiments and distance constraints applied simultaneously (Wells *et al.*, 1994).

the enzyme, and an ester linkage of the substrate's carboxylate group was constructed with the $-\text{CH}_2\text{OH}$ side chain of Ser-195. The conformation of the acyl moiety of the substrate in the active site of the reaction intermediate differs significantly from that of the free substrate in solution and is torsionally similar to the nearly eclipsed structure of high potential energy with respect to the $\text{C}^\beta\text{-C}^\gamma$ bond in Fig. 18. Torsional alterations induced in the substrate by binding to the enzyme to form a catalytically productive acylenzyme reaction intermediate underlie the basis of specificity of substrate recognition in the enzyme-catalyzed reaction (Wells *et al.*, 1994).

5.2.2. Carboxypeptidase A

Applying cryoenzymologic methods to elucidate the reaction mechanism of carboxy peptidase A, an important example of a proteolytic enzyme in all major biochemistry textbooks (*cf.*, Parson, 1993; Stryer, 1995), brought perhaps the greatest amount of new information about its mechanism of action than for any other enzyme. For instance, by using organic aqueous solvents and subzero temperatures, kinetic (Makinen *et al.*, 1976, 1979, 1982), nucleophile trapping (Sander, 1984; Sander and Witzel, 1985), and spectroscopic (Kuo and Makinen, 1982; Kuo *et al.*, 1983; Kuo and Makinen, 1985; Mustafi and Makinen, 1994) studies show that (1) reaction for both ester and peptide hydrolysis catalyzed by carboxypeptidase A proceeds by formation of a mixed anhydride, acylenzyme intermediate; (2) metal-bound water is responsible for hydrolytic breakdown of the acylenzyme; and (3) metal ion becomes penta-liganded in the acylenzyme reaction intermediate to accommodate coordination of both the metal-bound water molecule and the carbonyl oxygen of the scissile bond. In contrast results of x-ray studies of enzyme-inhibitor complexes (Quioco and Lipscomb, 1971; Christianson and Lipscomb, 1989) and chemical (Breslow and Wernick, 1977) and kinetic (Vallee *et al.*, 1983; Vallee and Galdes, 1984) studies were invoked earlier to suggest that (1) the reaction proceeds through a general base-catalyzed mechanism; (2) the substrate displaces the metal-bound water; and (3) the active site metal ion remains tetra-liganded throughout the reaction. These vastly different interpretations of the reaction mechanism derive simply by chemical and structural characterization of a true reaction intermediate.

Kuo *et al.* (1983) demonstrated that *O*-[3-(2,2,5,5-tetramethyl-1-oxypyrrolinyl)-propen-2-oyl]-*L*- β -phenyllactate, (TEPOPL), a spin-label analog of the highly specific substrate *O*-(para-chlorocinnamoyl)-*L*- β -phenyllactate, is an esterolytic substrate of Carboxypeptidase A with high catalytic reactivity. Cryokinetic studies were carried out to stabilize a reaction intermediate of carboxypeptidase A formed with TEPOPL for combined ENDOR and molecular graphics-based structural analysis of the mixed anhydride (acylenzyme) intermediate (Mustafi and Makinen, 1994). Tyrosine residues were acetylated to distinguish resonances of

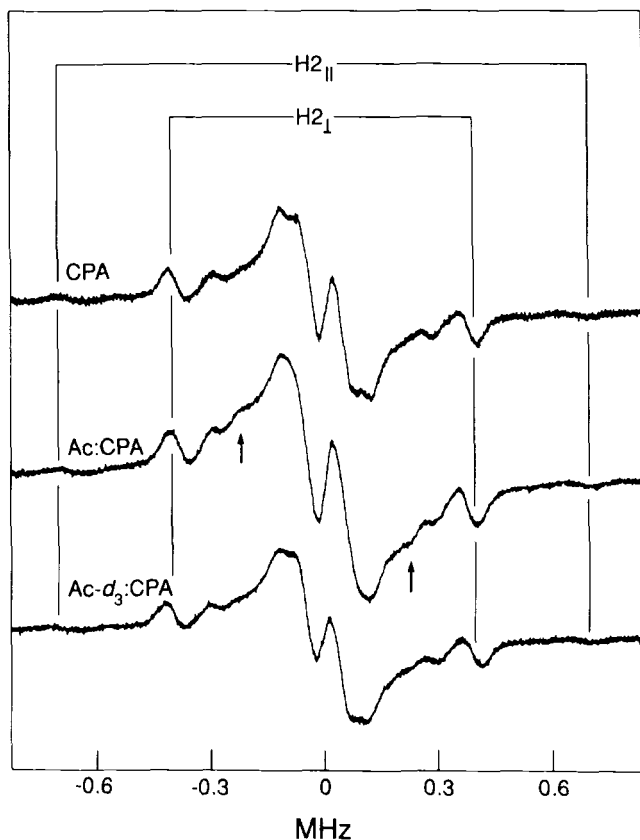
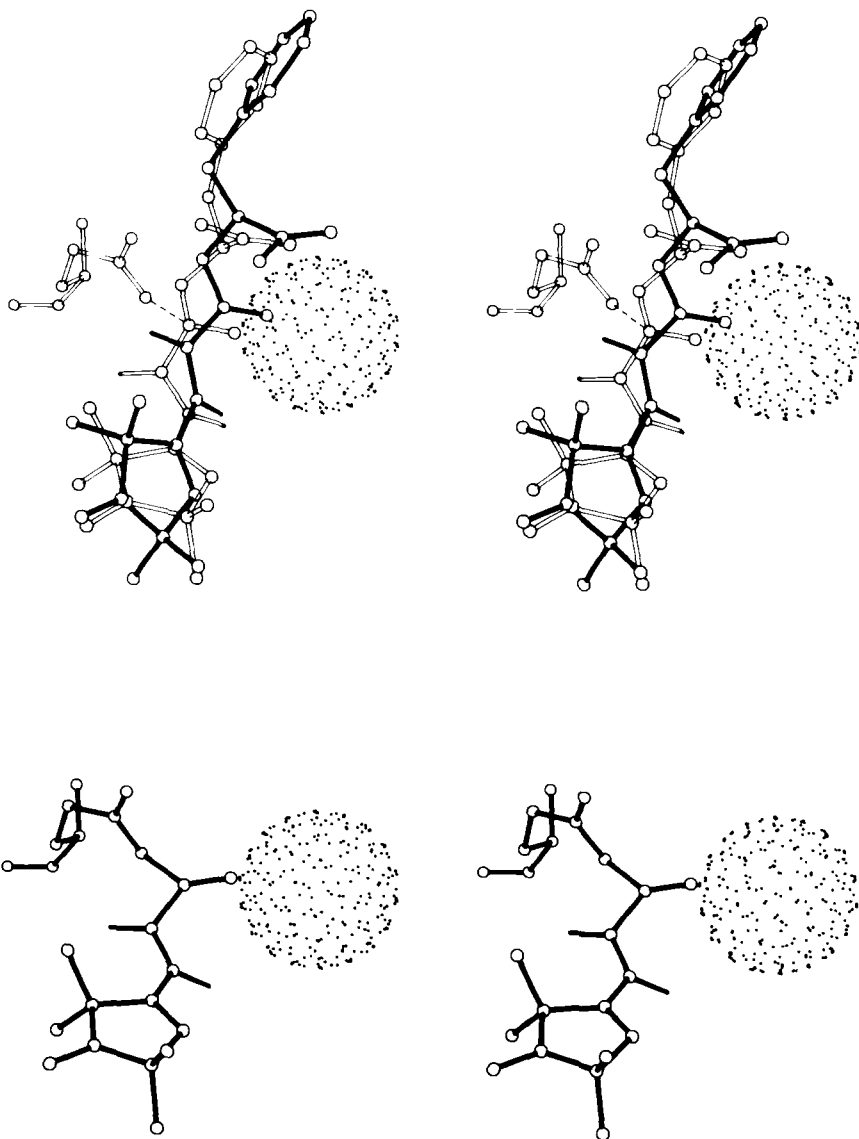


Figure 31. Proton ENDOR spectra of reaction intermediates of [α -D]TEPOPL formed with carboxypeptidase A (CPA) (*top spectrum*), acetyl-CPA (*middle spectrum*), and d_3 -acetyl-CPA (*bottom spectrum*). Line splittings corresponding to principal hfc components for H^{β} in the propenoyl portion of the substrate are indicated by the stick diagram. Resonance features for acetyl protons are indicated by arrows. The acetylated enzyme was shown to catalyze substrate hydrolysis similarly to the active enzyme with no significant change in K_M . Reprinted with permission from Mustafi and Makinen (1994).

Figure 32. Stereodiagram of the conformation of TEPOPL and the spin-labeled propenoyl moiety in the active site of carboxypeptidase A. In the upper diagram, the structure of intact, bound TEPOPL (*solid bonds*), derived from modeling studies, is compared to that of the putative tetrahedral adduct (*open bonds*). The intact TEPOPL molecule was modeled in the active site on the basis of the ENDOR defined structure of the spin-labeled ethyl propenoate analog (Mustafi *et al.*, 1990a). Also illustrated in this diagram is the Glu-270 residue (*open bonds*). The broken line connects the tetrahedral carbon of the substrate to the incoming nucleophilic O^{i2} of Glu-270. Comparing relative positions of the phenyllactate side chain shows that retaining the side chain in a position similar to that of the intact substrate requires torsional rotation around the ester C-O bond as well as around O-C $^{\alpha}$, C $^{\alpha}$ -C $^{\beta}$ and C $^{\beta}$ -C $^{\gamma}$ bonds on subsequent formation of the tetrahedral adduct, in accord with stereoelectronic requirements. The



bottom diagram illustrates the spin-labeled propenoyl moiety in mixed anhydride linkage with the side chain of Glu-270. In both diagrams the Zn^{2+} ion is shown as a dotted surface of 2.0 Å radius. Careful inspection of the propenoyl side chain shows that the change in conformation of the propenoyl moiety from that in the free substrate to that in the (mixed anhydride) acylenzyme corresponds to torsional alteration of the spin-labeled propenoyl moiety. Reprinted with permission from Mustafi and Makinen (1994).

Tyr-198 or Tyr-248 from other residues in the active site and to determine their positions relative to the nitroxyl group in the reaction intermediate. Figure 31 shows ENDOR spectra of the reaction intermediate to illustrate proton resonances from the H^β position of the α -deuterio substrate analog [α - 2H]TEPOPL and from the CH_3 -group of acetyl-Tyr-198 of the chemically modified enzyme. Figure 32 shows conformation of the substrate in the active site based on ENDOR studies.

An important aspect of the structural analysis of the reaction intermediate of carboxypeptidase A in Fig. 32 is that the ENDOR spectrum of the reaction intermediate can be accounted for only by a mixed anhydride acylenzyme species in which the spin-labeled propenoyl moiety has covalently acylated the carboxylate group of Glu-270 (Mustafi and Makinen, 1994). Kinetic and spectroscopic results for stabilizing the intermediate in a ternary organic aqueous (40% MeOH:20% EGOH:40% H_2O) cosolvent mixture at $-60^\circ C$ were compared to those in aqueous, saturated NaCl at $-20^\circ C$. Both sets of results confirm a previous EPR-based structure analysis of the reaction intermediate (Kuo *et al.*, 1983) and extend the methodology to identify positions of active site amino acid side chains in the reaction intermediate.

6. FUTURE DIRECTIONS

6.1. Enhanced Resolution of ENDOR Spectra

To consider other areas in which to apply ENDOR spectroscopy of nitroxyl spin labels, we evaluate first those factors that govern the resolving power of ENDOR. The variety of ENDOR spectra presented in this chapter, particularly in Figs. 17, 29, and 31, demonstrate that resonances of distant protons are clustered near the free proton Larmor frequency according to the dipolar relationships depicted in Eq. (4). Thus, the intrinsic linewidth of ENDOR features limit the accuracy of identifying different classes of nuclei on the basis of the electron-to-nucleus separation r . As pointed out by Wells and Makinen (1988), to resolve the ENDOR lines of two closely spaced protons with r values of $\sim 7 \text{ \AA}$, electron-nucleus separations must differ by at least 0.2 \AA for a 20 kHz peak-to-peak separation. This is generally the linewidth of resonance features and the modulation depth of the rf field in our experiments. For r values of $\sim 10 \text{ \AA}$, electron-nucleus separations must differ by $\sim 1 \text{ \AA}$ for the same 20 kHz peak-to-peak separation. These estimates are readily borne out by results in Fig. 15 and Table 3 for spin-labeled methyl L-alanate. Two sets of hfc components were resolved for β -methyl protons differing in electron-proton separations by about 0.4 \AA for values of $r \sim 7.5 \text{ \AA}$. Torsional angle calculations constrained by ENDOR distances confirmed the interpretation that two of the β -methyl protons were equidistant from the unpaired electron in the nitroxyl

group, while the third was sufficiently further away to be resolved in the ENDOR spectrum.

While factors just described provide quantitative limits for ENDOR linewidths and electron-to-nucleus distances governing spectral resolution, another factor that must be addressed to study macromolecules is that disordered hydrogens in the protein provide overlapping contributions clustered around the Larmor frequency and these are an important source of dipolar broadening of the resonance features of interest. For instance, although β -methylene protons of aromatic side chains of spin-labeled amino acids were readily resolved for the free substrates or products (Wells *et al.*, 1990; Joela *et al.*, 1991; Jiang *et al.*, 1998), we were not able to identify β -methylene protons of the spin-labeled tryptophanyl residue in the acylenzyme reaction intermediate of α -chymotrypsin (Wells, 1987; Wells *et al.*, 1994) or of the spin-labeled L-phenylalaninal adduct in α -chymotrypsin (Jiang *et al.*, 1998) because of broad overlapping contributions from active site residues (*cf.*, Table 7). In further studies of macromolecules, it will be necessary to decrease or remove overlapping contributions of distant, disordered protons near the Larmor frequency. This objective can be met only by biosynthetic deuteration of proteins. In addition to eliminating overlapping resonances, generating a deuterated background should also improve the resolution of proton ENDOR features of individual residues because of decreased dipolar broadening.

There are three general patterns of deuterium protein enrichment that can be achieved by biosynthetic methods: Random fractional deuteration where all carbon-bound hydrogen positions are uniformly enriched to an intermediate level from 0–100%, selective incorporation of deuterated residues in a protiated background, and selective incorporation of protiated residues in a protein uniformly enriched with deuterium (LeMaster, 1989). Since a variety of isotope enrichment methods are applied in present day macromolecular structure analysis by multinuclear NMR methods, including deuterium (Crespi *et al.*, 1968; LeMaster, 1989; Venters *et al.*, 1995; Nietlispach *et al.*, 1996), this methodology can be similarly applied for ENDOR investigations by using strains of *E. coli* engineered to overproduce specific gene products. It is probable that not only background resonances can be eliminated but also the resolution of proton resonance features of both active site residues and the substrate will be enhanced against a deuterated background.

It was observed in NMR studies of proteins that the resolution and sensitivity of ^1H NMR experiments are improved by fractional deuteration because the dipole-dipole broadening by nearby ^1H nuclei is decreased (Crespi *et al.*, 1968; Markley *et al.*, 1968; LeMaster, 1989). Similarly eliminating the source of ^1H dipole-dipole broadening of ENDOR features should enhance resolution and increase sensitivity. Comparing ENDOR spectra of specifically deuterated analogs of spin-labeled amino acids, for instance, those of spin-labeled phenylalanine (Joela *et al.*, 1991), shows that individual proton resonance features are greatly enhanced by deuteration of nearby sites on the molecule.

In addition to chemical and biosynthetic methods for deuterium enrichment, enhancing spectral resolution may also be achieved through application of new developments in instrumentation, such as pulsed ENDOR (Schweiger, 1982; Togni *et al.*, 1993), ENDOR with higher frequency (20–35 GHz) EPR spectrometers, and stochastic ENDOR (Brüggeman and Niklas, 1994), which are known to provide substantial improvement in signal-to-noise and spectral resolution over that of continuous wave X-band methodology. We believe that these combined newer developments will extend investigation of structure-function relationships of biological macromolecules by ENDOR spectroscopy. When directed toward problems that cannot be readily addressed by other physical methods and demand precise characterization of local structure, the rewards of applying ENDOR spectroscopy can be great. We personally feel that our initiatives to characterize true intermediates of enzyme-catalyzed reactions, as described in Sec. 5, are modest beginnings compared to the wealth of structural information yet to be gained by studying macromolecular structure and function through ENDOR spectroscopy.

6.2. Enzyme Reaction Intermediates

Applying EPR methods to characterize structural properties of true catalytically competent enzyme reaction intermediates requires a paramagnetic probe that is not chemically modified in the course of the reaction. Naturally occurring paramagnetic sites in enzymes often exhibit such spectroscopic properties as high anisotropy, which renders structural analysis difficult [*cf.*, Hurst *et al.* (1985)], or they undergo changes in spin and oxidation state through chemical modification in the course of the reaction. Structural characterization of enzyme reaction intermediates by EPR and ENDOR, thus, requires introduction of an artificial, stable paramagnetic probe. This requirement can be addressed incisively by introducing nitroxyl spin-labeled molecules as catalytically specific, spectroscopic substrate-probes in the active site as a direct means of investigating the structural basis of enzyme action. An important objective in such studies is of course to design a spectroscopic substrate-probe that does not perturb the enzyme from its native functional structure. By carefully selecting the attachment site of the spin label to the substrate, we found that spin-labeled substrates can be synthesized that according to kinetic criteria exhibit high specificity comparable to that of “classical” substrates. Table 8 lists a variety of spin-labeled substrates synthesized in our laboratory that illustrate this point; kinetic parameters of structurally similar “classical” substrates are provided for comparison.

In our laboratory we endeavored to develop a method of three-dimensional structure determination and conformation analysis of cryokinetically stabilized enzyme reaction intermediates by applying ENDOR spectroscopy, and the results employing α -chymotrypsin and carboxypeptidase A provide general guiding principles for further applying this methodology to a variety of enzyme-catalyzed

Table 8
Comparison of Steady-State Kinetic Parameters of Classical and Structurally Similar Spin-Labeled Substrates

Enzyme	Substrate ^a	k_{cat} (sec ⁻¹)	K_M ($\times 10^3$ M)	Ref.
α -chymotrypsin	Methyl <i>N</i> -acetyl-L-tryptophanate	27.7	0.095	<i>b</i>
	Methyl <i>N</i> -(spin-label)-L-tryptophanate	4.5	0.05	<i>c</i>
carboxypeptidase A	<i>N</i> -(carbobenzoxy)-glycyl-L-phenylalanine	24.1	1.95	<i>d</i>
	<i>N</i> -(spin-label)-glycyl- <i>p</i> -nitro-L-phenylalanine	91.0	1.0	<i>e</i>
	<i>O</i> -(<i>p</i> -chlorocinnamoyl)-L- β -phenyllactate	73.0	0.098	<i>f</i>
	<i>O</i> -[(3-(2,2,5,5-tetramethyl-1-oxypyrrrolinyl)-propen-2-oyl)-L- β -phenyllactate	2.3	0.096	<i>g</i>
papain	<i>N</i> -(carbobenzoxy)- <i>p</i> -nitrophenyl glycinate	5.2	0.008	<i>h</i>
	<i>N</i> -(spin-label)- <i>p</i> -nitrophenyl glycinate	3.9	0.009	<i>i</i>
β -lactamase	6- <i>N</i> -benzyl-penicillanic acid	1920	0.065	<i>j</i>
	6- <i>N</i> -(spin-label)-penicillanic acid	1810	0.087	<i>k</i>
Horse liver alcohol dehydrogenase	Benzyl alcohol	2.4	0.083	<i>l</i>
	3-(2,2,5,5-tetramethyl-1-oxypyrrrolinyl)-2-propen-1-ol	12.8	2.2	<i>m</i>
	Benzaldehyde	3.0	0.020	<i>n, o</i>
	3-(2,2,5,5-tetramethyl-1-oxypyrrrolinyl)-2-propenal	32.0	1.48	<i>p</i>

^aSpin label designates the [2,2,5,5-tetramethyl-1-oxypyrrrolinyl-3-carboxy] group covalently attached at the carbonyl carbon position to the amine nitrogen of the amino acid.

^bZerner and Bender, 1964.

^cWells *et al.*, 1994.

^dDavis *et al.*, 1968.

^eHinds, D. A., and Makinen, M. W., unpublished observations.

^fMakinen *et al.*, 1979.

^gKuo *et al.*, 1983.

^hGlazer, A. N., and Smith, E. L., 1971.

ⁱSchlunk, P., and Makinen, M. W., unpublished observations.

^jChristensen *et al.*, 1990.

^kMustafi and Makinen, 1995.

^lMaret and Makinen, 1991.

^mMustafi *et al.*, 1993b; Boisvert *et al.*, 1993.

ⁿWeidig *et al.*, 1977.

^oJacobs *et al.*, 1974.

^pBoisvert *et al.*, 1993.

reactions. Since reaction intermediates are accumulated in fluid organic aqueous cosolvent mixtures that form glasses upon freezing, there appears to be no deleterious effect on protein structure. The concentration of the intermediate, as just described, can be made high ($> 10^{-3}$ M), aiding signal detection. As demonstrated in Sec. 4, ENDOR provides a precise means for determining structures of the free substrate and product. We find that the structure and conformation of the free substrate and product are conformationally distinct from that of the enzyme-bound molecule (Wells *et al.*, 1994; Mustafi and Makinen, 1994). This structural comparison yields important insights into the molecular basis of the specificity of substrate recognition by the enzyme and how the substrate is conformationally (torsionally) altered during the binding process to be accommodated into the active site.

It is important to carry out further studies in this direction to unravel details of the structural basis of enzyme catalytic action by monitoring catalytically productive stereochemical interactions in the active site. For all of the enzymes listed in Table 8, cryoenzymologic studies have been carried out with "classical" substrates (Cartwright and Fink, 1981). Extending such studies to include spin-labeled substrates for ENDOR structural investigations of reaction intermediates can therefore be relatively straightforward.

6.3. Spin-Labeled Proteins for ENDOR

From this chapter it is evident that ENDOR spectroscopy of nitroxyl spin labels is most incisively applied to problems where local structural details must be precisely determined. While we demonstrated that the nitroxyl group can be used as the paramagnetic probe for assigning geometric locations of protons and fluorine substituents up to 11 Å from the unpaired electron (Wells and Makinen, 1988; Wells *et al.*, 1990; Joela *et al.*, 1991; Wells *et al.*, 1994), biosynthetic methods for deuteration of proteins, as described in Sec. 6.1., ensure that adequate resolution of resonance features can be achieved for structural analysis. However, the application of ENDOR with nitroxyl spin label probes need not be viewed only as a method suitable for enzyme reaction intermediates. This methodology is well-designed to investigate structure-function relationships of biological macromolecules in general on a variety of problems, for example protein folding, formation of multicomponent complexes, and photoactivated conformational changes in protein structure.

The method of site-directed spin-labeling of proteins, based on analysis of EPR spectra, has proven to be a useful approach for investigating protein structure and dynamics (Hubbell and Altenbach, 1994). This methodology could be further extended by applying ENDOR spectroscopy. The general approach is to incorporate single reactive cysteine residues biosynthetically into proteins to provide points of attachment for nitroxyl spin labels. Reaction of the spin label (2,2,5,5-tetramethyl-1-oxyprolinyl-3-methyl) methane thiolsulfonate (Berliner *et al.*, 1982) according to the reaction scheme in Diagram 6 is highly specific. The technique is based on

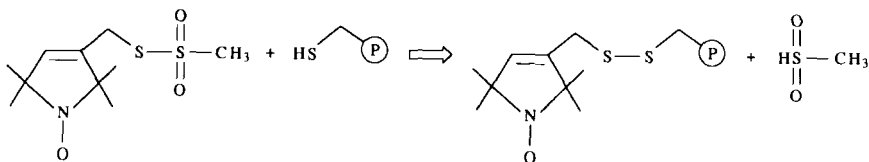


Diagram 6.

the use of methyl methane thioisulfonate to incorporate radioisotopically labeled methyl groups into proteins to quantify the number of free sulfhydryl residues (Kenyon and Bruice, 1977). The spin label reagent reacts with both exposed and buried cysteine residues.

Site-directed spin labeling was applied to determine topology in membrane proteins, locate helical and β -sheet regions in proteins, and to follow protein conformational changes (Hubbell and Altenbach, 1994). Using a thioisulfonate derivative with the unsaturated five-membered oxypyrrolinyl ring, as shown in the preceding reaction diagram, ensures that the spin label probe is suitable as a structural probe for ENDOR spectroscopy. Coupled with biosynthetic methods for random or site-specific deuteration of proteins, site-specific spin labeling, thus could be advantageously applied with ENDOR spectroscopy to determine structure and conformation in a variety of structure-function studies of biological macromolecules.

ACKNOWLEDGMENT. This work was supported by a grant from the National Institutes of Health (GM 21900).

REFERENCES

- Ament, S. S., Wetherington, J. B., Noncrief, J. W., Flohr, K., Nochizuki, M., and Kaiser, E. T., 1973, *J. Am. Chem. Soc.* **95**:7896.
- Atherton, N. M., and Shackleton, J. F., 1980, *Mol. Phys.* **39**:1471.
- Atherton, N. M., and Shackleton, J. F., 1984, *Chem. Phys. Lett.* **103**:302.
- Bates, R. B., Hurby, V. J., and Kriek, G. R., 1979, *Acta Crystallogr.* **B35**:188.
- Bauer, R. S., and Berliner, L. J., 1979, *J. Mol. Biol.* **128**:1.
- Benner, S. A., 1988, Stereoelectronic analysis of enzymatic reactions, in *Mechanistic Principles of Enzyme Activity*. (J. Liebman and A. Greenberg eds.) (VCA, New York), pp. 27-74.
- Berliner, L. J., 1970, *Acta Crystallogr.* **B26**:198.
- Berliner, L. J., ed., 1976, *Spin Labeling: Theory and Application* (Academic, New York).
- Berliner, L. J., 1978, *Methods Enzymol.* **49**:418.
- Berliner, L. J., Grunwald, J., Hankovszky, H. O., and Hideg, K., 1982, *Anal. Biochem.* **119**:450.
- Biehl, R., Plato, M., and Möbius, K., 1975, *J. Chem. Phys.* **63**:3515.
- Boeyens, J. C. A., and Kruger, G. J., 1970, *Acta Crystallogr.* **B26**:668.

- Boisvert, W. E., Mustafi, D., Kasa, S., Makinen, M. W., Halpern, H. J., Yu, C., Barth, E., and Peric, M., 1993, Kinetically specific spin label substrates of liver alcohol dehydrogenase and liver aldehyde dehydrogenase, in *Enzymology and Molecular Biology of Carbonyl Metabolism 4* (H. Weiner, D. W. Crabb, and T. G. Flynn, eds.) (Plenum, New York), pp. 501–12.
- Boles, M. O., Girven, R. J., and Gane, P. A. C., 1978, *Acta Crystallogr.* **B34**:461.
- Bondi, A., 1964, *J. Phys. Chem.* **68**:441.
- Breslow, R., and Wemick, D. L., 1977, *Proc. Natl. Acad. Sci. USA* **74**:1303.
- Brüggeman, W., and Niklas, J. R., 1994, *J. Magn. Reson.* **A108**:25.
- Brustolon, M., Maniero, A. L., and Segre, U., 1985, *Mol. Phys.* **55**:713.
- Bürgi, H. B., Dunitz, J. D., and Shefter, E., 1974a, *Acta Crystallogr.* **B30**:1517.
- Bürgi, H. B., Dunitz, J. D., Lehn, J. M., and Wipff, G., 1974b, *Tetrahedron* **30**:1563.
- Capiomont, A., 1972, *Acta Crystallogr.* **B28**:2298.
- Capiomont, A., Bordeaux, D., and Lajzerowicz, J., 1972, *C. R. Acad. Sci., Paris* **275C**:317.
- Capiomont, A., Chion, B., Lajzerowicz-Bonneteau, J., and Lemaire, H., 1974, *J. Chem. Phys.* **60**:2530.
- Cartwright, S. J., and Fink, A. L., 1981, *CRC Crit. Rev. Biochem.* **11**:145.
- Chen, R., Gorenstein, D. G., Kennedy, W. P., Love, G., Nurse, D., and Schultz, R. M., 1979, *Biochemistry* **18**:921.
- Chien, J. C. W., and Dickinson, L. C., 1981, EPR crystallography of metalloproteins and spin-labeled enzymes, in *Biological Magnetic Resonance*, vol. 3 (L. J. Berliner and J. Reuben, eds.) (Plenum, New York), pp. 155–212.
- Christensen, H.; Martin, M. T.; and Waley, S. G., 1990, *Biochem. J.* **266**:853.
- Christianson, D. W., and Lipscomb, W. N., 1989, *Acc. Chem. Res.* **22**:62.
- Cohen, A. H., and Hoffman, B. M., 1973, *J. Am. Chem. Soc.* **95**:2061.
- Cook, R. J., and Whiffen, D. H., 1964, *Proc. Phys. Soc. London* **84**:845.
- Coppens, P., 1967, *Science* **158**:1577.
- Cotrait, P. M., and Barrans, Y., 1974, *Acta Crystallogr.* **B30**:510.
- Crespi, H. L., Rosenberg, R. M., and Katz, J. J., 1968, *Science* **161**:795.
- Davis, R. C., Riordan, J. F., Auld, D. S., and Vallee, B. L., 1968, *Biochemistry* **7**:1090.
- Davis, T. D., Christofferson, R. E., and Maggiora, G. N., 1975, *J. Am. Chem. Soc.* **97**:1347.
- Deslongchamps, P., 1983, *Stereoelectronic Effects in Organic Chemistry* (Pergamon, Oxford, UK).
- Douzou, P., 1977, *Cryobiochemistry* (Academic, New York).
- Duke, E. M. H., Hadfield, A., Walters, S., Wakatsuki, S., Bryan, R. K., and Johnson, L. N., 1992, *Phil. Trans. Roy. Soc. Lond.* **A340**:245.
- Duke, E. M. H., Wakatsuki, S., Hadfield, A., and Johnson, L. N., 1994, *Protein Sci.* **3**:1178.
- Espie, J. C., and Rassat, A., 1971, *Bull. Soc. Chim. Fr.* **12**:4385.
- Evans, J. N. S., Appleyard, R. J., and Shuttleworth, W. A., 1993, *J. Am. Chem. Soc.* **115**:1588.
- Feher, G., 1956, *Phys. Rev.* **103**:834.
- Feher, G., 1959, *Phys. Rev.* **114**:1219.
- Fields, R. A., and Hutchison, C. A., Jr., 1985, *J. Chem. Phys.* **82**:1711.
- Glazer, A. N., and Smith, E. L., 1971, Papain and other protein sulfhydryl proteolytic enzymes, in *The Enzymes*, vol. 3 (P. D. Boyer, ed.) (Academic, New York) pp. 501–46.
- Griffith, O. H., Cornell, D. W., and McConnell, H. M., 1965, *J. Chem. Phys.* **43**:2909.
- Gullion, T., and Schaefer, J., 1989, *Adv. Magn. Reson.* **13**:57.
- Hajdu, J., Acharya, K. R., Stuart, D. I., Barford, D., and Johnson, L. N., 1988, *Trends Biochem. Sci.* **13**:104.
- Hamilton, C. L., and McConnell, H. M., 1968, Spin labels, in *Structural Chemistry and Molecular Biology* (A. Rich and N. Davidson, eds.) (W. H. Freeman, San Francisco), pp. 115–49.
- Hayat, H., and Silver, B. L., 1973, *J. Phys. Chem.* **77**:72.
- Henderson, T. A., Hurst, G. C., and Kreilick, R. W., 1985, *J. Am. Chem. Soc.* **107**:7299.

- Hess, G. P., 1971, Chymotrypsin—Chemical Properties and Catalysis, in *The Enzymes*, vol. 3 (P. D. Boyer, ed.) (Academic, New York), pp. 213–48.
- Hoffman, B. M., and Gurbiel, R. J., 1989, *J. Magn. Reson.* **82**:309.
- Hoffman, B. M., Martinsen, J., and Venters, R. A., 1984, *J. Magn. Reson.* **59**:110.
- Hoffman, B. M., Venters, R. A., and Martinsen, J., 1985, *J. Magn. Reson.* **62**:537.
- Hubbell, W. L., and Altenbach, C., 1994, *Curr. Opin. Struct. Biol.* **4**:566.
- Hurst, G. C., Henderson, T. A., and Kreilick, R. W., 1985, *J. Am. Chem. Soc.* **107**:7294.
- Hutchison, C. A., Jr., and McKay, D. B., 1977, *J. Chem. Phys.* **66**:3311.
- Hwang, J. S., Mason, R. P., Hwang, L. P., and Freed, J. H., 1975, *J. Phys. Chem.* **79**:489.
- Hyde, J. S., and Subczynski, W. K., 1984, *J. Magn. Reson.* **56**:125.
- Iijima, H., Dunbar J.B., Jr. and Marshall, G. R., 1987, *Proteins: Struct. Funct. Genet.* **2**:330.
- Jacobs, J. W., McFarland, J. T., Wainer, I., Jeanmaier, D., Ham, C., Hamm, K., Wnuk, M., and Lam, M., 1974, *Biochemistry* **13**:60.
- Jarvie, T. P., Went, G. T., and Mueller, K. T., 1996, *J. Am. Chem. Soc.* **118**:5330.
- Jenzen, E. G., Oehler, U. M., Haire, L., and Kotake, Y., 1986, *J. Am. Chem. Soc.* **108**:6858.
- Jiang, F. S., Tsai, S. W., Chen, S., and Makinen, M. W., 1998, *J. Phys. Chem.* **B102**:4619.
- Joela, H., Mustafi, D., Fair, C. C., and Makinen, M. W., 1991, *J. Phys. Chem.* **95**:9135.
- Jost, P. C., and Griffith, O. H., 1978, *Methods Enzymol.* **49**:369.
- Karplus, M., and Fraenkel, G. K., 1961, *J. Chem. Phys.* **35**:1312.
- Kasa, S., Huuskonen, J., and Makinen, M. W., 1996, manuscript in preparation.
- Keana, J. F. W., *Chem. Rev.* **78**:37.
- Kenyon, G. A., and Bruice, T. W., 1977, *Methods Enzymol.* **47E**:407.
- Kirn, B. L., Greiner, S. P., and Kreilick, R. W., 1995, *Mol. Phys.* **84**:511.
- Kirby, A. J., 1983, *The Anomeric Effect and Related Stereoelectronic Effects at Oxygen* (Springer-Verlag, Berlin).
- Kirste, B., Krüger, A., and Kurreck, H., 1982, *J. Am. Chem. Soc.* **104**:3850.
- Kreilick, R. W., 1967, *J. Phys. Chem.* **46**:4260.
- Kotake, Y., Tomita, Y., and Kuwata, K., 1985, *J. Phys. Chem.* **89**:207.
- Kuo, L. C., and Makinen, M. W., 1982, *J. Biol. Chem.* **257**:24.
- Kuo, L. C., and Makinen, M. W., 1985, *J. Am. Chem. Soc.* **107**:5255.
- Kuo, L. C., Fukuyama, J. M., and Makinen, M. W., 1983, *J. Mol. Biol.* **163**:63.
- Kurreck, H., Kirste, B., and Lubitz, W., 1988, *Electron Nuclear Double-Resonance Spectroscopy of Radicals in Solution: Application to Organic and Biological Chemistry* (VCH, New York).
- Lajzerowicz-Bonneteau, J., 1976, Molecular structures of nitroxides, in *Spin Labeling* (L. J. Berliner, ed.) (Academic, New York), pp. 239–49.
- Lee, B., and Richards, F. M., 1971, *J. Mol. Biol.* **55**:379.
- Lee, S., Ames, D. P., and Brown, I. M., 1984, *J. Chem. Phys.* **81**:5272.
- Leigh, J. S., Jr., 1970, *J. Chem. Phys.* **52**:2608.
- LeMaster, D. M., 1989, *Methods Enzymol.* **177**:23.
- Leniart, D. S., Vedrine, J. C., and Hyde, J. S., 1970, *Chem. Phys. Lett.* **6**:637.
- Makinen, M. W., and Fink, A. L., 1977, *Annu. Rev. Biophys. Bioeng.* **6**:301.
- Makinen, M. W., and Kuo, L. C., 1983, Spin label probes of enzyme action, in *Magnetic Resonance in Biology*, vol. 2 (J. S. Cohen, ed.) (Wiley, New York), pp. 53–94.
- Makinen, M. W., and Mustafi, D., 1995, The vanadyl ion: molecular structure of coordinating ligands by electron nuclear double-resonance spectroscopy, in *Metal Ions in Biological Systems*, vol. 31 (H. Sigel and A. Sigel, eds.) (Marcel Dekker, New York), pp. 89–127.
- Makinen, M. W., Kuo, L. C., Dymowski, J. J., and Jaffer, S., 1979, *J. Biol. Chem.* **254**:356.
- Makinen, M. W., Yamamura, K., and Kaiser, E. T., 1976, *Proc. Natl. Acad. Sci. USA* **73**:3882.
- Makinen, M. W., Fukuyama, J. M., and Kuo, L. C., 1982, *J. Am. Chem. Soc.* **104**:2667.
- Maret, W., and Makinen, M. W., 1991, *J. Biol. Chem.* **266**:20636.

- Markley, J. L., Potter, I., and Jardetzky, O., 1968, *Science* **161**:1249.
- McConnell, H. M., and McFarland, B. G., 1970, *Quart. Rev. Biophys.* **3**:91.
- McConnell, H. M., and Strathdee, J., 1959, *Mol. Phys.* **2**:129.
- Möbius, K., and Biehl, R., 1979, Electron-nuclear-nuclear TRIPLE resonance of radicals in solutions, in *Multiple Electron Resonance Spectroscopy* (M. M. Dorio and J. H. Freed, eds.) (Plenum, New York), pp. 475–507.
- Möbius, K., and Lubitz, W., 1987, ENDOR spectroscopy in photobiology and biochemistry, in *Biological Magnetic Resonance*, vol. 7 (L. J. Berliner and J. Reuben, eds.) (Plenum, New York), pp. 129–247.
- Moffat, K., 1989, *Annu. Rev. Biophys. Biophys. Chem.* **18**:309.
- Morrisett, J. D., 1976, The use of spin labels for studying the structure and function of enzymes, in *Spin Labeling* (L. J. Berliner, ed.) (Academic, New York) pp. 273–338.
- Mustafi, D., and Joela, H., 1995, *J. Phys. Chem.* **99**:11370.
- Mustafi, D., and Makinen, M. W., 1992, *Appl. Magn. Reson.* **3**:321.
- Mustafi, D., and Makinen, M. W., 1994, *J. Biol. Chem.* **269**:4587.
- Mustafi, D., and Makinen, M. W., 1995, *J. Am. Chem. Soc.* **117**:6739.
- Mustafi, D., Boisvert, W. E., and Makinen, M. W., 1990a, *Biopolymers* **29**:45.
- Mustafi, D., Sachleben, J. R., Wells, G. B., and Makinen, M. W., 1990b, *J. Am. Chem. Soc.* **112**:2558.
- Mustafi, D., Wells, G. B., Joela, H., and Makinen, M. W., 1990c, *Free Radical Res. Commun.* **10**:95.
- Mustafi, D., Joela, H., and Makinen, M. W., 1991, *J. Magn. Reson.* **91**:497.
- Mustafi, D., Boisvert, W. E., and Makinen, M. W., 1993a, *J. Am. Chem. Soc.* **115**:3674.
- Mustafi, D., Boisvert, W. E., and Makinen, M. W., 1993b, *J. Am. Chem. Soc.* **115**:3683.
- Naruto, S., Motoc, J., Marshall, G. R., Daniels, S. B., Sofia, M. J., and Katzenellenbogen, J. A., 1985, *J. Am. Chem. Soc.* **107**:5262.
- Neiman, M. B., Rozantsev, E. G., and Mamedova, Yu. G., 1962, *Nature* **196**:472.
- Nietlispach, D., Clowes, R. T., Broadhurst, R. W., Ito, Y., Keeler, J., Kelly, M., Ashurst, J., Oschkinat, H., Domaille, P. J., and Laue, E. D., 1996, *J. Am. Chem. Soc.* **118**:407.
- Ohnishi, S., and McConnell, H. M., 1965, *J. Am. Chem. Soc.* **87**:2293.
- Ohzeki, F., Kispert, L. D., Arroyo, C., and Steffan, M., 1982, *J. Phys. Chem.* **86**:4011.
- Page, M. I., 1987, *Adv. Phys. Org. Chem.* **23**:165.
- Parson, W. W., 1993, Chapter 9, Mechanisms of enzyme catalysis, in *Biochemistry* (G. Zubay, ed.) (Wm. C. Brown, Dubuque, Iowa), pp. 219–53.
- Press, W. H., Flannery, B. P., Teukolsky, S. A., and Vetterling, W. T., 1986, *Numerical Recipes: Art of Scientific Computing* (Cambridge University Press, Cambridge, UK), pp. 269–73.
- Quiocho, F. A., and Lipscomb, W. N., 1971, *Adv. Prot. Chem.* **25**:1.
- Rist, G. H., and Hyde, J. S., 1970, *Chem. Phys.* **52**:4633.
- Rozantsev, E. G., 1970, *Free Nitroxyl Radicals* (Plenum, New York).
- Rozantsev, E. G., Neiman, M. B., and Mamedova, Yu., G., *Izv. Akad. Nauk SSSR, Ser. Khim.* **1963**:1509.
- Sander, M. E., 1984, Nachweis der Kovalenten Zwischenstufe bei der Carboxypeptidase A und Untersuchungen zum Nucleotidienzym der Phosphodiesterase aus Schlangengift, Ph. D. diss. Wilhelms Universität, Münster, Germany.
- Sander, M. E., and Witzel, H., 1985, *Biochem. Biophys. Res. Comm.* **132**:681.
- Scheidig, A. J., Pai, E. F., Schlichting, I., Corrie, J., Reid, G. P., Wittinghofer, A., and Goody, R. S., 1992, *Phil. Trans. Roy. Soc. Lond.* **A340**:263.
- Schlichting, I., Almo, S. C., Rapp, G., Wilson, K., Petratos, K., Lurtfer, A., Wittinghofer, A., Kabsch, W., Pai, E. F., Petsko, G. A., and Goody, R. S., 1990, *Nature* **345**:309.
- Schultz, G. E., and Schirmer, R. H., 1979, Chapter 2, Structural implications of the peptide bond, in *Principles of Protein Structure* (Springer-Verlag, New York), pp. 17–26.
- Schweiger, A., 1982, *Structure and Bonding* **51**:1.
- Sinnott, M. L., 1988, *Adv. Phys. Org. Chem.* **24**:113.

- Stoddard, B. L., Koenigs, P., Porter, N., Petratos, K., Petsko, G. A., and Ringe, D., 1991, *Proc. Natl Acad. Sci. USA* **88**:5503.
- Stone, T. J., Buckman, T., Nordio, P. L., and McConnell, H. M., 1965, *Proc. Natl. Acad. Sci. USA* **54**:1010.
- Stryer, L., 1995, Chapter 9, Catalytic Strategies, in *Biochemistry*, 4th ed. (W. H. Freeman, San Francisco), pp.207–36.
- Togni, A., Rist, G., Rihs, G., and Schweiger, A., 1993, *J. Am. Chem. Soc.* **115**: 1908.
- Turley, J. W., and Boer, F. P. B., 1972, *Acta Crystallogr.* **B28**:1641.
- Vallee, B. L., Galdes, A., Auld, D. S., and Riordan, J. F., 1983, Carboxypeptidase A, in *Metal Ions in Biology*, vol 5 (T. G. Spiro, ed.) (Wiley, New York), pp. 25–75.
- Vallee, B. L., and Galdes, A., 1984, *Adv. Enzymol. Rel. Areas Mol. Biol.* **56**:283.
- Venters, R. A., Huang, C. C., Farmer, B. T., II, Trolard, R., Spicer, L. D., and Fierke, C. A., 1995, *J. Biomol. NMR* **5**:339.
- Wang, C. L. A., Calvo, K. C., and Klapper, M. H., 1981, *Biochemistry* **20**:1401.
- Weidig, C. F., Halvorson, H. R., and Shore, J. D., 1977, *Biochemistry* **16**:2916.
- Wells, G. B., 1987, Determination of the Molecular Conformations of Spin-Labeled Molecules by ENDOR Spectroscopy: Structure at the Active Site of an Acyl-Enzyme of α -Chymotrypsin and Implications for the Reaction Mechanism, Ph. D. Thesis, The University of Chicago, Chicago, Illinois.
- Wells, G. B., and Makinen, M. W., 1988, *J. Am. Chem. Soc.* **110**:6343.
- Wells, G. B., Mustafi, D., and Makinen, M. W., 1990, *J. Am. Chem. Soc.* **112**:2566.
- Wells, G. B., Mustafi, D., and Makinen, M. W., 1994, *J. Biol. Chem.* **269**:4577.
- Wolfenden, R., 1976, *Annu. Rev. Biophys. Bioeng.* **5**:271.
- Zemer, B., and Bender, M. L., 1964, *J. Am. Chem. Soc.* **86**:3669.

This page intentionally left blank

Site-Directed Spin Labeling of Membrane Proteins and Peptide-Membrane Interactions

Jimmy B. Feix and Candice S. Klug

1. INTRODUCTION

Site-directed spin labeling (SDSL) has emerged as a powerful method for examining structure-function relationships in proteins. It is particularly useful in studying large membrane proteins that are not amenable to study by modern nuclear magnetic resonance (NMR) methods and do not readily crystallize. The sensitivities of spin label electron spin resonance (ESR) spectra to molecular dynamics on an appropriate time scale and interactions with paramagnetic relaxation agents have also proven useful in studying small peptides and their association with membranes. The ability to specifically introduce labeling sites at a series of selected residues in a given protein or peptide greatly enhances the ability of the spin-labeling technique to provide detailed information on structure and dynamics.

Jimmy B. Feix and Candice S. Klug • National Biomedical ESR Center, Biophysics Research Institute, Medical College of Wisconsin, Milwaukee, WI 53226.

Biological Magnetic Resonance, Volume 14: Spin Labeling: The Next Millennium, edited by Berliner. Plenum Press, New York, 1998.

2. THE SDSL PARADIGM

SDSL consists of (1) manipulating the system of interest so that it contains a single reactive amino acid residue, usually a cysteine, that may be selectively modified with an appropriate spin label; (2) selectively labeling the site; (3) examining the functional viability of the mutants, preferably before and after spin labeling; and (4) characterizing the spin-labeled site by a variety of ESR methods. This approach was introduced as an adjunct to the original spin-labeling technique (Ogawa and McConnell, 1967; Hubbell and McConnell, 1968; McConnell and McFarland, 1970; reviewed in Berliner, 1976, 1979) by Hubbell and coworkers, who recognized that the rapid advancement in site-directed mutagenesis could solve a problem that had plagued spin labeling since its inception—the relative scarcity of proteins containing unique reactive cysteines. Indeed its relatively low abundance makes cysteine the residue of choice in SDSL studies; however lysine residues can also be readily spin labeled. Alternatively, small peptides (i.e., less than 50 amino acids) may be simply prepared using solid-phase synthesis with cysteine or lysine residues at desired labeling sites.

Early applications of SDSL were previously reviewed (Millhauser, 1992; Hubbell and Altenbach, 1994a, 1994b). At present the method appears generally applicable to any protein with a cloned gene that can be expressed, with the exception of proteins containing multiple essential disulfide bonds that may become scrambled by introducing additional cysteines. These proteins may later become amenable to SDSL when their folding pathways are more fully understood. However for other proteins containing natural disulfide bonds and/or multiple cysteines, such as rhodopsin and FepA, introducing additional cysteine residues has not disrupted their native structure. SDSL provides information on local structure, polarity, accessibility to various solutes, and dynamic conformational changes in response to a given stimulus or perturbation. As illustrated in this chapter, the ability to study selected single sites in addition to compiling such information for several sites in the same protein may provide numerous insights into its structural and functional dynamics.

The growth of SDSL stems from a number of unrelated developments that combined to enable experiments that could not have previously been accomplished. In addition to advances in site-directed mutagenesis and solid-phase peptide synthesis, introduction of the loop-gap resonator (Froncisz and Hyde, 1982) permitted ESR studies on relatively small amounts of protein with good sensitivity, and saturation studies using either continuous wave (CW) or time domain techniques on aqueous samples without the problems associated with sample heating due to high microwave power. Using gas-permeable sample capillaries (Popp and Hyde, 1981) allowed control and manipulation of O_2 concentration without subjecting sensitive biological samples to deoxygenation by freeze-pump methods. The ensu-

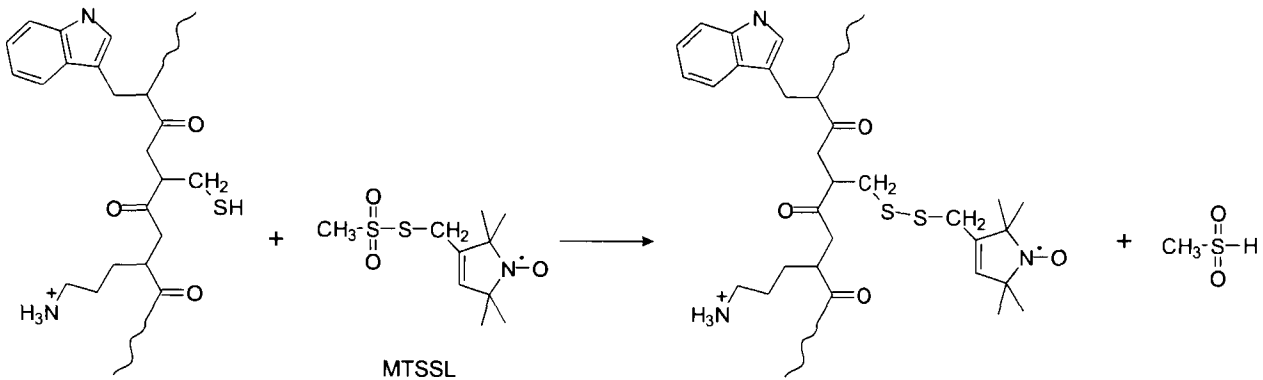
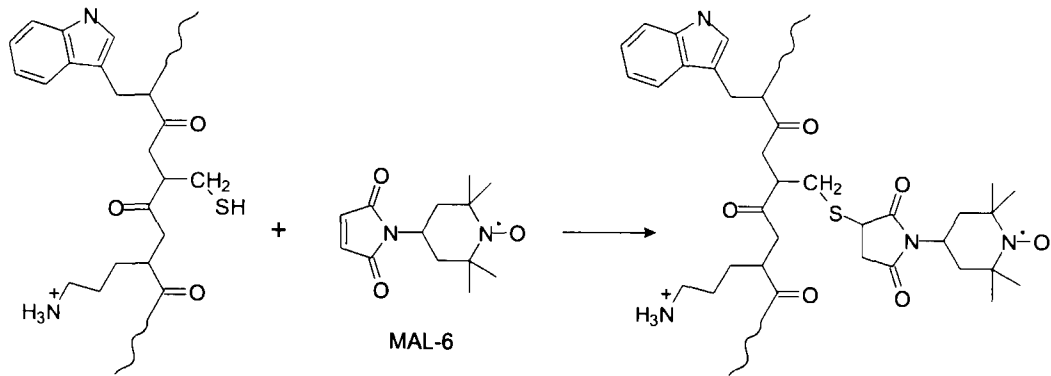
ing ease of saturation studies greatly complemented the traditional sensitivity of the ESR spectrum to spin label motion.

2.1. Spin Labeling Cysteine

Cysteine residues may be modified with a variety of reagents (Means and Feeny, 1971; Berliner, 1983; Gaffney, 1976), but is most often spin labeled with either methanethiosulfonate or a maleimide. The methanethiosulfonate spin label 1-oxyl-2,2,5,5-tetramethylpyrroline-3-methylmethanethiosulfonate (MTSL; Scheme 1) was initially introduced as a sulfhydryl-specific label that was readily released by mild reducing agents, greatly facilitating spin label quantitation (Berliner *et al.*, 1982; Berliner, 1983). On the other hand, maleimide labels, such as 2,2,6,6-tetramethyl-4-maleimidopiperidine-1-oxyl (MAL-6) form stable thio-ether bonds (Scheme 1), which is of value in systems where reducing equivalents are present. MTSL has the distinct advantage of specificity for the cysteine sulfhydryl moiety of proteins, whereas MAL-6 can also modify the amino group of lysines. MTSL readily labels sites in both hydrophilic and hydrophobic environments, although partial denaturation may be needed to modify sites buried in protein tertiary structure. MTSL has a relatively small molecular volume, similar to the natural tryptophan or phenylalanine side chains, so it represents a minimal perturbation. One of the emerging lessons of SDSL is that proteins are remarkably resilient with regard to structure and function following cysteine mutagenesis and MTSL labeling.

2.2. Spin Label Motion in SDSL

The sensitivity of ESR spectra to nitroxide motion is a fundamental aspect of spin labeling extensively reviewed in previous monographs in this series (Berliner, 1976, 1979; Berliner and Reuben, 1989). Spin labels attached to single cysteine residues in a protein so often exhibit spectra composed of at least two motional components that this is the rule rather than the exception (e.g., Todd *et al.*, 1989; Greenhalgh *et al.*, 1991; Altenbach *et al.*, 1990; Resek *et al.*, 1993; Mchaourab *et al.*, 1996; Klug *et al.*, 1997). Although in principle such spectra may arise from anisotropic motion in a single population (Meirovich and Freed, 1984), in spin-labeled proteins they are more likely the result of alternative conformations of the nitroxide relative to the peptide backbone (Resek *et al.*, 1993; Mchaourab *et al.*, 1996). This result is somewhat fortuitous, since changes in relative intensities of motional components serve as a sensitive indicator of a conformational change (e.g., Ogawa and McConnell, 1967). Changes in relative populations of motional components provide evidence of structural alterations in systems containing multiple spin-labeled sites (Butterfield *et al.*, 1976), and these are even more informative when dealing with a single labeled site. Such effects have allowed time-resolved



Scheme 1. Labeling reactions for the MTSL and MAL-6 spin labels with cysteine. For MTSL, the resultant side chain is similar in molecular volume to that of tryptophan.

ESR studies of the membrane insertion of colicin E1 (Shin *et al.*, 1993), structural changes in rhodopsin on photoactivation (Farahbakhsh *et al.*, 1993), and receptor dynamics during *in vivo* transport of ferric enterobactin and colicin B by FepA (Jiang *et al.*, 1997).

2.3. CW Saturation in SDSL

Changes in spin label motion or relative intensities of motional components may provide compelling evidence of structural change at a labeled site. In membranes however, where motion is often damped, the accessibility of a given site to various fast-relaxing agents (e.g., paramagnetic metal complexes, molecular oxygen) may be more informative in characterizing the overall protein structure and (by inference) the precise nature of conformational changes. Accessibilities are implied by Heisenberg exchange rates, which are directly determined by using either time domain methods (e.g., saturation recovery measurement of the electron spin lattice relaxation time T_{1e}) or empirical CW saturation methods. Since the latter requires no specialized instrumentation beyond a conventional spectrometer and a loop-gap resonator, it has been the method of choice. A typical set of CW saturation

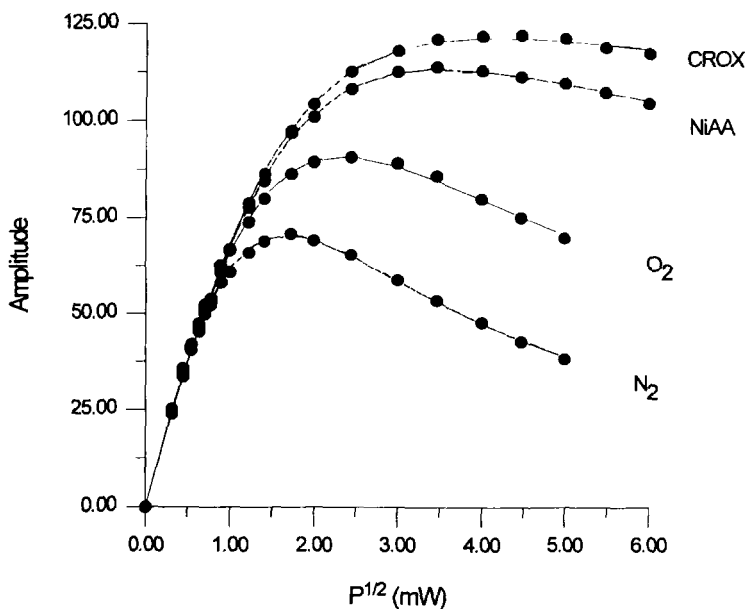


Figure 1. Representative CW saturation curves for MTSL-labeled cysteine in a hydrophilic environment. The $P_{1/2}$ values increase in the order $N_2 < O_2 < NiAA < CROX$.

curves is shown in Fig. 1. At low incident microwave power, the first derivative peak-to-peak amplitude shows a linear increase with $P^{1/2}$, as expected for a Lorentzian line (Poole, 1983). As the spin system begins to saturate, the increase in amplitude becomes less than linear with respect to $P^{1/2}$, reaches a maximum, and then decreases. The curves are fit to the function (Altenbach *et al.*, 1994; Yu *et al.*, 1994):

$$A = Y P^{1/2} \left[1 + (2^{1/\epsilon} - 1) \frac{P}{P_{1/2}} \right]^{-\epsilon} \quad (1)$$

where A is the peak-to-peak amplitude of the first derivative center line (in arbitrary units), P is the incident microwave power, Y is a scaling parameter, ϵ is a parameter related to the homogeneity of the line with $\epsilon = 0.5$ and $\epsilon = 1.5$ limits for inhomogeneous and homogeneous saturation, respectively (Altenbach *et al.*, 1994); and $P_{1/2}$, the half-saturation parameter, is the power at which the amplitude is exactly half that which would be observed in the absence of saturation (Subczynski and Hyde, 1981; Altenbach *et al.*, 1989a). $P_{1/2}$ is a function of $1/(T_{1e}T_{2e})$:

$$P_{1/2} = \frac{(2^{2/3} - 1)}{(\gamma^2 \Lambda^2 T_{1e} T_{2e})} \quad (2)$$

where γ is the electron gyromagnetic ratio and Λ is a constant dependent on the cavity or resonator (Poole, 1983; Altenbach *et al.*, 1989a). Interactions with paramagnetic species that shorten the nitroxide T_{1e} make saturation more difficult to achieve, resulting in an increase in $P_{1/2}$.

In the limit where interaction between the relaxation agent and the spin label is dominated by Heisenberg exchange, the change in the nitroxide spin lattice relaxation rate ($1/T_{1e}$) is proportional to the bimolecular collision frequency W_x :

$$T_{1e}^{-1} - T_{1e}^{\circ-1} = f p W_x \quad (3)$$

where $^{\circ}$ refers to the absence of a paramagnetic relaxation agent, p is the collision efficiency, and f is a statistical factor (Subczynski and Hyde, 1981).

Since $1/T_{2e}$ is typically about an order of magnitude faster than $1/T_{1e}$ for nitroxides in the liquid phase, as a first approximation it can be assumed unchanged by the relaxation agent, so that:

$$\Delta P_{1/2} = P_{1/2} - P_{1/2}^{\circ} \propto \frac{1}{T_{1e} T_{2e}} - \frac{1}{T_{1e}^{\circ} T_{2e}^{\circ}} \propto \frac{W_x}{T_{2e}} \quad (4)$$

(Altenbach *et al.*, 1989a). Thus for a given line width, $\Delta P_{1/2}$ is proportional to the collision frequency between the spin label and relaxation agent. Measuring the change in the half-saturation parameter $\Delta P_{1/2}$ is the basis of CW saturation accessibility studies.

Curves in Fig. 1 were generated with three samples (one for O_2 and N_2 and one each for NiAA and CROX) of spin labeled protein. Due to the high microwave B_1 field per unit power in the loop-gap resonator (5–9 G of B_1 field per watt; Froncisz and Hyde, 1982), it is typically possible to obtain a full saturation curve from 0.1–50 mW incident microwave power. Because the electric field component of microwaves is largely confined to a region outside the resonator, problems due to sample heating are virtually eliminated. Sufficient microwave powers to obtain full saturation curves are typically not attained in a conventional rectangular cavity, and sample heating may be troublesome. Thus with a small investment of sample, one can obtain relative bimolecular collision frequencies between the spin label and a variety of paramagnetic relaxation agents.

Accessibility studies with complementary relaxation agents are most informative, especially for membrane-exposed sites. Many early studies relied on chromium(III) oxalate [potassium tris(oxalatochromate); CROX] as a fast-relaxing, polar reagent confined almost exclusively to the aqueous phase. Although a very effective reagent, CROX carries a negative charge (–2 to –3 at physiological pH) that influences its interactions. More recent experiments introduced a number of polar, neutral paramagnetic complexes, including nickel(II) acetylacetonate (NiAA) and nickel(II) ethylenediaminediacetate (NiEDDA) (Altenbach *et al.*, 1994), and chromium maltolate (Burchfield *et al.*, 1994). These compounds are found mostly in the aqueous phase, but do partition into the lipid bilayer (discussed later). In addition, molecular O_2 is a very effective nonpolar relaxation agent, O_2 preferentially partitions into lipid bilayers relative to the surrounding aqueous phase at a ratio of approximately 10:1, and it exhibits a depth-dependent concentration gradient in the membrane (Windrem and Plachy, 1980; Subczynski and Hyde, 1981) with maximum concentration at the bilayer center. The O_2 produces changes in $1/T_{1e}$ that are linear in concentration (Hyde *et al.*, 1990), as expected for a bimolecular-collision based mechanism, and it is readily introduced and removed from samples in a nondestructive fashion. Although its small size makes O_2 accessible to most sites, it does not penetrate the hydrophobic core of folded water-soluble proteins (Calhoun *et al.*, 1988), and it may thus have little effect on relaxation rates of truly buried sites.

Inverse concentration profiles of oxygen and the polar Ni(II) complexes in a lipid bilayer can be exploited to measure the depth of lipid-exposed sites in a membrane (Altenbach *et al.*, 1994). Altenbach *et al.* (1994) defined the parameter Φ such that:

$$\Phi = \ln \left[\frac{\Delta P_{1/2} (NP)}{\Delta P_{1/2} (P)} \right] \quad (5)$$

where NP refers to the nonpolar reagent (typically O_2) and P the polar reagent (e.g., NiAA or NiEDDA). This relation results from the fact that $\Delta P_{1/2}$ is directly

proportional to the collision frequency with a given relaxation agent, W_x (Eq. 4), which in turn depends on the local concentration of that particular species at the site of the nitroxide.

To obtain depth measurements of lipid-exposed sites in a membrane, Φ is calibrated for the system under study using n-doxyl phosphatidylcholine (PC) spin labels (Dalton *et al.*, 1987) as standards (Altenbach *et al.*, 1994; Qin and Cafiso, 1996; Klug *et al.*, 1997). We observed an essentially linear relationship between Φ and bilayer depth for 7-, 10-, and 12-doxylPC (Fig. 2), which agrees with the original observations of Altenbach *et al.* (1994). We also find that 5-doxylPC gives a Φ value slightly greater than predicted for linear dependence; this may be due to its localization in the aqueous/hydrophobic interface. The 16-doxylPC gives Φ values significantly lower than expected for its position in the membrane (Altenbach *et al.*, 1994) due to the tendency of this label to undergo vertical fluctuations toward the membrane surface (Feix *et al.*, 1984, 1987). It is noteworthy that the dependence of Φ on depth varies depending on the composition of the host membrane. Thus a calibration curve must be established for each new membrane or micellar system studied.

Using bacteriorhodopsin in model membranes (discussed later), Φ varied linearly with bilayer depth across the lipid-exposed surface of a transmembrane α -helix (Altenbach *et al.*, 1994). This initial study employed NiAA and O_2 , and since both are relatively small molecules, the authors argued that differences in accessibility from steric constraints (i.e., local structure around the nitroxide) tended to cancel. This argument is less certain when the larger NiEDDA complex is used as the polar relaxation agent, although values based on relative accessibilities to O_2 and NiEDDA have shown good reliability in providing bilayer depths (e.g., Fig. 2). Nonetheless it is worth remembering that local tertiary structure in a protein

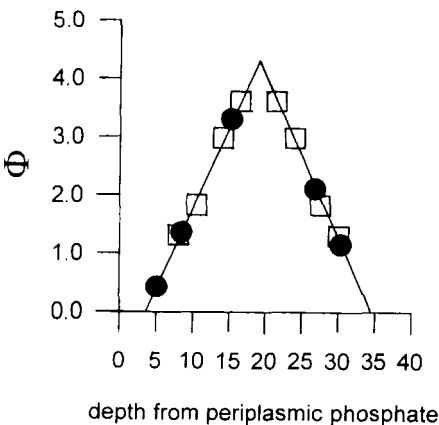


Figure 2. Dependence of Φ on membrane depth. NiEDDA and O_2 were the polar and nonpolar relaxation agents, respectively. Open squares represent data (in order of increasing depth) from 5-, 7-, 10-, and 12-doxylphosphatidylcholine spin labels (PCSLs) reflected through the membrane center to give a symmetric bilayer. Closed circles represent data for (from left to right) MTSL-labeled Q245C, L247C, L249C, A251C, and Y253C found in a transmembrane β -strand in FepA. Straight lines are extrapolations of data from 7-, 10-, and 12-PCSLs (C. S. Klug and J. B. Feix, unpublished data).

may influence results, particularly at sites where nitroxide motion indicates a sterically hindered environment (e.g., Altenbach *et al.*, 1996). Φ is independent of ESR line shape, since effects of T_{2e} on $\Delta P_{1/2}$ (Eq. 4) cancel.

3. SDSL OF MEMBRANE PROTEINS

Perhaps the most effective way to appreciate the utility of SDSL is to consider how it is applied in investigating membrane proteins and peptide-membrane interactions. The representative studies that follow illustrate how SDSL provides insight into protein structure and conformational dynamics.

3.1. Structure-Function Studies of α -Helical Membrane Proteins

SDSL began with studies of the soluble C-terminal domain of colicin E1 (Todd *et al.*, 1989) and four single-cysteine mutants of bacteriorhodopsin (Flitsch and Khorana, 1989; Altenbach *et al.*, 1989a). Since then rhodopsin and bacteriorhodopsin (bR) have been by far the most extensively studied membrane proteins using this technique, with much of the basic methodology used in SDSL was developed in these systems.

3.1.1. Bacteriorhodopsin

Bacteriorhodopsin, an integral membrane protein found in the purple membrane of *Halobacterium halobium*, functions as a light-driven proton pump. It is proposed to contain seven membrane-spanning α -helices, designated A-G, based on hydrophobicity analysis and cryoelectron microscopy (Baldwin *et al.*, 1988). Like many bacterial membrane proteins, bR contains no native cysteines, making it an attractive candidate for SDSL.

Of the initial four single-cysteine mutants of bR, three were quantitatively labeled with MTSL (or another spin label based on pyridine disulfide) in the presence of SDS/urea, then refolded, with regeneration of the bR chromophore used to assess natively like structure (Altenbach *et al.*, 1989a). To establish the location of spin labeled sites in the folded bR tertiary structure, accessibility to O_2 and CROX was determined by CW saturation. Although unusually high concentrations of relaxation agents (100% O_2 and 50 mM CROX) were used in this early study, results were consistent with the localization of two sites in interhelical loops and another site buried in the membrane.

In a subsequent seminal study that introduced nitroxide scanning, 18 consecutive single-cysteine mutants in bR were generated and analyzed, beginning at the C-terminal end of helix D, traversing an interhelix loop, and extending well into helix E (Altenbach *et al.*, 1990). When $\Delta P_{1/2}$ values for O_2 were plotted against residue number, a striking 3.6 residue/turn periodicity was observed, coincident

with that of an α -helix (Fig. 3). A pronounced spike in $\Delta P_{1/2}$ values for CROX identified the location of the interhelix loop, and O_2 accessibility data led to a model for the orientation of helix E with respect to the rest of the seven-helix bundle. This work demonstrated the power of SDSL in providing refined structural data for an integral membrane protein. Key elements of the SDSL methodology—CW saturation experiments, employing a loop-gap resonator to minimize sample requirements, and using MTSL as a sulfhydryl-specific labeling reagent—were introduced to the general scientific community, and it was established that a protein may sustain numerous different cysteine substitutions without undue disruption of its native structure.

3.1.2. Rhodopsin

Rhodopsin is the light-sensitive protein-chromophore complex found in the vertebrate retinal rod outer segment (ROS) membrane. On photon absorption by the 11-*cis*-retinal chromophore, rhodopsin passes through several intermediate states. One such state, the meta II (MII) state, binds and activates the specialized G-protein transducin. Rhodopsin is a member of the family of G-protein-coupled receptors that contain seven transmembrane α -helices. Electron cryomicroscopy of two-dimensional crystals provided structural data on the transmembrane helices (Unger and Schertler, 1995), and a model of the membrane topology was proposed based on sequence comparisons with other G-protein-coupled receptors (Baldwin, 1993). This model served as an excellent starting point for designing SDSL studies on rhodopsin; results from SDSL studies have in turn refined the model (e.g., Farahbakhsh *et al.*, 1995a; Farrens *et al.*, 1996).

Unlike bR, rhodopsin contains ten native cysteine residues. In isolated ROS membranes, Farahbakhsh *et al.* (1992) demonstrated that it was possible to selectively label a single site with stoichiometric amounts of a *p*-chloromercuribenamide

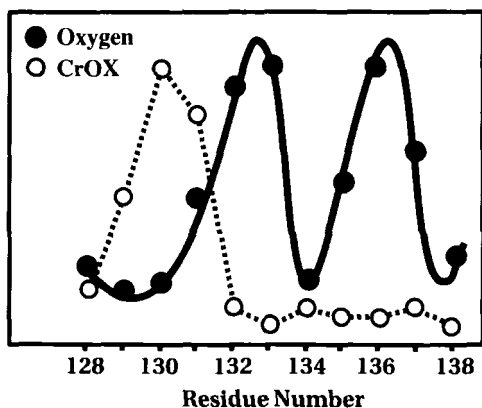


Figure 3. Accessibility of MTSL-labeled side chains in bacteriorhodopsin to oxygen and CROX. The 3.6 residue/turn periodicity in $\Delta P_{1/2}(O_2)$ is indicative of an α -helix (from Altenbach *et al.*, 1990).

spin label, with a second site also labeling at higher spin label:protein ratios. To establish the location of the uniquely labeled native cysteine, accessibilities to CROX and O_2 were determined and compared to values obtained for lipid analog spin labels intercalated into the ROS membrane bilayer. Two important advances in SDSL methodology arose from this approach. First, since $1/T_{2e}$ is proportional to line width, $\Delta P_{1/2}$ values were corrected for differences in T_{2e} among different sites by dividing each $\Delta P_{1/2}$ by the peak-to-peak width of the center line (ΔH_0):

$$\Delta P'_{1/2} = \frac{\Delta P_{1/2}}{\Delta H_0} \quad (6)$$

This corrected value was then converted into the dimensionless accessibility parameter Π by normalizing to the half-saturation power and line width of a DPPH standard to compensate for differences in the amount of microwave field per unit microwave power among resonators.

$$\Pi = \Delta P'_{1/2} \cdot \frac{\Delta H_0(\text{DPPH})}{P_{1/2}(\text{DPPH})} \quad (7)$$

Correcting for line width differences was important in this study, given the extreme differences in T_{2e} observed among lipid analog spin labels and between these labels and a protein-bound nitroxide. Normalizing resonator performance was the first attempt to put CW saturation parameters on a scale that was reliably compared between laboratories.

In addition to introducing Π , this study was the first to consider the ratios of collision rates among the nitroxide and different relaxation agents as a way of assessing local polarity; the argument was that ratios of accessibility parameters tend to eliminate effects due to local structure, providing a better measure of the hydrophobicity of the spin label environment. A linear relationship was observed between $\Pi_{\text{CROX}}/\Pi_{O_2}$ and the bilayer depth of the nitroxide for a series of lipid analog spin labels intercalated into the ROS membrane. Comparing this parameter for the spin labeled cysteine indicated a binding site in the head group region of the bilayer, helping to identify the modified residue (Farahbakhsh *et al.*, 1992). This concept was further developed into the depth parameter Φ (Eq. 5) using model bilayers containing reconstituted bR (Altenbach *et al.*, 1994, previously discussed).

Much of the remaining SDSL work on rhodopsin focused on elucidating structural changes both induced by light absorption and involved in transducin activation. For example, selectively labeling rhodopsin in ROS membranes at either C140 or C316 (accomplished by alternately protecting each cysteine with 4,4-dithiopyridine) with MTSL results in spectra that contain two motional components (Farahbakhsh *et al.*, 1993). Photoexcitation of rhodopsin results in a marked decrease in the more mobile spectral component of MTSL bound to C140, with a

concomitant increase in the strongly immobilized component, reflecting a conformational change in the region of the protein occupied by C140. Effects were apparently not global, since little change was observed at C316. This illustrates one of the key advantages of SDSL, the ability to detect local conformational changes without respect to global changes in protein structure.

To examine the physiological relevance of these effects, time-resolved ESR studies were used to examine light-induced changes in spin label motion. Kinetics of the decrease in the more mobile MTSL-C140 population closely matched the increase in A_{380} that is associated with formation of the MII state under a variety of conditions, thereby providing an important link between structural changes observed by SDSL and optical changes in the chromophore.

To further analyze light-induced structural changes by SDSL, a synthetic rhodopsin gene was developed and five mutants constructed, each containing a single reactive cysteine (Resek *et al.*, 1993). Mutant gene constructs were placed in an appropriate plasmid vector and expressed in mammalian COS-1 cells. Cysteine labeling site environments were characterized by accessibility to CROX, NiAA, and O_2 using CW saturation. The photoinduced conformational change previously noted was confirmed for MTSL-C140 in lauryl maltoside micelles (which support MII formation), but not in digitonin (which does not support MII formation). Perhaps more importantly this study demonstrated that it was possible to express a vertebrate protein in an eukaryotic cell line to obtain sufficient material for SDSL.

With the preceding genetic approach, Khorana, Hubbell and coworkers produced more than 50 additional rhodopsin mutants, focused primarily in the C-D (Ridge *et al.*, 1995; Farahbakhsh *et al.*, 1995a) and E-F (Yang *et al.*, 1996; Altenbach *et al.*, 1996) interhelical loops. Each mutant was functionally characterized according to its spectral properties and the ability to activate transducin, the MTSL-labeled cysteine localized with respect to the membrane by examining accessibility to O_2 and NiEDDA in dodecyl maltoside (DM) micelles, and examined for conformational changes at the spin label site on photoactivation. The Π values for O_2 and NiEDDA confirmed that most residues under study were in a hydrophilic environment, as indicated by higher accessibility to NiEDDA than to O_2 . Because differences in Φ are often relatively small among labeling sites exposed to the aqueous phase, variation in e^Φ , which is simply the ratio $\Delta P_{1/2}(O_2)/\Delta P_{1/2}(NiEDDA)$, was compared for mutants at 20 consecutive sites in the C-D loop (Farahbakhsh *et al.*, 1995a) and 30 consecutive mutants encompassing the E-F interhelical loop (Altenbach *et al.*, 1996). In both studies sharp changes in e^Φ occurred at the hydrophilic/hydrophobic interface, definitively showing the insertion of these helices into the nonpolar core of the DM micelle and presumably the membrane bilayer. In the E-F interhelical domain, a periodicity in both $\Phi(NiEDDA)$ and $\Phi(O_2)$ was evident, indicating regular secondary structure, and accessibilities to O_2 and NiEDDA were in phase with one another. As discussed

later, this is a characteristic of aqueous domains, where residues are either exposed or completely buried in the tertiary structure of the protein. In contrast accessibilities to polar and nonpolar relaxation agents for membrane-spanning domains are typically out of phase. Similar variability was observed in the reciprocal line width of the center line (ΔH_0^{-1}), although the periodicity was less well-defined.

To explore dynamic effects of photoactivation on rhodopsin structure, this large collection of site-specific mutants was surveyed for alterations in its conventional ESR spectra. Most spectra were relatively unchanged, reflecting only minor perturbations in spin label motion; however for a handful of mutants, changes in rotational mobility after photobleaching were quite dramatic. Results were interpreted in terms of rigid-body motions of the helices with respect to one another, causing changes in helix-helix interactions (Farahbakhsh *et al.*, 1995a; Altenbach *et al.*, 1996).

3.1.3. SDSL Using Double Cysteines

To test the concept of rigid-body helix movement in more detail, rhodopsin mutants were constructed containing *two* reactive cysteines, and the spatial proximity of those cysteines was determined based on their ability to form disulfide bonds and by examining spin-spin interactions between the two sites after spin labeling. Farrens *et al.* (1996) explored static dipolar interactions between a single site in helix C and a series of sites near the cytoplasmic end of helix F. Rigid-lattice ESR spectra were recorded (i.e., in a frozen micellar solution at 183 K) before and after photoactivation. Dipolar interactions between sites in relatively close proximity (10–20 Å in this study) resulted in a marked spectral broadening and loss of signal amplitude. Dipolar interaction decreased after photoactivation for three mutant pairs, increased for one pair, and remained relatively unchanged for another. Mild oxidation with Cu(phenanthroline) resulted in disulfide bond formations between all but one of the pairs. Interestingly, disulfide formation precluded the ability of these otherwise functional mutants to activate transducin, suggesting that helix movement relative to one another is a functionally important conformational change.

Distance constraints provided by the preceding experiments were used to construct a model of the photoinduced conformational change in rhodopsin. Results from SDSL studies could be matched only by postulating both a tilt and a rotation of helix F (Fig. 4). Clearly, the insight from such studies are far beyond what is currently available from crystallography.

This same approach was used to examine interaction between single sites near the cytoplasmic ends of helices A (H65C) and G (C316) (Yang *et al.*, 1996). The spectrum of the MTSL-labeled double mutant was compared with the computational sum of the single-mutant spectra at room temperature and at 183 K. Even at room temperature, dipolar interactions in the doubly labeled mutant produced

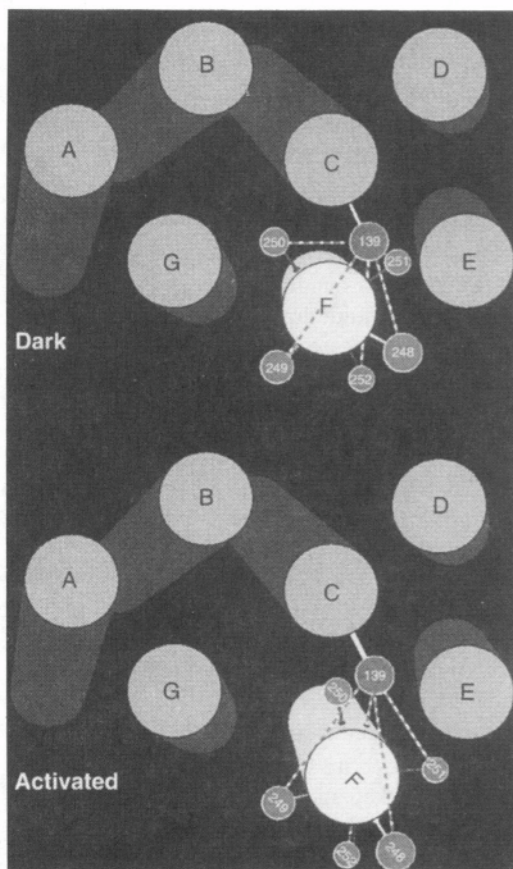


Figure 4. Model depicting structural changes occurring on photoactivation of rhodopsin, as indicated by SDSL studies using double-cysteine mutants. Both a tilt and a rotation of helix F are needed to satisfy changes in the distance from MTSL-C139 (on helix C) to sites shown on helix F (from Farrens *et al.*, 1996).

marked broadening of the spectra in the dark state. Photoactivation largely eliminated the broadening, indicating displacement of labeled sites from one another. As expected, single mutants produced powder spectra in the frozen state. Samples frozen in the dark state showed extreme broadening, but samples frozen after photoactivation showed much less broadening, although some dipolar interaction was suggested by failure of the spectrum to return to baseline in the regions between the center line and both the low- and high-field turning points. Simulations on frozen state spectra gave distance separations between the two nitroxides of 10 ± 3 Å in the dark state and 15 ± 4 Å after photoactivation.

3.1.4. Additional Double Cysteine SDSL

Using spin-spin interactions between two suitably placed cysteines is a powerful method of analyzing structure and conformational dynamics. These effects

can arise from either dipolar (as discussed) or exchange (Fiori *et al.*, 1993; Qin and Cafiso, 1996; Wertz *et al.*, 1996) mechanisms. In the rhodopsin studies, the effects of dipolar interactions on ESR spectra were simulated using a model that assumes an isotropic distribution of the interspin vector (as expected for a powder or frozen solution) and of the relative orientations of the two nitroxides (Farahbakhsh *et al.*, 1995b). Under such conditions, the observed effect is general line broadening (Likhtenshtein, 1976; Steinhoff *et al.*, 1991; Anthony-Cahill *et al.*, 1992). Under very favorable conditions where the two nitroxides have specific relative orientations, broadening can be resolved into a definitive splitting of the lines (Pake, 1948; Beth *et al.*, 1984; Hustedt *et al.*, 1997). A different method, based on Fourier transform deconvolution, was also introduced (Rabenstein and Shin, 1995). In each case quantitation is possible in the 8–25 Å range. Below 8 Å, through-space exchange dominates, and nitroxides are essentially in contact. Rigorously, all of the preceding methods require complete immobilization of the nitroxide for quantitative analysis. Due to the way that spin labels are tethered to the peptide backbone, this almost always requires going to a frozen solution. Nonetheless, it is noteworthy that Yang *et al.* (1996) observed qualitative effects at room temperature that were easily interpretable as evidence of spin-spin interaction. Mchaourab *et al.* (1997) recently introduced a convolution method for room temperature distance measurements based on dynamic modulation of the dipole-dipole interaction by rotational motion. Unfortunately, such analysis requires relatively narrow ESR lines and moderately fast rotation of the protein, both of which are seldom observed for membrane proteins. As a general theme, interaction *patterns* between one fixed site and a series of sites in a region of interest provide useful insights into conformational changes and the way that distinct regions of a protein pack together in a tertiary structure (Farrens *et al.*, 1996; Mchaourab *et al.*, 1997). The use of double mutants is developing into an important site-directed spin labeling technique.

3.2. SDSL of the Ferric Enterobactin Receptor FepA

The ferric enterobactin receptor FepA, is an 81-kDa integral membrane protein found in *E. coli* and many related enteric bacteria. FepA is responsible for the acquisition of iron *via* binding and transport of the complex ferric enterobactin (FeEnt). Enterobactin is a 750 Da cyclic triester of dihydroxybenzoylserine that is secreted into the extracellular environment in response to low iron availability (Neilands, 1981). The association constant between enterobactin and ferric iron is estimated at 10^{52} (Harris *et al.*, 1979), the largest known for any ferric complex. The FeEnt complex binding and uptake by FepA thus allows enteric bacteria to compete effectively for extremely limited amounts of iron present *in vivo*.

The ferric enterobactin receptor of gram-negative bacteria differs from any other protein studied by site-directed spin labeling thus far. In contrast to α -helices comprising rhodopsin and bacteriorhodopsin, the membrane-spanning region of

FepA is thought to be composed of a series of antiparallel β -strands. Hydrophobicity analysis of the FepA primary structure also suggests that the transmembrane domain must indeed be composed of β -strands, since there are no stretches of hydrophobic residues long enough to span the bilayer in an α -helical configuration (Murphy *et al.*, 1990). In addition, several crystal structures have emerged in recent years for bacterial outer-membrane porins (e.g., Weiss *et al.*, 1991; Cowan *et al.*, 1992; Kreuzsch *et al.*, 1994; Schirmer *et al.*, 1995). Porins form nonspecific, open channels that allow diffusion of solutes with molecular weights less than ca. 600 Da through the outer membrane. Structural characteristics common to all crystallized porins are a transmembrane β -barrel with an aqueous central channel and surface loops that fold back into the channel, limiting access and determining the exclusion limit of the pore. FepA is thus thought to represent a further development of porins where surface loops have evolved not only to limit channel access, but also to bind a specific ligand with high affinity. SDSL studies of FepA have focused on determining structure and conformational changes that occur in ligand-binding surface loop upon association of FeEnt and in verifying the hypothesis that the transmembrane domain is composed of antiparallel β -strands.

3.2.1. Surface-Loop Domain

Initial SDSL studies on FepA focused on two residues, E280 and E310, located in the large cell-surface loop containing the ligand-binding site, as well as preliminary studies examining labeling two native cysteines present in wild type FepA (Liu *et al.*, 1994). Using protein purified by differential extraction of the OM with Triton X-100 followed by ion exchange chromatography on DEAE-cellulose (Hollifield and Neilands, 1978), native cysteines could be labeled only after both reduction with a thiol-reducing agent (e.g., DTT) and unfolding in 6 M urea. These results indicated that native cysteines were disulfide-linked and also buried in what is evidently a highly restricted site. Essentially no labeling of native cysteines was observed at urea concentrations less than 4 M, and only partial labeling could be obtained from 4–6 M urea. These results agree with subsequent studies demonstrating the unfolding of the FepA ligand-binding domain in this same range of denaturant concentrations (Klug *et al.*, 1995). In contrast both E280C and E310C mutants were readily labeled with MTSL during a 4-hour incubation at 4 °C without the addition of either a reducing agent or denaturant. Consequently these studies indicated the ability to introduce and spin label unique cysteines in FepA without first having to delete native cysteine residues. This important conclusion must be individually evaluated for each protein under study.

Conventional CW ESR spectra of MTSL-labeled E280C and E310C produced strongly immobilized spectra at room temperature (Liu *et al.*, 1994). It is remarkable that despite the hydrophilic nature of the surface loop as a whole, each of these labels resides in a highly restricted environment with little freedom of rotational

motion. This was further borne out by CW saturation studies on the accessibility of these sites to O_2 and CROX (Liu *et al.*, 1994). Thus it appears that the ligand-binding surface loop of FepA exits in a tightly packed conformation having a large number of tertiary contacts, perhaps by analogy to porins, folding back into the transmembrane channel.

3.2.2. β -Barrel Domain

SDSL was used as the first direct experimental test of the β -strand model for FepA (Klug *et al.*, 1997). This was also the first SDSL study of a transmembrane β -strand. Nine consecutive residues comprising a proposed β -strand immediately adjacent to the ligand-binding domain were individually mutated to cysteine, labeled with MTSL, and examined for accessibility to paramagnetic relaxation agents in a reconstituted liposome system. Figure 5 shows relative collision rates with O_2 and NiEDDA. Both reagents show a striking biphasic periodicity that is characteristic of β -sheet structure; accessibilities to polar and nonpolar reagents are precisely 180° out of phase. Odd-numbered residues (Q245C, L247C, L249C, A251C, Y253C) are relatively more exposed to O_2 , indicating that they face the lipid phase of the bilayer and even-numbered residues (S246C, E248C, E250C, G252C) are more exposed to NiEDDA, indicating that these sites are oriented toward the aqueous channel. Thus, SDSL confirms that these residues form a transmembrane β -strand and provide strong support for the β -barrel model of the channel domain.

The phase relationship of Φ values for O_2 and NiEDDA is worth comment. As previously noted, for the transmembrane β -strand in FepA, $\Phi(O_2)$ and $\Phi(NiEDDA)$ are *out of phase* (Fig. 5). Residues on the polar side of the sheet are solvent-exposed, in this case extending into the hydrophilic channel through which FeEnt must presumably pass, while residues on the hydrophobic side are sequestered from the aqueous solvent but remain accessible to high concentrations of O_2 found in the membrane. Conversely in soluble proteins containing β -strands, the hydrophobic face is typically buried through tertiary interactions, so it is inaccessible to both polar and nonpolar relaxation agents. Consequently, Φ values retain the characteristic periodicity of 2, but are in phase. This is precisely what was observed for retinal-binding protein (Hubbell *et al.*, 1996), which was the first example of β -strand secondary structure studied by SDSL in a soluble β -sheet protein.

3.2.3. Denaturation of FepA and Use of SDSL in Protein Folding Studies

In the past few years there has been explosion of interest in understanding protein folding mechanisms. Most studies use circular dichroism (CD), uv-vis, or fluorescence spectroscopy to monitor *global* changes in protein structure as a function of temperature or denaturant concentration. In contrast SDSL is able to follow *local* structural changes in a specified spin-labeled site. Given that

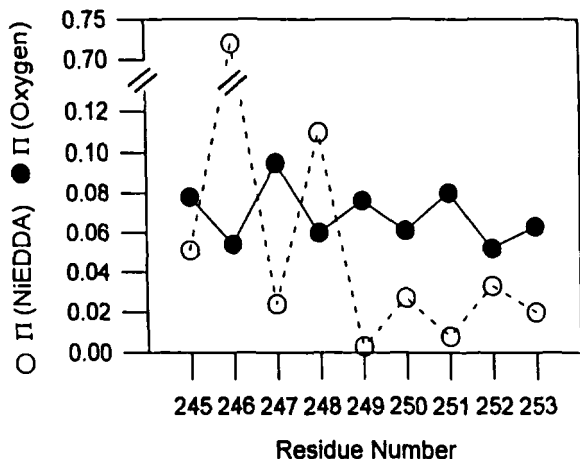


Figure 5. Accessibilities of MTSL-labeled residues in a transmembrane β -strand of FepA. The alternating periodicity seen with both reagents is indicative of a β -sheet secondary structure (from Klug *et al.*, 1997).

many proteins (and essentially all membrane proteins) consist of multiple domains, which in general have differing stabilities, SDSL offers enormous advantages for providing a more well-defined understanding of folding-unfolding processes.

To characterize the thermodynamic stability of the ligand-binding domain of FepA, changes in the rotational mobility of MTSL bound at E280C were followed as a function of denaturant concentration (Klug *et al.*, 1995). Unfolding of the region surrounding E280C with either guanidine hydrochloride (Gdn-HCl) or urea resulted in conversion from a native environment where spin label motion was strongly restricted to a rotationally mobile state (Fig. 6). In the native state, spin label accessibility to hydrophilic relaxation agents was partially limited, whereas following denaturation the nitroxide became fully accessible to CROX. These changes and an increase in the isotropic hyperfine coupling constant suggest that the large surface loop containing E280C becomes unfolded on denaturation, thereby converting into a random coil configuration extending into the aqueous phase.

The fraction of protein in the denatured state can be quantitated by comparing integrated signal intensities before and after spectral subtraction of the rotationally mobile component (using the fully denatured spectrum obtained in 4-M Gdn-HCl for subtraction). Plots of the fraction of unfolded protein (i.e., freely mobile spins) against denaturant concentration produced curves (Fig. 7) typical of rapid cooperative unfolding (reviewed by Pace, 1986). Modeling this process as a two-state equilibrium between native and denatured states provides a Gibbs free

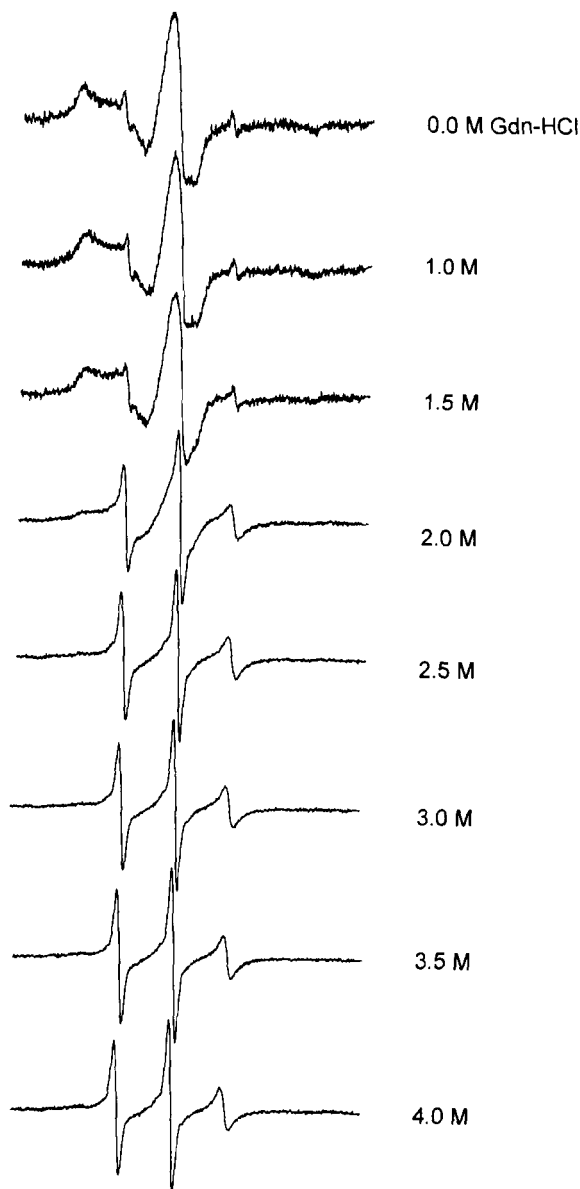


Figure 6. Changes in ESR spectra of FepA that accompany denaturation. FepAE280C-MTSL was denatured by guanidine-HCl at indicated concentrations. The ESR spectra of purified MTSL-E280C in detergent micelles were recorded at room temperature. Appearance of a sharp, rotationally mobile component indicates unfolding of the protein. To quantitate the fraction of denatured protein, the spectrum of fully denatured FepA (in 4.0-M guanidine) was used for spectral subtraction (from Klug *et al.*, 1995).

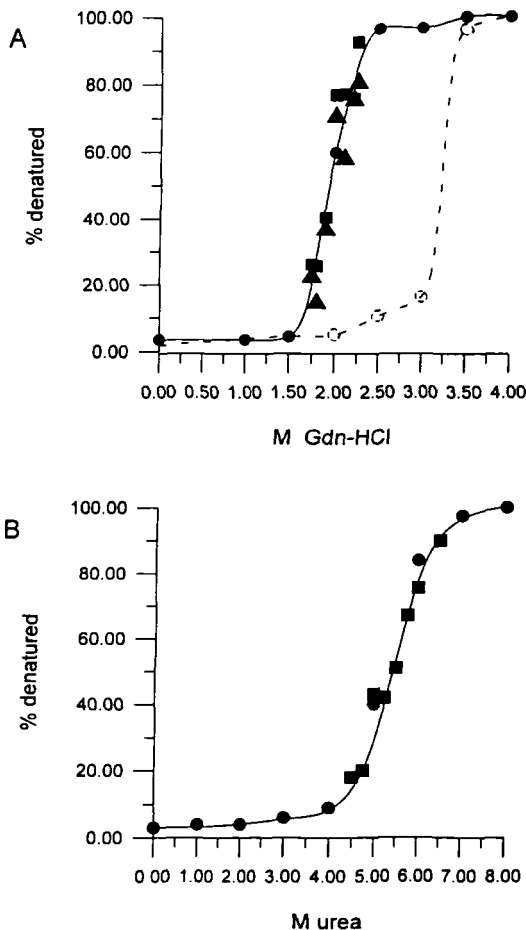


Figure 7. Guanidine-HCl denaturation curves for MTSL-E280C FepA. Percentage of denatured protein is determined by double integrating spectra before and after subtracting the denatured component. Different symbols represent independent experiments. Open circles are from data immediately after guanidine-HCl addition, while the closed data points are after 24 hours at room temperature. The curves are consistent with guanidine-HCl being the more potent denaturant (from Klug *et al.*, 1995).

energy of unfolding for the region of the protein surrounding the spin label, in this case 6.2 ± 0.6 kcal/mol. The kinetics of unfolding decreased markedly in the presence of bound ferric enterobactin, demonstrating an *in vitro* ligand-induced stabilization of the surface loop occupied by E280C. This approach can be used to compare thermodynamic stabilities in different regions of a protein, as well as to compare stabilities of different mutants. Using the spin-labeling approach in conjunction with other spectroscopic methods (i.e., CD) provides information on global versus local stability (Gibney *et al.*, 1997).

Although the preceding study was reasonably well-fit with a two-state model, spin labeling also provides evidence of stable or quasi-stable folding intermediates. These may show up as either complex denaturation curves with multiple transitions

(e.g., Lindgren *et al.*, 1995) or as spectral components with motional characteristics distinct from either the native or fully unfolded state (Lindgren *et al.*, 1995; Svensson *et al.*, 1995).

3.2.4. Ligand-Induced Conformational Changes in FepA

The nature of structural changes that occur with ligand binding and how binding results in transport or transmembrane signaling are key questions about any ligand-gated receptor. For FepA it was interesting to characterize structural changes that may occur on FeEnt binding *in vitro*. Effects of FeEnt binding on spin label motion and accessibility were examined using E280C and E310C, spin labeled with MTSL and reconstituted into liposomes (Liu *et al.*, 1994). Ligand binding produced a small concentration-dependent change in conventional ESR spectra, with decreased motion at both sites. These changes were confirmed using saturation transfer ESR, which is more sensitive to effects in the slow-motion regime (Thomas *et al.*, 1976). The FeEnt binding did not in itself alter the CW saturation properties of either site (of interest, since the ligand contains high-spin ferric iron, discussed later), but it did alter accessibilities of both sites to O₂. Thus, this study demonstrated that the large extracellular ligand-binding surface loop of FepA does indeed undergo a conformational change on ligand binding *in vitro*. Observed changes were distinct from those seen *in vivo* (Jiang *et al.*, 1997).

3.3. Metal-Nitroxide Distance Measurements

3.3.1. FepA

The fact that the ligand for FepA, ferric enterobactin, contains high-spin Fe³⁺ (Pecoraro *et al.*, 1983) conveniently allows distance measurements from the bound ligand to various spin labels as a way of defining the ligand-binding site in FepA. Yet despite the apparent proximity of MTSL-E280C and MTSL-E310C to the ligand-binding site, there was no effect of FeEnt on their ESR spectra, at least at room temperature. This was not surprising, since the metal is not an effective broadening agent if its spin lattice relaxation time T_{1m} is much less than the magnitude of the metal nitroxide spin-spin coupling (Hyde *et al.*, 1979; Budker *et al.*, 1995). It is likely that low-temperature studies will be required to lengthen T_{1m} of the Fe³⁺ to observe its dipolar effects. Alternatively, it may be possible to replace iron with a metal having more desirable relaxation properties, although this will require verification that the complex is recognized by the receptor.

Time domain ESR techniques that examine effects of the faster relaxing metal ion on nitroxide relaxation properties can in principle be used to measure longer distances than can be determined by CW techniques. Budker *et al.* (1995) observed a strong effect of the low-spin heme iron in methemoglobin on the phase memory time of a spin label at a distance of 15 Å using spin echo ESR and distances were

accurately measured for spin-labeled low-spin iron porphyrins in the range of 10–15 Å using saturation recovery ESR to observe the nitroxyl T_{1e} (Rakowsky *et al.*, 1995). Interaction between high-spin iron and a stable semiquinone radical in neuronal nitric oxide synthase was observed by both CW saturation (at 6 K) and saturation recovery (at 22 K), but it was not interpreted in terms of distance (Galli *et al.*, 1996).

A double electron-electron resonance (DEER) spin echo technique was used to measure a distance of 20 Å between nitroxides in a biradical and it was suggested that this approach should be capable of determining distances up to 50 Å (Larsen and Singel, 1993). Data derived from a related “2+1” spin echo method applied to distance measurements between nitroxides attached to two different subunits of hemoglobin indicated a distance of 34 Å (Raitisring *et al.*, 1992). These methods should also be applicable to measuring metal-nitroxide distances, although they remain to be more fully tested in biological systems.

The preceding studies were all performed at low temperatures (4–70 K) and the effects of freezing the protein, usually in the presence of a cryoprotectant, such as glycerol, is a concern. Nonetheless studies of methemoglobin (Budker *et al.*, 1995) and frozen micellar solutions of rhodopsin (Yang *et al.*, 1996; Farrens *et al.*, 1996) gave results consistent with their accepted structure.

3.3.2. Lac Permease

Kaback, Hubbell, and coworkers carried out an extensive series of SDSL experiments on the Lac permease, a bacterial inner membrane protein that transports lactose into the cytoplasm (He *et al.*, 1995; Voss *et al.* 1995a, 1995b). They introduced two important advances to SDSL methodology: Engineering histidine residues into the protein structure as metal-binding sites for determining helix proximity and metal-nitroxide distance measurements between the engineered histidine-metal site and a spin-labeled cysteine residue.

Lac permease contains 12 transmembrane helices. To determine the packing arrangement of the helices and the relative proximity of sites along the transmembrane helices, histidine residues were substituted on the inner faces of helices at sites thought to interact in the native structure (He *et al.*, 1995). These mutants were assayed for transport activity and the ability to bind Mn^{2+} . Manganese binding was quantitated by observing the decrease in the Mn^{2+} signal amplitude that accompanied association with the metal with the protein. Only sites in close proximity bound Mn^{2+} . When metal binding was titrated, a transition midpoint with a pK of 6.2 was observed, confirming histidines as the metal binding site.

Voss *et al.* (1995b) further studied the structure of Lac permease by introducing a series of spin labels along one helix and making distance measurements to Cu^{2+} bound to six contiguous histidines introduced into a turn between helices. Distance-dependent broadening of spin label spectra was observed when Cu^{2+} was bound to

the protein. Metal-nitroxide distances in the range of 8-25 Å were estimated using Leigh theory (Leigh, 1970). These measurements were made at room temperature on spectra that were not at the rigid limit but in good agreement with distances estimated from modeling the helix. This was somewhat surprising, since Leigh theory is rigorously valid only for rigid-limit spectra, and it offers promise for measuring metal-nitroxide distances in the intermediate motional regime.

This approach was further developed using T4 lysozyme (Voss *et al.*, 1995a) for which distances based on crystallographic data are available. Distances were measured from a Cu^{2+} ion bound at an engineered bis-histidine site and spin-labeled cysteine mutations along a well-defined α -helix. Consistent distance measurements were made using Leigh theory at both room temperature and in the frozen state. The effects of having less than stoichiometric occupancy of the metal site were also considered. Together these studies provide optimism that reliable metal-nitroxide distance measurements can be made even at room temperature. This approach is a powerful addition to the SDSL technique, and it can be applied to both natural metalloproteins and proteins containing engineered metal-binding sites.

4. SDSL STUDIES OF PEPTIDE-MEMBRANE INTERACTIONS

The ability of SDSL to distinguish between membrane-bound and soluble forms of spin-labeled peptides and to provide information on the localization of the spin-labeled site with respect to the lipid bilayer makes it a valuable technique in studying peptides whose biological activity involves association with, or incorporation into, the cell membrane. Such peptides can be obtained with unique labeling sites by either molecular genetic methods or solid-phase synthesis. Several examples follow that illustrate how SDSL can be used to define factors that influence membrane binding and insertion.

4.1. Diphtheria Toxin

Diphtheria toxin (DT) contains both a catalytic domain and a translocation (T) domain. The T-domain binds to a eukaryotic cell membrane receptor, and after endocytosis, it delivers the catalytic domain to the cytoplasm, where it causes cell death by inhibiting protein synthesis. A conformational change, elicited by the low pH of the endosomal compartment, initiates insertion of the T-domain into the endosomal membrane, ultimately resulting in transport of the catalytic subunit. Although this is a common theme for many toxins, mechanistic details of this process are poorly understood.

Zhan *et al.* (1995) generated four cysteine mutants in the T-domain of DT and examined conformational changes accompanying exposure to low pH in solution and in the presence of membrane vesicles. Two of the four MTSL-labeled mutants

experienced changes in their CW spectra with a shift to a solution at pH 4.6, both consistent with increased immobilization. All four mutants showed motional changes at pH 4.6 with vesicles present; three had decreased motion, and one showed an increase in spin label mobility. Changes in NiEDDA and O_2 accessibility in going from a solution at pH 8 to the membrane-bound state at pH 4.6 were more revealing. One buried site was converted into a lipid environment with a high Π_{O_2} , whereas another site changed from an exposed location with high accessibility to both O_2 and NiEDDA to a location buried in the protein tertiary fold. This study thus provides an excellent example of dynamic conformational changes inferred from comparing static accessibilities.

In a further SDSL study of the diphtheria toxin T-domain, 21 consecutive cysteine mutants were constructed spanning a helical segment (helix 9 in the transmembrane domain, TH9). In the crystal structure of soluble DT, TH9 is inaccessible to solvent due to helix packing (Choe *et al.*, 1992; Bennett *et al.*, 1994); it was proposed to insert into the endosomal membrane as part of a helical hairpin along with an adjacent helix TH8.

In a manner reminiscent of transmembrane helices of bacteriorhodopsin (Altenbach *et al.*, 1990; Fig. 3), accessibilities to O_2 and NiEDDA showed a marked 3.5 residue periodicity throughout the sequence, indicative of α -helical secondary structure (Oh *et al.*, 1996). The periodicities of Π_{NiEDDA} and Π_{O_2} were 180° out of phase. This phase relationship is consistent with either of two conformations in the membrane: One where the helix lies along the plane of the bilayer surface and one where the helix spans the membrane with an aqueous channel on one side and the lipid bilayer on the other. Depth measurements based on Φ were able to resolve the two possible models suggested by accessibility, thus showing that this segment of the T-domain inserts into the bilayer as a transmembrane α -helix and providing strong evidence that TH9 participates in the formation of an aqueous transmembrane channel.

4.2. Cecropins

Cecropins are small peptides in the range of 35–39 amino acids produced by a variety of insect species as a primitive form of immunological defense against bacterial infection (Steiner *et al.*, 1981). These peptides have potent antibiotic activity, but interestingly these do not hemolyze human erythrocytes. They induce membrane leakage in liposomes (Steiner *et al.*, 1988) and form voltage-gated ion channels in planar bilayers (Christensen *et al.*, 1988). A cecropin analog was isolated from porcine intestine (Lee *et al.*, 1989), raising speculation that they may be widespread among many species.

Cecropins have no native cysteine residues, although they do contain 6–7 lysines that with two arginine residues make them highly positively charged. To examine the structure and membrane interactions of these peptides, a single-

cysteine mutant of cecropin AD, one of the more potent analogs, was prepared by solid-phase synthesis and spin labeled with MTSL (Mchaourab *et al.*, 1993). This peptide was largely unstructured in aqueous solution, giving rise to a sharp three-line ESR spectrum, but it could be induced to undergo conformational transitions by adding the helix-promoting solvent hexafluoro-2-propanol (HFP). This confirmed earlier NMR studies indicating the formation of a helix-turn-helix motif in 15% HFP (Holak *et al.*, 1988). In addition, spin label studies demonstrated aggregate formation at lower HFP concentrations as a preliminary step toward structural organization, and it was suggested that this process may be related to channel formation in membranes.

Unlike diphtheria toxin, cecropins partition between the membrane and aqueous phases. In the presence of liposomes, MTSL-labeled cecropin AD gives a distinct two-component spectrum that is a superposition of a rapidly rotating aqueous component with a subnanosecond rotational correlation time (τ_c) and a membrane-bound component with slower motion (Fig. 8). It was shown that for such a spectrum, the amplitude of the high-field line can be used to determine the fraction of peptide free in solution, therefore providing a direct measure of the extent of binding (Castle and Hubbell, 1976; Archer *et al.*, 1991). This approach can be used to characterize peptide-membrane interactions as a function of pH, ionic strength, membrane surface charge, lipid acyl chain composition, and a number of other experimental variables. For MTSL-cecropin AD, it was shown that

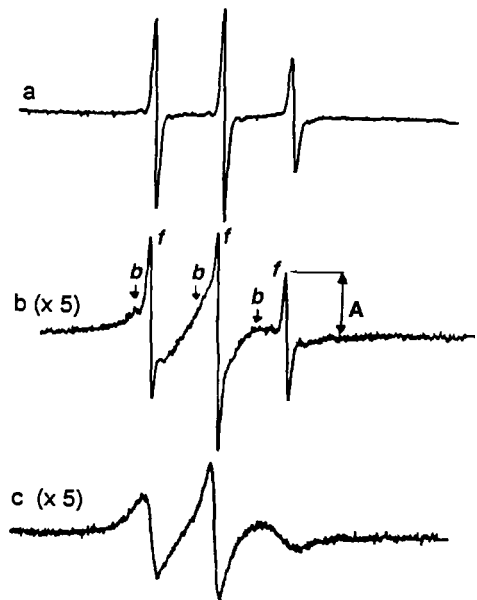


Figure 8. ESR spectra of MTSL-cecropin AD (a) in solution, (b) in the presence of POPC/POPG (9:1) vesicles, and (c) as in (b) with the addition of 50 mM CROX. Spectrum (b) shows an equilibrium between membrane bound peptide (noted as *b*), and peptide free in solution (noted as *f*). The amplitude of the high-field line of the free component from peak maximum to baseline (noted as *A*) is used to quantitate the amount of peptide in solution (from Mchaourab *et al.*, 1994).

membrane binding was cooperative and dependent on pH, surface charge, and alkyl chain length. In addition, accessibility to O_2 was used to determine the depth of spin-labeled residue in the bilayer for the membrane-bound component (Mchaourab *et al.*, 1994). Thus, these SDSL studies allowed determination of physical parameters governing membrane insertion of cecropins and identification of the membrane orientation of the inserted peptide.

4.3. Alamethicin

Alamethicin is a 20-amino acid fungal peptide containing eight residues of the atypical amino acid α -methylalanine and no cysteines. Alamethicin produces voltage-gated ion conductance across lipid bilayers, and has been intensively studied as a model for voltage-gated ion channels.

Spin-labeled derivatives of alamethicin were prepared with the nitroxide attached at either the N- or C-terminus, or at cysteine residues introduced during solid-phase synthesis (Archer *et al.*, 1991; Barranger–Mathys and Cafiso, 1996). Like the cecropins, these peptides partition between the lipid bilayer and the aqueous phase, yielding two-component spectra similar to those in Fig. 8 (Archer *et al.*, 1991). Analysis of these spectra demonstrated cooperativity in membrane binding. Free energy of binding becomes more negative as the peptide:lipid ratio increases, which is consistent with earlier studies based on changes in CD spectra. Spin-labeled derivatives showed no evidence of spin-spin interactions or concentration-dependent changes in τ_c , indicating that aggregation does not play a role in cooperativity. The CW saturation accessibility studies were used to map depths of specific residues in the membrane and showed that the peptide was inserted into the membrane parallel to the bilayer normal, supporting a model where the peptide is in an extended conformation and refuting an alternative bent configuration (Barranger–Mathys and Cafiso, 1996). Thus again SDSL was able to provide insights into the process of membrane association and the structure and organization of the peptide in the membrane-bound state that are not readily available through other spectroscopic techniques.

4.4. Influenza Virus Hemagglutinin

A similar SDSL approach was used to examine a model for the membrane insertion of a 40-amino acid loop of the influenza virus hemagglutinin, HA (Yu *et al.*, 1994). Influenza HA also undergoes a pH-dependent conformational change that initiates fusion of the viral and endosomal membranes, delivering the viral genome into the cell cytoplasm (Carr and Kim, 1993; Bullough *et al.*, 1994). Two mutants of the HA peptide containing single-cysteine substitutions were prepared by solid-phase synthesis, labeled with MTSL, and their membrane-binding equilibria studied as a function of solution pH. In solution, these peptides yielded spectra

characteristic of rapid motion. One peptide lost significant signal amplitude at a low pH without substantial line shape change, suggesting the formation of an equilibrium between monomers and an oligomer where nitroxides were in such close proximity as to be effectively exchange-broadened into the baseline. This effect was reversible, providing confidence that the loss in amplitude was not due to chemical reduction of the nitroxide.

Both peptides showed a decrease in spin label motion upon binding to phospholipid vesicles, allowing quantitation of their membrane-binding equilibria as previously described for cecropin and alamethicin. Oxygen accessibility confirmed that nitroxides were inserted into the lipid bilayer, apparently near the membrane surface, since they retained some exposure to CROX. Membrane-binding isotherms as a function of pH closely followed those observed for HA-induced fusion, thereby providing evidence supporting the physiological relevance of ESR studies.

4.5. Melittin

Melittin is a water soluble 26-amino acid peptide that is the principle component of bee venom. It causes cell lysis and forms voltage-gated ion channels in planar lipid bilayers (Tosteson and Tosteson, 1981). As with many membrane-active peptides, it contains a high percentage of cationic residues, with three lysines and two arginines in addition to the positive charge carried on the N-terminus. Altenbach and Hubbell (1988) spin labeled melittin with the amino-specific nitroxide, succinimidyl-2,2,5,5-tetramethyl-3-pyrroline-1-oxyl-3-carboxylate (SSL). Using reverse-phase HPLC, they were able to isolate all 16 statistically possible reaction products, containing 0, 1, 2, 3, or 4 attached spin labels. Of most use were the singly labeled species derivatized with SSL at either Lys7, Lys21, Lys23, or at the N-terminus. Each of these species possessed hemolytic activity comparable to native melittin, and the Lys7 and N-terminally spin-labeled species were shown to form voltage-gated channels (Tosteson *et al.*, 1990).

As monomers, all singly labeled mutants gave spectra characteristic of rapid motion in aqueous solution, with rotational correlation times in the 1–2 nanosecond range. Salt-induced tetramer formation decreased spin label mobility in all cases and produced apparent spin-spin broadening. Effects of motion and spin-spin interactions could be separated by diluting spin-labeled peptides with enough unlabeled melittin so that the average spin concentration was less than one per tetramer, clearly indicating that both a decrease in motion and the onset of spin-spin broadening occurred upon tetramer formation at all four labeling sites.

To separate dipolar effects from Heisenberg exchange, spin-labeled tetramers were examined in frozen solution. With excess unlabeled melittin present, typical powder spectra were obtained. However marked dipolar broadening was observed for each of the tetramers composed of purely spin-labeled peptide. Although the broadening was somewhat greater for the Lys7-SSL peptide than for other isomers,

the presence of four interacting spin labels precluded quantitative analysis of the spin-spin interaction.

In addition, these peptides were also used to examine the interaction of melittin with membranes. Binding singly labeled species resulted in a decrease in nitroxide mobility at all four sites, with essentially identical spectra observed for neutral and negatively charged bilayers. In contrast to many other small peptides (e.g., cecropins, alamethicin, HA), 100% binding was observed in each case. The absence of spin-spin broadening led to the important conclusion that membrane-bound melittin was monomeric and all four sites were at least qualitatively exposed to CROX.

The orientation of melittin in the membrane was further studied using CW saturation and saturation recovery (SR) methods (Altenbach *et al.*, 1989b). Accessibility to CROX was ordered as Lys7 > Lys21 > Lys23, with the N-terminal label showing two populations with different accessibilities. However, compared to hydrophobic sites in integral membrane proteins, all melittin sites had relatively high CROX accessibilities. Consistent with this, a model was proposed where the peptide lies horizontally along the membrane surface in an α -helical configuration with Lys7 oriented toward the aqueous phase and Lys23 oriented toward the membrane interior (Altenbach *et al.*, 1989b). An important point of methodological interest in this study was that the dependence of collision frequency on both CROX concentration and spin label position determined by CW saturation and SR were in agreement.

5. CONCLUSION

In summary, SDSL is rapidly becoming a mature technique with which to approach questions related to structure-function relationships in proteins. This ESR method is uniquely suited to membrane proteins, and it can provide information on systems that are not amenable to modern NMR and crystallographic methods. SDSL methods are adept at defining local secondary structure (e.g., α -helix and β -strand) through nitroxide-scanning experiments and the sensitivity of the ESR spin label spectrum to molecular motion can give insights into both local and global conformational changes that accompany such events as ligand binding and denaturation. Continued improvements in methods for making distance measurements for both nitroxide:nitroxide and metal:nitroxide pairs will enhance the future application of the site-directed spin-labeling approach even further.

ACKNOWLEDGMENTS This work was supported by NIH grants GM51339, GM22923, and RR01008.

REFERENCES

- Altenbach, C., and Hubbell, W. L., 1988, *Proteins: Structure, Function, and Genetics* **3**:230.
- Altenbach, C., Flitsch, S. L., Khorana, H. G., and Hubbell, W. L., 1989a, *Biochemistry* **28**:7806.
- Altenbach, C., Froncisz, W., Hyde, J. S., and Hubbell, W. L., 1989b, *Biophys. J.* **56**:1183.
- Altenbach, C., Marti, T., Khorana, H. G., and Hubbell, W. L., 1990, *Science* **24**:1088.
- Altenbach, C., Greenhalgh, D. A., Khorana, H. G., and Hubbell, W. L., 1994, *Proc. Natl. Acad. Sci. USA* **91**:1667.
- Altenbach, C., Yang, K., Farrens, D. L., Farahbakhsh, Z. T., Khorana, H. G., and Hubbell, W. L., 1996, *Biochemistry* **35**:12470.
- Anthony-Cahill, S. J., Benfield, P. A., Fairman, R., Wasserman, Z. R., Brenner, S. L., Stafford III, W. L., Altenbach, C., Hubbell, W. L., and DeGrado, W. F., 1992, *Science* **255**:979.
- Archer, S. J., Ellena, J. F., and Cafiso, D. S., 1991, *Biophys. J.* **60**:389.
- Baldwin, J. M., Henderson, R., Beckman, E., and Zemlin, F., 1988, *J. Mol. Biol.* **202**:585.
- Baldwin, J. M., 1993, *EMBO J.* **12**:1693.
- Barranger-Mathys, M., and Cafiso, D. S., 1996, *Biochemistry* **35**:498.
- Bennett, M. J., and Eisenberg, D., 1994, *Protein Sci.* **3**:1464.
- Berliner, L. J., ed., 1976, *Spin-Labeling Theory and Applications* (Academic, New York).
- Berliner, L. J., ed., 1979, *Spin-Labeling. Theory and Applications II* (Academic, New York).
- Berliner, L. J., Grunwald, J., Hanovszky, H. D., and Hideg, K., 1982, *Anal. Biochem.* **119**:450.
- Berliner, L. J., 1983, *Ann. N. Y. Acad. Sci.* **414**:153.
- Berliner, L. J., and Reuben, J., eds., 1989, *Biological Magnetic Resonance*, vol. 8 (Plenum, New York).
- Beth, A. H., Robinson, B. H., Cobb, C. E., Dalton, L. R., Trommer, W. E., Birktoft, J. J., and Park, J. H., 1984, *J. Biol. Chem.* **259**:9717.
- Budker, V., Du, J. L., Seiter, M., Eaton, G. R., and Eaton, S. S., 1995, *Biophys. J.* **68**:2531.
- Bullough, P. A., Hughson, F. M., Skehel, J. J., and Wiley, D. C., 1994, *Nature* **371**:37.
- Burchfield, J., Telehowski, P., Rosenberg, R. C., Eaton, S. S., and Eaton, G. R., 1994, *J. Magn. Reson.* **B104**:69.
- Butterfield, D. A., Roses, A. D., Appel, S. H., and Chesnut, D. B., 1976, *Arch. Biochem. Biophys.* **177**:226.
- Calhoun, D. B., Englander, S. W., Wright, W. W., and Vanderkooi, J. M., 1988, *Biochemistry* **27**:8466.
- Carr, C. M., and Kim, P. S., 1993, *Cell* **73**:823.
- Castle, J. D., and Hubbell, W. L., 1976, *Biochemistry* **15**:4818.
- Choe, S., Bennett, M. J., Fujii, G., Curmi, P. M. G., Kantardjieff, K. A., Collier, R. J., and Eisenberg, D., 1992, *Nature* **357**:216.
- Christensen, B., Fink, J., Merrifield, R. B., and Mauzerall, D., 1988, *Proc. Natl. Acad. Sci. USA* **85**:5072.
- Cowan, S. W., Schirmer, T., Rummel, G., Steiert, M., Ghosh, R., Pauptit, R. A., Jansonius, J. N., and Rosenbusch, J. P., 1992, *Nature* **358**:727.
- Dalton, L. A., McIntyre, J. O., and Fleischer, S., 1987, *Biochemistry* **26**:2117.
- Farahbakhsh, Z. T., Altenbach, C., and Hubbell, W. L., 1992, *Photochem. Photobiol.* **56**:1019.
- Farahbakhsh, Z. T., Hideg, K., and Hubbell, W. L., 1993, *Science* **262**:1416.
- Farahbakhsh, Z. T., Ridge, K. D., Khorana, H. G., and Hubbell, W. L., 1995a, *Biochemistry* **34**:8812.
- Farahbakhsh, Z. T., Huang, Q.-L., Ding, L.-L., Altenbach, C., Steinhoff, H.-J., Horwitz, J., and Hubbell, W. L., 1995b, *Biochemistry* **34**:509.
- Farrens, D. L., Altenbach, C., Yang, K., Hubbell, W. L., and Khorana, H. G., 1996, *Science* **274**:768.
- Feix, J. B., Popp, C. A., Venkataramu, S. D., Beth, A. H., Park, J. H., and Hyde, J. S., 1984, *Biochemistry* **23**:2293.
- Feix, J. B., Yin, J.-J., and Hyde, J. S., 1987, *Biochemistry* **26**:3850.
- Fiori, W. R., Miick, S. M., and Millhauser, G. L., 1993, *Biochemistry* **32**:11957.
- Flitsch, S. L., and Khorana, H. G., 1989, *Biochemistry* **28**:7800.

- Froncisz, W., and Hyde, J. S., 1982, *J. Magn. Reson.* **47**:515.
- Gaffney, B. J., 1976, Chemistry of spin labels, in *Spin Labeling* (L. J. Berliner, ed.) (Academic, New York), pp. 183–238.
- Galli, C., MacArthur, R., Abu-Soud, H. M., Clark, P., Stuehr, D. J., and Brudvig, G. W., 1996, *Biochemistry* **35**:2804.
- Gibney, B. R., Johansson, J. S., Rabanal, F., Skalicky, J. J., Wand, A. J., and Dutton, P. L., 1997, *Biochemistry* **36**:2798.
- Greenhalgh, D. A., Altenbach, C., Hubbell, W. L., and Khorana, H. G., 1991, *Proc. Natl. Acad. Sci. USA* **88**:8626.
- Harris, W., Carrano, C. J., Cooper, S. R., Sofen, S., Avdeef, A., McArdle, J., and Raymond, K. N., 1979, *J. Amer. Chem. Soc.* **101**:6097.
- He, M., Voss, J., Hubbell, W. L., and Kaback, H. R., 1995, *Biochemistry* **34**:15661.
- Holak, T. A., Engstrom, A., Kraulis, P. J., Lindeberg, G., Bennich, H., Jones, T. A., Groenenborn, A. M., and Clore, G. M., 1988, *Biochemistry* **27**:7620.
- Hollifield, W. C., Jr., and Neilands, J. B., 1978, *Biochemistry* **17**:1922.
- Hubbell, W. L., and McConnell, H. M., 1968, *J. Am. Chem. Soc.* **93**:314.
- Hubbell, W. L., and Altenbach, C., 1994a, *Curr. Opin. Struct. Biol.* **4**:566.
- Hubbell, W. L., and Altenbach, C., 1994b, Site-directed spin labeling of membrane proteins, in *Membrane Protein Structure: Experimental Approaches* (S. H. White, ed.) (Oxford University Press, London), pp. 224–48.
- Hubbell, W. L., Mchaourab, H., Altenbach, C., and Lietzow, M. A., 1996, *Structure* **4**:779.
- Hustedt, E. J., Smirnov, A. I., Laub, C. F., Cobb, C. E., and Beth, A. H., 1997, *Biophys. J.* **74**:1861.
- Hyde, J. S., Swartz, H. M., and Antholine, W. E., 1979, Spin label spin probe method, in *Spin Labeling II* (L. J. Berliner, ed.) (Academic, New York), pp. 71–113.
- Hyde, J. S., Yin, J.-J., Feix, J. B., and Hubbell, W. L., 1990, *Pure & Appl. Chem.* **62**:255.
- Jiang, X., Cao, Z., Foster, S. B., Feix, J. B., Payne, M. A., Newton, S. M. C., and Klebba, P. E., 1997, *Science* **276**:1261.
- Klug, C. S., Su, W., Liu, J., Klebba, P. E., and Feix, J. B., 1995, *Biochemistry* **34**:14230.
- Klug, C. S., Su, W., and Feix, J. B., 1997, *Biochemistry* **36**:13027.
- Kreusch, A., Neubuser, A., Schiltz, E., Weckesser, J., and Schulz, G. E., 1994, *Protein Sci.* **3**:58.
- Larsen, R. G., and Singel, J. D., 1993, *J. Chem. Phys.* **98**:5134.
- Lee, J.-Y., Boman, A., Chuanxin, S., Andersson, M., Jörnvall, H., Mutt, V., and Boman, H. G., 1989, *Proc. Natl. Acad. Sci. USA* **86**:9159.
- Leigh, J. S., Jr., 1970, *J. Chem. Phys.* **52**:2608.
- Likhtenshtein, G. I., 1976, *Spin-Labeling Methods in Molecular Biology* (Wiley, New York).
- Lindgren, M., Svensson, M., Freskgård, P.-O., Carlsson, U., Jonasson, P., Mårtensson, L.-G., and Jonsson, B.-H., 1995, *Biophys. J.* **69**:202.
- Liu, J., Rutz, J. M., Klebba, P. E., and Feix, J. B., 1994, *Biochemistry* **33**:13274.
- McConnell, H. M., and McFarland, B. G., 1970, *Quart. Rev. Biophys.* **3**:91.
- Mchaourab, H. S., Hyde, J. S., and Feix, J. B., 1993, *Biochemistry* **32**:11895.
- Mchaourab, H. S., Hyde, J. S., and Feix, J. B., 1994, *Biochemistry* **33**:6691.
- Mchaourab, H. S., Lietzow, M. A., Hideg, K., and Hubbell, W. L., 1996, *Biochemistry* **35**:7692.
- Mchaourab, H. S., Oh, K. J., Fang, C. J., and Hubbell, W. L., 1997, *Biochemistry* **36**:307.
- Means, G. E., and Feeney, R. E., 1971, *Chemical Modification of Proteins* (Holden-Day, San Francisco).
- Meirovitch, E., and Freed, J., 1984, *J. Phys. Chem.* **88**:4995.
- Millhauser, G. L., 1992, *TIBS* **17**:448.
- Murphy, C. K., Kalve, V. I., and Klebba, P. E., 1990, *J. Bacteriol.* **172**:2736.
- Neilands, J. B., 1981, *Ann Rev. Biochem.* **50**:715.
- Ogawa, S., and McConnell, H. M., 1967, *Proc. Natl. Acad. Sci. USA* **58**:19.
- Oh, K. J., Zhan, Q., Cui, C., Hideg, K., Collier, R. J., and Hubbell, W. L., 1996, *Science* **273**:810.

- Pace, C. N., 1986, *Methods Enzymol.* **131**:266.
- Pake, G. E., 1948, *J. Chem. Phys.* **16**:327.
- Pecoraro, V. L., Wong, G. B., Kent, T. A., and Raymond, K. N., 1983, *J. Am. Chem. Soc.* **105**:4617.
- Poole, C. P., 1983, *Electron Spin Resonance* (Wiley, New York).
- Popp, C. A., and Hyde, J. S., 1981, *J. Magn. Reson.* **43**:249.
- Qin, Z., and Cafiso, D. S., 1996, *Biochemistry* **35**:2917.
- Rabenstein, M. D., and Shin, Y.-K., 1995, *Proc. Natl. Acad. Sci. USA* **92**:8239.
- Raitsimring, A., Peisach, J., Lee, H. C., and Chen, X., 1992, *J. Phys. Chem.* **96**:3526.
- Rakowsky, M. H., More, K. M., Kulikov, A. V., Eaton, G. R., and Eaton, S. S., 1995, *J. Am. Chem. Soc.* **117**:2049.
- Resek, J. F., Farahbakhsh, Z. T., Hubbell, W. L., and Khorana, H. G., 1993, *Biochemistry* **32**:12025.
- Ridge, K. D., Zhang, C., and Khorana, H. G., 1995, *Biochemistry* **34**:8804.
- Schirmer, T., Keller, T. A., Wang, Y.-F., and Rosenbusch, J. P., 1995, *Science* **267**:512.
- Shin, Y.-K., Levinthal, C., Levinthal, F., and Hubbell, W. L., 1993, *Science* **259**:960.
- Steiner, H., Hultmark, D., Engström, A., Bennich, A., and Boman, H. G., 1981, *Nature* **292**:246.
- Steiner, H., Andreu, D., and Merrifield, R. B., 1988, *Biochim. Biophys. Acta* **939**:260.
- Steinhoff, H.-J., 1988, *J. Biochem. Biophys. Methods* **17**:237.
- Steinhoff, H.-J., Dombrowsky, O., Karim, C., and Schneiderhahn, C., 1991, *Eur. Biophys. J.* **20**:293.
- Subczynski, W. K., and Hyde, J. S., 1981, *Biochim. Biophys. Acta* **643**:283.
- Svensson, M., Jonasson, P., Freskgård, P.-O., Jonsson, B.-H., Lindgren, M., Mårtensson, L.-G., Gentile, M., Borén, K., and Carlsson, U., 1995, *Biochemistry* **34**:8606.
- Thomas, D. D., Dalton, L. R., and Hyde, J. S., 1976, *J. Chem. Phys.* **65**:3006.
- Todd, A. P., Cong, J., Levinthal, F., Levinthal, C., and Hubbell, W. L., 1989, *Proteins: Structure, Function, and Genetics* **6**:294.
- Tosteson, M. T., and Tosteson, D. C., 1981, *Biophys. J.* **36**:109.
- Tosteson, M. T., Alvarez, O., Hubbell, W. L., Bieganski, R. M., Altenbach, C., Caporales, L. H., Levy, J. J., Nutt, R. F., Rosenblatt, M., and Tosteson, D. C., 1990, *Biophys. J.* **58**:1367.
- Unger, V. M., and Schertler, G. F., 1995, *Biophys. J.* **68**:1776.
- Voss, J., Salwinski, L., Kaback, H. R., and Hubbell, W. L., 1995a, *Proc. Natl. Acad. Sci. USA* **92**:12295.
- Voss, J., Hubbell, W. L., and Kaback, H. R., 1995b, *Pmc. Null Acad. Sci. USA* **92**:12300.
- Weiss, M. S., Abele, U., Weckesser, J., Welte, W., Schiltz, E., and Schulz, G. E., 1991, *Science* **254**:1627.
- Wertz, S. L., Savino, Y., and Cafiso, D. S., 1996, *Biochemistry* **35**:11104.
- Windrem, D. A., and Plachy, W. Z., 1980, *Biochim. Biophys. Acta* **600**:655.
- Yang, K., Farrens, K. D., Altenbach, C., Farahbakhsh, Z. T., Hubbell, W. L., and Khorana, H. G., 1996, *Biochemistry* **35**:14040.
- Yu, Y. G., King, D. S., and Shin, Y.-K., 1994, *Science* **266**:274.
- Zhan, H., Oh, K. J., Shin, Y.-K., Hubbell, W. L., and Collier, J. L., 1995, *Biochemistry* **34**:4856.

This page intentionally left blank

Spin-Labeled Nucleic Acids

Robert S. Keyes and Albert M. Bobst

1. INTRODUCTION

Numerous spectroscopic techniques have been used to investigate structure-function relationships of nucleic acids. These investigations are often limited however because the nucleic acid signals monitored by such techniques as ultraviolet, fluorescence, circular dichroism (CD), infrared, or nuclear magnetic resonance (NMR) spectroscopy are too complicated to be rigorously examined due to interference from surrounding molecules. The concept of using a reporter group to analyze local macromolecular conformations and interaction processes can on the other hand help simplify a complex biological system, provided due regard is given to inherent possible nitroxide perturbations. While nitroxide labels as reporter groups have been successfully applied to analyze many different systems, spin labeling nucleic acids has not been so prevalent. As pointed out earlier (Bobst, 1979), the application of nitroxide labeling to the field of nucleic acids can in principle be divided into two groups. In one group the nitroxide is attached to small ligands known to interact with nucleic acids; in the other group the label is directly linked to the nucleic acid lattice.

While the chemistry required to attach a label covalently to a small nucleic-acid-binding ligand is relatively straightforward provided the ligand contains an

Robert S. Keyes and Albert M. Bobst • Department of Chemistry, University of Cincinnati, Ohio 45221-0172.

Biological Magnetic Resonance, Volume 14: Spin Labeling: The Next Millennium, edited by Berliner. Plenum Press, New York, 1998.

appropriate functional group, the challenge of introducing a reporter group sequence specifically into a nucleic acid is substantial. Significant progress was made in preparing and characterizing nucleic acids with probes covalently attached to well-defined sites as well as in developing theoretical concepts to analyze their EPR spectra. This chapter focuses on these more recent developments.

Nucleic acids offer a number of potentially reactive sites for covalently attaching a tethered nitroxide. However it is difficult to achieve base and sequence-specific spin labeling through direct chemical modification if only the four common bases are present and a chemically reactive base analog is absent. Alkylation of DNA with various hydrazine mustard spin labels were found to give some preferential labeling of the four bases (Raikova *et al.*, 1982, 1983). Some of the labels had a strong denaturing effect on double-stranded DNA (Ivanov *et al.*, 1983); studies on DNA fragments of plasmid pBR322 suggested sequence-dependent spin labeling (Weygand-Durasevic and Susic, 1990). Selective modification was achieved in the case of T4 phage DNA using a nongluco-sylated mutant and spin labeling hydroxyl groups of the hydroxymethyl-2-deoxycytidines (Kamzolova, 1987).

New synthetic approaches have been developed that make it possible to spin label oligonucleotides sequence specifically with great accuracy by either chemical or enzymatic means or a combination of both approaches. Nucleotides labeled by chemical oligonucleotide synthesis offers the possibility of synthesizing spin-labeled oligonucleotides with any desired sequence in relatively large amounts (5–10 OD). Sequence-specific enzymatic incorporation of appropriate spin-labeled substrates into DNA with a variety of enzymes yields spin-labeled oligonucleotides and polynucleotides with some limitation in the possible sequences and in somewhat smaller quantities (0.2–1 OD). However the chemical synthesis approach requires elaborate protocols to ensure the preservation of nitroxide during various chemical reaction steps; it also necessitates complicated purification procedures to yield pure spin-labeled oligonucleotides. Such difficulties do not arise with enzymatically prepared spin-labeled nucleic acids.

In principle it is also possible to synthesize oligonucleotides first with adopting groups, then to modify these groups specifically with appropriate reporter groups, such as fluorophores (Gibson and Benkovic, 1987; Haralambidis *et al.*, 1987) or nitroxides (Fidanza and McLaughlin, 1989). Unfortunately this approach can readily lead to side reactions giving rise to other labeled products exhibiting additional motional states. In view of the great sensitivity of electron paramagnetic resonance (EPR) spectroscopy, which can detect picomole quantities of a nitroxide, the adopting group approach for spin labeling nucleic acids is believed to be less reliable than methods discussed in detail in this chapter.

Besides the difficulty of preparing clean products containing sequence specifically incorporated nitroxides, a fundamental issue concerns the accuracy with which a tethered nitroxide reflects the motion of the assembly to which it is attached.

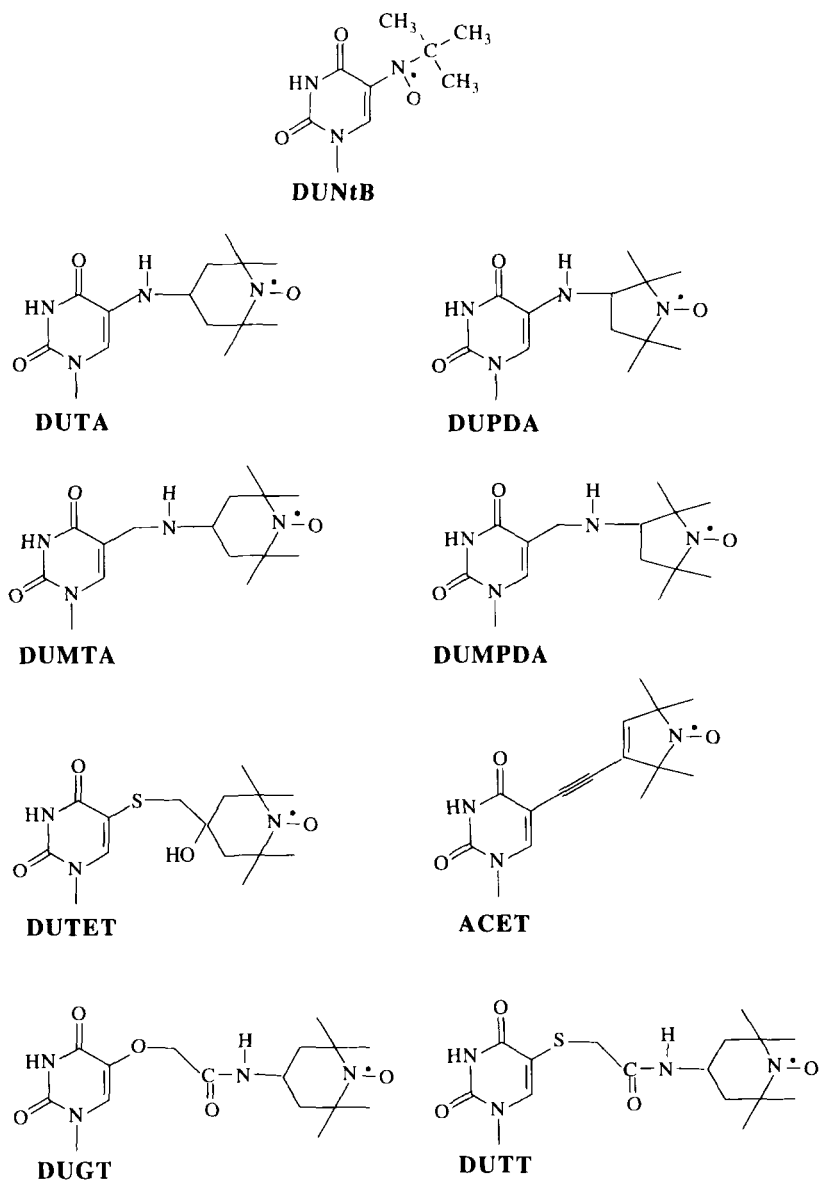
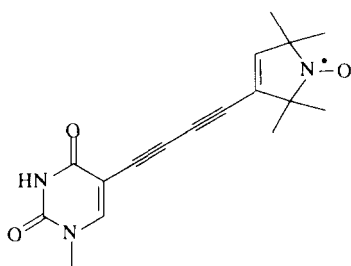
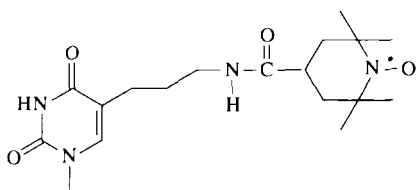
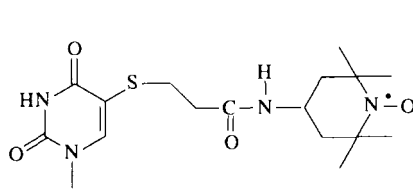
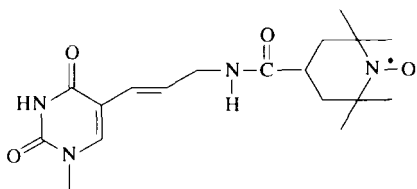
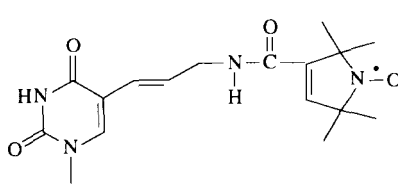
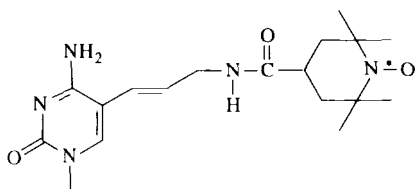
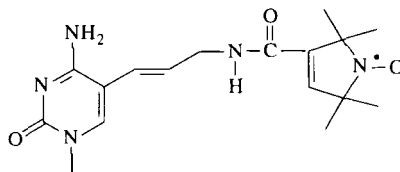


Figure 1(a). Chemical structures of spin-labeled deoxyridine and deoxycytidine derivatives in order of increasing tether size that were incorporated into DNA sequences.

**DIACET****DUPAT****DUMPT****DUAT****DUAP****DCAT****DCAP****Figure 1(b).**

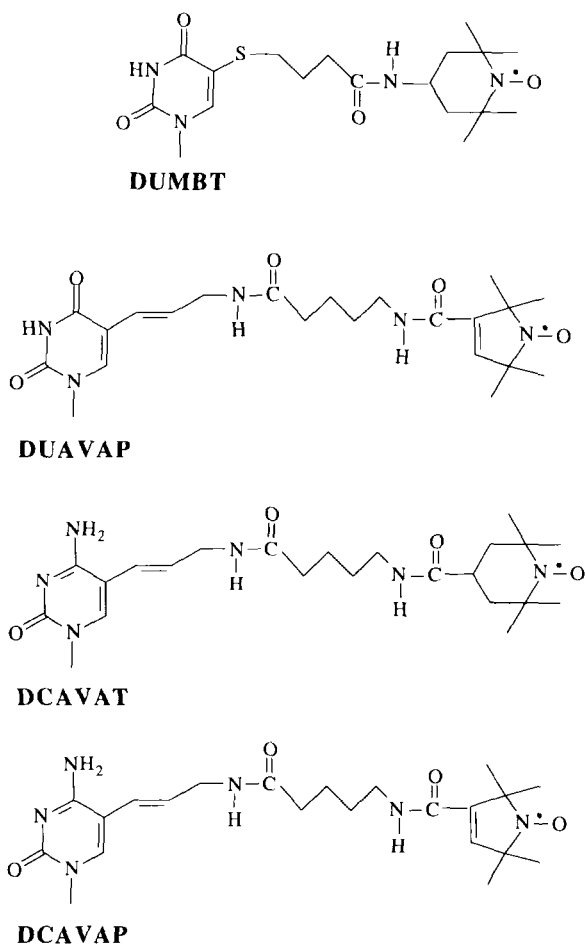


Figure 1(c).

It would be ideal to attach the nitroxide rigidly to prevent independent label motion without causing structural perturbation. However the design of such ideal labels for nucleic acids has to this point remained elusive. Figure 1 lists in order of increasing tether length chemical structures of spin-labeled bases that were incorporated into nucleic acid sequences by chemical oligonucleotide synthesis or enzymatic techniques.

This chapter reviews synthesizing and characterizing spin-labeled nucleic acids, theoretical analyses of resulting EPR spectra, and biological applications of spin-labeled nucleic acids. Emphasis is placed on research performed since the last

review from this laboratory (Bobst, 1979). [In the meantime a few reviews dealing specifically with spin-labeling nucleic acid were published (Kamzolova and Postnikova, 1981a, 1981b; Nöthig-Laslo *et al.*, 1987).]

2. SYNTHESSES OF SPIN-LABELED NUCLEIC ACIDS

2.1. Chemical Oligonucleotide Synthesis

Chemical synthesis of spin-labeled oligonucleotides can in principle be achieved by using either phosphoramidite or phosphotriester chemistry to incorporate spin-labeled bases into oligonucleotides. In view of the reaction conditions required for either method, it was found helpful first to evaluate the stability of 5- and 6-membered ring nitroxides under these required conditions. For instance it is well-known that the chemical stability of a nitroxide is strongly affected by a number of chemicals (for a review on nitroxide chemistry, see Aurich, 1989).

The phosphotriester method is usually preferred for sensitive modified bases (Kaplan and Itakura, 1987), because the coupling unit for phosphoramidite chemistry is relatively reactive. On the other hand the coupling yield of the former method is about 90%, whereas the latter one gives yields close to 100%. A high-coupling yield is particularly important when preparing long oligomers. While the phosphoramidite method is advantageous with its high-coupling yields, it calls for an oxidation step not required with phosphotriester chemistry. Unfortunately the nitroxide undergoes a 10–20% destruction under published oxidation conditions consisting of 0.1-M I_2 in $H_2O/2,6$ -lutidine/THF (Atkinson and Smith, 1984).

Regarding the chemistry common with phosphotriester and phosphoramidite chemistry, the acidic detritylation step can be potentially hazardous to the nitroxide moiety. While protonation of the nitroxide group does not change the oxidation level of the molecule, stabilization due to delocalization of the unpaired electron is essentially lost (Aurich, 1989). Various detritylation conditions, including protic, aprotic, and Lewis acids, were explored, and detritylation protocols were found that cause minimal damage to the nitroxide (Duh, 1990; Kryak, 1990).

Since phosphotriester chemistry does not need an oxidation step, it was originally the preferred method in this laboratory to prepare spin-labeled oligonucleotides. Subsequently we discovered that the phosphoramidite protocol of Pharmacia requires only 0.01-M I_2 for the oxidation step. When repeating EPR experiments with this tenfold lower I_2 concentration, the rate of nitroxide destruction was significantly reduced. In view of the possibility of working with less I_2 , we prepared some DUTA-labeled oligomers with the phosphoramidite protocol of Pharmacia. Reaction products were then purified in the same way as spin-labeled material obtained by phosphotriester chemistry. It was determined that EPR-specific activity (A_{EPR}) (see Sec. 3.2) of the oligomer prepared by phosphotriester chemistry

was still by about 20% greater than the A_{EPR} of a product obtained by the phosphoramidite method (Persichetti *et al.*, 1991).

2.1.1. Synthesis of Some Spin-Labeled Building Blocks for the Phosphotriester or Phosphoramidite Method

The one-atom-tethered C-5 spin-labeled nucleosides DUTA, 5-[(1-Oxyl-2,2,6,6-tetramethyl-4-piperidinyl)amino]-2'-deoxyuridine (Bobst *et al.*, 1983) and DUPDA, 5-[(1-Oxyl-2,2,5,5-tetramethyl-3-pyrrolidinyl)amino]-2'-deoxyuridine (Duh, 1990) are obtained by a condensation reaction between 4-amino-TEMPO or 3-amino-PROXYL with 5-hydroxy-2'-deoxyuridine (Fig. 2). The method, originally described for DUTA by Bobst *et al.* (1983), was applied more recently to the synthesis of DUPDA (Duh, 1990). The DUTA and DUPDA are very stable under basic deprotection conditions (conc. NH_3 at 25–60 °C).

Figure 3 shows the addition of six- and five-membered nitroxide rings to 3,5-dUCHO (4) to form DUMTA (5) and DUMPDA (6), respectively. The synthetic method for preparing these 2-atom-tethered nitroxides is relatively simple and

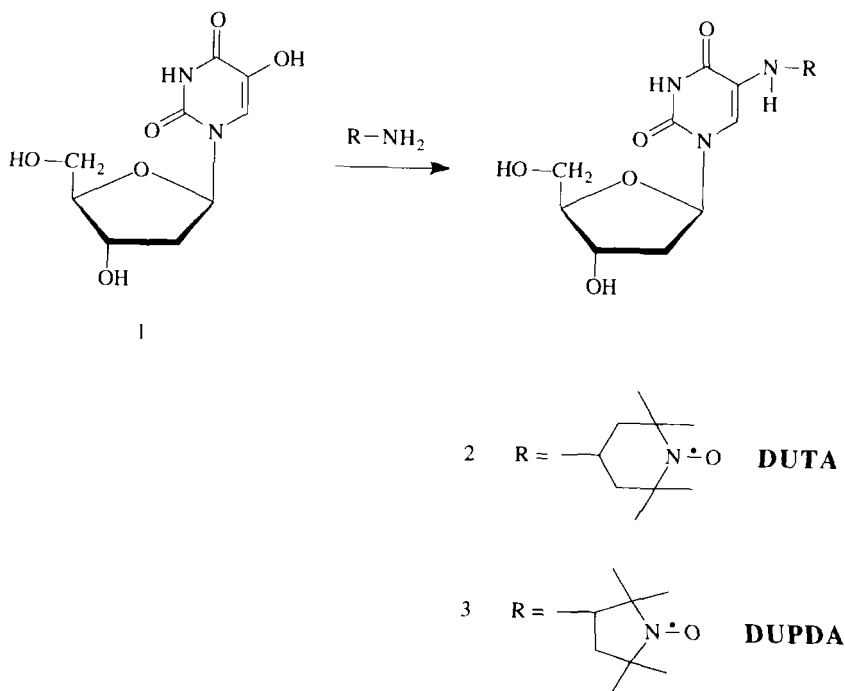


Figure 2. Condensation of 4-amino-TEMPO or 3-amino-PROXYL with 5-hydroxy-2'-deoxyuridine (1) to yield DUTA or DUPDA, respectively.

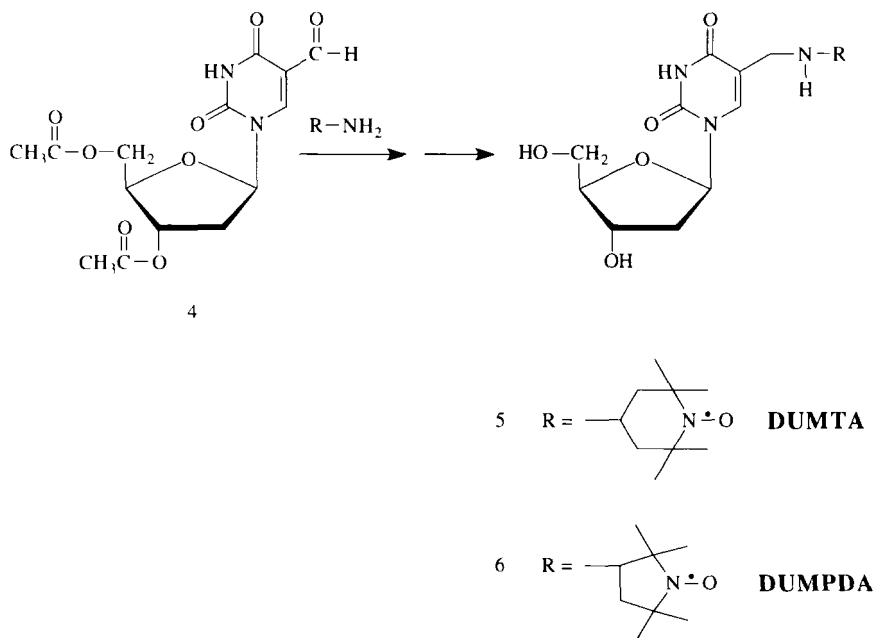


Figure 3. Formation of DUMTA or DUMPDA from 3,5-dUCHO (4) with 4-amino-TEMPO or 3-amino-PROXYL, respectively, through a condensation and a subsequent reduction step.

economical. The EPR spectra of spin-labeled nucleosides are typical for uridine analogs labeled with five- and six-membered ring nitroxides (Kryak and Bobst, 1990).

2.1.2. Phosphotriester Synthesis

Spin-labeled oligonucleotides are synthesized according to standard solid-phase phosphotriester chemistry, as described in Gait (1984). Coupling time with spin-labeled derivatives is usually increased by about a factor of two compared to the time needed for unlabeled derivatives. Spin-labeled oligonucleotides are cleaved from the support and deblocked at internucleotide phosphates by treatment with cone. NH₃ overnight at 55 °C. The trityl group is removed by a short exposure to 40% (v/v) acetic acid; after neutralization with cone. NH₃, the spin-labeled material is desalted with a Bio Gel P-2 column before FPLC purification.

2.1.3. Phosphoramidite Synthesis

Reaction steps required for synthesis are shown with Fig. 4. Preparation of d(T)₇(DUTA)d(T)₇ from the phosphoramidites, DMTr-DUTA-PA and commer-

cially available 5'-O-DMTr-thymidine-3'-(2-cyanoethyl-N,N-diisopropyl)phosphoramidite can be achieved with DMTr-dT-CPG as the solid support on a fully automated Pharmacia Gene™ Assembler DNA Synthesizer™. Synthesis is carried out with the Pharmacia protocol with the exception of about doubling coupling time for the spin-labeled derivative. Note: Pharmacia protocol calls for only 0.01-M I₂, while standard protocol for the Applied Biosystems 380B™ instrument requires 0.1-M I₂. Unlike phosphotriester synthesis, capping is carried out after each coupling, and the final detritylation is directly performed on the column. The final product is removed from the solid support by heating the support in conc. NH₃ for 16 h.

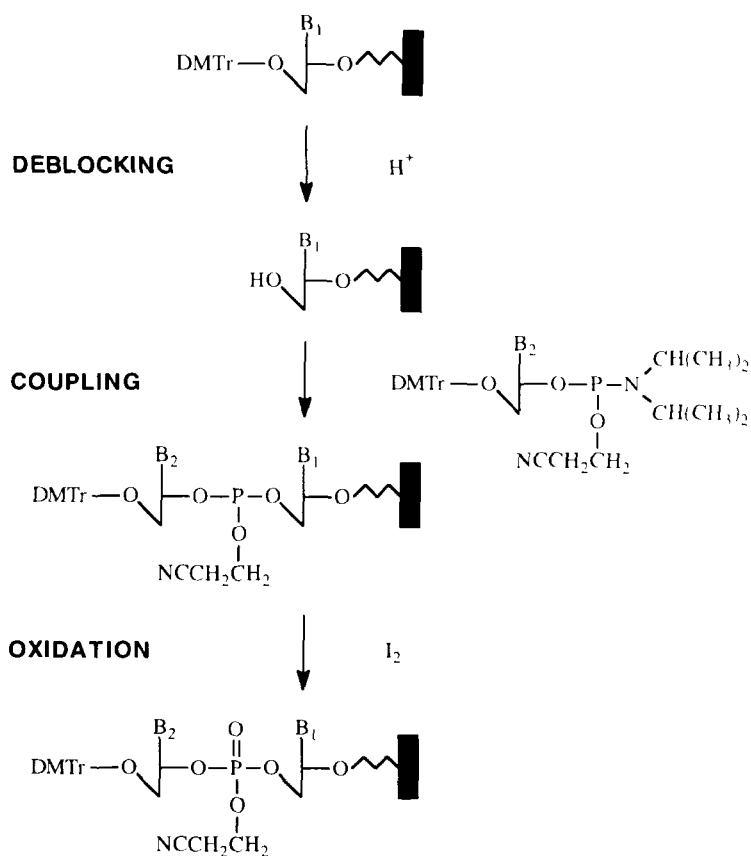


Figure 4. Reaction cycle of phosphoramidite synthesis to prepare a spin-labeled oligonucleotide. The B₁ is one of the four possible starting bases attached to the support. Extension of the oligonucleotide occurs in the 3'-5' direction by adding phosphoramidites containing an unlabeled or spin-labeled base B₂.

2.1.4. Purification of Spin-Labeled Oligonucleotides by FPLC

Considerable effort has to be put into purifying spin-labeled oligomers by HPLC and/or FPLC to isolate pure products with optimal A_{EPR} values; however these can be considerably reduced when using steel columns together with acetonitrile as a solvent component. Fully deprotected oligonucleotides are best purified by anion exchange Mono Q FPLC using a sodium hydroxide/sodium chloride gradient (pH 12). The last major peak usually contains the desired material, which, depending on the spin-labeled derivative used, may contain pure material. Most often however, it is necessary to add a reverse-phase ProRPC FPLC purification step with an acetonitrile/triethylammonium gradient (pH 7.0).

2.1.5. Enzymatic Digestion of Spin-Labeled Oligonucleotides and HPLC Analysis of Digest

The base composition of spin-labeled nucleic acids can be verified by enzyme digestion and subsequent HPLC analysis. The 0.1 OD₂₆₀ of FPLC-purified spin-labeled oligomer is digested with a 0.1 unit of alkaline phosphatase in 50-mM Tris-HCl, pH 8.5, 10-mM MgCl₂ in a total volume of 150 μ l for 1 h before adding 0.02 unit of phosphodiesterase, then keeping the mixture for 16 h at room temperature. An aliquot of the digestion is analyzed by reverse-phase chromatography with a Delta-Pak™ C-18 column (Waters, Inc.™) (Duh and Bobst, 1991).

2.2. Enzymatic Incorporation of Spin-Labeled Substrates

Our laboratory developed a variety of nitroxide-labeled uridine, deoxyuridine, and deoxycytidine derivatives to serve as substrates for nucleic-acid-synthesizing enzymes. Either template-independent enzymes, such as polynucleotide phosphorylase (Bobst and Torrence, 1978; Hakam *et al.*, 1980; Kao *et al.*, 1983; Toppin *et al.*, 1983a) and terminal deoxynucleotidyl transferase (Toppin *et al.*, 1983b; Bobst *et al.*, 1984a), or template-dependent enzymes, such as reverse transcriptase from *avian myeloblastosis virus* (Warwick-Koochaki *et al.*, 1983), DNA polymerase I from *E. coli* (Pauly *et al.*, 1987; Strobel *et al.*, 1989), T-4 DNA polymerase (Pauly *et al.*, 1989), *Micrococcus luteus* DNA polymerase (Strobel *et al.*, 1995), and *AmpliTag* DNA polymerase Stoffel fragment (Strobel *et al.*, 1995) were used for this purpose. The enzymatic incorporation of spin-labeled substrates was successful provided the tether used to couple the nitroxide to the base exhibited some flexibility. The only labeled derivative to fail as a substrate for any polymerase so far tested was the one-atom tethered DUTA (Toppin, 1983). However DUTA's excellent thermal stability, its chemical stability, and its ease of preparation on a large scale made the one-atom-tethered compound a good candidate for sequence-specific incorporation by chemical oligonucleotide synthesis (see Sec. 2.1).

2.2.1. Preparation of Spin-Labeled Lambda Phage DNA by Nick Translation or End Replacement

The spin-labeled thymidine analogs ppp-DUAT, ppp-DUPAT, and ppp-DUAVAP were incorporated into lambda phage DNA by nick translation (Pauly *et al.*, 1989). Control experiments with [^3H]dATP to monitor incorporation kinetics show that these analogs are good substrates in a nick translation system. Preparation of radiolabeled and spin-labeled lambda phage DNA is best carried out in polypropylene tubes. Each reaction requires 30 μl of a solution of 0.1-M Tris-HCl (pH 7.5), 0.01-M MgCl_2 , 0.001-M dl-dithiothreitol, 22- $\mu\text{g/ml}$ nuclease free BSA, 1.5- μg lambda phage DNA, 2.4 nmol each of dGTP, dCTP, [^3H]dATP (spec. activity 650 Ci/mol), and 0.5-nmol TTP as well as 1.9 nmol of the spin-labeled thymidine analog ppp-dL (in the absence of TTP, the resulting lambda phage DNA spectrum exhibits significant broadening due to Heisenberg spin exchange. (For an analysis of broadened EPR spectra due to a large incorporation of nitroxides into a single-stranded nucleic acid lattice, see Kao and Bobst, 1986.) The 10 μl of Pol I/DNAse I in 50-mM Tris-HCl (pH 7.5), 5-mM Mg acetate, 1-mM 2-mercaptoethanol, 0.1-mM phenylmethylsulphonyl fluoride, 50% (v/v) glycerol, and 100- $\mu\text{g/ml}$ nuclease-free BSA are added before incubating the mixture at 16 $^\circ\text{C}$. At appropriate time intervals 3- μl samples are spotted on Whatman DE81 filters, then counted. After establishing an optimal nick translation conditions, the reaction is carried out without tritiated material and scaled up threefold. After incubation at 16 $^\circ\text{C}$ for 90 min, 10- μl 0.1-M Na_2EDTA (pH 8.0) and 2.5- μl 5% (w/v) SDS are added to stop incorporation.

The ppp-DUAVAP was incorporated into Hind-III-restriction fragments of lambda phage DNA by end replacement with T-4 DNA polymerase. For that purpose 10 μl of a solution of 50-mM Tris-acetate (pH 7.9), 50-mM sodium acetate, 10-mM magnesium acetate, 0.5-mM dl-dithiothreitol, 100- $\mu\text{g/ml}$ nuclease-free BSA is added to 10 μl of 0.3-M sodium acetate containing 5.5 μg of chloride-free Hind III digested lambda phage DNA. This mixture is incubated together with 5 units of T-4 DNA polymerase for 15 min at 37 $^\circ\text{C}$, then 7 μl of a solution containing 3 nmol each of dATP, dGTP, and dCTP are added together with 2 μl an aqueous solution containing 3.8-nmol ppp-DUAVAP. After incubation at 37 $^\circ\text{C}$ for 35 min, the reaction is stopped by adding 10- μl 0.3-M Na_2EDTA (pH 8.0) and 2.5-ml 5% (w/v) SDS.

2.2.2. End Filling with Klenovv Fragment

Figure 5 shows the enzymatic reaction required for end filling a partially complementary 17mer with the large DNA polymerase (Klenow) fragment. The reaction leads to the formation of a 26mer containing a sequence specifically incorporated spin-labeled nucleotide (L). The L corresponds to analogs DUAT,



Figure 5. Sequence-specific incorporation of spin-labeled nucleotide L by first hybridizing two partially complementary 17mers, then end filling to form a 26mer. (Reprinted with permission from Bobst *et al.*, 1988.)

DUAP, or DUAVAP; from Fig. 5 it is apparent that positioning L in the 26mer can be readily changed by changing the position of the A residue in the 17mer.

Preparation of radiolabeled and spin-labeled 26mer is best carried out in propylene tubes with 0.2-nmol 17mer, 4-nmol ppp-DUAT or 4-nmol ppp-DUAP or 4-nmol ppp-DUAVAP, 30-nmol [³H]dGTP (specific activity 17 cpm/pmol), and 6.6 units of a Klenow fragment in a total volume of 102 μ l containing 0.14-M Tris-HCl, 0.05-M NaCl, pH 7.8, 0.014-M MgCl₂, 1.4-mM dl-dithiothreitol, and 28- μ g/ml bovine serum albumin. The mixture is incubated at room temperature, and 5- μ l aliquots are withdrawn at appropriate time intervals, spotted on Whatman DE 81 filters, then counted. Kinetics of dGMP incorporation showed that spin-labeled analogs are excellent substrates. After establishing the best reaction conditions, end filling is done without the radiolabel; by increasing individual component amounts fourfold, about 0.4 nmol of spin-labeled 26mer can be isolated. As noted earlier (Bobst *et al.*, 1988), sequence specifically spin-labeled oligonucleotides prepared enzymatically are more easily purified than those prepared by chemical oligonucleotide synthesis.

2.2.3. Spin Labeling with *M. luteus* DNA Polymerase or Taq DNA Polymerase

With *M. luteus* DNA polymerase, polymerization reactions (650 μ l) are conducted in 1.5-ml polypropylene tubes containing H₂O, 380 μ l; 0.8-M KH₂PO₄ (pH 7.5), 50 μ l; 1.25-mM dl-DTT, 50 μ l; 76-mM MgCl₂, 50 μ l; 6-mM dCTP, 25 μ l [50- μ l dCTP and 0- μ l dLTP for synthesizing (dG-dC)_n]; 6-mM dLTP, 25 μ l; 6-mM dGTP, 50 μ l; (dI-dC)_n template primer at 0.05 OD₂₅₁/ μ l in H₂O, 5 μ l; and 15 units *M. luteus* DNA Polymerase (1 U/ μ l) buffered in 0.2-M KH₂PO₄ (pH 7.4), 0.1-M NaCl, 1.5-mM Na₂EDTA, and 50% (v/v) glycerin, 15 μ l. Reactions are incubated at 37 °C for 10–12 hours, then terminated by adding 3-M NaCl, 45-mM Na₂EDTA (200 μ l). Deproteinization is carried out in 3-ml glass tubes by extraction with CHCl₃/isoamyl alcohol (5:2, v/v). After centrifugation at 1750g, the aqueous DNA-containing layer is drawn off, then transferred to another glass tube. The extraction procedure is repeated four times before separating polymers from the unincorporated nucleotides by size exclusion chromatography (Strobel *et al.*, 1995).

With Taq DNA Polymerase, the reaction (per ml) in 10-mM Tris-HCl (pH 8.3), 10-mM KCl, 4-mM $MgCl_2$, 1-mM dATP, 1-mM dTTP, 4-mM-dGTP, and 4-mM ppp-DCAVAP contains 100-mg pRDZ8/pUC8 hybrid and 100 units of *AmpliTaq* DNA Polymerase. The reaction mixture (with mineral oil layered on top of it) is incubated at 70 °C, and after 45 min, the reaction is supplied with dCTP to bring its concentration to 4 mM. The reaction is stopped after 2 hours by extracting three times with phenol and three times with $CHCl_3$ /isoamyl alcohol (24:1, v/v). The DNA is loaded onto a Sephacryl S-200 (16 × 340mm) size-exclusion column, then eluted with 0.04-M NH_4HCO_3 (pH 7.5). The DNA-containing eluate is collected and freeze dried repeatedly (Strobel *et al.*, 1995).

2.2.4. Purification of Enzymatically Spin-Labeled Nucleic Acids

Purification of spin-labeled DNA for EPR analysis is usually accomplished by exclusion chromatography over a Sephadex G-50 column with 150-mM NaCl, 15-mM Na-citrate pH 7 with 0.1% (w/v) SDS. Polymer-containing fractions are concentrated by centrifugation with an Amicon K-30 Centricon filtration device, and the buffer is exchanged by washing through the Centricon filter three times with 1.5 ml of a 10-mM Tris-HCl, 10-mM NaCl buffer pH 7.9.

In Fig. 6 FPLC elution profiles confirm that a 26mer prepared enzymatically has the same retention time as a 26mer constructed with a DNA synthesizer. The EPR spectrum in the inset also establishes that the enzymatically incorporated nitroxides endure the FPLC analysis condition (Keyes *et al.*, 1996).

2.3. Spin Labeling Oligonucleotides by Spin Trapping

A procedure was developed for making a 0-tether spin-labeled 15mer containing DUNtB as the main reporter group (Bobst *et al.*, 1997). A 15mer containing a C5-iodo-deoxyuridine placed in position 8 was prepared by phosphoramidite chemistry, purified by FPLC, then irradiated in the presence of the spin trap 2-methyl-2-nitrosopropane (MNP) (Fig. 7a). Originally irradiation was carried out with a 150-W Xenon lamp and an Oriel™ filter #59423 (transmission at 260 nm and higher) to yield a stable spin adduct nitroxide ($t_{1/2} = 36$ h at 4 °C in solution) with a primary triplet ($A = 15$ G) due to the ^{14}N nucleus and some additional secondary splitting. Earlier studies with C5-iodo-uridine showed that the formation of RUNtB, the RNA analog of DUNtB, under similar irradiation conditions displayed only a triplet spectrum with $A = 15$ G after purification with a small reverse phase cartridge (Sep-Pak™, Waters, Inc.™) (Ozinskas, 1981). However removing the secondary splitting formed on irradiating C5-iodo-deoxyuridine embedded in an oligodeoxynucleotide has so far not been successful. It is believed that this splitting arises from an additional trapped species that may originate from an H-abstraction radical formed in the (5') position in view of spin-trapping studies

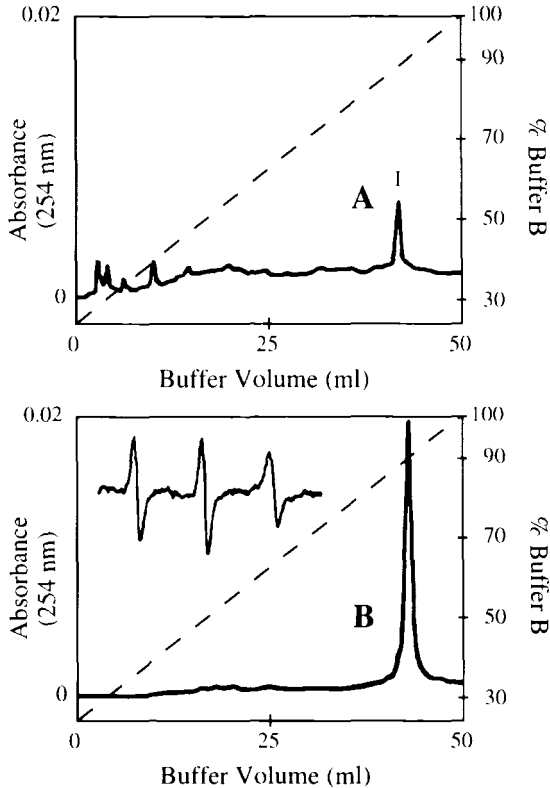


Figure 6. The MonoQ HR 5/5 FPLC elution profiles of (a) 0.04 OD₂₆₀ of 26mer CCCACCCGCGAATTCGCGGGTGGGG (Peak I) prepared by phosphoramidite chemistry; (b) 0.08 OD₂₆₀ of enzymatically prepared 26mer with DUAP label in position 11; EPR spectrum (*inset*) of aliquot of peak fraction eluting at same buffer concentration (0.7-M NaCl, 0.01-M NaOH) as Peak I in (a). (Reprinted with permission from Keyes *et al.*, 1996).

by others (Kuwabara *et al.*, 1981). Changing the irradiation source to a Liconix™ HeCd laser (325 nm, power output 8 mW/cm²) decreased secondary splitting by about 30%. Capillary electrophoresis (CE) analysis of the DUNtB-labeled 15mer showed that the oligomer is not fragmented by the laser (Fig. 7b). (Note: We refer to the spin-trapped 15mer as the DUNtB-labeled 15mer out of convenience; the 15mer is of uniform size, but besides DUNtB it contains a covalently bound minor EPR active contamination.) The EPR spectra obtained after annealing DUNtB-labeled (dT)₁₅ to either (dA)₁₅ or (dA)₄₅ are given in Fig. 7c; these indicate that the EPR signal responds to the change in duplex size (see Sec. 4.2).

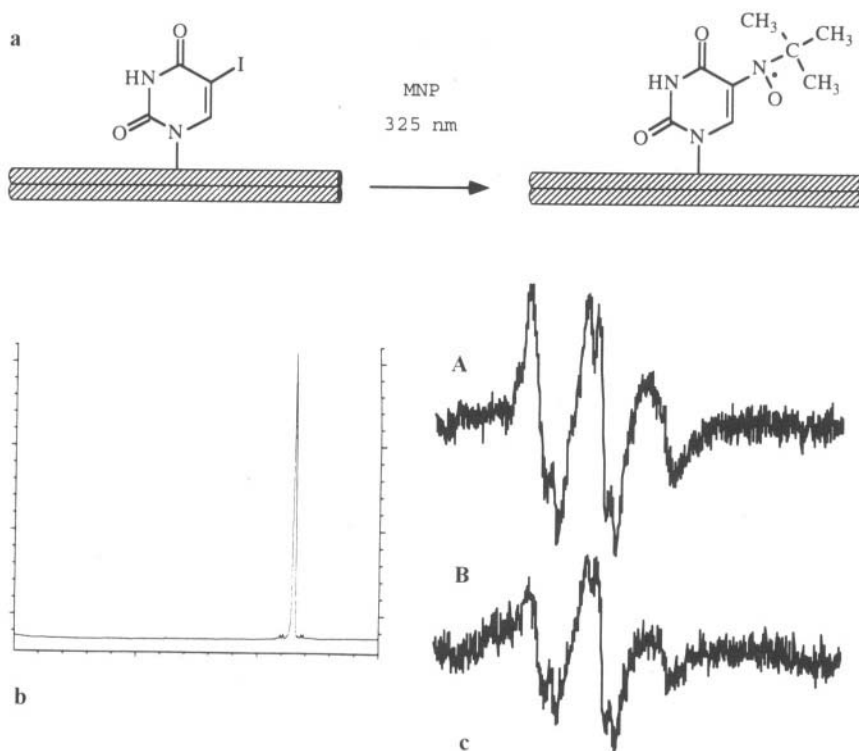


Figure 7. (a) Synthesis scheme of DUNtB-labeled (dT)₁₅ using MNP as trap, (b) CE profile of DUNtB-labeled (dT)₁₅, (c) EPR spectra of DUNtB-labeled (dT)₁₅ annealed to (dA)₁₅ (A) and (dA)₄₅ (B).

3. CHARACTERIZATION OF SPIN-LABELED NUCLEIC ACIDS

3.1. Free Spin Test

To record the EPR signal from a spin label incorporated into a nucleic acid accurately, background signals must be minimized. In contrast to NMR spectroscopy where inherent insensitivity is almost an advantage when dealing with sample purity [as much as 5% impurity in an NMR sample does not usually interfere with a one- or two-dimensional NMR spectrum (Parraga and Klevit, 1991)], the high sensitivity of EPR spectroscopy detects the slightest EPR-active impurity. The greatest potential source of an extraneous signal is from unincorporated labels. These free spins yield sharp lines of large amplitude that can mask other signals. Sometimes an incorporated spin label produces a line shape broad enough so that a free spin is clearly seen as a second spectral component, but this is not always the case.

Table 1
EPR-Specific Activities (A_{EPR}) of Two-Atom-Tethered Nucleotides

Compound	A_{EPR}^a (BU/OD) $\times 10^{-3} \pm 20\%$	A_{EPR}^b (cm/OD) $\pm 20\%$	A_{EPR} (poly-L-lysine complex) ^c
	(uncomplexed)	(uncomplexed)	A_{EPR} (uncomplexed)
DUMPDA	4400	900	na
DUMTA	2900	590	na
DUMPDA-(dT) ₁₁	420	86	0.20–0.30
(dT) ₄ -DUMPDA-(dT) ₇	330	67	0.15–0.25
(dT) ₅ -DUMPDA-(dT) ₆	330	67	0.15–0.25
(dT) ₆ -DUMPDA-(dT) ₅	330	67	0.15–0.25
(dT) ₇ -DUMPDA-(dT) ₄	330	67	0.15–0.25
(dT) ₇ -DUMPDA-(dT) ₇	250	51	0.15–0.25
(dT) ₇ -DUMTA-(dT) ₇	200	41	0.15–0.25

^aMeasured at room temperature in a flat cell (56 × 16 × 2 mm) with a Bruker TM₁₁₀ cavity on a Bruker ESP 300™ spectrometer at X-band (10⁵ receiver gain, 1.6-G modulation amplitude, 30-mW microwave power, 1024 address resolution, 164-ms conversion time providing a DR = 18, and 164-ms time constant).

^bMeasured at room temperature in a flat cell (56 × 16 × 2 mm) with a Varian TM₁₁₀ cavity on a Varian E-104™ spectrometer at X-band (10⁴ receiver gain, 1.6-G modulation amplitude, 30-mW microwave power, 120-s sweep time, and 128-ms time constant)

^cPoly-L-lysine to oligomer ratio of 2.0 (based on residue concentration)

A free spin test can be applied to a spin-labeled nucleic acid solution to verify that there is no unincorporated label present. An assay using poly-L-lysine was found to be the most effective means of detecting minute amounts of noncovalently bound probes in nucleic acids (Bobst, 1979). Poly-L-lysine is a polycation at neutral pH that binds to the polyanion nucleic acid, thereby restricting the mobility of incorporated spin labels. If free spins are present, their diffusion rate is not affected (see Bobst, 1979, Fig. 4). About 10–20 nmol (amount of nucleotide) of a spin-labeled oligomer is titrated with aliquots of a poly-L-lysine stock solution until broadening of the EPR line shape is essentially complete; with 10mers–15mers, this requires a poly-L-lysine to nucleotide ratio of 1.7 to 2 (Table 1). When the test is applied to spin-labeled polymers, a 1 to 1 ratio saturates available lattices due to a higher binding affinity. In the case of free spin contamination, one or more gel chromatography steps with either Sephacryl or Bio-Gel usually eliminates the problem.

3.2. EPR-Specific Activity of Spin-Labeled Nucleic Acids

Although it is difficult and tedious to quantify EPR signal intensity when preparing spin-labeled oligonucleotides by chemical or enzymatic synthesis to

yield sequence-specific EPR-active nucleic acids, it is beneficial to do so to compare the quality of the labeled products from synthesis to synthesis. Mild conditions used to prepare enzymatically labeled nucleic acids cause little damage to the nitroxide moiety, thereby making it possible routinely to synthesize labeled material with EPR signal intensities that vary little from one preparation to another. This was found not to be the case with spin-labeled oligonucleotides prepared by chemical synthesis.

The relatively harsh chemistry encountered in oligonucleotide synthesis makes it necessary to follow the integrity of the nitroxide moiety during various reaction steps by EPR. By keeping experimental conditions (solvent, temperature, etc.) and instrument parameters constant (Dalal *et al.*, 1981) and normalizing for concentration, A_{EPR} can be determined for spin-labeled nucleic acids (Strobel, 1992). The A_{EPR} is expressed as S/OD , where S is the absolute h_0 signal intensity (peak-to-peak height) of the center field line and optical density (OD) is the nucleic acid concentration at neutral pH, where $\text{OD} = \text{Abs}_{260}/\text{ml}$. The A_{EPR} is measured under very specific conditions (Strobel *et al.*, 1991), since signal intensity is influenced by a number of variables, including the cavity filling factor (η), cavity quality factor (Q), and incident microwave power (Dalal *et al.*, 1981). Power saturation studies are performed to ensure that spectra are recorded under nonsaturating conditions where EPR signal intensity is proportional to microwave power. Although the number of nitroxides is directly proportional to the area under the EPR absorption curve and it is normally obtained by double integration of the spectrum, values of integrated numbers can often be misleading due to subtle problems with the base line (Ireland, 1984). Therefore it is more convenient routinely to quantify the EPR signal measuring peak-to-peak height of h_0 for a particular category of compounds characterized by the same line shape. Peak height is a good approximation in the motional-narrowing region ($10^{-11} < \tau < 10^{-9}$), where lines are Lorentzian.

To quantify the EPR signal from a Varian E-104 spectrometer, the Bobst group developed a standard based on the height of the centerfield peak. The magnitude of h_0 is measured in centimeters (where Varian digital units are converted into centimeters within the acquisition program). This value is normalized to 1 OD and a receiver gain (RG) of 10,000. Therefore standardized values are recorded in cm/OD at 10,000 RG; these are calculated by:

$$\text{Varian } A_{\text{EPR}} (\text{cm}/\text{OD}) = \frac{h_0 (\text{cm})}{\text{Abs}(\text{OD}) \times \text{RG}/10,000} \quad (1)$$

When operating more than one EPR spectrometer in a lab, it is often necessary to compare spectra from the different instruments (Keyes, 1994) quantitatively. A case where Varian E-104 and Bruker ESP 300 spectral data are compared illustrates how this can be done. Spectral data are acquired on the Bruker ESP 300 EPR spectrometer through the ER 023M signal channel. The sweep time for an experi-

ment equals the number of data points sampled (i.e., x -axis resolution) multiplied by the time taken for each data point to be converted from its analog signal into its digital representation (i.e., conversion time). When a conversion time is chosen, it automatically sets the digitizer resolution (DR) with a value from 9–22. The digitizer resolution determines the number of bits that will represent full-scale voltage, which in turn will represent the maximum y -scale resolution of a particular spectrum. The larger the digitizer resolution, the greater the resulting digitized intensity values during acquisition.

After acquisition data on the ESP 300 are displayed on the computer monitor so that the resulting spectrum fills a large part of the screen. The computer changes scale, ranging from 9 to 32, to accommodate the intensities of a particular spectrum. The magnitude of the scale is defined by a scaling factor (SF) that is the power to which two is raised to achieve a particular scale:

$$\text{Scale} = 2^{\text{SF}} \quad (2)$$

For example a scaling factor of 16 provides a scale of 65,536. Since the data baseline is defined to be zero so that intensities take both positive and negative values; in this case the bottom edge of the spectral display corresponds to $-32,768$ and the top edge represents $32,768$. For a single scan, the scaling factor equals the digitizer resolution. When spectra are time-averaged (in the Add mode), the scaling factor increases further as spectral intensity sums become larger.

Such factors as receiver gain, type of cavity, sample concentration, sample volume, different EPR cells, and variations in microwave source can influence the magnitude of an EPR signal (Dalal *et al.*, 1981). If a measure of the A_{EPR} is required, then standards must be established to allow valid comparisons. Comparing two spectra from the same EPR spectrometer is straightforward: If the same cell, cavity, and sample volume are maintained and the microwave source has not changed between measurements, then the EPR signal is linearly related to both receiver gain and sample concentration. However when comparing spectra from two different EPR spectrometers, an empirical conversion factor must be determined to account for instrument differences.

For the Bruker ESP 300 EPR spectrometer, the definition of A_{EPR} was extended and a relationship developed to compare A_{EPR} values between the two instruments. There are three differences between Varian and Bruker definitions. First h_0 is defined in terms of digital bits of peak intensity, which are arbitrarily called Bruker units (BU). Note: The number of BU depends on the digitizer resolution (DR) set when the spectrum is taken (i.e., at a DR of 17, maximum voltage of the signal channel is divided into $2^{17} = 131,072$ units; minimum and maximum values are $-65,536$ and $65,536$, respectively). A second distinction in calculating A_{EPR} is the difference in time averaging between the two instruments. When multiple scans are taken with the Varian E-104, the acquisition program averages spectral data over the number of scans (NS) to provide the final spectrum (Ireland *et al.*, 1983); the

Bruker ESP 300 program sums spectral intensities of each scan to yield the final spectrum. Therefore intensities of a Bruker spectrum expressed in BU is divided by NS. A third difference is that the ESP 300 receiver gain is normalized to 100,000 rather than 10,000 as with the E-104. Thus for a given DR, A_{EPR} for a Bruker spectrum is

$$\text{Bruker } A_{\text{EPR}} (\text{BU}/\text{OD}) = \frac{h_0(\text{BU})}{\text{NS} \times \text{Abs}(\text{OD}) \times \text{RG}/100,000} \quad (3)$$

Varian and Bruker A_{EPR} values are related by an empirically determined conversion factor (CF) (Strobel, 1992). The relationship is

$$\text{Bruker } A_{\text{EPR}} (\text{BU}/\text{OD}) = \text{Varian } A_{\text{EPR}} (\text{cm}/\text{OD}) \times \text{CF} \quad (4)$$

where CF = 4900 is defined at a DR of 18. Note: The CF depends on the two spectrometers being compared due to variations in machine characteristics, such as the quality of the microwave source and noise level of the detector diode. These properties may change as a function of time, so CF must periodically be redetermined.

Table 1 lists both Bruker and Varian A_{EPR} values of some spin-labeled mono- and oligonucleotides (Kryak, 1990). The A_{EPR} values quantitatively follow expected trends in signal intensity. Since the monomer, 12mer, and 15mer molecules are 100%, 8.3%, and 6.7% spin-labeled, respectively, their S/OD reflects the effective spin dilution. The A_{EPR} values of the DUMPDA-labeled 12mer and 15mer are 7.5–9.5% and 5.7%, respectively, of the DUMPDA monomer A_{EPR} ; these correlate well with the percent labeling. For a given system, the six-membered ring spectra contain broader peaks than those of the five-membered ring; thus their amplitudes and corresponding A_{EPR} are smaller.

3.3. Influence of Spin Label on Native Nucleic Acid Duplex Conformation

Whenever a probe is placed in a system, there is usually a trade-off between sensitivity to the system and perturbation of the system. With respect to nitroxide spin labels, it was found that when the reporter group is attached to the base by a four-atom tether, there is no perturbation of the native RNA duplex (Langemeier and Bobst, 1981). The uv-melting study (260 nm) of DNA 26mers spin labeled with either DUAT or DUAP also indicated no destabilization of the helix based on the T_m value (Bobst *et al.*, 1988). Both labeled and unlabeled oligomers yielded nearly identical melting profiles. In contrast Froehler *et al.* (1992) demonstrated that the presence of a propyne group in the C5 position of pyrimidine bases stabilizes the DNA duplex. Examining the melting profile of a monoacetylene-labeled dodecamer indicates both hypochromic stabilization of the helix prior to the melting transition and an increase in the T_m value (Spaltenstein *et al.*, 1988). This increase

in duplex thermostability caused by propyne is currently used by others who employ nucleotide bases chemically modified by adding a propyne group to increase dramatically the affinity of antisense oligonucleotides to their target sequence (Wagner *et al.*, 1996). For this reason conclusions based on studies performed with spin labels containing such acetylenic tethers as ACET and DIACET (Fig. 1) (Hustedt *et al.*, 1993a, 1995) are questionable. In a recent study, an attempt to include a nitroxide reporter group within the ring system of a base analog resulted in significant destabilization of the helix (Miller *et al.*, 1995).

Another test of the influence of the spin label on DNA conformation involves monitoring whether or not a repair enzyme excises the modified nucleotide from the duplex. A preliminary study with the *uvrABC* protein complex showed that substituting a five-atom-tethered nitroxide in position C5 of thymidine does not cause distortional sites in the duplex (Kao and Bobst, 1985).

3.4. Evaluation of Spin-Label Rigid-Limit Tensors

Zeeman and hyperfine splittings result from the interaction of the nitroxide's paramagnetic electron with the static magnetic field and nitroxide nitrogen, respectively. These two effects induce primary electronic energy level splittings defining the EPR spectrum. The first two terms of the spin Hamiltonian represent these primary interactions, and these are generally the most important energy contributions:

$$\mathcal{H} = \beta_e \mathbf{g} \cdot \mathbf{H} \cdot \mathbf{S} + \mathbf{A} \cdot \mathbf{I} \cdot \mathbf{S} + \text{dipolar terms} \quad (5)$$

The \mathbf{g} and \mathbf{A} tensors represent both the magnitude and anisotropy of the Zeeman and hyperfine splittings. They are generally defined with respect to their diagonal elements:

$$\mathbf{g} = \begin{bmatrix} g_{xx} & 0 & 0 \\ 0 & g_{yy} & 0 \\ 0 & 0 & g_{zz} \end{bmatrix} \quad \mathbf{A} = \begin{bmatrix} A_{xx} & 0 & 0 \\ 0 & A_{yy} & 0 \\ 0 & 0 & A_{zz} \end{bmatrix} \quad (6)$$

An immobilized nitroxide determines values of an EPR spectrum's rigid-limit \mathbf{g} and \mathbf{A} tensors. The goal is to achieve an environment for the spin-labeled system that does not allow residual motion faster than the rigid limit ($\tau > 10^{-6}$ s) and also maintains a polarity similar to that in the solvent in dynamics experiments. Both changes in motion and solvent polarity (including hydrogen bonding) affect tensor values (Hwang *et al.*, 1975).

Different methods have been used to determine rigid-limit magnetic tensors (Keyes and Bobst, 1995). Freezing or lyophilizing the spin-labeled sample immobilizes the nitroxide and provides solvent interactions, but it can also result in hydrogen bonding (Hustedt *et al.*, 1993a). Johnson (1981) proposed a two-state

model to separate effects due to hydrogen-bonded and nonbonded states. This approach helped explain hydrogen-bonding observations of Hwang *et al.* (1975), but it did not work for systems described by Keyes and Bobst (1995).

Another approach involves preparing an aqueous solution of the spin label in glycerol or sucrose, then cooling the sample without freezing. This provides an effective environment for reducing nitroxide motion while minimizing hydrogen bonding beyond what occurs with water in an aqueous solution (Hustedt *et al.*, 1993a). Table 2 lists experimental tensor values of four spin-labeled nucleotides. The isotropic \bar{g} and \bar{A} values for DUMTA, DUAT, and DUAP were determined from spectra taken at room temperature (Keyes and Bobst, 1995). Because the frequency meter provided only three significant figures, the \bar{g} value was determined relative to a chromium standard (Cr^{3+} in a polyethylene matrix) (Bobst *et al.*, 1984b) according to the relationship:

$$g_{NO} = g_{Cr} \times \frac{H_{Cr}}{H_{NO}^{CF}} \quad (7)$$

where H_{Cr} is the field value of the major peak of Cr^{3+} , H_{NO}^{CF} is the field value of the nitroxide centerfield peak, and $g_{Cr} = 1.9804 \pm 0.0002$. The value for \bar{A} was taken as the difference between the center field line and either the up- or down-field line that were symmetrically split.

The rigid-limit values are measured in a 75% (w/w) glycerol aqueous solution at 233 K. The value of A_{zz} is obtained as half the field difference between the two extreme peaks; g_{zz} was calculated from the field position midpoint between the two extrema relative to a chromium standard according to Eq. (7). The other g and A diagonal elements are obtained by simulating spectra with a rigid-limit routine

Table 2
Spin Label Rigid-limit Magnetic Tensor Values^a

Compound	g_{xx}	g_{yy}	g_{zz}	\bar{g}	1/3Tr			\bar{A} (G)	1/3Tr	
					g	A_{xx} (G)	A_{yy} (G)		A_{zz} (G)	A (G)
DUMTA ^b	2.0096	2.0067	2.0028	2.0063	2.0064	7.47	7.21	36.3	16.9	17.0
DUAT ^b	2.0096	2.0067	2.0028	2.0064	2.0064	7.47	7.49	36.9	17.0	17.3
DUAP ^b	2.0090	2.0066	2.0029	2.0062	2.0062	6.25	5.70	36.0	16.1	16.0
ACET ^c	2.0076	2.0059	2.0029	2.0055	2.0055	6.27	10.1	32.2	16.2	16.2

^aIn general, errors in hyperfine splitting values are reported to be ± 0.5 G, while g -value tolerances vary from ± 0.0001 – ± 0.0005 (Hustedt *et al.*, 1993a; Pasenkiewicz-Gierula *et al.*, 1983)

^bKeyes and Bobst (1995).

^cHustedt *et al.* (1993a); ¹⁴N A-tensor values tabulated here were obtained by multiplying the ¹⁵N A-tensor elements by the ratio of the gyromagnetic ratios for the two spins 0.7131.

(Hustedt *et al.*, 1993b; Keyes and Bobst, 1995). Tensor elements for ACET are determined in a 51 % (w/w) sucrose buffer at 273 K (Hustedt *et al.*, 1993a).

The consistency of a set of rigid-limit tensor elements can be tested by either measuring the isotropic (i.e., fast limit) values $\bar{\mathbf{g}}$ and $\bar{\mathbf{A}}$ or determining partially averaged tensor elements when motion is introduced within the EPR time scale (see Sec. 4.1.3). Tensors must exhibit rotational invariance where traces remain constant for different motional rates and equal three times the isotropic values $\bar{\mathbf{g}}$ and $\bar{\mathbf{A}}$ (i.e., $\bar{\mathbf{g}} = 1/3\text{Tr } \mathbf{g} = 1/3\text{Tr } \mathbf{g}'$ and $\bar{\mathbf{A}} = 1/3\text{Tr } \mathbf{A} = 1/3\text{Tr } \mathbf{A}'$, where the prime indicates an averaged tensor). Variance in tensor traces indicates that rigid-limit values may have been affected by differences in environmental polarity.

4. MOTIONAL ANALYSIS OF SPIN-LABELED NUCLEIC ACIDS

4.1. Theoretical Approaches to Modeling Nucleic Acid Dynamics

Various approaches can be used to analyze nucleic acid dynamics. Molecular dynamics (MD) attempts to model the classic trajectory of all atoms in the molecule according to a force field (Fritsch *et al.*, 1993). This is helpful in addressing femtosecond-to-picosecond dynamic processes, but slower motional modes on the nanosecond time scale and longer are difficult to model with MD, since the algorithms are computationally intensive. By grouping atoms together and taking larger time steps between iterations, Brownian dynamics yields trajectories that provide a detailed simulation of DNA diffusion, including collective bending, twisting modes, and global tumbling (Robinson *et al.*, 1992). Alternatively by making a few simplifying assumptions, theoretical frameworks can be formulated that contain very few adjustable parameters but still provide a realistic model of DNA motion. The weakly bending rod model of Schurr and coworkers (Schurr *et al.*, 1992), the slowly relaxing local structure (SRLS) model of Freed's group (Polimeno and Freed, 1995), and the model-free approach of Lipari and Szabo (1982) are three such schemes.

Robinson and Drobny (1995) describe and compare the weakly bending rod model with the model-free approach. This model pictures the DNA as a series of coupled oscillators consisting of base pairs connected by Hookean springlike bonds. The dynamics are characterized by the effect of global tumbling, collective bending, and twisting modes on diffusion of an individual base pair element. This model has four adjustable parameters; D_{\parallel} and D_{\perp} describe axially symmetric diffusion of the DNA helix and the twisting and bending force constants.

The SRLS model and the model-free approach are more generalized motional frameworks (Fig. 8). In the SRLS model internal dynamics diffuse within a surrounding cage that relaxes more slowly. Internal and global motions are effectively modeled as two rigid rotors at a fixed angle coupled by an interaction

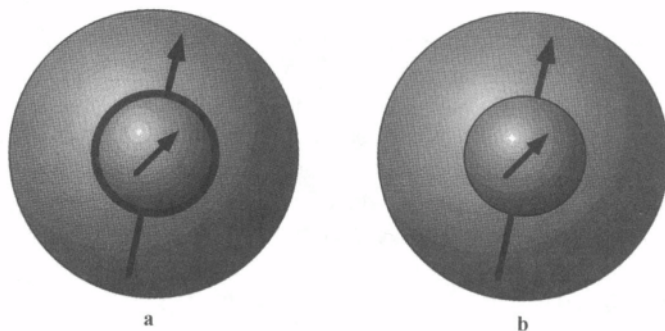


Figure 8. Internal and global dynamics can be modeled as a rotor with either axial or spherical symmetry. (a) The SRLS model couples the two rotors through an interaction potential; (b) in the model-free approach, the internal rotor is decoupled from the global rotor.

potential. The diffusion of each rotor is characterized by correlation times and an order parameter. For DNA oligomer diffusion, the cage rotor diffuses axially symmetrically with a magnitude of D_{\parallel} and D_{\perp} . The internal rotor can also be described by an axially symmetric diffusion tensor.

The model-free approach decouples global dynamics from internal dynamics as motionally independent processes. For a DNA helix global diffusion is also described by D_{\parallel} and D_{\perp} as in the other two models. Internal dynamics are described by an order parameter and an internal correlation time. These two model-independent parameters of internal motion can be related to bending and twisting modes (Robinson and Drobny, 1995).

Two other motional components complicate the dynamics picture. First individual bases within a base pair experience independent fluctuations that are not coupled to other base pairs. The magnitude of these motions range from small amplitude librations to large amplitude base pair opening/closing reactions. This spectrum of values is due to the kinetics of base pair oscillations resulting in a large population of small-amplitude fluctuations, where only a small population of large-amplitude base pair openings permit hydrogen exchange. Opening reactions were monitored by NMR using hydrogen exchange; these occur on the 10^{-3} – 10^{-1} s time scale (Leroy *et al.*, 1988; Folta–Stogniew and Russu, 1994). Although some researchers argue that most base oscillations are limited to small amplitudes ($< 10^{\circ}$) (Allison *et al.*, 1982; Schurr and Fujimoto, 1988; Hustedt *et al.*, 1993a, 1995), a large body of data suggests that magnitude is considerably larger (Eimer *et al.*, 1990; Georghiou *et al.*, 1996 and references therein).

The other motion to be considered when a probe is used to monitor nucleic acid dynamics is the probe itself relative to the base. An ideal dynamics probe does not introduce perturbation into the system it is monitoring but accurately reports the actual base motion; this is difficult to achieve in practice. The compromise is

between effectively coupling a probe to the system while introducing minimal perturbation (see Sec. 3.3.).

These two motions can be included in dynamics models by correlating motional parameters to independent base and probe motions. However if a model is applied to interpret the meaning of motional parameters in terms of specific contributions, such as bending modes, then the ability to interpret experimental data correctly depends on the suitability of the model.

4.2. Spin-Labeled Nucleic Acid Dynamics Detected by EPR

From the previous analysis, the dynamics of DNA can be broken down into specific contributions or modes. For instance the motion of an individual base consists of twisting, tilting, and torsional components. However due to difficulties in separating these numerous contributions, motions are generally classified into sets of increasing scope. These include base oscillations of different amplitudes, multiple base opening breathing reactions, collective bending and twisting modes, and global tumbling. These various motions all have similar time scales (at least for oligomers) such that motions are coupled and on the EPR time scale, these all influence the spectral line shape. The spin label is progressively coupled to the dynamics of the nucleic acid depending on the motional coupling between various components (Fig. 9).

To interpret EPR spectra of spin-labeled nucleic acids quantitatively and consistently, a motional model is used to explain spectral features. In the case of fast motions, relative peak heights and widths provide the necessary information for determining rates and anisotropy (Nordio, 1976; Bobst, 1979; Marsh, 1989). However for slower motions, the entire line shape is simulated according to the motional model. There are essentially two ways that motion is introduced into spectral simulations of spin-labeled nucleic acids. The first is by modeling the diffusion of the label around one or more axes while rigid-limit magnetic tensors are kept fixed. The rate of motion is characterized by correlation times. The second method assumes there is very fast diffusion (i.e., fast motional limit), so magnetic tensors are preaveraged by moving them from their rigid-limit values toward their fast-limit values. The rate of diffusion is often not quantifiable in this case, so averaged tensors are used to measure the geometry of motion or to determine an order parameter.

4.2.1. Measuring Motional Rates

In fast rotational diffusion where nitroxide magnetic anisotropies' average results in three sharp lines, perturbation theory can be applied to extract motional rates from line widths and heights (Nordio, 1976; Bobst, 1979; Marsh, 1989). This motional-narrowing region extends from about 10^{-11} – 10^{-9} s. When dynamics occur

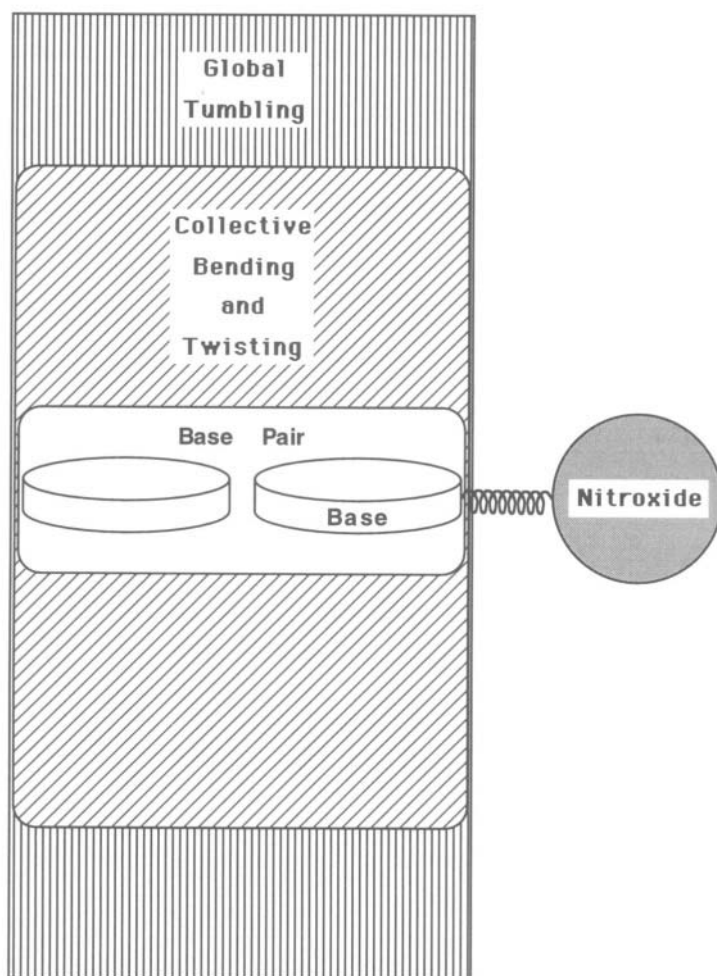


Figure 9. The reporter group monitors DNA dynamic processes according to the degree of coupling to each mode. The nitroxide ring is coupled to base dynamics through a tether linkage. The spin-labeled base is coupled to another base; together these experience base pair motion. This base pair is coupled to the collective bending and twisting of all base pairs in the helix. Finally collective modes are coupled to the global tumbling. (Reprinted with permission from Keyes and Bobst, 1995.)

on the time scale of nanoseconds or slower (10^{-9} – 10^{-6}), magnetic interactions become orientation-dependent, so the **g** and **A** tensor anisotropies are apparent in the line shape. Slow motional spectra are more sensitive to the model used for microscopic diffusion than are fast motional spectra (Freed, 1998). For these slower motions, the entire line shape must be simulated to determine motional rates. The

current standard approach to this problem is to solve the Stochastic Liouville equation (SLE) of motion for a given set of rigid-limit tensors with various values for the correlation time, then fit the resulting line shape to experimental spectra (Freed, 1976; Schneider and Freed, 1989a, 1989b).

Correlation time provides a measure of spin correlation decay. For an axially symmetric system, it is related to diffusion coefficients by:

$$\tau_{\parallel} = \frac{1}{(6D_{\parallel})} \quad (8)$$

$$\tau_{\perp} = \frac{1}{(6D_{\perp})} \quad (9)$$

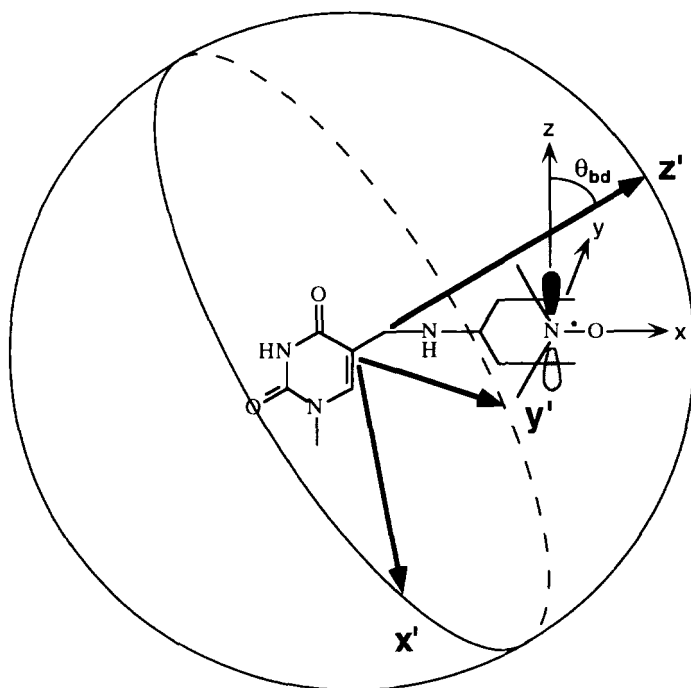


Figure 10. In the base disk model, the principal magnetic axis z passes through the nitroxide $2p_z$ orbital as in the case of the dynamic cylinder model. However the principal diffusion axis z' is defined by the first tether bond originating from the C5 position of the pyrimidine base. The two axes are tilted with respect to each other by an angle θ_{bd} . (Reprinted with permission from Keyes and Bobst, 1995.)

Kao *et al.* (1983) developed an axially symmetric motional model for spin-labeled nucleic acids termed the base disk model (Fig. 10). The principal diffusion axis corresponds to the first tether bond connecting the spin label to the C5 position of the nucleotide base. The principal magnetic axis runs through the $2p_z$ orbital of the nitroxide nitrogen atom to make an angle θ_{bd} , defined as the tilt angle, with the principal diffusion axis.

This model was successfully applied to many different spin-labeled systems, which resulted in well-characterized values for model parameters (Kao *et al.*, 1983; Kao and Bobst, 1985; Pauly *et al.*, 1987; Strobel *et al.*, 1990a, 1990b; Keyes and Bobst, 1995; Keyes *et al.*, 1997). The τ_{\parallel} primarily represents motion of the nitroxide about the tether; thus its magnitude is strongly tether-dependent. There is an approximately linear relationship between tether length and τ_{\parallel} (Keyes *et al.*, 1997). The τ_{\perp} correlates well with motion of the base within the duplex; it is sensitive to changes in both conformation and global tumbling (Keyes and Bobst, 1995; Keyes *et al.*, 1997). The B-to-Z transition was effectively monitored for a randomly labeled dG-dC polymer (Strobel *et al.*, 1990b; see Sec. 5.3); τ_{\perp} indicated that a motional slowing of the base dynamics from 4 ns to 7 ns occurred during the conformational change.

4.2.2. Measuring Motional Restriction

When diffusion of a nitroxide is fast on the EPR time scale, the \mathbf{g} and \mathbf{A} tensors can be averaged to account for the motion. The averaging method used to simulate spectral data is determined by the motional model chosen. A particular geometry of motion is associated with the model. This type of analysis can yield amplitudes as well as order parameters. An important characteristic of motionally averaging magnetic tensors is that the trace of tensor matrices must remain constant when dynamics change. This follows from the property that second-rank tensors are rotationally invariant. If the trace changes, this indicates that environment polarity is varying.

Van *et al.* (1974) developed three models for tensor averaging when a spin label is undergoing fast anisotropic motion. The first is when rapid rotation occurs about a single molecular axis not necessarily coincident with a nitroxide axis. For this model, tensors average according to:

$$\mathbf{A}'_{\parallel} = A_{zz} \cos^2\theta + A_{yy} (1 - \cos^2\theta) + (A_{xx} - A_{yy}) \sin^2\theta \cos^2\psi \quad (10)$$

$$\mathbf{A}'_{\perp} = A_{zz} \frac{1}{2(1 - \cos^2\theta)} + A_{yy} \frac{1}{2(1 + \cos^2\theta)} + (A_{xx} - A_{yy}) \frac{1}{2(1 - \sin^2\theta \cos^2\psi)} \quad (11)$$

where \mathbf{A}'_{\parallel} and \mathbf{A}'_{\perp} are the axially symmetric averaged hyperfine tensor elements and A_{xx} , A_{yy} , and A_{zz} are rigid-limit values. The θ and ψ are standard Euler angles

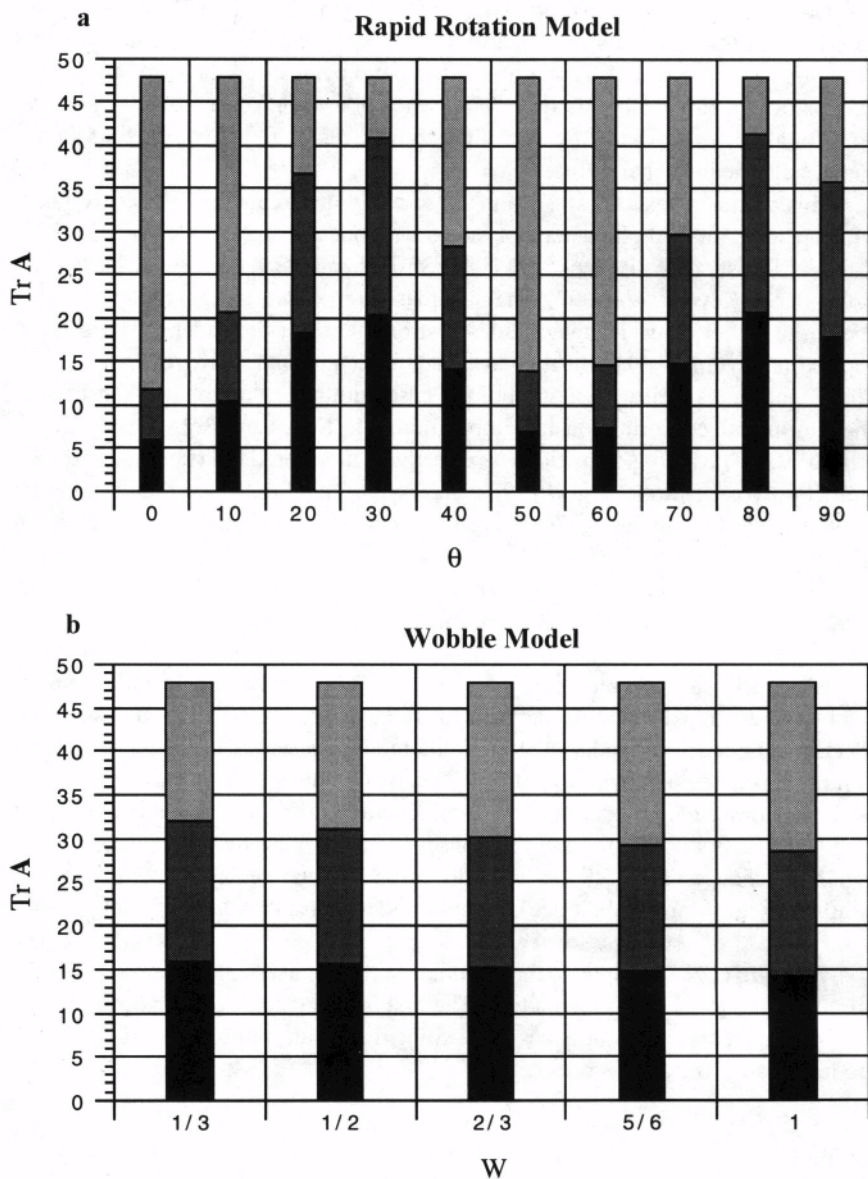


Figure 11. Models for averaging the magnetic \mathbf{g} and \mathbf{A} tensors of DUAP (Table 2). As the degree of averaging changes, rotational invariance is seen by the constant tensor trace evident in the total bar height of the graphs. (a) $A_{xx} = A_{yy} = A_{\perp}$ (■ and ▨) and $A_{zz} = A_{\parallel}$ (■) due to rapid rotation about a molecular axis as a function of the tilt angle θ , where $\psi = 0^\circ$; (b) wobbling of an axis within a cone results in $A_{xx} = A_{yy} = A_{\perp}$ (■ and ▨) and $A_{zz} = A_{\parallel}$ (■), where $\theta = 40^\circ$ and $\psi = 0^\circ$.

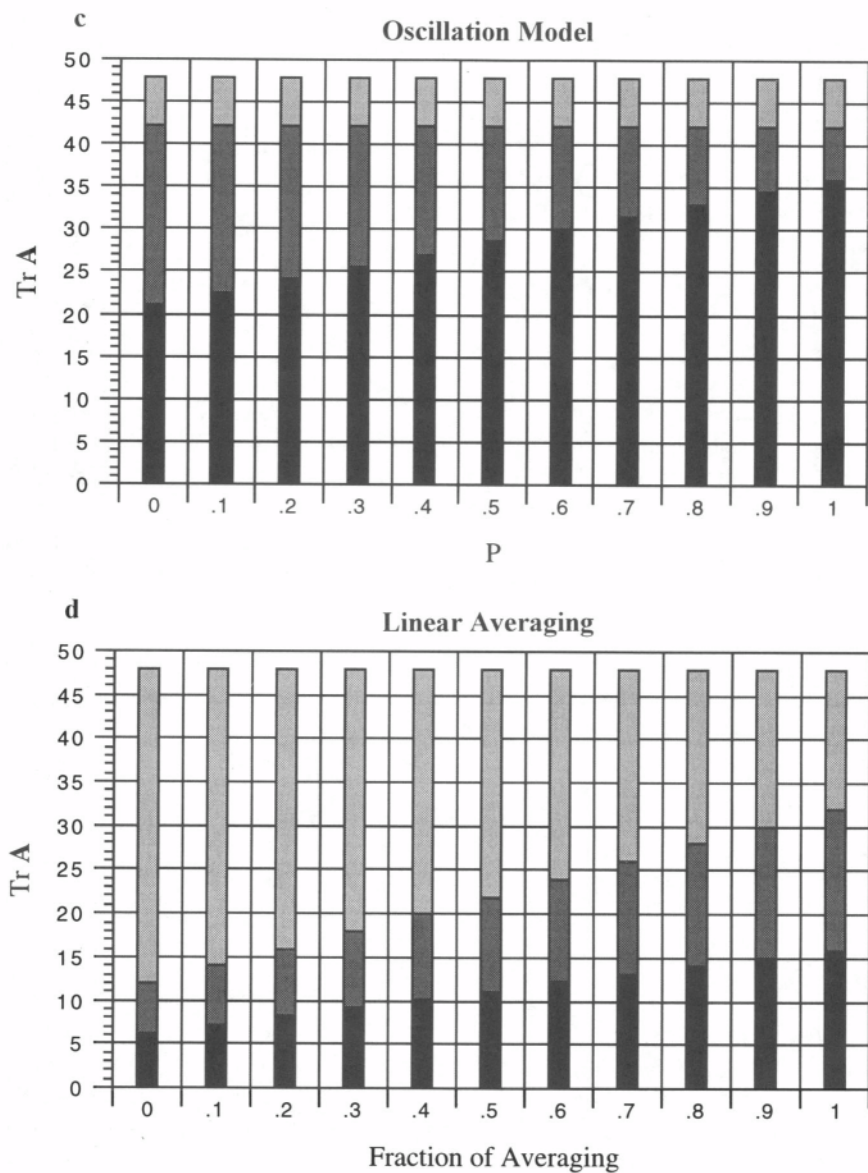


Figure 11. (c) oscillation within a restricted angle about a single axis yields A_{xx} (■), A_{yy} (▣), and A_{zz} (◐); (d) A_{xx} (■), A_{yy} (▣), and A_{zz} (◐) when a linear averaging model is applied.

defining nitroxide magnetic axes orientation with respect to the molecular diffusion coordinate system. The θ is the tilt angle between the principal magnetic and principal diffusion axes; ψ is the angle of rotation about the principal magnetic axis. Figure 11a shows that averaged hyperfine tensor elements change as a function of θ . Note: Although individual elements change in value, the tensor trace remains constant.

The Wobble model (Fig. 11 b) allows the principal diffusion axis to randomly walk over a section of a sphere's surface, thereby restricting motion to a cone with half-angle γ ; the axis points to all allowed directions with equal probability. The tensor averaging for this wobble model follows:

$$\mathbf{A}_{\parallel}^w = \mathbf{A}_{\perp}^r + (\mathbf{A}_{\parallel}^r - \mathbf{A}_{\perp}^r)W \quad (12)$$

$$\mathbf{A}_{\perp}^w = \mathbf{A}_{\perp}^r + (\mathbf{A}_{\parallel}^r - \mathbf{A}_{\perp}^r) 1/2(1 - W) \quad (13)$$

where \mathbf{A}_{\parallel}^r and \mathbf{A}_{\perp}^r are defined according to Eqs. (10) and (11). Thus this model also maintains axial symmetry and depends on Euler angles θ and ψ . The W is a wobble parameter ranging from $1/3-1$; $W = 1/3$ corresponds to $\gamma = 90^\circ$, where Eqs. (12) and (13) describe isotropic diffusion [i.e., $\mathbf{A}_{\perp}^w = \mathbf{A}_{\parallel}^w = 1/3(\mathbf{A}_{\parallel}^r + 2\mathbf{A}_{\perp}^r) = \bar{A}$]. When $W = 1$, $\gamma = 0^\circ$, so Eqs. (12) and (13) reduce to Eqs. (10) and (11) for the Rapid Rotation model. Figure 11 b depicts tensor averaging for the Wobble model as a function of W .

The Oscillation (Fig. 11 c) model restricts spin label diffusion to motions in a plane. Oscillations occur with a half-amplitude α resulting in averaging that is not axially symmetric:

$$A_{x'x'}^o = A_{xx} + (A_{zz} - A_{xx}) \frac{1}{2(1+P)} \quad (14)$$

$$A_{y'y'}^o = A_{zz} - (A_{zz} - A_{xx}) \frac{1}{2(1+P)} \quad (15)$$

$$A_{z'z'}^o = A_{yy} \quad (16)$$

where nitroxide axes (x, y, z) coincide with molecular axes (x', y', z'). The P ranges in value from $0-1$; $P = 1$ when $\alpha = 0^\circ$, so Eqs. (14)–(16) become rigid limit. At the other extreme, $P = 0$ when $\alpha = 90^\circ$, representing large amplitude oscillations, and the oscillation model approaches the rapid rotation model for $\theta = 90^\circ$. Traces illustrated in Fig. 11 c show that the hyperfine elements A_{xx} and A_{yy} average for the oscillation model as the A_{zz} element remains constant for different values of P . The

g tensor is averaged for various models by equations equivalent to Eqs. (14)–(16) for hyperfine tensors, where g_{xx} , g_{yy} , and g_{zz} are substituted for A_{xx} , A_{yy} , and A_{zz} .

An extension of the previous approach involves embedding the rapidly diffusing label within a slowly tumbling macromolecule. Hustedt *et al.* (1993a) developed this framework for nucleic acid oligomers spin labeled with an acetylene-tethered nitroxide. Duplex global tumbling is modeled as a rigid cylinder diffusing according to the hydrodynamic equations of Tirado and García de la Torre (1980):

$$D_{\perp} = \frac{3kT [\ln(p) + \delta_1]}{\pi\eta L^3} \quad (17)$$

$$D_{\parallel} = \frac{kT}{(1 + \delta_2)A\pi\eta LR^2} \quad (18)$$

where δ_1 and δ_2 are end-effect correction factors parametrized by Spaltenstein *et al.* (1989a):

$$\delta_1 = -0.661 + 0.891(p^{-1}) \quad (19)$$

$$\delta_2 = 0.688(p^{-1}) - 0.202(p^{-2}) \quad (20)$$

and

$$p = \left(\frac{L}{2R} \right) \quad (21)$$

Remaining parameters are Boltzmann's constant ($k = 1.38063 \times 10^{-16}$ erg/K), temperature (K), viscosity (erg s/cm^3), cylinder length ($L = \text{number of base pairs} \times 3.4 \text{ \AA}$), and cylinder radius (\AA); constant A equals 3.841.

Internal dynamics are characterized by a mean-square amplitude, and these are divided into contributions from bending and probe/base librations. This averaging model yields values interpreted in terms of the dynamic persistence length within the weakly bending rod framework. Although a tether that rigidly couples the nitroxide to motions of the base plane may seem to be an ideal probe, attaching a propyne group to the C5 position of a pyrimidine base was found to stabilize the DNA helix (Froehler *et al.*, 1992). This may be the reason that monoacetylenic tethers resulted in near-rigid-limit EPR spectra (Hustedt *et al.*, 1993a, 1995). The relative insensitivity of these labels to motional effects leads to uncertainty in the persistence length of several hundred angstroms (Keyes *et al.*, 1997). If the monoacetylenic spin label stabilizes the duplex as near-rigid-limit spectra seem to suggest, then it is doubtful that changes in internal dynamics of a duplex, such as those associated with a helix conformational change, are observed.

Hustedt *et al.* (1995) extended earlier work by employing a diacetylene-tethered nitroxide that yielded spectra containing considerably faster motional components (Kirchner *et al.*, 1990). This spin label was modeled in terms of rapid uniaxial rotation coupled to the globally diffusing cylinder to account for increased motion. However simulating experimental data according to this model yielded poor fits in the up-field line, which suggests that uniaxial rotation was not in the fast motional limit. When the authors simulated EPR data according to the base disk model (Sec. 4.2.1), a good fit was obtained. Hustedt and coworkers state that the value of 9 ns obtained for τ_{\perp} argues against the ca. 4-ns base dynamics seen with more flexible tethers. It may be that as in the case of the monoacetylenic tether, propyne stabilization of base stacking is restricting base motion. Since both monoacetylenic and diacetylenic tethers inherently possess the potential to perturb DNA dynamics due to the presence of the propyne group, a similar conclusion is expected with either one of the probes.

Keyes and Bobst (1995) used a similar approach, termed the dynamic cylinder model (Fig. 12) to interpret their EPR spectra from a two-atom-tethered spin label attached to oligomers of various lengths. The principal magnetic axis through the $2p_z$ orbital of the nitroxide nitrogen is at an angle θ_{dc} (Note: The θ_{dc} corresponds to θ_{tilt} in Hustedt *et al.*, 1993a) with respect to the principal diffusion axis of the cylinder. In the dynamic cylinder model, internal dynamics are interpreted according to a simple linear averaging of magnetic tensors (Fig. 11d). This yields an order parameter defined as:

$$S = \frac{\sum_{i=x,y,z} |A'_{ii} - (1/3)TrA'|}{\sum_{i=x,y,z} |A_{ii} - (1/3)TrA|} \quad (22)$$

where A_{ii} represents a rigid-limit element and A'_{ii} is an averaged value. Although this model does not have axial symmetry, averaging is approximately axially symmetric when $A_{xx} \equiv A_{yy}$, which is often the case (see Table 2). As defined by Eq. (22), S varies linearly as tensor elements move from their rigid-limit values toward the isotropic value. This method of calculating the order parameter can be derived (Griffith and Jost, 1976) from the second Legendre polynomial of the excursion angle (Saupe, 1964). The S indicates motional restriction of the spin-labeled base. Because there is some independent motion of the nitroxide with respect to the base, S of the spin label is somewhat smaller than that of the base itself. However since it was demonstrated that nitroxide is coupled to the base (see Sec. 5.3), the order parameter serves as a valuable characterization of spin-labeled base dynamics.

Figure 13a and b shows experimental spectra and dynamic cylinder simulations for series of two- (DUMTA, Keyes and Bobst, 1995) and five- (DUAP, Keyes *et*

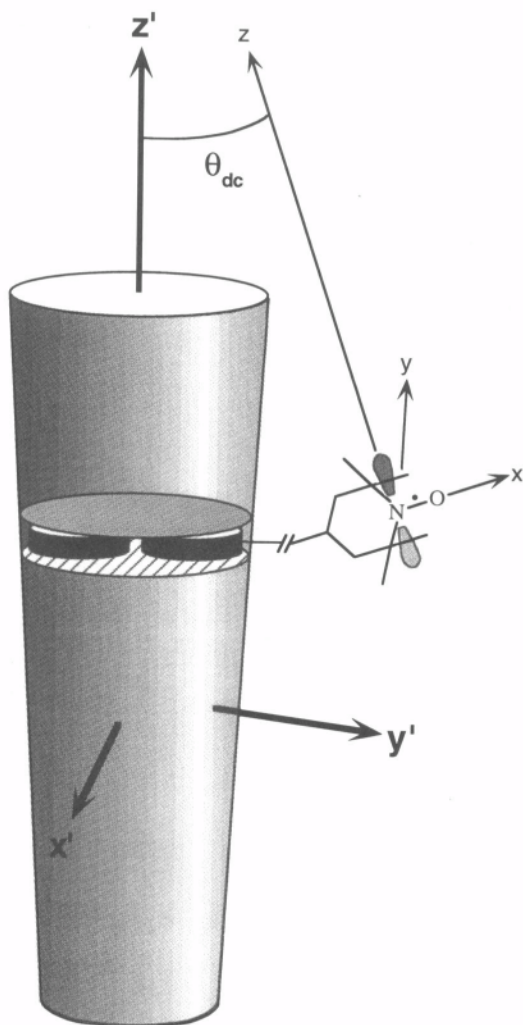


Figure 12. Magnetic and diffusion coordinates for the dynamic cylinder model. The principal magnetic axis z is coincident with the symmetry axis of the nitroxide $2p_z$ orbital. The principal diffusion axis z' , which corresponds to the helix long axis is at an angle θ_{dc} with respect to z . (Reprinted with permission from Keyes and Bobst, 1995.)

al., 1997) atom-tethered nucleic acids, respectively. Line shape features of both spectral series change in response to the decreasing global tumbling rate due to increasing cylinder size (τ_{rb} is the rigid-body correlation time of the DNA helix, Keyes and Bobst, 1995). The order parameter [Eq. (22)] for DUAP is smaller than that for DUMTA as a result of increased nitroxide mobility on the longer tether. The DUAP was also shown to be sensitive to local motional effects arising from conformational changes (Secs. 5.3 and 5.4) and protein binding (Sec. 5.6). The

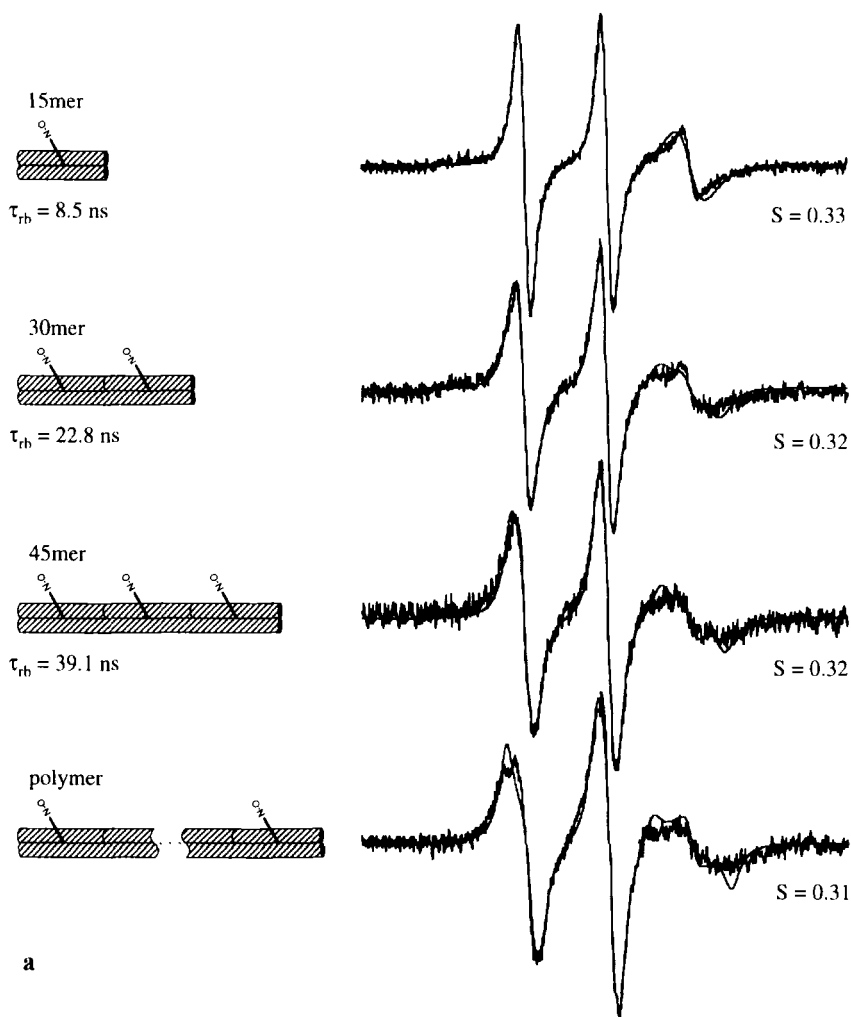


Figure 13. Experimental EPR spectra and dynamic cylinder simulations of two- (DUMTA) and five- (DUAP) atom-tethered nucleic acids demonstrating their sensitivity to helix length. (a) 15mer: $(dT)_7DUMTA(dT)_7(dA)_{15}$, 30mer: $[(dT)_7DUMTA(dT)_2]_2(dA)_{30}$, 45mer: $[(dT)_7DUMTA(dT)_3]_3(dA)_{45}$, and polymer: $[(dT)_7DUMTA(dT)_7]_m(dA)_n$.

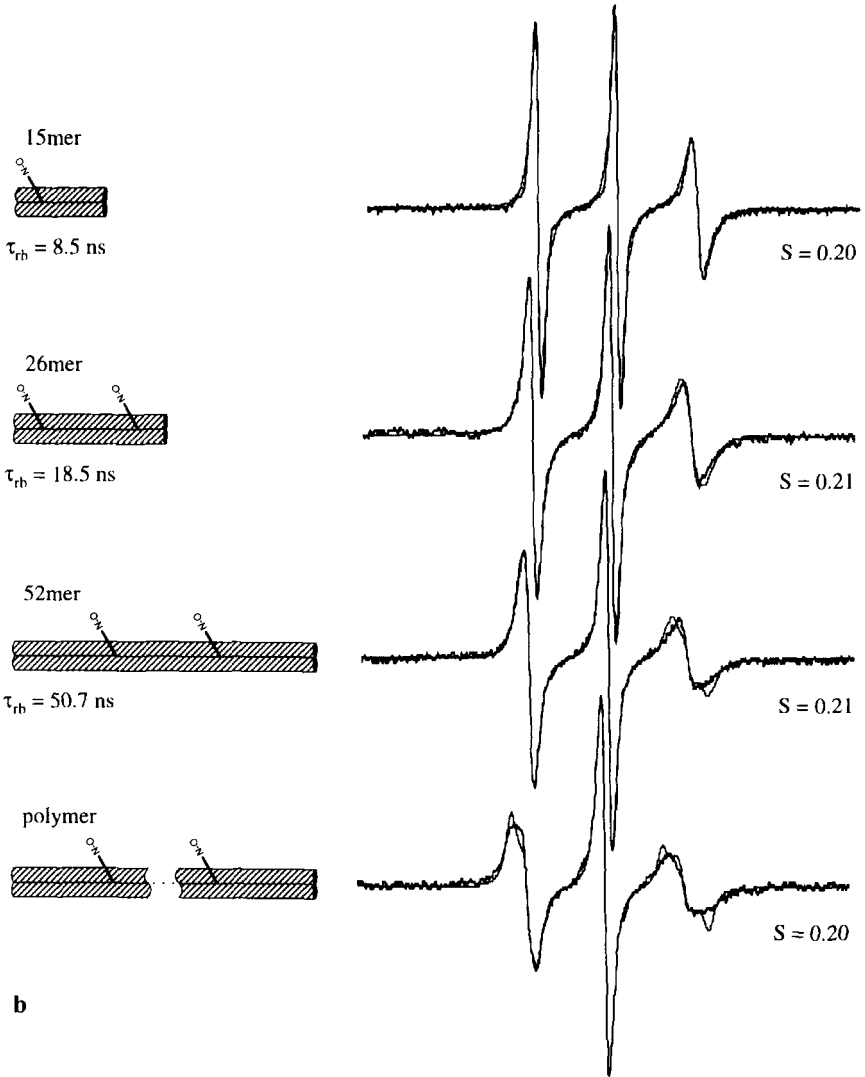


Figure 13. (b) 15mer: 5'CCCCAGAATTCGCCC3'
 3'GGGGLCTTAAGCGGG5' ($L = \text{DUAP}$),

26mer: 5'CCCCACCGCGAATTCGCGGGLGGGG3'
 3'GGGGLGGGCGCTTAAGCGCCCACCC5',

52mer: 5'CCCCCCCCCCCCCCCCACCGCGAATTCGCGGGLGGGGGGGGGGGGGGGGGG3'
 3'GGGGGGGGGGGGGGGGLGGGCGCTTAAGCGCCCACCCGGGGGGGGGGGGGG5',

and polymer: $(\text{dT, DUAP})_n(\text{dA})_n$. Spectra were recorded on sample volumes of 190 μl containing 0.2–0.5 $\text{OD}_{261\text{nm}}/\text{ml}$ of DNA at room temperature. (Reprinted with permission from Keyes *et al.*, 1997.)

longer tethered spin label DUAP was used for many biological studies because of benefits incorporating spin labels enzymatically into DNA (Sec. 3.2).

Timofeev and Samarianov (1993, 1995) developed a simulation approach that uses a framework similar to that of Hustedt *et al.* (1993a). Spin label dynamics are considered to arise from two independent reorientation processes consisting of label diffusion relative to the macromolecule and diffusion of the macromolecule itself. Macromolecular motion is described by an effective correlation time. Label dynamics are assumed to be chaotic, rapid, and anisotropic. Magnetic tensors are averaged according to models like those of Van *et al.* (1974). Groups of spin-labeled macromolecules with similar dynamic properties are defined as clusters. Each cluster is characterized by the same averaged \mathbf{g} and \mathbf{A} tensors. The EPR spectral simulation is calculated by assigning a weight to each cluster, then summing contributions.

4.2.3. Correlating Motional Parameters

In some cases it is helpful to extract both the rate and geometry from an EPR spectrum. Polnaszek and Freed (1975) developed what they term the SRLS model, where the internal dynamics are characterized by both a correlation time and an order parameter. Relaxation due to global motion, solvent structure, or other nonlocal phenomena are considered to contribute to a slowly relaxing cage that surrounds internal dynamics. Simulating 250-GHz EPR spectra according to the SRLS model resulted in better line shape fits than when a Brownian motional model was used (Polimeno and Freed, 1995). The model-free approach of Lipari and Szabo (1982) derived a similar theoretical framework for NMR; however it is not directly applicable to EPR due to the way slow motional effects contribute to line shape. Robinson and Drobný (1995) compare an application of the model-free approach to Schurr's weakly bending rod model for interpreting DNA dynamics.

Steinhoff (1988) presents a simple graphic correlation between the order parameter and rotational correlation time. A series of EPR spectra were generated for different correlation times using the axially symmetric diffusion program of Freed (1976). These spectra were then fitted with a rigid-limit program that yielded averaged magnetic tensor values from which values of S were calculated. The resulting plot yielded a sigmoidal relationship between the two parameters when there was a large increase in S from about 0.2–0.8 as correlation time increased from about 2×10^{-9} to 10^{-8} s (see Steinhoff, 1988, Fig. 3).

Both the base disk model and the dynamic cylinder model are special cases of the SRLS model. When the local structure relaxes beyond the rigid limit, then the internal dynamics of the base disk model remain. If internal dynamics diffuse rapidly and are decoupled from the global tumbling, then the dynamic cylinder model results. These two models were empirically correlated to determine both the

order parameter and correlation time for internal dynamics (Keyes and Bobst, 1995).

5. BIOLOGICAL APPLICATIONS OF SPIN-LABELED NUCLEIC ACIDS

The sensitivity of spin-labeled bases to nucleic acid dynamics has allowed a number of biological structures and phenomena to be observed. The A-RNA (Kao *et al.*, 1983; Kao and Bobst, 1985), B-DNA (Bobst *et al.*, 1984a; Kao and Bobst, 1985; Pauly *et al.*, 1987; Bobst *et al.*, 1988; Pauly *et al.*, 1989; Strobel *et al.*, 1989, 1991; Hustedt *et al.*, 1993a; Keyes and Bobst, 1995; Hustedt *et al.*, 1995), Z-DNA (Strobel *et al.*, 1990a, 1990b, 1995), a mismatch-bearing DNA sequence (Spaltenstein *et al.*, 1989a), a hairpin loop (Spaltenstein *et al.*, 1989b), and an AAA triplet-induced bend (Bobst *et al.*, 1996a) are all nucleic acid structures successfully monitored with spin-labeled bases. Studies were performed on interactions of spin-labeled nucleic acids with single-strand binding proteins, the *EcoRI* endonuclease (Keyes *et al.*, 1996), and the Homeodomain (Bobst *et al.*, 1996b); biomolecular associations between membranes and nucleic acids were examined by incorporating spin labels into nucleic acids as well (Zhdanov *et al.*, 1994). Recently progress was made in using spin-labeled psoralen probes to study DNA dynamics (Spielmann *et al.*, 1995) to obtain a better understanding of the signal involved in recognizing DNA lesions.

5.1. Spin-Labeled Nucleic Acids As Monitors in Biological Studies

Enzymatically prepared spin-labeled copolymers of $(U)_n$ were tested for their ability to direct polyphenylalanine synthesis *in vitro* with *E. coli* B enzymes and ribosomes (Ozinskas *et al.*, 1981). Spin-labeling the C5 position did not alter the amount of polyphenylalanine formed in comparison to $(U)_n$, while C4 spin-labeled copolymers reduced phenylalanine incorporation by 70–75% of the $(U)_n$ control levels. The EPR studies on *E. coli* tRNA^{Phe} labeled in position 8 revealed that this tRNA exists in solution as a mixture of two conformers. The equilibrium of the conformers was found to depend on pH, Mg^{2+} concentration and on whether the tRNA was deacetylated or not (Bondarev *et al.*, 1982). It was inferred that there are no overall structural rearrangements on aminoacylation or peptidylation of tRNA^{Phe}.

The effect of nitroxide radicals incorporated into nucleic acid duplexes on interferon-inducing activity was investigated by spin labeling the $(C)_n$ strand of the $(I)_n(C)_n$ duplex chemically or enzymatically to various degrees. It was found that spin-labeled interferon inducers maintain their activity provided $(I)_n(C)_n$ duplexes contain no less than approximately 16 uninterrupted base pairs (Bobst *et al.*, 1981).

It was concluded that double-helical segments of approximately 16 base pairs partitioned by nonintrahelical residues suffice to trigger the interferon response.

Yeast tRNA^{Tyr} spin labeled in the isopentenyladenosine residue adjacent to the anticodon was analyzed by EPR as a function of temperature at various spermine/tRNA ratios. Based on Scatchard plots analyses, it was estimated that two to three new binding sites are created for divalent cations on binding spermine to tRNA^{Tyr} (Nöthig-Laslo *et al.*, 1981, 1985). The EPR spectrum of the uncomplexed spin-labeled tRNA^{Tyr} changed to a spectrum with extensively broadened lines on adding *E. coli* ribosomes, thereby suggesting P-site binding (Weygand-Durasevic *et al.*, 1984).

The relative affinity of avian myeloblastosis virus reverse transcriptase for (U)_n and a series of (U)_n analogs were measured directly in solution by EPR (Warwick and Bobst, 1984). It was shown that the affinity of (U)_n for reverse transcriptase can be affected by modifying the (U)_n matrix as well as by the molecular weight of the polynucleotide.

Polyribonucleotides spin labeled at the 2'-OH (Petrov and Sukhorukov, 1980) were used to determine exchange kinetics in duplexes with EPR stop-flow measurements (Petrov *et al.*, 1985). A slow exchange in the minute time scale was determined with polymers, whereas the exchange with the nucleoside adenosine took a few milliseconds.

The 4-Amino-2,2,6,6-tetramethylpiperidiny 1-1-oxy was covalently linked to the UCUA 3'-terminus of the yeast 5S rRNA to facilitate base pair proton peak assignments by NMR (Lee and Marshall, 1987); namely, proton NMR signals from the hydrogen bond imino protons of base pairs closest to the nitroxide exhibit substantial peak broadening, which gives a starting point for base pair sequencing. This approach makes it possible to sequence eight of the nine base pairs in the terminal helix by primary and secondary nuclear overhauser enhancements (NOEs).

5.2. Spin-Labeled Hybridization Probes

Since their inception nucleic acid hybridization techniques relying on radioactively labeled probes predominated, mainly for reasons of sensitivity, over nonradioactive probes in research and diagnostics laboratories. However increasing public concern for the environment has magnified the acuteness of some problems inherent to radioisotopes, such as personnel exposure, storage, purchase and disposal cost, and record keeping and monitoring. User safety and economic factors coupled with short shelf lives and long development times caused the waning use of radioisotopic probes, and in turn spawned the development of many nonradioactive nucleic acid probes. A nitroxide-labeled oligonucleotide is an example of a nonradioactive hybridization probe. It was shown that such probes, which possess

EPR signatures characteristic of single- and double-stranded nucleic acids, can be readily detected at the picomole level in a loop-gap resonator (Strobel *et al.*, 1991).

Figure 14 shows the hybridization assay components with corresponding EPR spectra: A centrally labeled 15mer, a complementary polymer, and a right-handed duplex with the reporter molecule positioned within the major groove. The experimental EPR spectra represent 3.3 pmol of an oligomer probe as DUMPDA-labeled $(dT)_{15}$ before (*top*) and after (*bottom*) annealing to a large excess of $(dA)_n$.

The S/N in the duplex spectrum in Fig. 14 is the result of a 14-minute acquisition period. It would be difficult to extract meaningful numerical values from spectra with S/N values much below that of the duplex spectrum. Without increasing acquisition time, one method of enhancing S/N, and thus lowering the detection limit, is through signal conditioning by a Fourier transformation. Since broad EPR lines arising from nitroxides are low in frequency as compared to noise, successfully separating high-frequency noise from the low-frequency nitroxide signal is readily accomplished. After the EPR spectrum is recorded, it is transformed, the high-frequency portion of the spectrum is deleted, then the spectrum is retransformed back into the familiar three-line nitroxide line shape with a substantially reduced noise level. Figure 14 shows an example of an S/N increase realized with Fourier transformations. The two duplex spectra represent the same data, but the bottom spectrum was digitally filtered where most of the high-frequency noise was eliminated without distorting the low-frequency (nitroxide line shape) EPR signal of interest. In this case an approximate factor of four increase in S/N is gained with the on-board Bruker Fourier Transform software. This in turn further reduces the amount of spin-labeled probe required for detection.

The large difference in the EPR signature observed between unhybridized and hybridized nitroxide-labeled oligonucleotides should facilitate detecting single-base mismatches. The mobility of a mismatched base is greater than the corresponding paired base, so the order parameter is smaller in the case of an unpaired base. Such probes may be important in EPR assays designed specifically to detect point mutations directly.

The detection limit of this solution phase assay is set by the minimum number of nitroxides that can be measured by the EPR spectrometer to give spectra with an S/N usable for analyses. The EPR spectra in Fig. 14 represent this limit achieved with $(dT)_7$ -DUMPDA- $(dT)_7$ and the LGR. With signal conditioning the limit is further reduced by a factor of three to four, so that no more than 1 pmole of target DNA is required for detection. This makes the EPR assay only slightly less sensitive than a solution phase fluorescence assay (Morrison *et al.*, 1989) within similar time frames. In view of the possibility of one millionfold target amplification by PCR technology, the need for methods capable of ultrasensitive target detection no longer exists.

The di- and pentanucleotides spin labeled with 4-amino-2,2,6,6-tetramethylpiperidine-N-oxyl (4-amino-TEMPO) at the 5'-end internucleotide linkage,

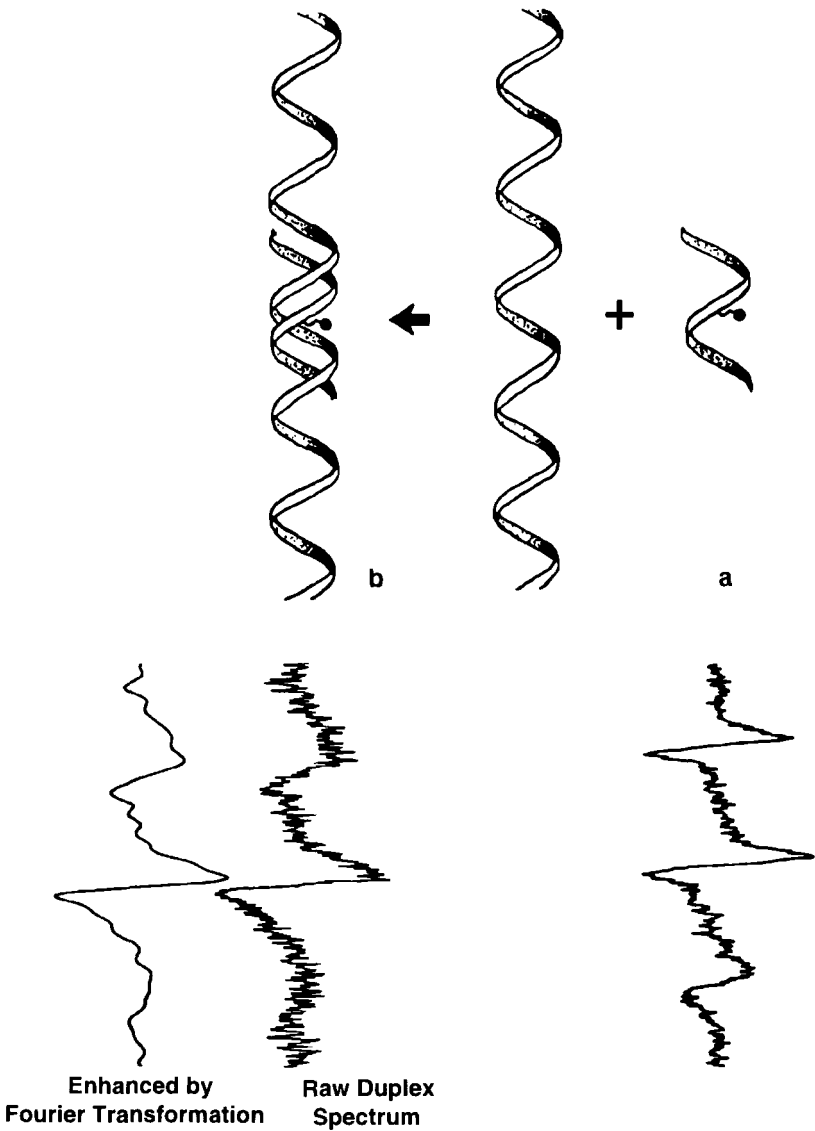


Figure 14. Hybridization and corresponding experimental EPR spectra of DUMPDA-labeled single- and double-stranded DNA obtained with a loop-gap resonator. Buffered in $2 \mu\text{l}$ of 0.1-M NaCl , 0.01-M sodium cacodylate ($\text{pH } 7.0$), and 0.01-M MgCl_2 ; (a) $50\text{-pmol (dT)}_7\text{-DUMPDA-(dT)}_7$ (3.3-pmol probe); (b) $50\text{-pmol (dT)}_7\text{-DUMPDA-(dT)}_7$ annealed to an excess of $(\text{dA})_n$, 630 pmol . An EPR spectrum of the hybridized probe illustrating signal-to-noise enhancement by Fourier transformation is shown next to the raw duplex spectrum. (Reprinted with permission from Strobel *et al.*, 1991).

dTpLT and dTpLTpTpTpT, were also successfully prepared (Makino *et al.*, 1988, 1989) with the aid of H-phosphonate intermediates. Significant spectrum broadening was observed on adding the $(A)_n$ to the spin-labeled pentanucleotide, thereby indicating duplex formation. To prepare oligos through spacers, such diamines as ethylenediamine and hexamethylenediamine were first introduced at the 5'-end internucleotide bond (Murakami *et al.*, 1989). The same group succeeded in enhancing the sensitivity of the EPR hybridization assay significantly by substituting 4-amino-2,2,6,6-tetramethylpiperidine-N-oxyl with either 4-amino-2,2,6,6-tetramethylpiperidine- ^{15}N -oxyl or 4-amino-2,2,6,6-tetramethylpiperidine- ^{15}N -oxyl- d_{16} (Makino *et al.*, 1993). Such 4-amino-TEMPO-labeled oligonucleotides were also used to monitor hybrid formation in a M13mp8 single-stranded DNA containing an *Eco*RI recognition site (Murakami *et al.*, 1993).

Thus nitroxide-labeled probes join the small number of nucleic acid probes using spectroscopic labels to facilitate the direct detection of hybridization. The ease of analysis as well as the potential for automation with EPR hybridization assay makes it suitable for large-scale testing, and it also offers the potential of direct *in vivo* target detection. In conclusion the availability of probes with high A_{EPR} values, the use of an LGR, and spectral signal conditioning collectively form an EPR-based DNA hybridization assay that requires only picomole quantities of a spin-labeled oligomer.

5.3. Detecting Local Z-DNA Conformations

The sensitivity of a five-atom-tethered spin label in detecting a change in nucleic acid conformation was demonstrated with DCAT, a cytidine analog of DUAP (Strobel *et al.*, 1990a, 1990b; Keyes *et al.*, 1997). The EPR spectrum of $(dG-dC)_n$ spin labeled with DCAT showed significant line broadening when placed in 4.5-M NaCl. Circular Dichroism confirmed that the effect was the result of a B-to-Z conformational transition. The EPR broadening was attributed to a nucleic acid conformational change, and not just to a viscosity change of the solution, and verified by running control experiments with spin-labeled $(dA-dT)_n$, since $(dA-dT)_n$ is known not to undergo a salt dependent B-to-Z transition. Indeed no EPR line shape change was observed between the low and high salt EPR spectra (Strobel *et al.*, 1990b). The B-Z effect was also observed with more flexible 11-atom-tethered labels in both a $(dG-dC)_n$ polymer (Strobel *et al.*, 1990a) and a plasmid containing a Z-forming region (Strobel *et al.*, 1995).

Molecular models of the B- and Z-DNA conformations (Fig. 15) show that the nitroxide is positioned further from the helix in the Z form. If the spin label reported only probe motion independent of the base, as was suggested (Spaltenstein *et al.*, 1989a), then the Z-DNA line shape would reflect faster nitroxide diffusion. In fact the EPR spectrum indicates that slower motion is occurring. This observation

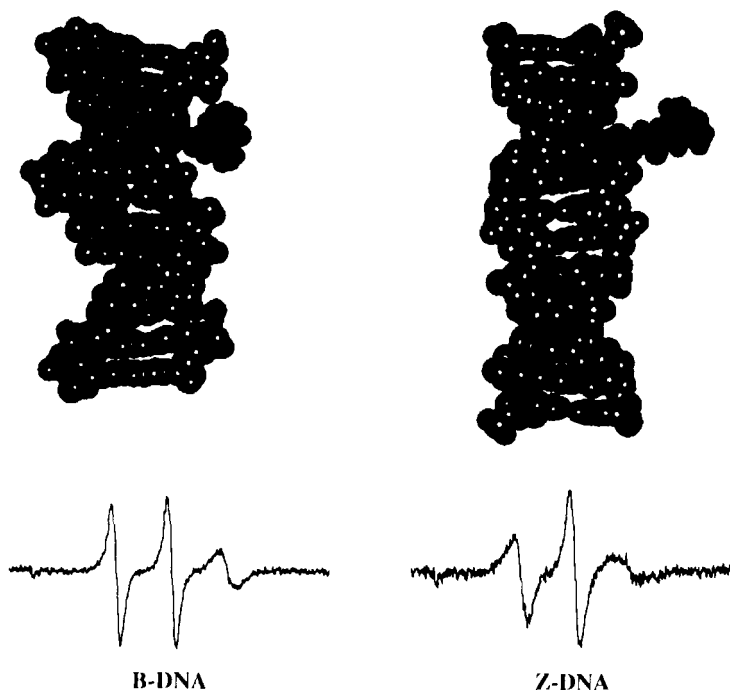


Figure 15. Space-filling models and EPR spectra (Strobel *et al.*, 1990a) of DCAT-labeled B- and Z-DNA. Models illustrate that the tether places the nitroxide further from the helix in Z-DNA than in B-DNA. However the EPR spectrum of the Z-DNA indicates that the nitroxide motion is slower and more restricted.

supports the claim that nitroxide dynamics are coupled to base dynamics; thus the spin label is sensitive to conformational changes.

A motional analysis of the DCAT-labeled B- and Z-DNA EPR spectra according to the dynamic cylinder model indicates that the order parameter increases from 0.15 to 0.26. This suggests that the bases are motionally restricted in the Z form (Keyes *et al.*, 1997). This increased base ordering is also observed in the 11-atom-tethered systems (Strobel *et al.*, 1995). These results are consistent with the hypothesis that Z-DNA is more rigid than B-DNA with a correspondingly greater persistence length (Hagerman, 1988).

There is evidence that several human genetic diseases, including fragile X syndrome, myotonic dystrophy, and spinocerebellar ataxia type 1, are associated with the presence of defined ordered sequence DNA (dosDNA) (Wells and Sinden, 1993; Sinden, 1994; Chastain *et al.*, 1995; Godde and Wolffe, 1996). Various conformations can form from dosDNA, including bends, cruciforms, intramolecular triplexes, Z-DNA, and quadruplexes. The connection between structural and

dynamic features of these alternative DNA structures and their mutagenic influence on humans most likely involves various mechanisms, including DNA replication, repair, and recombination. Two possible conformations arising from *dosDNA*, namely, Z-DNA and bending (see Sec. 5.4) were successfully detected by EPR.

Recent attention focused on biophysical properties of expanded CTG trinucleotide repeats. The CTG repeats from genes associated with various diseases confer anomalous rapid electrophoretic gel mobility on DNA (Chastain *et al.*, 1995). For instance linear nontreated *HindIII/EcoRI* fragments migrate anomalously fast; the 164 bp (CTG)₁₇ fragment migrates as 156bp, and the 263bp (CTG)₅₀ fragment migrates as 232 bp (Pearson and Sinden, 1996). The anomalous gel mobility is consistent with a 20% increase in DNA persistence length, which is most readily explained by a reduction in flexibility relative to canonical DNA. This increase in rigidity is similar to the phenomenon observed in the B-to-Z transition by EPR.

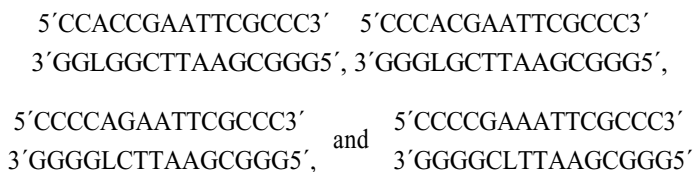
5.4. Detecting Local DNA Bending

One of the most exciting areas of current research in nucleic acid conformations is that of bending (Crothers *et al.*, 1990; Hagerman, 1992; Sinden, 1994). The ability of DNA to adopt curvature in its helical axis is important in nucleosome structure, gene regulation, and the formation of higher order nucleoprotein complexes (Love *et al.*, 1995; Jacobson and Tjian, 1996). For example the formation of a bend in the arabinose operon was found to repress expression of the Ara proteins (Schleif, 1992). Energetics favor bending toward one groove or the other using the sugar phosphate backbone as a hinge (Hagerman, 1992). Even a small sequence-induced bend can greatly reduce the energy required to achieve a full bend in a protein complex (Crothers, 1994).

A global bend results from the accumulation of a series of localized structural distortions that occur in phase (i.e., every helical turn) with one another. These large conformational changes were detected by gel migration assays where curvature of the nucleic acid slows the diffusion. Studies on the sequence dependence of DNA bending indicate that A-tracts are associated with significant bending. Currently there is discussion as to whether bending occurs within an A-tract or at its junction with flanking sequences.

Individual base pair steps contribute to bending to various degrees depending on the particular bases involved. The global result of these localized effects depends on a statistical average over the helix length (Zhurkin *et al.*, 1991). Crystallographic studies attempted to categorize the effect of specific base pair steps on the resulting nucleic acid curvature (Young *et al.*, 1995). Whether a bend occurs toward the major or minor groove also depends on individual base pair steps (Zhurkin *et al.*, 1991; Young *et al.*, 1995).

With its ability to detect local conformational changes, spin-labeling studies should yield further insight into sequence-dependent effects of bending. To this end initial studies were performed with the four DUAP-labeled DNA 15mers



(Bobst *et al.*, 1996). Three of these contain the AATT sequence with the DUAP spin label located in different positions. The fourth 15mer contains AAATT spin-labeled within the AAA triplet. It was found that when an A-tract occurs in both strands, a sequence as short as A₃ results in bending (Hagerman, 1985).

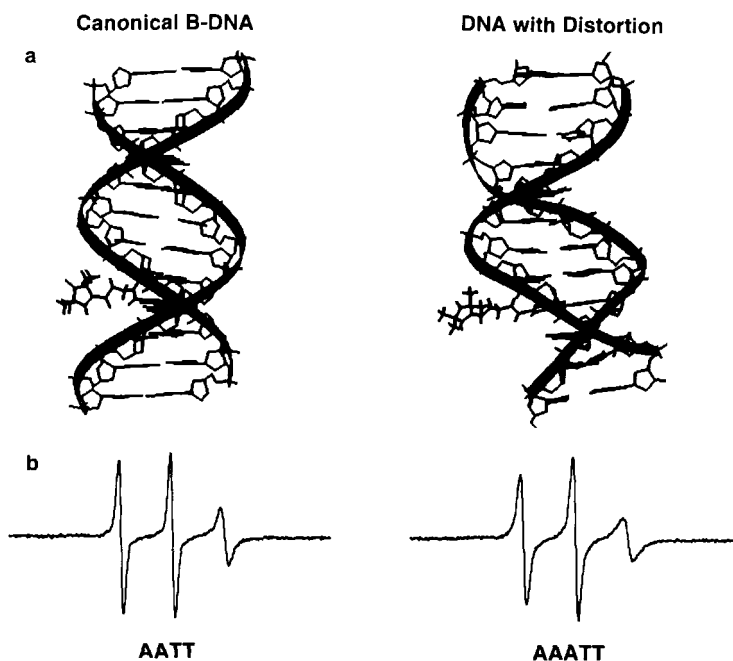


Figure 16. (a) Molecular model (NDB BDL011) of the DUAP-labeled (L) sequence

5'CGCAAATTCGCG3' with the backbone ribbon shown (*right*) to illustrate a structural distortion 3'GCGLTTAAGCGC5'

with respect to a canonical B-DNA 12mer (*left*). (b) The EPR spectra of AATT- (*left*) and AAATT- (*right*) containing 15mers, where structural distortion results in motional restriction of DUAP.

Experimental EPR spectra are nearly identical except for the AAATT-containing sequence that displays a distinct broadening in all three lines. Figure 16 illustrates that a structural distortion in the DNA helix results in a motionally restricted spectrum with respect to canonical DNA. When simulated according to the dynamic cylinder model, the spectra of AATT sequences yield an order parameter of 0.20, while the spectrum of the AAATT sequence contains increased ordering where S is 0.32. This increased ordering is similar to that in the B-Z transition (see Sec. 5.3), where S increased from 0.15 to 0.26. Since global diffusion was assumed to be constant for all four oligomers, increased ordering indicates that the spin-labeled base is experiencing greater motional restriction due to a localized structural change. Since DUAP places the nitroxide in the major groove, this restriction in the AAA triplet sequence appears to result from narrowing the major groove due to bending. These results correlate with crystallographic studies that found AA steps compress the major groove (Young *et al.*, 1995).

5.5. Relative Binding Affinities of Single-Strand Nucleic Acid Binding Proteins

A number of cellular processes involve single-strand binding proteins, including replication, recombination, and repair. During transcription these proteins function by maintaining strand separation at the replication fork, and these protect the strand from nuclease activity. By exhibiting highly cooperative nonspecific binding, proteins form a tight coat along the single strand that contains a sequence of all four bases. However single-strand binding proteins can also function in a feedback control loop that requires base preference. For instance gene 32 protein of bacteriophage T4 regulates its own synthesis by maintaining a difference in affinity for DNA and RNA. Gene 32 protein preferentially binds all available single-stranded DNA, then binds to its own mRNA, thus repressing its production (Russel *et al.*, 1976).

To quantify the binding affinity of a protein for a particular sequence, an EPR competition assay using spin-labeled nucleic acids was developed and applied to a variety of systems (Bobst *et al.*, 1982a, 1982b; Warwick-Koochaki *et al.*, 1983; Bobst *et al.*, 1984b, 1985; Keyes and Bobst, 1993). Due to the difficulty in experimentally determining absolute binding affinities, this approach yields a binding affinity ratio K_A/K_B between two nucleic acid sequences A and B. A spin-labeled nucleic acid is prepared that serves as a monitor of protein binding. Protein is added to the labeled lattice to achieve an initial fraction of saturation F_i . An unlabeled nucleic acid is then titrated into the solution; this results in protein being pulled from the labeled lattice onto the unlabeled lattice. A second experiment is performed with an equivalent amount of protein using an unlabeled lattice with a different sequence. This experiment is terminated when the same final fraction of saturation F_f of the labeled lattice is reached as in the first experiment. The smaller

the amount of unlabeled lattice required to pull a given amount of protein, the greater the affinity of the protein for that lattice. The ratio of binding affinities for lattices A and B can be derived in terms of the number of free binding sites S remaining on the lattices at the end of competition experiments (Keyes and Bobst, 1993):

$$\frac{K_A}{K_B} = \frac{S_B}{S_A} \quad (23)$$

This inverse relationship corresponds to the intuitive recognition that the fewer the number of free binding sites on the unlabeled lattice, the greater the binding constant.

Equation (23) expresses a thermodynamic relationship that is independent of the model used to define S . If the absolute binding constant is being determined, then a statistical analysis accounting for site overlap such as that found in the linear lattice model of McGhee and von Hippel (1974) is the proper approach. However when the ratio of binding constants is calculated for systems displaying moderate-to-high cooperativity, a Scatchard-type model of nonoverlapping sites can be used in the analysis. The affinity ratio relationship for nonoverlapping sites (Bobst *et al.*, 1982a) is

$$\frac{K_A}{K_B} = \frac{(N_{i_b}/S_B) - P_i[1 - (F_j/F_i)]}{(N_{i_a}/S_A) - P_i[1 - (F_j/F_i)]} \quad (24)$$

Table 3
Affinity Ratios for Various Single-Strand Binding Proteins

Competition System (Case A:Case B)	$N_{i_a}:N_{i_b}$ (nmol)	P_i (nmol)	K_A/K_B
<i>Gene 5 (s=4)</i>			
poly dT:fd DNA	9:3000	1.5	998
fd DNA:poly A	9:85	1.3	21
<i>Gene 32 (s=10)</i>			
poly dT:poly dI	130:440	2.4	3.9
poly dI:poly I	440:1270	2.4	3.0
<i>SSB (s=65)</i>			
poly dT:fd DNA	26:88	0.14	4.7
fd DNA:poly A	12:225	0.13	61

where N_l is the moles of unlabeled nucleic acid residue, s is the stoichiometric ratio of nucleic acid residue to protein, P_l is the total amount of protein, and $[1 - (F_l/F_l)]$ represents the fraction of protein stripped from the labeled lattice. The main advantages of this approach are that all variables are experimentally determined and such complicating factors as secondary structure (e.g., hairpins) and multiple intrinsic binding constants due to differences in the protein's base preference are subsumed in the analysis. Data obtained by this approach for three single-strand binding proteins are summarized in Table 3 (Keyes and Bobst, 1993).

5.6. Monitoring the Dynamics of *EcoRI* Endonuclease and Homeodomain Protein Spin-Labeled Oligonucleotide Complexes

Site-specific protein nucleic acid interactions are involved in the fundamental processes by which information flows through living systems. Interaction mechanisms often involve deformation of the nucleic acid lattice; examples include the DNA kink that forms within the *EcoRI* endonuclease complex (Kim *et al.*, 1994) and bending (see Sec. 5.4). In gene control various modes of action are proposed to explain how binding a protein to a control site can be transmitted to the coding region to regulate transcription.

The site-specific *EcoRI* endonuclease was thoroughly studied to determine what interactions define specificity and how the protein and nucleic acid respond due to binding. The *EcoRI* endonuclease consists of two identical subunits that recognize the inverted repeat



The protein nucleic acid complex was the first to be cocrystallized (Frederick *et al.*, 1984); its structure was determined to 2.8-Å resolution by x-ray crystallography (Kim *et al.*, 1990; Duan *et al.*, 1996). Studies indicate that a pair of hydrogen bonds to each of the six cognate base pairs determines sequence specificity.

The *EcoRI* complex contains a localized disruption of DNA helix that was termed the *EcoRI* kink (Kim *et al.*, 1994). There is uncertainty about whether the kink is present in the free binding site or induced by protein binding. Recent MD calculations suggest that the kink is an example of a molecular strain (Kumar *et al.*, 1994). It was proposed that these local structural changes may extend beyond the binding site to induce long-range effects allosterically in the DNA. Whether such action at a distance involves transmitting a structural deformation or forming a bend are questions of interest.

To explore the boundary of the DNA binding site as it is occupied by the *EcoRI* endonuclease and to monitor structural distortions propagated along the DNA duplex, a 26mer sequence was constructed that contains the *EcoRI* recognition site flanked on both sides by spin labels in three different positions (Table 4) (Keyes *et*

al., 1996). By choosing three positions at increasing distances from the *EcoRI* binding site, the extent of a structural change beyond the site can be detected. Since the DUAP spin label was well-characterized in terms of its sensitivity to changes in both local conformation and global tumbling (see Sec. 4.2.2), it was selected as the probe.

The EPR spectra indicated that only in the position closest to the binding site (position 6) was there a small decrease in the mobility of the spin label corresponding to an order parameter increase from 0.20 to 0.25 (Table 4). The constancy of the trace of the hyperfine tensor that can be calculated from Table 4 also suggests that the spectral effect is not due to attraction to the *EcoRI* endonuclease, since nitroxide interaction with the polar protein surface would change the trace. Similar MD nitroxide trajectories are observed for DUAP-labeled 26mers with and without bound *EcoRI* protein, thereby supporting this conclusion (Keyes *et al.*, 1996). The small position 6 effect is attributed to some deformation in the major groove of the DNA at this location due to endonuclease binding; this is similar to a bending distortion observed with DUAP at an AAA triplet (Bobst *et al.*, 1996a; see Sec. 5.4). These results indicate that although a subtle conformational change occurs close to the binding site, there is no significant structural variation propagated along the DNA helix.

Furthermore spectral line shapes apparently do not reflect the change in molecular volume of the macromolecule due to protein binding. The global dynamics of the uncomplexed 26mers are modeled satisfactorily by hydrodynamic Eqs. (17) and (18) for a cylinder. According to molecular modeling, the protein nucleic acid complex can be approximated as a 70-Å sphere (Fig. 17a). The Stokes-Einstein equation provides the correlation time for the hydrodynamic diffusion of a sphere:

$$T = \frac{4\pi\eta r^3}{3kT} \quad (25)$$

where r is the radius of the sphere. Modeling the complex as a 70-Å sphere ($T = 44$ ns) resulted in a simulation that did not fit the up-field line well. Since DUAP was shown to monitor global diffusion successfully (Keyes *et al.*, 1997), this was unexpected. A satisfactory simulation can be obtained for *EcoRI* complexes if the global tumbling rate is increased to 19.5 ns. Cassol *et al.* (1993) found that the influence of global dynamics on EPR line shapes of macromolecules containing long tether spin labels was greatest in the upfield line. They discovered that by increasing the global dynamics rate, multiple turning points evident in this line were averaged into a smooth peak.

This suggests that one or more additional relaxation processes contribute to line shape. The MD simulations performed on the *EcoRI* endonuclease complex indicate that there are long-range correlations within the system (Rosenberg *et al.*,

Table 4
Simulation Parameters Used to Determine S for 26mers and *EcoRI* Endonuclease Complexes

Compound	g'_{xx}	g'_{yy}	g'_{zz}	A'_{xx}	A'_{yy}	A'_{zz}	S	T_{\parallel}	T_{\perp}	θ_{dc}	B
11-DUAP(<i>EcoRI</i>)26mer ^a	2.0069	2.0061	2.0056	12.9 G	15.0 G	20.3 G	0.21	7.5 ns	34.2 ns	50°	1.14 G
11-DUAP(<i>EcoRI</i>)Complex	2.0069	2.0061	2.0055	12.9 G	15.0 G	20.2 G	0.21	19.5 ns	19.5 ns	n/a	1.23 G
9-DUAP(<i>EcoRI</i>)26mer ^b	2.0069	2.0061	2.0056	12.9 G	15.0 G	20.3 G	0.21	7.5 ns	34.2 ns	50°	1.14 G
9-DUAP(<i>EcoRI</i>)Complex	2.0069	2.0061	2.0055	12.9 G	15.0 G	20.2 G	0.21	19.5 ns	19.5 ns	n/a	1.23 G
6-DUAP(<i>EcoRI</i>)26mer ^c	2.0075	2.0055	2.0057	13.4 G	14.7 G	20.1 G	0.20	7.5 ns	34.2 ns	50°	1.05 G
6-DUAP(<i>EcoRI</i>)Complex	2.0073	2.0058	2.0054	12.0 G	15.3 G	21.0 G	0.25	19.5 ns	19.5 ns	n/a	1.15 G

^a5'CCACCCCGCGAATTCGCGGGGGLGG3'
 3'GGLGGGGCGCTTAAGCGCCCCACCS'

^b5'CCCACCCGCGAATTCGCGGGGGLGGG3'
 3'GGGGLGGGCGCTTAAGCGCCCACCCS'

^c5'CCCCCAGCGAATTCGCLGGGGGGG3'
 3'GGGGGGGLCGCTTAAGCGACCCCCCS'

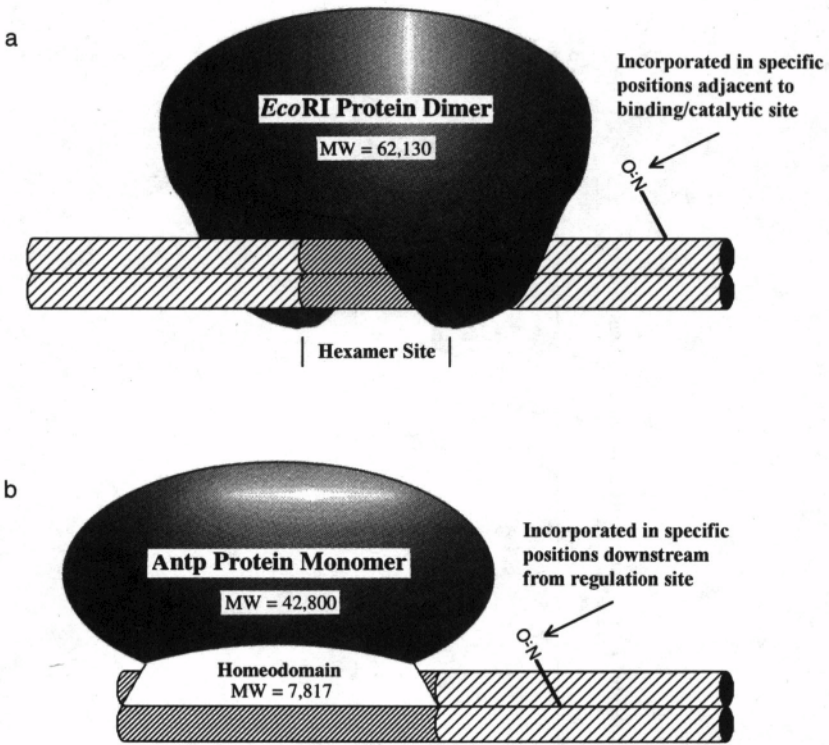


Figure 17. (a) Binding *EcoRI* endonuclease to a spin-labeled 26mer significantly increases molecular volume relative to the uncomplexed 26mer cylinder that results in a decreased global tumbling rate. As a first approximation, the complex can be modeled as a 70-Å sphere. (b) Complexes of a spin-labeled 26mer with either the HD or full-length Antp protein possess different molecular volumes and correspondingly different rates of global diffusion.

1994). These MD results support the hypothesis that mutually induced motions exist between the protein and nucleic acid. Experimental EPR observations are also consistent with the system behaving as a dynamic unit of coupled fluctuations.

From studies of regulatory genes within the fruitfly, *Drosophila melanogaster* (McGinnis *et al.*, 1984; Scott and Weiner, 1984), a 180-bp DNA sequence common to many eukaryotic regulatory genes (e.g., worms, frogs, and mice) was found (Levine and Hoey, 1988). This sequence motif was termed the homeobox, since it was first found in homeotic genes of *Drosophila*. The homeobox encodes the 60 amino acid homeodomain (HD) which corresponds to the DNA-binding domain of the much larger full-length HD protein. The HD is the region responsible for the sequence-specific recognition capability of the full-length HD proteins that act as transcription factors to regulate target genes. The global mode of binding the *Antp*

HD monomer to a 14mer DNA duplex was determined by NMR spectroscopy (Otting *et al.*, 1990). The complete structure of the *Antp* (C39S) HD-DNA complex was determined by NMR in solution (Billeter *et al.*, 1993). Crystal structure determinations of the engrailed and Mat a2 HD-DNA complexes showed that these proteins have a binding mode similar to the *Antp* HD (Kissinger *et al.*, 1990; Wolberger *et al.*, 1991). The HD-DNA complex also revealed that the structure of the free HD is largely preserved in the complex; the dissociation constant is on the order of $1.6 \times 10^{-9} M^{-1}$ by gel mobility shift assay (Gehring *et al.*, 1994), and the cognate decanucleotide sequence is d(AGCCATTAGA) (Gehring, private communication). Comparing the backbone structure of the helix-turn-helix motif of five prokaryotic gene-regulatory proteins with that of the *Antp* HD revealed that these motifs are readily superimposable (Qian *et al.*, 1989; Gehring *et al.*, 1990).

A model system was developed to study the effect of the *Antennapedia* (C39S) HD regulatory protein on the DNA 26mer



containing the HD cognate sequence (indicated by the bar) and to determine the extent of structural distortions induced on complex formation. The two-atom-tethered spin label DUMPDA was incorporated into position 8 using a combination of phosphoramidite and enzymatic synthesis techniques. Gel mobility shift assays demonstrate that both the HD and full-length protein bind to the 26mer.

The EPR spectra of the 26mer before and after titration with HD indicate that very little change occurs in the line shape. Repeating this experiment with full-length protein resulted in the same effect. Both the HD (MW = 7817) and full-length protein (MW = 42,800) complexes yield similar line shapes. These results are unexpected due to the sensitivity of two- and five-atom-tethered spin labels to changes in the molecular volume (Keyes and Bobst, 1995; Keyes *et al.*, 1997). However these observations corroborate those made with the *EcoRI* endonuclease complex regarding intermediate molecular volume-independent relaxation processes; these observations actually extend *EcoRI* results, since two proteins of very different volume produce the same line shape change (Fig. 17b). In this case fluctuations within the complex may drive a side chain scanning process at the protein-DNA interface subsequent to binding to the DNA. It was suggested that functionally important side chains may form a fluctuating network of short-lived contacts with nucleotide bases and interfacial water molecules (Gehring *et al.*, 1994).

The dynamics of nucleic acid and protein molecules consist of various components including residue fluctuations, collective residue motion, and global tumbling. These results suggest that a protein nucleic acid complex may exhibit a different set of dynamics from those of individual molecules, and it may behave as

a dynamical entity resulting from coupled molecular fluctuations between the protein and nucleic acid.

6. CONCLUSIONS

Major progress was made during recent years in applying spin-labeled nucleic acids to biological systems due to the synthesis of new spin-labeled nucleic acid substrates recognized by a variety of nucleic acid polymerizing enzymes. The ready availability of oligonucleotides of defined sequence to serve as templates or primers has made it possible to incorporate spin-labeled bases sequence-specifically enzymatically into DNAs of small as well as large molecular weight. Secondly the synthesis of phosphotriester and phosphoramidate derivatives of spin-labeled nucleotides made it practical routinely to incorporate spin-labeled bases sequence specifically into oligonucleotides with a DNA synthesizer. In addition better analytical methods based on HPLC, FPLC, and CE technology can now be routinely used to verify the quality of spin-labeled nucleic acids. Progress in designing and automating EPR instrumentation and data collection also makes it feasible to work quantitatively with small amounts of spin-labeled oligonucleotides that can serve for instance as hybridization probes with as little as picomole amounts of material. Lastly new theoretical models were developed to allow the extraction of motional ordering and of global and local motion rates from spin-labeled nucleic acid EPR spectra. Success in addressing the question of how to decouple global motion from internal motions now makes it possible to work on gaining a more comprehensive understanding phenomena involving nucleic acids that are critical in cellular development.

REFERENCES

- Allison, S. A., Shibata, J. H., Wilcoxon, J., and Schurr, J. M., 1982, *Biopolymers* **21**:729.
- Atkinson, T., and Smith, M., 1984, Solid-phase synthesis of oligodeoxyribonucleotides by the phosphotriester method, in *Oligonucleotide Synthesis, a Practical Approach* (M. J. Gait, ed.) (IRL, Oxford, UK), p. 35.
- Aurich, H. G., 1989, Nitroxides, in *Nitrones, Nitronates, and Nitroxides* (E. Breuer, H. G. Aurich, and A. Nielsen, eds.) (Wiley, New York), p. 313.
- Billeter, M., Qian, Y. Q., Otting, G., Müller, M., Gehring, W., and Wüthrich, K., 1993, *J. Mol. Biol.* **234**:1084.
- Bobst, A. M., and Torrence, P. F., 1978, *Polymer* **19**:115.
- Bobst, A. M., 1979, Applications of spin labeling to nucleic acids, in *Spin Labeling II: Theory and Applications* (L. J. Berliner, ed.) (Academic, New York), p. 291.
- Bobst, A. M., Langemeier, P. W., Torrence, P. T., and De Clercq, E., 1981, *Biochemistry* **20**:4798.
- Bobst, A. M., Langemeier, P. W., Warwick-Koochaki, P. E., Bobst, E. V., and Ireland, J. C., 1982a, *J. Biol. Chem.* **257**:6184.
- Bobst, A. M., Sinha, T. K., Langemeier, P. W., and Prairie, R. L., 1982b, *Computers & Chemistry* **4**:45.

- Bobst, A. M., Ozinskas, A. J., and de Clercq, E., 1983, *Helv. Chem. Acta* **66**:534.
- Bobst, A. M., Kao, S.-C., Toppin, R. C., Ireland, J. C., and Thomas, I. E., 1984a, *J. Mol. Biol.* **173**:63.
- Bobst, A. M., Ireland, J. C., and Bobst, E. V., 1984b, *J. Biol. Chem.* **259**:2130.
- Bobst, A. M., Pauly, G. T., Keyes, R. S., and Bobst, E. V., 1988, *FEBS Lett.* **228**:33.
- Bobst, E. V., Bobst, A. M., Perrino, F. W., Meyer, R. R., and Rein, D. C., 1985, *FEBS Lett.* **181**:133.
- Bobst, E. V., Keyes, R. S., Cao, Y. Y., and Bobst, A. M., 1996a, *Biochemistry* **35**:9309.
- Bobst, E. V., Keyes, R. S., Resendez-Perez, D., Gehring, W., and Bobst, A. M., 1996b, *Biophys. J.* **70**:A157.
- Bobst, E. V., Keyes, R. S., and Bobst, A. M., 1997, manuscript in preparation.
- Bondarev, G. N., Isaeva-Ivanov, V. V., Isaeva-Ivanova, L. S., Kirillov, S. V., Kleiner, A. R., Lepekhin, A. F., Odinzov, V. B., and Fomichev, V. N., 1982, *Nucl. Acids Res.* **10**:1113.
- Cassol, R., Ferrarini, A., and Nordio, P. L., 1993, *J. Phys. Chem.* **97**:2933.
- Chastain, P. D., Eichler, E. E., Kang, S., Nelson, D. L., Levene, S. D., and Sinden, R. R., 1995, *Biochemistry* **34**:16125.
- Crothers, D. M., 1994, *Science* **266**:1819.
- Crothers, D. M., Haran, T. E., and Nadeau, J. G., 1990, *J. Biol. Chem.* **13**:7093.
- Dalal, D. P., Eaton, S. S., and Eaton, G. R., 1981, *J. Magn. Reson.* **44**:415.
- Duan, Y., Wilkosz, P., and Rosenberg, J. M., 1996, *J. Mol. Biol.* **264**:546.
- Duh, J.-L., 1990, *Incorporation of Deoxyuridylic Acid Substituted in Position 5 with One-Atom-Tethered Nitroxides into Oligonucleotides by the Phosphotriester Method*, Ph.D. diss., University of Cincinnati, Cincinnati, OH.
- Duh, J.-L., and Bobst, A. M., 1991, *Helv. Chim. Acta* **74**:739.
- Eimer, W., Williamson, J. R., Boxer, S. G., and Pecora, R., 1990, *Biochemistry* **29**:799.
- Fidanza, J. A., and McLaughlin, L. W., 1989, *J. Am. Chem. Soc.* **111**:9117.
- Folta-Stogniew, E., and Russu, I. M., 1994, *Biochemistry* **33**:11016.
- Frederick, C. A., Grable, J., Melia, M., Samudzi, C., Jen-Jacobson, L., Wang, B.-C., Greene, P., Boyer, H. W., and Rosenberg, J. M., 1984, *Nature* **309**:327.
- Freed, J. H., 1976, Theory of slow-tumbling ESR spectra for nitroxides, in *Spin Labeling: Theory and Applications* (L. J. Berliner, ed.) (Academic, New York), pp. 53–132.
- Freed, J. H., 1998, Line widths, line shapes, and spin relaxation in the one- and two-dimensional ESR of organic radicals and spin labels, in *Foundations of Modern EPR* (G. Eaton, S. Eaton, and K. Salikhov, eds.) (World Scientific), pp. .
- Fritsch, V., Ravishanker, G., Beveridge, D. L., and Westhof, E., 1993, *Biopolymers* **33**:1537.
- Froehler, B. C., Wadwani, S., Terhorst, T. J., and Gerrard, S. R., 1992, *Tetrahedron Lett.* **33**:5307.
- Gait, M. J., 1984, An introduction to modern methods of DNA synthesis, in *Oligonucleotide Synthesis, a Practical Approach* (M. M. Gait, ed.) (IRL Press.), p. 1.
- Gehring, W. J., Müller, M., Affolter, M., Percival-Smith, A., Billeter, M., Qian, Y. Q., Otting, G., and Wüthrich, K., 1990, *Trends Genet.* **6**:323.
- Gehring, W. J., Qian, Y. Q., Billeter, M., Furukubo-Tokunaga, K., Schier, A. F., Resendez-Perez, D., Affolter, M., Otting, G., and Wüthrich, K., 1994, *Cell* **78**:211.
- Georghiou, S., Bradrick, T. D., Philippatis, A., and Beechem, J. M., 1996, *Biophys. J.* **70**:1909.
- Gibson, K. J., and Benkovic, S. J., 1987, *Nucleic Acid Research* **15**:6455.
- Godde, J. S., and Wolffe, A. P., 1996, *J. Biol. Chem.* **271**:15222.
- Griffith, O. H., and Jost, P. C., 1976, Lipid spin labels in biological membranes, in *Spin Labeling: Theory and Applications* (L. J. Berliner, ed.) (Academic, New York), pp. 453–523.
- Hagerman, P. J., 1985, *Biochemistry* **24**:7033.
- Hagerman, P. J., 1988, *Ann. Rev. Biophys.* **17**:265.
- Hagerman, P. J., 1992, *Biochem. Biophys. Acta* **1131**:125.
- Hakam, A., Thomas, I. E., and Bobst, A. M., 1980, *Int. J. Biol. Macromol.* **2**:49.
- Haralambidis, J., Chai, M., and Tregear, G. W., 1987, *Nucl. Acids Res.* **15**:4857.

- Hustedt, E. J., Spaltenstein, A., Kirchner, J. J., Hopkins, P. B., and Robinson, B. H., 1993a, *Biochemistry* **32**:1774.
- Hustedt, E. J., Cobb, C. E., Beth, A. H., and Beechem, J. M., 1993b, *Biophys. J.* **64**:614.
- Hustedt, E. J., Kirchner, J. J., Spaltenstein, A., Hopkins, P. B., and Robinson, B. H., 1995, *Biochemistry* **34**:4369.
- Hwang, J. S., Mason, R. P., Hwang, L.-P., and Freed, J. H., 1975, *J. Phys. Chem.* **79**:489.
- Ireland, J. C., Willet, J. A., and Bobst, A. M., 1983, *J. Biochem. Biophys. Meth.* **8**:49.
- Ireland, J. C., 1984, *Physical and Chemical Interactions of Adriamycin and Daunomycin with Spin Labeled Nucleic Acids*, Ph.D. diss., University of Cincinnati, Cincinnati, OH.
- Ivanov, I., Raikova, E., Raikov, Z., Yaneva, J., and Kaffaliev, D., 1983, *Int. J. Biochem.* **15**:433.
- Jacobson, R. H., and Tjian, R., 1996, *Science* **272**:827.
- Johnson, M. E., 1981, *Biochemistry* **20**:3319.
- Kamzolova, S. G., and Postnikova, G. B., 1981a, *Q. Rev. Biophys.* **14**:223.
- Kamzolova, S. G., and Postnikova, G. B., 1981b, *Molekulyarnaya Biologiya* **15**:272.
- Kamzolova, S. G., 1987, *Biokhimiya* **52**:1577.
- Kao, S.-C., Polnaszek, C. E., Toppin, C. R., and Bobst, A. M., 1983, *Biochemistry* **22**:5563.
- Kao, S.-C., and Bobst, A. M., 1985, *Biochemistry* **24**:5465.
- Kao, S.-C., and Bobst, A. M., 1986, *J. Magn. Res.* **67**:125.
- Kaplan, B. E., and Itakura, K., 1987, DNA synthesis on solid supports and automation, in *Synthesis and Applications of DNA and RNA* (S. A. Narang, ed.) (Academic, New York), p. 9.
- Keyes, R. S., 1994, *Probing Nucleic Acid Dynamics and Protein-Nucleic Acid Interactions*, Ph.D. diss., University of Cincinnati, Cincinnati, OH.
- Keyes, R. S., and Bobst, A. M., 1993, *Biophys. Chem.* **45**:281.
- Keyes, R. S., and Bobst, A. M., 1995, *Biochemistry* **34**:9265.
- Keyes, R. S., Bobst, E. V., Cao, Y. Y., and Bobst, A. M., 1997, *Biophys. J.* **72**:282.
- Keyes, R. S., Cao, Y. Y., Bobst, E. V., Rosenberg, J. M., and Bobst, A. M., 1996, *J. Biomol. Struct. Dyn.*, in press.
- Kim, Y., Choi, J., Grable, J. C., Greene, P., Hager, P., and Rosenberg, J. M., 1994, Studies on the canonical DNA-Eco RI endonuclease complex and the Eco RI kink, in *Structural Biology: State of the Art*, vol. 1 (R. H. Sarma and M. H. Sarma, eds.) (Adenine, New York), pp. 225-46.
- Kim, Y., Grable, J. C., Love, R., Greene, P. J., and Rosenberg, J. M., 1990, *Science* **249**:1307.
- Kirchner, J. J., Hustedt, E. J., Robinson, B. H., and Hopkins, P. B., 1990, *Tetrahedron Lett.* **31**:593.
- Kissinger, C. R., Liu, B., Martín-Blanco, E., Kornberg, T. B., and Pabo, C. O., 1990, *Cell* **63**:579.
- Kryak, D. D., 1990, *Sequence Specific Incorporation of Deoxyuridylic Acid Substituted in Position 5 with Two-Atom-Tethered Nitroxides into Oligothymidylic Acids by Phosphotriester Chemistry*, Ph.D. diss., University of Cincinnati, Cincinnati, OH.
- Kryak, D. D., and Bobst, A. M., 1990, *Nucleosides Nucleotides* **9**:1015.
- Kumar, S., Duan, Y., Kollman, P. A., and Rosenberg, J. M., 1994, *J. Biomol. Struct. Dyn.* **12**:487.
- Kuwabara, M., Lion, Y., and Riesz, P., 1981, *Int. J. Radiat. Biol.* **39**:491.
- Langemeier, P. W., and Bobst, A. M., 1981, *Arch. Biochem. Biophys.* **208**:205.
- Lee, K. M., and Marshall, A. G., 1987, *Biochemistry* **26**:5534.
- Leroy, J. L., Kochoyan, M., Huynh-Dinh, T., and Guéron, M., 1988, *J. Mol. Biol.* **200**:223.
- Levine, M., and Hoey, T., 1988, *Cell* **55**:537.
- Lipari, G., and Szabo, A., 1982, *J. Am. Chem. Soc.* **104**:4546.
- Love, J. J., Li, X., Case, D. A., Giese, K., Grosschedl, R., and Wright, P. E., 1995, *Nature* **376**:791.
- Makino, K., Murakami, A., Nagahara, S., Nakatsuji, Y., and Takeuchi, T., 1988, *Nucl. Acids Res. Symp. Ser.* **20**:89.
- Makino, K., Murakami, A., Nagahara, S., Nakatsuji, Y., and Takeuchi, T., 1989, *Free Rad. Res. Comms.* **6**:311.

- Makino, K., Nagahara, S., Konishi, Y., Mukae, M., Ide, H., and Murakami, A., 1993, *Free Rad. Res. Comms.* **19**:S109.
- Marsh, D., 1989, Experimental methods in spin-label spectral analysis, in *Spin Labeling: Theory and Applications, vol. 8, Biol. Magn. Reson.* (L. J. Berliner and J. Reuben, eds.) (Plenum, New York), p. 255.
- McGhee, J. D., and von Hippel, P. H., 1974, *J. Mol. Biol.* **86**:469.
- McGinnis, W., Levine, M., Hafen, E., Kuroiwa, A., and Gehring, W. J., 1984, *Nature* **308**:428.
- Miller, T. R., Alley, S. C., Reese, A. W., Solomon, M. S., McCallister, W. V., Mailer, C., Robinson, B. H., and Hopkins, P. B., 1995, *J. Am. Chem. Soc.* **117**:9377.
- Morrison, L. E., Halder, T. C., and Stols, L. M., 1989, *Anal. Biochem.* **183**:231.
- Murakami, A., Nagahara, S., Takeuchi, T., and Makino, K., 1989, *Nucl. Acids Res. Symp. Ser.* **21**:89.
- Murakami, A., Mukae, M., Nagahara, S., Konishi, Y., Ide, H., and Makino, K., 1993, *Free Rad. Res. Comms.* **19**:S117.
- Nordio, P. L., 1976, General magnetic resonance theory, in *Spin Labeling: Theory and Applications* (L. J. Berliner, ed.) (Academic, New York), p. 5.
- Nöthig-Laslo, V., Weygand-Durasevic, I., Zivkovic, T., and Kucan, Z., 1981, *Eur. J. Biochem.* **117**:263.
- Nöthig-Laslo, V., Weygand-Durasevic, I., and Kucan, Z., 1985, *J. Biomol. Struct. Dyn.* **2**:941.
- Nöthig-Laslo, V., Podravec, M., and Kucan, Z., 1987, *Period. Biol.* **89**:3.
- Otting, G., Qian, Y. Q., Billeter, M., Müller, M., Affolter, M., Gehring, W. J., and Wüthrich, K., 1990, *EMBO J.* **9**:3085.
- Ozinskas, A. J., 1981, Synthesis of C5-substituted Pyrimidine Nucleosides as Antiviral Agents and Characterization of Nitroxide Labeled Polynucleotides as Molecular Probes, Ph.D. diss., University of Cincinnati, Cincinnati, OH.
- Ozinskas, A. J., Devanesan, P. D., Keller, S. J., and Bobst, A. M., 1981, *Nucl. Acids Res.* **9**:5483.
- Parraga, G., and Klevit, R. E., 1991, *Meth. Enzymol.* **208**:63.
- Pauly, G. T., Thomas, I. E., and Bobst, A. M., 1987, *Biochemistry* **26**:7304.
- Pauly, G. T., Bobst, E. V., Bruckman, D., and Bobst, A. M., 1989, *Helv. Chim. Acta* **72**:110.
- Pearson, C. E., and Sinden, R. R., 1996, *Biochemistry* **35**:5041.
- Persichetti, R. A., Sinden, R. R., Duh, J.-L., and Bobst, A. M., 1991, *Synthetic Commun.* **21**:1013.
- Petrov, A. I., and Sukhorukov, B. I., 1980, *Nucl. Acids Res.* **8**:4221.
- Petrov, A. I., Ebert, B., Damerau, W., and Sukhorukov, 1985, *Stud. Biophys.* **107**:161.
- Polimeno, A., and Freed, J. H., 1995, *J. Phys. Chem.* **99**:10995.
- Polnaszek, C. F., and Freed, J. H., 1975, *J. Phys. Chem.* **79**:2283.
- Qian, Y. Q., Billeter, M., Otting, G., Müller, M., Gehring, W. J., and Wüthrich, K., 1989, *Cell* **59**:573.
- Raikova, E., Ivanov, I., Kaffaliev, D., Demirov, G., and Raikov, Z., 1982, *Int. J. Biochem.* **14**:41.
- Raikova, E. T., Kaffaliev, D. N., Ivanov, I. G., Zakhariyev, S. G., and Golovinsky, E. V., 1983, *Biochem. Pharmacology* **32**:587.
- Robinson, B. H., and Drobny, G. P., 1995, *Methods Enzymol.* **261**:451.
- Robinson, B. H., Slutsky, L. J., and Auteri, F. P., 1992, *J. Chem. Phys.* **96**:2609.
- Rosenberg, J. M., Kumar, S., Duan, Y., and Kollman, P., 1994, *Proceedings of International Conference on Computational Physics II*:228.
- Russel, M., Gold, L., Morrisset, H., and O'Farrell, P. Z., 1976, *J. Biol. Chem.* **251**:7263.
- Saupe, A., 1964, *Z. Naturforsch.* **19A**:161.
- Schleif, R., 1992, *Ann. Rev. Biochem.* **61**:119.
- Schneider, D. J., and Freed, J. H., 1989a, Calculating slow motional magnetic resonance spectra, in *Spin Labeling: Theory and Applications, vol. 8, Biol. Magn. Reson.* (L. J. Berliner and J. Reuben, eds.) (Plenum, New York), p. 1.
- Schneider, D. J., and Freed, J. H., 1989b, Spin relaxation and motional dynamics, in *Lasers, Molecules, and Methods, vol. 73, Adv. Chem. Phys.* (J. O. Hirschfelder, R. E. Wyatt, and R. D. Coalson, eds.) (Wiley, New York), p. 387.

- Schurr, J. M., and Fujimoto, B. S., 1988, *Biopolymers* **27**:1543.
- Schurr, J. M., Fujimoto, B. S., Wu, P., and Song, L., 1992, Fluorescence studies of nucleic acids, in *Topics in Fluorescence Spectroscopy, vol. 3. Biological Applications* (J. R. Lakowicz, ed.) (Plenum, New York), pp. 137–229.
- Scott, M. P., and Weiner, A. J., 1984, *Proc. Natl. Acad. Sci. U.S.A.* **81**:4115.
- Sinden, R. R., 1994, DNA Bending, in *DNA Structure and Function* (Academic, New York), p. 58.
- Spaltenstein, A., Robinson, B. H., and Hopkins, P. B., 1988, *J. Am. Chem. Soc.* **110**:1299.
- Spaltenstein, A., Robinson, B. H., and Hopkins, P. B., 1989a, *Biochemistry* **28**:9484.
- Spaltenstein, A., Robinson, B. H., and Hopkins, P. B., 1989b, *J. Am. Chem. Soc.* **111**:2303.
- Spielmann, H. P., Chi, D.-Y., Hunt, N. G., Klein, M. P., and Hearst, J. E., 1995, *Biochemistry* **34**:14801.
- Steinhoff, H.-J., 1988, *J. Biochem. Biophys. Meth.* **17**:237.
- Strobel, O. K., Bobst, E. V., and Bobst, A. M., 1989, *Arch. Biochem. Biophys.* **273**:597.
- Strobel, O. K., Keyes, R. S., and Bobst, A. M., 1990a, *Biochemistry* **29**:8522.
- Strobel, O. K., Keyes, R. S., and Bobst, A. M., 1990b, *Biochem. Biophys. Res. Commun.* **166**:1435.
- Strobel, O. K., Kryak, D. D., Bobst, E. V., and Bobst, A. M., 1991, *Bioconjugate Chem.* **2**:89.
- Strobel, O. K., 1992, *An Investigation of Z-DNA by Electron Paramagnetic Resonance Spectroscopy*, Ph.D. diss., University of Cincinnati, Cincinnati, OH.
- Strobel, O. K., Keyes, R. S., Sinden, R. R., and Bobst, A. M., 1995, *Arch. Biochem. Biophys.* **324**:357.
- Timofeev, V. P., and Samarianov, B. A., 1993, *Appl. Magn. Reson.* **4**:523.
- Timofeev, V., and Samarianov, B., 1995, *J. Chem. Soc. Perkin Trans.* **2**:2175.
- Tirado, M. J., and García de la Torre, J., 1980, *J. Chem. Phys.* **73**:1986.
- Toppin, C. R., 1983, *Synthesis of Analogues of Uridine and 2'-Deoxyuridine Spin Labeled at Positions 4 or 5 as Substrates for RNA and DNA Polymerizing Enzymes*, Ph.D. diss., University of Cincinnati, Cincinnati, OH.
- Toppin, C. R., Thomas, C. R., and Bobst, A. M., 1983a, *Helv. Chim. Acta* **66**:1966.
- Toppin, C. R., Thomas, C. R., Bobst, E. V., and Bobst, A. M., 1983b, *Int. J. Biol. Macromol.* **5**:33.
- Van, S. P., Birrell, G. B., and Griffith, O. H., 1974, *J. Magn. Reson.* **15**:444.
- Wagner, R. W., Matteucci, M. D., Grant, D., Huang, T., and Froehler, B. C., 1996, *Nature Biotechnol.* **14**:840.
- Warwick-Koochaki, P. E., Hakam, A., and Bobst, A. M., 1983, *FEBS Lett.* **152**:157.
- Warwick-Koochaki, P. E., and Bobst, A. M., 1984, *Arch. Biochem. Biophys.* **228**:425.
- Wells, R. R., and Sinden, R. R., 1993, Defined ordered sequence DNA, DNA structure, and DNA-directed mutation, in *Genome Analysis, vol. 7: Genome Rearrangement and Stability* (K. Davies and S. T. Warren, eds.) (Cold Spring Harbor Laboratory Press, Plainview), p. 107.
- Weygand-Durasevic, I., Nöthig-Laslo, V., and Kucan, Z., 1984, *Eur. J. Biochem.* **139**:541.
- Weygand-Durasevic, I., and Susic, S., 1990, *Biochem. Biophys. Acta* **1048**:38.
- Wolberger, C., Vershon, A. K., Liu, B., Johnson, A. D., and Pabo, C. O., 1991, *Cell* **67**:517.
- Young, M. A., Ravishanker, G., Beveridge, D. L., and Berman, H. M., 1995, *Biophys. J.* **68**:2454.
- Zhdanov, R. I., Volkova, L. A., Kuvichkin, V. V., and Petrov, A. I., 1994, *Appl. Magn. Reson.* **7**:115.
- Zhurkin, V. B., Ulyanov, N. B., Gorin, A. A., and Jernigan, R. L., 1991, *Proc. Natl. Acad. Sci. U.S.A.* **88**:7046.

Spin Label Applications to Food Science

Marcus A. Hemminga and Ivon J. van den Dries

1. INTRODUCTION

In general food systems are multicomponent, multiphase systems with complicated structures that in most cases are not in equilibrium. In such systems, a variety of changes often occurs, most of which are only partly understood. These macroscopic changes are induced on a molecular level by structural changes in the molecules and by molecular motions. An example is the glass-rubber transition of solid food materials, which is important for processing, quality, and storage stability of food. Below the glass transition temperature, very low molecular mobility predicts good food stability. For example, knowledge about molecular processes in food systems is important for new food products developed for magnetron ovens of which the quality after manufacturing should remain constant upon freezing for storage and heating for consumption. Of special concern in this respect is including and limiting diffusion of water and small organic molecules that act as plasticizers of the food material. Most of the basic work in this area was been carried out in sugar water systems used to model much more complicated food systems.

Marcus A. Hemminga and Ivon J. van den Dries • Department of Molecular Physics, Wageningen Agricultural University, 6703 HA Wageningen, The Netherlands.

Biological Magnetic Resonance, Volume 14: Spin Labeling: The Next Millennium, edited by Berliner. Plenum Press, New York, 1998.

Electron spin resonance (ESR) spectroscopy and saturation transfer (ST) ESR are suitable magnetic resonance tools for obtaining information about the rotational mobility of nitroxide spin-labeled molecules over a very large motional range of rotational correlation times τ_R of eight decades from 10^{-3} – 10^{-11} s. Conventional ESR is sensitive in the motional region for τ_R values from 10^{-11} – 10^{-6} s. In the motional region for $\tau_R > 10^{-6}$ s, ST-ESR may be used to obtain spectra sensitive to molecular motions to a final limit of $\tau_R \approx 10^{-3}$ s. This limit can be further increased to τ_R values up to 10^4 s by using the integral of ST-ESR spectra (van den Dries *et al.*, 1998). For glassy systems it was found that this information is related to the presence of molecular cavities, solvent interactions, and arrangement of the hydrogen-bonded network in the matrix.

Another application of ESR and ST-ESR spectroscopy is found in the study of wheat proteins. The bread-making quality of flours is related to the quantity and nature of glutenins and gliadins, which are water-insoluble proteins that form a network, called gluten, established on hydration and subsequent mixing. The ESR and ST-ESR spectroscopy are used in this case to provide information about the protein network by specifically labeling cysteine residues of proteins with nitroxide spin labels.

The application of ESR and ESR to food and related model systems is still scarce, and the present chapter reviews some of the author's work carried out in collaboration with European scientists. Note: The ESR spin labeling is also used to relate the properties of sugar-water systems with desiccation tolerance of biological objects (Dzuba *et al.*, 1993a,b; Golovina and Tikhonov, 1994; Buitink, *et al.*, 1998).

2. SPIN LABELS

In general food systems do not possess intrinsic paramagnetism; hence in the unlabeled state these do not give rise to an ESR spectrum. Introducing a stable free radical (spin label) is a method using ESR spectroscopy to study specific molecular environments within a food system. The spin label almost exclusively used is the nitroxide radical, which has very high stability.

Figure 1 shows two useful examples of spin-labeled molecules for application in food materials. Nitroxide spin label I (4-hydroxy-TEMPO, which is often referred to as TEMPOL) is an alcohol derivative applied to monitor changes in hydrogen bond formations in carbohydrate water systems. To spin label proteins, several nitroxide analogues of standard protein modifying agents can be used, e.g., maleimide, iodoacetamide, and isothiocyanate derivatives. These agents are capable of labeling nucleophilic groups by aqueous reaction, particularly sulphhydryl or amino groups; specificity to some extent depends on reaction conditions. It is generally observed that amino groups are not labeled very extensively at pH values below their pK_a , thus sulphhydryl group labeling is normally favored at a neutral pH.

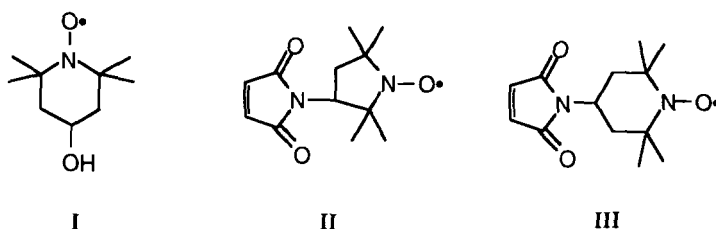


Figure 1. Chemical structure of nitroxide spin labels most suitable in motional analysis of food materials: Spin label I is the TEMPOL spin label; Spin labels II and III are maleimide spin labels used mainly to label cysteine groups of protein molecules covalently.

In the present chapter results obtained with maleimide spin label II (3-maleimido-PROXYL) or spin label III (4-maleimido-TEMPO) covalently attached to sulphhydryl groups of gluten are discussed. Spin label II was used in some sugar water model studies as well. Because of the high sensitivity of ESR spectroscopy, only a small amount of labeling (< 0.5 wt%) is required.

Nitroxide radicals have a three-line nitrogen hyperfine spectrum whose splitting varies with the orientation of the nitroxide moiety with respect to the externally applied magnetic field; this is necessary to obtain ESR spectra, and this makes ESR spectra very sensitive to rotational motions, as Fig. 2 illustrates. The nitroxide group can be attached to various molecules with different functionality. The motion of the nitroxide then directly reflects the motion of the labeled part. Note: With the spin label technique, a foreign molecule whose properties deviate from the system's natural components is introduced into the system, by adding chemical and steric perturbations. When spin labeling biomolecules, the perturbation is generally relatively small. If small spin label molecules are examined in solutions, this effect is explicitly taken into account.

Spin label ESR spectroscopy is complementary to nuclear magnetic resonance (NMR) spectroscopy in determining molecular motion. However the advantage of spin label ESR is that this information is obtained from specifically labeled sites in the system. As compared to optical methods, the technique does not require transparent samples; therefore it is applicable to virtually all food systems.

3. ANALYSIS OF ESR AND ST-ESR SPECTRA

The major use of spin label ESR to food systems is in determining the molecular motion of nitroxide spin labels. Molecular motion is generally expressed by an isotropic rotational correlation time τ_R . Figure 2 shows a survey of various motional regions and characteristic ESR spectra for isotropic motion of nitroxide spin labels. The success and importance of the spin label method in studying molecular dynamics is based on the fact that g and A tensors are anisotropic; this makes ESR

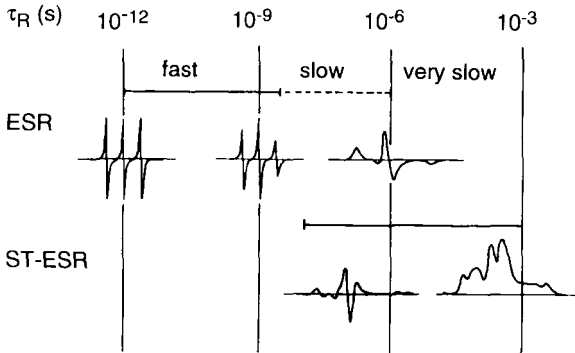


Figure 2. Survey of various motional regions and the corresponding characteristic ESR and second harmonic quadrature ST ESR spectra for isotropic motion of a nitroxide spin label with rotational correlation time τ_R [reprinted from Hemminga, 1983 with kind permission from Elsevier Science-NL].

spectra critically dependent on the orientation of the spin label in space (Hemminga, 1983). The principal values of g and A tensors of nitroxides are given by:

$$\mathbf{g} = \begin{pmatrix} 2.009 & 0 & 0 \\ 0 & 2.006 & 0 \\ 0 & 0 & 2.002 \end{pmatrix} \quad (1)$$

$$\mathbf{A} = \begin{pmatrix} 0.6 & 0 & 0 \\ 0 & 0.6 & 0 \\ 0 & 0 & 3.2 \end{pmatrix} \text{ (in mT)} \quad (2)$$

These values may differ slightly from one system to another depending on the polarity of the environment.

When nitroxide spin labels are allowed to tumble rapidly in an isotropic way, as in the case of a liquid, tensor components are completely averaged to the isotropic values:

$$g_{\text{iso}} = \frac{1}{3} (g_{xx} + g_{yy} + g_{zz}) \quad (3)$$

$$A_{\text{iso}} = \frac{1}{3} (A_{xx} + A_{yy} + A_{zz}) \quad (4)$$

This arises for $\tau_R < 10^{-11}$ s; the ESR spectrum consists of three sharp lines of equal height, with a splitting $A_{\text{iso}} \approx 1.5$ mT, and center determined by g_{iso} . As the motion becomes progressively slower, there is differential broadening of lines in the spectrum, while line positions remain constant. This is the fast motional region,

where the rotational correlation time (in s) may be obtained directly from spectra by the simple relation (Knowles *et al.*, 1976):

$$\tau_R = 6.5 \times 10^{-10} \Delta B_0 (\sqrt{h_C/h_H} - 1) \quad (5)$$

where h_H and h_C are the heights of the high field and central lines in the ESR spectra, respectively; ΔB_0 is the line width of the central line in Tesla (T). The rotational motion of spin labels is assumed to be isotropic. Note: Equation (5) applies for ESR spectra obtained in the X-band microwave region at a microwave frequency of about 9.5 GHz.

For values of $\tau_R > 3 \times 10^{-9}$ s, averaging tensor components is no longer complete; line position and line shape distortions are observed. This region is called the slow motional region. In this motional region it is possible to characterize changes in spectral line shape by an empirical Eq. (6), where A'_{zz} is one-half the separation of outer hyperfine extremes in the ESR spectrum, and A_{zz} is the rigid limiting value for the same quantity.

$$\tau_R = a \left[1 - \frac{A'_{zz}}{A_{zz}} \right]^b \quad (6)$$

From computer simulations (Freed, 1976) it is possible to determine constants a and b , which depend on the nature of the motion of the spin label and the intrinsic line width of the spectra. For a Brownian diffusion model $a = 1.09 \times 10^{-9}$ s and $b = -1.05$ (Hyde, 1978). This model was employed in analyzing ESR spectra of labels in glassy materials (Le Meste and Simatos, 1980; Roozen and Hemminga, 1990).

In the very slow motional region ($\tau_R > 10^{-6}$ s), the rigid powder spectrum is reached for conventional ESR, in which the full effects of anisotropic g and A tensor interactions are observed. The powder line shape is then insensitive to the rate of molecular motion; this region is called the slow motional region. It is possible however, to obtain line shapes sensitive to even slower motions by carrying out ESR spectroscopy under saturation conditions. This nonlinear ESR technique is referred to as ST ESR spectroscopy. This method measures the transfer of saturation throughout a spectrum by reorientational molecular motions. Therefore the shape of ST-ESR spectra is not only sensitive to molecular motion but also depends on saturation properties of the spin label.

Figure 2 shows a survey of characteristic ST-ESR spectra, recorded in quadrature (90° out-of-phase with respect to field modulation) at the second harmonic, where the final limit of sensitivity for molecular motions is $\tau_R \approx 10^{-3}$ s. Maximal effects in ST-ESR spectra arise if the spin lattice relaxation time T_1 and field modulation frequency ν_m obey the following equation:

$$\tau_R \approx T_1 \approx \frac{1}{2\pi\nu_m} \quad (7)$$

Since T_1 is about 10^{-5} – 10^{-6} s, ST-ESR spectroscopy is most sensitive to values of τ_R around 10^{-5} – 10^{-6} s and to modulation frequencies around 100 kHz. In ST-ESR spectroscopy the rotational correlation time τ_R is usually obtained empirically from calibration curves of the line shape against the value of τ_R obtained from reference spectra of spin labels in suitable solvents (Thomas *et al.*, 1976; Hemminga, 1983; Hemminga and De Jager, 1989).

Recently it has been found that beyond the upper limit of sensitivity for rotational mobility ($\tau_R \approx 10^{-3}$ s), ST-ESR spectra are still sensitive to saturation recovery, governed by T_1 , in competition with field modulation. Because T_1 is still dependent on τ_R for $\tau_R > 10^{-3}$ s, the integral of the ST-ESR spectra is sensitive to τ_R . This provides a means to measure extremely long rotational correlation times up to $\tau_R \approx 10^4$ s (van den Dries *et al.*, 1998). This method gives a further extension by seven decades for the rotational correlation time, as compared to the method of analyzing the line shape using calibration curves.

4. MOLECULAR MOTION IN LIQUID SAMPLES

Before discussing the properties of spin labels in glassy materials, we illustrate the application of ESR spectroscopy to spin labels in the liquid state. A remarkable finding is that spin labels often rotate faster in liquids than expected on basis of their volume. To describe this effect, a modified Stokes–Einstein relationship was successfully employed; it is given by (McClung and Kivelson, 1968; Kivelson *et al.*, 1970; Dote *et al.*, 1981; Roozen and Hemminga, 1990):

$$\tau_R = \left(\frac{\eta V}{k_b T} \right) k + \tau_0 \quad (8)$$

where τ_R is the rotational correlation time, η is the solvent viscosity, k_b is Boltzmann's constant, V the volume of the rotating molecule, T the absolute temperature, τ_0 is the zero viscosity rotational correlation time, and k a dimensionless interaction parameter. The parameter k is a measure of coupling rotational motions of the spin label to shear modes of the fluid. In many cases interaction parameter $k \leq 1$, and k is independent of temperature and viscosity. However, parameter k depends on specific solvent spin label interactions and the geometry of molecules considered, since nonspherical molecules must displace a solvent as they rotate. This can be expressed as follows (Hoel and Kivelson, 1975):

$$k = S(1 - \theta) + \theta \quad (9)$$

Table 1
Van der Waals Volume V and Shape Parameter θ for Different Spin Labels

Spin Label	θ (-)	V (\AA^3)
I	0.05	180
II	0.10	310

Source: Roozen and Hemminga, 1990.

where S is the stickiness factor that depends on coupling between the rotating molecule and the liquid. If $S = 0$, there is no interaction, so molecules experience complete slip conditions. For $S = 1$, boundary layer conditions are completely sticking. The parameter θ is the ratio of the effectiveness of torques under slip to those under stick conditions; it depends on the geometry of the rotating molecule. Values derived from hydrodynamic theory were tabulated for prolate and oblate spheroids as a function of the ratio of the short and long molecular axes (Hu and Zwanzig, 1974). For nitroxide spin labels I (TEMPOL) and II, these values were determined by means of Stuart Bribleb atomic models, as given in Table 1 (Roozen and Hemminga, 1990). To study variations of the stickiness factor S with solvent composition, the value for θ is considered to be independent of temperature and solvent effects.

For nonspherical molecules, the stickiness factor S can be negative; this implies that molecules displace less solvent as expected on the basis of their geometry. This is the case for example when a cavity is formed whose spin label can carry out free rotation. The parameter k then equals zero, so that S equals $-\theta/(1 - \theta)$ [see Eq. (9)].

4.1. Glycerol Water Systems

To analyze the interaction between the spin label and the solvent in glycerol water mixtures at temperatures above the freezing point, graphs of values for τ_R versus η/T were plotted according to the modified Stokes-Einstein Eq. (8). To obtain values for k from the slope of these graphs, the volume of the spin label is considered to be independent of the solution composition (Roozen and Hemminga, 1990). In the temperature range considered here, k was found to be independent of temperature. Graph intercepts (τ_0) are from 10^{-10} – 10^{-12} s, which agrees with results of other studies (Kivelson *et al.*, 1970).

Figure 3 shows the resulting stickiness factor S as a function of the glycerol content in different glycerol water mixtures. For both spin labels, a decrease in S with an increasing glycerol content is observed to a glycerol content of 95 wt%, which agrees with other work on glycerol water solutions (Le Meste and Voilley, 1988). The decrease in S implies that both spin labels interact stronger with water than with glycerol molecules; therefore at increasing glycerol contents, the slip

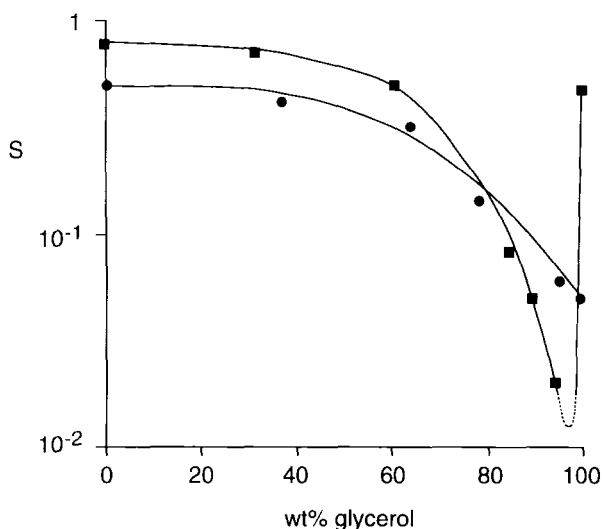


Figure 3. Stickiness parameter S as a function of the glycerol content for glycerol water mixtures for TEMPOL spin label I (●) and spin label II (■) [reprinted with permission from Roozen and Hemminga (1990). © 1990 American Chemical Society].

increases. Clearly glycerol is sufficiently more basic in character than water to behave as a hydrogen acceptor rather than as an amphoteric compound. The TEMPOL spin label I is a secondary alcohol, so it slightly prefers to accept a hydrogen bond rather than to offer it. Spin label II is a di-ketone, so it is a stronger base than TEMPOL spin label I. The decrease in S with glycerol content in aqueous glycerol mixtures is therefore in agreement with the acid base aspects of hydrogen bond formation (Roozen and Hemminga, 1990).

Above 95 wt% glycerol, an extreme increase in S of spin label II is observed. This is not the case for TEMPOL spin label I, which shows a continuous decrease to anhydrous glycerol. This arises because TEMPOL spin label I hardly interacts with anhydrous glycerol; however spin label II interacts strongly with this solvent. This is explained by the fact that due to its relatively strong basic character, this spin label forms a solvation shell with the amphoteric glycerol molecules. If a small amount of water is added to anhydrous glycerol, glycerol molecules in the solvation shell of spin label II are replaced by smaller water molecules. This leads to a decrease of its hydrodynamic volume, giving rise to the minimum of parameter S at low water contents (Roozen and Hemminga, 1990).

Observed differences between values for parameter S of the two spin labels at low glycerol contents are relatively small. Since S is independent of the molecular shape of spin labels, this is explained by a different dynamic behavior of spin labels

(i.e., anisotropic and internal motion) as well as by uncertainties of values calculated for V and θ (Roozen and Hemminga, 1990).

4.2. Sucrose Water Systems

For sucrose water mixtures the interaction parameter k as a function of the sucrose content is given in Fig. 4. The value of k at which the stickiness factor S becomes negative is indicated by Arrow 1 in Fig. 4. At concentrations above 40 wt% sucrose, a decrease of k is observed; this point is indicated by Arrow 2.

In Fig. 4 we see that the value of the interaction parameter k in sucrose-water mixtures from 0–40 wt% (corresponding to 3.4 molH₂O/mol) is constant and close to 1. This arises because the spin label molecules can form many hydrogen bonds with the liquid. Due to the relative basic character of spin labels, they form hydrogen bonds with water rather than with sucrose molecules (Roozen and Hemminga, 1990).

At concentrations above 40 wt% sucrose, a decrease in parameter k is observed (Arrow 2 in Fig. 4) because fewer hydrogen bonds are formed between spin labels and the solvent. This agrees with the conclusions of Flink (1983) that sucrose water mixtures at concentrations over 30–40 wt% sucrose change from a solution of

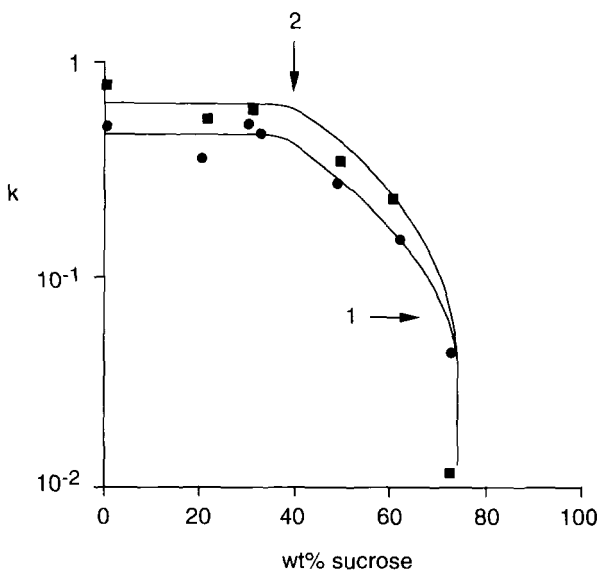


Figure 4. Interaction parameter k as a function of the sucrose content in sucrose water mixtures for TEMPOL spin label I (●) and spin label II (■). Arrow 1 indicates the value for k where the stickiness factor S becomes negative. Arrow 2 indicates the sucrose content where k starts to decrease [reprinted with permission from Roozen and Hemminga (1990). © American Chemical Society].

hydrated sucrose molecules to a sucrose water phase, where all water molecules directly or indirectly (i.e., as a second layer) are involved in hydrogen bonds with sucrose (Roozen and Hemminga, 1990).

Arrow 1 in Fig. 4 shows that parameter k equals θ [thus S becomes negative; see Eq. (9)] at about 70 wt% sucrose (corresponding to 11 mol $\text{H}_2\text{O}/\text{mol}$). A negative value of S indicates the formation of cavities. Such cavities may be formed if spin labels are not part of the lattice. Since the ESR technique is based on a labeling method, it is possible that cavities are not a property of the lattice but induced by spin labels themselves. Nevertheless hydrogen binding spin labels with surrounding molecules gives indirect information about the lattice (Roozen and Hemminga, 1990).

5. MOLECULAR MOBILITY IN SUGAR WATER GLASSES

In carrying out ESR and ST-ESR spectroscopy on spin labels in sugar water glasses, results depend on the measuring protocol and the nonequilibrium state of the samples. For samples containing 20 wt% sugar in water, a protocol is followed where prior to ESR experiments, samples are quickly cooled to about 180 K. During this process the solution concentrates to a C'_g value of about 80 wt% for most sugars; as a result the solution goes into very high viscosity amorphous state and becomes a solid glass (see Fig. 5). The remaining water crystallizes as ice (Levine

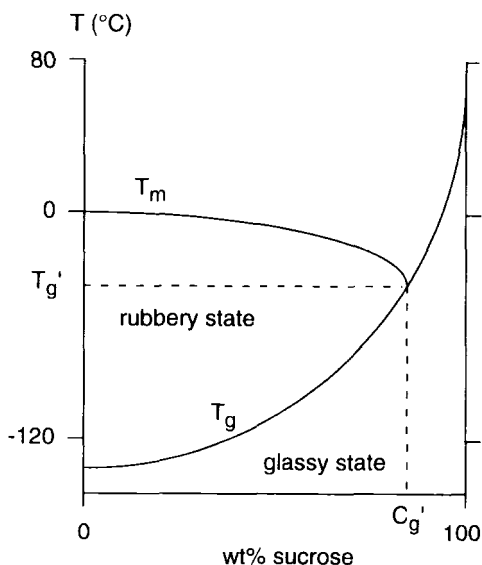


Figure 5. Simplified state diagram of temperature against sucrose content for an aqueous solution of sucrose. The T_m is the freezing curve and T_g the glass transition temperature curve; T'_g is the specific glass transition temperature of the maximally freeze concentrated solution, and C'_g (wt% solute in the glassy phase) is the corresponding composition.

and Slade, 1992). During ice crystallization spin labels are concentrated in the amorphous solution (Yoshioka, 1977; Roozen and Hemminga, 1990). The ESR and ST-ESR spectra are then recorded on heating the sample. When rewarming such a mixture, the Stokes viscosity of the amorphous solution starts to decrease above T'_g ; this is followed by ice melting above T_m .

Note: Such a measuring protocol and alternatives (such as annealing, or cycling) can be fully automated on a new range of computer-controlled ESR spectrometers, for example the Bruker ESR spectrometer ESP 330E™ with a nitrogen flow temperature control accessory.

5.1. Glassy State

This is a long lasting nonequilibrium state characterized by a spatially homogeneous distribution of molecules without a long-range lattice order. Amorphous materials show a glass transition where the solid phase displays a discontinuous change in the specific heat on changing temperature. An essential prerequisite for glass formation from a solution is that the cooling rate must be sufficiently fast to prevent nucleation and crystal growth. At the glass transition temperature, there is not only a sudden change in thermal and mechanical properties of the system but also an extreme decrease in molecular translation diffusion rates (Franks, 1985). In theory molecular mobility in glassy state systems is many orders of magnitude lower than in liquid systems (Roos, 1995). Below the glass transition temperature T_g , the very low molecular mobility predicts good stability in food products, such as ice cream, bakery products, meat, and fish.

Figure 5 shows the state diagram of a sugar water system where the glass transition temperature is a function of composition. Important parameters in the state diagram are T'_g , the specific glass transition temperature of the maximally freeze concentrated solution, and the corresponding composition C'_g (wt% solute in the glassy phase). At temperatures above T'_g (in the rubbery state), the sample becomes unstable in its supersaturated state, and it risks crystallization of the solute dictated by nucleation and crystal growth kinetics.

In general when a maximally frozen aqueous sugar solution is warmed from below its T'_g , there is a sudden increase in molecular mobility due to passing the glass-rubber transition. This mobility increase is followed by, and cannot always be separated from, a further strong increase in mobility due to subsequent ice melting and accompanying dilution of dissolved solids.

5.2. Sugar Water Systems

Figure 6 shows rotational correlation time for spin labels I and II after rewarming a rapidly cooled 20 wt% sucrose water mixture (Roozen and Hemminga, 1990). From -70 – -31 °C, $\log \tau_R$ decreases almost linearly with temperature; at

temperatures from -33 – -28 °C (as indicated by arrows in Fig. 6), τ_R exhibits a much stronger decrease. This strong increase in mobility arises from the mixture's melting transition, which is at -32 °C (Levine and Slade, 1988; Roos, 1995). Due to the glass transition, the Stokes viscosity of the concentrated amorphous solution decreases. The reduction of viscosity for a 20 wt% sucrose-water is from about 10^{12} Pa.s at the glass transition temperature to about 10^3 Pa.s at temperatures 20 °C above the glass transition (Franks, 1985). However the relative decrease in τ_R , as shown in Fig. 6, is much smaller. Note: A 20 wt% sucrose water mixture at temperatures below the glass transition consists of ice and a glassy sucrose water mixture. When the ice starts to melt due to the glass transition, the interaction parameter k increases strongly, as seen from Fig. 4. This effect reduces the decrease of τ_R due to the melting transition.

At -50 °C the rotational correlation time τ_R is about 10^{-4} s (Fig. 6), so that k is about 10^{-9} [given a viscosity of 10^{12} Pa.s (Franks, 1985)]. This very low value for the interaction parameter k implies that spin labels are present in cavities in the lattice of the amorphous solution, similar to those found in liquid samples. Figure 6 shows that spin label II is somewhat more mobile in the glassy sucrose system than TEMPOL spin label I. This may be due to the fact that lattice distortion due to the presence of TEMPOL spin label I is smaller than that arising from the presence of less spherical spin label II.

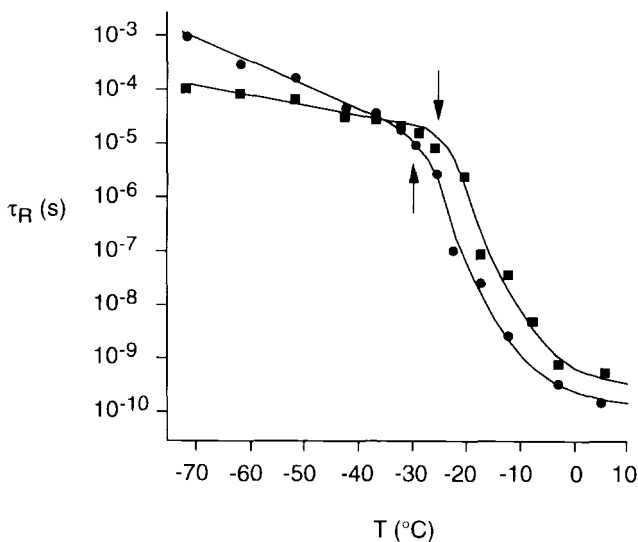


Figure 6. Rotational correlation time τ_R as a function of temperature in a 20 wt% sucrose water mixture for TEMPOL spin label I (●) and spin label II (■). The temperature at which τ_R starts to decrease sharply is indicated with an arrow [reprinted with permission from Roozen and Hemminga (1990). © American Chemical Society].

Table 2
Comparison of the Special Melting Temperatures (in K) of Various Carbohydrate Water Systems as Determined by ESR and DSC

Concentration (wt%)	Glucose		Fructose		Sucrose		Maltose	
	$T'_m{}^a$	$T'_m{}^b$	$T'_m{}^a$	$T'_m{}^b$	$T'_m{}^a$	$T'_m{}^b$	$T'_m{}^a$	$T'_m{}^b$
20	227	228	228	229	234	240	244	243
40	222	228	224	226	233	239	244	243
55	217	228	227	228	234	—	244	243

Source: van den Berg *et al.*, 1995.

^aDetermined by spin label ESR spectroscopy.

^bDetermined by DSC.

Similar observations were made about TEMPOL spin label I incorporated into various other water-carbohydrate (fructose, maltose, trehalose) systems. Table 2 compares and summarizes values for T'_m (the temperature of ice melting in freeze-concentrated systems) obtained with ESR and DSC (van den Berg *et al.*, 1995). In general there is a good agreement between ESR and differential scanning calorimetry (DSC) results. This observation confirms that for these carbohydrate-water systems there is a direct relation between molecular mobility and a change in specific heat given by macroscopic sample properties. However a change in mobility during warming up is often detected earlier by ESR than by DSC in 40 and 55 wt% glucose with 4° and 9°, respectively, and for 20 and 40 wt% sucrose with 6°. This effect may be related to a local interaction effect between the TEMPOL spin label I and saccharide, which is not exhibited in the DSC curves (van den Berg *et al.*, 1995).

Mobility in the glassy state is affected significantly by the initial carbohydrate concentration. In all cases the glassy system made from dilute 20 wt% concentration exhibits a higher mobility than systems with concentrations of 40 and 55 wt%. This effect of concentration is somewhat unexpected, since theoretically we would expect equal mobilities in maximally frozen systems produced with initially different concentrations. This effect may be caused by an inhomogeneous spin label distribution due to the amount and size of ice crystals in the sample (van den Berg *et al.*, 1995). However it may also be related to the fact that samples are quenched-cooled, so that they probably are not maximally freeze concentrated.

5.3. Molecular Mobility in Maltooligosaccharide Water Glasses

The rotational correlation time τ_R of TEMPOL spin label I in a 20 wt% maltooligosaccharide water mixture was determined similarly to sucrose water systems (Roozen *et al.*, 1991); Table 3 lists melting temperatures. A comparison

Table 3
Special Melting Temperature (T'_m) for Rapidly Cooled 20 wt% Maltooligosaccharide Water Mixtures (in °C)

Oligosaccharide	T'_m ^a	T'_m ^b
Maltotriose	-23	-23.5
Maltopentaose	18	-16.5
Maltoheptaose	-14	-13.5

^aDetermined by spin label ESR spectroscopy (± 1 °C) (Roozen *et al.*, 1991)

^bDetermined by differential scanning calorimetry (Levine and Slade, 1988)

with DSC results (Levine and Slade, 1988) shows an excellent agreement. For relatively dry sugar water systems, the ESR technique can be applied as well (see Fig. 7).

Figure 7 shows the rotational mobility of TEMPOL spin label I in a concentrated maltoheptaose-water mixture stored at an equilibrium relative humidity of 33% (Roozen *et al.*, 1991). The glass transition temperature T_g takes place at 42 °C. Due to higher viscosity, the value of τ_R at temperatures above T_g is higher than in samples where ice melts (see Fig. 6). In addition Fig. 7 shows the resulting curve

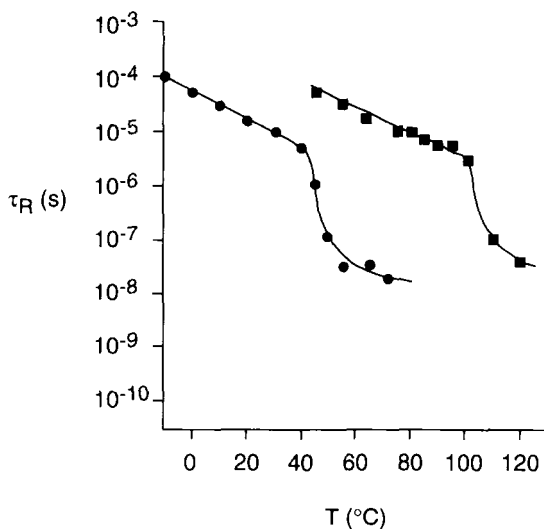


Figure 7. Rotational correlation time τ_R of TEMPOL spin label I as a function of temperature in a maltoheptaose water mixture stored at an equilibrium relative humidity of 33% (●) and oven dried for 16 hours at 100 °C (■) [reprinted with permission from Roozen *et al.* (1990)].

for a completely dried maltoheptaose sample. Due to a decrease in the water content, T_g shifts upward to about 100 °C, as may be qualitatively expected from the state diagram (Fig. 5).

The molecular mobility of the TEMPOL spin label I was examined using ESR and ST-ESR in 20 wt% sugar glasses consisting of a range of malto-n-ose molecules with $n = 1$ to 7 (M. Nijman *et al.*, unpublished results). Figure 8 shows results for extreme-case glucose ($n = 1$) and maltoheptaose ($n = 7$). Intermediate sugars fall systematically in between these two extremes. In addition to a change in glass transition in agreement with DSC results, Fig. 8 shows the mobility state of TEMPOL spin label I in the glassy material. We see that in maltoheptaose, mobility increases with respect to glucose. This result strongly indicates that free volume effects play a role in spin label mobility in the sugar lattice. Glucose molecules are relatively small, so these can be densely packed when concentrated in a glassy state. Maltoheptaose on the other hand is a glucose oligomer, which has a lower packing ratio in the glassy state; TEMPOL spin label I molecules can rotate more freely in its small holes as that in glucose.

Apart from the free volume effect, hydrophilic interactions (i.e., hydrogen bonds) between the sugar and TEMPOL spin label I can be expected to influence rotational correlation times τ_R . It is well-known that deuterated hydrogen bonds are stronger than protonated hydrogen bonds (March, 1985). Comparing the ESR analysis of a glucose sample made up in D_2O and H_2O shows a reduction of motion in the D_2O sample in the glassy state. This suggests that hydrophilic interactions effect the rotational motion of TEMPOL spin label I in sugar water systems. This

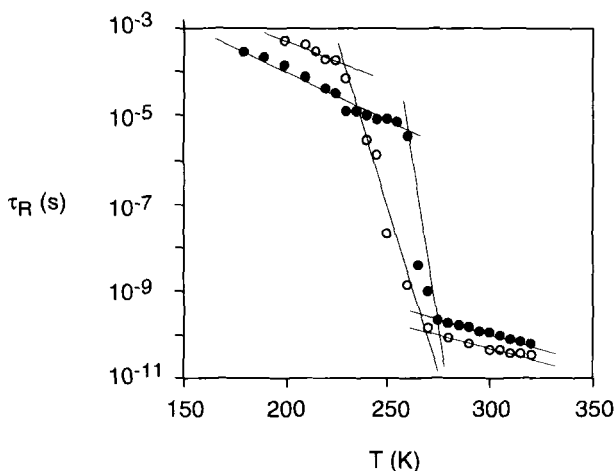


Figure 8. Rotational correlation time τ_R of TEMPOL spin label I as a function of temperature in 20 wt% glucose (○) and maltoheptaose (●) (M. Nijman *et al.*, unpublished).

also indicates that TEMPOL spin label I is able to probe molecular dynamics as well as molecular structure in glassy sugar water mixtures. It can also provide insight into the hydrogen-bonding network of the glass.

5.4. Glucose Water Systems

The molecular mobility of the TEMPOL spin label I in a 20 wt% glucose-water sample has been examined using both the L''/L ratio and the relative integrated intensity I_{rel} of the ST-ESR spectra (van den Dries *et al.*, 1998). The results are shown in Figure 9. Upon cooling this sample a phase separation takes place, because ice is formed. Upon rewarming, the melting of ice then starts at the melting temperature T_m . The process of ice formation upon cooling concentrates the remaining glucose solution containing the spin label, and finally the supersaturated solution undergoes a glass transition at a temperature T_g .

From Figure 9, it can be seen that the glass transition temperature T_g (210 K) and the melting temperature T_m (223 K) are well identified as breaks in the plot determined from the relative integrated intensity I_{rel} . These values of T_g and T_m are in agreement with the literature (Roos, 1995). Furthermore, τ_R values can be determined at temperatures far below the glass transition temperature T_g , i.e. τ_R can be determined in the glassy state up to a value of about 10^3 s. In contrast, the

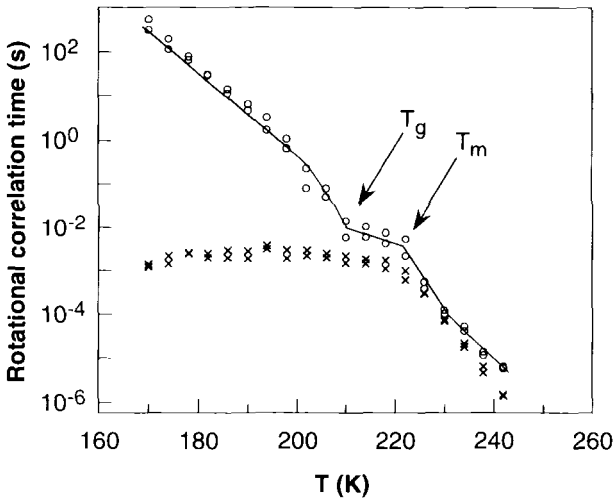


Figure 9. Rotational correlation time τ_R of the TEMPOL spin label I in a 20 wt% glucose-water system analyzed using the L''/L ratio (x) and the relative integrated intensity I_{rel} (O) obtained in glycerol (Fig. 3). The glass transition temperature T_g (210 K) and the melting temperature T_m (223 K) are indicated with an arrow (van den Dries *et al.*, 1998).

L''/L ratio levels off at a value of about 2.1, giving τ_R values around 10^{-3} s. At these values the limit of sensitivity for mobility for the L''/L ratio is reached. This effect can be explained by realizing that the L''/L ratio is almost insensitive to T_1 effects, and that changes in T_1 are the main cause for sensitivity for motion for $\tau_R > 10^{-3}$ s. This also implies that by using the relative integrated intensity I_{rel} of ST-ESR spectra, the range of sensitivity for mobility can be strongly extended, as compared to using the L''/L ratio.

5.5. Commercial Maltodextrin

It is interesting to compare results for model oligo-saccharides with those for materials used in the food industry, such as enzymatically converted starch, which is a mixture of dextrin molecules of different molecular weight. Figure 10 shows the rotational mobility of TEMPOL spin label I in a commercially available sample of maltodextrin (average molecular weight of 8000 Da) as a function of temperature (Roozen *et al.*, 1991). The sudden change in the temperature dependence of the rotational correlation time τ_R at 30 °C represents the glass-rubber transition.

By adding 8 wt% glucose to the polymer (Fig. 10), we observed a decrease of the glass transition temperature by 5 °C. This indicates that glucose acts as a plasticizer in maltodextrin. Several effects may contribute to this decrease: the addition of glucose results in a small increase in the water-to-dextrin ratio or glucose may act as a plasticizer to dextrin, although water molecules that interact with glucose molecules may not be able to plasticize the polymer chain.

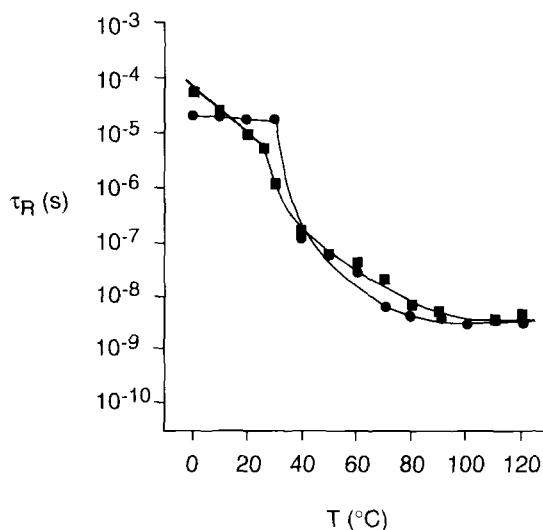


Figure 10. Rotational correlation time τ_R of the TEMPOL spin label I as a function of temperature in a maltodextrin water system; (●) 12.7 wt% water, (■) 12.7 wt% water and 8 wt% glucose [reprinted with permission from Roozen *et al.* (1991)].

5.6. Activation Energy for Molecular Reorientation

It was shown that the temperature dependency of the correlation time of spin labels in the glassy state is described by an Arrhenius-type equation (Roozen *et al.*, 1991):

$$\tau_R = \tau_a \exp(E_a/RT) \quad (10)$$

The parameter τ_a is a temperature-independent factor, R and T have their usual meaning; E_a is interpreted as an activation energy for molecular reorientation.

As discussed before TEMPOL spin label I is present in cavities in the glass; however values for τ_R and E_a indicate that the spin label does not rotate freely in the cavities. Activation energy E_a corresponds not only to the number and strength of hydrogen bonds formed between the spin label and its surrounding, but it is also determined by the free volume of the system. This latter effect is observed in Fig. 10 on adding glucose to maltodextrin, where the strong increase in E_a from 8 to 60 kJ/mol is related to the decrease in the free volume of the sample.

6. GLUTEN SYSTEMS

Gluten is a protein part of dough that gives it unique technological characteristics that make wheat the most widespread cereal. The protein network of gluten composed mainly of monomeric (gliadins) and polymeric (glutenins) water-insoluble storage proteins; these are associated into aggregates that interact by weak bonds (see Fig. 11) (Shewry *et al.*, 1994). The viscoelastic properties of gluten depend largely on relative proportions of the two components; too few gliadins compared to glutenins results in a rigid mass, while too many gliadins make it too slack. In native gluten the proportion of gliadins is about 40 wt%. Although it is accepted that gliadins contribute to flow and glutenins to elasticity (Kaufman *et al.*, 1986), the molecular basis of the functionality of the protein network of gluten is still unclear.

The ESR spectroscopy was used to understand the properties of functional gluten. Spin probing by using the small spin label TEMPO provided information about the compartmentation of the liquid phase of hydrated gluten. This showed the existence of lipid and aqueous phases (Pearce *et al.*, 1988; Hargreaves *et al.*, 1994b), and the presence of two different microenvironments in the water phase (Hargreaves *et al.*, 1994a; Hargreaves *et al.*, 1995b). In the application of ESR and ST-ESR spectroscopy to the study of gluten discussed here in more detail, we follow an approach where ESR spin labels are attached to polypeptide chains by covalently labeling SH groups. This provides information about polypeptide flexibility, depending on the organization and gliadin/glutenin ratio of the gluten (Hargreaves *et al.*, 1994b; Hargreaves *et al.*, 1995a; Hemminga, 1995).

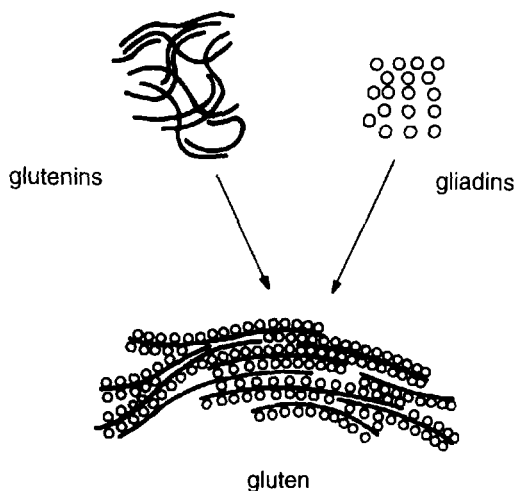


Figure 11. Schematic illustration of a gluten system consisting of glutenins and gliadins [reprinted with permission from Hemminga (1995)].

6.1. ESR Spectra

Figure 12 shows ESR spectra of a gluten system, labeled with maleimide spin label III. The spectrum consists of a mixture of labels at different positions on proteins; this gives rise to composite ESR spectra in which at least two populations of spin labels largely differing in molecular mobility can be observed. On increasing the temperature, there is a progressive transfer of spin labels with a slow motion to a more mobile population of spin labels. At 90 °C all spin labels are in the mobile state. Concomitantly the rotational correlation time τ_R of the mobile fraction decreases with increasing temperature. Two parameters are used to describe the spectra. The parameter R , given by the ratio h_i/h_m (see Fig. 12), reflects the number of immobile ($\tau_R > 10^{-7}$ s) with respect to mobile ($\tau_R < 10^{-8}$ s) spin labels. The rotational correlation time τ_R , determined from the sharp three-line spectrum according to Eq. 5, describes the molecular mobility of the mobile spin label population.

For the gluten system and various gliadin or glutenin-enriched fractions, parameters R and τ_R decrease monotonous with increasing temperature (Hargreaves *et al.*, 1995a; Hemminga, 1995), representing the increase in molecular dynamics by both a transfer of spin labels from the immobile to the mobile population and increased motion of mobile spin labels. This means that local molecular motion as sensed by the maleimide spin label attached to cysteine residues on the polypeptide chains changes gradually with temperature.

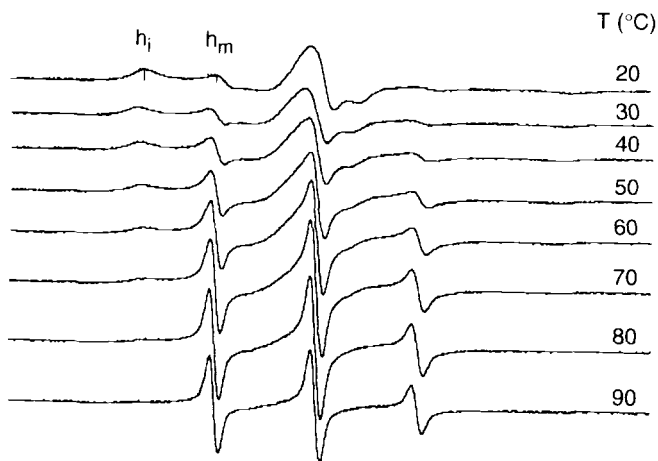


Figure 12. Conventional ESR spectra of gluten labeled with maleimide spin label III recorded at different temperatures. The parameter R is given by the ratio h_i/h_m . The total scan range is 10 mT [reprinted with permission from Hargreaves *et al.* (1995a). © 1995 American Chemical Society].

Strikingly the absence of a transition in the segmental flexibility of hydrated gluten proteins in the temperature range explored is opposite to the viscoelastic behavior of gluten. From rheological studies we find that the height of the rubbery plateau (G_N^0) decreases on heating from 10 to 50 °C (103 to 102 N/m²), then increases strongly, reaching 104 N/m² at 80 °C. The effect with ESR is therefore proposed to be related to a reduction of hydrogen bonds, possibly corresponding to a disruption of α -helices in the gluten system (Hargreaves *et al.*, 1995a; Hemminga, 1995).

Parameters R and τ_R show a linear dependence when drawn according to the Arrhenius equation (10). Activation energy E_a for the spin label motion derived from the τ_R values is about 13.5 kJ/mol, which is much lower than that found from rheological studies (90 kJ/mol). This difference may be explained if the activation energy of 90 kJ/mol represents the contribution of low-energy interactions (hydrogen bonds, hydrophobic interactions, and entanglement points) between two covalent bonds in the gluten, whereas the value of E_a determined by ESR spectroscopy (13.5 kJ/mol) is related to low-energy bonds in the immediate surrounding of the spin label; this corresponds to about one-sixth of the unit polymer bond (Hargreaves *et al.*, 1995a).

6.2. ST-ESR Spectra

Figure 13 shows ST-ESR measurements on maleimide spin-labeled gluten. Only approximate values for the rotational correlation time τ_R can be obtained in this case due to the spectral contribution of fast moving spin labels. Because of the

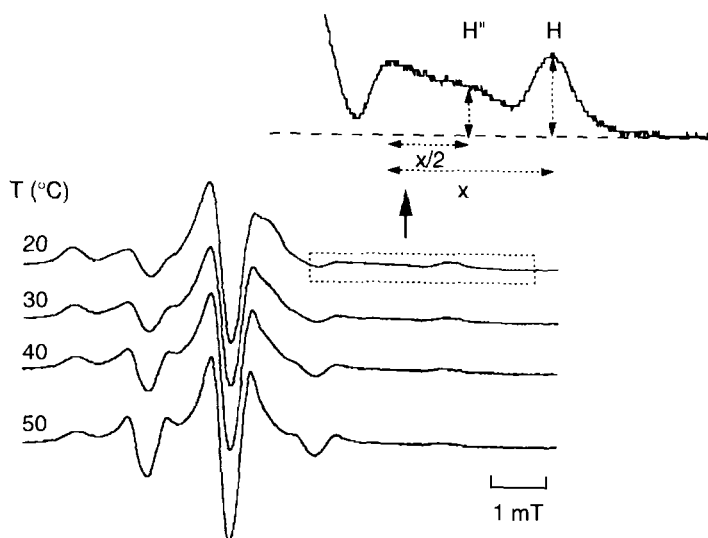


Figure 13. The ST-ESR spectra of gluten labeled with maleimide spin label III recorded at different temperatures. Insert shows an enlargement of the high-field part of the spectrum, with line heights H'' and H from which the rotational correlation time τ_R is estimated [reprinted with permission from Hargreaves *et al.*, (1995a). © 1995 American Chemical Society].

overlap of the mobile fraction, the high-field region is taken to calculate τ_R . Values of H''/H vary from 0.6–0.9. In comparing these values with those of reference experiments, it follows that τ_R is between 3×10^{-5} and 3×10^{-4} s for the slow moving population (Hargreaves *et al.*, 1995a). These large τ_R values, compared to those for the mobile fraction, stress the very slow motional properties of the immobile fraction. This suggests that the spin label is rigidly bound to the gluten with virtually no internal flexibility.

7. CONCLUSIONS

From the present overview we can conclude that spin label ESR and ST-ESR spectroscopy are useful techniques for providing physical insights into the molecular dynamics of food systems and related model systems.

Although spin labels provide only indirect information about their local environment, these techniques are especially powerful in obtaining data about molecular mobilities that can not be obtained in alternative ways. Taking into account the lower limit of conventional ESR is for values of rotational correlation times τ_R of

Table 4
Summary of Information Accessible with Spin Label ESR and
ST-ESR on Carbohydrate Water Systems

Description	Parameter
Molecular motion	τ_R
Activation energy for molecular motion	E_a
Slip and stickiness	k, S
Glass transition and melting temperatures	T_g, T_g', T_m'
Hydrogen bonds	
Free volume	
In lattice cavities	

about 10^{-11} s and the upper limit is around 10^{+4} s, it will be clear that a single set of equipment for ESR spectroscopy is able to cover an immense range of rotational molecular motions. In carbohydrate water systems, glass transition temperatures can be obtained that agree very well with those obtained from DSC measurements. In addition the technique provides information about hydrogen bonds and the presence of cavities in these systems. Table 4 summarizes the information accessible with spin label ESR and ST-ESR on carbohydrate-water systems. The ESR technique is also suitable for characterizing gluten proteins on a molecular basis. This information complements such techniques as microscopy and rheology, which reflect the macroscopic network organization.

Food materials are complex and heterogeneous systems. Up to now a strong emphasis was placed on applying the ESR spin label technique to model compounds. However this will make it possible to develop general rules for handling more complex systems in the future.

ACKNOWLEDGMENTS. Chapter 8 gives an overview of work carried out in collaboration with food scientists in France (Dominique Champion, Jeremy Hargreaves, Martine Le Meste, and Denise Simatos, from the Ecole Nationale Supérieure de Biologie Appliquée à la Nutrition et à l'Alimentation (ENSBANA) in Dijon; and Yves Popineau from the Institut National de la Recherche Agronomique (INRA) in Nantes); and The Netherlands (Cornelius van den Berg, Marcel Roozen, and Pieter Walstra from the Department of Food Science, Wageningen Agricultural University). We are very grateful for their enthusiastic collaboration. This research was partly financed by the European Union projects ECLAIR-AGRE-0052 and ERB-FAIR-CT96-1085.

APPENDIX: CALIBRATION PROCEDURE FOR ST-ESR SPECTRA

Calibration of ST-ESR Spectra

To carry out ST-ESR spectroscopy of spin labels in sugar water systems, it is necessary to calibrate ST-ESR spectra to the rotational correlation time τ_R . This is done by taking glycerol water systems as a reference system. The strategy of this calibration procedure is to select a reference system whose viscosity is known over a large temperature range and that resembles most carbohydrate molecules. The TEMPOL spin label I in anhydrous glycerol, which has a close chemical resemblance to carbohydrates, turns out to be the most suitable reference system for calibrating ST-ESR spectra. The calibration procedure is carried out in the following steps:

1. Conventional ESR spectra of TEMPOL spin label I in anhydrous glycerol are recorded between room temperature and 100 °C, and the rotational correlation time τ_R of the spin label is determined from ESR spectra using Eq. (6). A plot of τ_R against η/T is shown in Fig. A1. Data for viscosity

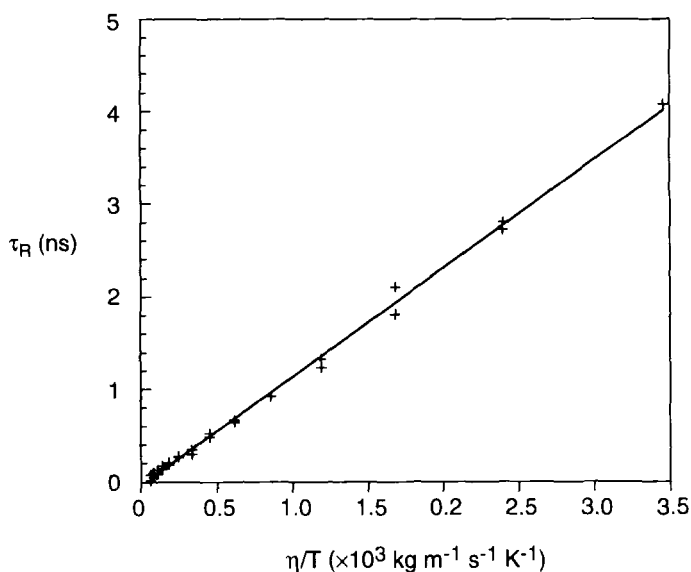


Figure A1. Rotational correlation time τ_R of the TEMPOL spin label I versus η/T in anhydrous glycerol. Values of τ_R were calculated from conventional ESR spectra using Eq. (5). Scan range, scan rate, time constant, and modulation amplitude were adjusted to avoid spectral distortion. The microwave power was 2 mW.

are obtained from (Glycerine Producers' Association, 1969). According to the modified Stokes Einstein equation (8), the slope yields a value for the interaction parameter k . The intercept at $\eta/T = 0$ gives τ_0 , the zero viscosity rotational correlation time, which is generally negligible.

- Since ST-ESR spectra are recorded in the temperature range from 170–280 K, we must know viscosities in this temperature range. However viscosity data of anhydrous glycerol are known only for temperatures above 240 K (Glycerine Producers' Association, 1969). Therefore known data are fitted to the Williams–Landel–Ferry (WLF) equation (Williams *et al.*, 1955):

$$\ln \frac{\eta}{\eta_s} = \frac{C_1(T - T_s)}{C_2 + (T - T_s)} \quad (11)$$

where T_s is a reference temperature, η_s the corresponding viscosity, and C_1 (–17.4) and C_2 (51.6) are universal constants. Using $T_s = T_g = 185$ K, this equation is then extrapolated to lower temperatures, as illustrated in Fig. A2. From this extrapolation the rotational correlation time τ_R of TEMPOL spin label I can be calculated as a function of temperature.

- In the final step, the ST-ESR spectra of TEMPOL spin label I in anhydrous glycerol are recorded at various temperatures in the low-temperature range (see Fig. A3). Line heights L and L'' that determine the characteristic low-field ratio L''/L are used to relate spectra to the rotational correlation

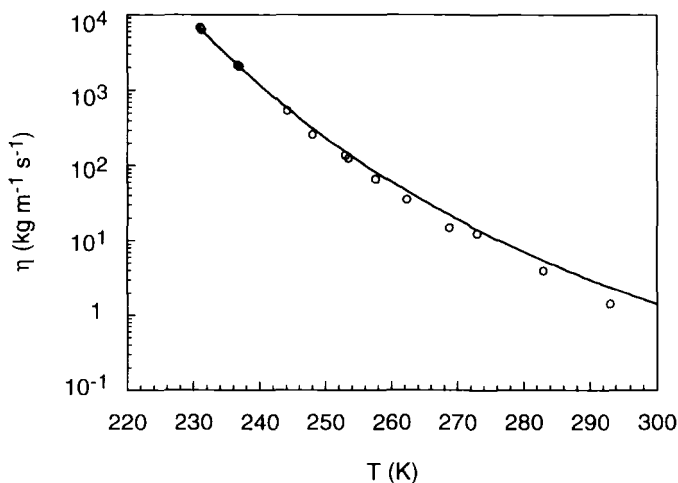
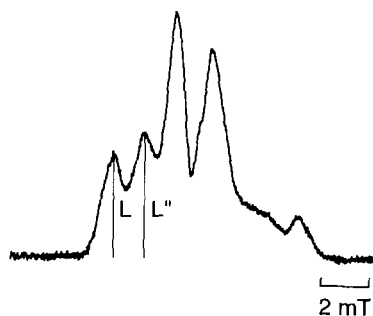


Figure A2. Viscosity of anhydrous glycerol versus temperature fitted to the Williams–Landel–Ferry (WLF) Equation (11).

Figure A3. Characteristic second harmonic quadrature ST-ESR spectrum of TEMPOL spin label I in anhydrous glycerol at a temperature of 230 K. The ST-ESR spectra were recorded under the following conditions: microwave power 100 mW, a modulation amplitude of 0.5 mT, and a modulation frequency of 50 kHz. Samples were contained in sealed 100 μ l capillaries with a height of 5 mm. The final concentration of the spin label was about 0.5 mg/ml. The absorption ST-ESR signal was measured 90° out-of-phase with respect to the field modulation. Line heights L and L'' determine the characteristic low-field ratio L''/L from which the rotational correlation time τ_R is derived.



time τ_R , as shown in Fig. A4. Alternatively, the relative integrated intensity I_{rel} can be taken to determine τ_R (van den Dries *et al.*, 1998). A comparison of the use of the L''/L ratio and the relative integrated intensity I_{rel} is given in Fig. A5. Note that the lineheight ratio L''/L levels off and loses motional sensitivity for values of τ_R above 10^{-2} s, whereas the relative integrated intensity I_{rel} continues to change in this τ_R region. The assumption in the calibration procedure is that the molecular motion

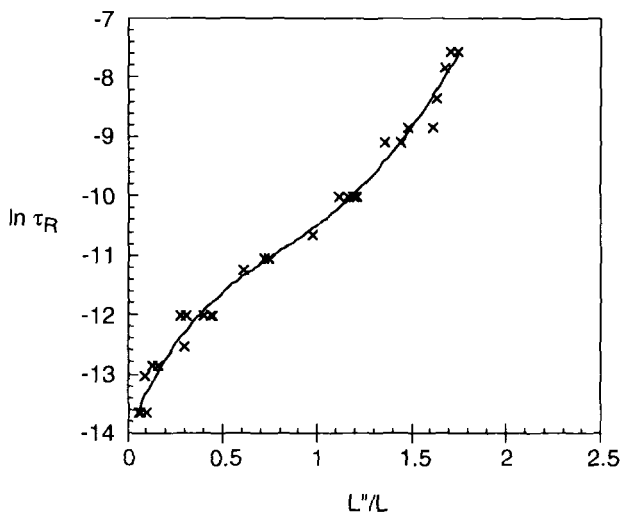


Figure A4. Calibration curve deduced from the low-field region of the second harmonic quadrature ST-ESR spectra. Points are fitted to a polynomial of order 4, given by $\tau_R = \exp\{-14.023 + 7.897 \times (L''/L) - 8.407 \times (L''/L)^2 + 4.870 \times (L''/L)^3 - 0.8244 \times (L''/L)^4\}$.

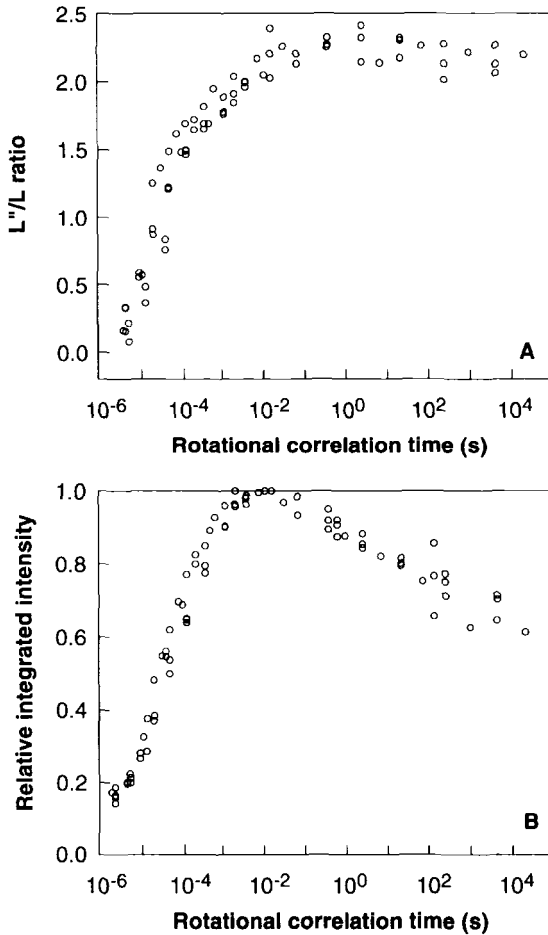


Figure A5. The L''/L ratio (A) and the relative integrated intensity I_{rel} (B) of the ST-ESR spectra of the TEMPOL spin label I in glycerol as a function of the rotational correlation time τ_R (van den Dries *et al.* 1998).

of TEMPOL spin label I is isotropic, and it has the same nature in glycerol water and sugar water systems. Furthermore it is assumed that the spin lattice relaxation time T_1 of TEMPOL and the dielectric properties of the systems are comparable.

The center-field ratio C'/C and the high-field ratio H''/H can be used for the calibration as well (Thomas *et al.*, 1976; Hemminga, 1983; Hemminga and De Jager, 1989). Since the center-field ratio is sensitive to small missettings of the phase

of the ST-ESR spectrum, it gives less accurate values for τ_R as compared to the ratio L''/L . The high-field ratio is often more difficult to determine. Therefore the low-field ratio is used to calibrate rotational correlation times in sugar water systems (Roozen and Hemminga, 1990; Roozen and Hemminga, 1991; Roozen *et al.*, 1991; van den Berg *et al.*, 1995).

NOTES

1. Note: In contrast to conventional ESR, which is generally carried out below saturation and with small-field modulation amplitudes, ST-ESR is a highly nonlinear ESR technique. To observe saturation transfer, the experiment is performed under saturating conditions, and high-field modulation amplitudes are used. Since the microwave field strength B_1 and field modulation amplitude B_m vary over the cavity, the resulting ST-ESR spectrum strongly depends on values and distribution of these parameters. Therefore care should be taken that all experimental conditions for the reference set and actual samples are the same. This also applies to the sample size and height (Hemminga *et al.*, 1984; Hemminga and De Jager, 1989).
2. In the literature spin-labeled hemoglobin in glycerol water systems is often used as a reference system. These reference data cannot be applied to TEMPOL spin label 1 in sugar water systems, because motional properties of large molecules, such as spin-labeled hemoglobin, are not directly comparable to those of the small molecule TEMPOL. To analyze ST-ESR spectra spin-labeled gluten (Hargreaves *et al.*, 1995a) however, spin-labeled hemoglobin was taken as a reference system.
3. In carrying out ESR spectroscopy on spin labels in glassy sugar water mixtures, we found it important routinely to take ST-ESR spectra and ESR spectra at the same temperature. Since these systems are generally not in equilibrium, it is important to check for phase separations (for example crystallization) in the sample and for spin label-spin label interactions (during freeze concentration the spin label is also concentrated) that may disturb τ_R determination. This is better observed in ESR than in ST-ESR spectra.

REFERENCES

- Buitink, J., Claessens, M. M. A. E., Hemminga, M. A., and Hoekstra, F. A., 1998, *Plant Physiol*, in press.
- Dote, J. L., Kivelson, D., and Schwartz, R. N., 1981, *J Phys. Chem.* **85**:2169.
- Dzuba, S. A., Golovina, Y. A., and Tsvetkov, Y. D., 1993a, *J. Magn. Reson. Ser. B* **101**:134.
- Dzuba, S. A., Golovina, Y. A., and Tsvetkov, Y. D., 1993b, *Appl. Magn. Reson.* **5**:31.
- Flink, J. M., 1983, Structure and structure transitions in dried carbohydrate materials, in *Physical Properties of Foods* (M. Peleg and E. B. Bageley, eds.) (AVI, Westport, CT), pp. 473–521.
- Franks, F., 1985, *Biophysics and Biochemistry at Low Temperatures* (Cambridge Univ. Press, Cambridge).
- Freed, J. H., 1976, Theory of slow-tumbling ESR spectra for nitroxides, in *Spin Labeling* (L.J. Berliner, ed.) (Academic, New York), pp. 53–132.
- Glycerine Producers' Association, 1969, *Physical properties of glycerine and its solutions* (Glycerine Producers' Ass., New York).
- Golovina, E. A., and Tikhonov, A. N., 1994, *Biochim. Biophys. Acta* **1190**:385.
- Hargreaves, J., Le Meste, M., Cornec, M., and Popineau, Y., 1994a, *J. Agric. Food Chem.* **42**:2698.

- Hargreaves, J., Le Meste, M., and Popineau, Y., 1994b, *J. Cereal Sci.* **19**:107.
- Hargreaves, J., Popineau, Y., Le Meste, M., and Hemminga, M. A., 1995a, *FEBS Lett.* **372**:103.
- Hargreaves, J., Popineau, Y., Marion, D., Lefebvre, J., and Le Meste, M., 1995b, *J. Agric. Fund Chem.* **43**:117.
- Hemminga, M. A., 1983, *Chem. Phys. Lipids* **32**:323.
- Hemminga, M. A., 1995, Analysis of molecular motions in food products, in *Magnetic Resonance in Food Science* (P. S. Belton, I. Delgadillo, A. M. Gil, and G. A. Webb, eds.) (Royal Society of Chemistry, Cambridge, UK), pp. 43–53.
- Hemminga, M. A., and De Jager, P. A., 1989, Saturation transfer spectroscopy of spin labels: Techniques and interpretation of spectra, in *Biological Magnetic Resonance. Spin Labeling—Theory and Applications*, vol. 8 (L. J. Berliner and J. Reuben, eds.) (Plenum, New York), pp. 131–78.
- Hemminga, M. A., de Jager, P. A., Marsh, D., and Fajer, P., 1984, *J. Magn. Reson.* **59**:160.
- Hoel, D., and Kivelson, D., 1975, *J. Chem. Phys.* **62**:1323.
- Hu, C. M., and Zwanzig, R., 1974, *J. Chem. Phys.* **60**:4354.
- Hyde, J. S., 1978, *Methods Enzymol* **49**:480.
- Kaufman, S. P., Hosoney, R. C., and Fennema, O., 1986, *Cereal Foods World* **31**:820.
- Kivelson, D., Kivelson, M. G., and Oppenheim, I., 1970, *J. Chem. Phys.* **52**:1810.
- Knowles, P. F., Marsh, D., and Rattle, H. W. E., 1976, *Magnetic Resonance of Biomolecules* (Wiley, London).
- Le Meste, M., and Simatos, D., 1980, *Cryo-Lett.* **1**:402.
- Le Meste, M., and Voilley, A., 1988, *J. Phys. Chem.* **92**:1612.
- Levine, H., and Slade, L., 1988, *Cryo-Lett.* **9**:21.
- Levine, H., and Slade, L., 1992, Glass transitions in foods, in *Physical Chemistry of Foods* (H. G. Schwartzberg and R. W. Hartel, eds.) (Marcel Dekker, New York), pp. 83–221.
- March, J., 1985, *Advanced Organic Chemistry* (Wiley, New York).
- McClung, R. E. D., and Kivelson, D. J., 1968, *Chem. Phys.* **59**:3380.
- Pearce, L. E., Davis, E. A., Gordon, J., and Miller, W. G., 1988, *Cereal Chem.* **65**:55.
- Roos, Y., 1995, *Phase Transitions in Foods* (Academic, San Diego).
- Roozen, M. J. G. W., and Hemminga, M. A., 1990, *J. Phys. Chem.* **94**:7326.
- Roozen, M. J. G. W., and Hemminga, M. A., 1991, *Spec. Publ.-R. Soc. Chem.* **82**:531.
- Roozen, M. J. G. W., Hemminga, M. A., and Walstra, P., 1991, *Carbohydr. Res.* **215**:229.
- Shewry, P. R., Miles, M. J., and Tatham, A. S., 1994, *Prog. Biophys. Mol. Biol.* **61**:37.
- Thomas, D. D., Dalton, L. R., and Hyde, J. S., 1976, *J. Chem. Phys.* **65**:3006.
- Van den Berg, C., van den Dries, I. J., and Hemminga, M. A., 1995, Molecular mobilities around the glass transition in sugar water systems, in *Magnetic Resonance in Food Science* (P. S. Belton, I. Delgadillo, A. M. Gil, and G. A. Webb, eds.) (Royal Society of Chemistry, Cambridge, UK), pp. 93–101.
- Van den Dries, I. J., De Jager, P. A., and Hemminga, M. A., 1998, *J. Magn. Reson.* **131**:241.
- Williams, M. L., Landel, R. F., and Ferry, J. D., 1955, *J. Am. Chem. Soc.* **77**:3701.
- Yoshioka, H., 1977, *Chem. Lett.* **10**:1153.

EPR Studies of Living Animals and Related Model Systems (*In Vivo* EPR)

Harold M. Swartz and Howard Halpern

1. INTRODUCTION

The aim of this chapter is to provide the reader with an understanding of what is *in vivo* Electron paramagnetic resonance (EPR), why it may be important, how it is carried out, what results were obtained with it so far, and where it may go in the future. This chapter is especially intended for readers who are not closely involved with these techniques but may become so in the future. Given these aims and the limitations of space, we do not consider the details of instrumentation, although this is certainly a critical aspect for the development of this field.

In this chapter *in vivo* EPR encompasses a range of techniques in which parameters of EPR spectra are obtained from functional multicellular systems. This chapter focuses on approaches that obtain EPR spectra or images directly from the

Note to the reader: At the authors' request the references in this chapter are arranged numerically rather than alphabetically as in the other chapters in this volume.

Harold M. Swartz • Department of Radiology, HB7785, Dartmouth Medical School, Hanover, New Hampshire 03755-3863. **Howard Halpern** • Department of Radiation and Cellular Oncology, University of Chicago, Chicago, Illinois 60637

Biological Magnetic Resonance, Volume 14: Spin Labeling: The Next Millennium, edited by Berliner. Plenum Press, New York, 1998.

functioning biological system and considers only in passing the often useful approaches in which samples are removed from the biological system, then studied by EPR. (Examples of the latter are studies that have demonstrated the occurrence of free radicals *in vivo* by administering spin traps, then removing tissue for study *in vitro*.⁽⁹¹⁾ We also do not cover the important related field in which EPR and Nuclear magnetic resonance (NMR) are combined to provide information with proton electron double-resonance imaging (PEDRI) and dynamic nuclear polarization (DNP), with the aim of providing spatial information on the distribution of paramagnetic substances by their effects on NMR images.^(58, 59, 119-129)

Even within this restricted definition, *in vivo* EPR encompasses a considerable range of techniques and studies, including microscopic imaging of small biological samples, such as spheroids, high-resolution spectroscopic studies of intact animals or isolated organs; and images obtained from isolated organs or intact animals.

This chapter emphasizes the current state of knowledge and directions that are likely to be pursued in the future. We have paid only modest attention to historical aspects. While major types of applications are considered and many major results summarized, there is no attempt to cover this field comprehensively because it is rapidly growing and therefore any such effort would soon be out of date. An attempt was made, however, to provide an up-to-date bibliography that covers pertinent literature at the time this chapter was completed (November 1996).

2. RATIONALE FOR DEVELOPING AND USING *IN VIVO* EPR

Much of the motivation for developing *in vivo* EPR initially arose from a desire to determine the real biological role and consequences of processes involving unpaired electron species, especially free radicals. The perception of a need for carrying out such studies in intact organisms was based on concerns that procedures required to remove samples for examination in conventional EPR spectrometers may alter significantly what was measured. While such goals remain valid and pertinent, other considerations have driven most developments of *in vivo* EPR. This occurred because it rapidly became obvious that the level of naturally occurring free radicals was so low, it was likely to be very difficult to observe them *in vivo*. Problems caused by these low levels are significantly augmented by the lower sensitivity of EPR when applied to such systems as live animals, which contain large amounts of lossy materials such as water (i.e., materials that nonresonantly absorb frequencies used for EPR).

Consequently the development of *in vivo* EPR occurred especially through two key elements: Going to lower frequencies (1.2 GHz or less), which decreases nonresonant losses due to water and adding stable paramagnetic materials to biological systems, so that the concentration of materials is sufficient to be measured. As a consequence initial principal applications of *in vivo* EPR were based on

measuring the distribution and environment of added paramagnetic materials. Using low frequency EPR, recently it was possible to obtain measurements from free radicals generated within the biological system, ^(44–46, 84, 85, 130) there were also a few studies *in vivo* using higher frequencies, such as X-band (9 GHz) to study blood in the tail ⁽¹³⁶⁾ and in extra corporeal circuits.⁽¹⁴⁷⁾

In view of the many formidable technical problems involved in doing EPR *in vivo* (details follow), there should be strong reasons for attempting such a difficult approach. The technical challenge of conducting such studies is probably not a sufficient reason for going beyond a demonstration of the feasibility of the techniques; instead the rationale should be based on information obtained, and this indeed is the case. A number of studies already demonstrated that *in vivo* EPR presents an opportunity to obtain valuable biomedical information that cannot be obtained by other methods or can be obtained better by EPR. *Better* includes obtaining better quality data, obtaining data more easily, or with less cost. One important aspect of the value of *in vivo* EPR is that data are obtained under the most physiological conditions. Recent developments enable studies to be made even in unanesthetized animals, avoiding some potential artifacts associated with anesthesia required for many other *in vivo* measurements in experimental animals.

Here we discuss the general principles of types of information available with *in vivo* EPR that are useful for both fundamental and applied studies. Later in this chapter we provide details about what types of information were so far especially valuable to obtain with *in vivo* EPR.

In vivo EPR can potentially provide both anatomical and functional information. Because EPR is a magnetic resonance technique, using magnetic field gradients allows spatial localization of the signal. This adds information on spatial localization to information on processes provided by the spectrum; potentially changes in the processes can then be studied over various anatomical regions in the animal.

Given the power of EPR to reflect local environment and the availability of many other excellent techniques for providing anatomical information, it is not surprising that the principal applications so far have focused on providing information on function. This was facilitated by the absolute specificity of EPR for unpaired electron species, principally free radicals and/or paramagnetic metal ions. Unpaired electron species can be either naturally occurring, in which case EPR provides a uniquely specific window on biochemical processes, or introduced, in which case there is a very specific label.

With most introduced paramagnetic materials, uses have usually involved exploiting the sensitivity of EPR spectra to the environment around the unpaired electron. Biologically useful aspects of the environment studied with *in vivo* EPR or related model systems include the amount of molecular oxygen, pH, molecular motion, viscosity, polarity, temperature, and redox potential. The latter is usually measured indirectly by monitoring the bioreduction of nitroxides. Another impor-

tant and growing set of applications uses paramagnetism as a label or tag to investigate such processes as local perfusion, permeability, and distribution of the molecule or structure on which the paramagnetic tag is located.

Although administering exogenous probes adds an element of invasiveness and experimental complication, it may allow an additional means of controlling the location from which an EPR signal arises. For example by modifying a small, otherwise nonessential group on the probe, the distribution in the aqueous compartment of a spin probe can be controlled.

The ultimate rationale for using EPR in specific experiment should depend on the value of data obtained, including considerations of alternative methods that could be used to obtain similar information. The value and, presumably the degree of *in vivo* EPR use, should be related to the usefulness of the information.

3. IMAGING AND SPECTROSCOPY

Imaging and spectroscopy can be quite different in their technical requirements and the type of information that can be obtained. Typically EPR imaging provides a one-, two-, or three-dimensional representation of the distribution of a particular parameter—most typically the intensity of the EPR spectrum of the paramagnetic species used for imaging. Spatially resolved data obtainable by imaging can be a rich source of information, especially if the imaged parameter can be directly related to a physiological process of interest, such as diffusion or the concentration of oxygen. Obtaining a good image, of course, requires a way of obtaining and presenting the spatial distribution of the paramagnetic species; most typically this involves magnetic field gradients and computer reconstruction with back projection or similar methods. Elements of the image (voxels) must have sufficient intensity to be differentiated from adjacent voxels; this requires a good signal-to-noise ratio and/or long periods of time. Thus potential limitations of imaging center on the time required to obtain an acceptable image. In addition the amount of information presented in the image may be limited.

In *in vivo* spectroscopy high-resolution spectra are obtained from a defined volume of a whole animal (including human subjects). The volume from which spectra are obtained can be as large as the animal (currently small rodents are the largest size animal from which spectra have been obtained from the entire animal) or as small as a microscopic crystal in an animal tissue. Most typically data are obtained from a region of the animal defined by a combination of the detector's sensitive volume and the location of the paramagnetic material. The major strength of spectroscopy is its ability to provide the full range of information potentially available in an EPR spectrum, including such parameters as motion, concentration of oxygen, pH, polarity, etc. Any or all of these processes can in principal be studied simultaneously, and these can be followed through time. The major limitation of

spectroscopy is the lack of spatial information with the detail obtainable from imaging. This includes not only the failure to indicate the distribution of the phenomenon being investigated but perhaps more importantly, combining information from different regions or processes whose differences are of critical biological importance. For example EPR spectra in a tumor should ideally be used to characterize differences between the tumor and adjacent normal tissues; however if only a single spectrum is obtained from the entire sensitive volume, then it contains contributions from both tumor and normal tissues.

The spectral spatial technique yields aspects of both imaging and spectroscopy. In principle it is possible to obtain complete spectra from very small volumes, then use any or all of the spectral line shape to provide a one-, two-, or three-dimensional image based on that spectroscopic feature. This approach may be especially feasible with the high resolution obtainable at higher frequencies, but technical difficulties must be confronted at lower frequencies, including the development of paramagnetic materials with narrow lines, as discussed later.

On the other hand it is possible, especially with particulate or otherwise localized paramagnetic materials, to obtain high-quality spectra from several sites simultaneously in the presence of a gradient to separate spectra.⁽¹⁶⁶⁾ The latter approach is especially promising for measuring oxygen concentration with such particulate paramagnetic materials as lithium phthalocyanine or fusinite. This hybrid technique is included in the section on *in vivo* spectroscopy, since its use especially has emphasized spectroscopic considerations.

Recently we conceptualized another way that spectroscopy and imaging can be combined to provide maximum benefits from the strengths of each; this involves using imaging to define areas of interest and spectroscopy to follow processes with sensitivity and specificity. Any imaging modality can be used, such as magnetic resonance imaging (MRI), CAT scanning, or EPR imaging, to define macroscopic regions of interest (e.g., areas of tumor with good blood flow, areas of tumor with poor blood flow, and nontumor regions), then EPR imaging techniques can be used to collect spectroscopic data from these biologically relevant areas of interest. The result would then be EPR spectra from volumes that involve the biological processes that are being investigated. Defined regions need not correspond to simple geometric shapes because they can be defined and shaped to the extent of the resolution available with gradients used for the EPR-imaging process.

4. POTENTIAL CONSTRAINTS ON *IN VIVO* EPR

In spite of their potential attractiveness, *in vivo* EPR studies developed slowly because of formidable technical problems. We now describe the major types of problems and how they may be overcome. The reader should not be overwhelmed by this long list. Despite these problems, very fruitful experiments have already

been carried out, and the rate of such successful experiments appears to be increasing rapidly, including extending the technique to new areas.

4.1. Nonresonant Absorption of the Exciting Frequency (Usually Microwaves)

The usual EPR frequencies used to yield well-resolved spectra (i.e., 9 GHz and higher) are readily absorbed by materials with a high dielectric constant, such as water, and most functional biological systems have a water content as high as 90%. As a consequence conventional EPR spectra usually cannot be obtained from most functional biological systems whose dimensions exceed 1 millimeter. The most feasible solution to this problem so far was to use lower frequencies. This was effective, but of course it results in a very significant decrease in the sensitivity of the EPR experiment.

For very small objects, such as the tumor model spheroids, higher frequency EPR can successfully be used if samples are small enough and/or oriented to minimize interactions with the electric field.

4.2. Concentration of Paramagnetic Species

EPR spectroscopy of course requires the presence of paramagnetic materials. In living systems, however, concentrations of free radicals or other paramagnetic species with relaxation times suitable for measurement at room temperature are very low. Consequently with the exception of melanin and perhaps the ascorbyl radical, it is unlikely that any presently envisioned EPR instrumentation will be able to obtain a useful signal-to-noise based on naturally occurring paramagnetic species at body temperatures. Melanin, the pigment responsible for the dark color of hair and skin, is a stable-free radical; in some tissues the concentration is sufficiently high, so that it may be detectable by EPR in functional biological systems. The ascorbyl radical occurs in lower concentrations than melanin, but because of its very narrow line width, it was observed in some tissue preparations and it may be detectable *in vivo* under suitable conditions.⁽¹⁴⁷⁾

One solution to the problem is to increase the concentration of paramagnetic materials that occur as a result of cellular functions. This can be accomplished by administering drugs, etc., to generate free radical intermediates and/or using such methods as spin trapping to stabilize radicals produced by metabolism. The latter method has the potential of increasing the amount of free radicals by prolonging their lifetimes, so that the concentration builds up for a species whose lifetime ordinarily leads to a steady-state level too low to be detected directly by EPR.

The more general solution to the problem, however, is to add stable paramagnetic materials to the system, then use these as the basis for imaging or spectroscopy. This has the potential disadvantage of requiring the addition of a substance, usually

by injection; consequently there is the potential for toxic effects from these substances. There is also a potential upper concentration limit for materials introduced before encountering significant spin–spin interactions that significantly alter the resulting line shape; this limit is a function of the spin probe used. To consider concentration-dependent effects, common materials that have been used can be divided into two groups: Molecular free radicals, such as nitroxides, which have one unpaired electron in every molecule and particulates, such as coal, which have unpaired electrons distributed throughout the particle. The latter have essentially no concentration-dependent changes and reasonably narrow line widths affected by pO_2 ; therefore these have been used mostly to measure oxygen.

On the other hand such molecular free radicals as nitroxides have concentration-dependent effects on the spectra over essentially the whole range of useful concentrations; this may be a critical factor in interpreting results from *in vivo* EPR. The extent of the effect can be decreased by using a charged species, so that electrostatic effects decrease the ease of molecules approaching each other. Halpern *et al.*⁽⁶⁷⁾ developed an elegant method to account for spin–spin interactions with a nitroxide used for pO_2 measurements; this method may be applicable to other free radicals as well. Some general solutions are to overmodulate the signal to overwhelm concentration-dependent broadening or to correct for concentration-dependent line broadening by estimating the concentration by integration or from Heisenberg spin exchange theory. The latter is especially difficult to do accurately. Newer, very narrow-line, infusible, stable free radicals developed by Nycomed, Inc., have a line width that is essentially independent of concentration. These were designed to make access to the unpaired electron by another free radical far more difficult than for simpler molecules, such as oxygen. These free radicals are sufficiently bulky to prevent paramagnetic centers from overlapping when two molecules collide, so there is only a small probability of spin exchange; hence there is no concentration broadening until high concentrations are reached. Oxygen on the other hand still has easy access to the paramagnetic center of free radicals; therefore it broadens the spectral line.

4.3. Bioreduction

Bioreduction (or more generally metabolism) of added paramagnetic materials is another potential limiting factor. This is especially important with nitroxides, but it can occur with other species as well. It can be decreased by appropriately selecting nitroxide species: Nitroxides based on the pyrrolidine ring are inherently much more stable to bioreduction than those based on the piperidine or doxyl rings. (Ref. 92 provides a comprehensive summary of interactions of nitroxides with biological systems.)

4.4. Excretion

Excretion of added paramagnetic materials is another source of limitation. The most common route for excretion of soluble species is by the kidneys, and unless charged species are attached to macromolecules such as polysaccharide polymers⁽⁹⁰⁾, these are excreted fairly rapidly. Particulate paramagnetic materials may remain at the site of administration indefinitely, but it is also possible for some of them to be removed through phagocytosis by macrophages.^(52, 53, 191)

4.5. Physiological Motions

Some of the same factors that make *in vivo* EPR so valuable, i.e., the ability to provide data under fully physiological conditions, lead to significant technical problems. Physiological conditions imply a variety of motions associated with the normal functions of circulatory, respiratory, and intestinal systems, and voluntary motions can also occur, especially in conscious subjects. When we try to deal with the latter by anesthetizing the animal, other problems may occur due to changes in physiology associated with the anesthesia.⁽¹⁰⁸⁾

The motions cause several different problems. They can be a source of noise from microphonics and/or changing the tuning of the resonator; they can move the paramagnetic species into a region out of the applied magnetic field, secondary (gradient) magnetic field, or modulation field; or change the distribution of the microwave field. The most obvious effects lead to increased noise, and these are likely to be detected, then, to a greater or lesser extent, corrected. The more subtle effects may change spectral shape without causing obvious noise, therefore these can be especially troublesome.

4.6. Accurate Localization of Paramagnetic Materials

Physiological motion can contribute to another potential problem; Inaccurate localization of the site of paramagnetic materials; nonuniformity of applied and gradient fields can also contribute to this problem. These problems are especially important in imaging studies because they can lead to errors in the apparent distribution of paramagnetic species. New approaches to generating high uniformity gradients will improve this situation considerably.⁽⁶¹⁾

4.7. Penetration of Microwaves

Penetration of exciting radiation is perhaps the most pervasive limitation. This leads to a need to trade off sensitivity (which increases with frequency) and penetration depth (which decreases with frequency). A measure of penetration is skin depth, the depth at which an electromagnetic wave diminished to 37% (1/e) of its initial amplitude; at X-band (9.5 GHz frequency) this is less than 1.0 mm in

tissue; at L-band (1.5 GHz frequency) this is less than 10 mm, and at 250 MHz, this is approximately 6 cm.^(60, 61, 159)

5. SENSITIVITY CONSIDERATIONS FOR *IN VIVO* EPR

5.1. Concentrations of Naturally Occurring Free Radicals and Other Paramagnetic Materials *In Vivo*

The capabilities of *in vivo* EPR and consequently directions of instrumental development and choices of instrumental conditions for specific applications are closely tied to the levels of paramagnetic materials that can be measured with the required signal/noise. Most free radicals produced in physiological reactions (e.g., free radical intermediates from enzymatic reactions) are in the submicromolar concentration range. As noted later, direct detection *in vivo* of such a low concentration is very difficult using existing instrumental approaches. On the other hand when the application involves paramagnetic species at higher concentrations due to particular conditions of the experiment (e.g., administering of a stable free radical or the metabolizing a drug to a free radical intermediate), these low levels of naturally present paramagnetic species have the advantage of reducing background signals from paramagnetic species other than those being measured.

Several approaches were successfully used to achieve levels of paramagnetic species detected *in vivo*; these include administering such precursors as drugs or metal ions that were converted into paramagnetic species *in vivo*, using spin traps to stabilize free radical intermediates, and administering stable free radicals.

5.2. Sensitivity of *in Vivo* EPR Spectrometers

The ultimate limitation of any noninvasive analytical method is the limiting signal/noise for the lowest possible amount (i.e., concentration) of material. The reduction of frequency usually employed with *in vivo* EPR (to overcome the problem of nonresonant absorption of the microwave by aqueous components of tissues, which dominate at conventional EPR frequencies) results in a theoretical decrease in signal proportional to frequency squared. In addition to the decrease in sensitivity, however, there is a decrease in noise for nonlossy samples proportional to the frequency to the one-half power; ⁽¹⁾for lossy samples it is directly proportional to the frequency.⁽²⁰⁶⁾ For the latter, sensitivity or signal-to-noise ratio diminishes more nearly proportional to the operating frequency. Given the large increase in the accessible volume of a living sample, the molar concentration sensitivity of the EPR technique may even increase at lower frequency.^(1, 60, 74)

As mentioned elsewhere in addition to decreasing the frequency by almost an order of magnitude (e.g., to L-band), there is also usually a much reduced resonator

Q due to the still considerable lossiness of tissues (factors of 5–10 depending on the final loaded Q with a live animal). Consequently the theoretical decrease in sensitivity can amount to a factor of 50 to 1000 versus a commercial X-band spectrometer with a flat cell in a TE_{102} or TM_{110} cavity. Hence one of the challenges was to redesign and optimize L-band spectrometer bridges and resonators. While bridge designs vary somewhat from lab to lab, the loop-gap resonator proved to be very useful for many investigators. An advantage of loop-gap resonators is their very large filling factors, making efficient use of the electromagnetic energy they store in the sample. This more than offsets their lower Q values, giving a much higher signal-to-noise ratio for extremely small samples or those with high non-resonant absorption of electromagnetic radiation.⁽³⁸⁾ The geometry of loop-gap resonators at 1.1 GHz can be suitable for inserting a mouse or small rat.^(39, 151)

Although sensitivity in a live animal is difficult to compare precisely from lab to lab, since spectrometers, resonators, and exact conditions of animal placement vary, some comparisons can be made on phantoms of aqueous nitroxide solutions. To date both Zweier and Kuppusamy (Ref. 202) and Koscielniak and Berliner (Ref. 94) have reported successfully detecting of concentrations of $\approx 0.5 \mu\text{m}$ for *nonisotopically* substituted Tempo or CTPO.

6. RESULTS OF *IN VIVO* EPR SPECTROSCOPY OF FUNCTIONAL BIOLOGICAL SYSTEMS

6.1. Initial Studies

The pioneering experiment by Feldman *et al.* published in 1975⁽³⁴⁾ is usually considered to be the first *in vivo* EPR spectroscopic study. There were in fact earlier unpublished studies by Rowlands and colleagues at the Southwest Research Institute on whole animals using low-frequency EPR and injection of nitroxides into mice which then were placed inside a rectangular cavity. The signal-to-noise ratio however was very poor, so resulting data were quite limited; and the experiments were never published in the refereed literature. There was a published study by Hutchinson and Mallard in 1971 in which they discussed their development of an EPR instrument designed for *in vivo*; while they were able to obtain spectra from excised guinea pig liver, they were not able to obtain data from an intact mouse.⁽⁷⁶⁾ Hutchinson also provided an analysis of the potential optimum frequency for *in vivo* EPR.⁽⁷⁵⁾ There were also some unpublished studies in which the tail of a mouse was inserted into the EPR cavity of an X-band spectrometer and data were obtained from free radicals circulating in the blood.

In the study by Feldman *et al.*,⁽³⁴⁾ they implanted a resonator in the liver of a rat, then administered high doses of the nitroxide, Tempol. They observed an EPR spectrum with a relatively poor signal-to-noise ratio, but they were able to follow

the pharmacokinetics of the disappearance of the nitroxide in a semiquantitative manner. They also reported the spectrum of a spin-labeled drug obtained *in vivo* by the same apparatus.

Subsequently there have been a large number of studies in which EPR spectra were obtained from functional biological systems, and some recent reviews are available.^(13, 173, 174, 180) Rather than provide a comprehensive review, we discuss some of the more promising and extensively investigated areas of applications. Note: Some of the most interesting and important uses of *in vivo* EPR techniques combine other techniques, such as NMR, where the specificity and sensitivity of EPR is used to interpret measurements made with the other techniques (e.g., Refs. 6, 7, 23, 33, 47, 48).

6.2. Types of Studies with *in Vivo* EPR Spectroscopy

6.2.1. Level of Oxygen in Tissues

The use of *in vivo* EPR to measure the concentration or partial pressure of oxygen in tissues has received the most attention because there is great need for such measurements and EPR oximetry appears to have distinct advantages.^(52, 67, 171, 172, 174-176, 178) Many of these advantages arise from the development of oxygen-sensitive particulate materials that combine a high degree of sensitivity to the pO_2 with favorable biological properties, including inertness to such factors as oxidation and pH,^(52, 53, 109, 179, 191, 177) leading to the possibility of taking repeated measurements from the same site over long periods of time, without undesirable side effects. This technique has now been applied to measure pO_2 in skin,^(68, 179) brain,⁽¹⁰⁸⁾ the peritoneal cavity,⁽¹⁷⁰⁾ skeletal muscle,^(19, 51) cardiac muscle,⁽⁹⁶⁾ liver,^(86, 148) kidneys,⁽⁸²⁾ and tumors.^(6, 53, 54, 63, 153, 179) There appears to be considerable potential for its application to clinical medicine, especially in radiation oncology and peripheral vascular disease;^(54, 63, 153, 154, 180) the feasibility of using a material already approved for use in humans, India ink, was shown.⁽⁵³⁾

6.1.2. Reactive Intermediates

In vivo EPR spectroscopy appears to have considerable potential for applications in a number of other areas as well. Initially the possibility of detecting reactive intermediates was a strong factor in the interest in *in vivo* EPR techniques, but that proved to be more difficult than anticipated by some because of low steady-state concentrations of reactive intermediates and the lack of spin-trapping systems that are sufficiently stable *in vivo*. Recently, however, some progress was made with trapping sulfite anion radicals⁽⁸⁵⁾ and thiyl radicals⁽⁸⁴⁾ and directly detecting a paramagnetic ion intermediate, Cr(V).^(113, 114) Spin trapping ionizing radiation-induced hydroxyl radicals *in vivo* was also recently reported.⁽⁶⁵⁾

There has also been significant and growing progress in detecting radical intermediates of such drugs and xenobiotics as nitrosobenzene, ^(45, 46) as discussed in the following section.

These direct demonstrations of the occurrence of free radicals *in vivo* provide powerful support for such indirect methods as chemiluminescence; ⁽²²⁾ *in vivo* spin trapping where spin traps are administered, then tissues or fluids extracted, and spin adducts measured; ⁽⁹¹⁾ fast freezing after adding spin traps; and spin trapping in effluents from organs. ⁽¹⁶⁵⁾

6.1.3. Pharmacokinetics

There appears to be great potential for the use of *in vivo* EPR in the study of pharmacokinetics and other aspects of interactions of drugs *in vivo*. ⁽¹⁶⁹⁾ Initially *in vivo* spectroscopy emphasized studies of the distribution and metabolism of the nitroxides per se, as part of the development of the system and also in recognition of the potential use of nitroxides as both active agents themselves (e.g., as imaging agents for EPR, contrast agents for MRI, or as redox markers) and potential labels for other agents. ^(8, 9, 15, 34, 35, 55, 77, 79, 96, 116, 143, 146, 158, 160, 183, 187, 188, 190, 201) Subsequently more specific uses of nitroxides in pharmacokinetic studies have emerged; ⁽¹³⁴⁾ these were used to follow the mechanisms of drug delivery systems, ^(131, 133) measure local changes in pH, ⁽⁴⁹⁾ and to measure perfusion ⁽⁴⁷⁾ and absorption. ^(49, 135, 136) *In vivo* EPR spectroscopy was also useful in directly following free radical intermediates of some drugs. ^(45, 46, 130) In a related type of study, *in vitro* EPR spectroscopy provided critical information on the status of an MRI contrast agent based on a complex of paramagnetic manganese ⁽⁴⁸⁾ and followed the fate of Mn^{++} encapsulated in liposomes; ⁽⁷⁾ with the current state of instrumental development, these studies could probably now be done *in vivo*.

6.3. Specific Results Obtained with *in Vivo* EPR Spectroscopy

6.3.1. Biodistribution and Metabolism of Administered Free Radicals

These studies have had a prominent role in initial studies with *in vivo* EPR, and these continue to be an area of intense interest. Interest arises from using both nitroxides as imaging/tracing agents and their potential as therapeutic (e.g., superoxide dismutases) and diagnostic agents (e.g., contrast agents for NMR).

6.3.1.1. Nitroxides and Other Soluble Stable Free Radicals These studies usually involve administering a nitroxide by injection, although some studies employed absorption through the skin or the lungs. The concentration of nitroxide is followed by measuring the rate of disappearance of nitroxides in either the whole animal (usually by inserting a mouse or small rat entirely into a resonator) or in localized regions. Localization is usually achieved on the basis of the sensitive region characteristic for the particular configuration of the animal and the resonator,

although more complex approaches are possible that could provide more control of the volume being studied. Examples of the latter include delineating the sensitive volume by the shape of the effective modulation field or by the region of magnetic field homogeneity.

The kinetics observed are a result of the usual factors affecting distribution of drugs: Uptake into the circulation, diffusion from the circulatory system, diffusion into tissues, excretion, and metabolism to products. The latter has proven to be an extremely important aspect because of the tendency of nitroxides to be bioreduced to the corresponding nonparamagnetic hydroxylamines. Relative rates of reduction *in vivo* appear to parallel those observed in cellular suspensions, with the reduction occurring primarily intracellularly. Piperidine- and doxyl-type nitroxides are reduced fairly rapidly, and pyrroline and pyrrolidine nitroxides are more resistant to reduction. As in cells *in vivo* there can also be enzymatic and nonenzymatic oxidation of hydroxylamines back to nitroxides. (Ref. 92 provides an extensive summary of literature on the interactions of nitroxides with biological systems, including *in vivo* studies.) Similar studies in the isolated beating heart indicate that metabolism of nitroxides is similar under these conditions.⁽¹⁰²⁾

A few studies used higher frequency EPR (X-band) to make measurements in rodent tails; taking advantage of the relatively low lossiness of this structure it is therefore possible to tune a conventional spectrometer with the tail inserted in the resonant structure.^(15, 115, 135, 136) Pharmacokinetics of nitroxides was also studied at X-band by using extracorporeal circulation through the EPR resonator.^(150, 158, 192, 193) In rats blood levels of the commonly used nitroxide CTPO were followed after single, multiple, and continuous IP injections. Urine was periodically sampled to indicate the role of renal excretion for this nitroxide.⁽¹⁵⁾ Using a similar approach absorption into the blood of an inhaled volatile nitroxide (di-tert-butyl-nitroxide or DTBN) was demonstrated, and the constant for its disappearance from blood was measured to be $k = 0.08 \text{ min}^{-1}$.⁽¹³⁶⁾ This study also demonstrated an important capability of *in vivo* EPR: In a single spectrum DTBN spectra arising from two different environments differing in polarity were observed. Similarly the transcutaneous absorption rate into the blood was studied.⁽¹³⁵⁾

A paramagnetic metal in the form of dextran magnetite was also studied with this approach.⁽⁷⁷⁾ Although spectra were very broad, they were sufficiently intense to enable the pharmacokinetics of different preparations of the dextran magnetite to be followed quantitatively.

Most studies used low-frequency EPR in the range of 0.7–1.2 GHz, especially at the higher end of this range, to follow rates of change of the concentration of nitroxides *in vivo* in both the whole animal and specific regions. Lifetimes *in vivo* tend to be relatively short due to both bioreduction and excretion. By placing the resonator over the bladder, the rate of excretion by the kidney can be followed; this turns out to be the major excretory route for most nitroxides. The rate of metabolism to nonparamagnetic hydroxylamine can be determined by combining the measure-

ment over the bladder (to measure losses due to excretion of active nitroxide) with a second measurement over another region or the whole animal.^(8, 9) Relative rates of bio-reduction of nitroxides *in vivo* parallel those of nitroxides in isolated cells, with most of the reduction occurring intracellularly (and hence greatly influenced by factors that affect entrance of the nitroxides into cells), and the structure of the ring on which the nitroxide group is located.⁽⁹²⁾

Other factors affecting the pharmacokinetics of the nitroxides which have been studied by *in vivo* EPR techniques include the effects of the concentration of oxygen that is breathed,^(24, 25, 35, 118, 146, 158, 190) the effects of multiple repeated injections of nitroxides or continuous infusions on the kinetics of the concentration of the nitroxides,^(15, 79, 117) the effects of age,⁽⁵⁵⁾ the effect of food restriction,⁽⁵⁵⁾ the mode of administration,^(135, 136) the effect of heating,⁽¹¹⁶⁾ the role of the lungs,^(182, 183, 184, 185) the effect of anti-oxidants,^(182, 189, 198) the effects of ischemia-reperfusion,⁽¹⁹⁰⁾ and the effect of binding to macromolecules.^(89, 90, 103, 199)

Some very useful data have been obtained by following the pharmacokinetics in isolated organs, where it is possible to investigate variables that occur at the tissue level such as metabolism and compartmentalization from other factors that occur at the whole organism level such as distribution and excretion.^(160, 201, 203)

6.3.1.2. Particulate Paramagnetic Materials Several different particulate paramagnetic materials were used extensively to measure molecular oxygen (and to a very limited extent, nitric oxide), including several types of carbon-based materials (coals, chars, India ink) and lithium phthalocyanine. These are generally quite unreactive materials—stable to oxidation, reduction, and extremes of pH. It is not surprising, therefore that these materials have essentially no demonstrated metabolic interactions. Their distribution is primarily affected by their size. Most typically these materials are injected directly into tissues in which measurements are to be made. Particles too large to be incorporated into cells tend to remain indefinitely in the tissues, causing little or no reaction. Smaller particles may be taken into cells in the vicinity, especially phagocytic cells, but unless the concentration is very high, there is no apparent deleterious effect from such particles. If particles are injected into the blood stream, larger particles are trapped in the first capillary network that they encounter, (i.e., if injected into a vein, they localize in the lungs; if injected into an artery, they localize in the organ supplied by that artery.) Particles small enough to pass through capillary networks are removed from the blood if they are in the range readily phagocytized by reticuloendothelial cells; this is the case with India ink, which has particles of carbon in the range readily phagocytized. Consequently these then concentrate selectively in the liver in the highly phagocytic Kupffer cells.⁽¹⁴⁸⁾

6.3.1.3. Paramagnetic Materials in Supramolecular Structures The distribution and the subsequent metabolism of paramagnetic materials are likely to be altered if contained in such structures as liposomes or aggregates of albumin.^(7, 8, 20, 21, 51, 110, 138, 178) In this type of situation, the paramagnetic material can act as a

tag or tracer to monitor structures where they are located. *In vivo* EPR spectroscopy was used to follow such aggregates to determine how long they stay in the circulatory system and the factors affecting their integrity and/or distribution. Some of these studies take advantage of the metabolism of nitroxides to obtain more information than that available from an inert tag: e.g., using readily metabolizable nitroxides trapped inside a liposome, these remain paramagnetic only while the liposome wall remains fully intact; consequently the disappearance of the EPR signal is an excellent marker for the loss of integrity of the liposome wall. These structures can also be used to make the trapped environment more optimal for measurement; e.g., by trapping a lipid-rich environment (e.g., cyclohexane) within an albumin microsphere, the sensitivity of a nitroxide to the concentration of oxygen can be enhanced several fold because of the greater solubility of oxygen in lipids.⁽¹¹⁰⁾ A similar use of lipophilic materials to enhance sensitivity to oxygen was previously used by placing a gas-permeable capsule containing a nitroxide (Tempone) in paraffin oil in the peritoneum of a mouse.⁽¹⁷⁰⁾

6.3.2. Perfusion Studies

The perfusion of tissue is an important parameter in both physiology and pathophysiology; while there are a number of other methods available to measure perfusion *in vivo*, they all have some significant limitations. The feasibility of using *in vivo* EPR for this type of measurement was demonstrated using the washout of injected nitroxides.⁽⁴⁷⁾ Potential advantages of this approach include the specificity of the end point of wash out for the administered nitroxide (due to selectivity of EPR of paramagnetic materials and the lack of significant amounts of other paramagnetic materials in tissues at concentrations that would be detectable by *in vivo* EPR), the ability to vary the type of behavior by the material used for tagging (using the availability of nitroxides with different charges, solubilities, etc.), and the potential for combining measurement of perfusion with measurements of redox status and pO_2 (using the rate of reduction of the nitroxide for redox status and the line width dependency of the nitroxide on pO_2).

6.3.3. Direct Observation of Free Radical Intermediates from Drugs and/or Metabolism

The potential for directly observing free radicals *in vivo* was an important motivation for developing *in vivo* EPR techniques. This has, however, proven to be a challenging task because relatively high concentrations of free radicals needed to detect them *in vivo*. The detectable concentration is a function of a number of factors including line widths of the radical; sites where it occurs; and such instrumental parameters as effective microwave power, overall sensitivity of the instrument, and stability of the spectrometer. The latter may be especially important because with sufficient stability, averaging techniques can be used quite effectively. In general

the lower limit of detectability of free radicals is likely to be 10–100 micromolar or greater.

In spite of potential difficulties, some notable successes have now been reported in observing free radical intermediates of drugs or other administered compounds, and it seems likely that this approach will receive considerable attention in the future. Fujii *et al.*^(44–46) followed the kinetics of the generation and decay of the toxin nitrosobenzene in the mouse; with the addition of experiments on isolated tissues and *in vitro* models, they proposed the metabolic pathway involved.

Mader *et al.* demonstrated that *in vivo* EPR can be used to follow the metabolism of some drugs that have free radical products. They studied the metabolism of anthralin in the skin of mice by using the same formulation of the drug as that used for human applications.⁽¹³⁰⁾ They were able to demonstrate the formation of a free-radical-containing polymer derived from anthralin and also to determine some factors affecting the amount of polymer formed. (Antioxidants reduced the amount of polymer detected by EPR.)

6.3.4. Spin Trapping Free Radicals

The usual spin traps are nonparamagnetic materials which become converted to relatively stable spin adducts on reacting with many types of free radicals. This technique was applied with great success in model systems; there are, however, considerable technical problems in carrying out spin trapping *in vivo*. The principal limitation is probably the paucity of spin traps whose spin adducts have sufficient stability in the presence of cells, especially water soluble spin adducts derived from oxygen-centered radicals.^(112, 162, 163) Another significant problem is the relatively high concentration of spin traps usually needed for effective trapping of reactive free radicals; concentrations in the range of 10–50 millimolar are often used to compete effectively for reactive free radicals because such free radicals react with a variety of substances. Despite these limitations direct *in vivo* spin trapping has now been reported for the sulfite radical anion⁽⁸⁵⁾ and the hemoglobin-thiyl radical.⁽⁸⁴⁾

The potential value of using *in vivo* EPR in this type of investigation was illustrated in these studies by determining factors that affect the amount of detectable spin adduct. Due to the complexity of interactions *in vivo*, it would be very difficult to determine such overall effects only by the use of model systems, because of the involvement of physiological parameters such as biodistribution and compensatory physiological changes in response to the biochemical events.

There have also been a number of indirect *in vivo* studies where free radicals were spin-trapped *in vivo*, then tissues or fluids were extracted and studied *ex vivo* at 9 GHz (see Ref. 91). These studies usually use lipophilic spin traps/adducts because these have sufficient stability to be extracted, especially when extracted into organic solvents. This approach was also used to demonstrate that chromium

can generate free radicals *in vivo*, which can then be trapped and studied *ex vivo*.⁽⁸⁷⁾ The validity of the indirect *in vivo* type of experiment was confirmed by direct *in vivo* spin trapping of the hemoglobin-thiyl radical, which was previously reported using the technique of extraction with *ex vivo* analysis.^(84, 142)

A special type of spin trapping was successfully used *in vitro* and *in vivo* to detect nitric oxide. This approach is based on the formation of stable complexes of nitric oxide with metal (usually iron) containing dithiocarbamates. Komarov *et al.*⁽⁹³⁾ took advantage of the relatively small amount of lossy material in the tail of a mouse to study spin-trapped nitric oxide at a relatively high frequency, 3.5 GHz (S-Band), using a dithiocarbamate to trap the nitric oxide. This appears to be the first report of *in vivo* trapping of nitric oxide. This technique was extended by the same group to study such problems as the role of nitric oxide in shock syndromes.^(106, 107) Zweier and associates extended this approach to measure at L-band in functioning, isolated hearts;^(205, 206) they were also able to obtain images based on complexes with nitric oxide in the isolated heart⁽¹⁰⁰⁾ and brain⁽⁹⁹⁾. Another group demonstrated directly the trapping nitric oxide *in vivo* and followed the time course of its detectability, although quantitative measurements were not possible with this system.⁽¹⁵⁷⁾ Given the potential importance of nitric oxide in physiology and pathophysiology and the complexity of its production, interactions, and metabolism/reactions, it seems likely that using *in vivo* EPR to study nitric oxide *in vivo* will be very productive. Note: Useful studies of the role of nitric oxide may also be made less directly by using EPR oximetry to study the effects of nitric oxide on local pO₂, as recently illustrated in the kidney.^(82, 83)

6.3.5. Direct Studies of Metal Ions

While most paramagnetic metal ions have very short relaxation times, so they are difficult to detect at physiologically pertinent temperatures, there are some interesting exceptions. *In vivo* EPR studies were used to study some of these and more such studies seem possible. The potential advantage of such studies rests on the fact that *in vivo* systems are so complex that it seems essential eventually to demonstrate the occurrence of postulated mechanisms by direct *in vivo* studies.

Chromium is an especially interesting metal ion because of the potential link to carcinogenesis of the widely occurring nonparamagnetic Cr(VI). The pathway is postulated to occur via conversion to paramagnetic states that are thought to react with such key molecules as DNA, perhaps by catalyzing a Fenton-like reaction with endogenous hydrogen peroxide. The paramagnetic intermediate Cr(V) was successfully detected *in vivo* in mice, and some of the factors affecting its concentration were studied.^(113, 114)

The vanadyl metal ion was also studied *in vivo* in rats.⁽¹⁶¹⁾ Researchers circulated blood through the EPR cavity using a surgical connection between an artery and a vein.

Iron in the form of dextran magnetite was studied in the circulation of living rats, using 9-GHz EPR and the tail for measurements.⁽⁷⁷⁾

6.3.6. Measurements of pH

The extent of the hyperfine splitting of the three lines of the spectrum of the nitrogen atom in nitroxides is sensitive to a number of environmental factors that affect the charge distribution around the nitrogen atom, including pH. This was exploited by developing nitroxides with a relatively large pH-sensitive change in specific pH ranges. Using a set of such nitroxides, we can use EPR spectroscopy to follow changes in pH in model systems with considerable accuracy and sensitivity. This capability was extended to *in vivo* EPR, providing perhaps a unique capability to follow pH changes noninvasively at sites where appropriate nitroxides are located. The feasibility and usefulness of this approach was demonstrated for following the pH in the stomach⁽⁴⁹⁾ and polymeric implants used for drug delivery.⁽¹³³⁾ In principle, this approach can be used at any site *in vivo* where a pH-sensitive nitroxide can be localized and its spectrum measured.

6.3.7. Monitoring the Functioning of Implanted Drug Delivery Systems

In vivo EPR studies of implanted drug delivery systems provide useful information for noninvasively following some key aspects of the functioning of drug delivery systems. These include pH within the implant, penetration of water, and the mobility of tagged material. These studies take advantage of the sensitivity of EPR spectra of nitroxides to environmental factors, including pH (by changes in hyperfine splitting) and molecular motion (by changes in the shape of spectra, since more freely moving nitroxides exhibit less anisotropy in their EPR spectra). Using this approach several different types of polymers used to deliver drugs in experimental animals and human patients were characterized using *in vivo* EPR.^(131, 133, 134, 137, 168) There were also studies that used naturally occurring EPR signals in certain drug delivery systems; these were due to high doses of ionizing radiation, which are sometimes used to sterilize drug delivery systems.⁽¹³²⁾ Radiation-induced free radicals are stable as long as they are relatively immobile, and not accessible to such solvents as water. Therefore their line shapes indicate their mobility; as water penetrates sites where they are located, the intensity of the EPR signal decreases.

Using such data, conclusions may be drawn about the mechanism of release of the drug which occurs *in vivo*. This type of use of *in vivo* EPR is likely to become more widespread because of the importance of implanted drug delivery systems, the lack of alternative ways of following their *in vivo* functioning (except for following drug levels in the blood), and the location of implanted drugs near the surface where *in vivo* EPR is especially sensitive.⁽¹³⁴⁾

6.3.8. Measuring Transport in the Skin

These studies are aimed at following various clinically and/or experimentally important processes involving transport through the skin. A paramagnetic label, usually a nitroxide, is used to follow penetration of the drug through the skin directly or to follow the penetration of a larger molecule or structure (e.g., a liposome) to which the paramagnetic label is attached. Studies usually use high-resolution spectroscopy to follow a parameter that changes as the paramagnetic material is transported through the skin. It is sometimes feasible to follow the transport into the blood by monitoring blood levels of transcutaneously administered nitroxides,⁽¹³⁵⁾ although due to subsequent metabolism and distribution, it may be a complex task to use such data to determine the kinetics of the absorption process.

A number of studies exploited the ability of EPR imaging to follow the passage of nitroxides through the skin,^(26-30, 40-42, 69, 70) which are described in the section on imaging. The studies usually use either a 1-, 2-, or 3-dimensional image to follow the process directly.

6.3.9. Measuring Oxygen in Specific Organ Systems

The measurement of oxygen in tissues has been a major area of application of *in vivo* EPR and is likely to be a dominant use in the future as well. As noted previously this is because of the ability of *in vivo* EPR to make such measurements and the experimental and clinical need for such information.

The sensitivity of EPR spectra to oxygen occurs because molecular oxygen is paramagnetic (it is a stable triplet with two unpaired electrons); therefore it affects paramagnetic properties of other paramagnetic molecules. The effect is usually manifested by a change in relaxation times, leading to line broadening. Other parameters of the spectra can also be used to observe the effect (e.g., changes in relaxation times, decreases in resolution of superhyperfine splitting). The effects of oxygen may also occur because of other mechanisms, especially changes in the localization of unpaired electrons in such complex paramagnetic systems as coals and lithium phthalocyanine.

Two principal types of information about oxygen are obtained with EPR techniques used *in vivo*: the *concentration of oxygen* ($\{O_2\}$) and the *partial pressure of oxygen* (pO_2). With small molecules having one unpaired electron (molecular-free radicals) such as nitroxides, effects of oxygen on the EPR spectra are directly proportional to collision rates for oxygen with molecules; therefore these reflect the $\{O_2\}$ (assuming that diffusion rates do not change). In contrast many of the particulate oxygen-sensitive paramagnetic particles, such as coals, India ink, and lithium phthalocyanine, respond to the pO_2 . Depending on circumstances, one of these parameters may be preferable for a particular study, but the most important

aspect is to understand which parameter is being measured in the study and what factors may affect the validity and/or the interpretation of that measurement.

While in principle the maximum information on the level of oxygen within tissues would be in the form of images which reflect the relative or absolute levels of oxygen, in practice it may be difficult to have sufficient sensitivity to make such an image; therefore required information is often obtained by a single measurement using EPR spectroscopy. It is also possible to obtain measurements at several sites using spectroscopy in the presence of magnetic field gradients combined with injections of oxygen-sensitive paramagnetic materials at two or more discrete sites. The usefulness of this approach was demonstrated in the heart, kidney, and brain.^(82, 108, 166)

6.3.9.1. Brain and Spinal Cord The metabolism of the brain usually involves a high rate of oxidative phosphorylation, so the brain is potentially quite vulnerable to changes in pO_2 . The EPR oximetry provides a potentially useful method to follow changes in the pO_2 directly under various physiological and pathophysiological conditions. This seems especially useful for situations in which repeated measurements of brain pO_2 are needed over a period of time. Lithium phthalocyanine was especially useful for *in vivo* studies of the pO_2 in the central nervous system because of its sensitivity to the relatively high concentrations of oxygen that occur normally in these tissues. Some results were already obtained with *in vivo* EPR on pO_2 in the brain as a function of breathing gas by using various anesthetics, on adaptations to chronic hypoxia of the type likely to occur at high altitudes, and on the extent of ischemia and reperfusion.^(108, 109, 111) These studies included measuring pO_2 simultaneously, at more than one site, which provides a very effective comparison between the experimentally manipulated side and the control side in the brain. EPR oximetry was also used to follow effects of ionizing radiation on pO_2 in the spinal cord (unpublished, Dartmouth group).

6.3.9.2. Heart Measuring pO_2 or $[O_2]$ in the beating heart is important because of the significant role which oxygen has in this organ with a high rate of aerobic metabolism. EPR oximetry provides a means of making measurements in a non-destructive way with the required accuracy and sensitivity for these measurements. While a few studies were carried out in the heart *in situ* in the rat, most EPR oximetry studies of the heart used an isolated beating heart. These studies provided some excellent insights into various physiological parameters affecting the level of oxygen in the wall of the heart, the effects of some drugs on pO_2 in the heart, and effects of such treatments as ischemic preconditioning.^(36, 37, 57, 56, 109) The relationship of the amount of oxygen in the heart to oxidative damage associated with ischemia reperfusion injury is a particular focus for many of the studies reported; this approach appears to be quite fruitful.^(96, 160, 204)

Preliminary measurements of the concentration of oxygen in the heart were also made using dynamic nuclear polarization techniques; this technique may

become a useful approach, especially for noninvasive measurements in large subjects, including humans.⁽⁵⁹⁾

6.3.9.3. Skeletal Muscle The measurement of pO_2 in skeletal muscle is important for understanding the energetics of muscle function. It is especially valuable to be able to relate pO_2 to measurements of key metabolites, such as those measured by NMR (e.g., ATP, inorganic phosphate, and lactic acid). EPR oximetry appears capable of making the desired measurement of pO_2 in skeletal muscle; some results were reported using both carbon-based materials and lithium phthalocyanine^(19, 51, 52) and also nitroxides in cyclohexane-filled albumin microspheres.⁽¹¹⁰⁾ More extensive use of these measurements seems likely in the near future given the value of such data.

6.3.9.4. Liver The liver has a very complex blood supply, receiving blood from both the hepatic artery and the portal vein. It also has a complex microscopic anatomy with regard to circulation of blood, with input from the portal triad, distribution by the sinusoids, then collection by the central veins. Consequently the liver has a number of pathophysiological conditions that seem to be affected by local pO_2 , but the number of direct measurements of pO_2 in the liver is very limited. Thus EPR oximetry was used to study pO_2 in the liver, and some useful data have already emerged.^(51, 53, 86, 148, 149, 173) It is possible to use different physical properties of paramagnetic materials and/or the effect of how they are administered on their localization within the liver to obtain measurements at functionally different sites within the liver. Using either liposomes of the appropriate size or particles of India ink results in the selective accumulation of the paramagnetic material in the Kupffer cells, which provides measurements of the pO_2 at this site. Average global pO_2 can be obtained by using macroscopic materials as lithium phthalocyanine crystals. Preliminary evidence from using such both types of measurements in the same animal, indicates that pO_2 in Kupffer cells may be lower than in hepatocytes. Effects of acute ligation on pO_2 were also studied. The effects on pO_2 in Kupffer cells from the hepatotoxin carbon tetrachloride, were followed over a 2-week period by using India ink particles which localized in Kupffer cells.⁽¹⁴⁸⁾

6.3.9.5. Kidney The kidney has a very complex blood supply with regard to both variations within different parts of the kidney and changes due to physiological and pathophysiological factors. To date the number of measurements of levels of oxygen in the kidney are limited because of technical difficulties involved. Difficulties arise because of the deep location of the kidneys, the complex pattern of blood supply within the kidney, and the motion of kidneys due to respiration; therefore EPR oximetry may be very important for this organ. Some results were already reported for EPR measurements of pO_2 in both isolated perfused kidneys and *in vivo*.^(82, 83, 109) Techniques used for these measurements included simultaneous measurements in the cortex and medulla of the kidney; these are useful because of their different blood supplies and different responses to changes in the circulatory system. As expected from results with other techniques, the baseline pO_2 of the

cortex was higher than that of the medulla. In response to an injection of endotoxin the pO_2 of the medulla increased, while that of the cortex decreased, so that the two became approximately equal. This effect could be eliminated by administering of an inhibitor of nitric oxide synthase, suggesting that the effect was mediated by nitric oxide.

6.3.9.6. Skin and Underlying Tissues Using EPR oximetry to measure oxygen in the skin has a number of attractive aspects. The skin is a tissue that can be subject to a number of processes which should be greatly affected by the amount of oxygen, including burns and wounds, especially with regard to factors which may affect the rate of healing. If we extend the definition of skin to include immediately underlying tissues including some muscles, then skin encompasses a region of great potential clinical importance: The status of tissues at risk in peripheral vascular disease.⁽¹⁸¹⁾ Because of its location, the skin is fully accessible to the relatively higher frequency *in vivo* EPR (e.g., 1 GHz), unlike many other sites where depth of sensitivity can be limiting.

To date there are only a few reported studies of EPR oximetry on skin,^(53, 68, 179) but this seems likely to change in the near future. Areas that are likely to receive particular emphasis include wound healing and peripheral vascular disease. There is considerable potential for early clinical studies using EPR oximetry on skin, including the advantage of India ink for EPR oximetry. India ink is the usual source of black pigment already used extensively in humans for both decorative tattoos and a number of medical applications (marking margins for radiation therapy, surgical margins in operative fields, and tracing lymphatics). Its usefulness in EPR oximetry was demonstrated, and the feasibility of using preexisting tattoos was shown.^(53, 148, 149, 179)

6.3.9.7. Tumors The response of tumors to ionizing radiation and in some cases, to chemotherapy, is greatly affected by the local amount of oxygen. Sensitivity decreases by as much as a factor of 3 when partial pressure is below 5–10 torr. EPR oximetry has the potential to make such measurements accurately and perhaps most importantly, on a repeated basis; therefore there is considerable interest in using EPR oximetry to measure oxygen in tumors, and some very promising results were obtained.

So far most studies were done at 1 GHz, but by using a very low-frequency *in vivo* EPR spectrometer (250 ± 20 MHz), Halpern *et al.*^(66, 67) measured the concentration of oxygen in a fibrosarcoma in mice and the effect of perfluorocarbon/carbogen on the oxygen concentration, using a specially designed nitroxide that may also provide information on viscosity.

Using particulate oxygen-sensitive paramagnetic materials, the group at Dartmouth demonstrated the potential value of *in vivo* EPR for following pO_2 in tumors.^(6, 23, 53, 54, 63, 153, 179) Their experimental approach usually involves placing one or more deposits of oxygen-sensitive paramagnetic materials at sites of interest in rodents, then taking repeated measurements over several days or weeks using

restrained but awake animals and a surface detector. Their results include the following:

- Measuring pO_2 in several different types of tumors
- Following changes in pO_2 during growth
- Measuring effects of therapy on pO_2 in tumors
- Using radiation-induced changes in pO_2 to enhance the effectiveness of subsequent doses of radiation by delivering these doses when pO_2 was relatively high
- Combining EPR oximetry with NMR techniques, especially to enhance the interpretation of NMR studies, so that the latter can be more widely used.

These approaches may provide clinical physicians with a method for individualizing therapy for each patient by selecting type and timing of treatment based on the pO_2 measured in the patient's tumor both initially and then during the course of therapy. ⁽¹⁵⁴⁾

6.3.10. Ischemia Reperfusion

An important role of free radicals in the damage associated with ischemia and reperfusion was postulated, and considerable indirect evidence was accumulated using model systems. Recently data indicating the occurrence of increased amounts of free radicals on reperfusion was demonstrated in *in vitro* samples in a number of different species, including rodents,^(201, 206) horses,⁽¹⁶⁴⁾ and man using spin traps and in rodents using chemiluminescence.⁽²²⁾ Attempts to demonstrate such effects directly *in vivo* are underway, but these are technically difficult because of the limited stability of spin adducts.

While direct studies of the kinetics of free radicals in ischemia reperfusion injury are difficult, many phenomena associated with ischemia reperfusion can be studied successfully. This is the driving force for many spectroscopic^(36, 37, 56, 57, 200–205) and imaging^(95–98, 101, 103) studies in isolated hearts (see the section on imaging).

The effects of acute ischemia in the liver were also studied in preliminary experiments.⁽⁸⁶⁾

6.3.11. Indicators of Oxidative Stress and/or Redox Metabolism

Several different approaches were suggested for using *in vivo* EPR to measure parameters related to oxidative stress or the redox state in an animal: The rate of metabolism of nitroxides, the level of ascorbyl radicals, and the generation of free radicals. All of these approaches address a topic of great contemporary interest: The role of oxidative damage in various diseases and types of pathophysiology. It is not yet clear whether any of these approaches with *in vivo* EPR will lead to widely useful assays, but it certainly seems possible. The rationale for using the rate of metabolism of nitroxides to measure oxidative stress is their metabolism is oxygen-

dependent and if the nitroxides interact with strong redox reagents, such as reactive free radicals, they are changed to a nonparamagnetic state.⁽⁹²⁾

The basis for using ascorbyl radical is the key role ascorbate has in redox metabolism and observing ascorbyl radicals in biological systems. The latter is facilitated by the very narrow and characteristic pattern of the lines of the EPR spectrum of the ascorbyl radical, which makes it readily detected (Ref. 147 reviews this topic). The ascorbyl radical was studied *in vivo* in a rat with X-Band, using an extracorporeal circulatory loop that flowed through an aqueous sample cell in the EPR spectrometer. This method used an injection of ferric citrate and/or ascorbate to generate the signal that was observed.⁽¹⁹²⁾

6.3.12. *In Vivo* Dosimetry of Unplanned Exposures to Ionizing Radiation

Ionizing radiation generates large numbers of free radicals. *In vivo* most of these react very rapidly, then disappear, but in some tissues, such as bone, teeth, and hair, where diffusion of the induced paramagnetic centers is restricted, these EPR centers can be very long lived. As early as 1967 it was suggested that these could be used for retrospective dosimetry of significant radiation exposures.⁽¹⁷⁾ With the development of *in vivo* EPR techniques, the principles of design for spectrometers to be used specifically for *in vivo* dosimetry were described and prototypes constructed to take measurements in teeth *in vivo*.^(81, 197) This method was applied to determine exposure dose in the Chernobyl accident. The usefulness of this approach remains to be demonstrated, but the method seems quite promising for potentially significant exposures where conventional dosimetry is inadequate.

7. RESULTS OF *IN VIVO* EPR IMAGING OF FUNCTIONAL BIOLOGICAL SYSTEMS

There are a number of very promising uses for information obtainable from EPR imaging. Like NMR imaging, EPR imaging can be done in two ways. The first is analogous to proton density imaging. The goal is to image parameters related to the concentration distribution of an infused spin probe, basically signal height. The spin probes imaged heretofore have been nearly entirely nitroxides. Here, the imaging algorithm regards the spectral shape as a complication. The effects due to the spectral shape can be eliminated or minimized through the process of deconvolution.^(11, 61, 155) Since the fluid compartment in which a nitroxide distributes can be altered by modest changes in the nitroxide structure, this form of imaging has significant implications for the study of pharmacokinetics. Since nitroxides can be covalently attached to other molecules of interest, they hold the promise of following drug distribution as in nuclear medicine.

A second use for EPR imaging lies in spectral spatial imaging, where the spectral shape is incorporated into the image to become an additional dimension.⁽¹³⁹⁾ Thus a spectrum is obtained at each spatial point in the image. The spectral information described in the spectroscopy section is available at each point in the image. In this sense spectral spatial images are more analogous to relaxographic imaging⁽¹⁰⁵⁾ and ³¹P chemical shift imaging,⁽¹⁸⁾ also referred to as spectroscopic imaging.⁽¹⁴⁵⁾ They may, however, contain a larger pool of physiologic information and higher specificity than measurements made with MRI. Spectroscopic parameters provide information (e.g., oxygen concentrations, polarity, and microviscosity) about the fluid compartment in which the spin probe distributes; thus the spectral spatial image gives an anatomic map of physiologically relevant parameters in living tissue.

The large amount of information provided by imaging occurs at a cost in sensitivity, as noted earlier. It is important to recognize, however, that the number of projections necessary to reconstruct three-dimensional volume with N^3 voxels is approximately $= 1/2 N^2$. Thus an increase in voxel spatial resolution requires less than a proportional increase in the number of gradient spectra to be obtained. This can be further compensated for by taking extra time to obtain images and developing narrower line width spin probes. The latter give higher signal per molecule, better spatial resolution, and higher sensitivity to physiologically relevant aspects of the fluid compartment. Effort is currently being devoted to spin probe development,^(50, 64) and there are further indications that this effort continues in several laboratories. Model studies^(140, 141) have allowed development of algorithms to extract spectra with relatively low gradients; extraction of oxygen concentrations from phantoms was studied as well.^(195, 196)

While there were other earlier reports of imaging substances by EPR,⁽⁸⁸⁾ the first actual applications to biological systems were reported by Berliner and Fujii in 1985 on plant specimens.⁽¹²⁾ It was necessary to work at a lower than conventional frequency (1 GHz), where they employed a primitive single flat-loop coil system adapted to a Varian E-4 console.⁽¹⁵²⁾ The object was placed concentrically through the (ca. 10-mm diameter) loop. The first paper⁽¹²⁾ showed the gradient projection spectra of Tempol in the capillaries of a celery stem, while another looked at coleus roots.⁽⁴³⁾ The first application to living animals was also from the same laboratory, where a cross-sectional image of the nitroxide CTPO was followed in an implanted melanoma tumor in the tail of a mouse using one-dimensional, filtered back-projection reconstruction methods.⁽¹⁴⁾

7.1. Imaging Studies of Pharmacokinetics of Nitroxides

More recently several low-field imaging studies of whole mice or organs were reported.^(2-5, 80-90, 144, 156) These used primarily the first of the two strategies for imaging, producing concentration images of radical species within each voxel of

the sample. They were aimed at the pharmacokinetics of nitroxides in a living sample or organ preparation.

Working at radio frequency (280 MHz), the nitroxide 2,2,5,5-tetramethylpyrrolidine-1-oxyl-3-carboxylic acid (PCA) was studied in the rat abdomen and thorax.⁽¹⁵⁶⁾ Another study involved time sequences of images of a series of nitroxides differing principally in the polarity of their side groups (3-trimethylaminomethyl iodide, 3-carboxy, 3-hydroxymethyl- and 3-carbamoyl-). This showed reproducible differences in the timing of the change from hepatic to bladder location depending on nitroxide polarity.⁽⁶²⁾ The signal-to-noise ratio for these images was modest, and it will must be enhanced to obtain quantitatively useful data. In a related study, it was shown that by covalently binding a nitroxide (Tempo) to a macromolecule (dextran), the lifetime of the imaging agent can be greatly extended; this probably occurs by preventing the nitroxide from entering cells where bioreduction usually occurs.^(89, 90, 199) Similar results were reported in the isolated heart using a polynitroxylated albumin.⁽¹⁰³⁾ A lipophilic nitroxide (16-doxyl stearate) was also imaged using 0.7-GHz EPR imaging; the authors concluded that this agent crosses the blood-brain barrier.⁽⁷¹⁾ The availability of paramagnetic agents that cross the blood-brain barrier may be an important factor in facilitating the study of the central nervous system. Studies with water-soluble nitroxides previously indicated that these do not readily cross the blood-brain barrier.⁽⁸⁰⁾

Extensive work with myocardial imaging of nitroxide distribution in rat heart models was pursued by the Johns Hopkins group.^(97, 98, 101, 103, 104) They described the development and optimization procedures for obtaining high-quality three-dimensional spatial EPR images of large lossy samples at 1 GHz. Strategies for selecting optimized parameters for projection acquisition, instrumentation, and algorithms to correct drifts in microwave frequency and inaccuracies in static and gradient magnetic fields were described.⁽⁹⁸⁾ Image reconstruction was performed using a two-stage, filtered back-projection method with spectral deconvolution. With this instrumentation, correction algorithms, and image reconstruction method, spatially accurate three-dimensional images of radical distribution were observed in complex phantoms using 0.5-mM nitroxide. Working with a high gradient system (up to 150 G/cm [15 mT/cm]), these workers developed sophisticated deconvolution methods to generate high-resolution images of the rat heart from deuterated nitroxides with line widths on the order of several hundred mG (tens of mT). They project spatial resolutions in three-dimensional phantoms with 10-20 G/cm gradients as low as 0.2 mm with spectral deconvolution.^(98, 104) Images of the rat heart confirmed the ability to image coronary arteries in the rat heart with diameters as small as to 0.2 mm.⁽¹⁰¹⁾

Effects of physical factors (local pressure) were followed in the myocardial walls of the isolated heart during the cardiac cycle, showing in detail the distribution through various stages.⁽⁹⁷⁾

7.2. Imaging Studies of Tumors and Tumor Oxygenation

EPR imaging of tumors has considerable potential for defining aspects of the physiology of tumors. It was driving force for instrumental development.^(61, 63, 152, 167) Berliner *et al.* demonstrated the potential of EPR imaging of tumors by publishing low-resolution images of a melanoma in a rat tail using 1.5-GHz EPR.⁽¹⁴⁾ The image derived was a two-spatial-dimensional image of nitroxide concentration distributions in tumors. It demonstrated heterogeneities that appeared to indicate hypovascular regions in the tumors.

Several studies in model systems demonstrated the potential of EPR imaging for measuring and imaging oxygen concentrations in living systems. Tumor measurements are of particular importance because the radiation response of tumors is sensitive to oxygen: It diminishes in regions with low oxygen tension or concentration. Halpern *et al.*⁽⁶⁷⁾ published an oxygen-sensitive two-dimensional (one spatial dimension), full spectral spatial image of a mouse tumor. In this proof of principle study, the oxygen tension resolution was approximately 5 torr, and spatial resolution was one mm. Analysis of the image with spectral fitting promises a quantitative map of oxygen concentrations. Even this initial tumor image shows lower oxygen tension in the center of the tumor mass than in the periphery, consistent with the expectation of an hypoxic tumor core. Improved resolution may be necessary for this technique to be of clinical relevance, although even that is controversial.^(72, 73)

7.3. Imaging of Diffusion in Skin and Related Systems

In view of the accessibility of the skin and underlying structures and the importance of processes occurring within the skin, it is not surprising that EPR imaging techniques focused on this system. Earliest studies used isolated skin and other tissues to image the diffusion of nitroxides.^(26–30) Bio-reduction was a moderate problem, but it could be overcome by using appropriate oxidizing substances and/or inactivating reducing systems.

The EPR imaging studies were undertaken with the modulated field gradient technique to investigate biophysical and biochemical properties of skin. This technique employed specific nitroxide spin probes, and included X-band studies of biopsies.^(40–42, 69, 70, 151) Modulated field gradients make it possible to obtain an EPR spectrum in a selected volume. Using this method, a distinct increase in polarity from epidermis toward lower dermis was observed with the spin label *di-t-butyl-nitroxide* (DTBN). The effect of the natural antioxidant dihydroliipoate on skin membrane polarity was studied by EPR imaging. One- and two-dimensional EPR images of the persistent free radical *di-t-butyl-nitroxide* were shown with two-dimensional images in skin biopsies with an actual point distinction resolution of 25 microns.

Selective imaging of lipid-rich and lipid-poor regions of isolated subcutaneous tissue were obtained by using four different approaches/principles: Differential solubility of oxygen in lipid versus aqueous compartments, nitroxides with different lipophilicities, differences in viscosity, and differences in concentrations of metal ions.⁽¹⁰⁾ These results suggest that *in vivo* EPR has the potential for providing very useful data on pharmacokinetics and pathophysiology that involve lipid-rich tissues as an important part of the system.

7.4. Imaging Studies of the Concentration of Nitric Oxide

Images showing the spatial distribution of nitric oxide in the isolated heart were obtained using iron dithiocarbamates.⁽¹⁰⁰⁾ They were able to follow the distribution and timing of nitric oxide concentrations under ischemia. Using a similar approach but freezing the organ before imaging, the distribution of nitric oxide was also imaged in the brain.⁽⁹⁹⁾ Frozen tissue can be used for these experiments because unlike nitroxides, the three-line EPR spectrum of nitric oxide can usually be resolved even when the molecule to which it is attached is immobilized.

7.5. Imaging Studies at the Microscopic Level

Functional biological systems were studied in only a few studies at the microscopic level by EPR imaging, usually using higher frequencies. Dobrucki and colleagues demonstrated that very useful images could be obtained from multicellular spheroids which are widely used models for tumors.^(31, 32, 195) The most definitive results were obtained in imaging the viability of cells in the spheroid. The viability was imaged on the basis that viable cells are able to exclude paramagnetic metal ions and therefore in the presence of nitroxides which could penetrate cells, the spectra could be seen only from the viable cells, which were able to exclude the paramagnetic ions which were placed in the suspension. Microscopic imaging of teeth was suggested as a means of obtaining detailed information on the absorption of ionizing radiation.⁽⁷⁸⁾ Finally, X-Band studies of skin biopsies just described approach microscopic resolution.

7.6. Use of Gated and Pulsed Methods to Obtaining Images

in vivo EPR presents several challenges and opportunities for methods that provide time resolution. Some of the most demanding challenges, as noted previously, are various motions that occur *in vivo*. Important physiological information is available if data can be obtained that are synchronized with such physiological cycles as heart rate and respiration. Testa *et al.*⁽¹⁸⁶⁾ reported success in synchronizing signal acquisition from a moving perfused beating heart in EPR-imaging experiments. The apparatus was a low-frequency bridge at 1.5 GHz, with a reentrant

cavity for sample and air coils for field gradients. Kuppusamy *et al.* elegantly used gating techniques to follow infused radicals in a heart with three-dimensional imaging.⁽⁹⁷⁾

7.7. Using of Pulsed Methods in *In Vivo* EPR

The possibility of carrying out pulsed FT *in vivo* EPR was frequently discussed but until recently, there were few if any real attempts at pulsed EPR and imaging at low frequency (L-band or lower).⁽¹⁶⁾ Concerns include short relaxation times of radicals, microphonics, and long ring-down times. Also the larger the resonator, the greater the power needed to achieve the same B1 at the sample. Last but not least, the power required for each pulse is high. If the dead time of the duty cycle of the pulse source and amplifier are large, there may be little advantage compared to a single acquisition with C.W. with high filtration.

In principle, however, the buildup of sensitivity through acquisition of multiple signals or free induction decay gives the same theoretical advantage to *in vivo* pulsed EPR as it does to NMR. The limiting difficulty appears to be that the time scale of EPR is a factor of 10^5 – 10^6 shorter. This means that data must be acquired nearly a million times more rapidly and pulses of high power must be generated, shaped, then allowed to dissipate in times of the same order of magnitude. This presents problems that have recently begun to be solved with evolving state-of-the-art equipment. Limitations on the field or frequency interval of the EPR spectrum excited in a single pulse arise from limits on available power; this forces compromise on the spectral interval to be detected with a pulse spectrometer operating at frequencies low enough for tissue penetration. Nonetheless Bourg *et al.*⁽¹⁶⁾ from the NIH developed a sensitive pulsed radio frequency (300 MHz) spectrometer, and more recently, then accumulated enough of the FID of nitroxide to obtain a usable signal by using a state-of-the-art homemade transient recording unit. While we also note that FT approaches in, e.g., IR or NMR, offer a multichannel advantage for a spectrum rich in features, an EPR spectrum of perhaps two-to-three lines does not appear to take advantage of this technique fully. We recall, however, that natural abundance C-13 NMR was not possible until the advent of the pulsed FT NMR spectrometer.

7.8. Review of Spectral Spatial-Imaging Studies

The spectral spatial approach was successfully used in several studies to obtain data from functioning biological systems. Woods *et al.* described the conceptual basis for this approach, especially for imaging of oxygen.⁽¹⁹⁴⁻¹⁹⁶⁾ While this approach has the potential for providing the most extensive data possible from *in vivo* EPR, it also has the greatest technical difficulties because of the need for high signal/noise and spatial resolution. Halpern *et al.*⁽⁶⁷⁾ reported a spectral spatial image of a tumor indicating a hypoxic tumor center as previously noted. Kup-

pusamy *et al.* developed techniques described by Woods *et al.* and applied these very elegantly to the isolated heart.^(95, 96) They reported the results of preliminary studies of three-dimensional spectral spatial images of free radicals infused into the heart and large vessels,⁽⁹⁶⁾ of gated images to resolve changes during the cardiac cycle,⁽⁹⁷⁾ and of four-dimensional spectral spatial images of an oxygen-sensitive char suspension.⁽⁹⁵⁾

7.9. Issues in EPR Imaging

Resolution is the key limitation in an imaging modality and *in vivo* EPR experiences major difficulties in this regard. Consider the fact that the typical line width for, e.g., a freely tumbling nitroxide is 0.5–1.0 G, which corresponds to a complete proton NMR spectral width several times over! That is, the magnitude of field gradients required for EPR versus NMR imaging of the same resolution should be about 100-fold larger, which requires some unique engineering tasks. By choosing totally perdeuterated N-15-labeled nitroxides, this requirement is somewhat relieved. The optimal imaging agent for EPR should, however, have even lower intrinsic line widths, preferably in the low-mG range. Spectral technique changes must be implemented (reduction of modulation field frequency and amplitude as well as electromagnetic radiation power), but these should not confuse the fact that even under these conditions narrower line spin probes give more robust signals. Magnetic susceptibility differences *in vivo* can distort lines but only if spin probes, like water, have access to protein-bound iron and copper, which is unlikely. Of course these concerns are in addition to homogeneity and stability requirements that were also discussed.

The Nycomed company (Oslo, Norway) produced a new type of stable free radicals that appear capable of providing the stability and narrow line widths of an ideal EPR-imaging agent, but to date these are not generally available. As more ideal imaging agents do become available, microwave and magnetic field absolute homogeneity and stability must be much higher than that typically found in X-Band laboratory EPR spectrometers. At the lower frequencies used for *in vivo* measurements, however, fractional homogeneity and stability requirements are relaxed. For example at 1 GHz relative homogeneity and stability are one-tenth that (1 part in 3×10^5 versus 1 part in 3×10^6) at X-Band. A number of technical aspects of *in vivo* EPR imaging must be dealt with before it can be regularly applied to biological problems; nonetheless it has high a potential for analyzing tissue physiology. EPR microscopy on small biological objects, such as cells, has great potential, and it should compete effectively with MRI.

A major improvement in both resolution and information content in *in vivo* EPR imaging is attainable by designing specific targeted spin labels/spin probes to be localized in specific organs and suborganelles. Other forms of targeting include specific fluid compartments, e.g., extracellular water (using highly polar molecular

substituents on a nitroxide), intracellular water (using ester molecular substituents), or intravascular water (using albumen bound nitroxides). The literature abounds with examples of site-specific spin labels and membrane probes that can be adapted to *in vivo* problems. A sensitivity problem may exist unless the localized spin probe reaches a significantly high concentration; for example spin probes targeted for specific cell surface receptors or labeled antibodies may not reach a high enough level for detection unless each label is polymeric.

8. SUMMARY AND CONCLUSIONS

In vivo EPR techniques have a surprisingly long history, but they began to yield data of direct biomedical value only very recently. The nature of the data, and the high rate of developments now occurring, lead to an optimistic assessment of the future for these approaches. The role of high-resolution EPR imaging is likely to be limited, but under the right conditions it can, provide very useful data. EPR spectroscopy is likely to be a more widespread and versatile approach because of the wider range of systems in which it can be used to obtain a useful signal/noise. Hybrid approaches, especially spatially resolved EPR imaging at several sites simultaneously may be especially useful. While the direction of developments for the next 50 years (or even the next 10 years) cannot be predicted with certainty, we can predict with a high degree of confidence that these techniques will be used increasingly and productively.

REFERENCES

1. Abragam, A., 1961, *Principles of Nuclear Magnetism* (Oxford/Clarendon Press, Oxford, U.K.).
2. Alecci, M., Colacicchi, S., Indovina, P. L., Momo, F., Pavone P., and Sotgiu, A., 1989, *Phys. Med.* **5**:99.
3. Alecci, M., Colacicchi, S., Indovina, P. L., Momo, F., Pavone, P., and Sotgiu, A., 1990, *Magn Reson. Imaging* **8**:59.
4. Alecci, M., Ferrari, M., Passariello, R., Quaresima, V., Sotgiu, A., and Ursini, C. L., 1992, Electron paramagnetic resonance: two-dimensional imaging of water-soluble nitroxide-free radical in whole rat, in *Proceedings of 11th Annual Meeting of the Society for Magnetic Resonance in Medicine* (Society of Magnetic Resonance in Medicine, Berkeley), p. 4410.
5. Alecci, M., Ferrari, M., Quaresima, V., Sotgiu, A., and Ursini, C. L., 1994, *Biophys. J.* **67**:1274.
6. Bacic, G., Liu, K. J., O'Hara, J. A., Harris, R. D., Szybinski, K., Goda, F., and Swartz, H. M., 1993, *Magn. Reson. Med.* **30**:568.
7. Bacic, G., Niesman, M. R., Magin, R. L., and Swartz, H. M., 1990, *Magn. Reson. Med.* **13**:44.
8. Bacic, G., Nilges, M. J., Magin, R. L., Walczak, T., and Swartz, H. M., 1989, *Magn. Reson. Med.* **10**:266.
9. Bacic, G., Nilges, M. J., Walczak, T., and Swartz, H. M., 1989, *Phys. Med.* **5**:307.
10. Bacic, G., Walczak, T., Demsar, F., and Swartz, H. M., 1988, *Magn. Reson. Med.* **8**:209.
11. Berliner, L. J., and Fujii, H., 1985, *Science* **227**:517.

12. Berliner L. J., and Fujii, H., 1985, Electron paramagnetic resonance (EPR) imaging and *in vivo* ESR, in *Magnetic Resonance in Biology and Medicine*. (G. Govil, G. L. Khetrpal, and A. Saran, eds.) (Tata-McGraw-Hill, Bombay), pp. 101-18.
13. Berliner L. J., and Fujii, H., 1992, Some applications of ESR to *in-vivo* animal studies and EPR imaging, in *In Vivo Spectroscopy, Biological Magnetic Resonance*, vol. 11 (L. J. Berliner and J. Reuben, eds.) (Plenum, New York), pp. 307-19.
14. Berliner, L. J., Fujii, H., Wan, X., and Lukiewicz, S. J., 1987, *Magn. Reson. Med.* **4**:380.
15. Berliner L. J., and Wan, X., 1989, *Magn. Reson. Med.* **9**:430.
16. Bourg, J., Krishna, M. C., Mitchell, J. B., Tschudin, R. G., Pohida, T. J., Friauf, W. S., Smith, P. D., Metcalfe, J., Harrington, F., and Subramanian, S., 1993, *J. Magn. Reson.* **102**:112.
17. Brady, J. M., Aarestad, N. O., and Swartz, H. M., 1968, *Health Physics* **15**:43.
18. Brown, T. R., Kincaid, B. M., and Ugurbil, K., 1982, *Proc. Nat. Acad. Sci.* **79**:3523.
19. Chan, H. C., Glockner, J., and Swartz, H. M., 1989, *Biochim. Biophys. Acta* **1014**:141.
20. Chan, H. C., Magin, R. L., and Swartz, H. M., 1989, *Biochem. Biophys. Methods* **18**:271.
21. Chan, H. C., Sun, K., Magin, R. L., and Swartz, H. M., 1990, *Bioconjugate Chem.* **1**:32.
22. Chance, B., and Gao, G., 1994, *Environ. Health Perspect.* **102**:29.
23. Chen, K., Ng, C. E., Zweier, J. L., Kuppusamy, P., Glickson, J. D., and Swartz, H. M., 1994, *Magn. Reson. Med.* **31**:668.
24. Colacicchi, S., Alecci, M., Gualtieri, G., Quaresima, V., Ursini, C. L., Ferrari, M., and Sotgui, A., 1993, *J. Chem. Soc. Perkin Transactions* **2**:2077.
25. Colacicchi, S., Ferrari, M., Gualtieri, G., Santini, M. T., and Sotgiu, A., 1989, *Phys. Med.* **5**:297.
26. Demsar, F., Cevc P., and Schara, M., 1986, *J. Magn. Reson.* **69**:258.
27. Demsar, F., and Kristl, J., 1989, *Phys. Med.* **5**:321.
28. Demsar, F., Schara, M., and Kveder, M., 1986, *Pharm. Vest.* **37**:131.
29. Demsar, F., Swartz, H. M., and Schara, M., 1988, *Magn. Reson. Med. Biol.* **1**:17.
30. Demsar, F., Walczak, T., Morse P.D., II; Bacic, G., Zolnai, Z., and Swartz, H. M., 1988, *J. Magn. Reson.* **76**:224.
31. Dobrucki, W., Demsar, F., Walczak, T., Woods, R. K., Bacic G., and Swartz, H. M., 1990, *Br. J. Cancer* **61**:221.
32. Dobrucki, J. D., Sutherland, R. M., and Swartz, H. M., 1991, *Magn. Reson. Med.* **19**:42.
33. Dunn, J. F., Ding, S., O'Hara, J. A., Liu, K. J., Rhodes, E., Weaver, J. B., and Swartz, H. M., 1995, *Magn. Reson. Med.* **34**:515.
34. Feldman, A., Wildman, E., Bartolinini, G., and Piette, L. H., 1975, *Phys. Med. Biol.* **20**:602.
35. Ferrari, M., Colacicchi, S., Gualtieri, G., Santini, M. T., and Sotgiu, A., 1990, *Biochem. Biophys. Res. Comm.* **166**:168.
36. Friedman, B. J., Grinberg, O. Y., Isaacs, K., Ruuge, E. K., and Swartz, H. M., 1996, *Magn. Reson. Med.* **35**:214.
37. Friedman, B. J., Grinberg, O. Y., Isaacs, K., Walczak, T. M., and Swartz, H. M., 1995, *J. Mol. Cell. Cardiol.* **27**:2551.
38. Froncisz W., and Hyde, J. S., 1982, *J. Magn. Reson.* **47**:515.
39. Froncisz, W., and Oles, T., 1989, *J. Magn. Reson.* **82**:109.
40. Fuchs, J., Freisleben, H. F., Groth, N., Herrling, T., Zimmer, G., Milbradt, R., and Packer, L., 1991, *Free Rad. Res. Comm.* **15**:245.
41. Fuchs, J., Freisleben, H. F., Groth, N., Herrling, T., Zimmer, G., Milbradt, R., and Packer, L., 1992, *J. of Investigative Dermatology* **98**:713.
42. Fuchs, J., Groth, N., Herrling, T., and Packer, L., 1994, *Methods in Enzymology* **233**:140.
43. Fujii, H., and Berliner, L. J., 1985, *Magn. Reson. Med.* **2**:275.
44. Fujii, H., Koscielniak, J., and Berliner, L. J., 1995, *In vivo* ESR observation of bioradical metabolites in living animals, *Bioradicals Detected by ESR Spectroscopy* (H. Ohya-Nishiguchi and L. Packer, eds.) (Birkhauser Verlag, Basel), pp. 155-62.

45. Fujii, H., Zhao, B., Koscielniak, J., and Berliner, L. J., 1994, *Magn. Reson. Med.* **31**:77.
46. Fujii, H., Zhao, B., Koscielniak, J., and Berliner, L. J., 1995, *Magn. Reson. Med. (Japan)* **6**:97.
47. Gallez, B., Bacic, G., Dunn, J., Goda, F., Jiang, J., O'Hara, J., and Swartz, H. M., 1996, *Magn. Reson. Med.* **35**:97.
48. Gallez, B., Bacic, G., and Swartz, H. M., 1996, *Magn. Reson. Med.* **35**:14.
49. Gallez, B., Mader, K., and Swartz, H. M., 1996, *Magn. Reson. Med.* **36**:694.
50. Gillies, D. G., Sutcliffe, L. H., Wu, X., and Belton, P. S., 1996, *Food Chemistry* **55**:349.
51. Glockner, F., Chan, H. C., and Swartz, H. M., 1991, *Magn. Reson. Med.* **20**:123.
52. Glockner, J. F., and Swartz, H. M., 1992, *In vivo EPR oximetry using two novel probes: fusicitin and lithium phthalocyanine*, in *Oxygen Transport to Tissue XIV* (W. Erdmann and D. F. Bruley, eds.) (Plenum, New York), pp. 229–34.
53. Goda, F., Liu, K. J., Walczak, T., O'Hara, J. A., and Swartz, H. M., 1995, *Magn. Reson. Med.* **33**:237.
54. Goda, F., O'Hara, J. A., Rhodes, E. S., Liu, K. J., Dunn, J. F., Bacic, G., and Swartz, H. M., 1995, *Canc. Res.* **55**:2249.
55. Gomi, F., Utsumi, H., Hamada, A., and Matsuo, M., 1993, *Life Science* **52**:2027.
56. Grinberg, O. Y., Friedman, B. J., and Swartz, H. M., 1997, *Intramyocardial pO₂ measured by EPR*, *Oxygen Transport to Tissue XIX* (D. K. Harrison and D. T. Delpy, eds.) (Plenum, New York), pp. 261–268.
57. Grinberg, O. Y., Grinberg, S. A., Friedman, B. J., and Swartz, H. M., 1996, *Myocardial oxygen tension and capillary density in the isolated perfused rat heart during pharmacological intervention*, *Oxygen Transport to Tissue XVIII* (E. M. Nemoto and J. C. Lamanna, eds.) (Plenum, New York), pp. 171–182.
58. Grucker, D., 1990, *Mag. Reson. Med.* **14**:140.
59. Grucker, D., and Chambron, J., 1993, *Mag. Reson. Imaging* **11**:691.
60. Halpern, H. J., and Bowman, M. K., 1991, *Low-frequency EPR spectrometers: MHz range*, in *EPR Imaging and in vivo EPR*, (G. R. Eaton, S. S. Eaton, K. Ohno, eds.) (CRC Press, Boca Raton), pp. 45–63.
61. Halpern, H. J., Bowman, M. K., Spencer, D. P., van Polen, J., Dowey, E. M., Massoth, R. J., Nelson, A. C., and Teicher, B. A., 1989, *Rev. Sci. Instr.* **60**:1040.
62. Halpern H. J., Peric, M., Yu, C., Barth, E. D., Boisvert, W., Makinen, M. W., Pou, S., and Rosen, G. M., 1996, *Biophys. J.* **71**:403.
63. Halpern, H. J., Spencer, D. P., van Polen, J., Bowman, M. K., Massoth, R. J., Teicher, B. A., Downy, E. M., and Nelson, A. C., 1986, *Radia. Oncol./Bio./Phys.* **12**:117.
64. Halpern H. J., Teicher, B. A., Lin, Y. L., Bowman, M. K., Nguyen, T. D., and Spencer, D. P., 1990, *J. Magn. Reson.* **90**:40.
65. Halpern, H. J., Yu, C., Barth, E. D., Peric, M., and Rosen, G. M., 1995, *Proc. Natl. Acad. Sci. USA* **92**:887.
66. Halpern, H., Yu, C., Peric, M., Barth, E., Karczmar, G., River, J., Grdina, D., and Teicher, B., 1996, *Rad. Res.* **145**:610.
67. Halpern, H., Yu, C., Peric, M., Barth, E. D., Grdina, D., and Teicher, B., 1994, *Proc. Nat. Acad. Sci. USA* **91**:13047.
68. Hatcher, M. E., and Plachy, W. Z., 1993, *BBA* **1149**:73.
69. Herrling, T., 1994, *Arzneimittel-Forschung* **44**:1047.
70. Herrling, T., Groth, N., Thiessenhusen, K-U, Fuchs, J., and Ewert, U., 1992, *Spectral-spatial skin imaging with modulated gradient and simultaneous field scan (MOSS)*, in *Magnetic Resonance Microscopy* (Blumich and Kuhn, eds.), pp. 1–10.
71. Hiramatsu, M., Oikawa, K., Hiroyuki, N., Akitane, M., Ogata, T., and Kamada, H., 1995, *Brain Res.* **697**:44.

72. Hockel, M., Knoop, C., Schlenger, K., Vorndran, B., Baussmann, E., Mitze, M., Knapstein, P. G., and Vaupel, P., 1993, *Radiother. Oncol.* **26**:45.
73. Hockel, M., Vorndran, B., Schlenger, K., Baussmann, E., and Knapstein, P. G., 1993, *Gynecol. Oncol.* **51**:141.
74. Houlst, D. I., Chen, C. N., and Sank, V. J., 1986, *Magn. Reson. Med.* **3**:730.
75. Hutchinson, J. M. S., 1971, Electron Spin Resonance Spectrometry on the Whole Mouse *in vivo*: Optimum Frequency Considerations, 1971, *J. of Physics (E), Scientific Instruments* **4**:703.
76. Hutchinson, J. M. S., and Mallard, J. R., 1971, Spectrometry on the Whole Mouse *In Vivo*: a 100 MHz Spectrometer, *J. of Physics, (E), Scientific Instruments* **4**:237.
77. Iannone, A., Magin, R. L., Walczak, T., Federico, M., Swartz, H. M., Tomasi, A., and Vannini, V., 1991, *Magn. Reson. Med.* **22**:435.
78. Ikeya, M., and Furusawa, M., 1988, *Oral Radiol.* **4**:133.
79. Ishida, S., Kumashiro, H., Tsuchihashi, N., Ogata, T., Ono, M., Kamada, H., and Yoshida, E., 1989, *Phys. Med. Bio.* **4**:1317.
80. Ishida, S., Matsumoto, S., Yokoyama, H., Mori, N., Kumashiro, H., Tsuchihashi, N., Ogata, T., Yamada, M., Ono, M., Kitajima, T., Kamada, H., and Yoshida, E., 1992, *Magn. Reson. Imag.* **10**:109.
81. Ishii, H., and Ikeya, M., 1990, (Japan) *J. Appl. Physics* **29**:871.
82. James, P. E., Bacic, G., Grinberg, O. Y., Goda, F., Dunn, J., Jackson, S. K., and Swartz, H. M., 1996, *Free Rad. Biol. Med.* **21**:25.
83. James, P. E., Goda, F., Grinberg, O. Y., Szybinski, K. G., and Swartz, H. M., 1996, Intrarenal Oxygenation Measured by EPR Oximetry and the Effects of Bacterial Endotoxin, in *Oxygen Transport to Tissue XVIII* (E.M. Nemoto and J.C. Lamanna, eds.) (Plenum, New York), pp. 557–568.
84. Jiang, J., Liu, K. J., Jordan, S., Swartz, H., and Mason, R., 1996, *Arch. Biochem. Biophys.* **330**:266.
85. Jiang, J., Liu, K. J., Shi, X., and Swartz, H. M., 1995, *Arch. Biochem. Biophys.* **319**:570.
86. Jiang, J., Nakashima, T., Shima, T., Liu, K. J., Goda, F., and Swartz, H. M., 1996, *J. of Appl. Physiol.* **80**:552.
87. Kadiiska, M. B., Xiang, Q. H., and Mason, R. P., 1994, *Chem. Res. in Toxicology* **6**:800.
88. Karthe, W., and Wehrsdorfer, J., 1979, *J. Magn. Reson.* **33**:107.
89. Kazama, S., Takashige, G., Yoshioka, H., Tanizawa, H., Ogata, T., Koscielniak, J., and Berliner, L. J., 1996, *Magn. Reson. Med.* **36**:547.
90. Kazama, S., Yoshioka, H., Tanizawa, H., and T. Ogata, 1996, *Magn. Reson. Med.* (Japan) **6**:74.
91. Knecht, K. T., and Mason, R. P., 1993, *Arch. Biochem. Biophys.* **303**:185.
92. Kocherginsky, N., and Swartz, H. M., 1995, Nitroxide spin labels, reactions in biology and chemistry, in (CRC Press, Boca Raton).
93. Komarov, A., Mattson, D., Jones, M. M., Singh, P. K., and Lai, C. -S., 1993, *Biochem. Biophys. Res. Comm.* **195**:1191.
94. Koscielniak J., and Berliner, L. J., Optimization of Low Frequency Spectrometers form *in vivo* EPR, *to be published*.
95. Kuppusamy, P., Chzhan, M., Samouilov, A., Wang, P., and Zweier, J. 1994, *J. Magn. Reson.* **107**:116.
96. Kuppusamy, P., Chzhan, M., Vij, K., Shteynbuk, M., Lefer, D. J., Giannella, E., and Zweier, J. L., 1994, *Proc. Nat. Acad. Sci. USA* **91**:3388.
97. Kuppusamy, P., Chzhan, M., Wang, P., and Zwier, J., 1996, *Magn. Reson. Med.* **35**:323.
98. Kuppusamy, P., Chzhan, M., and Zweier, J. L., 1995, *J. Magn. Reson. Series B.* **106**:122.
99. Kuppusamy, P., Ohnishi, S. T., Numagami, Y., Ohnishi, T., and Zweier, J., 1995, *J. Cerebral Blood Flow Metab.* **15**:899.
100. Kuppusamy, P., Wang, P., Samouilov, A., and Zweier, J., 1996, *Magn. Reson. Med.* **36**:219.
101. Kuppusamy, P., Wang, P., and Zweier, J., 1995, *Magn. Reson. Med.* **34**:99.

102. Kuppusamy, P., Wang, P., and Zweier, J., 1995, *Magn. Reson. Chem.* **33**:S123.
103. Kuppusamy, P., Wang, P., Zweier, J., Krishna, M. C., Mitchell, J. B., Ma, L., Trimble, C. E., and Hsia, C. J., 1996, *Biochem.* **35**:7051.
104. Kuppusamy, P., and Zweier, J., 1996, *Magn. Reson. Med.* **35**:316.
105. Labadie, C., Lee, J. -H., Gabor, V., and Springer, C. S., 1994, Relaxographic Imaging, *J. Magn. Reson.* **105**:99.
106. Lai, C. -S., and Komarov, A. M., 1994, *FEBS Lett.* **345**:120.
107. Lai, C. -S., and Komarov, A. M., 1995, Dithiocarbamate spin traps for in vivo detection of nitric oxide production in mice, in *Bioradicals Detected by ESR Spectroscopy*, (H. Ohya-Nishiguchi, L. Packer, eds.), (Birkhauser, Basel), pp. 163–171.
108. Liu, K. J., Bacic, G., Hoopes, P. J., Jiang, J., Dunn, J. F., and Swartz, H. M., 1995, *Brain Res.* **685**:91.
109. Liu, K. J., Gast, P., Moussavi, M., Norby, S. W., Vahidi, N., Walczak, T., Wu, M., and Swartz, H. M., 1993, *Proc. Natl. Acad. Sci. USA* **90**:5438.
110. Liu, K. J., Grinstaff, M., Jiang, J., Suslick, K., Swartz, H. M., and Wang, W., 1994, *Biophys. Journal* **67**:896.
111. Liu, K. J., Hoopes, P. J., Rolett, E. L., Beerle, B., Azzawi, A., Goda, F., Dunn, J. F., and Swartz, H. M., 1997, Effect of anesthesia on cerebral tissue oxygen and cardiopulmonary parameters in rats, *Oxygen Transport to Tissue XVIII* (E.M. Nemoto and J.C. Lamanna, eds.) (Plenum, New York), pp. 33-40.
112. Liu, K. J., Jiang, J. J., Ji, L. L., Shi, X., and Swartz, H. M., 1996, *Res. Chem. Intermed.* **22**:499.
113. Liu, K. J., Jiang, J., Swartz, H. M., and Shi, X., 1994, *Arch. Biochem Biophys* **313**:248.
114. Liu, K. J., Shi, X., Jiang, J., Goda, F., Dalai, N., and Swartz, H. M., 1995, *Arch. Biochem. Biophys.* **323**:33.
115. Lukiewicz, S. J., 1988, Direct in vivo ESR monitoring of blood level of nitroxide NMR contrast agents in mice at X-Band (9.3 GHz), abstract 116 (*Second European Conf. on NMR in Medicine and Biology, Berlin*).
116. Lukiewicz, S., Cieszka, S. K., Wojcik, K., Lackowska, B., Markowska, E., Pajak, S., Elas, M., and Dubis, K., 1989, *Phys. Med.* **5**:315.
117. Lukiewicz, S. J., Sochanik, A. S., and Lukiewicz, S. G., 1985, *Soc. Magn. Reson. Med.* **21**:1240.
118. Lukiewicz, S. J., Cieszka, K., Lackowski, B., Markowska, E., and Wojcik, K., 1987, In vivo ESR study on the influence of O₂ on biological half-lives of NMR contrast agents in murine tumors, Vol. 1, in *Proceedings of 6th Annual Meeting* (Society of Magnetic Resonance in Medicine, Berkeley), p. 236.
119. Lurie, D., 1994, *MAGMA* **2**:267.
120. Lurie, D., 1995, Imaging using the electronic overhauser effect, in *Encyclopedia of Nuclear Magnetic Resonance*, (John Wiley & Song, New York), pp. 2481–486.
121. Lurie, D., Bussell, D., Bell, L., and Mallard, J., 1988, *J. Magn. Reson.* **76**:366.
122. Lurie, D., Hutchison, J. M. S., Bell, L., Nicholson, I., Bussell, D., and Mallard, J., 1989, *J. Magn. Reson.* **84**:431.
123. Lurie, D., Hutchison, J. M. S., Bell, L. H., Nicholson, I., Bussell, D. M., and Mallard, J. R., 1989, *Phys. Med.* **5**:85.
124. Lurie, D., McLay, J., Nicholson, I., and Mallard, J., 1991, *J. Magn. Reson.* **95**:191.
125. Lurie, D. J., and Nicholson, I., 1993, Proton-electron double-resonance imaging of exogenous and endogenous free radicals in vivo. Proceedings of the International School of Physics, Enrico Fermi Course 123, *Nuclear Magnetic Double Resonance* (B. Maraviglia, ed.), (North Holland, Amsterdam), pp. 485–503.
126. Lurie, D., Nicholson, I., Foster, M., and Mallard, J., 1990, *Phil. Trans. R. Soc. Lond.* **333**:453.
127. Lurie, D., Nicholson, I., and Mallard, J., 1991, *J. Magn. Reson.* **94**:197.
128. Lurie, D., Nicholson, I., and Mallard, J., 1991, *J. Magn. Reson.* **95**:405.

129. Lurie, D., Nicholson, I., McLay, J. S., and Mallard, J. R., 1992, *Appl. Magn. Reson.* **3**:917.
130. Mäder, K., Bacic, G., and Swartz, H. M., 1995, *J. Invest. Derm.* **104**:514.
131. Mäder, K., Borchert, H.-H., Stösser, R., Groth, N., and Herrling, T., 1991, *Pharmazie* **46**:439.
132. Mäder, K., Domb, A., and Swartz, H. M., 1996, Gamma sterilization induced radicals in biodegradable drug delivery systems, *Appl. Radiat. Isotopes* **47**:1669.
133. Mäder, K., Gallez, B., Liu, K. J., and Swartz, H. M., 1996, *Biomaterials* **17**:457.
134. Mäder, K., Gallez, B., and Swartz, H. M., 1996, *Appl. Radial. Isotopes* **47**:1663.
135. Mäder, K., Stösser, R., and Borchert, H.-H., 1992, *Pharmazie* **47**:946.
136. Mäder, K., Stösser, R., and Borchert, H.-H., 1993, *Free Rad. Biol. Med.* **14**:339.
137. Mäder, K., Stösser, R., Borchert, H.-H., Mank, R., and Nerlich, B., 1991, *Pharmazie* **46**:341.
138. Magin, R. A., Wright, S. M., Niesman, M. R., Chan, H. C., and Swartz, H. M., 1986, *Magn. Reson. Med.* **3**:440.
139. Maltempo, M. M., 1986, *J. Magn. Reson.* **69**:156.
140. Maltempo, M. M., Eaton, S. S., and Eaton, G. R., 1987, *J. Magn. Reson.* **72**:449.
141. Maltempo, M. M., Eaton, S. S., and Eaton, G. R., 1988, *J. Magn. Reson.* **77**:75.
142. Maples, R., Eyer, P., and Mason, R., 1989, *Mol. Pharmacol.* **37**:311.
143. Masuda, S., Utsumi, H., and Hamada, A., 1992, In vivo ESR studies on radical reduction in ischemia paw oedema of whole mice, in *Oxygen Radicals* (K. Yagik, M. Kondo, E. Niki, and T. Yoshikawa, eds.) (Elsevier, Amsterdam), pp 75–178.
144. Masumizu, T., Tatebe, T., Masuda, S., Mutou, E., Utsumi, H., and Hamada, A., 1991, *Magn. Reson. Med. (Japan)* **2**:63.
145. Maudsley, A. A., Hilal, S. K., Simon, H. E., Wittekoek, S., 1984, *Radiology* **153**:745.
146. Miura, Y., Utsumi, H., and Hamada, A., 1992, *Biochem. Biophys. Res. Comm.* **182**:1108.
147. Mori, A., Wang, X., and Liu, J., 1994, *Methods in Enzymology* **233**:149.
148. Nakashima, T., Jiang, J., Goda, F., Shima, T., and Swartz, H. M., 1995, *Magn. Reson. Med.* **34**:888.
149. Nakashima, T., Jiang, J., Goda, F., Shima, T., and Swartz, H. M., 1995, *Magn. Reson. Med. (Japan)* **6**:158.
150. Nakai, M., Tamura, H., Hosokawa, H., Yamaoka, K., and Sakurai, H., 1995, *Magn. Reson. Med. (Japan)* **6**:34.
151. Nilges, M. J., Walczak, T., and Swartz, H. M., 1989, *Phys Med.* **5**:195.
152. Nishikawa, H., Fujii, H., and Berliner, L. J., 1985, *J. Magn. Reson.* **62**:79.
153. O'Hara, J. A., Goda, F., Liu, K. J., Bacic, G., Hoopes, P. J., and Swartz, H. M., 1995, *Rad. Res.* **144**:224.
154. O'Hara, J., Goda, F., and Swartz, H. M., 1996, Potential for EPR oximetry to guide treatment planning for tumors, *Oxygen Transport to Tissue XVIII*, (E.M. Nemoto and J.C. Lamanna, eds.) (Plenum, New York), pp. 233–242.
155. Ohno, K., 1982, *J. Magn. Reson.* **50**:145.
156. Quaresima, V., Alecci, M., Ferrari, M., and Sotgiu, A., 1992, *Biochem. Biophys. Res. Comm.* **183**:829.
157. Quaresima, V., Takehara, H., Tsushima, K., Ferrari, M., and Utsumi, H., 1996, *Biochem. Biophys. Res. Comm.* **221**:729.
158. Quaresima, V., Ursini, C. L., Gualtieri, G., Sotgiu, A., and Ferrari, M., 1993, *Biochimica et Biophysica* **1182**:115.
159. Roschmann, P., 1987, *Med. Phys.* **14**:922.
160. Rosen, G. M., Halpern, H. J., Brunsting, L. A., Spencer, D. S., Strauss, K. E., Bowman, M. K., and Wechsler, A. S., 1988, *Proc. Natl. Acad. Sci. USA* **85**:7772.
161. Sakurai, H., and Nakai, M., 1993, *Trace Nutrients Research* **10**:83.
162. Samuni, A., Samuni, A., and Swartz, H. M., 1989, *Free Rad. Biol. Med.* **7**:37.
163. Samuni, A., Samuni, A., and Swartz, H. M., 1989, *Free Rad. Biol. Med.* **6**:179.
164. Sertyn, D., 1994, *Can. J. Vet. Res.* **58**:309.

165. Shandelya, S. M. L., Kuppusamy, P., Weisfeldt, M., and Zweier, J., 1992, *Circ.* **87**:536.
166. Smirnov, A. I., Norby, S. W., Clarkson, R. B., Walczak, T., and Swartz, H. M., 1993, *Magn. Reson. Med.* **30**:213.
167. Sotgiu A., 1985, *J. Magn. Reson.* **65**:206.
168. Stösser, R., Mader, K., Borchert, H.-H., Herrmann, W., Schneider, G., and Liero, A., 1995, *Magn. Reson. Med. (Japan)* **6**:349.
169. Stösser, R., Mader, K., Borchert, H.-H., Hermann, W., Schneider, G., and Liero, A., 1995, Pharmaceutical aspects of ESR investigations on drug delivery systems, tissues and living systems, in *Bioradicals Detected by ESR Spectroscopy* (H. Ohya-Nishiguchi and L. Packer, eds.) (Birkhauser Verlag, Basel), pp. 301–20.
170. Subczynski, W. K., Lukiewicz, S., and Hyde, J. S., 1986, *Magn. Reson. Med.* **3**:747.
171. Swartz, H. M., 1995, Concentration of oxygen is too important of a variable to be ignored in experiments studying oxidative damage! in *Oxygen Paradox* (K. J. A. Davies and F. Ursini, eds.) (CLEUP Univ. Press, Padova Italy), pp. 105–22.
172. Swartz, H. M., Bacic, G., Friedman, G., Goda, F., Grinberg, O. Y., Hoopes, P. J., Jiang, J., Liu, K. J., Nakashima, T., O'Hara, J. A., and Walczak, T., 1995, Measurement of pO₂ in vivo, including human subjects by electron paramagnetic resonance, in *Oxygen Transport to Tissue XVI* (M. C. Hogan *et al.*, eds.) (Plenum, New York), pp. 119–28.
173. Swartz, H. M., Bacic, G., Gallez, B., Goda, F., James, P., Jiang, J., Liu, K. J., Mader, K., Nakashima, T., O'Hara, J., Shima, T., and Walczak, T., 1995, *In vivo* EPR spectroscopy, in *Bioradicals Detected by ESR Spectroscopy* (H. Ohya-Nishiguchi and L. Packer, eds.) (Birkhauser Verlag, Basel), pp. 285–99.
174. Swartz, H. M., Boyer, S., Brown, D., Chang, K., Gast, P., Glockner, J. F., Hu, H., Liu, K. J., Moussavi, M., Nilges, M., Norby, S. W., Smirnov, A. I., Vahidi, N., Walczak, T., Wu, M., and Clarkson, R. B., 1992, Use of EPR for the measurement of the concentration of oxygen *in vivo* in tissues under physiologically pertinent conditions and concentrations, in *Oxygen Transport to Tissue XIV* (W. Erdmann and D. F. Bruley, eds.) (Plenum, New York), pp 221–28.
175. Swartz, H. M., Boyer, S., Gast, P., Glockner, J. F., Hu, H., Liu, K. J., Moussavi, M., Norby, S. W., Walczak, T., Vahidi, N., Wu, M., and Clarkson, R. B., 1991, *Magn. Reson. Med.* **20**:333.
176. Swartz, H. M., Gast, P., Glockner, J., Hu, H., Ji, L. L., Liu, K. J., Nilges, M., Norby, S. W., Vahidi, N., Walczak, T., Wu, M., and Clarkson, R. B., 1991, Importance of measuring the concentration of oxygen appropriately and how this might be done, in *Oxidative Damage and Repair* (Oxford, Pergamon Press, Inc.), pp. 415–20.
177. Swartz, H. M., and Glockner, J. F., 1989, *Phys. Med.* **5**:109.
178. Swartz, H. M., and Glockner, J. F., 1991, Measurement of oxygen by ESRI and ESRS, in *EPR Imaging and in vivo EPR* (G. R. Eaton, S. S. Eaton, and K. Ohno, eds.) (CRC, Boca Raton, FL), pp. 262–90.
179. Swartz, H. M., Liu, K. J., Goda, F., and Walczak, T., 1994, *Magn. Reson. Med.* **31**:229.
180. Swartz, H. M., and Walczak, T., 1993, *Phys. Med.* **9**:41.
181. Swartz, H. M., and Walczak, T., 1996, *Chem. Intermed.* **22**:511.
182. Takeshita, K., Hamada, A., and Utsumi, H., 1995, *Magn. Reson. Med. (Japan)* **6**:255.
183. Takeshita, K., Utsumi, H., and Hamada, A., 1991, *Biochem. Biophys. Res. Comm.* **177**:874.
184. Takeshita, K., Utsumi, H., and Hamada, A., 1992, ESR study on radical clearance system in lung of whole mouse, in *Oxygen Radicals* (Yagi, K., Kondo, M., Niki, E., and Yoshikawa, T., eds.) (Excerpta Medica, Amsterdam), pp. 171–74.
185. Takeshita, K., Utsumi, H., and Hamada, A., 1993, *Biochem. Molec. Internat.* **29**:17.
186. Testa, L., Gualtieri, G., and Sotgiu, A., 1993, *Phys. Med. Biol.* **38**:259.
187. Utsumi, H., Masuda, S., Muto, E., and Hamada, A., 1991, *In vivo* ESR studies on pharmacokinetics of nitroxide radical in whole mice, in *Oxidative Damage and Repair* (M. J. Davies, ed.) (Pergamon, New York), pp. 165–70.

188. Utsumi, H., Muto, E., Masuda, S., and Hamada, A., 1990, *Biochem. Biophys. Res. Comm.* **177**:1342.
189. Utsumi, H., and Takeshita, K., 1995, *In vivo* ESR measurement of free radical reactions in living animals using nitroxyl probes, in *Bioradicals Detected by ESR Spectroscopy*. (H. Ohya-Nishiguchi, and L. Packer, eds.) (Birkhauser, Basel), pp. 321–34.
190. Utsumi, H., Takeshita, K., Miura, Y., Masuda, S., and Hamada, A., 1993, *Free Rad. Res. Comm.* **19**:S219.
191. Vahidi, N., Clarkson, R. B., Liu, K. J., Norby, S. W., Wu, M., and Swartz, H. M., 1994, *Magn. Reson. Med.* **31**:139.
192. Wang, X., Liu, J., Yokoi, I., Kohno, M., and Mori, A., 1992, *Free Rad. Biol. Med.* **12**:121.
193. Wang, I., Yokoi, I., Liu, J., Hiramatsu, M., and Mori, A., 1993, *Med. Sci. Res.* **21**:401.
194. Woods, R. K., Bacic, G. G., Lauterbur, P. C., and Swartz, H. M., 1989, *J. Magn. Reson.* **84**:247.
195. Woods, R. K., Dobrucki, J. W., Glockner, J., Morse, P. D. II, and Swartz, H. M., 1989, *J. Magn. Reson.* **85**:50.
196. Woods, R. K., Hyslop, W. B., and Swartz, H. M., 1989, *Phys. Med.* **5**:121.
197. Yamanaka, C., Ikeya, M., and Hara, H., 1993, *Appl. Radial. Isotopes* **44**:77.
198. Yokoyama, H., Ogata, T., and Hiramatsu, M., 1995, *Magn. Reson. Med. (Japan)* **6**:267.
199. Yoshioka, H., Tanizawa, H., Ogata, T., and Kazama, S., 1995, *Biol. Pharm. Bull.* **18**:1572.
200. Zweier, J. L., Chzhan, M., Ewert, U., Schneider, G., and Kuppusamy, P., 1994, *J. Magn. Reson.* **105**:52.
201. Zweier, J. L., and Kuppusamy, P., 1988, *Proc. Natl. Acad. Sci. USA* **85**:5703.
202. Zweier, J., and Kuppusamy, P., 1989, *Phys. Med.* **5**:289.
203. Zweier, J. L., and Kuppusamy, P., 1991, *Phys. Med.* **7**:29.
204. Zweier, J. L., Thompson-Gorman, S., and Kuppusamy, P., 1991, *J. Bioenergetics Biomembranes* **23**:855.
205. Zweier, J. L., Wang, P., and Kuppusamy, P., 1995, *J. Biol. Chem.* **270**:304.
206. Zweier, J. L., Wang, P., Samouilov, A., and Kuppusamy, P., 1995, *Nat. Med.* **1**:804.

Appendix: Corrections for Anisotropically Averaged Hyperfine Splittings and Order Parameters from Pseudopowder Electron Paramagnetic Resonance (EPR) Line Shapes

An Update for Slow-Motion Contributions to Lipid Spin Label Spectra from Membranes

Derek Marsh and Karl Schorn

In the first volume of this series (Berliner, 1976), consideration was given to corrections that must be made to extract order parameters from the EPR spectra of lipid spin labels in randomly oriented membrane dispersions (Gaffney, 1976; Griffith and Jost, 1976). A similar analysis leading to a somewhat different correction was also given previously by Hubbell and McConnell (1971). A hybrid of these results, depending on the range of order parameters studied ($0 \leq S_{app} < 0.45$ or 0.45

Derek Marsh and Karl Schorn • Max-Planck-Institut für biophysikalische Chemie, D-37108 Göttingen, Germany.

Biological Magnetic Resonance, Volume 14: Spin Labeling: The Next Millennium, edited by Berliner. Plenum Press, New York, 1998.

$\leq S_{app} \leq 1$) was given later by Marsh (1985), based on results of simulations presented by Griffith and Jost (1976). These corrections were widely used to analyze membrane EPR spectra from doxyl-labeled lipid chains, and these continue to be so. The purpose of this appendix is to update these corrections to account for components of lipid chain motion in fluid membranes that are now known to be in the slow regime of conventional nitroxide EPR spectroscopy (compare Freed, 1976; Schneider and Freed, 1989).

Restricted anisotropic rotation of spin-labeled lipid chain segments in fluid membranes is specified by an order tensor with principal element S_{zz} (relative to the membrane normal). This limited anisotropic reorientation results in the following principal elements of the partially motionally averaged hyperfine tensor (see, e.g., Seelig, 1976; Marsh and Horváth, 1989):

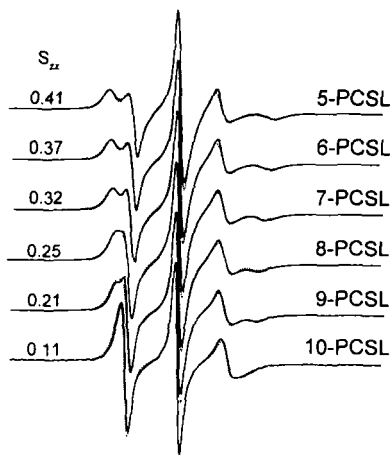
$$A_{||} = a_o + (2/3)\Delta A \cdot S_{zz} \quad (1)$$

$$A_{\perp} = a_o - (1/3)\Delta A \cdot S_{zz} \quad (2)$$

where with a ^{14}N -hyperfine tensor $\mathbf{A} = (A_{xx}, A_{yy}, A_{zz})$, the isotropic hyperfine coupling constant is $a_o = (1/3)(A_{xx} + A_{yy} + A_{zz})$ and the maximum extent of the axial hyperfine anisotropy is $\Delta A = A_{zz} - 1/2(A_{xx} + A_{yy})$. Here it is assumed that the z -principal axis of the ^{14}N -hyperfine tensor is oriented parallel to the molecular axis, as for stereospecifically doxyl- or proxyl-labeled lipid chains. It is also assumed that the nonaxiality of the ^{14}N -hyperfine tensor is small, as is found experimentally, such that only the S_{zz} principal element of the ordering tensor is required to describe its anisotropic motional averaging.

For a powder pattern EPR line shape or a partially averaged EPR spectrum resulting from fast anisotropic reorientation in an unoriented membrane suspension, the splitting between the outer hyperfine extrema of the first-derivative spectrum $2A_{\max}$ is rigorously equal to $2A_{||}$ (Weil and Hecht, 1963; Hubbell and McConnell, 1971). However the effective splitting of the inner hyperfine extrema A_{\min} is complicated by spectral overlap in this region of the (pseudo-)powder line shape. Previous corrections proposed to determine order parameters from randomly oriented samples related this effective inner splitting $2A_{\min}$ to the true value of the hyperfine splitting given by $2A_{\perp}$ (Hubbell and McConnell, 1971; Griffith and Jost, 1976; Gaffney, 1976). These empirical corrections were based on the simulation of powder spectra corresponding to the motionally averaged hyperfine tensor $\mathbf{A}' = (A_{\perp}, A_{\perp}, A_{||})$. These corrections therefore correspond to fast partial motional averaging of the hyperfine anisotropy. Unlike the situation in soap systems, which exhibit fast motional averaging and high order (Schindler and Seelig, 1971; Seelig, 1976), EPR spectra from chain-labeled lipids in fluid phospholipid membranes contain important features corresponding to motional components that are slow on the conventional nitroxide EPR time scale (Lange *et al.*, 1985; Moser *et al.*, 1989).

Figure 1. Experimental EPR spectra (solid lines) and simulations using the VAR model (dotted lines) for different positional isomers of the n-PCSL phosphatidylcholine spin labels in dimyristoyl phosphatidylcholine/dimyristoyl glycerol (58:42) mol/mol bilayers at 60°C. The order parameters S_{zz} used in the simulations are indicated in the figure. Total scan range = 100 G (Schorn and Marsh, 1996).



In the pseudopowder EPR spectra from spin-labeled lipids in fluid phospholipid bilayers or biological membranes, the low-field perpendicular peak is characteristically less deep than that of the central line (see Fig. 1); this feature is reversed in soap systems, and it cannot be reproduced by simulations based on fast motional narrowing theory (Schindler and Seelig, 1973; Seelig, 1976). Furthermore the high-field parallel peak is less deep than the overshoot feature from the high-field perpendicular peak (see experimental spectra in Fig. 1); this feature is not reproduced (for $S_{zz} \leq 0.7$) by previous simulations used to obtain corrections for calculating order parameters (see Griffith and Jost, 1976; Gaffney, 1976).

To account for slow-motional contributions with spin-labeled lipids in membranes, spectral simulations were made using the very anisotropic reorientation (VAR) model (see Meirovitch *et al.*, 1984). This is the very simplest of the slow motional models that emulates, although it does not describe exactly, anisotropic local ordering in macroscopically unoriented samples. Nevertheless it was found to be very successful in systematically representing spin label EPR spectra from a variety of different lipid spin labels in bilayer membranes over a wide range of temperature and membrane lipid compositions (Schorn and Marsh, 1996). Figure 1 shows representative simulations of experimental spectra from different positional isomers of the 1-acyl-2-(n-doxyl stearyl)-phosphatidylcholines (n-PCSL) in fluid lipid membranes. Unlike the fast-motional analysis, experimental spectra can be fitted with a high degree of precision by simulations using the VAR model. Further refinement of the model is not justified by the relatively low resolution obtained in experimental spectra from nonaligned membrane samples.

The EPR spectra were simulated for ^{14}N -nitroxide spin labels at a microwave frequency of 9.0 GHz for the full range of molecular order parameters. $S_{zz} = 0-1$

by using the VAR model (Schorn and Marsh, 1997). The spin Hamiltonian parameters used were $A = (5.9 \text{ G}, 5.4 \text{ G}, 32.9 \text{ G})$ and $g = (2.0076, 2.0072, 2.0021)$ (Schorn and Marsh, 1996). This g -tensor differs slightly from single-crystal values for a doxyl nitroxide (Jost *et al.*, 1971) because it has reduced nonaxiality to account in part for some of the effects of rapid *trans-gauche* isomerism not explicitly included in the model. Dynamic parameters and intrinsic line widths were chosen to reproduce experimental spectra typical of n-PCSL spin labels in membranes (see Schorn and Marsh, 1996; compare Fig. 1). Splittings between the outer peaks ($2A_{\text{max}}$) and between the inner peaks ($2A_{\text{min}}$) in simulated spectra were measured to establish empirical corrections that must be made to obtain the true hyperfine splittings $2A_{\parallel}$ and $2A_{\perp}$, respectively, which are used to determine the order parameter S_{zz} from Eqs. (1) and (2).

Values of $2A_{\text{max}}$ measured from the simulated spectra vary linearly with S_{zz} from $2A_{\text{max}} \approx 2a_o$ for $S_{zz} = 0$ to $2A_{\text{max}} \approx 2A_{zz}$ for $S_{zz} = 1$ (Schorn and Marsh, 1997), as would be predicted by Eq. (1) from motional narrowing theory. For spectra that contain contributions from slow motional components however, this is neither an avoidable nor necessarily expected result. It arises from a balance of the effects parallel and perpendicular components of the diffusion tensor have on the outer spectral line positions. Although somewhat fortuitous, this simple result corresponds best to experimental spectra in this model (Schorn and Marsh, 1996; see Fig. 1); it has the advantage that the relationship $A_{\parallel} = A_{\text{max}}$ normally used may be retained to a reasonable degree of approximation.

Values of the inner splittings $2A_{\text{min}}$ obtained from the simulated spectra do not correspond to Eq. (2) nor to those obtained previously from fast motional narrowing simulations. The dependence of A_{min} on the order parameter is linear, at least over the range $S_{zz} = 0.05\text{--}0.8$ (for values outside this range, the inner splitting is difficult to resolve). This leads to the following relation for the A_{\perp} motionally averaged tensor element (Schorn and Marsh, 1997):

$$A_{\perp} = A_{\text{min}} + 1.29 \text{ G} - 1.75 \text{ G} \cdot S_{zz} \quad (3)$$

This correction is similar in form to that introduced previously from motional narrowing simulations (Gaffney, 1976) except that in the latter case, both numerical terms had a value of 1.4 G.

Finally, the order parameter may be expressed in terms of the experimentally accessible parameter $S_{\text{app}} = (A_{\text{max}} - A_{\text{min}})/\Delta A$ by using Eqs. (1)–(3) with $A_{\parallel} = A_{\text{max}}$:

$$S_{zz} = 1.069 S_{\text{app}} - 0.051 \quad (4)$$

where $\Delta A = 27.2 \text{ G}$. This very simple form allows immediate estimation of S_{zz} by using values of A_{max} and A_{min} obtained from experimental spectra. If necessary a further correction may be applied to account for differences in spin label environ-

ment polarity by using the ratio of the isotropic hyperfine coupling constants (Hubbell and McConnell, 1979; Gaffney, 1976; Jost and Griffith, 1976). The hyperfine tensor used here to determine the corrections corresponds to a value of $a_o = 14.7$ G, which is reasonably close to the mean value for doxyl labels in the acyl chain regions of lipid membranes (Marsh and Watts, 1981).

Including the polarity correction, which corresponds to $a'_o = (1/3)(2A_{\perp} + A_{\parallel})$, gives rise to a quadratic equation for S_{zz} . The solution of this may be approximated by:

$$S_{zz} = \frac{1}{7} (A_{\max} + 2A_{\min}) - \sqrt{\left[\frac{1}{7} (A_{\max} + 2A_{\min})\right]^2 - 0.46(A_{\max} - A_{\min}) + 0.6} \quad (5)$$

where A_{\max} and A_{\min} are expressed in gauss. Values for the order parameter obtained in this way agree quite well with those obtained by direct simulations, such as are given in Fig. 1 (Schorn and Marsh, 1997). The method may therefore be used with experimental spectra to yield order parameters that closely approximate those obtained by spectral simulations using the VAR slow motional model.

REFERENCES

- Berliner, L. J., 1976, ed. *Spin Labeling. Theory and Applications* (Academic, New York).
- Freed, J. H., 1976, Theory of slow tumbling ESR spectra for nitroxides, in *Spin Labeling. Theory and Applications* (L. J. Berliner, ed.) (Academic, New York), p. 53.
- Gaffney, B. J., 1976, Practical considerations for the calculation for order parameters for fatty acid or phospholipid spin labels in membranes, in *Spin Labeling. Theory and Applications* (L. J. Berliner, ed.) (Academic, New York), p. 567.
- Griffith, O. H., and Jost, P. C., 1976, Lipid spin labels in biological membranes, in *Spin Labeling. Theory and Applications* (L. J. Berliner, ed.) (Academic, New York), p. 453.
- Hubbell, W. L., and McConnell, H. M., 1971, *J. Am. Chem. Soc.* **93**:314.
- Jost, P. C, Libertini, L. J., Hebert, V. C, and Griffith, O. H., 1971, *J. Mol. Biol.* **59**:77.
- Lange, A., Marsh, D., Wassmer, K.-H., Meier, P., and Kothe, G., 1985, *Biochemistry* **24**:4383.
- Marsh, D., 1985, ESR probes for structure and dynamics of membranes, in *Spectroscopy and the Dynamics of Molecular Biological Systems* (P. M. Bayley and R. E. Dale, eds.) (Academic, London), p. 209.
- Marsh, D., and Horváth, L. I., 1989, Spin-label studies of the structure and dynamics of lipids and proteins in membranes, in *Advanced EPR. Applications in Biology and Biochemistry* (A. J. Hoff, ed.) (Elsevier, Amsterdam), p. 707.
- Marsh, D., and Watts, A., 1981, ESR spin label studies of liposomes, in *Liposomes: from Physical Structure to Therapeutic Applications* (C. G. Knight, ed.) (Elsevier/North-Holland, Amsterdam), p. 139.
- Meirovitch, E., Nayeem, A., and Freed, J. H., 1984, *J. Phys. Chem.* **88**:3454.
- Moser, M., Marsh, D., Meier, P., Wassmer, K.-H., and Kothe, G., 1989, *Biophys. J.* **55**:111.
- Schindler H., and Seelig, J., 1973, *J. Chem. Phys.* **59**:1841.
- Schneider, D., and Freed, J. H., 1989, Calculating slow motional magnetic resonance spectra, a user's guide, in *Spin Labeling. Theory and Applications. Biological Magnetic Resonance*, vol. 8 (L. J. Berliner and J. Reuben, eds.) (Plenum, New York), p. 1.
- Schorn, K., and Marsh, D., 1996, *Chem. Phys. Lipids* **82**:7.

Schorn, K., and Marsh, D., 1997, *Spectrochim. Acta A* **53**:2235.

Seelig, J., 1976, Anisotropic motion in liquid crystalline structures, in *Spin Labeling. Theory and Applications* (L. J. Berliner, ed.) (Academic, New York), p. 373.

Weil, J. A., and Hecht, H. G., 1963, *J. Chem. Phys.* **38**:281.

Contents Of The Previous Volume In This Series

SPIN LABELING: THEORY AND APPLICATIONS, VOLUME 8, (1989)

Chapter 1

Calculating Slow Motional Magnetic Resonance Spectra: A User's Guide

David J Schneider and Jack H. Freed

Chapter 2

Inhomogeneously Broadened Spin-Label Spectra

Barney Bales

Chapter 3

Saturation Transfer Spectroscopy of Spin Labels: Techniques and Interpretation of Spectra

M. A. Hemminga and P. A. de Jager

Chapter 4

Nitrogen-15 and Deuterium Substituted Spin Labels for Studies of Very Slow Rotational Motion

Albert H. Beth and Bruce H. Robinson

*Chapter 5***Experimental Methods in Spin-Label Spectral Analysis***Derek Marsh**Chapter 6***Electron–Electron Double Resonance***James S. Hyde and Jim B. Feix**Chapter 7***Resolved Electron–Electron Spin–Spin Splittings in EPR Spectra***Gareth R. Eaton and Sandra S. Eaton**Chapter 8***Spin-Label Oximetry***James S. Hyde and Witold K. Subczynski**Chapter 9***Chemistry of Spin-Labeled Amino Acids and Peptides: Some New Mono- and Bifunctionalized Nitroxide Free Radicals***Kálmán Hideg and Olga H. Hankovsky**Chapter 10***Nitroxide Radical Adducts in Biology: Chemistry, Applications, and Pitfalls***Carolyn Mottley and Ronald P. Mason**Chapter 11***Advantages of ^{15}N and Deuterium Spin Probes for Biomedical Electron Paramagnetic Resonance Investigations***Jane H. Park and Wolfgang E. Trommer*

Chapter 12

Magnetic Resonance Study of the Combining Site Structure of a Monoclonal Anti-Spin-Label Antibody

Jacob Anglister

Appendix

Approaches to the Chemical Synthesis of ^{15}N and Deuterium Substituted Spin Labels

Jane H. Park and Wolfgang E. Trommer

Index

This page intentionally left blank.

Index

- Absorption, 90
Accessibility parameter, π , 69
ACET, 285, 302–304
Acetyl-carboxypeptidase, 238
Acetylsalicylic acid, 131, 132
Acetylcholine, 158, 172
Acetylcholinesterase
 enzymatic activity by ESR, 157
 modified by biradical disulfide, 159,
 160
Acetylthiocholine, 158
Activation energy, for molecular motion,
 356, 358, 360
Affinity, 298, 302, 320, 327–328
Alamethicin, 276
Alcohol dehydrogenase, 159–161
Alkylating nitroxide, 141, 147
Amidino nitroxide, 140
Amino nitroxide, 122, 140
3-Amino-PROXYL, 289, 290
4-Amino-TEMPO, 289, 290, 321, 323
Androstane spin label: *see* ASL
Angiotensin, spin-labeled, 141
Anisotropic rotational diffusion, 29
Anisotropy, hyperfine, 88
Apocytochrome *c*, 66
L-Arginine, 169, 171, 172
Arrhenius equation, 356, 358
(ASL) 3-doxyl-17 β -hydroxy-5 α -androstane,
 33, 88–90
A tensor, 341, 343
 isotropic value, 342
 principal value, 342
ATPase, Na⁺K⁺, 65
 vacuolar, 73
Azido nitroxide, 140
Bacteriorhodospin, 258–260
 α -helices, 259–260
Benzocaine, 131, 132
Bi(di)radical
 disulfide, 149
 exchange integral, 124, 150
 pH-sensitivity, 123, 125, 151
Bilayer membrane, 42, 73
Binomial distribution
 hyperfine multiplet, 6
 spinlabelpopulation, 11
Bioreduction, 373
Bovine serum albumin (BSA), 100–103
Broadening
 homogeneous, 53
 inhomogeneous, 6, 9, 14, 16, 54–55, 85, 90, 93
C-5 spin-labeled nucleoside (DUPDA), 285, 289
C-5 spin-labeled nucleoside (DUTA), 285, 288,
 289, 292
Capillary electrophoresis (CE), 296, 297, 334
 gas permeable, 94
Carbodiimide nitroxide, 140
 spin label, 77
Carbohydrate, 340, 351, 360
Carboxypeptidase A, 237, 243
 acetyl, 238
 mixed anhydride reaction intermediate of, 237
 spin-labeled substrates, 237

- Cavity
 in a glass, 356
 in a lattice, 345, 348, 350, 360
 microwave, 365
- Cecropins, 274–276
- Center-field ratio: *see* Line height ratio
- Chromium oxalate, paramagnetic relaxant, 69
- α -Chymotrypsin, 231–232, 243
 spin-labeled acylenzyme, 233, 236
 transition state inhibitor analog, 231
- Coat protein, M13, 71
- Comparative X- and W-band, EPR, 84–93
 bovine serum albumin, spin-labeled fatty acid binding, 100–102
 3-doxyl-17 β -hydroxy-5 α -androstane in O-xylene, 88–90
 doxyl stearic acid labels in phospholipid membranes, 97–100
 mixtures of phenyl-tert-butylnitron spin adducts, 90–93
 perdeuterated TEMPONE in toluene, 85–88
 small spin labels in phospholipid membranes, 95–97
 spin labeled phospholipids and proteins, 95–105
 spin labeled proteins
 immobilized labels, 102–104
 mobile labels, 104–105
- Correlation time, 29, 33, 35, 78, 305–306, 308, 315, 318–319, 330; *see also* Rotational correlation time
- Cryoenzymology, 230
- Crystallization, 348, 349
 crystals, 351
 formation, 354
 ice, 150
 melting, 349–352
- CSL (3-doxylcholestane) cholestane spin probe, 90
- CTPO, 33, 35–36, 379, 391; *see also* Spin label
- CW saturation, 255–256
 fast acting agents, 255
- Cysteine labeling, 152, 154–156, 159, 340–341, 356–357
- Cytochrome *c*, 66
- Cytochrome P-450 reductase, 159, 160
- DCAT, 286, 323, 324
- DCAVAP, 287, 295
- Degeneracy, 47
- Denaturation of FepA, 267–271
- Deoxygenation, CW HF EPR experiments, 93–95
- Desiccation tolerance, 340
- Deuterium hyperfine, 85
- Dextrin, 355
- DIACET, 286, 302
- Di-*t*-butylnitroxide, DTBN, 393
- Diagnostic intensity ratio, inhomogeneous broadening, 9, 14, 16
- Dielectric properties, 364
- Differential scanning calorimetry, 351–353, 360; *see also* DSC
- Diffusion, 349
 Brownian, 343
 rotational, 29, 77
 slow rotational, 77
 spin, 30, 35
 translational, 39–40, 63–65, 349
 water, 339
- Diffusion coefficient, translational, 39–40, 65
- 3,4-Dihydro-1,2-diazete, 1,2-dioxides, 168, 169
- 5,5-Dimethyl-1-pyrroline-N-oxide, 158
- 1,2-dipalmitoyl-*sn*-glycero-3-phosphatidylcholine (DPPC), 96, 97
- Diphtheria toxin, 273–274
- Dipolar interaction, 40, 72, 263, 265 (END) electron nuclear dipolar, 35
 spin–spin interactions, 11
- Dipolar relaxation, 40, 72
- Dipole coupled nitroxide labels, 104
- Dipole–dipole interaction, 40, 72
- Distance measurements, 40, 73
- Dispersion, 90
- Distance measurements
 metal–nitroxide, 271–273
 nitroxide–nitroxide, 263–265
- Disulfide
 biradical, 149
 thiol–disulfide exchange, 149, 150
- Dithiocarbamates, 162, 167
- Dithioerythritol, 149, 160
- DMPC (1,2-dimyristoyl-*sn*-glycero-3-phosphocholine), 94–100
- DMPC-DSPC, 17–21
- DMPG spin label, 67–68
- B*-DNA, 319, 323–324, 326
- Z*-DNA, 323–325

- Domains
 disconnected, 19
 size, 11, 13
- Dosimetry, by EPR, 390
- Double cysteines, 263–265
 dipolar interactions, 263
 distance, 263
- Double labeling, 66
- Dough, 356
- 3-Doxyl-17 β -hydroxy-5 α -androstane (ASL),
 88, 89
- Doxyl stearic acid, 94, 95, 97–102
- DPPC (1,2-dipalmitoyl-*sn*-glycero-3-
 -phosphatidylcholine), 96–99
- DSPC spin label (DMPCSL), 17–20, 34, 68, 70
- DTBN, di-*t*-butylnitroxide, 393
- DUAP, 286, 294, 296, 301, 303, 310, 314–318,
 323, 326, 327, 330
- DUAT, 286, 293, 294, 301, 303
- DUAVAP, 287, 293, 294
- DUMPDA, 285, 289, 290, 298, 301, 321, 322
- DUMTA, 285, 290, 298, 303, 315, 316
- DUNtB, 285, 295–297
- DUPAT, 286, 293
- DUPDA, 5-[(1-Oxyl-2,2,5,5-tetramethyl-3-
 pyrrolidinyl)amino]-2'-deoxyuridine,
 285, 289
- DUTA, 5-[(1-Oxyl-2,2,6,6-tetramethyl-4-
 piperidinyl)amino]-2'-deoxyuridine,
 285, 288, 289, 292
- Drug delivery systems, measurement in tissues,
 377
- DSC, *see also* Differential scanning calorime-
 try
 molecular, 341, 354, 357, 359
- Electron–nuclear dipolar interaction (END), 35
- Electron relaxation, mechanism, 28
- Electrostatic potential
 human serum albumin, 147, 148, 159
 phospholipid membranes, 138, 139, 143–146
- Enaminoketone nitroxide, 128
- Endothelium-derived relaxing factor, EDRF,
 168
- ENDOR
 angle-selected, 190
 basis of torsion angle search, 187–188
 constraints, 209
¹H, 109
¹⁹F, 190, 216
 shift, 190
- Enzymatic synthesis
 digestion of spin-labeled oligomers, 292
 incorporation, 284, 292–294, 299
 spin labeled oligonucleotides, 284, 292,
 299
 spin labeling, 284, 292–295, 299
 template-independent enzymes, 292
 template dependent enzymes, 292
AmpliTaq DNA polymerase, 292, 294,
 295
 DNA polymerase I, 292
 DNA polymerase, Klenow fragment,
 293, 294
M. luteus DNA polymerase, 292, 294
 reverse transcriptase, 292
 T-4 DNA polymerase, 292, 293, 295
- Enzyme reaction intermediates, 229, 242
- EPR (electron paramagnetic resonance) or ESR
 (electron spin resonance)
 CW, 252, 255
 CW saturation, 255–257
 orientation selection in ENDOR, 187
 signal quantitation, 299–301
 specific activity, AEPR, 288, 289, 292,
 298–301
 spin echo, 271
- Exchange interaction, 42, 265, 256, 85, 86, 91,
 93
 frequency, 68
 Heisenberg, 27, 42–43, 45, 47, 50, 63, 66,
 72, 85, 86, 91, 93, 265, 256, 293
 rate, 46
 two-site, 43, 50, 59
- FepA, 252, 265–272
- Ferric enterobactin, 265, 271–272
- Field modulation, 343, 344
 amplitude (B_m), 365
 frequency ν_m , 343
- Fluid phase, 16
- Gaussian lineshape, 7, 13
- Food stability, 339–341, 355, 359; *see also*
 Stability
- Free radicals, 378
 biodistribution and measurement in vivo,
 378
 drug intermediate, 381
- Free spin test, 297, 298
- Free volume: *see* Volume
- Freeze concentrated solution, 348, 349, 365

- Freeze pump-thaw, 93, 94
 Fructose, 351
- g*-factor shift, 97
 tensor, 341, 343
- Gas permeable capillary, 94
- Gel phase, 16, 97
 interdigitated, 75
 membranes, 62–64, 73
- Gene-32 protein, 327–328
- Glass, 343, 348–353, 356
 carbohydrate-water, 351
 glucose-water, 354
 maltodextrin-water, 355
 maltoheptaose-water, 352
 specific transition temperature (T_g'), 348, 349
 sucrose-water, 350
 sugar-water, 348, 353, 365
 transition (T_g), 349–354, 355, 360
- Glass–rubber transition, 339, 349, 355
- Gliadin, 356, 357
- Glucose, 351, 353–356
- Glutathione
 ESR detection, 152, 153
 intracellular, 155, 156
 spin labeled, 132, 141
- Gluten, 356–360
 maleimide spin labeled, 341, 356–360
- Glutenin, 356
- Glycerol, 345, 346, 354, 361–365
 glycerol water, 345, 361, 364, 365
- Heisenberg spin exchange, 27, 42–43, 45, 47,
 50, 63, 66, 72, 85, 86, 91, 93, 265,
 256, 293
- α -helix, 259–260, 274
 in gluten, 358
- Hemagglutinin, 276–277
- Hemoglobin, 159
 spin labeled, 32, 34, 365
- High-field ratio: *see* Line height ratio
- Homogenous broadening, 53
- Human growth hormone, recombinant, 104–
 105
- Human serum albumin
 electrostatic potential, 147–148, 159
 reaction with disulfide biradicals, 155
 spin-labeled, 147–149, 159
- Hybridization, 320–323, 334
- Hydrodynamic theory, 345
- Hydrodynamic volume, 34–36; *see also* Volume
- Hydrogen bond, 340, 346–348, 353, 356, 358, 360
 network, 354
- Hydroxylamine, 127
- Hydroxy-TEMPO, (TEMPOL), 31, 33, 35–36,
 340–341, 376
 ^{15}N derivative, 31–35
- Hyperfine, 83–105
 anisotropy, 406
 coupling, 192
 deuterium, 85
 interaction, 192
 isotropic, 406
 principal axes, 196
 tensor, 196
- Ice, 350
 crystallization, 348, 349
 crystals, 351
 formation, 354
 melting, 349–352
- Imidazolidine nitroxides, 113, 122, 125, 127,
 140, 141, 145, 150, 174, 175; *see*
also Imidazoline nitroxides
- Imidazoline nitroxides
 pK, 114–122, 127–129, 140, 142–143
 protonation, functional groups, 113, 122
 spin-labeling reagents, 140
- 2-Imidazoline-3-oxides, 175; *see also* Nitronyl
 nitroxides
- Inhomogeneous broadening, 6, 9, 14, 16,
 54–55, 85, 90, 93
- Interaction parameter (*k*), 344, 347, 350, 362
- Interactions
 ligand–protein, 271–272
 peptide–membrane, 273–278
- In vivo EPR, 367–404
 rationale, 368
 potential constraints, 371
 sensitivity considerations, 375
 pH measurement, 134, 135
 spin trapping, 382
- Iodoacetamide nitroxide, 140, 340
- Isothiocyanate nitroxide, 140, 340
- Isotropic hyperfine coupling, 406
- K**, interaction parameter, 344, 347, 350, 362
- Kaolin, pH in mesopores, 130, 131
- Lac permease, 271–272
- β -lactamase, 243
- L-band EPR, 375–376

- Lever rule, 17
- Line height ratio
 center-field ratio C'/C , 364
 high-field ratio H''/H , 359, 364
 low-field ratio L''/L , 354, 355, 362–365
 R parameter (h_i/h_m), 357
- Ligand–protein interaction, 271–272
- Linewidth parameters, 84, 85, 87, 91
- Lineshape, Lorentzian, 6, 9, 13
- Lipid
 bilayer, 16, 42, 73
 exchange, 59
 phase diagram, 17
 protein interactions, 59, 62
 spin label, 33, 59, 63, 69, 405
 translational diffusion, 63
- Lipopolysaccharide, 173
- Liposomes
 nitronylnitroxide incorporation, 169, 171
 pH in the inner volume, 132
 transmembrane transport, 138, 139
- Liver alcohol dehydrogenase, 243
- Loop-gap resonator, 252, 321
- Lorentzian lineshape, 6, 9, 13
- Lysine labeling, 104–105
- T4 lysozyme, 273
- M13 bacteriophage coat protein, 71
- MAL-6, 254
 spin labeling, 253
- Maleimide spin label (MSL), 2,2,6,6-tetra-
 methyl-4-maleimidopiperidine-1-oxyl,
 34, 77, 102–103, 253–254, 341
- Maltodextrin, 355, 356
- Maltoheptaose, 352, 353
- Malto-oligosaccharide, 351
- Maltopentaose, 352
- Maltose, 351
- Maltotriose, 352
- McConnell, Harden, 1–2
- Melittin, 277–278
- Melting temperature (T_m), 354, 360
 special (T_m'), 351, 352, 360
- Membrane, 59, 64, 66, 405
 gel phase, 62–64, 73
- Membrane depth, 257–258
- Membrane proteins, 251–259
 bacteriorhodopsin, 258, 259–260
 FepA, 252, 265–272
 lac permease, 272–273
 rhodopsin, 260–264
- Metal ions, measurement in tissues, 377
- N-methoxy-N-nitrosoamines, 68
- S-Methyl-2-nitrosopropane (MNP), spin trap-
 ping, 91, 295–297, 382
- Microscopic ordering, 99
- Microwave power saturation, 299
 cavity, 365
- Microwave radiation
 field strength (B_1), 365
 frequency, 343
 X-band, 343
- MNP (S-methyl-2-nitrosopropane)
 spin trapping, 91, 295–297, 382
- Mobility, *see* motion
- Modulation, field
 amplitude, 361, 363, 365
 Zeeman, 58
 frequency, 343, 363
 Zeeman, 56, 58
- Molecular distances, 104
- Molecular dynamics (MD), 304, 330, 332
- Molecular modeling, 206, 223
- Motion
 isotropic, 341, 342, 364
 molecular, 341, 344, 349, 353
 rotational, 341, 352
 sensitivity for, 343, 355, 363
- Motional region
 fast, 342
 slow, 343
 very slow, 343
- MSL (2,2,6,6-tetramethyl-4-
 maleimidopiperidine-1-oxyl), male-
 imide spin label, 34, 77, 102–103,
 253–254, 341
- MTSL, 1-oxyl-2,2,5,5-tetramethylpyrroline-3-
 methylmethanethiosulfonate,
 244–245, 253–255
- Multilamellar vesicles, 96
- Myelin proteolipid protein, 59–60
- Na^+K^+ -ATPase, 65
- Ni^{2+} ions, paramagnetic relaxant, 71, 76
- N-methoxy-N-nitrosoamines, 68
- Nitric oxide, *see also* NO
 donors, 168
 ESR detection, 162
 reaction with nitronylnitroxides, 162–168
 synthase, 169, 171, 172
- N^{ω} -monomethyl-L-arginine, 172, 174
- N^{ω} -nitro-L-arginine, 172, 174

- Nitronyl nitroxides
 histidine analog, 123
 incorporated protonation, 112
 NO liposome, 168–172
 reaction with NO, 162–168, 172
 spin-labeled angiotensin, 141
- Nitroprusside, 168
- Nitroxide, *see also* spin label
 alkylating, 141, 147
 amidino, 140
 amino, 122, 140
 3-amino-PROXYL, 289, 290
 4-amino-TEMPO, 289, 290, 321, 323
 azido, 140
 bioreduction, 373
 carbodiimide spin label, 77, 140
 enaminoketone, 128
 imaging, 390
 iodoacetamide, 140, 340
 isothiocyanate, 140, 340
 5-membered ring, 285–289
 6-membered ring, 285–289
 metabolism, 378
 MSL (2,2,6,6-tetramethyl-4-maleimidopiperidine-1-oxyl), maleimide spin label, 34, 77, 102–103, 253–254, 341
 MTSL (1-oxyl-2,2,5,5-tetramethylpyrrolidine-3-methylmethanethiosulfonate), 244–245, 253–255
 pH sensitive nitroxides, 384
 pharmacokinetics, 391
 succinimido, 140
 SSL (succinimidyl-2,2,5,5-tetramethyl-3-pyrrolidine-1-oxyl-3-carboxylate), 104, 105
 TEMPO (2,2,6,6-tetramethyl-piperidine-1-oxyl), 95–97, 356
 TEMPOL (Hydroxy-TEMPO, TANOL), 31, 33, 35–36, 340–341, 340, 345, 346, 350–356, 361, 365, 376
¹⁵N derivative, 31–35
 TEMPONE (2,2,6,6-tetramethyl-piperidone-1-nitroxide), 32, 85–87, 94
- S-Nitroso-N-acetylpenicillamine (SNAP), 172
- NMR, 341
- NO, *see also* Nitric oxide
 donors, 168
 ESR detection, 162
 reaction with nitronyl nitroxides, 162–168
 synthase, 169, 171, 172
- Nuclear relaxation, 26, 37, 39, 50
 mechanisms, 35
- Oligonucleotides, spin labeled chemical synthesis, 284, 287–291, 299, 334
- Oligosaccharide, 351, 352
- OmpA, presequence, 21
- Order parameter, 314, 315, 318, 405
 tensor, 406
- Oxygen
 measurement in tissues, 377, 385
 paramagnetic relaxant, 40, 69
 particulate paramagnetic materials for measuring, 380
 in tumors, 388
- 5-[(1-Oxyl-2,2,5,5-tetramethyl-3-pyrrolidinyl)amino]-2'-deoxyuridine (DUPDA), 285, 289
- 5-[(1-Oxyl-2,2,6,6-tetramethyl-4-piperidinyl)amino]-2'-deoxyuridine (DUTA), 285, 288, 289, 292
- Π, accessibility parameter
 definition, 261
 periodicity, 267, 268, 274
- Φ-values, 257–267
 definition, 257–259
 depth, 257–258
 for FepA mutants, 258, 267–268
 for lipids, 258
- P_{1/2}, definition, 256
- Papain, 243
- Paramagnetic relaxant
 chromium oxalate, 69
 ions, 40
 Ni²⁺ ions, 71, 76
 oxygen, 40, 69
- Partitioning, 96
- PBN, Phenyl-*tert*-butylnitron, 91, 92
- PD-TEMPONE (perdeuterated 2,2,6,6-tetramethyl-4-piperidone-1-oxyl), 86–88, 93
- Peptide-membrane interactions, 273–278
- Peptides
 alamethicin, 276
 cecropins, 274–276
 diphtheria toxin, 273–274
 hemagglutinin, 276–277
 melittin, 277–278
- Periodicity, 268
- PGSL phosphatidyl glycerol spin label, 67–71
- pH measurement
 in cross-linked polyelectrolytes, 130
 in kaolin, 130, 131
 in phospholipid vesicles, 132

- pH measurement (*cont.*)
in tissues, 377
in vivo, 134, 135
in water-in-oil systems, 131
in zeolites, 130, 131
- pH sensitive nitroxides, 384
biradicals, 124, 125
iminonitroxides, 112
nitronylnitroxides, 112, 122
spin labeling reagents, 140
triradicals, 125
- Pharmacokinetics, 378, 391–392
- Phase diagram, lipid, 17
- Phase separation, 365
- Phase transition, 97, 98, 100
- Phenyl-*tert*-butylnitronone (PBN), 91, 92
- Phenyl radical, 91, 92
- Phosphatidylcholine, 134, 143, 169
- Phospholipid, 94, 95
- Phospholipid membranes
electrostatic potential, 138–139, 143–146
intraliposomal pH, 132
surface potential, 143–146
transmembrane potential, 138, 139
transmembrane transport, 137–140
- Phosphoramidite chemistry, 288, 291, 295–296
- Phosphotriester chemistry, 288–291
- Plasticizer, 355
- POBN, α -(4-pyridyl-1-oxide)-*N*-*tert*-butyl nitronone, 172
- Point-dipole
approximation, 196
dihedral angle, 217
 β -lactam group, 224
- Point of connectivity, 17
- Poisson distribution
inhomogeneous broadening, 7
spin label population, 11
- Polarity, 97, 103
- Powder pattern, 88, 406
- PreOmpA, 21
- Protein, wheat, 356
- Proton exchange
isotopic effect, 130
pK for nitroxides, 112, 114–122, 125, 127–129, 140, 142–147
rate constants, 111, 129
titration curve, 111, 115, 135, 144, 145
- Proton transport
in aqueous glycerol, 135–137
across phospholipid membrane, 137, 138
- Purification, spin-labeled oligonucleotides, 292, 295–296,
- Pulsed EPR, in vivo studies, 395
- α -(4-pyridyl-1-oxide)-*N*-*tert*-butyl nitronone (POBN), 172
- Reactive intermediates, in tissues, 377
- Recombinant human growth hormone, 104–105
- Relaxation agents, 251, 255, 257
- Relaxation
dipolar, 40, 72
enhancement, paramagnetic, 37, 69, 72
nuclear, 26, 37, 39, 50
time, effective spin lattice (T_1), 26, 37, 45, 47, 50, 343, 344, 355, 364
- Resolution, EPR spectra, 90, 97
- Rheological studies, 358, 360
- Rhodopsin, 252, 260–264
- Rigid limit, spectra, 88, 97
- Ripple phase, 97
- Rotational correlation time, 29, 33, 35, 78, 341–344, 349, 350, 355–359, 361, 365
calibrations, 78
isotropic, 341
- Rotational diffusion, 29, 77
- Rozantsev, Eduard, 2–4
- Rubbery state, 349
- Sample deoxygenation, CW HF EPR experiments, 93–95
- Saturation, 24, 45, 52, 343, 365
CW, 25, 52, 255–256
first derivative, 53, 55
integrated intensity, 53, 55
parameter, 52
progressive, 55ff, 59, 68, 70–71
recovery, 272, 344
transfer, 343, 365
- Saturation transfer EPR, *see* ST-ESR
- SDSL (site-directed spin labeling), 251–252
depth, 257–258
membrane proteins, 259
- Simulation, 304, 306, 314, 316, 330, 331
- Site-directed spin labeling (SDSL), 251–252
depth, 257–258
membrane proteins, 259
- Slip, 345, 360
- Slow motional effects, 86, 90, 102, 105, 405, 407
- Slowly relaxing local structure (SRLS), 304, 305, 318

- S-Methyl-2-nitrosopropane (MNP), spin trapping, 91, 295–297, 382
- S-Nitroso-N-acetylpenicillamine (SNAP), 172
- Spectral densities, 28, 40, 84, 85, 91, 93
- Spin label, 339–342, 348, 356
- accessibility, 255
 - carbodiimide, 77
 - CTPO, 33
 - deuteriated, 185
 - fast limit values, 306
 - g** tensors, 302–303, 307, 310
 - immobile, 357, 359
 - lipid, 33, 59, 63, 69, 405
 - mobile, 357
 - molecular shape, 345–346
 - molecular structure, 185
 - motion, 253
 - oxypyrrolinyl, 185
 - rigid-limit tensors, 302
 - A** tensors, 302–303, 307, 310
 - SSL (succinimidyl 2,2,5,5-tetramethyl-3-pyrroline-1-oxyl-3-carboxylate), 104, 105; *see also* Nitroxide
 - sulfonic acid, 132, 138
 - triple spectroscopy, 201
- Spin labeled
- 26-mer, 293–296, 301, 329, 331, 333
 - g** tensors, 302–303, 307, 310
 - amino acids, 211
 - deoxycytidine analog
 - DCAT, 286, 323, 324
 - DCAVAP, 287, 295
 - fatty acid, 97–102
 - methane thiol-sulfonate, 244
 - methylalanate, 184, 211–215
 - methyl tryptophanate, 215, 218–219
 - oligonucleotides, 284, 287–288, 290–292, 294
 - chemical synthesis, 284, 287–291, 299, 334
 - enzymatic synthesis, 284, 292, 299
 - penicillin, 208–209, 221, 233
 - phenylalanine, 219, 220
 - proteins, 82–105
 - thymidine analogs, 285–287, 293
 - ACET, 285, 302–304
 - DUAP, 286, 294, 296, 301, 303, 310, 314–318, 323, 326, 327, 330
 - DUAT, 286, 293, 294, 301, 303
 - DUAVAP, 287, 293, 294
 - DUMPDA, 285, 289, 290, 298, 301, 321, 322
 - DUMTA, 285, 290, 298, 303, 315, 316
 - DUPA, 286, 293
- Spin labeling
- cysteine, 253
 - double cysteines, 263–265
 - with MAL-6, 253
 - membrane proteins, 259–273
 - with MTSL, 253
 - sequence-specific, 284, 293–294, 296, 299
 - site-directed, 251, 252
- Spin pH probes, 110, 115, 130, 132, 140
- Spin–spin interactions, 11
- Spin trapping, 91, 382, 295
- C5-iodo-deoxyuridine, 295
 - in vivo EPR, 382
 - 2-methyl-2-nitrosopropane (MNP), 295–297
 - POBN, α -(4-pyridyl-1-oxide)-N-tert-butyl nitron, 172
- SRLS (slowly relaxing local structure), 304, 305, 318
- Stability
- food, 339, 349
 - nitroxide, 340
 - storage, 339
- Starch, 355
- State diagram, 348, 349, 353
- Statistical distribution, spin labels, 13
- ST-ESR, 56, 58, 62, 64–65, 74, 76–77, 340–343, 348, 356–359, 365
- calibration spectrum, 344, 354, 363
 - integral measuring protocol, 348–349
 - phase reference experiments, 359
 - reference spectra, 365
 - spectrum, 344, 361
- Stickiness parameter *S*, 345–347, 360
- Stokes–Einstein equation modified, 344, 345, 362
- Structure, nitroxide spin labels, 341
- Succinimido nitroxide, 140
- Succinimidyl-2,2,5,5-tetramethyl-3-pyrroline-1-oxyl-3-carboxylate (SSL), 104, 105
- Sucrose, 347–351
- Sugar, 339–341, 348–354, 361, 364, 365
- Sulfonic acid spin label, 132, 138
- Superhyperfine, 88, 89
- Superoxide radical, reaction with thiols, 158
- T_1 : *see* Spin-lattice relaxation time
- TEMPO, (2,2,6,6-tetramethyl-piperidine-1-oxyl), 33, 95, 96, 97, 356
- TEMPOL (Hydroxy-TEMPO), 31, 33, 35–36, 340–341, 340, 345, 346, 350–356, 361, 365, 376
- ^{15}N derivative, 31–35

- TEMPONE (2,2,6,6-tetramethyl-4-piperidone-1-nitroxide), 32, 63, 85, 86, 87, 94
- Tensor: *see* A tensor; g tensor
- TEPOPL,O-[3-(2,2,5,5-tetramethyl-1-oxypyrrrolinyl)-propen-2-oyl]-L- β -phenyllactate, 237-240
- 2,2,5,5-tetramethyl-1-oxypyrrrolinyl-3-carbonyl)-L-alanate (methyl-L-alanate spin label), 184-186, 192-193, 195, 198-201
- 2,2,5,5-tetramethyl-1-oxypyrrrolinyl-3-carboxylic acid, 201-206
- 4-(2,2,5,5-tetramethyl-1-oxypyrrrolinyl-3-carbonyl)-L-phenylalaninal, 231-237
- 3-(2,2,5,5-tetramethyl-1-oxypyrrrolinyl)-2,4-pentadienal, 225-227
- 3-(2,2,5,5-tetramethyl-1-oxypyrrrolinyl)-2,4-pentadienoic acid, 225-228
- 3-(2,2,5,5-tetramethyl-1-oxypyrrrolinyl)-2-propanamide, 207
- Thiocholine, 158
- Thioglycerol, 113, 169-170
- Thiols
- in the blood, 156
 - ESR detection, 149, 155-157
 - in isolated organs, 156-157
- Thiols(*cont.*)
- spin-labeling SH-groups, 159
 - thiol-disulfide exchange, 149, 150
- Translational diffusion, lipids, 63
- Trehalose, 351
- Trichloromethyl radical, 91, 92
- Triradicals, 123, 125
- Valinomycin, 139
- Van der Waals volume: *see* Volume
- VAR (very anisotropic reorientation) model, 407
- Varian E-104, 298-301
- Very anisotropic reorientation (VAR) model, 407
- Viscosity, 344, 349, 350, 362
- Voigt lineshape, 7, 13
- Volume
- free, 353, 356, 360
 - hydrodynamic, 346
 - Van der Waals, 345
- W-band EPR, 83-107
- Williams-Landel-Ferry (WLF) equation, 362
- X-band EPR: *see* Microwave radiation
- Zeolites, pH in mesopores, 130, 131